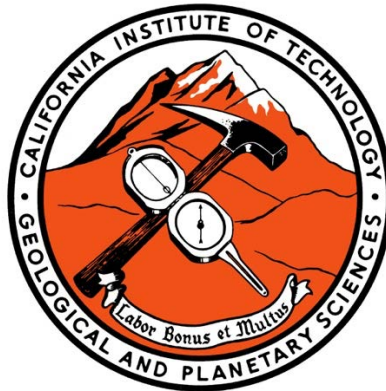


Crystalline Records of
Mafic Arc Magmas Across
the Sierra Nevada Batholith,
California

Thesis by

Juliet Ryan-Davis

In Partial Fulfillment of the Requirements for
the Degree of
Doctor of Philosophy



CALIFORNIA INSTITUTE OF TECHNOLOGY
Pasadena, California

2025

(Defended April 29, 2025)

© 2025

Juliet Ryan-Davis

ORCID: 0000-0001-7048-5937

ACKNOWLEDGEMENTS

From the very beginning, I knew I would feel nostalgic when the time came to move on from the timeless buildings of Caltech. I have been sincerely grateful for the support and cheer of the people within them, and for being lucky enough to participate in many exceptional scientific opportunities and excursions that were formative.

Claire Bucholz, I couldn't have dreamed up a better advisor for myself. You buoyed me through the pipeline and repaired any leaks that might have been there through your guidance and example of effective, balanced, hard work. I have also been so grateful for our conversations, and I look forward to many more.

To my collaborators: Jade Star Lackey, you've been like a fairy-godgeologist to me throughout my career, professionally and personally. Your lab and home in Claremont have been a haven to me during some unavoidable "lows" including during the aftermath of having our belongings destroyed in the Eaton Fire. Tom Sisson, I am likewise grateful for your steady guidance, and friendship. Every minute with you in the field was so valuable to my development as a petrologist and field geologist, I appreciate your mentorship.

To my committee: Ed Stolper, your encouragement has meant more to me than I think you know. Paul Asimow, your generosity and patience—ranging from explaining thermodynamics one-on-one to taking on division-wide endeavors—are admirable to any observer, and tangibly helped me through all seven years. John Eiler, I have appreciated the mix of seriousness and levity you bring to conversations, and through them I have learned to be (hopefully) clear and articulate in framing thoughts and questions.

One of the "highs" of these projects was the fieldwork. I was joined in the field by many intrepid women—first and foremost, my gratitude goes to Grace Hruska, who scaled Kings Canyon multiple times with me, and otherwise voluntarily adventured across California by my side. Let's do it again! Likewise, Maddie Lewis, whose own projects are braided with the ones documented here, led the charge up the eastern slopes of the Sierra. Anahi Carrera was the best "blind date" field partner (set up by our advisors) that anyone could have come by. Xenia Boyes, Amanda Bednarick and Sarah Zeichner are the three daring dear friends who were game to join me on many long days (in addition to Makayla

Betts, though the plans fell through!), plus Jen Bass, Ery Hughes, Babsi Ratschbacher, and Pond Sirorattanakul, who made time to join as well. Many others (Cedar Grove horses and packers, employees of state and federal land management agencies) were also instrumental.

Mark Garcia and Chi Ma at Caltech, I could not have done the work or analyses without your cheerful assistance. Likewise, to the many staff and faculty members of the GPS Division, it is a privilege to have had your support and guidance from coursework to fieldwork and beyond. In particular, François Tissot, Joann Stock, Jean-Philippe Avouac, Jen Shechet, Julie Lee, and Julia Zuckerman, thank you for everything.

I appreciated friendship and helping hands from many lab and officemates (Oliver Wilner, Emma Sosa, Shane Houchin, Hojjat Kaveh). I am also indebted to undergraduate and high-school assistants who were a joy to work with (Emma Bertran, Lily Coffin, Graham Brady). “The Pit” (Xenia, Makayla, Sarah, Ren Marquez, Shaelyn Silverman, Elliott Mueller, Sergio Parra, Philip Woods, Emily Miaou, Carl Swindle and Haoyu Li), you all are among the brightest people I know, and it was an honor to spend time together.

A number of remarkable mentors and friends from my years at the USGS nudged me forward and on track, and I am forever grateful. Wes Hildreth and Judy Fierstein, I cherish every moment we’ve had together, and wish for many more. Andy Calvert and Julie Donnelly-Nolan, your encouragement has meant so much to me. The faculty at Middlebury College laid the groundwork for me to pursue geology with enthusiasm and curiosity. Ray Coish, please enjoy these mafic rocks! Fellow MiddKids Cailey Condit and Victor Guevarra, we’ve come so far since pre-pre season... thank you for your advice and friendship.

To all my friends: I’ve missed you as I hammered away these many months and years. I can’t wait to play with you! Karen Atkins and Dessa D’Aquila are my California family. Susanne Henning (Oma), I am so glad that you could spend so much time caring for Augie. I would not have finished without your help. To my brother Jonah and my parents, Cindy Ryan and Franklin Davis, thank you for always reminding me what really matters. Luna, my dog, reminded me to go outside, drink water, and counterproductively helped in the field.

To Stephen, whatever I write is an understatement. Your unwavering support has sustained me. I cannot believe I am lucky enough to have built a family together with you. Augie, being your mom is the light on my path. I love you both so much more than rocks.

Dedicated to my family.

*Thank you for your love and generosity, for sunset walks,
and for stopping to smell the roses with me.*

And to the neighborhood of Altadena.

ABSTRACT

Our planet Earth is unique among the rocky planets of the solar system in having compositionally evolved continental crust—the reason for life as we know it. Processes that create continental crust occur at subduction zones where magmas differentiate, evolving from primary mantle-derived basalt to produce a diverse range of compositions that erupt at arc volcanoes and comprise the bulk of the continental crust. Many processes for differentiation have been proposed, yet, recognizing and evaluating the role of pre-existing crust in these processes remains challenging.

This thesis includes two studies of mafic intrusions in the Sierra Nevada batholith—the well-studied Mesozoic continental arc of the western North American Cordillera. The studies are grounded in field and petrographic observations. By targeting the intrusive record, they document the time-integrated effects of mafic magmatism over tens of millions of years within a volcanic arc.

Chapter 2 is a petrologic study of the most primitive intrusive rocks of the batholith, exposed in the Emigrant Gap complex. The complex ranges compositionally from ultramafic cumulates to intermediate granodiorite. The petrology, geochemistry and field relationships of these plutonic rocks reveal that—in addition to crystallization—open-system processes (melt-mush reactions and hybridization between the mafic products and a crustally contaminated felsic magma) produced the distinctive geochemical and petrologic trends of the complex.

Chapters 3 and 4 represent a broad study of mafic intrusions within a 250 km by 100 km swath of the central Sierra Nevada ($37\pm0.5^\circ\text{N}$ latitude). This regional perspective on mafic magmatism spans \sim 110 million years and crosses several tectonically-assembled belts, each with distinctive geology. The two chapters document systematic differences in field relationships and geochemistry of the mafic intrusions that vary by geologic belt, as the mafic magmas interacted with heterogeneous crust. Chapter 3 presents field relationships, ages, and major and trace element chemistry. Chapter 4 presents isotopic compositions (O, Hf, Sr, and Nd), revealing that contamination of mafic magmas by \sim 10–20% assimilation of the local crustal column is inevitable, and that it occurs early during differentiation.

PUBLISHED CONTENT AND CONTRIBUTIONS

Chapter II.

Ryan-Davis, J., Bucholz, C.E. and Sisson, T.W., *In review*, Shallow differentiation of primitive arc magmas at the Jurassic Emigrant Gap complex, Sierra Nevada, California. *Journal of Petrology*.

Ryan-Davis, J., Bucholz, C.E. and Sisson, T.W., 2024, Emigrant Gap complex whole-rock major and trace element chemistry. *Interdisciplinary Earth Data Alliance (IEDA)*. <https://doi.org/10.60520/IEDA/113590>

J.R.D. conceptualized the project, performed the fieldwork and most of the labwork, analyzed the data, interpreted the results, and wrote the manuscript.

MANUSCRIPTS IN PREPARATION

Chapter III.

Ryan-Davis, J., Bucholz, C.E., Lackey, J.S., Lewis, M.J., Kylander-Clark, A. and Wilner, O.D., *In preparation*, Sierra Nevada upper-crustal mafic intrusions record arc migration into thickened continental crust. *For: GSA Bulletin*.

J.R.D. participated in conceptualization of the project, performed the fieldwork, almost all labwork and microbeam analyses, interpreted the results, and wrote the manuscript.

Chapter IV.

Ryan-Davis, J., Bucholz, C.E. Lackey, J.S., Kylander-Clark, A., Lewis, M.J., Kitajima, K. and Valley, J.W., *In preparation*, Upper-crustal mafic intrusions fingerprint early, geologically-controlled contamination in a continental arc. *For: Earth and Planetary Science Letters*.

J.R.D. participated in conceptualization of the project, performed the fieldwork, almost all labwork and microbeam analyses, interpreted the results, and wrote the manuscript.

TABLE OF CONTENTS

Acknowledgements	iii
Abstract	vi
Published Content and Contributions	vii
List of Illustrations	x
List of Tables	xii
Nomenclature	xiv
I. Introduction	1
II. Shallow Differentiation of Primitive Arc Magmas at the Jurassic Emigrant Gap Complex, Sierra Nevada, California	13
Abstract	14
Introduction	15
Geologic background	17
Field relationships of Emigrant Gap	18
Sampling and analytical methods	21
Whole-rock geochemistry	23
Mineral chemistry	26
Discussion	31
Conclusions	45
Acknowledgements	46
Data availability statement	46
References	47
Figures	65
Tables	82
Appendix 1	84
References	101
Supplementary figures	104
III. Sierra Nevada Upper-Crustal Mafic Intrusions Record Arc Migration Into Thickened Continental Crust	118
Abstract	119
Introduction	119
Sampling and analytical methods	125
Field relationships of mafic intrusions across the transect	130
Geochronology results	132
Whole-rock geochemistry	134
Mineralogy and mineral chemistry	138
Discussion	143
Conclusions	161
Acknowledgements	162

References.....	163
Figures	188
Tables.....	204
Appendix 1	216
Supplementary figures	216
Appendix 2	223
References.....	225
Tables.....	228
Concordia and MSWD plots.....	230
Appendix 3	260
IV. Upper-Crustal Mafic Intrusions Fingerprint Early, Geologically-Controlled Contamination in a Continental Arc..... 278	
Abstract.....	279
1. Introduction	280
2. Sample suite and geologic context.....	283
3. Methods	288
4. Isotopic systematics of parental mafic magmas across the batholith..... 289	
5. Isotopic fingerprints depend on location across the upper plate..... 293	
6. Quantification of the degree of assimilation in parental mafic magmas... 295	
7. Implications for the generation of felsic crust..... 301	
8. Conclusions	304
Acknowledgements	305
References.....	305
Figures	323
Tables.....	328
Appendix 1	330
Methods.....	330
References.....	340
Supplementary figures	350
Supplementary tables	354

LIST OF ILLUSTRATIONS

Chapter I.

Ch. 1 Figure 1. An interpreted cross section	1
Ch. 1 Figure 2. Nisenan Land and residential sites.	2

Chapter II.

Ch. 2 Figure 1. Geologic map overview.....	65
Ch. 2 Figure 2. Geologic map of the Emigrant Gap complex.	66
Ch. 2 Figure 3. Anastomosing dunite field photograph.....	67
Ch. 2 Figure 4. Ultramafic rocks of the main suite.	69
Ch. 2 Figure 5. Gabbronorite field photograph.	70
Ch. 2 Figure 6. Mafic to intermediate rocks of the main suite..	72
Ch. 2 Figure 7. Whole rock chemistry.....	73
Ch. 2 Figure 8. Gabbronorite types distinguished by REE chemistry	74
Ch. 2 Figure 9. Detailed transect in the Lake Valley ultramafic body.	75
Ch. 2 Figure 10. Olivine Mg# versus Ni symbolized by rock type.....	76
Ch. 2 Figure 11. Emigrant Gap clinopyroxene compositions.....	77
Ch. 2 Figure 12. Schematic illustration of the Emigrant Gap complex	79
Ch. 2 Figure 13. alphaMELTS model results (pressure vs. total H ₂ O concentration)	80
Ch. 2 Figure 14. Normative olivine-clinopyroxene-quartz	81
Ch. 2 Figure A 1. Ultramafic rocks of the main and Cisco Butte.....	105
Ch. 2 Figure A 2. Mafic to felsic rocks of the complex.	107
Ch. 2 Figure A 3. BSE image of low-Cr orthopyroxene.....	108
Ch. 2 Figure A 4. Harker diagrams of whole-rock compositions	109
Ch. 2 Figure A 5. Trace-element spider diagrams	110
Ch. 2 Figure A 6. Spinel compositions compared to spinels from	111
Ch. 2 Figure A 7. Hisogram of anorthite (An) content in plagioclase.....	112
Ch. 2 Figure A 8. Mg# versus NiO concentration in spinels	113
Ch. 2 Figure A 9. Whole rock SiO ₂ vs. Al ₂ O ₃ for feldspar-bearing	114
Ch. 2 Figure A 10. Emigrant Gap whole rock compositions.....	115
Ch. 2 Figure A 11. alphaMELTS model results (P versus H ₂ O).....	117

Chapter III.

Ch. 3 Figure 1. Overview bedrock map of the Sierra Nevada	189
Ch. 3 Figure 2. Study area map with sample locations and ages.	190
Ch. 3 Figure 3. Overview field photos of mafic intrusions.	191
Ch. 3 Figure 4. Field photos of contacts relationships.	192
Ch. 3 Figure 5. Field photos of metamorphic xenoliths.	194
Ch. 3 Figure 6. Field photos of cumulate textures in	195
Ch. 3 Figure 7. Field photos of interactions with felsic intrusions	196
Ch. 3 Figure 8. Whole-rock geochemistry and legend of symbols.	197
Ch. 3 Figure 9. K_2O in all whole-rock samples across the transect.	198
Ch. 3 Figure 10. Whole rock A) $(La/Sm)_{CN}$ and B) Sr/Y vs. distance	199
Ch. 3 Figure 11. Representative petrography.....	200
Ch. 3 Figure 12. A) Mineral Mg#, and B) Calculated equilibrium melt	201
Ch. 3 Figure 13. A) Th/U versus Zr/Hf in zircon.	202
Ch. 3 Figure 14. Plots of “copious fractionation intervals”.....	203
Ch. 3 Figure A 1. Field photos of amphibole pegmatoid segregations	216
Ch. 3 Figure A 2. Harker diagrams of major and minor oxides	217
Ch. 3 Figure A 3. Plot of Modified Alkali Lime Index (MALI):	218
Ch. 3 Figure A 4. Whole rock $(Dy/Yb)_{CN}$ versus distance (km)	218
Ch. 3 Figure A 5. Whole rock Nb versus Sm. Symbols as in Fig. 8.	219
Ch. 3 Figure A 6. Whole rock Sr/Sr^* vs Eu/Eu^* . Symbols as in Fig. 8.	219
Ch. 3 Figure A 7. Al_2O_3 versus Mg#	220
Ch. 3 Figure A 8. Relations between Fe/Mg in coexisting minerals	221
Ch. 3 Figure A 9. Calculated oxygen fugacity (by zircon TE's)	222
Ch. 3 Figure A 10. A comparison of crustal thickness calculations	222

Chapter IV.

Ch. 4 Figure 1. Overview of the study area and ages.....	323
Ch. 4 Figure 2. Distance versus zircon isotope ratios.	324
Ch. 4 Figure 3. Binary mixing models of assimilants.....	325
Ch. 4 Figure 4. Schematic cartoon of isotopic fingerprints.....	326
Ch. 4 Figure 5. Age versus O and Hf isotope ratios in zircon.....	327
Ch. 4 Figure A 1. Mantle xenolith Sr and Nd isotope ratios	350
Ch. 4 Figure A 2. Plot of the range in $\delta^{18}O$ versus $\varepsilon Hf_{(t)}$	351
Ch. 4 Figure A 3. Plot of $^{87}Sr/^{86}Sr_{(t)}$ versus $\varepsilon Nd_{(t)}$	352
Ch. 4 Figure A 4. Plot of whole-rock TAS diagram	353

LIST OF TABLES

Chapter II.

Ch. 2 Table 1. Calculated temperature and pressure of crystallization	82
--	----

Supplementary Data File:

Ch. 2 Table S1. Whole-rock geochemistry of the Emigrant Gap complex.	
Ch. 2 Table S2. Representative modal abundances by μ ED-XRF mapping and phase analysis.	
Ch. 2 Table S3. Chrome-spinel EPMA analyses.	
Ch. 2 Table S4. Olivine EPMA analyses.	
Ch. 2 Table S5. Clinopyroxene EPMA analyses.	
Ch. 2 Table S6. Orthopyroxene EPMA analyses.	
Ch. 2 Table S7. Plagioclase EPMA analyses.	
Ch. 2 Table S9. Biotite EPMA analyses.	
Ch. 2 Table S9. Fe-Ti oxide EPMA analyses.	
Ch. 2 Table S10. Amphibole EPMA analyses.	
Ch. 2 Table S11. EPMA analytical conditions.	
Ch. 2 Table S12. alphaMELTS modeling input compositions.	
Ch. 2 Table S13. EarthChem Aleutians whole rock chemistry.	

Chapter III.

Ch. 3 Table 1. U-Pb zircon ages for mafic intrusions.....	204
Ch. 3 Table 2. Representative anhydrous mafic mineral.....	208

Ch. 3 Table A2- 1. U-Pb and trace element analysis conditions	228
Ch. 3 Table A2- 2. Session averages of Hf isotope measurements.....	229

Supplementary Data File:

Ch. 3 Table S1. Zircon U-Pb age and trace element (TE) analyses.	
Ch. 3 Table S2. Whole-rock geochemistry of central Sierra Nevada mafic intrusions.	
Ch. 3 Table S3. Olivine EPMA analyses of western and central belt mafic intrusions.	
Ch. 3 Table S4. Clinopyroxene EPMA analyses of western and central belt mafic intrusions.	
Ch. 3 Table S5. Orthopyroxene EPMA analyses of western and central belt mafic intrusions.	
Ch. 3 Table S6. EPMA analytical conditions.	

Chapter IV.

Ch. 4 Table 1. Endmember arc magma and assimilant	328
Ch. 4 Table 2. Amount of assimilation by belt	329

Ch. 4 Table A 1. Analytical conditions for hafnium isotope	354
Ch. 4 Table A 2. Session averages of Hf isotope.....	355

Supplementary Data File:

Ch. 3 Table S1. Summary of isotopic analyses of mafic intrusions.
Ch. 3 Table S2. Zircon hafnium isotope analyses with corresponding age and $\delta^{18}\text{O}$.
Ch. 3 Table S3. Zircon oxygen isotope analyses.
Ch. 3 Table S4. Whole-rock strontium and neodymium isotope analyses.
Ch. 3 Table S5. Compiled data for binary mixing model endmember compositions.

NOMENCLATURE

Arc. An arcuate chain of volcanoes that forms above a subduction zone.

Batholith. A mountain range-sized group of igneous intrusions of magma that crystallized underground.

Compositionally evolved. Not primitive in composition (see below), with the connotation of being felsic (although some mafic magmas are compositionally more evolved than others).

Cumulate. An igneous rock that has had interstitial melt extracted by some process, resulting in an accumulation of minerals, and thus, compositionally no longer resembles a bulk magma.

Felsic. Feldspar ($(\text{Na},\text{K})\text{AlSi}_3\text{O}_8$ – $\text{CaAl}_2\text{Si}_2\text{O}_8$) and silica (SiO_2)-rich.

Mafic. Magnesium (Mg) and iron (Fe)-rich.

Parental magma. Magma that formed the crystals and other derivative magma of interest.

Petrology. The study of the composition, mineralogy, texture, and conditions of the formation of rocks (and minerals).

Pluton. An intrusion of magma that crystallized underground into a mappable body of rock.

Primitive magma. Magma that is derived from the mantle and has not been modified in significantly composition (*i.e.*, has not (yet) experienced differentiation).

INTRODUCTION



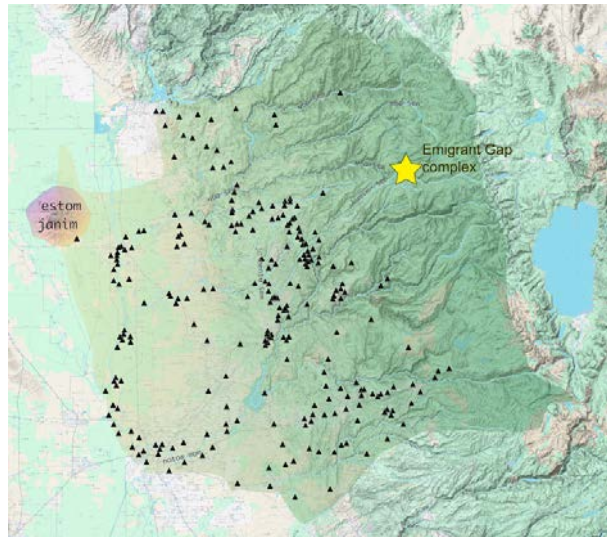
Ch. 1 Figure 1. North American Cordillera
An interpreted cross section. Painted on Silk (J. Ryan-Davis, 2022).

PREFACE

If you are a geologist and have never visited the Sierra Nevada, you may wonder why so many geological studies focus on this California mountain range. Prior to my first time setting foot in the range when I moved to the eastern Sierra for a summer internship, I had already encountered Sierra Nevada geology through college assignments to calculate tectonic rates and hydrological volumes based on offset drainages and a closed basin lake sited in the Sierra Nevada. At the time, these seemed to me to be imagined “textbook” systems constructed solely for the purpose of the homework exercise. When I arrived at the shoreline of Mono Lake only months later, it became obvious that these were real places—they just happened to be ideal representations of Earth science problems.

This is partly because of the spectacular exposures of the Sierra Nevada, particularly in the east because of the combined effects of glaciation, tectonic uplift, and dryness of the ecosystem there. The area hosts exposures of geological features of interest to most subdisciplines of Earth science, from volcanology to limnology. Further, the range has sparked the imagination and interest of naturalists and scholars with its enticing, beautiful features. It seems instinctive to wonder what formed the patterns and colors of the idyllic views, and every stony crag and peaceful lake (Fig. 1). They have been carefully crafted by thousands to millions of years of natural forces, including human activity of Indigenous peoples, and (at least in part) preserved from overprinting by modern Anthropocene activities by their remoteness in the wilderness.

The two study areas within the Sierra Nevada that are the focus of this dissertation are the ancestral homelands of dozens of Indigenous Tribes. Although many of those Tribes were nearly wiped out of existence during the Gold Rush and Mission eras, they continue to live on these lands today. The central Sierra Nevada region, the focus of Chapters 3 and 4, was a major trading route from the western foothills over to the Owens Valley east of the mountain range. Many of the trails and paths that I walked on to collect samples were first walked many centuries ago. The ancestral homelands of the Nisenan Tribe are situated in the northern Sierra Nevada, where the Emigrant Gap complex is located (the subject of Chapter 2). They are one of 48 California Tribes that were unlawfully terminated by the U.S. government in the 1960's by the California Rancheria Termination Acts. To attempt to reciprocate for sampling and studying their land (Ryan-Davis and Scalice, 2022), and partly in service of the Tribe's efforts to restore federal recognition, I digitized records of Nisenan sites and territories for a working reference map of their homelands (Fig. 2; Tatsch, 2006).



Ch. 1 Figure 2. Nisenan Land and residential sites.

For the purposes of the following research studies, this preface on the Sierra Nevada is also meant to explain why I sought to study a mountain range that has already been so thoroughly studied. The many decades of geologic examination of the intrusions of the batholith and their metamorphic host rocks (*i.e.*, Bateman et al., 1963; Kistler and Peterman, 1973, 1978; Chapman et al., 2012) provide a detailed framework for targeted questions about

arc magmatic processes. Perhaps somewhat surprisingly, the intrusive complex that hosts the most primitive rocks of the batholith has had limited previous study (James, 1971; Kelemen, 1989; Wracher, 1991). The major project presented in Chapters 3 and 4 spans from the best-exposed rocks of the eastern Sierra, described above, to the brush-covered and often privately owned rubbly outcrops of the western Sierra Nevada foothills, which in many cases have rarely been visited by geologists.

This preface is also partly for insight into the inspiration and joy that provided motivation for this dissertation, which were such an important aspect of the work but would be otherwise left out.

CRYSTALLINE RECORDS OF MAFIC ARC MAGMAS

Partial melting of mantle peridotite produces basalt, which forms the crusts of most of the planetary bodies in our solar system (L.P.I., 1981). Yet, on Earth, an additional stage of processing of that basalt produces more evolved continental crust (Taylor, 1989). Such differentiation to produce more evolved melts and ultimately crust mainly occurs at subduction zones (Gill, 1981; Taylor and McLennan, 1985; Rudnick, 1995). This is thought to occur in the lower crust, resulting in a mafic lower crust and more evolved upper crust (Saleeby, 2003; Greene et al., 2006; Otamendi et al., 2012; Jagoutz, 2014).

The exact process of differentiation within subduction zones is described by multiple possible models which are actively discussed and frequently debated. These can be summarized by two opposing models, wherein hydrous flux-driven partial melting of the mantle wedge produces mantle-derived basalts, which either (1) undergo fractional crystallization or solidification and then partial melting to directly produce more evolved compositions (Bowen, 1928; Grove and Baker, 1984; Sisson et al., 2005; Jagoutz and Klein, 2018; Müntener and Ulmer, 2018) or (2) incorporate pre-existing crust either through wholesale assimilation or mixing/homogenization with partial melts of the pre-existing crust (Hildreth and Moorbath, 1988; Annen et al., 2006; Reubi and Blundy, 2009). These two paradigms have been summarized as (1) mantle-dominated or (2) crust-dominated models (Moyen et al., 2021; Jacob et al., 2021). In theory, they will result in different geochemical signatures that are either mantle-like or crust-like.

In practice, part of the reason for the ambiguity between these options is that the recycling of pre-existing crust into the mantle wedge via subduction could impart crustal geochemical signatures into the least differentiated mafic magmas of an arc system (“source contamination” of Cornet et al., 2022). That mantle contamination could explain any crust-like isotopic signatures of arc magmas and potentially also mask any further crustal contamination that may occur in the upper plate of the subduction zone (“path contamination”; Cornet et al., 2022). Identifying systematic changes within an arc that relate either to the source (*i.e.*, arc-parallel heterogeneity related to what is being subducted along strike) or to the path of ascent through the crustal column (heterogeneity related to the composition of the upper plate) can help to elucidate this issue.

The work presented in this dissertation targets the products of mafic arc magmas to examine the earliest stages of differentiation. By studying both (A) the most primitive of these mafic products within a system and (B) how they vary across an arc in space and time, these studies attempt to reconcile opposing views into a more unified model.

The crystallized intrusions that make up an arc batholith provide a time-integrated record of the processes that occurred at a subduction zone. The Mesozoic Sierra Nevada batholith mainly consists of evolved intrusions, but ubiquitously scattered among these are mafic intrusions, even in the upper-crustal exposures. These are the crystallized products of basalt to basaltic andesite magmas that are typically not primitive (as reflected in lower MgO and higher Al₂O₃ concentrations than expected for mantle melts) and are often characterized by cumulate lithologies. Pressures recorded by most of the rocks of the batholith (aside from its southernmost portions) are upper-crustal. Thus, by studying these mafic intrusions of the Sierra Nevada batholith, we can understand the mafic, earlier stages of differentiation and their contributions to the upper continental crust.

Chapter 2 provides a rare example of the earliest stages of differentiation of primitive arc magmas in the upper crust. The study documents the field geology, petrology, and major and trace element chemistry of the ~35 km² mid-Jurassic Emigrant Gap complex, located in the northern Sierra Nevada. Distinct from most mafic intrusions of the Sierra Nevada batholith, the mafic complex features ultramafic rocks including dunite, wehrlite and clinopyroxenite, though it is dominated by gabbronorite. The complex formed at shallow

levels in the upper crust. The results presented in Chapter 2 show that the concentric structure of dunite surrounded by clinopyroxene-rich cumulates and then gabbronorite to diorite represents conduits through which primitive arc magmas ascended. Based on the petrology and chemistry of the rocks, the magmas parental to the mafic complex were relatively dry ($\sim 0.5\text{--}2$ wt.% H_2O) compared to typically hydrous parental arc magmas (Sisson and Layne, 1993; Plank et al., 2013). Their ascent to shallow levels could have been facilitated by regional extension.

Shallow differentiation of water-poor (<2 wt.% H_2O) mafic magmas is expected to produce an iron-enriched (tholeiitic) differentiation trend (Grove and Bryan, 1984; Grove et al., 2013). The main crystallization sequence has early crystallizing, low-anorthite plagioclase and conspicuously absent amphibole, with abundant orthopyroxene instead, resembling the tholeiitic differentiation series petrologically. However, the overall intrusive complex characteristically follows a calc-alkaline differentiation trend, which is distinctive and common among arc magmas. This is the result of hybridization between the mafic complex and an adjacent, closely-related granodioritic intrusion, which produces mixing trends geochemically between the two. That more evolved intrusion has abundant evidence for assimilation of crustal materials, including metasedimentary xenoliths. These results confirm previous hypotheses for how mixing and interaction between subduction zone magmas and pre-existing crust are at least in part responsible for the calc-alkaline trend (Kuno, 1950, 1959; Grove et al., 1982; Blatter et al., 2013).

Returning to the processes that drive differentiation, the Emigrant Gap complex also reveals that the mafic melts reacted with previously crystallized mushes within the conduits of the system. This type of percolative flow of melts that react with existing crystals has been described mostly in mid-ocean ridge settings (Kelemen et al., 1997; Lissenberg and Dick, 2008; Boulanger et al., 2023). Such melt-mush reaction has only rarely been identified in arc settings, but could be an important mechanism for generating arc crust (Bouilhol et al., 2015; Blundy, 2022). The Emigrant Gap complex is thus an ideal setting to explore this open-system process and its implications for arc magmatism going forward.

Chapters 3 and 4 together provide a regional, trans-batholithic view of mafic intrusions across the Sierran arc throughout its Jurassic to Cretaceous activity. Because the Sierra

Nevada formed on heterogeneous crust, this transect approach tests what role the upper plate has played in determining differences among these mafic intrusions. The intrusions are not primitive, representing basalt to basaltic andesite parental magmas that experienced earlier differentiation, likely in the lower crust (Sisson et al., 1996; Lewis et al., 2021, 2024). Further, they had relatively hydrous parental mafic magmas, demonstrated by their abundant amphibole and calcic plagioclase.

Their geochemistry and petrography reveal systematic changes that correspond to their geologic context. The framework of the pre-existing heterogeneous crust that the batholith was constructed on has been documented based on isotopic studies of the felsic intrusions as well as documentation of the various affinities of the metamorphic wallrocks (Bateman, 1963; Kistler and Peterman, 1973, 1978; Attia et al., 2018). The tectonic assembly of the framework rocks produced distinctive arc-parallel belts with variable crust and lithosphere.

The results presented in Chapter 3 show that during the Cretaceous, the intrusion of mafic magmas migrated from west to east, along with the more evolved rocks of the batholith, focusing during waning arc activity in the high elevations of the range. With this migration, changes in field relationships between the mafic and felsic intrusions corresponds to which of the tectonically assembled belts they intrude into. Mafic magmas that ascended through the thickest crust in the high Sierra, where magmatism had occurred for several tens of millions of years, produced mafic intrusions that are magmatically commingled with their host felsic intrusions. Their parental magmas were hydrous, with early-crystallizing amphibole. This may be due to the rheology of weakened and magmatically primed crust there. By comparison, mafic intrusions into thinner, dense, accreted oceanic crust in the western part of the batholith show evidence for less hydrous parental magmas, are larger in volume, and intrude with tabular geometries.

Chapter 4 documents systematic isotopic trends in the mafic intrusions along the transect, related to which tectonically assembled crustal belt they intrude. The results indicate that the parental mafic magmas were modified by minor assimilation, of ~10–20% in most cases, with extreme cases up to ~40%. This means that mafic magmas experience assimilation during early differentiation, without concomitant compositional evolution beyond basalt to basaltic andesite. This has been shown to be thermodynamically feasible,

and to likely occur in the lower crust (Reiners et al., 1995; Heinonen et al., 2022; Pimenta-Silva et al., 2024). Thus, although contaminated, the mafic magmas that ascended into the upper crust were initially mantle-derived.

Further, the results of this study have implications for how to interpret other isotopic data regarding crustal growth versus recycling or reworking over time. They show that the geochemistry of arc magmatic products, and particularly their isotopic composition, depends on the crustal column that they ascended through and interacted with. This is readily observable when the locus of arc magmatism migrates from juvenile, accreted (oceanic) crust into more ancient continental crust, which each have distinctive isotopic compositions, as is the case in the Sierra Nevada batholith (DePaolo, 1981; Chapman et al., 2017; Sundell and Macdonald, 2022).

Oxygen and hafnium isotope analyses in zircon (in addition to limited bulk-rock strontium and neodymium isotope analyses) presented here demonstrate the effect of heterogeneous crust on geochemical signatures. This serves as a cautionary message for studies using zircon that attempt to document crustal recycling or reworking versus generation of new crust over time throughout Earth's history. In their spatial, geologic context, the geochemical signatures of these mafic intrusions are clearly controlled by the local crustal column. In studies that lack geologic context, such as detrital zircon studies, shifts in isotopic composition of a similar magnitude can be interpreted as secular changes in recycling of crust versus mantle-dominated crustal growth. However, a more unified view of the process, revealed by these studies, is not one of drastically different processes over time, but rather of variation in the composition of crust sampled by magmas during ascent through the upper plate resulting from migration of the locus of magmatism.

Thus, a mantle- versus crust-dominated system can be reconciled as one that necessarily includes both inputs into arc magmas to derive the geochemical trends observed in arcs. It seems that these opposing paradigms and models mainly arise from attempts that focus on the variable chemistry of arc magmas. In considering the problems with a focus on the processes, rather than their chemical outcomes, a more cohesive understanding becomes attainable.

REFERENCES

Annen, C., Blundy, J.D., and Sparks, R.S.J., 2006, The genesis of intermediate and silicic magmas in deep crustal hot zones: *Journal of Petrology*, 47, 505–539, doi:10.1093/petrology/egi084.

Attia, S., Paterson, S.R., Cao, W., Chapman, A.D., Saleeby, J., Dunne, G.C., Stevens, C.H., and Memeti, V., 2018, Late Paleozoic tectonic assembly of the Sierra Nevada prebatholithic framework and western Laurentian provenance links based on synthesized detrital zircon geochronology: *Special Paper of the Geological Society of America*, 540, 267–295, doi:10.1130/2018.2540(12).

Bateman, P.C., Clark, L.D., Huber, N.K., Moore, J.G., and Rinehart, C.D., 1963, The Sierra Nevada batholith—A synthesis of recent work across the central part: U.S. Geological Survey Professional Paper, 414-D, 1–46.

Blatter, D.L., Sisson, T.W., and Hankins, W. Ben, 2013, Crystallization of oxidized, moderately hydrous arc basalt at mid- to lower-crustal pressures: Implications for andesite genesis: *Contributions to Mineralogy and Petrology*, 166, 861–886, doi:10.1007/s00410-013-0920-3.

Blundy, J., 2022, Chemical Differentiation by Mineralogical Buffering in Crustal Hot Zones: *Journal of Petrology*, 63, 1–36, doi:10.1093/petrology/egac054.

Bouilhol, P., Schmidt, M.W., and Burg, J.P., 2014, Magma transfer and evolution in channels within the arc crust: The pyroxenitic feeder pipes of Sapat (Kohistan, Pakistan): *Journal of Petrology*, 56, 1309–1342, doi:10.1093/petrology/egv037.

Boulanger, M., and France, L., 2023, Consequences of melt-mush reactions on mush-dominated magma reservoirs: The melt flush process exemplified at mid-ocean ridges: *Journal of Petrology*, 64, 1–20, doi:10.7185/gold2023.16597.

Bowen, N., 1928, *The Evolution of the Igneous Rocks*: Princeton, New Jersey, Princeton University Press, 334 p.

Chapman, A.D., Saleeby, J.B., Wood, D.J., Piasecki, A., Kidder, S., Ducea, M.N., and Farley, K.A., 2012, Late cretaceous gravitational collapse of the southern sierra nevada batholith, California: *Geosphere*, 8, 314–341, doi:10.1130/GES00740.1.

Cornet, J., Laurent, O., Wotzlaw, J.F., Antonelli, M.A., Otamendi, J., Bergantz, G.W., and Bachmann, O., 2022, Reworking subducted sediments in arc magmas and the isotopic diversity of the continental crust: The case of the Ordovician Famatinian crustal section, Argentina: *Earth and Planetary Science Letters*, 595, 117706, doi:10.1016/j.epsl.2022.117706.

Gill, J., 1981, *Orogenic Andesites and Plate Tectonics*. Springer, Berlin Heidelberg, New York.

Greene, A.R., DeBari, S.M., Kelemen, P.B., Blusztajn, J., and Clift, P.D., 2006, A detailed geochemical study of island Arc crust: The Talkeetna Arc section, south-central Alaska: *Journal of Petrology*, 47, 1051–1093, doi:10.1093/petrology/egl002.

Grove, T.L., and Bryan, W.B., 1983, Fractionation of pyroxene-phyric MORB at low pressure: An experimental study: *Contributions to Mineralogy and Petrology*, 84, 293–309, doi:10.1007/BF01160283.

Grove, T.L., and Baker, M.B., 1984, Phase equilibrium controls on the tholeiitic versus calc-alkaline differentiation trends: *Journal of Geophysical Research*, 89, 3253–3274.

Grove, T.L., Gerlach, D.C., and Sando, T.W., 1982, Origin of calc-alkaline series lavas at Medicine Lake Volcano by fractionation, assimilation and mixing: *Contributions to Mineralogy and Petrology*, 80, 160–182, doi:10.1007/BF00374893.

Grove, T.L., Kinzler, R.J., and Bryan, W.B., 1992, Fractionation of Mid-Ocean Ridge Basalt (MORB), *in* *Geophysical Monograph 71*, American Geophysical Union, 281–310, doi:10.1029/gm071p0281.

Hildreth, W., and Moorbath, S., 1988, Crustal contributions to arc magmatism in the Andes of Central Chile: *Contributions to Mineralogy and Petrology*, 98, 455–489, doi:10.1007/BF00372365.

Jacob, J.B., Moyen, J.F., Fiannacca, P., Laurent, O., Bachmann, O., Janoušek, V., Farina, F., and Villaros, A., 2021, Crustal melting vs. fractionation of basaltic magmas: Part 2, Attempting to quantify mantle and crustal contributions in granitoids: *Lithos*, 402–403, doi:10.1016/j.lithos.2021.106292.

Jagoutz, O., 2014, Arc crustal differentiation mechanisms: *Earth and Planetary Science Letters*, 396, 267–277, doi:10.1016/j.epsl.2014.03.060.

Jagoutz, O., and Kelemen, P.B., 2015, Role of arc processes in the formation of continental crust: *Annual Review of Earth and Planetary Sciences*, 43, 363–404, doi:10.1146/annurev-earth-040809-152345.

Jagoutz, O., and Klein, B., 2018, On the importance of crystallization-differentiation for the generation of SiO₂-rich melts and the compositional build-up of ARC (and continental) crust: *American Journal of Science*, 318, 29–63, doi:10.2475/01.2018.03.

James, O.B., 1971, Origin and emplacement of the ultramafic rocks of the Emigrant Gap area, California. *Journal of Petrology*, 12, no. 3, 523–560.

Kelemen, P.B., 1989, Combined crystal fractionation and reaction with ultramafic rock in basaltic magma: origin of dunite in the calc-alkaline Emigrant Gap plutonic complex, northern Sierra Nevada. *EOS Abstracts Spring Meeting*, 70, no. 15, V42A-01 1330H.

Kelemen, P.B., Koga, K., and Shimizu, N., 1997, Geochemistry of gabbro sills in the crust-mantle transition zone of the Oman ophiolite: Implications for the origin of the oceanic lower crust: *Earth and Planetary Science Letters*, 146, 475–488, doi:10.1016/s0012-821x(96)00235-x.

Kistler, R.W., and Peterman, Z.E., 1973, Variations in Sr, Rb, K, Na, and initial Sr⁸⁷/Sr⁸⁶ in mesozoic granitic rocks and intruded wall rocks in Central California: *Bulletin of the Geological Society of America*, 84, 3489–3512, doi:10.1130/0016-7606(1973)84<3489:VISRKN>2.0.CO;2.

Kistler, R.W., and Peterman, Z.E., 1978, Reconstruction of crustal blocks of California on the basis of initial strontium isotopic compositions of Mesozoic granitic rocks: *Geological Survey Professional Paper* 1071, 1–17.

Kuno, H., 1950, Petrology of Hakone volcano and the adjacent areas, Japan: *Geological Society of America Bulletin*, 61, 957–1020.

Kuno, H., 1959, Origin of Cenozoic petrographic provinces of Japan and surrounding areas: *Bulletin of Volcanology*, 20, 37–76.

Lewis, M.J., Bucholz, C.E., and Jagoutz, O.E., 2021, Evidence for polybaric fractional crystallization in a continental arc: Hidden Lakes mafic complex, Sierra Nevada batholith, California: Contributions to Mineralogy and Petrology, 176, 1–27, doi:10.1007/s00410-021-01844-y.

Lewis, M.J., Ryan-Davis, J.R., and Bucholz, C.E., 2024, Mafic intrusions record mantle inputs and crustal thickness in the eastern Sierra Nevada batholith, California, USA: Bulletin of the Geological Society of America, 136, 1808–1826, doi:10.1130/B36646.1.

Lissenberg, C.J., and Dick, H.J.B., 2008, Melt-rock reaction in the lower oceanic crust and its implications for the genesis of mid-ocean ridge basalt. *Earth and Planetary Science Letters*, 271, 311–325. <https://doi.org/10.1016/j.epsl.2008.04.023>

L.P.I., 1981, Basaltic volcanism on the terrestrial planets. Lunar and Planetary Institute, Houston, Texas, 1286 p.

Moyen, J.F., Janoušek, V., Laurent, O., Bachmann, O., Jacob, J.B., Farina, F., Fiannacca, P., and Villaros, A., 2021, Crustal melting vs. fractionation of basaltic magmas: Part 1, granites and paradigms: *Lithos*, 402–403, 106291, doi:10.1016/j.lithos.2021.106291.

Müntener, O., and Ulmer, P., 2018, Arc crust formation and differentiation constrained by experimental petrology: *American Journal of Science*, 318, 64–89, doi:10.2475/01.2018.04.

Otamendi, J.E., Ducea, M.N., and Bergantz, G.W., 2012, Geological, petrological and geochemical evidence for progressive construction of an Arc crustal section, sierra de valle fértil, famatinian Arc, Argentina: *Journal of Petrology*, 53, 761–800, doi:10.1093/petrology/egr079.

Plank, T., Kelley, K.A., Zimmer, M.M., Hauri, E.H., and Wallace, P.J., 2013, Why do mafic arc magmas contain ~4wt% water on average? *Earth and Planetary Science Letters*, 364, 168–179, doi:<https://doi.org/10.1016/j.epsl.2012.11.044>.

Reubi, O., and Blundy, J., 2009, A dearth of intermediate melts at subduction zone volcanoes and the petrogenesis of arc andesites : *Nature*, 461, 1269–1273, doi:10.1038/nature08510.

Rudnick, R.L., 1995, Making continental crust: *Nature*, 378, 571–578.

Ryan-Davis, J., and Scalice, D., 2022, Co-creating ethical practices and approaches for fieldwork. *AGU Advances*, 3, e2022AV000762. doi: 10.1029/2022AV000762

Saleeby, J., Ducea, M., and Clemens-Knott, D., 2003, Production and loss of high-density batholithic root, southern Sierra Nevada, California: *Tectonics*, 22, 1604, doi:10.1029/2002TC001374.

Sisson, T.W., and Layne, G.D., 1993, H₂O in basalt and basaltic andesite glass inclusions from four subduction-related volcanoes: *Earth and Planetary Science Letters*, 117, 619–635, doi:[https://doi.org/10.1016/0012-821X\(93\)90107-K](https://doi.org/10.1016/0012-821X(93)90107-K).

Sisson, T.W., Grove, T.L., and Coleman, D.S., 1996, Hornblende gabbro sill complex at Onion Valley, California, and a mixing origin for the Sierra Nevada batholith: *Contributions to Mineralogy and Petrology*, 126, 81–108, doi:10.1007/s004100050237.

Sisson, T.W., Ratajeski, K., Hankins, W.B., and Glazner, A.F., 2005, Voluminous granitic magmas from common basaltic sources: *Contributions to Mineralogy and Petrology*, 148, 635–661, doi:10.1007/s00410-004-0632-9.

Tatsch, S.J., 2006, The Nisenan: dialects and districts of a speech community. University of California, Davis, 496 p.

Taylor, S.R., 1989, Growth of planetary crusts. *Tectonophysics*, 161, 148–156.

Taylor, S.R., and McLennan, S.M., 1985, The Continental Crust: Its Composition and Evolution. Blackwell, Oxford.

Wracher, M.D., 1991, The petrology, geochemistry, and geochronology of the Emigrant Gap composite pluton, and its structural relationship to the Shoo Fly Complex. San Diego State University, 98 p.

SHALLOW DIFFERENTIATION OF PRIMITIVE ARC
MAGMAS AT THE JURASSIC EMIGRANT GAP COMPLEX,
SIERRA NEVADA, CALIFORNIA

Ryan-Davis, J., Bucholz, C.E. and Sisson, T.W., (*Chapter 2*), Shallow differentiation of primitive arc magmas at the Jurassic Emigrant Gap complex, Sierra Nevada, California. *In review: Journal of Petrology*.

Juliet Ryan-Davis¹, Claire E. Bucholz¹, Thomas W. Sisson²

¹*California Institute of Technology, 1200 E. California Blvd, Pasadena, CA 91104, USA*

²*U.S. Geological Survey, 350 Akron Rd, Moffett Field, CA 94035, USA*

ABSTRACT

The mafic Emigrant Gap complex and adjacent granodiorite expose ultramafic to silicic intrusive rocks that preserve the chemical and thermal evolution of primitive mafic arc magmas and their open-system interactions in the upper crust during mid-Jurassic growth of the Sierra Nevada batholith (California). We present field and petrographic observations and mineral and whole-rock chemistry of the $\sim 35 \text{ km}^2$ ultramafic to dioritic Emigrant Gap complex and an adjacent penecontemporaneous $\sim 90 \text{ km}^2$ granodiorite. In the Emigrant Gap complex proper, four roughly central masses of dunite, wehrlite, and olivine clinopyroxenite are flanked or surrounded by subtly banded gabbronorite and non-layered diorite. The ultramafic rocks are cumulates formed from near-liquidus minerals of primitive arc magmas that accumulated in steep feeder zones, with substantial modification by melt-mush reaction as primitive melts repeatedly transited the mush-filled conduits. The dominant gabbronoritic rocks are the variably accumulative products of more advanced crystallization-differentiation of arc tholeiitic basalts and basaltic andesites. The adjacent granodiorite intrusion originated separately and preserves field and geochemical evidence for assimilation of metasedimentary rocks. Open-system hybridization between the gabbronoritic mushes and the granodioritic magma produced an intervening body of two-pyroxene diorite. We infer that the ultramafic rocks and gabbronorite of the Emigrant Gap complex crystallized from near-primary arc basalts to basaltic andesites at $\sim 0.15\text{--}0.3 \text{ GPa}$, with estimated fO_2 of $\geq \text{FMQ} + 1$ and dissolved H_2O concentrations of only $\sim 0.5\text{--}2 \text{ wt.\%}$. Notably, the Emigrant Gap complex is distinct from other Mesozoic plutons in the Sierra Nevada batholith because of (1) its abundance of mafic and ultramafic rocks with characteristics indicating crystallization from relatively primitive mafic melts and (2) the low inferred H_2O concentrations of its parental magmas, indicated by a near absence of igneous amphibole and by the intermediate rather than calcic compositions of plagioclase. The ascent of primitive, relatively dry magmas into the upper crust of the Mesozoic arc was likely facilitated by a Jurassic regional extension event.

INTRODUCTION

Differentiation of primitive, mantle-derived magmas in subduction-zone settings produces evolved, buoyant continental crust (*e.g.*, Rudnick and Fountain, 1995). Consequently, most exposed arc magmatic products, both intrusive and extrusive, whether mafic or felsic, are typically evolved rather than primary mantle-derived compositions even when mafic. Studying products of the most primitive arc magmas is essential to fully understand arc differentiation from the earliest stages. Typically, mafic and ultramafic cumulates derived from primitive arc magmas are exposed in the lower crust of exhumed arcs, or as xenoliths brought up from those depths (Kay and Kay, 1985; Debari et al., 1987; Debari and Sleep, 1991; Greene et al., 2006; Jagoutz et al., 2009; Jagoutz, 2010; Jagoutz, 2014; Otamendi et al., 2012; Walker et al., 2015; Guo et al., 2020). By contrast, shallow mafic plutons are typically less primitive, representing more evolved stages of mafic magmatism (*i.e.*, Lewis et al., 2023).

In this contribution we document one of the most primitive sizeable intrusions of the Mesozoic Sierra Nevada batholith, providing a window into the crystallization products of the early stages of arc magma differentiation. The Sierra Nevada batholith is known mainly for its large granodiorite, tonalite, and granite plutons, but scattered among these are coeval smaller intrusions of hornblende gabbro and diorite, most of which are non-primitive (as shown by low concentrations of Mg, Ni and Cr, alongside high Al concentration). Some of the small mafic intrusions contain cumulates formed by crystallization-differentiation of evolved H₂O-rich arc basaltic magmas at upper crustal depths, including well-layered olivine hornblendites at Onion Valley (Sisson et al., 1996) and other amphibole-rich and often plagioclase-bearing cumulates within other <5 to 25 km² mafic plutons (*e.g.*, Frost, 1987; Lewis et al., 2023). The least fractionated among these intrusions in the main Sierra Nevada batholith, the Stokes Mountain complex, hosts modest volumes of well layered mafic-ultramafic cumulates (Clemens Knott and Saleeby, 1999). In the northern Sierra Nevada and Klamath Mountains, primitive mafic to ultramafic intrusions

associated with intermediate plutons are more common and intruded into the Foothills ophiolite belts and Upper Paleozoic to Jurassic mélanges (e.g., Saleeby and Sharp, 1980a and 1980b; Saleeby, 1982; Snode et al., 1982).

The focus of this study is one such complex in the Northern Sierra Nevada, located at Emigrant Gap, California (Fig. 1) near U.S. Interstate Highway 80 slightly west of Donner Pass. The Mid-Jurassic Emigrant Gap complex sits inboard (eastward) of many of the other Jurassic peridotite to diorite complexes, and was emplaced into Paleozoic to lower-Mesozoic volcano-sedimentary terranes rather than ophiolitic basement. Until now, it has been most extensively mapped and documented petrologically by James (1971). The Emigrant Gap complex exhibits many features of the “Alaskan-type” mafic-ultramafic intrusive complexes of the North American Cordillera (e.g., Irvine, 1974; Snode et al. 1982; Himmelberg and Loney, 1995; Nixon et al., 2024) and it has been described as such based on its ultramafic to felsic concentric structure, rock types, early clinopyroxene crystallization, late intrusion of hydrous magmas that crystallized as coarse-grained amphibole-plagioclase pegmatitic rocks, and its co-located intermediate (diorite to monzodiorite) plutons. However, the most abundant rocks of the Emigrant Gap complex differ from other mafic-ultramafic complexes of the Cordillera, and Alaskan-type intrusions generally (*i.e.*, Nixon et al., 2015), because they consist chiefly of orthopyroxene-bearing gabbro and gabbronorite with only minor to trace igneous amphibole.

In this study we employ whole-rock and mineral geochemistry together with field relationships to interpret the petrogenesis of the Emigrant Gap complex and its associated intermediate plutons, from dunite through granodiorite. We relate this to the global understanding of arc magmatism based on experimental petrology studies, exposed lower-crustal arc sections, and the compositions of arc volcanic rocks. We infer the physiochemical conditions of emplacement of the parental magmas (P, T, fO_2 , H_2O concentration), which bear on the geodynamic inference that regional extension allowed primitive magmas to ascend to the upper crust and differentiate at Emigrant Gap.

GEOLOGIC BACKGROUND

The Emigrant Gap complex comprises a $\sim 5 \times 10$ km, oval-shaped (long axis NE–SW), ~ 35 km 2 body of ultramafic and mafic igneous intrusive rocks (Fig. 1c). To the north, the mafic complex is bordered by an associated ~ 90 km 2 hornblende-biotite granodiorite pluton that extends ~ 15 km NNE. Together, these have been described as the Emigrant Gap composite pluton (James, 1971; Wracher 1991), but herein we consider the Emigrant Gap complex proper as solely the ultramafic through dioritic rocks. Owing to its size, location, and composition, we treat the granodiorite as a separate but associated pluton, itself possibly composite. To the east, south, and southwest, the Emigrant Gap complex is intrusive into dominantly greenschist facies metasedimentary and metavolcanic rocks of the Paleozoic Northern Sierra Terrane and the Jurassic Sailor Canyon and Tuttle Lake Formations (Fig. 1c, 2). Contacts with metamorphic rocks are sharp and steep and an ~ 800 m wide contact metamorphic aureole is distinguished by prominent andalusite and cordierite porphyroblasts in pelitic units (James, 1971; Wracher, 1991). Recent study of a shear zone developed along the eastern side of the complex near Cisco Butte inferred temperatures of deformation of 550–750 °C close to the contact (Leuchter, 2022), consistent with the presence of sillimanite + K-feldspar assemblages in the innermost aureole (Wracher, 1991). Emplacement of the complex at upper crustal depths is indicated by the low metamorphic grade outside of the aureole, the widespread andalusite and cordierite developed in the aureole, and an absence of garnet, kyanite, or other metamorphic minerals diagnostic of high pressures.

The Emigrant Gap complex and granodiorite are Middle Jurassic in age. The majority of plutons nearby are Cretaceous, excepting the Devonian Bowman Lake batholith, with the closest Jurassic plutons intruding the Smartville complex 30–40 km to the west (Harwood et al., 2014; Cecil et al., 2012; Saleeby et al., 1989 and other references in Irwin and Wooden, 2001; Kulow et al., 1997; Kulow, 1996; John et al., 1994; Hanson et al., 1988; Evernden and Kistler, 1970). The two-pyroxene diorite of the complex has a bulk zircon U-Pb age of ~ 164 Ma (Saleeby et al., 1989;

Girty et al., 1993). In the northern part of the hornblende-biotite granodiorite, mafic and ultramafic rocks potentially associated with Emigrant Gap are exposed as the ~168 Ma mafic complex of Beyers Lake located at Black Buttes (Hill, 1994), and a few other small, isolated localities of “two pyroxene diorite” or quartz monzonite (light purple units in Fig. 1c; Saucedo and Wagner, 1992; Skinner, 1992; Girty et al., 1993; Hill, 1994; Schweickert et al., unpublished, *in* John et al., 1994). The hornblende-biotite granodiorite pluton has a U-Pb zircon age of 166.5 ± 2.6 Ma on the dominant exposed granodiorite (Cecil et al., 2012). Consistent with these geochronologic results, our field observations of hybridization indicate coeval emplacement of the hornblende-biotite granodiorite with the mafic rocks of Emigrant Gap (described in detail below; also in James, 1971; Wracher 1991).

In this study, we focus on the ultramafic to mafic Emigrant Gap complex and the southern portion of the hornblende-biotite granodiorite. We do not document most of the granodiorite or other associated (ultra-)mafic bodies.

FIELD RELATIONSHIPS OF EMIGRANT GAP

Accurate mapping, field, and petrographic observations of the complex by James (1971) were foundational for our study. We provide an overview of the rock types here, with more detailed field and petrographic descriptions of each in Appendix 1 of this chapter. The Emigrant Gap complex comprises four separated bodies of ultramafic rocks surrounded successively by gabbronorite and a heterogeneous two-pyroxene diorite intrusion. Three ultramafic bodies that we designate part of the “main suite” crop out south of Lake Valley Reservoir (from west to east: Onion Valley, Monumental Ridge, Lake Valley. Note that this is different than the Onion Valley described in Sisson et al., 1996). They contain dunite and olivine clinopyroxenite, with some ($\sim <5\%$) wehrlite representing a gradational transition in modal clinopyroxene abundance between dunite and olivine clinopyroxenite (Fig. 2). These ultramafic bodies are typically 1.5–2 km across with steep, relatively sharp contacts against gabbronorite (however, these contacts are usually covered and not observable). Relative age relations of the ultramafic units

with gabbronorite are not obvious aside from occasional inclusions of ultramafic rock in gabbronorite near these bodies suggesting that at least some ultramafic rocks formed prior to the main gabbronorite intrusion. The ultramafic bodies are heterogeneous internally, with steeply dipping lenses to patchy and sheet-like domains of dunite interleaved with olivine clinopyroxenite (Fig. 3, 4b,f, A1d), but the ultramafic masses lack the well-defined, laterally continuous modal and grain-size variations typical of layered cumulates. Olivine clinopyroxenite contains trace amounts of orthopyroxene (<1 modal %, Fig. 4e,g, A3), and trace patches of amphibole in some clinopyroxene, interpreted to be products of igneous peritectic reactions. A transect through the core of the Lake Valley body is described in more detail below.

Gabbronorite (\pm olivine, \pm biotite) makes up the greatest exposure area of the complex. These are medium-grained rocks with well-developed moderately to steeply dipping igneous foliation defined mainly by aligned plagioclase laths (Fig. 5, 6c–f). Concordant with that foliation is a widespread but generally subtle modal banding defined by gradational changes in the relative abundances of plagioclase and pyroxenes (Fig. 5, 6). As with the ultramafic masses, sharply defined, repetitive, and laterally continuous modal and (or) grain-size layering, characteristic of well-layered cumulates, is absent. Small (cm to m-scale), sharply bounded transgressive masses of gabbronorite distinctly rich in either pyroxene (melagabbronorite) or plagioclase (leucogabbronorite) locally cut the banded gabbronorite (Fig. 5, 6). These transgressive masses have mineral assemblages, sizes, and habits similar to those of the host gabbronorite and likely represent locally remobilized portions of the gabbronoritic crystal mush. Some are clearly folded at outcrop scale, documenting dynamic mobility of the solidifying mush (Fig. 6b).

A “two-pyroxene diorite” intrusion (James, 1971; light blue unit in Fig. 2) surrounds the gabbronorite and separates it from the large granodiorite pluton to the northwest. The two-pyroxene diorite unit comprises a heterogeneous quartz monzodioritic to granodioritic zone mostly exposed north and west of the ultramafic

bodies, between gabbronorite to the south and amphibole-biotite granodiorite to the north (Fig. 1c, 2).

We do not focus on the fourth ultramafic body at Cisco Butte in this study, as its rocks are complicated by synmagmatic felsic and amphibole-bearing intrusions that affected their petrography and chemistry. However, we describe it briefly here and in Appendix 1 of this chapter. The Cisco Butte body differs from the three ultramafic bodies to the southwest, as it contains no dunite, and its olivine clinopyroxenite locally contains up to 5–10 modal % dark (igneous) amphibole surrounding pyroxene. Further, some of the clinopyroxenite is brecciated by coarse, pegmatitic amphibole gabbro (“pyroxenite breccia” unit of James, 1971; Fig. 2, A1f). Gabbroic rocks of Cisco Butte typically contain igneous amphibole as rims or oikocrysts (up to 1 mm wide) around pyroxene, unlike the generally amphibole-free gabbronorite that constitutes the bulk of the complex to the southwest (discussed further below).

Dikes of the hornblende-biotite granodiorite north of the Emigrant Gap complex crosscuts mafic units of the complex, establishing a younger relative age. The main body of this pluton is mapped as extending north of Black Buttes for ~4 km, and encloses other two-pyroxene diorite masses, but the pluton has had limited study and has been described as gradational with two-pyroxene diorite along its western margin (Wracher, 1991). Contacts of the granodiorite against gabbro at Cisco Butte observed in this study are sharp (Fig. A2f) and indicate the granodiorite is the younger intrusion, with crystals and scattered xenoliths of mafic rocks included in the granodiorite. Angular and rounded dark gray, micaceous metasedimentary xenoliths are common along with the more abundant fine-grained mafic enclaves (<~10 cm in diameter) that are commonly present in Sierra Nevada granitoids.

Mafic, intermediate, and felsic dikes striking northeast-southwest to north-south intrude wallrocks and each other along the eastern side of the Emigrant Gap complex in the region of Cisco Butte, and east of Lake Valley Reservoir. A plagioclase-porphyritic granodiorite intrusion that is ~120 m across by Lake Valley reservoir contains ultramafic xenoliths similar to Emigrant Gap rocks. The

plagioclase-porphyritic granodiorite is also exposed as dikes, which were sampled for this study (Fig. A2g–h). A few very fine-grained to aphanitic mafic dikes and one felsic quartz porphyry dike with aphanitic groundmass were observed and sampled (Fig. A2h). Other unstudied plagioclase porphyry dikes and small intrusions have been mapped intruding the metamorphic rocks east of Emigrant Gap (Harwood et al., 1995; Harwood et al., 2014).

SAMPLING AND ANALYTICAL METHODS

118 samples were collected from the Emigrant Gap complex. Sampling focused on the ultramafic rocks (57 of 118 samples), including a detailed transect through dunite lenses within wehrlite and clinopyroxenite in the Mears–Lake Valley ultramafic body. Representative samples of gabbronorite, gabbros, and intermediate plutonic rocks, including portions with accumulated crystals (mela- and leucogabbro segregations), were also collected. Four fine-grained mafic to coarser porphyritic felsic dikes from the margins of the complex are included in the suite. Polished thin sections of 75 samples were examined using a petrographic microscope.

XRF and ICP-MS whole-rock geochemistry

83 samples from the Emigrant Gap complex, including of dikes and the associated granodiorite, were analyzed for bulk-rock geochemistry by XRF, performed at Hamilton Analytical Laboratory (HAL) at Hamilton College, New York following protocols described in Appendix 1 of this chapter (Conrey et al., 2023). A further 3 samples (EG-22-97, EG-22-98, EG-22-100) were analyzed at the California Institute of Technology (Caltech) following protocols described in Bucholz and Spencer (2019; Table S1). Fragments of the glass pellets from bulk-rock XRF measurements were mounted in epoxy and analyzed by laser ablation ICP-MS at HAL for 41 trace and rare earth elements (see Appendix 1 of this chapter). An additional 4 samples of metasedimentary rocks in contact with the complex and 6 of mafic intrusive rocks from the complex at Black Buttes to the north were also analyzed at HAL (reported in Table S1).

Modal abundances and electron probe microanalysis (EPMA)

Modal mineral abundances of 20 representative samples were measured using a Bruker M4 Tornado energy dispersive micro-XRF to map the chemical compositions across entire thin sections. The Bruker software was then used to compute phase maps of each section, binning areas with similar compositions by principal component analysis to identify major mineral phases and their cumulative areas across the thin section. The normalized (modal) abundances for these sections are reported in Table S2. Details of these methods are reported in Appendix 1 of this chapter.

We analyzed the chemical compositions of major mineral phases from 50 samples (including 12 from the Cisco Butte suite) by electron microprobe (EPMA) at Caltech (see Table S11e for samples and phases). The JEOL JXA-8200 Superprobe with five tunable wavelength-dispersive spectrometers (WDS) was used for all analyses, except for samples EG-19-07, -30, -63, -68, and EG-22-100, 101A, 101B, 103A, 103B and 104, which were analyzed with a newer JEOL JXA-iHP200F field emission electron microprobe, with the same standards and analytical methods (analytical methods in Appendix 1 of this chapter and table S11 in the Supplementary Data File).

Approximately 10–30 individual grains of olivine, clinopyroxene, orthopyroxene and plagioclase of all representative textures were analyzed in each sample, if present, aiming for 6 spot analyses per grain (3 cores, 3 towards the rim). Due to their lesser abundance, ~1–8 grains of biotite and amphibole were targeted per sample where present, scattering ~3–10 spots on each grain. Up to 20 grains of chromite and 15 grains of Fe-Ti oxides, with 1–6 spots (targeting cores, and checking rims where grains were large enough) were analyzed where present, both as inclusions within silicate minerals or as interstitial grains. A few analyses on cracks, on non-stoichiometric (altered) areas of a mineral, or straddling multiple phases were excluded from the final dataset. Sample averages for each phase (and number of analysis spots of each phase per sample) are reported in Tables S2–S9. Where compositional variations were distinguishable between cores and rims or where the

same mineral occurs in multiple distinct textures (*i.e.*, as inclusions and as interstitial grains), they are averaged separately and reported.

WHOLE-ROCK GEOCHEMISTRY

Major-element chemistry

Whole-rock major- and trace-element chemical compositions and locations for the 83 analyzed samples are reported in Table S1 (Ryan-Davis et al., 2024). Published whole-rock chemical compositions (James, 1971; Wracher, 1995) are also plotted (Fig. 7, A4). Samples from Cisco Butte are plotted for comparison and completeness and are described in Appendix 1 of this chapter.

Main suite rocks plot as transitional between calc-alkaline and tholeiitic in Fe- versus Si-enrichment (Miyashiro, 1974; Kay and Kay, 1994; Zimmer et al., 2010), which is consistent with their mineralogy. Feldspar-bearing rocks are metaluminous, magnesian, and calcic using the modified alkali-lime index (MALI: $\text{Na}_2\text{O} + \text{K}_2\text{O} - \text{CaO}$), except for a high-Si keratophyre dike (Wracher, 1991) which is peraluminous (Frost et al., 2001).

Main suite and intermediate rocks

Whole-rock magnesium number ($100 * \text{Mg} / [\text{Mg} + \text{Fe}_T]$, molar, where Fe_T is total iron) decreases through ultramafic and mafic rocks of the main suite with increasing SiO_2 in the order of dunite (Mg# 83–88, SiO_2 40.0–41.8 wt.%) > olivine clinopyroxenite (Mg# 79–85, SiO_2 47.8–51.7 wt.%) > olivine gabbronorite and gabbronorite (Mg# 53–74, SiO_2 50.9–52 wt.%, up to 55.7 wt.% including altered monzogabbronorite). These whole-rock chemical variations correlate with the relative modal abundances of olivine, clinopyroxene, and feldspar (Fig. 7a) (note that no wehrlite samples were analyzed, as they are gradational between dunite and olivine clinopyroxenite and neither abundant nor adequately fresh). Intermediate-composition rocks shift to a relatively constant Mg# (48–57) in two-pyroxene dioritic

to granodioritic rocks (SiO_2 55.8–60.7 wt.%) and hornblende-biotite granodiorite ($\text{Mg}^{\#}$ 45–53, SiO_2 61.5–66.8 wt.%).

Dunite samples, as expected, have low concentrations of Al_2O_3 , CaO , K_2O , P_2O_5 , and incompatible minor and trace elements (less than 0.8 wt.% Al_2O_3 , 0.1–2.6 wt.% CaO and <0.02 wt.% K_2O ; Fig. 7c, A4). Olivine clinopyroxenite samples are similar, but with slightly higher concentrations of Al_2O_3 (up to 2.0 wt.%) and elevated CaO (13.1–19.2 wt.%). One dunite locality is anomalous in containing widespread but minor interstitial clinopyroxene, orthopyroxene, and plagioclase. That dunite has a comparatively low $\text{Mg}^{\#}$ (76 at 40.1 wt.% SiO_2 ; Fig. 7a), exceptionally high FeO_{t} (19.3 wt.%) and also high Al_2O_3 , MnO , and P_2O_5 that contrasts with the other analyzed dunite samples; this anomalous dunite is interpreted as having been infiltrated by and reacted with a transiting mafic melt. Olivine gabbronorite samples are relatively uniform in composition and similar to the ultramafic rocks in their respectively primitive $\text{Mg}^{\#}$ (72–74) and low concentrations of incompatible oxides (SiO_2 50.9–52.3 wt.%, K_2O 0.3–0.4 wt.%), whereas olivine-free gabbronorite samples vary more widely and systematically in composition ($\text{Mg}^{\#}$ 53–65, SiO_2 51.7–55.7 wt.%, K_2O 0.6–1.8 wt.%; Fig. 7, A4). Melagabbronorite and leucogabbronorite segregations are characterized by low and high SiO_2 , respectively (51.8 and 55.3 wt.%); these samples include the highest in TiO_2 (0.66 wt.% in a melagabbronorite), and in Al_2O_3 (20.2 wt.% in a leucogabbronorite) and almost the highest Na_2O (4.0 wt.%) in the entire series (Fig. 7, A4).

Samples from the two-pyroxene diorite unit and the hornblende-biotite granodiorite pluton define near-linear trends on variation diagrams, with compositions that classify them as gabbronoritic to hornblende-biotite granodioritic in all major oxides (and trace elements, described below). Progressing from gabbronorite to hornblende-biotite granodiorite, most major oxides either increase or decrease in broadly linear fashions with increasing SiO_2 except for TiO_2 , MgO , Na_2O , K_2O and P_2O_5 . These oxides exhibit kinks in their variation diagrams at ~55 wt.% SiO_2 , marking a distinct transition from gabbronorite to more evolved rock types.

The whole-rock aluminum saturation index [ASI = molar Al/(2Ca+Na+K)] increases with SiO₂ in the feldspar-bearing rocks from ~0.5 in gabbronorite to near 1 in biotite-amphibole granodiorite. Ultramafic rocks have low ASI values (<0.4 in dunite and <0.1 in clinopyroxenite), reflecting the abundance of Ca-rich clinopyroxene in these samples. Notably, all rocks in the main suite have ASI values that are lower at any given SiO₂ concentration than the common plutonic rocks of the Sierra Nevada batholith (Fig. 7b).

Dikes

Three analyzed felsic dikes have diverse SiO₂ concentrations of ~61–73.1 wt.% and are similar to the intermediate plutonic rocks of the main suite in their major element compositions. Mafic dikes have low-to-moderate MgO concentration (4.6–7.9 wt.% in aphanitic samples, up to 13.9 wt.% in coarser dikes that have accumulative amphibole) and lower SiO₂ (47.4–52.5 wt.%) than the main suite gabbronorite, plotting as tholeiitic. They also have comparatively elevated concentrations of Al₂O₃ and TiO₂, and slightly elevated concentrations of FeO* and Na₂O.

Trace-element chemistry

Feldspar-bearing rocks of the main suite have elevated concentrations of K, Sr, Cs, Rb, Ba and Pb, alongside relative depletions in high-field strength elements (Nb, Ta, Zr, Hf, Ti; Fig. A5). All rocks except for wehrlite to olivine clinopyroxenite exhibit elevated chondrite normalized (subscript CN) light rare earth element (LREE) contents relative to heavy rare earth element (HREE) contents: (La/Yb)_{CN} = ~2–10.5 in gabbronorite through diorite, and 6–15 in hornblende-biotite granodiorite. Clinopyroxene-rich wehrlite, olivine clinopyroxenite, and olivine gabbronorite displays more muted enrichments in LREE relative to HREE with (La/Yb)_{CN} = ~1. Dunite has low overall concentrations in most trace elements (<0.01 to 1 times chondrite) and flat normalized REE patterns.

Rare earth element (REE) patterns of gabbronorite samples distinguish different types (Fig. 8), which are also spatially and petrographically distinctive. Olivine gabbronorite, located closest to the ultramafic bodies at Black Mountain, has low overall REE concentrations compared to the gabbronorite that makes up the majority of the intrusion. The most widely exposed olivine-free gabbronorite has a slight positive Eu anomaly ($\text{Eu/Eu}^* = 1.17\text{--}1.23$), contrasting with monzogabbronorite that crops out near the contact with diorite ($\text{Eu/Eu}^* = 0.97\text{--}1.08$). Gabbronorite bands and segregations defined by variations in modal mineralogy (relatively more or less pyroxene versus plagioclase) have distinctive chemistry. Pyroxene-rich melagabbronorite has a distinct negative Eu anomaly ($\text{Eu/Eu}^* = 0.78$) and is enriched in the middle and heavy REE, whereas plagioclase-rich leucogabbronorite has a pronounced positive Eu anomaly ($\text{Eu/Eu}^* = 1.35$) and low HREE concentrations. The types of gabbronorite and their significance are discussed further below.

Whole-rock Ni and Cr concentrations decrease with decreasing modal abundances of olivine in the ultramafic rocks: dunite (800–1430 $\mu\text{g/g}$ Ni, ~1750–6300 $\mu\text{g/g}$ Cr) versus olivine clinopyroxenite and wehrlite (140–395 $\mu\text{g/g}$ Ni, 510–2170 $\mu\text{g/g}$ Cr). The olivine gabbronorite has up to ~190 $\mu\text{g/g}$ Ni and 630 $\mu\text{g/g}$ Cr, whereas the gabbronorite reaches a maximum of ~130 $\mu\text{g/g}$ Ni and 475 $\mu\text{g/g}$ Cr. Incompatible element concentrations increase with increasing SiO_2 in the gabbronorite samples. Sr concentrations are elevated in rocks with accumulated plagioclase (~545–845 $\mu\text{g/g}$) and are lower in gabbronorite (and gabbro) samples with less modal feldspar (~530–750 $\mu\text{g/g}$), whereas Sr concentrations are roughly constant in the diorite to granodiorite (~455–570 $\mu\text{g/g}$).

MINERAL CHEMISTRY

We report modal abundances and average mineral major and minor element compositions of chromite, olivine, clinopyroxene, orthopyroxene, plagioclase, biotite, and Fe-Ti oxides for analyzed samples of the main suite as a Supplementary

Data File (Tables S2–S7; Ryan-Davis et al., 2024). Average mineral compositions of amphibole and the Cisco Butte suite are discussed in Appendix 1 of this chapter.

In general, minerals are not strongly zoned, except for some samples with core and rim differences in plagioclase (Table S7). We first describe a detailed transect across pods and dikes of dunite within wehrlite and olivine clinopyroxenite in the Lake Valley ultramafic body (Fig. 9; also Fig. 3, 4b–f, A1b). We then describe the chemistry of major minerals in the overall order of magmatic evolution for the rocks of the main sequence, recognizing that because of replenishment and assimilation this need not correspond to a strict temporal progression.

Lake Valley ultramafic body transect through dunite pods

We collected 12 samples along a ~625 m transect across a set of dunite to wehrlite pods (or sheets), surrounded by olivine clinopyroxenite, within the Lake Valley ultramafic body (Fig. 9a). Most exposures there are olivine clinopyroxenite, although glacial drift and forested alluvium covers swales between outcrops. Dunite outcrops comprise 15–20% of the exposure; they are each up to ~120 m long with long axes striking ~25° and steeply dipping margins and internal fabric of olivine. Wehrlite comprises ~10% or less of the exposure. Regions between dunite pods have meter-scale patches and anastomosing sheets of dunite and lesser wehrlite within olivine clinopyroxenite (Fig. 3, 4f).

In dunite samples from the transect, the Mg# of chromite, olivine, and pyroxene is highest towards the edges of dunite pods, decreasing inward to the mixed dunite–wehrlite–olivine clinopyroxenite central region, including in a dunite “dike” at the center (Fig. 9b–c; Tables S3–S6). MnO concentrations in olivine and pyroxene increase slightly from dunite pod margins to the cores of dunite masses. The olivine in olivine clinopyroxenite has low Mg# and Ni concentrations and slightly elevated MnO concentrations compared to olivine from dunite. Clinopyroxene in surrounding clinopyroxenite away from the pods has lower Mg#, as does orthopyroxene in the olivine clinopyroxenite (Fig. 9c).

Chromite

Chromium-rich spinel from the main series, present in dunite and in lesser abundance in wehrlite, are more Fe-rich than chromite found in mantle peridotites (Fig. A6). They are mainly Fe-chromite, with some slightly more Fe-poor (Al-chromite) examples in more primitive dunite samples (Fig. A6). Some rims, where large enough to be analyzed, are Cr-magnetite (Fig. A6, Table S3). Chromite that forms a small (1–2 mm wide by ~5 cm) seam surrounding rounded olivine from a dunite pod in the Lake Valley ultramafic body transect (Fig. 4c–d) has higher Mg#, like chromite from more primitive dunite bodies, but is otherwise broadly similar in composition to nearby disseminated chromite.

Olivine

Olivine from the complex has lower Mg# (≤ 89) and Ni ($\leq 1600 \mu\text{g/g}$) than olivine from mantle ultramafic rocks (Fig. 10). Across all rock types, olivine MnO concentrations generally increase with decreasing Mg#, and CaO concentrations are low ($< 0.04 \text{ wt.}\%$) except in dunite samples with Mg# ≥ 87 (CaO = 0.06–0.11 wt.%), which have little to no clinopyroxene (Table S4).

In ultramafic rocks, Mg# of olivine decreases continuously from dunite (Mg# = 84–89) and wehrlite (Mg# = 87–87.5) to olivine clinopyroxenite (Mg# = 75–85; Fig. 10). Olivine in the sample of reacted dunite (with poikilitic orthopyroxene, plagioclase, and biotite) has anomalously low Mg# (78.2), but similar Ni concentration (874 $\mu\text{g/g}$) to olivine from other dunite samples. Ni concentrations in olivine are greatest in samples with relatively primitive chromite from large dunite bodies (Ni = ~1000–1400 $\mu\text{g/g}$), but are near constant for dunite from smaller bodies and in the transect in pods and in patches (Ni = ~800–1000 $\mu\text{g/g}$; Fig. 10).

In olivine gabbronorite, Ni concentrations increase (Ni = ~1000–1150 $\mu\text{g/g}$) as olivine Mg# decreases (from 82–80) while grain morphology changes from subhedral grains and inclusions in clinopyroxene to more rounded, resorbed grains (Fig. 10). Olivine from a fine-grained biotite-bearing olivine gabbronorite (1–2 cm wide) dike that crosscuts olivine gabbronorite (Fig. A2a–b) overlaps the range of

Mg# in olivine from dunite and olivine clinopyroxenite (Mg# = 83.8), and has elevated Ni (1000 $\mu\text{g/g}$).

Clinopyroxene

The only clinopyroxene variety found across the entire Emigrant Gap suite is augite. Neither pigeonite nor its inversion products have been identified. The most primitive clinopyroxene (Mg# = 90) is found in wehrlite, which is associated with dunite (*e.g.*, Fig. A1c–d). In ultramafic rocks, clinopyroxene has Mg# 90–82, and its Al_2O_3 concentrations ($\text{Al}_2\text{O}_3 = 1.17\text{--}2.65$ wt.%) increase with decreasing Mg# (Table S5). This trend reverses in plagioclase-bearing rocks with clinopyroxene Al_2O_3 concentrations continuously decreasing (from 3.63–1.43 wt.%) with decreasing Mg# (Mg# = 82–71; Fig. 11a). Clinopyroxene TiO_2 concentrations behave similarly. The Cr concentrations of clinopyroxene decrease continuously with Mg# (and lithology), with the greatest values in dunite (up to ~ 4900 $\mu\text{g/g}$ Cr, Mg# 89) and a clinopyroxene core in fine-grained gabbronorite (~ 5700 $\mu\text{g/g}$ Cr, Mg# 87.8; Fig. 11b). Clinopyroxene from the reacted dunite sample has relatively low Mg# compared to other ultramafic rocks (Mg# = 81.1) but elevated Cr concentration (~ 3000 $\mu\text{g/g}$ Cr). Rare resorbed clinopyroxene cores rimmed by amphibole in granodiorite are similar in composition to clinopyroxenes from the ultramafic rocks.

Orthopyroxene

Orthopyroxene in the ultramafic rocks is enstatite with Mg# 78–84 and low Al_2O_3 concentrations (<1.5 wt.%). As noted above for clinopyroxene, the orthopyroxene from plagioclase-bearing rocks defines a trend of decreasing Al_2O_3 concentrations (from a maximum of ~ 2 wt.%) with decreasing Mg# (Table S6). The Mg# of orthopyroxene in ultramafic rocks overlaps with that of orthopyroxene in olivine-bearing gabbronorite and olivine gabbronoritic fine-grained dikelets (Mg# 80–83). Poikilitic orthopyroxene in reacted dunite has elevated Al_2O_3 (and CaO and TiO_2) concentrations compared to other ultramafic samples, overlapping in composition with orthopyroxene from olivine gabbronorite, but has high Cr (~ 960

$\mu\text{g/g}$) resembling the orthopyroxene in ultramafic samples. Cr concentration decreases with decreasing Mg# in orthopyroxene, with elevated values in ultramafic rocks (maximum Cr = 1500 $\mu\text{g/g}$). An exception to this trend is peritectic orthopyroxene, which was identified texturally as orthopyroxene lenses rimming anhedral and fine-grained olivine (Fig. 4e,g, A3) in olivine gabbronorite, fine-grained dikelets (Fig. 6a–b, A2a–b), and olivine clinopyroxenite. In the peritectic orthopyroxene, Cr concentrations are \sim 200–390 $\mu\text{g/g}$ compared to orthopyroxene in ultramafic rocks with similar Mg# 82–84 with Cr \sim 760–1500 $\mu\text{g/g}$.

Plagioclase

Plagioclase in gabbronorite is subtly normally zoned with cores reaching a maximum of \sim An₅₉ and rims \sim An₅₅ (Table S7). Plagioclase in reacted dunite is An₅₄, similar to more evolved gabbronorite (An_{48–55}). In diorite, anorthite contents of plagioclase cores (An_{62–70}) and rims (to An₄₃) are higher and lower, respectively, than in plagioclase in gabbronorite. Diorite plagioclase rims overlap compositionally with plagioclase rims in granodiorite (An_{41–49}). Plagioclase in fine-grained olivine gabbronoritic dikelet has a distinctly high anorthite content (An_{81–84}). Plagioclase compositions from the amphibole-bearing intrusions of Cisco Butte extend to much higher anorthite content and are reversely zoned in some cases (An_{45–89}; Fig. A7 and Table S7).

Fe-Ti oxides

Fe-Ti oxides are nearly all magnetite, which is present but minor in olivine clinopyroxenite, but reaches 3–4 modal % in olivine gabbronorite and gabbronorite. The fine-grained olivine gabbronoritic dikelets have up to \sim 10 modal % magnetite. NiO concentration in magnetite correlates with Mg#, with a maximum of \sim 0.2 wt.% NiO in the dikelets (Table S8; Fig. A8). Ilmenite is present in melagabbronorite bands; ulvöspinel patches can be found in some ilmenite, probably formed by oxidation-precipitation. Ilmenite also occurs in symplectites of Fe-Ti oxides (both

ilmenite and magnetite) with biotite and quartz in coronas around clusters of orthopyroxene in diorite.

Biotite

Biotite is present in trace to accessory amounts in the ultramafic through gabbronoritic rocks, with biotite composition correlating with textural differences across rock types. In reacted dunite and in fine-grained olivine gabbronorite dikelets, biotite forms small (<1 mm) anhedral, interstitial patches between olivine and pyroxene. Limited analyses of biotite in these samples have Mg# of 82–87, and somewhat higher Al₂O₃ of ~14.5 to ~15.5 wt.% compared to biotite in gabbronorite and diorite (Mg# 50–70; Al₂O₃ 13–14 wt.%; Table S9).

Diorite and granodiorite have more abundant and coarser biotite (2–4 mm). In both rock types, biotite is commonly poikilitic, and in the diorite, forms anhedral coronas on pyroxenes with magnetite symplectites (particularly around clusters of small orthopyroxene grains; Fig. 6g, A2c). Biotite increases in Mg# (47–53) with decreasing TiO₂ from diorite (~3.7 wt.%) to granodiorite (2.5–3.2 wt.%). Biotite in the granodiorite has elevated Al₂O₃ (14.4–15 wt.%) compared to the overall decreasing trend with differentiation in the rest of the suite from ultramafic rocks and gabbronorite to diorite (down to ~13–14 wt.% Al₂O₃ in biotite from diorite).

DISCUSSION

Based on the geology, petrology, and geochemistry described above, we first propose an origin for the main suite that is consistent with the geochemical and field relations. Using this petrogenetic framework we then discuss the conditions of crystallization (P, T, *f*O₂, H₂O concentration) of the different suites of the Emigrant Gap complex and place these into broader context of arc tectonic environments. The Cisco Butte suite is discussed in Appendix 1 of this chapter.

Proposed origins of the Emigrant Gap intrusive suites

The ultramafic rocks and melt-rock reaction

Ultramafic rocks at Emigrant Gap lack the sharply defined, laterally extensive modal and/or grain size layering typical of some well-known mafic and ultramafic cumulates (e.g., Skaergaard, Stillwater Complex, Bushveld Complex). Instead, their rock types and fabrics dip steeply and interfinger closely and discontinuously. Although their compositions represent accumulations of the near-liquidus minerals of primitive melts (*i.e.*, olivine + spinel or olivine + clinopyroxene), the main process that formed the dunite, wehrlite and clinopyroxenite was not crystal settling, compaction, or other processes that are often proposed for cumulates. The transgressive ultramafic bodies at Emigrant Gap formed potentially partly by mineral accumulation in conduits and then textural equilibration during cooling (Fig. 4a,h, A1c), but also likely by reaction of more mafic melts (saturated with olivine \pm spinel \pm clinopyroxene) melts with pyroxenitic crystal mushes previously emplaced in the active upper crustal intrusion (Fig. 3, 4, 11). Clinopyroxenite bodies that contain interstitial olivine with trace orthopyroxene reaction rims also likely formed by similar melt percolation, during which olivine + melt \rightarrow orthopyroxene (Fig. 4e,g, A3).

Focused vertical flow of primitive and near-primitive melts through centralized conduits, some precipitating dominantly clinopyroxene, and others precipitating olivine and reacting with earlier clinopyroxene to produce dunite accounts for the “concentric” zonation of the ultramafic and mafic plutonic rocks at Emigrant Gap that also defines Alaskan-type complexes (Fig. 12). That olivine is limited to gabbronorite adjacent to the ultramafic bodies is evidence that relatively primitive magmas that passed through those localized conduits contributed to the gabbroic rocks forming nearby, rather than there having been a hiatus between the mafic and ultramafic rocks. Magma feeder channels in the deep crust of the Kohistan arc with similar field and petrographic textures (Fig. 4, 6) and clinopyroxene and olivine chemistry have been described (Bouilhol et al., 2015; Jagoutz et al., 2006), where

they are ~10 km in diameter, compared to the 1–2 km diameter of the ultramafic bodies at Emigrant Gap. Infiltration of reactive melts has been proposed as an integral differentiation process beyond simple crystallization-differentiation at other Alaska-type complexes (Irvine, 1974; Kelemen and Ghiorso, 1986; Nixon et al., 2024).

Geochemical and textural observations are consistent with this interpretation. For example, Ni concentrations in olivine from dunite, wehrlite, and olivine clinopyroxenite in the main suite decrease (from ~1630–490 $\mu\text{g/g}$ Ni) with decreasing olivine Mg# (88.5–74; green diamonds and triangles in Fig. 10, Table S4). However, in the dunite and pyroxenite from the Mears-Lake Valley transect (Fig. 9), Ni concentrations in olivine stay nearly constant ($\sim 900 \pm 70 \mu\text{g/g}$ average; open diamonds and triangles in Fig. 10). This relation suggests that lenses of dunite with Mg# between 82–88 formed not by progressive fractionation of olivine from a fixed volume of melt (which would cause progressive Ni depletion), but rather by olivine growth from a supply of melt with a relatively constant Ni concentration (assuming temperature did not vary significantly; Matzen et al., 2013; Matzen et al., 2017). We interpret this as evidence of persistent replenishment of percolating melt. Thin, mm to cm chromite seams that occur near steeply dipping planes of more abundant clinopyroxene in dunite (Fig. 4c–d, A1b) may also form by melt percolating through dunite, where primitive and orthopyroxene-saturated melts (reacting with dunite) mix, stabilizing chromite (Irvine, 1977; Arai and Yurimoto, 1994; Payot et al., 2013; Abumarah et al., 2020).

The introduction and reaction of melts percolating through pre-existing mushes has been described as reactive flow and “melt-flush” in mid-ocean ridge settings (Kelemen and Dick, 1995; Kelemen et al., 1997; Lissenberg and Dick, 2008; Boulanger et al., 2023), and has been more sparingly identified in the lower crustal exposures (~0.7 GPa) of exhumed oceanic arc plutonic rocks (Bouilhol et al., 2015), though it has been suggested as an important mechanism for generation of the arc crust (Blundy, 2022). The process of melts transiting through crystal-rich mushes captured at Emigrant Gap has implications for rheological models and geophysical

characteristics of sub-arc volcanic intrusions during active magmatic emplacement (and presumably, eruption of extracted melts).

Gabbronorite as a cumulate from near-primitive arc basalts to basaltic-andesites with variable melt trappings

Geochemical and field observations indicate that the main suite gabbronorite crystallized from arc basaltic to basaltic andesitic magmas with trace-element abundances similar to other primitive arc magmas (Fig. 8, A5). The full crystallization sequence of the main suite is captured in the olivine gabbronorite suites, which first crystallized olivine (\pm chromite), joined by clinopyroxene, then by plagioclase + (titano)magnetite and reached the reaction boundary olivine + melt \rightarrow orthopyroxene (Fig. 12). Interstitial liquids then crystallized minor biotite and in some cases K-feldspar, but with little to no calcic amphibole.

The majority of the samples from the most widely exposed member of Emigrant Gap's main suite, the gabbronorite, represent a mixture of accumulated minerals and melt. Olivine gabbronorite samples represent the crystallization products from the least evolved plagioclase-saturated melts accompanied by the most efficient escape of intercumulus liquids. Monzogabbronorite samples are the closest to preserving magmatic liquid compositions, whereas gabbronorite and leucogabbronorite samples contain excess accumulated plagioclase and melagabbronorite samples likewise accumulated pyroxene. These non-layered but subtly banded gabbronoritic partial cumulates have SiO_2 concentrations of basaltic to basaltic andesitic liquids owing to the intermediate composition of the plagioclase, the abundances of pyroxenes, the absence of amphibole, the scarcity of olivine, and the moderate abundances of Fe-Ti oxides. Strong enrichment of daughter liquids in SiO_2 would require low- SiO_2 cumulates (*i.e.*, amphibole gabbro and hornblendite, common elsewhere in the Sierra Nevada), and thus may have been limited at Emigrant Gap.

Spatially, the olivine gabbronorite and gabbronorite generally becomes more evolved compositionally and mineralogically moving northward away from Black

Mountain (Fig. 2, 12). These members can be subdivided and interpreted based on mineralogy and aspects of trace element geochemistry, although the distinctions between subdivisions are not sharp. Simplest is biotite-monzogabbronorite that occurs closest to the contact with the dioritic intrusion, which has neither positive nor negative Eu anomalies on chondrite-normalized plots (Fig. 8). The major-oxide composition of this group is like that of arc basalts to basaltic andesites with anhydrous-normalized SiO_2 concentrations of 52.1–55.7 wt.%, MgO of 9.7–5.7 wt.%, Na_2O of 2.1–3.1 wt.%, and P_2O_5 of 0.15–0.27 wt.%. The Al_2O_3 concentrations of this group are 17.2–13.6 wt.%, with the lower values outside the common range for arc volcanic rocks, so some monzogabbronorite samples may include minor accumulated pyroxenes. The CIPW normative plagioclase in monzogabbronorite is 42–54 wt.% An_{48-58} (computed with whole rock $\text{Fe}^{3+} = 0.15\sum\text{Fe}$). The biotite-monzogabbronorite group probably most closely approaches melt-rich magma compositions.

The more abundant main gabbronorite group requires a more complex origin due to its notable positive Eu anomalies. Excepting the positive Eu anomalies, the REE patterns of gabbronorite samples are similar to those of monzogabbronorite samples but with generally slightly lower overall REE concentrations and with less LREE enrichment, where subscript CN indicates chondrite normalized (Sun and McDonough, 1995): the median monzogabbronorite has $\text{La}_{\text{CN}} = 34$ and $\text{Lu}_{\text{CN}} = 7.3$, whereas the median gabbronorite has $\text{La}_{\text{CN}} = 25$ and $\text{Lu}_{\text{CN}} = 6.7$ (Fig. 8). Consistent with their positive Eu anomalies, the gabbronorite group includes plagioclase-rich leucocratic samples; the range in CIPW normative plagioclase is 49–56 wt.%. Major-oxide compositions of gabbronorite overlap with those of monzogabbronorite, with anhydrous-normalized SiO_2 concentrations of 51.7–54.2 wt.%, MgO of 9.0–5.3 wt.% and Na_2O of 2.7–3.3 wt.%. Gabbronorite samples lack conspicuous interstitial K-feldspar and have low P_2O_5 concentrations, consistent with a larger fraction of cumulative crystals and less trapped melt than in monzogabbronorite. Assuming the median biotite-monzogabbronorite composition with P_2O_5 of 0.2 wt.% represents that of the dominant melt and that cumulus mineral assemblages contain negligible

P_2O_5 , then the gabbronorites could have contained 55–90 wt.% trapped melt. Most exposed gabbronorite of the Emigrant Gap complex is this moderately accumulative type.

The olivine gabbronorite of the main suite, exposed only on Black Mountain, has mineral assemblages and whole-rock compositions consistent with appreciable accumulation of near-liquidus minerals. Besides conspicuous modal olivine, olivine gabbronorite samples are distinguished by their low overall REE abundances and smaller or absent LREE enrichments ($La_{CN} = 11.5\text{--}7.9$, $Lu_{CN} = 4.9\text{--}4.6$, $(La/Sm)_{CN} = 1.3\text{--}0.9$; Fig. 8). These are relatively plagioclase-poor rocks, reflected in their low whole-rock Al_2O_3 concentrations (12.9–12.1 wt.%), well below the common range for arc basalts and basaltic andesites, and in their low abundance and calcic composition of CIPW normative plagioclase (40 ± 2 wt.%, of $An_{60\text{--}63}$). The low P_2O_5 concentrations of these rocks indicate low fractions of trapped melt, estimated very approximately at 10–20 wt.%, again assuming that biotite-monzogabbronorite represents the trapped melt composition.

Single samples of a prominently pyroxene-rich zone (melagabbronorite) and plagioclase-rich zone (leucogabbronorite) are distinct from their host gabbronorite. The melagabbronorite differs from the other gabbronorite samples in its high concentrations of middle and heavy REE, its lack of LREE enrichment, and its prominent negative Eu anomaly, all characteristics consistent with its obvious accumulation of calcic clinopyroxene (Fig. 11). Unlike olivine gabbronorite, its normative plagioclase (An_{54}) is within the range of the normative and modal plagioclase in typical gabbronorite, although of lower normative abundance (28 wt.%). The melagabbronorite is thus a locally pyroxene-enriched cumulate from the somewhat differentiated magmas that created the common gabbronorite. The leucogabbronorite has a pronounced positive Eu anomaly like gabbronorite (and normative plagioclase of 66 wt.%, An_{50}) and enriched LREEs but depleted HREEs ($Lu_{CN} = 5$). These features and the high Al_2O_3 (19.8 wt.%) indicate that the leucogabbronorite is a locally plagioclase-enriched cumulate of the common gabbronorite. The compositions of the melagabbronorite and the leucogabbronorite

bracket the range of (monzo)gabbronorite compositions in all elements, indicating that they are mineral segregates from the bulk magma.

Open-system hybridization of gabbronorite and hornblende-biotite granodiorite produced the two-pyroxene diorite

The main crystallization-differentiation sequence described above includes ultramafic rocks and gabbronoritic rocks that are cogenetic products of primitive arc magmas. In contrast, the petrography and geochemistry of the heterogeneous two-pyroxene diorite to granodiorite intrusion of the main suite is consistent with it originating by hybridization between the gabbronorite of the main suite and the magmas that formed the associated hornblende-biotite granodiorite pluton (Fig. 12). Orthopyroxene in the gabbronorite is subhedral and relatively large (2–3 mm). However, in the two-pyroxene diorite, orthopyroxene forms 1 mm-sized clusters of rounded <0.25 mm grains with reaction-rim symplectites (Fe-Ti oxides, biotite, quartz and plagioclase) or disseminated <0.25 mm round orthopyroxene grains farther from the gabbronorite (Fig. 6g, A2c). Orthopyroxene in the two-pyroxene diorite likely originated from the gabbronorite but then broke down partly in the new hybrid melt. Plots of major and trace elements of the two-pyroxene diorite form linear arrays between gabbronorite and the granodiorite (*i.e.*, Fig. 7, A4, A9), that are consistent with (though not definitive evidence of) an origin via mixing.

The ~1 mm-sized orthopyroxene that disaggregated once the reaction occurred indicates that some or all of the gabbronorite had already crystallized extensively, and perhaps solidified completely, when hybridization occurred with the slightly younger granodioritic intrusion. The hornblende-biotite granodiorite and plagioclase-porphyritic granodiorite dikes (Fig. A2e–h) also contain xenoliths and xenocrysts from the mafic complex (*e.g.*, Mg# 88 in clinopyroxene rimmed by amphibole), reflecting further open-system interaction. Significantly, the granodiorite also contains angular, commonly foliated metasedimentary xenoliths (which are not observed in the mafic complex) reflecting additional open-system assimilation, likely at depths below the present level of exposure (Fig. 12). The source of the intermediate

pluton was thus a crustally contaminated magma, distinct from the near primitive parental magmas of the mafic complex.

Emigrant Gap compared to arc volcanic rocks

As described, most of the Emigrant Gap ultramafic through gabbronoritic rocks are accumulative, containing excesses of early-formed crystals that (1) precipitated directly from mafic melts ascending through centralized conduits (clinopyroxenite, some dunite), (2) became accumulative by partial escape of interstitial melts (gabbronorite), or (3) grew from replenishing melts transiting and reacting with earlier, conduit-filling pyroxenitic cumulates. Exceptions are some monzogabbronoritic rocks which may approach basaltic andesite melt compositions. A volcanic counterpart to the Emigrant Gap complex has not been confirmed, but nearby mid-Jurassic andesitic volcanic rocks of the Tuttle Lake formation have similar pyroxene phenocrysts, suggesting that the complex could have been the feeder system for a volcanic center.

Although the gabbronorite samples overlap in some compositional respects with transitional tholeiitic to calc-alkaline arc basaltic andesites (Fig. A10), they clearly differ from erupted arc magma compositions in other indicators, shown particularly well by their low ASI values and TiO_2 concentrations compared to volcanic arc rocks (Fig. A10g–h). The two lowest- SiO_2 mafic dike samples contain accumulated amphibole, so do not preserve melt compositions, but the other two mafic dike samples are fine-grained and equivalent in composition to tholeiitic arc basalt and basaltic andesite, whereas the felsic dikes classify as calc-alkaline (Fig. A10). Thus, some mafic melts associated with the complex were tholeiitic, while the gabbronorite samples of the main suite mainly plot as calc-alkaline, including the nearly basaltic andesitic monzogabbronorite group (Fig. A10). Thus, the Emigrant Gap complex represents the intrusive products and records some of the differentiation processes that occurred under a transitional, not strongly tholeiitic or calc-alkaline, arc volcano. Kay et al. (1983) identified a similar connection between volcanic rocks and the Finger Bay pluton, Alaska.

Parental magmas and crystallization conditions

We infer that mafic parental magmas that formed the Emigrant Gap complex were near-primitive oxidized basalts to basaltic andesites, with liquidus temperatures $>1100^{\circ}\text{C}$ (up to $\sim 1200^{\circ}\text{C}$, based on experiments). Present levels of exposure formed at a maximum of ~ 10 – 12 km depth below the surface (~ 0.3 GPa emplacement pressure), and could have been as shallow as ~ 5.5 km depth (~ 0.15 GPa). Detailed estimates based on mineral thermometry and barometry are in Appendix 1 of this chapter and are summarized in Tables 1 and S3–S10.

The sample-average Mg# of olivine in dunite spans 83.8–88.7, indicating equilibrium with a melt with an Mg# of 55–64 assuming a melt $\text{Fe}^{3+}/\sum\text{Fe} = 0.15$ and 8.5 wt% FeO_{T} to calculate Mg# (and olivine-melt Fe^{2+} -Mg K_D of 0.28; Sisson and Grove, 1993). Following these assumptions, melts parental to the main sequence gabbro-norite would have had Mg# spanning 45–55 based on Fe/Mg exchange equilibrium with olivine, as well as clinopyroxene ($K_D = 0.23$; Sisson and Grove, 1993) and orthopyroxene ($K_D = 0.284$; Beattie, 1993).

Comparing the main suite's crystallization sequence to experiments that vary oxygen fugacity ($f\text{O}_2$) and concentration of H_2O (*i.e.*, Feig et al., 2010), the parental magma to the main suite at Emigrant Gap was likely oxidized ($\sim \Delta\text{FMQ} = +1$ – $+3$), common for arc magmas (Sisson et al., 2005; Kelley and Cottrell, 2009; Rowe et al., 2009; Bounce et al., 2014; Bucholz and Kelemen, 2019). Controlling for other conditions, experiments performed with a magnesian basaltic andesite (52.2 wt.% SiO_2 , 7.9 wt.% MgO , normalized anhydrous) produced similar crystallization sequences to Emigrant Gap at 0.4 GPa, $\text{H}_2\text{O} \leq 3$ wt.%, and oxidized conditions, whereas a magnesian arc basalt (47.7 wt.% SiO_2 , 12.7 wt.% MgO , normalized anhydrous) did not reach orthopyroxene saturation under the same conditions (Pichavant and Macdonald, 2007). Experiments on an arc basalt intermediate between these two compositions (SiO_2 49.9 wt.%, MgO 8.7 wt.%) also did not saturate with near-liquidus orthopyroxene at 400 MPa, H_2O 2.0 wt.%, and oxidized

conditions (Blatter et al., 2013), further supporting that the mafic parental magmas to the Emigrant Gap complex were relatively silicic arc basalts or basaltic andesites.

Pressure and H₂O concentration of the main suite—evidence from thermodynamic modeling

The parental magmas of the Emigrant Gap complex likely had relatively low H₂O concentrations. Low-H₂O arc magmas are not the most typical arc magmas, yet they are widespread (Sisson and Grove, 1993a,b; Sisson and Bronto, 1998; Zimmer et al., 2010; Grove et al., 2012; Till, 2017; Rezeau et al., 2021; Rasmussen et al., 2022). The main petrologic observations that support low H₂O concentrations in the parental magmas are the near absence of igneous amphibole, the intermediate rather than high-An plagioclase of the main suite (a maximum of An₆₃ in olivine gabbro-norite), and the relatively early plagioclase crystallization near or before the onset of orthopyroxene crystallization (indicated by petrographic observations and by the decreasing Al₂O₃ in clinopyroxene with decreasing Mg# starting with gabbro-norite; Fig. 6a,c, 10a, A2a). Plagioclase thus likely joined the crystallizing assemblage when melts had Mg# ~45–50, based on Fe-Mg exchange with mafic minerals.

To place more quantitative constraints on the H₂O concentrations of the main suite's parental magmas and the suite's emplacement pressure (depth), we compare alphaMELTS modeling results to observed crystallization sequence and phase assemblages (Smith and Asimow, 2005; Gualda et al., 2012). The alphaMELTS simulations employed two representative primitive arc volcanic rock compositions (Table S12): an average of Aleutian high-Mg basalts (Turner and Langmuir, 2015), and the average of Izu-Bonin “enriched” high-Mg basaltic andesites and andesites (average composition #352 in supplemental dataset S1 of Schmidt and Jagoutz, 2017), the latter with a basaltic andesitic SiO₂ concentration of 53.0 wt.%. We sought to identify the conditions of pressure and total H₂O concentration for which those compositions would crystallize in the sequence: olivine (± spinel), clinopyroxene, plagioclase (with intermediate An compositions) + orthopyroxene (or plagioclase

shortly before orthopyroxene), with olivine then reacting to orthopyroxene. MELTS does a poor job predicting the stability of amphibole, so its absence (or presence) was not considered in evaluating the success of a simulation. Simulations explored 0.01–0.5 GPa in 0.01 GPa steps and total H₂O concentrations of 0.2–3.0 wt.% while keeping oxygen fugacity fixed to the nickel-nickel oxide buffer (considered appropriate for arc-related magmatic series; Kelley and Cottrell, 2009; Brounce et al., 2014).

A strong constraint on crystallization conditions is the petrographic requirement from Emigrant Gap rocks that plagioclase appeared either before or concurrent with orthopyroxene in the crystallization sequences. The suite lacks either harzburgite or websterite and plagioclase inclusions are observed in orthopyroxene. The intersection of plagioclase-in and orthopyroxene-in appearance curves across pressure and H₂O-concentration space at various extents of crystallization thus maps plausible conditions of crystallization at Emigrant Gap (Fig. 13). Plagioclase would appear before orthopyroxene at pressures less than that curve (above it, as plotted) and plagioclase would follow orthopyroxene at pressures greater than that curve (below it, as plotted).

Pressures of about 0.3 GPa marks the concurrent appearance of plagioclase and orthopyroxene for the average high-Mg arc basalt composition across the range of explored H₂O concentrations, whereas for the average high-Mg basaltic andesite composition, much lower pressures of about 0.15 GPa (or less) would be required for plagioclase to appear coincident with or to precede orthopyroxene (Fig. 13, A11). Primitive magmas as silicic as that average high-Mg basaltic andesite are less common in arcs, so ~0.15 GPa may represent a low-pressure limit for emplacement of the Emigrant Gap complex, and we take 0.15–0.3 GPa as the probable pressure range permissible from the alphaMELTS modeling, depending on how SiO₂-rich the dominant parental magmas were. This is consistent with contact aureole index mineralogy and calculated pressures of equilibration (Table 1; Appendix 1 of this chapter). Comparison to experimental liquid lines of descent and cumulate compositions at lower-crustal and mid- to upper-crustal pressures and various H₂O

conditions confirm that hydrous lower-crustal experiments are a poor match for Emigrant Gap main series rock compositions, and that drier and lower pressure experimental products are more similar (Fig. A10a–c). The Cisco Butte suite's geographic proximity and geologic continuity with the Emigrant Gap main suite are consistent with closely similar emplacement pressures, but the Cisco Butte suite's abundance of igneous amphibole and the calcic compositions of its plagioclase point to higher H₂O concentrations than for main suite magmas, perhaps >2–4 wt.% in the Cisco Butte parents.

Shallow level differentiation of mafic lavas: Emigrant Gap compared to other arc plutonic rocks

The Emigrant Gap complex represents the products of shallow (~0.15–0.3 GPa) differentiation of primitive arc basalts to basaltic andesites distinguished by low H₂O concentrations. Primitive intrusive rocks like Emigrant Gap are uncommon in shallowly exhumed arcs, whereas exposures of deeply exhumed arcs and mafic and ultramafic arc xenoliths indicate that primitive, mantle-derived arc magmas most often differentiate at the high pressures of the deep crust and shallow mantle (>0.8 GPa; DeBari and Coleman, 1989; DeBari and Sleep, 1991; Greene et al., 2006; Jagoutz et al., 2009; Jagoutz, 2010; Jagoutz, 2014). Mafic magmas may differentiate polybarically during ascent (Marxer et al., 2022), but the scarcity of primitive arc intrusions at middle and upper crustal depths (Lewis et al., 2023) nevertheless indicates that early differentiation is predominantly deep.

The shallow pressure of crystallization at Emigrant Gap is not, however, unique. Similar behavior has been found in other Sierra Nevada mafic complexes, where pressures are estimated to be 0.2–0.34 GPa (Sisson et al., 1996; Lewis et al., 2021), or shallower (<0.2 GPa at Stokes Mountain, indicated by its contact metamorphic assemblage; Clemens Knott, 1992). However, the H₂O concentrations inferred for the various Sierra Nevada mafic magmas are appreciably higher than for Emigrant Gap's main series. For example, all of these complexes contain high-An plagioclase and common or abundant amphibole. At Onion Valley, ~6 wt.%

dissolved H₂O was inferred from experimental phase equilibria and the presence of miarolitic cavities, and at Hidden Lakes, ~3 wt.% dissolved H₂O was inferred based on the crystallization sequence (Sisson et al., 1996; Lewis et al., 2021). Similarly, typical Alaskan-type complexes were emplaced at shallow levels with hydrous parental magmas (e.g., Nixon et al., 2024) demonstrated by the widespread presence of igneous amphibole.

Emigrant Gap whole-rock compositions are distinct from both dry (*i.e.*, mid-ocean ridge) and appreciably hydrous differentiation sequences, shown by Figure 13. On the olivine-clinopyroxene-quartz pseudoternary projection of Tormey et al. (1987) and Grove (1993), Emigrant Gap ultramafic cumulates fall on a mixing line between OLIVINE and CLINOPYROXENE components. This differs from the amphibole-rich cumulates common in hydrous mafic arc intrusions that plot in negative QUARTZ space owing to those cumulates' abundant low-SiO₂ igneous amphibole (Sierra Nevada: Sisson et al., 1996; Clemens-Knott, 1992; Lewis et al., 2021; Lewis et al., 2023; Alaskan-Type complexes: Himmelberg and Loney, 1995; Fig. 14). Differences in ASI and TiO₂ concentration of Emigrant Gap rocks relative to hydrous arc cumulates result from the high SiO₂ concentrations in gabbroite owing to the presence of orthopyroxene and abundant intermediate composition plagioclase, and the absence or scarcity of low-SiO₂ phases such as amphibole and abundant Fe-Ti oxides (Fig. A10d–e).

Shallow intrusion of low-H₂O primitive arc magmas: thin crust or an extensional tectonic event?

The other small but widespread upper crustal gabbroic and dioritic intrusions of the Sierra Nevada batholith solidified from somewhat evolved mafic arc magmas with high H₂O concentrations, resulting in high buoyancies and relatively low liquidus temperatures that presumably facilitated ascent through partly molten granitoid source regions and partly solidified granitoid intrusions (Sisson et al., 1996). The non-primitive Mg numbers and low concentrations of compatible trace elements of those hornblende-rich intrusions and associated cumulates indicate that

those wet mafic arc magmas derived from more primitive parents that differentiated deep in the sub-batholithic crust or uppermost mantle (Sisson et al., 1996; Lewis et al., 2023). Emigrant Gap therefore stands out in that primitive arc magmas reached the shallow crust in sufficient abundance to assemble a sizeable mafic-ultramafic intrusion (Fig. 12), and that those magmas had H₂O concentrations at the low end of what is typical for arcs.

Estimates for crustal thickness in the central Sierra Nevada arc throughout its protracted history vary from ~35 km in the Jurassic (the age of the Emigrant Gap complex) to >45–50 km in the Cretaceous as the result of significant shortening and magmatism (Lee et al., 2001; Cao et al., 2015; Lewis et al., 2023). In the northern Sierra Nevada in the vicinity of Emigrant Gap and in the Klamath Mountains, the batholith is thought to be ensimatic, built either on oceanic crust or oceanic crustal terranes accreted to the North American continental margin (Snoke et al., 1982; Saleeby et al., 1989). The folding and steep dips of Emigrant Gap’s wallrocks support the latter interpretation, so although emplacement of Emigrant Gap into thin, intraoceanic arc crust cannot be ruled out entirely, we consider it unlikely.

An alternative is that the Emigrant Gap complex was emplaced during an episode of regional extension in the mid-Jurassic that has been widely documented throughout the Sierra Nevada batholith (Chen and Moore, 1982; Saleeby and Dunne, 2015; Cao et al., 2015). The northern Sierra Nevada Foothills and Coast Range ophiolite belts of California are interpreted to have formed in a forearc or intra-arc extensional basin and then obducted (Saleeby, 1990). The ophiolite belts in the northern Sierra Nevada have igneous ages of 300 Ma, 200 Ma and 160 Ma (Saleeby, 1982) and are intruded by Jurassic peridotite to diorite mafic complexes (Fig. 1b; Saleeby and Sharp, 1980a and 1980b; Saleeby, 1982; Snoke et al., 1982). Thus, widespread mafic arc magmatism closely followed arc-related ophiolite formation during the Jurassic in the Sierra Nevada batholith (Saleeby and Sharp, 1980a and 1980b; Saleeby, 1982; Snoke et al., 1982; Beard and Day, 1987; Beard and Day, 1988; Day and Bickford, 2004; Saleeby, 2011; Saleeby and Dunne, 2015). This suggests that there may have been regional tectonic and stress-field controls during

that portion of the Jurassic that produced both atypically low-H₂O mafic arc magmas through a greater component of decompression melting, and that allowed those relatively dry primitive magmas to ascend and be emplaced in the upper arc crust (Kay and Kay, 1982; Kay and Kay, 1994).

CONCLUSIONS

The ~35 km² ultramafic to dioritic Emigrant Gap complex and an associated granodiorite pluton exposed in the northern Sierra Nevada batholith records a time-integrated intrusive record of the chemical and thermal history of upper crustal differentiation of primitive to evolved arc magmas that probably fed a Jurassic arc volcanic center. The main fractionation series of dunite, minor wehrlite, olivine clinopyroxenite and gabbronorite ± olivine ± biotite is amphibole poor. Ultramafic rocks formed from near-liquidus minerals of primitive magmas accumulating in sub-vertical conduit systems, with substantial melt-rock reaction as replenishing olivine ± clinopyroxene-saturated basaltic melts transited previously emplaced mushes. Crystallization-differentiation of resulting moderately fractionated basaltic to basaltic andesite magmas formed the main gabbronorite pluton. A two-pyroxene diorite intrusion then resulted from the open-system hybridization of the partly or fully solidified gabbronorite with a granodioritic magma that intruded to the north. The granodioritic magma originated at deeper crustal levels having already assimilated metasedimentary rocks. A small-volume amphibole-bearing ultramafic-to-mafic suite at Cisco Butte formed in a process akin to Emigrant Gap's main fractionation suite but with H₂O concentrations of its parental melts sufficiently high to produce widespread igneous amphibole, calcic plagioclase, and amphibole-plagioclase pegmatite matrix in intrusive breccias.

The intrusions crystallized at ~0.15–0.35 GPa, with the earliest crystallization of ultramafic rocks at temperatures $\geq 1115^{\circ}\text{C}$. The estimated $f\text{O}_2$ and water concentration of parental magmas of the main suite is $\geq \Delta\text{FMQ} + 1$ and ~0.5–2 wt.% H₂O, respectively. Trace element chemistry and geologic setting confirm that the Emigrant Gap complex formed in an arc setting during growth of the Mesozoic Sierra

Nevada batholith. Emigrant Gap's main suite is atypical for the Sierra Nevada batholith in its relatively dry and primitive character, reminiscent of arc tholeiites. Although the entire composite intrusive complex, including diorite and granodiorite, can be classified as calc-alkaline, this is a consequence of appreciable hybridism between gabbro (and other mafic to ultramafic cumulates) with an adjacent and slightly younger granodioritic intrusion derived in part from older crustal rocks. This open-system behavior led to the seeming paradox of a relatively dry mafic arc magmatic system that nevertheless produced a calc-alkaline rock series, reminiscent of Kuno's (1950, 1959) original open-system hypothesis for hypersthenic/calc-alkaline arc magmas. An extensional event during the Jurassic, or possibly relatively thin (oceanic?) crust in the Northern Sierra Nevada arc, are potential reasons for the unique character of the intrusive complex preserved at Emigrant Gap.

ACKNOWLEDGEMENTS

The authors thank Rick Conrey for whole-rock geochemical analyses, Chi Ma and Ted Present for analytical assistance, and Pond Sirorattanakul and Madeline Lewis for assistance in the field. Thanks to Mark Hampton of PG&E and Izaya Lewis, Michele Woods and Ernie Johnson of the U.S. Forest Service for assistance with permission for sampling. We are grateful to Shelly Covert, Ember Amador, and the California Heritage Indigenous Research Project for conversations about conducting research on the land at Emigrant Gap, which is the Ancestral Homeland of the Nisenan Tribe. This research was supported by NSF Grant EAR 2105371 awarded to C. Bucholz and by the USGS Volcano Hazards Program.

DATA AVAILABILITY STATEMENT

All geochemical data presented are available in the Supplementary Data File, as well as in the EarthChem Library doi: 10.60520/IEDA/113590. Natural samples are available at the California Institute of Technology.

REFERENCES

Arai, S. and Yurimoto, H., 1994, Podiform chromitites of the Tari-Misaka ultramafic complex, southwestern Japan, as mantle–melt interaction products. *Economic Geology*, 89, 1279–1288. doi:10.2113/gsecongeo.89.6.1279

Beard, J. S. and Day, H. W., 1987, Petrology and emplacement of reversely zoned gabbro–diorite plutons in the smartville complex, Northern California. *Journal of Petrology*, 29(5), 965–995. <https://doi.org/10.1093/petrology/29.5.965>

Beard, J. S. and Day, H. W., 1988, Petrology and emplacement of reversely zoned gabbro–diorite plutons in the Smartville complex, northern California. *Journal of Petrology*, 29, 965–995.

Beattie, P., 1993, The effect of partial melting of spinel peridotite on uranium series disequilibria: constraints from partitioning studies. *Earth and Planetary Science Letters*, 177, 379–391. doi:10.1016/0012-821X(93)90091-M

Blatter, D. L., Sisson, T. W. and Hankins, W. B., 2013, Crystallization of oxidized, moderately hydrous arc basalt at mid- to lower-crustal pressures: implications for andesite genesis. *Contributions to Mineralogy and Petrology*, 166, 861–886. <https://doi.org/10.1007/s00510-013-0920-3>

Blundy, J., 2022, Chemical differentiation by mineralogical buffering in crustal hot zones. *Journal of Petrology*, 63, 1–36. <https://doi.org/10.1093/petrology/egac054>

Bouilhol, P., Schmidt, M. W. and Burg, J. P., 2015, Magma transfer and evolution in channels within the arc crust: The pyroxenitic feeder pipes of Sapat (Kohistan, Pakistan). *Journal of Petrology*, 56(7), 1309–1342. <https://doi.org/10.1093/petrology/egv037>

Boulanger, M. and France, L., 2023, Cumulate formation and melt extraction from mush-dominated magma reservoirs: The melt flush process

exemplified at mid-ocean ridges. *Journal of Petrology*, 64, 1–20.
<https://doi.org/10.1093/petrology/egad005>

Brady, J. B., 2019, Igneous and metamorphic petrology, interactive diagrams, investigative tools, images, and information for students and teachers of petrology. <https://www.science.smith.edu/~jbrady/petrology/index.php>

Brounce, M. N., Kelley, K. A. and Cottrell, E., 2014, Variations in $\text{Fe}^{3+}/\sum\text{Fe}$ of Mariana arc basalts and mantle wedge fO_2 . *Journal of Petrology*, 55(12), 2513–2536. <https://doi.org/10.1093/petrology/egu065>

Bucholz, C. E. and Kelemen, P. B., 2019, Oxygen fugacity at the base of the Talkeetna arc, Alaska. *Contributions to Mineralogy and Petrology*, 174, 79. <https://doi.org/10.1007/s00410-019-1609-z>

Bucholz, C. E. and Spencer, C. J., 2019, Strongly peraluminous granites across the Archean-Proterozoic transition. *Journal of Petrology*, 60(7), 1299–1348. doi:10.1093/petrology/egz033

Bushey, J. C., Snock, A. W., Barnes, C. G., & Frost, C. D., 2006, Geology of the Bear Mountain intrusive complex, Klamath Mountains, California. Special Paper of the Geological Society of America, 410(303), 287–315.
[https://doi.org/10.1130/2006.2410\(14\)](https://doi.org/10.1130/2006.2410(14))

Cao, W., Paterson, S., Memeti, V., Mundil, R., Anderson, J. L. and Schmidt, K., 2015, Tracking paleodeformation fields in the Mesozoic central Sierra Nevada arc: Implications for intra-arc cyclic deformation and arc tempos. *Lithosphere*, 7(3), 296–320. doi:10.1130/L389.1

Cecil, M. R., Rotberg, G. L., Ducea, M. N., Saleeby, J. B., & Gehrels, G. E., 2012, Magmatic growth and batholithic root development in the northern Sierra Nevada, California. *Geosphere*, 8(3), 592–606.
<https://doi.org/10.1130/GES00729.1>

Chen, J. H. and Moore, J. G., 1982, Uranium-lead isotopic ages from the Sierra Nevada batholith, California. *Journal of Geophysical Research*, 87, 4761–4784. doi:10.1029/JB087iB06p04761

Chin, E. J., Shimizu, K., Bybee, G. M. and Erdman, M. E., 2018, On the development of the calc-alkaline and tholeiitic magma series: A deep crustal cumulate perspective. *Earth and Planetary Science Letters*, 482, 277–287. <https://doi.org/10.1016/j.epsl.2017.11.016>

Clemens-Knott, D., 1992, Geologic and isotopic investigations of the early Cretaceous Sierra Nevada batholith, Tulare Co., CA, and the Ivrea Zone, NW Italian Alps: Examples of interaction between mantle-derived magma and continental crust. PhD Thesis, California Institute of Technology.

Clemens-Knott, D. and Saleeby, J. B., 1999, Impinging ring dike complexes in the Sierra Nevada batholith, California: Roots of the Early Cretaceous volcanic arc. *Geological Society of America Bulletin*, 111(4), 484–496.

Clemens-Knott, D. and Gevedon, M., 2025, Zircon U-Pb-Hf isotope evidence from gabbros of the Summit Igneous Complex for a latest Jurassic rift through the southern Sierra Nevada arc crust, California, USA. in: Riggs, N., Putirka, K., Wakabayashi, J. (Eds.), *The Virtue of Fieldwork in Volanology, Sedimentology, Structural Geology, and Tectonics—Celebrating the Career of Cathy Busby*. Geological Society of America Special Paper, 1–34. [https://doi.org/https://doi.org/10/1130/2025.2563\(08\)](https://doi.org/https://doi.org/10/1130/2025.2563(08))

Conrey, R. M., Bailey, D. G., Singer, J. W., Wagoner, L. J., Parfitt, B., Hay, J., Keh, O., Chang, Z. and Huang, S., 2023, Combined use of multiple external and internal standards in LA-ICP-MS analysis of bulk geological samples using lithium borate fused glass. *Geochemistry: Exploration, Environment, Analysis*, 23(2): geochem2023-001.

Day, H. W. and Bickford, M. E. (2004) Tectonic setting of the Jurassic Smartville and Slate Creek complexes, northern Sierra Nevada, California. *Geological Society of America Bulletin*, 116, 1515–1528. doi:10.1130/B25416.1

DeBari, S. M., Kay, S. M., and Kay, R. W. (1987) Ultramafic xenoliths from Adagdak volcano, Aleutian Islands, Alaska: Deformed igneous cumulates from the Moho of an island arc, *Journal of Geology*, 95, 329-341.

DeBari, S. M. and Coleman, R. G., 1989, Examination of the deep levels of an island arc: evidence from the Tonsina ultramafic-mafic assemblage, Tonsina, Alaska. *Journal of Geophysical Research*, 94(B4), 4373–4391.

DeBari, S. M. and Sleep, N. H., 1991, High-Mg, low-Al bulk compositions for the Talkeetna island arc, Alaska: Implications for primary magmas and the nature of arc crust. *Geological Society of America Bulletin*, 103, 37–47.

Evernden, J. F. and Kistler, R. W., 1970, Chronology of emplacement of Mesozoic batholithic complexes in California and western Nevada. U.S. Geological Survey Professional Paper 623, 26p.

Feig, S. T., Koepke, J. and Snow, J. E., 2006, Effect of water on tholeiitic basalt phase equilibria: An experimental study under oxidizing conditions. *Contributions to Mineralogy and Petrology*, 152, 611–638.
doi:10.1007/s00410-006-0123-2

Feig, S. T., Koepke, J. and Snow, J. E., 2010, Effect of oxygen fugacity and water on phase equilibria of a hydrous tholeiitic basalt. *Contributions to Mineralogy and Petrology*, 160, 551–568. doi:10.1007/s00410-010-0493-3

Frost, R. B., Barnes, C. G., Collins, W. J., Arculus, R. J., Ellis, D. J. and Frost, C. D., 2001, A geochemical classification for granitic rocks. *Journal of Petrology*, 42(11), 2033–2048.

Frost, T. P., 1987, Sample localities, radiometric ages, descriptions, and major- and trace-element abundances of Late Jurassic mafic plutonic rocks, eastern Sierra Nevada, California. U.S. Geological Survey Open File Report, 87–484, 33 p.

Girty, G. H., Yoshinobu, A. S., Wracher, M. D., Girty, M. S., Bryan, K. A., Skinner, J. E., McNulty, B. A., Bracchi, K. A., Harwood, D. S. and Hanson, R. E., 1993, U-Pb zircon geochronology of the Emigrant Gap composite pluton, northern Sierra Nevada, California: Implications for the Nevadan Orogeny, in G. Dunn & K. McDougall (Eds.), Mesozoic Paleogeography of the Western United States-II, Pacific Section SEPM, Book 71, 323–332.

Gordeychik, B., Churikova, T., Shea, T., Kronz, A., Simakin, A. and Wörner, G., 2020, Fo and Ni relations in olivine differentiate between crystallization and diffusion trends. *Journal of Petrology*, 61(9), egaa083. doi:10.1093/petrology/egaa083

Greene, A. R., DeBari, S. M., Kelemen, P. B., Blusztajn, J. and Clift, P. D., 2006, A detailed geochemical study of island arc crust: The Talkeetna arc section, south-central Alaska. *Journal of Petrology*, 47(6), 1051–1093.

Grove, T. L., 1993, Corrections to expressions for calculating mineral components in “Origin of calc-alkaline series lavas at Medicine Lake Volcano by fractionation, assimilation, and Mixing” and “Experimental petrology of normal MORB near the Kane Fracture Zone: 22°–25°N, mid-Atlantic ridge”. *Contributions to Mineralogy and Petrology*, 114, 422–424.

Grove, T. L., Gerlach, D. C., Sando, T. W., 1982, Origin of calc-alkaline series lavas at Medicine Lake volcano by fractionation, assimilation and mixing. *Contributions to Mineralogy and Petrology*, 80, 160–182.

Grove, T. L., Kinzler, R. J. and Bryan, W. B., 1992, Fractionation of mid-ocean ridge basalt (MORB), in Morgan, J.P., Blackman, D.K. and Sinton, J.M., eds., *Mantle Flow and Melt Generation at Mid-Ocean Ridges*, Geophysical Monograph Series 71, 281–310.

Grove, T. L., Till, C. B. and Krawczynski, M. J., 2012, The role of H₂O in subduction zone magmatism. *Annual Reviews in Earth and Planetary Science*, 40, 413–39. doi:10.1146/annurev-earth-042711-105310

Gualda, G. A. R., Ghiorso, M. S., Lemons, R. V. and Carley, T. L., 2012, Rhyolite-MELTS: A modified calibration of MELTS optimized for silica-rich, fluid-bearing magmatic systems. *Journal of Petrology*, 53(5), 875–890. doi:10.1093/petrology/egr080

Guo, L., Jagoutz, O., Shinevar, W. J. and Zhang, H. F., 2020, Formation and composition of the Late Cretaceous Gangdese arc lower crust in southern Tibet. *Contributions to Mineralogy and Petrology*, 175, 58.

Hanson, R. E., Saleeby, J. B. and Schweikert, R. A., 1988, Composite Devonian island-arc batholith in the northern Sierra Nevada, California. *Geological Society of America Bulletin*, 100(3), 446–457.

Harwood, D. S., Fisher, G. Reid, J., & Waugh, B. J., 1995, Geologic map of the Duncan Peak and southern part of the Cisco Grove 7-1/2' quadrangles, Placer and Nevada Counties, California.

Harwood., D. S., Fisher, G. R. and Hanson, R. E., 2014, Geologic map of part of eastern Placer County, northern Sierra Nevada, California. California Geological Survey, Map Sheet 61, scale 1:48,000.

Hill, C.A., 1994, The petrology and geochemistry of the Middle Jurassic Black Buttes quartz monzodiorite, Sierra Nevada, California. M.S. Thesis, San Diego State University. 46 p.

Himmelberg, G. R., & Loney, R. A., 1995, Characteristics and petrogenesis of Alaskan-type ultramafic-mafic intrusions, southeastern Alaska. US Geological Survey Professional Paper 1564, 43 p.

Holland, T. and Blundy, J., 1994, Non-ideal interactions in calcic amphiboles and their bearing on amphibole-plagioclase thermometry. *Contributions to Mineralogy and Petrology*, 116, 433–447.

<https://doi.org/10.1007/BF00310910>

Hoover, J. D., 1989, The chilled marginal gabbro and other contact rocks of the Skaergaard intrusion. *Journal of Petrology*, 30, 441–476.
doi:10.1093/petrology/30.2.441

Irvine, T. N., 1974, Petrology of the Duke Island Ultramafic Complex Southeastern Alaska. In *GSA Memoirs* (Vol. 138).
<https://doi.org/https://doi.org/10.1130/MEM138>

Irvine, T. N., 1977, Origin of chromitite layers in the Muskox intrusion and other stratiform intrusions: A new interpretation. *Geology*, 5, 273–277.

Irwin, W. P. and Wooden, J. L., 2001, Map showing plutons and accreted terranes of the Sierra Nevada, California with a tabulation of U/Pb isotopic ages. USGS Open-File Report, 01-229, scale 1:1,000,000.

Jagoutz, O. E., 2010, Construction of the granitoid crust of an island arc. Part II: a quantitative petrogenetic model. *Contributions to Mineralogy and Petrology*, 160, 339–381. doi:10.1007/s00410-009-0482-6

Jagoutz, O. E., 2014, Arc crustal differentiation mechanisms. *Earth and Planetary Science Letters*, 396, 267–277.

Jagoutz, O., Müntener, O., Burg, J. P., Ulmer, P., & Jagoutz, E., 2006, Lower continental crust formation through focused flow in km-scale melt conduits: The zoned ultramafic bodies of the Chilas Complex in the Kohistan island arc (NW Pakistan). *Earth and Planetary Science Letters*, 242(3–4), 320–342. <https://doi.org/10.1016/j.epsl.2005.12.005>

Jagoutz, O. E., Burg, J. P., Hussain, S., Dawood, H., Pettke, T., Ilzuka, T. and Maruyama, S., 2009, Construction of the granitoid crust of an island arc. Part I: geochronological and geochemical constraints from the plutonic Kohistan (NW Pakistan). *Contributions to Mineralogy and Petrology*, 158, 739–755. doi:10.1007/s00410-009-0408-3

Jagoutz, O. and Schmidt, M. W., 2012, The formation and bulk composition of modern juvenile continental crust: The Kohistan arc. *Chemical Geology*, 298–299, 79–96. doi:10.1016/j.chemgeo.2011.10.022

James, O. B., 1971, Origin and emplacement of the ultramafic rocks of the emigrant gap area, California. *Journal of Petrology*, 12(3), 523–560. <https://doi.org/10.1093/petrology/12.3.523>

Janiszewski, H. A., Abers, G. A., Shillington, D. J. and Calkins, J. A., 2013, Crustal structure along the Aleutian island arc: New insights from receiver functions constrained by active-source data. *Geochemistry Geophysics Geosystems*, 14(8), 2977–2992. Doi:10.1002/ggge.20211

Jennings, C. W., with modifications by, Gutierrez, C., Bryant, W., Saucedo, G. and Wills, C., 2010, Geologic map of California: California Geological Survey, Geologic Data Map No. 2, scale 1:750,000.

John, D. A., Schweickert, R. A. and Robinson, A. C., 1994, Granitic rock in the Triassic-Jurassic magmatic arc of western Nevada and eastern California. USGS Open-File Report, 94-148, 1-61.

Kay, S. M. and Kay, R. W., 1982, Tectonic controls on tholeiitic and calc-alkaline magmatism in the Aleutian arc. *Journal of Geophysical Research*, 87(B5), 4051-4072.

Kay, S. M., Kay, R. W., Brueckner, H. K., & Rubenstein, J. L., 1983, Tholeiitic Aleutian Arc Plutonism: The Finger Bay Pluton, Adak, Alaska. *Contributions to Mineralogy and Petrology*, 99-116.

Kay, S. M. and Kay, R. W., 1985, Role of crystal cumulates and the oceanic crust in the formation of the lower crust of the Aleutian arc. *Geology*, 13, 461-464.

Kay, S. M. and Kay, R. W., 1994, Aleutian magmatism in space and time, in, Plafker, G. and Berg, H.C., eds., *The Geology of Alaska*: Boulder, Colorado, Geological Society of America, *The Geology of North America*, G-1.

Kays, M. A., and McBirney, A. R., 1982, Origin of the picrite blocks in the marginal border group of the Skaergaard intrusion, East Greenland. *Geochimica et Cosmochimica Acta*, 46, 23-30. doi: 10.1016/0016-7037(82)90287-3

Kelemen, P. B., and Ghiorso, M. S., 1986, Assimilation of peridotite in zoned calc-alkaline plutonic complexes: evidence from the Big Jim complex, Washington Cascades. *Contributions to Mineralogy and Petrology*, 94, 12-28.

Kelemen, P. B. and Dick, H. J. B., 1995, Focused melt flow and localized deformation in the upper mantle: juxtaposition of replacive dunite and ductile shear zones in the Josephine peridotite, SW Oregon. *Journal of Geophysical Research*, 100(B1), 423-438.
<https://doi.org/10.1029/94JB02063>

Kelemen, P. B., Koga, K. and Shimizu, N., 1997, Geochemistry of gabbro sills in the crust-mantle transition zone of the Oman ophiolite: Implications for the origin of the oceanic lower crust. *Earth and Planetary Science Letters*, 146(3–4), 475–488. [https://doi.org/10.1016/s0012-821x\(96\)00235-x](https://doi.org/10.1016/s0012-821x(96)00235-x)

Kelley, K. A. and Cottrell, E., 2009, Water and the oxidation state of subduction zone magmas. *Science*, 325(5940), 605–607. doi:10.1126/science.1174156

Krawczynski, M. J., Grove, T. L. and Behrens, H., 2012, Amphibole stability in primitive arc magmas: Effects of temperature, H₂O content, and oxygen fugacity. *Contributions to Mineralogy and Petrology*, 164, 317–339. doi:10.1007/s00410-012-0740-x

Kulow, M. J., 1996, Geology, petrology, age, and intrusive relations of Cretaceous plutons in the Donner Lake-Cisco Grove area, northern Sierra Nevada, California. MS Thesis, Texas Christian University, 123 p.

Kulow, M. J., Hanson, R. E. and Girty, G. H., 1997, The Big Bend shear zone: Early Cretaceous ductile deformation associated with pluton emplacement in the Northern Sierra terrane, California, in Girty, G.H., Hanson, R.E. and Cooper, J.D., eds., *Geology of the Western Cordillera: Perspectives from Undergraduate Research*, Society for Sedimentary Geology, Pacific Section, 82, 79–90.

Kuno, H. (1950) Petrology of Hakone volcano and the adjacent areas, Japan. *Bulletin of the Geological Society of America*, 61, 957–1020.

Kuno, H. (1959) Origin of Cenozoic petrographic provinces of Japan and surrounding areas. *Bulletin of Volcanology*, 20, 37–76.

Lee, C.-T., Rudnick, R. L. and Brimhall Jr., G. H., 2001, Deep lithospheric dynamics beneath the Sierra Nevada during the Mesozoic and Cenozoic as inferred from xenolith petrology. *Geochemistry, Geophysics, Geosystems*, 2(12), doi:10.1029/2001GC000152

Leuchter, E. R., 2022, Formation and emplacement of an ultramafic plutonic complex in continental crust constrained from structural, thermal and

rheological properties of contact aureole: A case study from the Emigrant Gap complex in California. MS Thesis, University of Nevada, Reno.

Lewis, M.J., Bucholz, C.E. and Jagoutz, O.E., 2021, Evidence for polybaric fractional crystallization in a continental arc: Hidden Lakes mafic complex, Sierra Nevada batholith, California. Contributions to Mineralogy and Petrology, 176(11), 90. <https://doi.org/10.1007/s00410-021-01844-y>

Lewis, M. J., Ryan-Davis, J. R. and Bucholz, C. E., 2023, Mafic intrusions record mantle inputs and crustal thickness in the eastern Sierra Nevada batholith, California, USA. Geological Society of America Bulletin, 136 (56), 1808–1826. <https://doi.org/10.1130/B36646.1>

Li, J., Kornprobst, J., Vielzeuf, D. and Fabriès, J., 1995, An improved experimental calibration of the olivine-spinel geothermometer. Chinese Journal of Geochemistry, 14(1), 68–77.

Lissenberg, C.J. and Dick, H.J.B., 2008, Melt-rock reaction in the lower oceanic crust and its implications for the genesis of mid-ocean ridge basalt. Earth and Planetary Science Letters, 271, 311–325.

<https://doi.org/10.1016/j.epsl.2008.04.023>

Marxer, F., Ulmer, P. and Müntener, O., 2022, Polybaric fractional crystallization of arc magmas: an experimental study simulating trans-crustal magmatic systems. Contributions to Mineralogy and Petrology, 177, 3.

<https://doi.org/10.1007/s00410-021-01856-8>

Matzen, A. K., Baker, M. B., Beckett, J. R. and Stolper, E. M., 2013, The temperature and pressure dependence of nickel partitioning between olivine and silicate melt. Journal of Petrology, 54(12), 2521–2545.
doi:10.1093/petrology/egt055

Matzen, A. K., Baker, M. B., Beckett, J. R., Wood, B. J. and Stolper, E. M., 2017, The effect of liquid composition on the partitioning of Ni between olivine and silicate melt. Contributions to Mineralogy and Petrology, 172, 3.
doi:10.1007/s00410-016-1319-8

McBirney, A. R., 1984, Igneous Petrology. Freeman, Cooper & Company, San Francisco.

McBirney, A. R., 1998, The Skaergaard layered series. Part V. Included trace elements. *Journal of Petrology*, 39, 255–276. doi: 10.1093/petroj/39.2.255

Molina, J. F., Cambeses, A., Moreno, J. A., Morales, I., Montero, P. and Bea, F., 2021, A reassessment of the amphibole-plagioclase NaSi-CaAl exchange thermometer with applications to igneous and high-grade metamorphic rocks. *American Mineralogist*, 106, 782–800. <https://doi.org/10.2138/am-2021-7400>

Murray, C. G., 1972, Zoned Ultramafic complexes of the alaskan type: Feeder pipes of andesitic volcanoes. *Memoir of the Geological Society of America*, 132(1967), 313–335. <https://doi.org/10.1130/MEM132-p313>

Mutch, E. J. F., Blundy, J. D., Tattich, B. C., Cooper, F. J. and Brooker, R. A., 2016, An experimental study of amphibole stability in low-pressure granitic magmas and a revised Al-in-hornblende geobarometer. *Contributions to Mineralogy and Petrology*, 171, 85. doi:10.1007/s00410-016-1298-9

Nandedkar, R. H., Ulmer, P. and Müntener, O., 2014, Fractional crystallization of primitive, hydrous arc magmas: An experimental study at 0.7 GPa. *Contributions to Mineralogy and Petrology*, 167, 1015. doi:10.1007/s00410-014-1015-5

Nixon, G.T., Manor, M.J., Jackson-Brown, S., Scoates, J.S. and Ames, D.E., 2015, Magmatic Ni-Cu-PGE sulphide deposits at convergent margins. In: Ames, D.E., Houlé, M.G. (eds) *Targeted Geoscience Initiative 4: Canadian Nickel-Copper-Platinum Group Elements-Chromium Ore Systems—Fertility, Pathfinders, New and Revised Models*. Geological Survey of Canada Open File 7856, 17–34.

Nixon, G.T., Manor, M.J., Scoates, J.S., Spence, D.W. and Milidragovic, D., 2024, Mineralogical constraints on magma storage conditions in ultramafic arc cumulates and the nature and role of cryptic fugitive melts:

Tulameen Alaskan-type intrusion, North American Cordillera. Contributions to Mineralogy and Petrology, 179, 103.
<https://doi.org/10.1007/s00410-024-02181-6>

Nye, C. L. and Reid, M., 1986, Geochemistry of primary and least fractionated lavas from Okmok volcano, central Aleutians: Implications for arc magmagenesis. *Journal of Geophysical Research*, 91(B10), 10271–10287.
<https://doi.org/10.1029/JB091iB10p10271>

Otamendi, J. E., Ducea, M. N. and Bergantz, G. W., 2012, Geological, petrological and geochemical evidence for progressive construction of an arc crustal section, Sierra de Valle Fértil, Famatinian Arc, Argentina. *Journal of Petrology*, 53(4), 761–800. doi:10.1093/petrology/egr079

Paster, T. P., Schauwcker, D. S., Haskin, L. A., 1974, The behavior of some trace elements during solidification of the Skaergaard layered series. *Geochimica et Cosmochimica Acta*, 38, 1549–1577. doi: 10.1016/0016-7037(74)90174-4

Pattison, D. R. M., 1992, Stability of andalusite and sillimanite and the Al₂SiO₅ triple point: constraints from the Ballachulish Aureole, Scotland. *The Journal of Geology*, 100, 423–446.

Payot, B. D., Arai, S., Tamayo Jr., R. A., Yumul Jr., G. P., 2013, Textural evidence for the chromite-oversaturated character of the melt involved in podiform chromitite formation. *Resource Geology*, 63(3), 313–319.
doi:10.1111/rge.12011

Pichavant, M. and Macdonald, R., 2007, Crystallization of primitive basaltic magmas at crustal pressures and genesis of the calc-alkaline igneous suite: Experimental evidence from St Vincent, Lesser Antilles arc. Contributions to Mineralogy and Petrology, 157, 535–558. doi:10.1007/s00410-007-0208-6

Putirka, K. D., 2008, Thermometers and barometers for volcanic systems. *Reviews in Mineralogy and Geochemistry*, 69, 61–120.
doi:10.2138/rmg.2008.69.3

Rasmussen, D. J., Plank, T. A., Roman, D. C. and Zimmer, M. M., 2022, Science. Magmatic water content controls the pre-eruptive depth of arc magmas. *Science*, 375(6585), 1169–1172. doi:10.1126/science.abm5174

Rezeau, H., Klein, B. Z. and Jagoutz, O., 2021, Mixing dry and wet magmas in the lower crust of a continental arc: New petrological insights from the Bear Valley Intrusive Suite, southern Sierra Nevada, California. *Contributions to Mineralogy and Petrology*, 176, 73. <https://doi.org/10.1007/s00410-021-01832-2>

Rowe, M. C., Kent, A. J. R. and Nielsen, R. L., 2009, Subduction influence on oxygen fugacity and trace and volatile elements in basalts across the Cascade volcanic arc. *Journal of Petrology*, 50(1), 61–69. <https://doi.org/10.1093/petrology/egn072>

Ryan-Davis, J., Bucholz, C.E. and Sisson, T.W., 2024, Emigrant Gap complex whole-rock major and trace element chemistry. *Interdisciplinary Earth Data Alliance (IEDA)*. doi: 10.60520/IEDA/113590

Saleeby, J. B. (1982) Polygenetic ophiolite belt of the California Sierra Nevada: Geochronological and tectonostratigraphic development. *Journal of Geophysical Research*, 87(B3), 1803–1824.

Saleeby, J. B. (1990) Geochronological and tectonostratigraphic framework of Sierran-Klamath ophiolitic assemblages, in Harwood, D.S. and Miller, M.M., eds., *Paleogeographic Relations: Sierra Nevada, Klamath Mountains, and Related Terranes*: Geological Society of America Special Paper 255, 93–114. <https://doi.org/10.1130/SPE255-p93>

Saleeby, J. (2011) Geochemical mapping of the Kings-Kaweah ophiolite belt, California—Evidence for progressive mélange formation in a large offset transform-subduction initiation environment, in Wakabayashi, J., and Dilek, Y., eds., *Mélanges: processes of formation and societal significance*. Geological Society of America Special Paper 480, 31–73, doi:10.1130/2011.2480(02)

Saleeby, J., & Sharp, W. (1980a) Chronology of the structural and petrologic development of the southwest Sierra Nevada foothills, California: Summary. *Geological Society of America Bulletin*, Part 1, 91, 317–320.

Saleeby, J., & Sharp, W. (1980b) Chronology of the structural and petrologic development of the southwest Sierra Nevada foothills, California. *Geological Society of America Bulletin*, Part 2, 91(6), 1416–1535.

Saleeby, J. B., Shaw, H. F., Niemeyer, S., Moores, E.M. and Edelman, S.H., 1989, U/Pb, Sm/Nd and Rb/Sr geochronological and isotopic study of Northern Sierra Nevada ophiolitic assemblages, California. *Contributions to Mineralogy and Petrology*, 102, 205–220.

Saleeby, J. and Dunne, G., 2015, Temporal and tectonic relations of early Mesozoic arc magmatism, southern Sierra Nevada, California. *Geological Society of America Special Paper* 513, 223–268.
doi:10.1130/2015.2513(05)

Saucedo, J. G. and Wagner, D. L., 1992, Geologic map of the chico quadrangle, California. California Division of Mines and Geology, Map No. 7A, scale 1:125,000.

Schmidt, M. W. and Jagoutz, O. (2017) The global systematics of primitive arc melts. *Geochemistry, Geophysics, Geosystems*, 18, 2817–2854.
doi:10.1002/2016GC006699

Schweickert, R. A., Bogen, N. L., Girty, G. H., Hanson, R. E., & Merguerian, C., 1984, Timing and structural expression of the Nevadan orogeny, Sierra Nevada, California: Discussion. *Bulletin of the Geological Society of America*, 95, 967–979.

Shejwalkar, A. and Coogan, L. A., 2013, Experimental calibration of the roles of temperature and composition in the Ca-in-olivine geothermometer at 1.0 MPa. *Lithos*, 177, 54–60. <http://dx.doi.org/10.1016/j.lithos.2013.06.013>

Sisson, T. W. and Grove, T. L., 1993, Experimental investigations of the role of H₂O in calc-alkaline differentiation and subduction zone magmatism. *Contributions to Mineralogy and Petrology*, 113, 143–166.

Sisson, T. W. and Grove, T. L., 1993, Temperatures and H₂O contents of low-MgO high-alumina basalts. *Contributions to Mineralogy and Petrology*, 113, 167–184.

Sisson, T. W., Grove, T. L. and Coleman, D. S., 1996, Hornblende gabbro sill complex at Onion Valley, California, and a mixing origin for the Sierra Nevada batholith. *Contributions to Mineralogy and Petrology*, 126, 81–108.

Sisson, T. W. and Bronto, S., 1998, Evidence for pressure-release melting beneath magmatic arcs from basalt at Galunggung, Indonesia. *Nature*, 391, 883–886.

Sisson, T. W., Ratajeski, K., Hankins, W. B. and Glazner, A. F., 2005, Voluminous granitic magmas from common basaltic sources. *Contributions to Mineralogy and Petrology*, 148, 635–661. doi:10.1007/s00410-004-0632-9

Sisson, T. W. and Moore, J. G., 2010, Osa Creek gabbro-granite ring complex, Sierra Nevada, CA, by degassing-driven subsidence of mafic-magmatic sheets. *American Geophysical Union, Fall Meeting 2010*, V11C-2294.

Skinner, J. E., 1992, Geochemical, geochronological and petrological characteristics of the quartz monzonite unit of the Emigrant Gap composite pluton, northern Sierra Nevada, California. BS Thesis, San Diego State University. 27 p.

Smith, P. M. and Asimow, P. D., 2005, Adiabat_1ph: A new public front-end to the MELTS, pMELTS, and pHMELTS models. *Geochemistry Geophysics Geosystems*, 6(1), Q02004. doi:10.1029/2004GC000816

Snoke, A. W., Sharp, W. D., Wright, J. E., & Saleeby, J. B., 1982, Significance of mid- Mesozoic peridotitic to dioritic intrusive complexes, Klamath mountains—western Sierra Nevada, California. *Geology*, 10(3), 160–166.
[https://doi.org/10.1130/0091-7613\(1982\)10<160:SOMPTD>2.0.CO;2](https://doi.org/10.1130/0091-7613(1982)10<160:SOMPTD>2.0.CO;2)

Snoke, A. W., Quick, J. E., & Bowman, H. R., 1981, Bear Mountain igneous complex, Klamath mountains, California: An ultrabasic to silicic cale-

alkaline suite. *Journal of Petrology*, 22(4), 501–552.
<https://doi.org/10.1093/petrology/22.4.501>

Sosa, E. S., Bucholz, C. E., Barickman, M. H., VanTongeren, J. A., Setera, J. B., Kay, S. M. and Kay, R. W., 2023, Petrology and geochemistry of Adak Island plutonic xenoliths: Implications for primitive magma generation and crustal differentiation in the Aleutian Island arc. *Journal of Petrology*, 64(10), egad073. <https://doi.org/10.1093/petrology/egad073>

Springer, R. K. (1980a). Geology of the Pine Hill intrusive complex, a layered gabbroic body in the western Sierra Nevada foothills, California: Summary. *Geological Society of America Bulletin*, Part 1, 91, 381–385.

Springer, R. K. (1980b). Geology of the Pine Hill intrusive complex, a layered gabbroic body in the western Sierra Nevada foothills, California. *Geological Society of America Bulletin*, Part II, 91, 1536–1626.

Sun, S. S. and McDonough, W. F., 1989, Geochemical and isotopic systematics of oceanic basalts: Implications for mantle composition and processes. *Geological Society, London, Special Publications*, 42, 313–345.
doi:10.1144/GSL.SP.1989.042.01.19

Takahashi, E., 1978, Petrological model of the crust and upper mantle of the Japanese island arcs. *Bulletin of Volcanology*, 41, 529–547.

Till, C. B., 2017, A review and update of mantle thermobarometry for primitive arc magmas. *American Mineralogist*, 102, 931–947.

Tilley, C. E. (1950). Some aspects of magmatic evolution. *Quarterly Journal of the Geological Society of London*, 106, 37–61. doi: 10.1144/GSL.JGS.1950.106.01-04.04

Tormey, D. R., Grove, T. L. and Bryan, W. B., 1987, Experimental petrology of normal MORB near the Kane fracture zone: 22°-25° N, mid-Atlantic ridge. *Contributions to Mineralogy and Petrology*, 96, 121–139.
<https://doi.org/10.1007/BF00375227>

Turner, S. J. and Langmuir, C. H., 2015, The global chemical systematics of arc front stratovolcanoes: Evaluating the role of crustal processes. *Earth and*

Planetary Science Letters, 422, 182–193.
<http://dx.doi.org/10.1016/j.epsl/2015.03.056>

Ulmer, P., Kaegi, R. and Müntener, O., 2018, Experimentally derived intermediate to silica-rich arc magmas by fractional and equilibrium crystallization at 1.0 GPa: An evaluation of phase relationships, compositions, liquid lines of descent and oxygen fugacity. *Journal of Petrology*, 59(1), 11–58. doi:10.1093/petrology/egy017

Villiger, S., Ulmer, P., Müntener, O. and Thompson, A. B., 2004, The liquid line of descent of anhydrous, mantle-derived, tholeiitic liquids by fractional and equilibrium crystallization—an experimental study at 1.0 GPa. *Journal of Petrology*, 45(12), 2369–2388. doi:10.1093/petrology/egh042

Villiger, S., Ulmer, P. and Müntener, O., 2007, Equilibrium and fractional crystallization experiments at 0.7 GPa: The effect of pressure on phase relations and liquid compositions of tholeiitic magmas. *Journal of Petrology*, 48(1), 159–184. doi:10.1093/petrology/egl058

Walker, B. A., Bergantz, G. W., Otamendi, J. E., Ducea, M. N. and Cristofolini, E. A., 2015, A MASH zone revealed: The mafic complex of the Sierra Valle Fértil. *Journal of Petrology*, 56(9), 1863–1896.

Warr, L.N., 2021, IMA-CNMNC approved mineral symbols. *Mineralogical Magazine*, 85(3), 291–320. doi:10.1180/mgm.2021.43

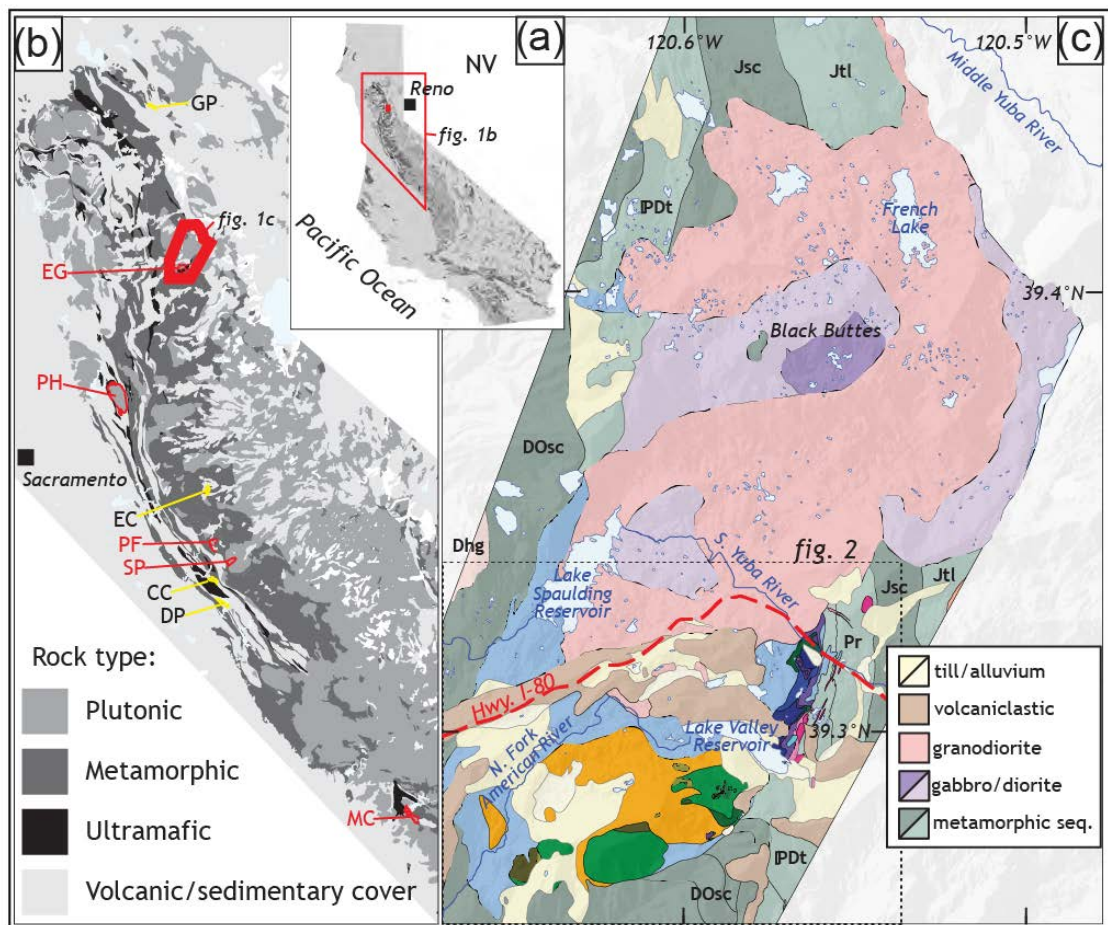
Weiser, P. E., Kent, A. J. R., Till, C. B., Donovan, J., Neave, D.A., Blatter, D. L. and Krawczynski, M. J., 2023, Barometers behaving badly I: Assessing the influence of analytical and experimental uncertainty on clinopyroxene thermobarometry calculations at crustal conditions. *Journal of Petrology*, 64(2), egac126. <https://doi.org/10.1093/petrology/egac126>

Wracher, M. D., 1991, The petrology, geochemistry, and geochronology of the Emigrant Gap composite pluton, and its structural relationship to the Shoofly Complex. M.S. Thesis, San Diego State University. 98 p.

Zimmer, M. M., Plank, T., Hauri, E. H., Yogodzinski, G. M., Stelling, P., Larsen, J., Singer, B., Jicha, B., Mandeville, C. and Nye, C. J., 2010, The role of

water in generating the calc-alkaline trend: New volatile data for Aleutian magmas and a new Tholeiitic Index. *Journal of Petrology*, 51(12), 2411–2444. doi:10.1093/petrology/egq062

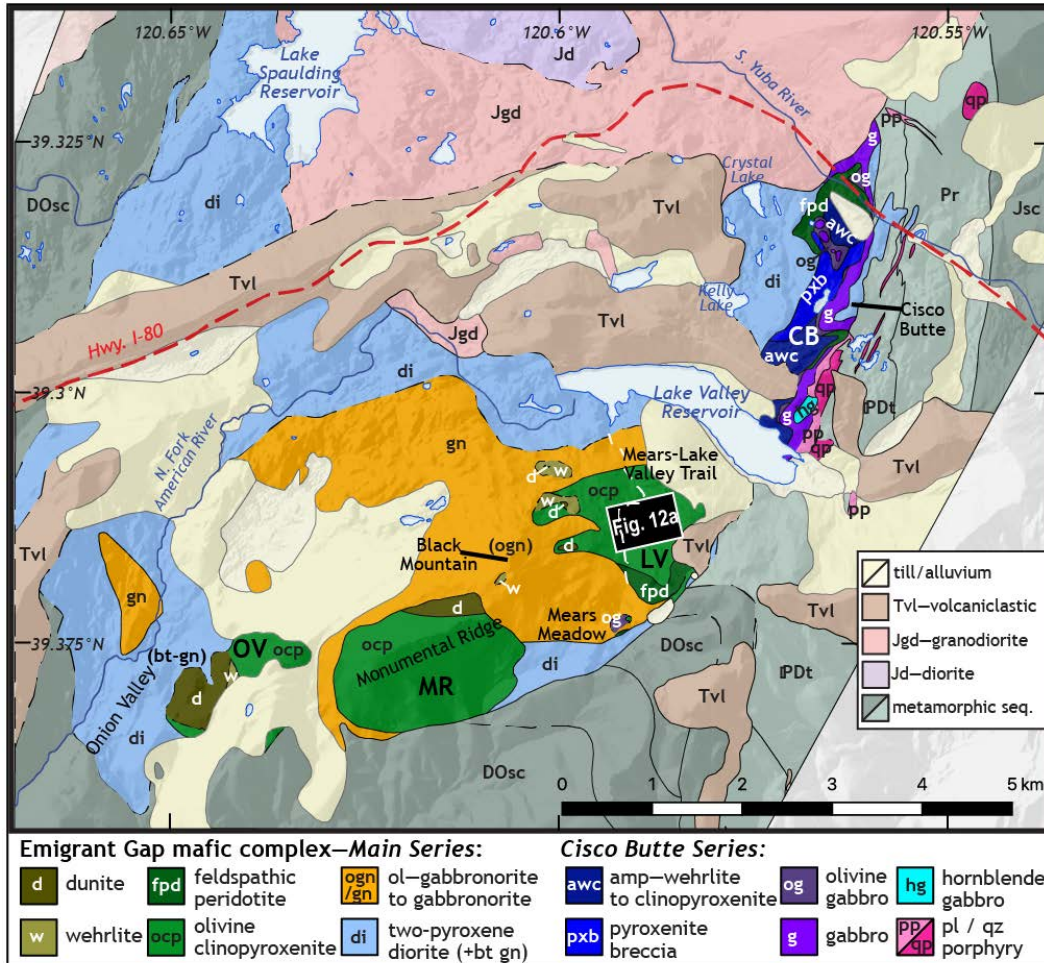
FIGURES



Ch. 2 Figure 1. Geologic map overview.

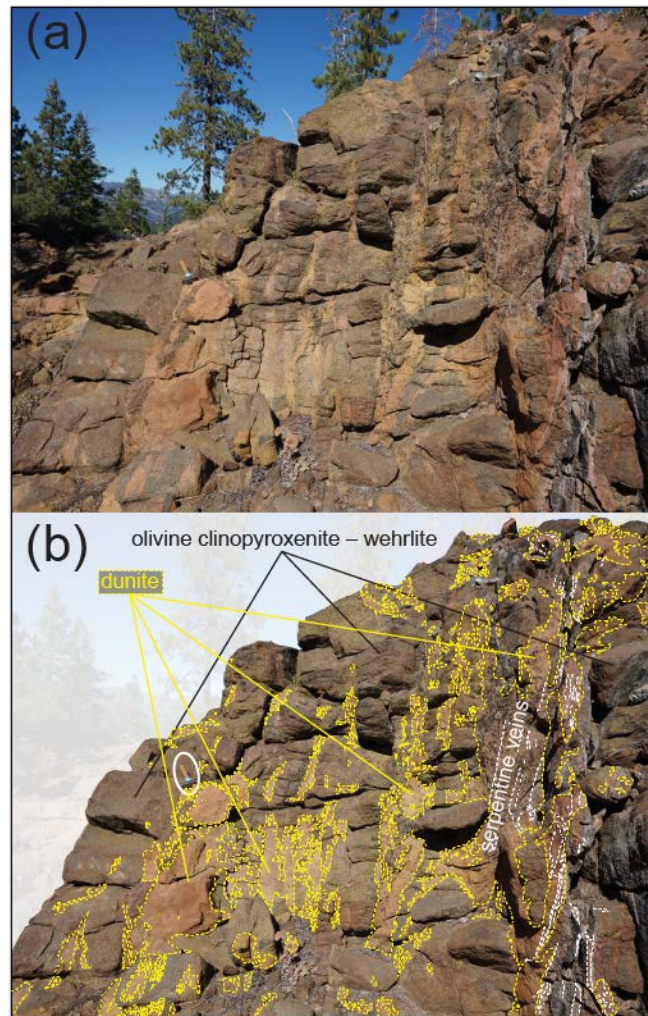
a. (inset) Location map with bedrock geology (modified from Jennings et al., 2010). **b.** Northern Sierra Nevada, showing ultramafic (mostly ophiolite) and metamorphic belts and their relationship to Mesozoic plutons. Lighter shades are volcanic rocks and unconsolidated or sedimentary units. Location of 1c outlined in bold red, Jurassic peridotite to diorite complexes similar in age (~145–170 Ma) to the Emigrant Gap complex (EG) are outlined in red; those in yellow are older (~200 Ma) or undated: GP=Grizzly Peak; PH=Pine Hill; EC=Esperanza Creek; PF=Parrot's Ferry; SP=Standard Pluton; CC=Chinese Camp; DP=Don Pedro; MC=Mill Creek. **c.** Overview map of the Emigrant Gap complex, including the hornblende-biotite granodiorite pluton and other diorite and gabbro bodies north of the main mafic complex in shades of purple. Contacts are dashed where inferred and lighter gray where bedrock is covered. Dhg=Bowman Lake batholith. Metamorphic sequences: DOsc=Shoo Fly Complex; PDt=Taylorville Sequence; Pr=Reeve Formation; Jsc=Sailor Canyon Formation; Jtl=Tuttle Lake Formation. Compiled from James (1971), Harwood et al. (1995), Wracher (1991), Saucedo and Wagner (1992), Skinner (1992), and Girty et al., 1993, Top edge in all panels is north, datum: NAD 83 HARN

CA State Plane Zone 3 (Lambert Conformal Conic). Hwy. I-80 is U.S. Interstate highway 80. The geology of the main mafic complex including a legend is shown in Figure 2 (outlined by dashed box).



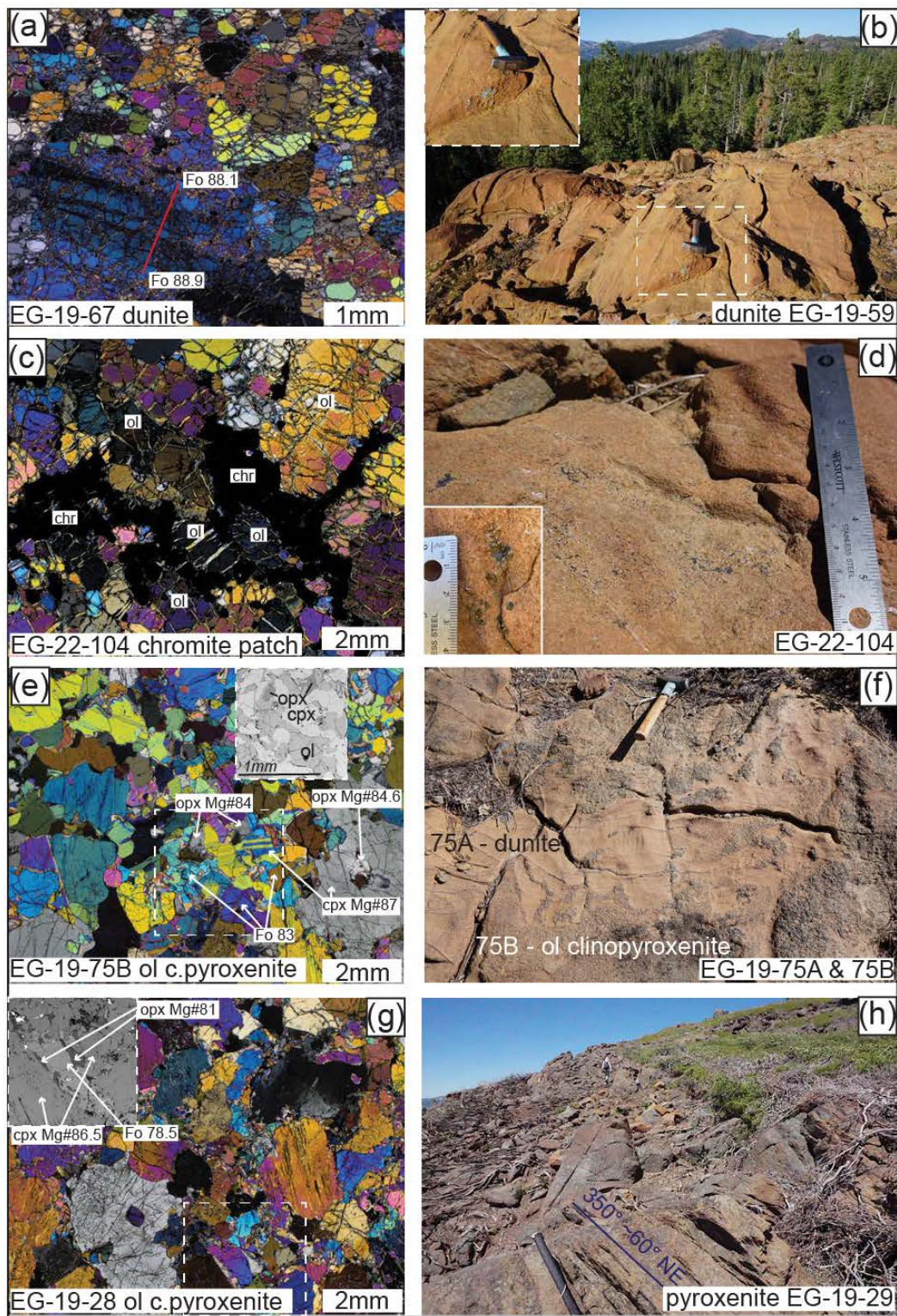
Ch. 2 Figure 2. Geologic map of the Emigrant Gap complex.

Unit abbreviations DOsc, Jd, Jgd, Jsc, Pr, PDt, Tvl as in Fig. 1. Mafic complex mapping is mainly from James (1971), Harwood *et al.* (1995), with updated contacts around mafic and ultramafic units (this study). Four ultramafic bodies: OV=Onion Valley; MR=Monumental Ridge; LV=Lake Valley; CB=Cisco Butte. Area in box in Lake Valley ultramafic body shown in Fig. 11. Hwy. I-80 is U.S. Interstate highway 80.



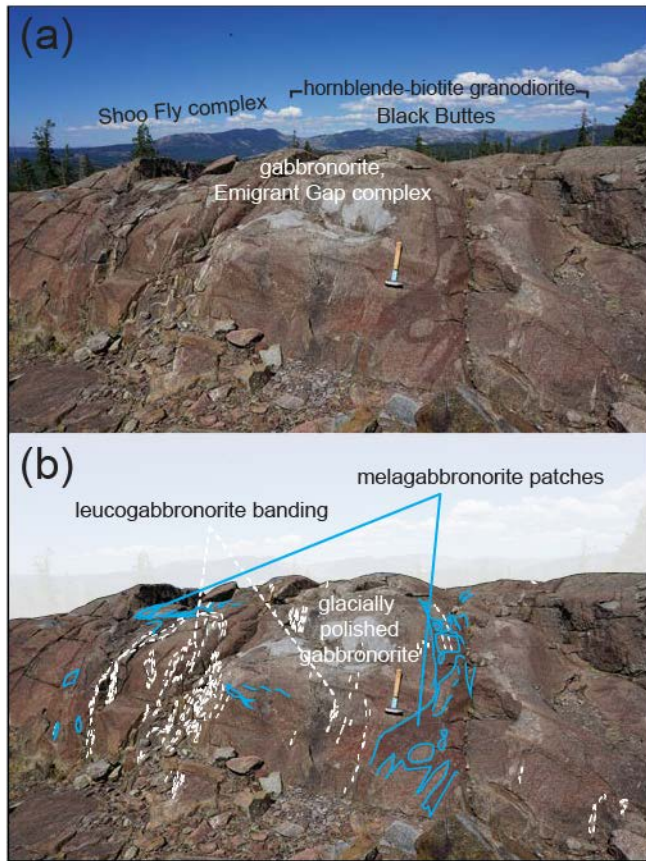
Ch. 2 Figure 3. Anastomosing dunite field photograph.

(a) Anastomosing dunite sheets and lenses in olivine clinopyroxenite to wehrlite in the central area between dunite lenses along a transect (documented in detail in Fig. 11). **(b)** Same photo with yellow dashed lines tracing dunite patches, and large serpentinite veins traced in white. Hammer is 37.5 cm long and handle points roughly north.



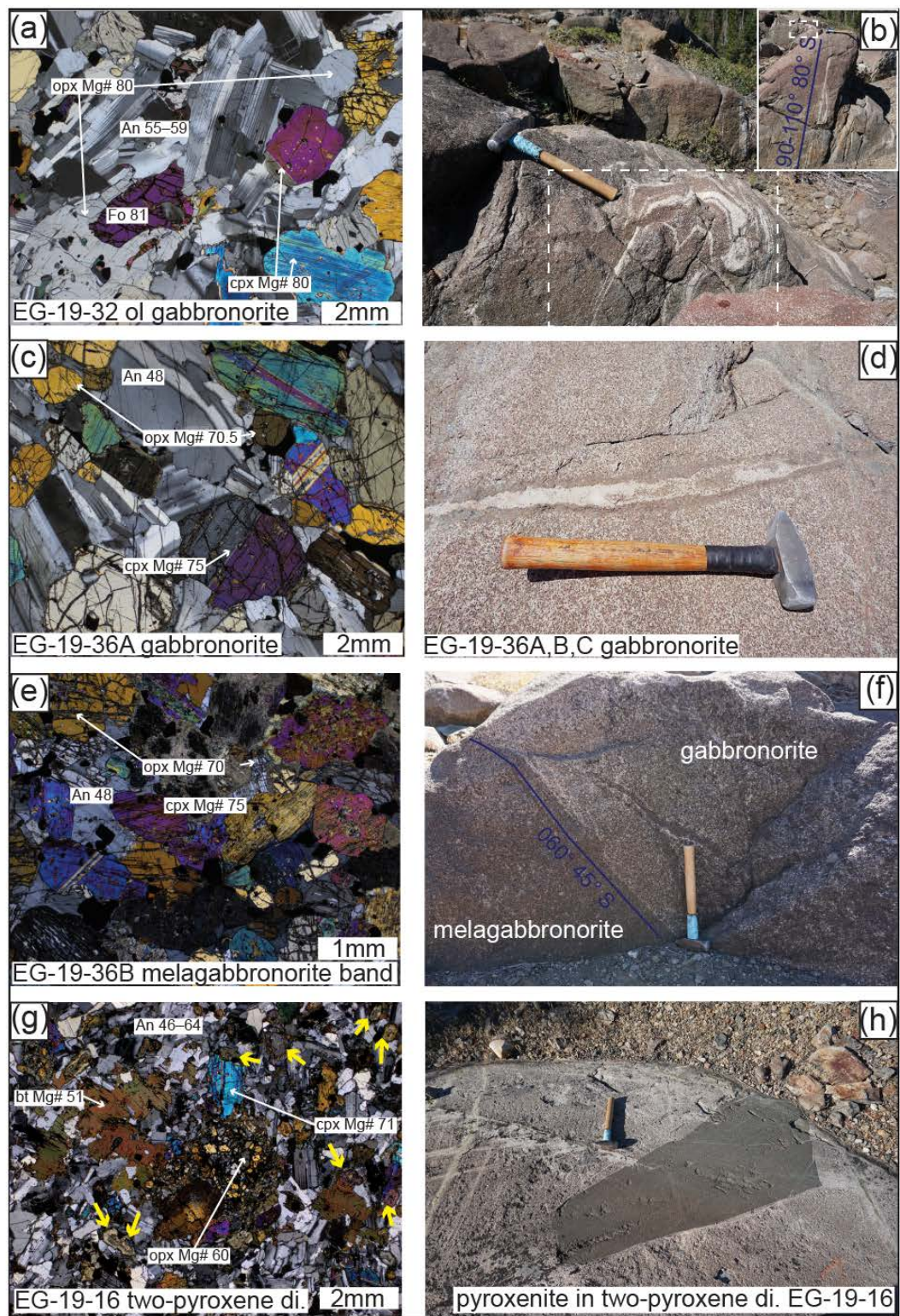
Ch. 2 Figure 4. Ultramafic rocks of the main suite.

(a, c, e, g) Cross-polarized photomicrographs with measured compositions labeled; **(b, d, f, h)** hammer in all field photos is 37.5 cm long, and handle points roughly north. Mineral names are abbreviated following Warr (2021), Fo is forsterite content expressed as a molar ratio of $100 \times \text{Mg}/(\text{Mg}+\text{Fe}_T)$. **(a)** Dunite with strained large olivine. Other subhedral to mosaic textured olivine grains are $\text{Fo}_{88.0-88.6}$. **(b)** Dunite pod, with dashed box (inset is closer view) outlining a region with clinopyroxene patches and band aligned with the subtle foliation of the dunite and nearby deformation in other dunite pods. **(c)** Chromite (black) patch around rounded olivine grains in dunite. **(d)** Chromite patches surrounding olivine in a dunite pod, with inset photo of nearby vug-like clinopyroxene. **(e)** Olivine clinopyroxenite (abbreviated ol c.pyroxenite) from between dunite pods, associated with dunite patches shown in (d). Dashed box outlines the area of the inset backscattered electron image (grayscale), to distinguish orthopyroxene (dark gray) from clinopyroxene (lightest gray) more obviously. Orthopyroxene is also found as an inclusion in a large clinopyroxene grain, as shown. **(f)** Intermingled relationship between dunite and olivine clinopyroxenite from between dunite pods (like Fig. 3). Dunite weathers with a lighter orangey surface, whereas olivine clinopyroxenite weathers with a rough, slightly resistant darker gray-green surface. **(g)** Olivine clinopyroxenite (abbreviated ol c.pyroxenite) from Monumental Ridge. Dashed box outlines area of inset backscattered electron image (grayscale), to distinguish orthopyroxene (dark gray) from clinopyroxene (middle gray) more obviously. **(h)** Olivine clinopyroxenite on Monumental Ridge, with fractures aligned with assumed subtle layering.



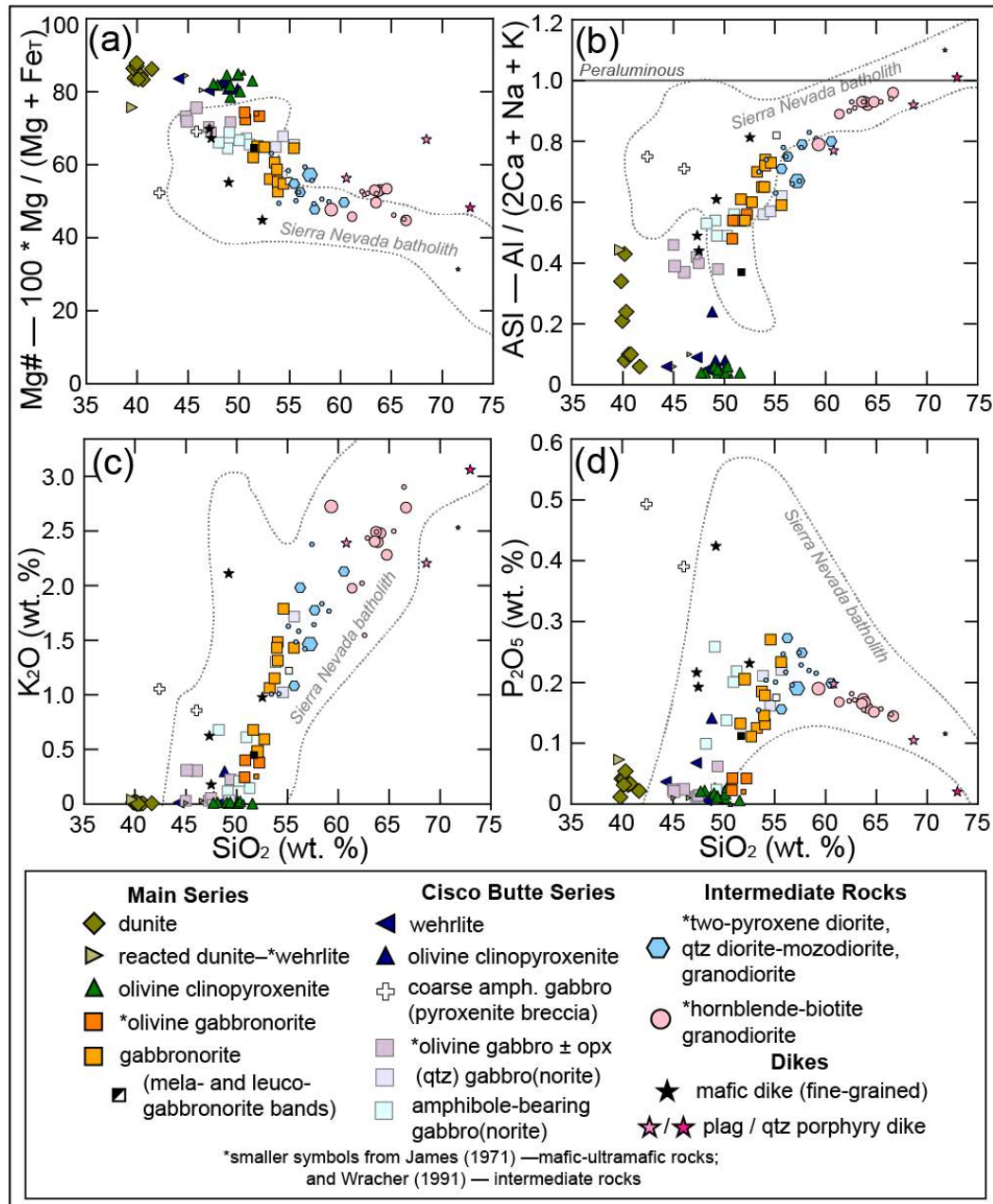
Ch. 2 Figure 5. Gabbronorite field photograph.

(a) View north-northwest of typical gabbronorite of the Emigrant Gap complex, with plagioclase- (light) and pyroxene- (dark) rich banding and transgressive patches. **(b)** Same photo as in (a) with blue outlines tracing darker (pyroxene-rich melagabbronorite) patches and white outlines tracing folded and deformed light (plagioclase-rich leucogabbronorite) banding. An exfoliated glacially polished patch is lighter gray, but the outcrop weathers reddish brown otherwise. Hammer is 37.5 cm long and handle points roughly north.



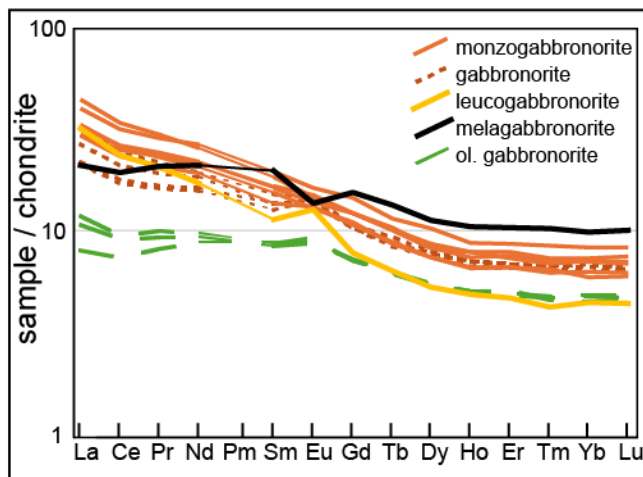
Ch. 2 Figure 6. Mafic to intermediate rocks of the main suite.

(a, c, e, g) Cross-polarized photomicrographs with measured compositions labeled; **(b, d, f, h)** hammer in all field photos is 37.5 cm long and handle points roughly north, vertical in (h). Mineral names are abbreviated following Warr (2021), Fo is forsterite content of olivine expressed as a molar ratio of $100 \times \text{Mg}/(\text{Mg}+\text{Fe}_T)$ and An is anorthite content of plagioclase. **(a)** Olivine gabbronorite, showing orthopyroxene engulfing and associated with olivine, and kink-bands in many subhedral plagioclase grains. Exsolution lamellae in clinopyroxene are common. **(b)** Olivine gabbronorite with folded modal banding and streaking. Inset is a wider view of the outcrop to show that streaking is pervasive across nearby blocks that are in place (dashed box around the region in the main photo). **(c)** Hypidiomorphic granular gabbronorite with some exsolution in clinopyroxene. **(d)** Gabbronorite with its subtle foliation ($\sim 300^\circ$ strike) crosscut by dike-like sheet with pyroxene concentrated along margins and in clusters surrounded by feldspar towards center (roughly N–S, steeply dipping NW). **(e)** Melagabbronorite band within the outcrop shown in (c–d), with some sericitization of interstitial plagioclase and alteration of pyroxenes (actinolite patches). **(f)** Gabbronorite with a melagabbronorite layer and narrower branching veins. **(g)** Two-pyroxene diorite (di.) with orthopyroxene in a raspberry-like cluster of small rounded to subhedral grains, which have coronas and intergrowths of biotite and/or Fe-Ti oxides. Yellow arrows identify orthopyroxene surrounded by actinolite. **(h)** Fine-grained homogeneous two-pyroxene diorite that includes a meter-sized angular block of pyroxenite that is injected by minor thin dikes of diorite. Bleached alteration zones with epidote are common.

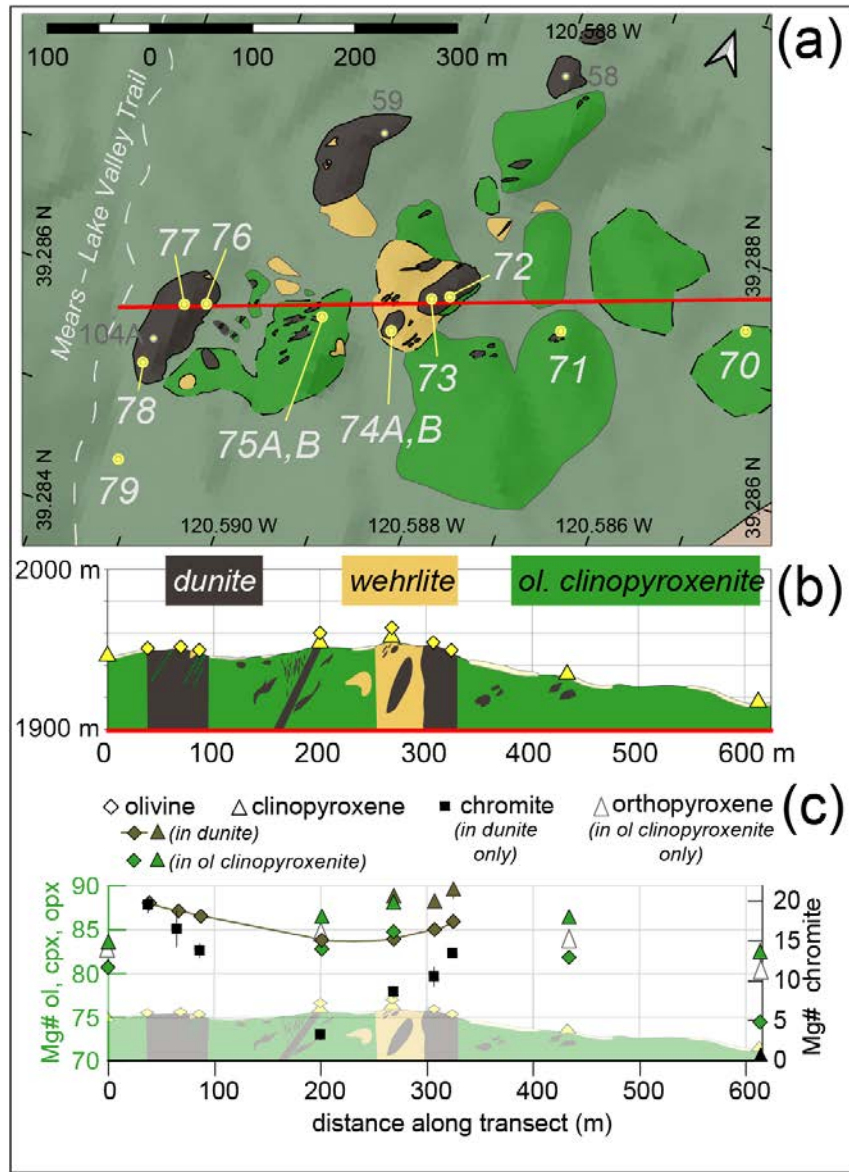


Ch. 2 Figure 7. Whole rock chemistry.

(a) Mg#, magnesium number $100 * \text{Mg} / [\text{Mg} + \text{FeT}]$ **(b)** ASI, aluminum saturation index **(c)** K₂O and **(d)** P₂O₅ versus SiO₂, in weight percent, for 103 samples (83 analyzed by XRF and ICP-MS in this study, smaller symbols from James (1971) and Wracher (1991) analyzed by wet chemistry and automatic X-ray spectrometry, respectively). All analyses are plotted on an anhydrous-normalized basis.

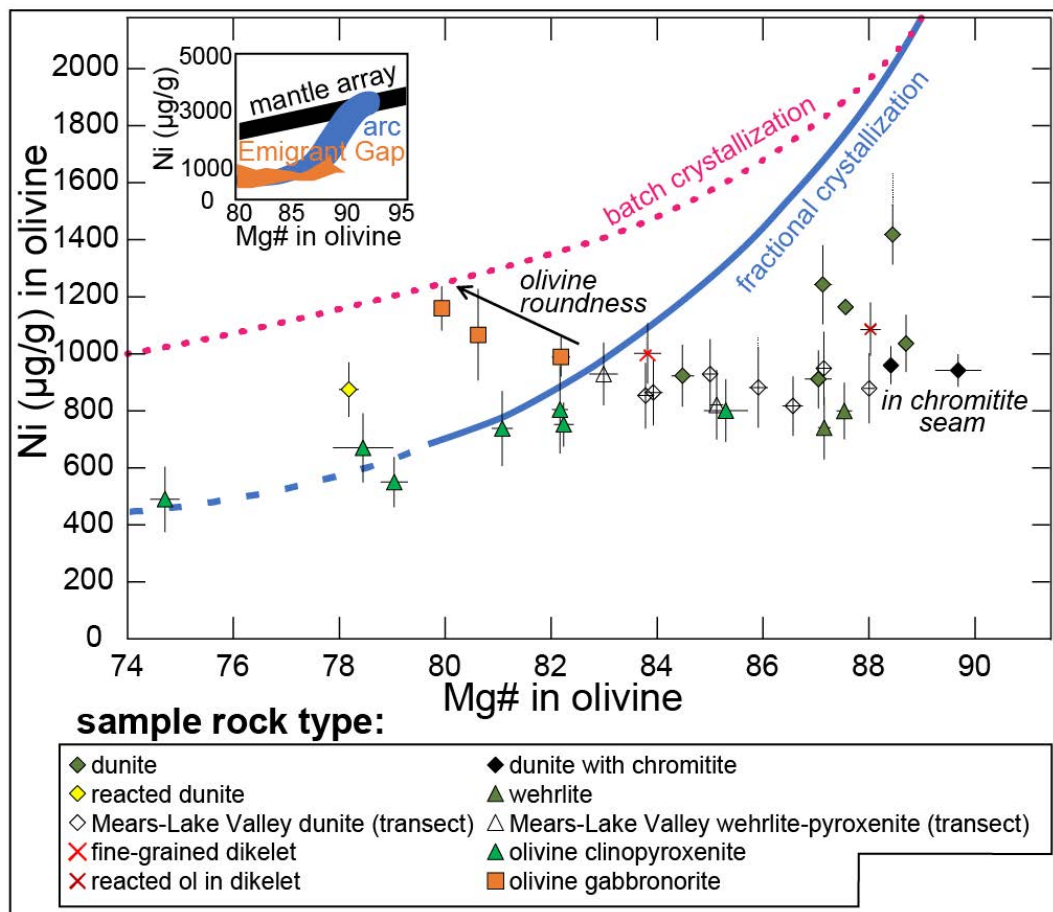


Ch. 2 Figure 8. Gabbronorite types distinguished by REE chemistry.
Patterns are chondrite-normalized (Sun and McDonough, 1995).

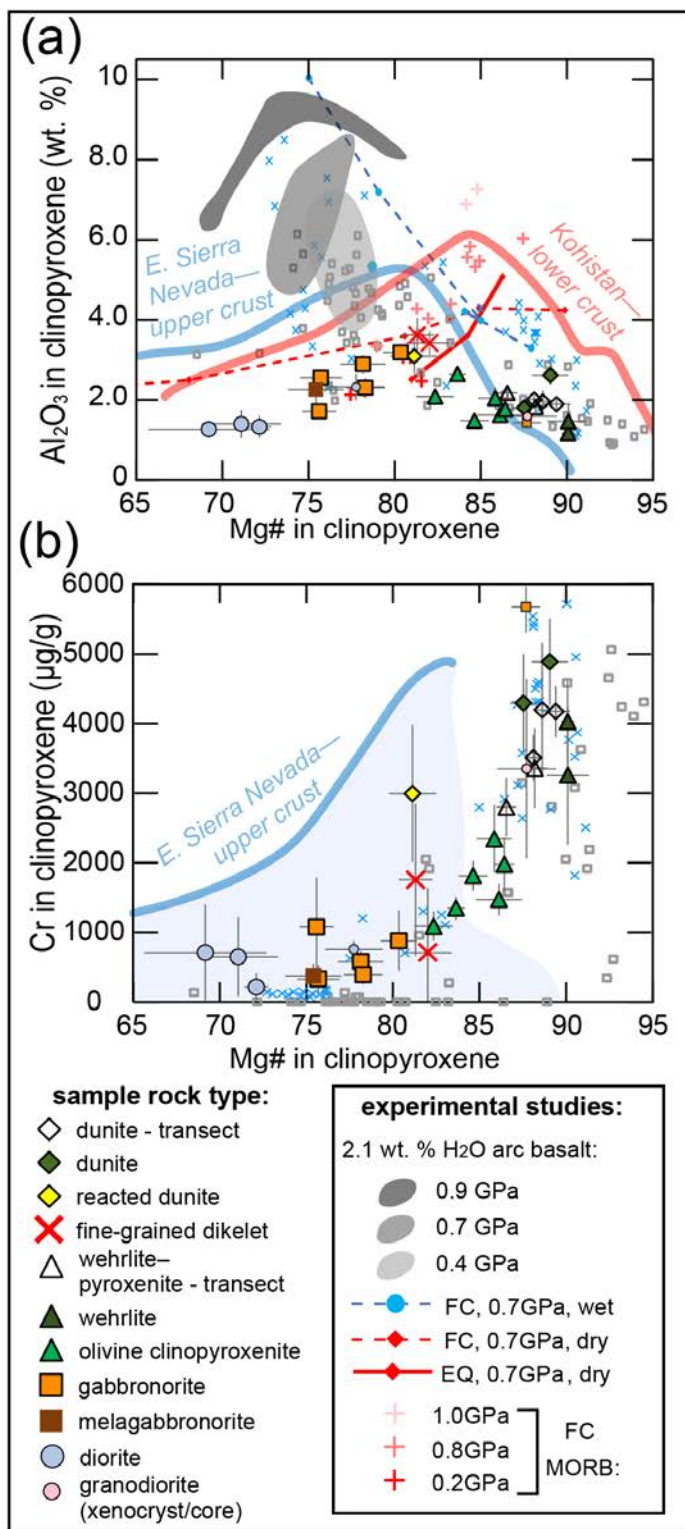


Ch. 2 Figure 9. Detailed transect in the Lake Valley ultramafic body.

(a) Map of outcrops and rock types showing sample locations (large numbers) without EG-19- prefix (Lat/Long: NAD83, location in Fig. 2). The surrounding ultramafic body is mapped as pyroxenite but is covered (gray-green background). Contacts are black where sharp, dashed where approximate, and light gray where covered. Samples excluded from the transect are smaller, in gray. Units are colored as in (b). **(b)** Interpreted cross section of the transect, with samples (diamonds = dunite; triangles = olivine clinopyroxenite) located on the surface. **(c)** Sample-average Mg# in olivine, clinopyroxene, chromite and orthopyroxene (see legend for symbology). Symbols cover error bars where not visible (1 sigma).

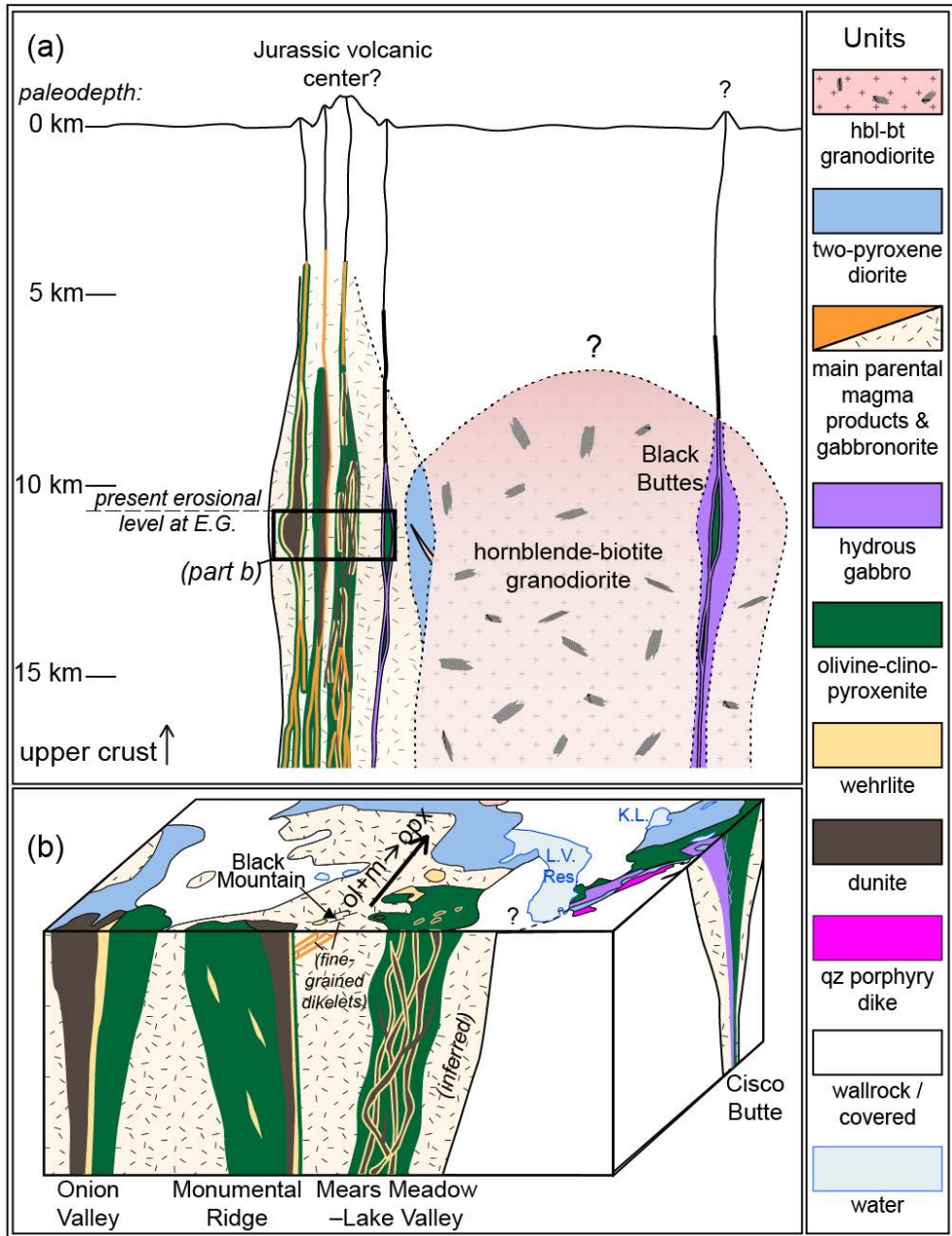


Ch. 2 Figure 10. Olivine Mg# versus Ni symbolized by rock type (plotted as sample averages with 1 standard deviation ranges; see legend for symbology). Fractional and batch (equilibrium) crystallization of olivine were modeled in alphaMELTS (using Aleutian basalt composition ID16—Nye and Reid, 1986—at 0.3 GPa, 1 wt.% H₂O, QFM + 1). The arrow describing olivine roundness applies only to an olivine gabbronorite sample with three distinguishable olivine types (orange squares). Inset plot shows Emigrant Gap olivine compositions (orange) compared to volcanic arc olivine from Kamchatka (blue; Gordeychik et al., 2020) and mantle olivine (black; Takahashi et al., 1987).

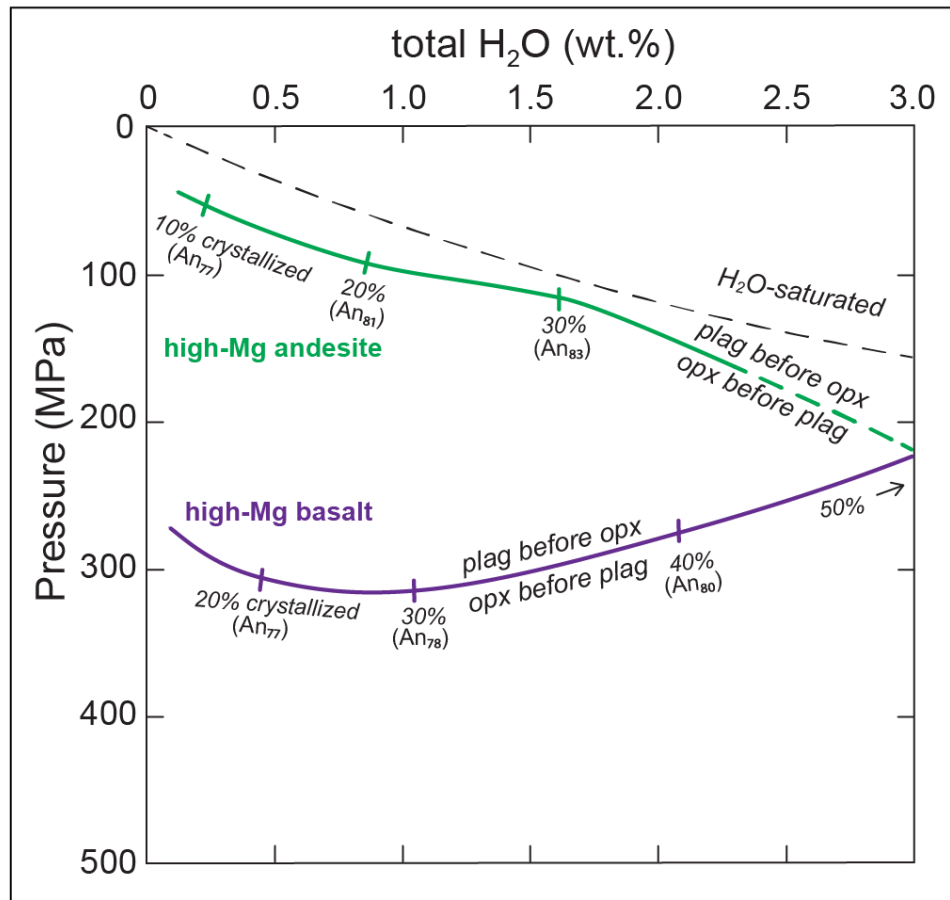


Ch. 2 Figure 11. Emigrant Gap clinopyroxene compositions symbolized by rock type (plotted as sample averages with 1 standard deviation ranges; see figure legends for symbology; smaller symbols of gabbronorite and diorite are grain cores, with elevated

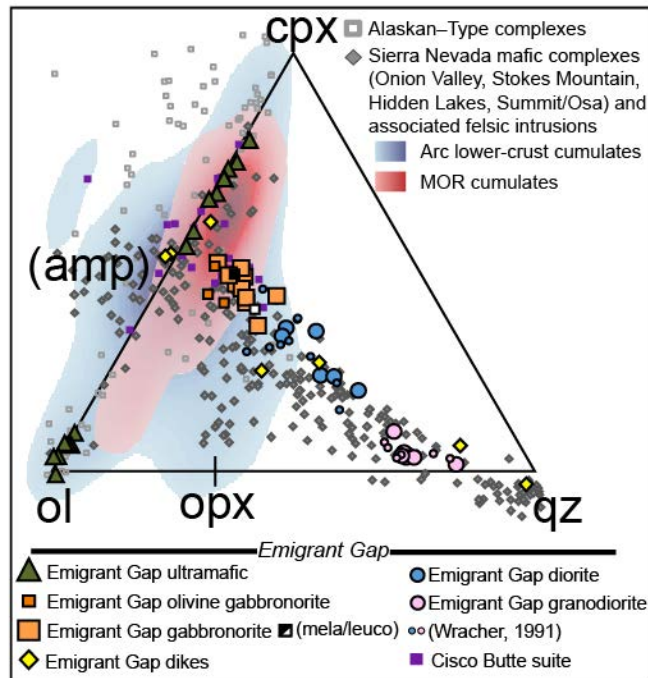
Mg# compared to typical compositions of the rock type). (a) Mg# versus Al_2O_3 in clinopyroxene from Emigrant Gap compared to clinopyroxene from Alaskan-type complexes (gray squares; Himmelberg and Loney, 1995), lower crust (blue x's; Adak Island xenoliths, Sosa et al. 2023; Kohistan arc, Jagoutz et al., 2007), upper-crustal gabbro (Sierra Nevada, Lewis et al., 2023) and experimental products. Emigrant Gap clinopyroxene has lower Al_2O_3 than lower-crustal clinopyroxene and products of water-rich experiments. Gray fields outline Blatter *et al.* (2013) equilibrium experiments on 2.1 wt.% H_2O arc basalt starting material at lower- to middle-crustal pressures. FC, 0.7 GPa dry and EQ, 0.7 GPa dry are fractional-crystallization and equilibrium experiments starting with anhydrous tholeiitic basalt at 0.7 GPa, (Villiger et al., 2007); FC, 0.7 GPa, wet are fractional-crystallization experiments on hydrous (3 to 10 wt.% H_2O) basalt to rhyolite at 0.7 GPa (Nandedkar et al., 2014); FC-MORB 1.0 GPa, 0.8 GPa and 0.2 GPa are fractional crystallization experiments on mid-ocean ridge basalt at the indicated pressures (Grove et al., 1992). (b) Mg# versus Cr in clinopyroxene from Emigrant Gap compared to clinopyroxene from Alaskan-Type, Adak xenolith, and upper-crustal Sierra Nevada samples, symbolized as in (a).



Ch. 2 Figure 12. Schematic illustration of the Emigrant Gap complex of a cross section in the upper crust showing the relationships between the rock types. **(a)** Overview showing how the Emigrant Gap complex represents sub-volcanic feeder channels in the upper crust, as described in the text. Nearby slightly older mafic complexes (*i.e.*, at Black Buttes) may share similarities to Emigrant Gap. **(b)** Closeup 3-D sketch of the geology of Emigrant Gap with interpreted subsurface features of each ultramafic body. Compositional evolution of gabbronorite away from Black Mountain is indicated by the arrow, olivine + melt reacts to orthopyroxene (ol + m → opx).



Ch. 2 Figure 13. alphaMELTS model results (pressure vs. total H_2O concentration) showing conditions under which two primitive arc magma compositions (Aleutian basalt, 50.8 wt.% SiO_2 ; Izu-Bonin high-Mg andesite, 53.0 wt.% SiO_2) would crystallize gabbro with plagioclase crystallizing prior to or co-crystallizing with orthopyroxene, consistent with Emigrant Gap petrography. The intersection of plagioclase-in and orthopyroxene-in curves (Fig. A7) and corresponding anorthite content of plagioclase at decreasing melt fraction are marked on the curves. Model details are described in the text.



Ch. 2 Figure 14. Normative olivine-clinoproxene-quartz pseudo-ternary projection from plagioclase after Tormey *et al.* (1987), Grove *et al.* (1982) and Grove (1993). Emigrant Gap whole-rock compositions (see legend) are compared to natural plutonic samples, including cumulates from mid-ocean ridge (MOR) and arc lower-crust (Chin *et al.*, 2018), and arc-intrusive complexes from Alaskan-Type intrusions (Himmelberg and Loney, 1995) and the Sierra Nevada batholith including other mafic intrusive complexes (Onion Valley, Sisson *et al.*, 1996; Stokes Mountain, Clemens-Knott, 1992; Hidden Lakes, Lewis *et al.*, 2021; Summit/Osa Creek and associated hypabyssal-volcanic series, Clemens-Knott and Gevedon, 2025; Sisson and Moore, 2010).

TABLES

Ch. 2 Table 1. Calculated temperature and pressure of crystallization using published geothermometers/barometers. Numbers surrounded by square brackets are for minerals that may be xenocrysts or disequilibrium textures. (*Continued on following page*).

Method	Mg# eq. melt (calc from olivine, ol-melt K_D 0.28)	Mg# eq. melt (calc from olivine, cpx-melt K_D 0.23)	T (°C)	Li et al., 1995	Sheiwalkar and Coogan 2013, eq. 13 (higher P), using 0.3 GPa as P estimate;	Putirka 2008, eq. 36 (using 0.3 GPa as P estimate); reported as P GPa as P estimate*	Molina et al., 2021 (± ~50°C)	Holland and Blundy, 1994 (± 40°C)	Mutch et al., 2016 (± 0.06)	Molina et al., 2021 (± 0.06)	Mutch et al., 2021 (± 0.06)	Molina et al., 2021 (± 0.06)
	($Fe_3/\Sigma Fe = 0.15$)	($Fe_3/\Sigma Fe = 0.15$)										
dunite	55–64	58–62		830– 1100	Ca-in-olivine (cpx exchange)	two- pyroxene	plag- amph.	plag- amph.	Al-in- amph.	plag- amph.	Al-in- amph.	two- pyroxene
reacted dunite	46	46	44	[690]	1100							
wehrlite	62–63	64		940–955	1075							
olivine clinopyroxenite	46–63	48–59	41–51		1050–1130	[870–940]**						
olivine gabbro	52–[64]	44–47	45–50		1080–1100	1010 / 930– 970						
gabbro	38–41	29–38				1000 / 870– 925	926	917– 926	0.3	0.35–0.4		
two-pyroxene diorite	31–34	18–22				895 / 830– 855	745	[680]– 690				
grandiorite		[58]						745– 780	0.21– 0.28			
<i>Cisco Butte sequence:</i>												
wehrlite	46–54	54–55		690								
olivine clinopyroxenite	50	53			1070							
gabbro	40–42	39–47	33–40		1065	895–930	822– 830	710		0.3	0.35–0.5	
amphibole gabbro		39–55	28–36			835–905		690– 780			0.4–0.5	

*Clinopyroxene and rare trace orthopyroxene may not be in equilibrium with olivine in the ultramafic rocks as required by the geothermometer, and a difference in pressure of 0.1 GPa would change the calculated temperature by ±50°C, so ol-cpx temperatures are considered estimates.

**Olivine clinopyroxenites have minor orthopyroxene along grain boundaries (usually of olivine), likely representing a reaction product from percolating melts so cpx-cpx in these rocks may not record equilibrium temperatures

APPENDIX 1

Field and petrographic descriptions

Dunite

Dunite is only present in the three ultramafic bodies southwest of Lake Valley Reservoir typically in the interiors of or adjacent to much larger masses of olivine clinopyroxenite. Dunite commonly forms elongate lenses or sheets (Fig. 4b,d, A1d) steeply in contact with and interleaved with olivine clinopyroxenite along their margins. The largest exposed dunite masses are ~300 by 500 m at the Onion Valley body, followed by a ~200 by 80 m lens (pervasively altered to serpentine and talc + magnetite along joints) in the Lake Valley body, and extending down in size to anastomosing vein or sheet-like dunite patches in olivine clinopyroxenite that are ~1 to 3 m long by ~10 to 50 cm wide (Fig. 3, 4d). The dunite is characterized by minor (<5-15%) serpentinization typically along joints or fractures, some ductile deformed and reddish-orange weathering, but are otherwise fresh and are not cross-cut intrusively by other rock types. Shearing is evident within dunite pods east of Black Mountain in the Lake Valley ultramafic body and is oriented parallel to the dunite pods' long axes. Dunite is common as inclusions, patches, and steeply dipping anastomosing sheets within wehrlite to olivine clinopyroxenite between larger isolated pods in the Lake Valley body (documented in detail in a transect, Fig. 9), and as small patches and steeply dipping sheets along Monumental Ridge.

Olivine comprises >95% modally of these rocks and ranges from ~0.5 to 3 mm, with up to 5% chromite and locally ~1–2% clinopyroxene as \leq 0.5 cm-sized patches, plus minor serpentine along grain boundaries and in fractures (Fig. 4a–d, A1c–d). Chromite is present as ~100 μ m inclusions within olivine or at junctions between grains, however in the dunite lenses, there are thin 1–3 mm wide by \leq 10 cm long vein-like seams of chromite around rounded olivine grains (Fig. 4c–d). Rare clinopyroxene locally encloses olivine poikilitically, but more commonly forms small, isolated patches at triple junctions between olivine crystals. Large (~2 to 3 mm) olivine grains have patchy recrystallization and sweeping extinction suggesting

strain, but surrounding, <2 mm olivine grains are interlobate and look unstrained (Fig. 4a). Olivine grain boundaries tend to be straight and polygonal in the dunite bodies that lack shearing, although some larger elongate grains are aligned. The small dunitic patches and dike-like domains are granoblastic polygonal textured and contain Cr-magnetite to magnetite rather than chromite.

One ~ 60 m 2 forested outcrop (Fig. A1b) located between ultramafic (dunite, wehrlite, and olivine clinopyroxenite) and olivine gabbronorite exposures has 75 modal % olivine (1-3.5 mm) with interstitial white plagioclase (5 modal %, up to 2 mm surrounding olivine) and oikocrystic clinopyroxene (12 modal %, up to 4 mm) and orthopyroxene (5 modal %, up to 4 mm), and anhedral magnetite (~ 3.5 modal %, up to 2 mm) associated with biotite (<1 modal %, up to 1 mm). It is texturally and chemically a dunite, with rounded olivine grains surrounded by gabbronoritic minerals (Fig. A1a), so we interpret it as a dunite that was infiltrated by and reacted with mafic melt. Only one sample of this “reacted dunite” was collected—it is not a main rock type of the complex but uniquely captures disequilibrium textures.

Wehrlite, olivine clinopyroxenite and clinopyroxenite

Main suite. Olivine clinopyroxenite is the most abundant ultramafic rock, although its olivine abundance is variable, in places decreasing to form nearly olivine-free clinopyroxenite, and in others increasing to form small patches and sheets of wehrlite that can locally approach dunite in their olivine abundances. Large masses (0.5–2 km) of dark green olivine clinopyroxenite form the bulk of the ultramafic bodies in the eastern half of the Onion Valley body, Monumental Ridge, and surrounding the Lake Valley dunite pods east of Black Mountain (Fig. 4g–h, A1c–d). The largest ultramafic mass, Monumental Ridge, is a 1 by 2 km mountain ridge made entirely of olivine clinopyroxenite laced sporadically with small, steeply dipping dunite sheets and patches. Olivine clinopyroxenite masses also flank the larger (map scale) dunite bodies at Onion Valley and Monumental Ridge, and olivine clinopyroxenite surrounds and grades into dunite and wehrlite in the Lake Valley ultramafic body. Clifffy exposures of olivine clinopyroxenite are common, and in

several places in the Onion Valley and Monumental Ridge bodies have cleavage that appears like subtle to cryptic cumulus layering (Fig. 4h), but prominent modal or grain-size layering typical of well-layered cumulates is lacking. Unlike the dunite lenses, the olivine clinopyroxenite lacks evidence for strong shearing. Contacts between olivine clinopyroxenite and the surrounding gabbronorite are rarely exposed but must be sharp over distances of less than one to several meters.

The clinopyroxene-rich rocks are typically xenomorphic granular (Fig. 4e,g, A1c,e). Olivine abundance is variable in olivine clinopyroxenite and wehrlite (10 to 55%) typically occurring as finer-grained (0.25-1 mm) slightly polygonal textured zones between coarser (1-4 mm) clinopyroxene crystals. Wehrlite has rounded clinopyroxene with polygonal-textured olivine surrounding it, with acute angles of olivine grain boundaries filling in some scalloped clinopyroxene margins (Fig. A1c). In olivine clinopyroxenite, some olivine is anhedral, intergrown within embayments in clinopyroxene (Fig. 4e,g A1e). Orthopyroxene is rare (<1 modal %), occurring as thin margins along grain boundaries within the finer-grained patches between cumulus clinopyroxene and olivine (Fig. 4e,g, A3). Thin exsolution lamellae, <1–25 μm wide, are widespread in clinopyroxene grains. Subgrains are developed in some large clinopyroxenes (Fig. 4g, A1e). There is no chromite and little (~1%) magnetite in these rocks. Locally, tiny (~10–20 μm) patches of amphibole (and rarely, biotite) are present at grain junctions and within clinopyroxene crystals.

Cisco Butte suite. In the Cisco Butte ultramafic body north of Lake Valley Reservoir, no dunite is exposed, and instead wehrlite is more common. Dark, igneous amphibole is widespread and conspicuous in the olivine clinopyroxenite and clinopyroxenite (Fig. A1g–h), forming interstitial patches between and surrounding pyroxenes in most samples. In these olivine clinopyroxenite and clinopyroxenite samples, some individual clinopyroxene crystals have inclusions of Fe-Ti oxides along cleavage planes and in discrete zones.

A distinctive pyroxenite breccia crops out as a 300 by 1500 m mass in the northeast part of the complex in and near Cisco Butte (Fig. A1f). The pyroxenite is brecciated by coarse-grained (up to 3 cm) amphibole gabbro, with widespread but

minor epidote and saussuritized feldspar. Pyroxenite blocks are angular to rounded, commonly 10–30 cm across, and many have thin rims of biotite and amphibole at their margins with the invasive coarse amphibole gabbro. Where exposed in cliffs of Cisco Butte, the unit is mostly pyroxenite penetrated pervasively by thin (sub-cm) anastomosing seams of finer-grained amphibole gabbro (Fig. A1f). Petrography within the brecciated pyroxenite blocks matches clinopyroxenite throughout Emigrant Gap but with minor amphibole ± biotite along grain boundaries.

Gabbronorite ± olivine ± biotite and gabbro

Main suite. Gabbronorite is the dominant rock type of the main suite, exposed south and west of Lake Valley Reservoir as reddish-weathering commonly glacially polished or cliffy outcrops (Fig. 5). Gabbronorite consists of subhedral to rounded clinopyroxene and orthopyroxene (both 2–3 mm) amongst generally more abundant plagioclase laths (1–3 mm), accompanied with minor magnetite (~3–4 modal %) and biotite (<1–4 modal %), plus accessory apatite and zircon. Plagioclase laths define a nearly pervasive, steeply dipping igneous foliation that is generally parallel with a macroscopic modal banding defined by gradual variations in the relative abundances of plagioclase and pyroxenes (Fig. 5, 6b).

The modal banding defined by gradual variations in plagioclase and pyroxene abundances is widespread in the gabbronorite and olivine gabbronorite and is concordant with igneous foliation, but this banding fails to form the sharply defined, laterally continuous, repetitive grain size and modal layering characteristic of well layered cumulates. Both the igneous foliation and the modal banding strike approximately 60–110° and dip 50–80° S near Black Mountain (Fig. 6b), and are rotated to scattered orientations (~250–300° strike, steep dips) farther north in gabbronorite without olivine. Some approximately m thick bands of melagabbronorite are sufficiently pyroxene-rich to be termed ‘feldspathic websterite’ (James, 1971). Modal banding is locally truncated along trough-like discontinuities draped by otherwise similar banded gabbronorite, and banding can also be truncated by syn-magmatic ‘hot’ faults that cannot be traced beyond single exposures (Fig. 5,

6b,f). Small dike-like and more irregular masses distinctly rich in plagioclase (leucogabbronorite) or pyroxenes (melagabbronorite, Fig. 5, 6d–f) also cut the banded gabbronorite, but these transgressive bodies cannot be traced beyond one or two outcrops. Minerals in these transgressive bodies are the same species with the same sizes and habits as those in the gabbronorite, and these small intrusions probably originated as locally remobilized and reinjected portions of the cogenetic mush. Some thin, plagioclase-rich bands or dikelets can be seen to be folded at outcrop scale. Collectively, these features are consistent with the gabbronorite mush having actively deformed as it solidified.

The most primitive gabbronorites contain minor amounts of olivine and crop out adjacent to the ultramafic bodies at Black Mountain; these olivine gabbronorites have less biotite (<1%) than the common olivine-free gabbronorites (Fig. 6a–d). Contacts between gabbronorite and ultramafic bodies are usually covered, but where exposed at the northern tip of the Monumental Ridge ultramafic body, the contact is sharp between olivine gabbronorite and ultramafic units (270° strike, 67°NW dip), with ultramafic modal mineralogy grading from pyroxenite adjacent to gabbronorite through wehrlite to dunite over a span of ~10 m away from the contact. Scattered rare blocks of clinopyroxenite, rounded to angular and up to 1.5 m long, are present in olivine gabbronorite, establishing that at least some ultramafic cumulates had formed prior to intrusion of gabbronorite. Several sets of thin (0.5–3 cm) fine-grained (<0.5 mm) planar olivine gabbronorite and gabbronorite dikelets (striking ~240° dipping ~40° N) sharply cut across foliation of the coarser olivine gabbronorite near the summit of Black Mountain (Fig. S2a,b).

Monzogabbronorite that appears similar to the main gabbronorite but has the more abundant biotite (4–6%), minor interstitial K-feldspar, and commonly saussuritic and greenish alteration including actinolite, separates portions of the gabbronorite along its northern margin from the two-pyroxene diorite. In Onion Valley close to the southwestern margin of the complex, gabbronorite is pervasively altered with abundant green actinolite and sericitized plagioclase. Fine-grained biotite-rich (~5%) outcrops of monzogabbronorite, also altered, surrounding and

penetrating the Onion Valley ultramafic body are mapped as part of the two-pyroxene diorite unit, described below. They are compositionally and mineralogically transitional between gabbronorite and the more intermediate dioritic rocks (with less biotite and feldspar than typical two-pyroxene diorite) and are included herein chemically as a type of gabbronorite.

Gabbronorite is texturally xenomorphic to hypidiomorphic granular (Fig. 6a,c). Clinopyroxene and orthopyroxene range in abundance from 25–30% and 10–25%, respectively, with 45–65% plagioclase, and typically 1–4% biotite. Olivine gabbronorite samples from Black Mountain contain embayed or rounded olivine (up to ~5%) that is typically rimmed by orthopyroxene (Fig. 6a). Plagioclase is less abundant (~30%) in olivine gabbronorites than in olivine-free gabbronorites, and small euhedral (Cr)-magnetite is associated with or enclosed by pyroxenes. Plagioclase has polysynthetic twins that in some samples are kinked, consistent with modest sub-solidus deformation. Magmatic biotite is anhedral and interstitial to plagioclase and pyroxene, commonly as patches between or along pyroxene grain boundaries. Amphibole is nearly absent in these rocks, except for trace scattered $<10\text{ }\mu\text{m}$ patches within some clinopyroxene crystals that likely formed as an igneous reaction product, and rare patches or rims on clinopyroxene of actinolite that are likely secondary subsolidus reaction products in places associated with chlorite and sericite within cracks or between mineral grains.

Cisco Butte suite. In contrast to the biotite-bearing gabbronorite of the main suite, mafic rocks of the Cisco Butte suite are dominated by (olivine) gabbro and amphibole-bearing gabbronorite. These rock types occur as ~10's of m wide bands that dip 75° to subvertical to the southeast and strike sub-parallel to the margins of the complex (~10–80°). Olivine gabbro has ~10–20% olivine. Many olivine gabbro bands are cumulate-textured, contain $<50\%$ plagioclase, and grade to olivine clinopyroxenite. Texturally, olivine (2–4 mm) forms clusters surrounding clinopyroxene and rims of Fe-Ti oxide, some as symplectite, whereas plagioclase (<1 mm) is mostly polygonal and/or interstitial. The texture differs distinctly from olivine gabbronorite of the main suite (where olivine is subhedral, like clinopyroxene).

Amphibole-bearing gabbronorite occurs along the easternmost margin of the Cisco Butte to Lake Valley Reservoir area. Orthopyroxene (0.25–1 mm) makes up <10% modally in the amphibole-bearing gabbronorites and is rounded. Subhedral to anhedral clinopyroxene (1–3 mm in diameter) is more abundant (~30–50%). Many clinopyroxene crystals have internal rings of Fe-Ti oxides, commonly along cleavage planes within a ring between the core and rim of the crystal. Dark, igneous amphibole forms ~0.5 mm rims on clinopyroxene and as small patches among pyroxene and/or olivine crystals and is <5% modally in most cases. A single ~100 m outcrop of oikocrystic amphibole gabbro (~40% amphibole) crops out near the margin of the complex between Cisco Butte and Lake Valley Reservoir. Gabbro within <150 m of felsic intrusive units (*i.e.*, hornblende-biotite granodiorite or porphyritic felsic dikes along the eastern margin, Fig. 2) is characterized by green actinolite and chlorite rims around clinopyroxene and have small patches of quartz with plagioclase, which is often saussuritized.

Intermediate rocks

Two-pyroxene quartz monzodiorite, tonalite, and granodiorite

The intrusion mapped collectively as a two-pyroxene diorite, tonalite, and granodiorite by James (1971) is heterogeneous and internally gradational, from quartz monzodiorite with clinopyroxene and orthopyroxene, to tonalite, to granodiorite (Fig. 6g–h, A2c–d). A glacially polished exposure of a nearly gabbronoritic portion is modally layered (Fig. A2d) and contains abundant ductilely deformed felsic granodiorite and aplite dikelets. Late fractures are bleached and are coated with patches of epidote. South of the ultramafic bodies, a thin region of this diorite is diffusely interfingered with metasedimentary wall rocks. This domain has seriate grain sizes (~0.1–2 mm) and contains scattered angular inclusions of pyroxenite (Fig. 6h).

Quartz monzodiorite is similar to the gabbronorite except that clinopyroxene (up to 6%) and orthopyroxene (1%) are less abundant whereas interstitial biotite is more abundant (~6–22%; Fig. 6g, A2c). Commonly, orthopyroxene has a frambooidal

shape of small (~20–40 μm) round pellets in clusters with anhedral biotite and Fe-Ti oxide coronas (Fig. 6g, A2c). In many samples these rounded small orthopyroxene grains are dispersed rather than clustered and have ~10 μm rims of actinolite with exsolution lamellae, suggestive of former inverted pigeonite.

Plagioclase is widely sericitized, and interstitial quartz (trace to 20%) and up to ~10% potassium feldspar and biotite are present in increasing abundance away from the contact with gabbronorite in more evolved (tonalite to granodiorite) samples. Orthopyroxene crystals are generally smaller (~0.2 mm) and associated with magnetite-quartz-biotite symplectites in these evolved samples. Dark (igneous) amphibole and/or actinolite form rims on pyroxenes, but amphibole never constitutes more than 10% modal abundance of the rock.

Hornblende-biotite granodiorite

The hornblende-biotite granodiorite consists of 30–35% quartz, 30–63% plagioclase, 0–16% K-feldspar, amphibole (hornblende), and biotite, with the low K-feldspar abundance of some samples indicating areas of tonalite. Quartz is anhedral and interstitial to K-feldspar and plagioclase. Hornblende varies in abundance, typically ~10–15%, as does biotite (14–20%), with biotite more abundant than amphibole, based on rocks in this study and reported by Wracher (1991) (Fig. A2e). Xenocrysts of pyroxenes in the granodiorite, likely derived from the local ultramafic rocks of Emigrant Gap, are rimmed by amphibole.

Methods

Whole-rock geochemistry

X-ray fluorescence spectrometry (XRF) at HAL

Samples were sawed to remove areas with visible alteration or weathering and sanded to remove saw marks, then sonicated in deionized water and dried. To ensure homogeneity of coarse-grained samples, ~100 to 600 g of each rock was crushed with steel hammer and chipmunk jaw crusher. At HAL, a subsample of each was

powdered in a Rocklabs tungsten carbide (WC) ring mill. Powders were heated overnight at 900°C in silica crucibles and weighed before and after to measure loss on ignition (LOI). Powder and Li-tetraborate flux (1:2) were mixed with a vortex mixer and fused twice in graphite crucibles at 1000 °C in a muffle furnace, following an adapted method described by Johnson et al., 1999, Ultramafic samples were additionally diluted with pure fused silica to prevent crystallization during quenching. Fused pellets were re-ground in a WC ring mill between fusions. The glass pellets were polished to a 15 µm surface on diamond lapping plates and sonicated in ethanol before analysis by the Thermo ARL Perform'X XRF spectrometer.

Analytical conditions for WDXRF were 45 kV and 45 mA, and a suite of 44 elements was measured. All measurement details are reported in Conrey et al. (2023) and can be accessed at <<https://www.hamilton.edu/academics/analytical-lab>>. Calibration using 77 reference materials, using revised values weighted more heavily than older values (Jochum et al., 2016). We report a subset of these results with all iron reported as FeO (SiO₂, TiO₂, Al₂O₃, FeO*, MnO, MgO, CaO, Na₂O, K₂O, P₂O₅, minimum F, minimum Cl, minimum SO₃ as weight percent oxide; minimum Br, minimum As, Zn as µg/g) as the trace elements were measured in the same samples by ICP-MS. Because the samples were ground using WC vessels, which are known to introduce Ta into samples, Ta values are not plotted as points in Figure A5.

Laser ablation inductively coupled plasma mass spectrometry (LA-ICP-MS)

Following WDXRF analysis, the fused glasses were analyzed by LA-ICP-MS at Colorado School of Mines using an Applied Spectra RESOlution SE ArF Excimer 193 nm laser coupled to an Agilent 8900 QQQ ICP-MS, following methods and operating parameters in Conrey et al., 2023, For quartz porphyry dike sample EG-19-37, a high-SiO₂ sample with low FeO* that would not couple well to the laser, ~35 mg of spec-pure Fe-oxide was added to the glass (which was fused a third time following XRF analysis) (Conrey et al., 2023). Laser ablation signals were reduced and background corrections were applied in the *Iolite* software package (Paton et al.,

2011), and further drift correction and data reduction, including internal standardization using multiple elements, was performed using new *HALite* software (Conrey et al., 2023).

Energy dispersive micro-XRF sample mapping (ED- μ XRF)

A M4 Tornado μ -EDXRF spectrometer (Bruker) was used for microXRF mapping of polished 30 μ m-thick thin sections. X-ray conditions used were 50 kV, 599 μ A, 30 W focused by a polycapillary lens with a 30 μ m beam diameter, generated by a rhodium tube, and measured by two 30 mm² silicon drift detectors (SDD) in the instrument with maximum pulse throughput of 130,000 cps. The continuous mapping step size (pixel size) used was 30 μ m, with a dwell time of 10 ms per pixel, where the stage speed was 3.0 mm/s. Each pixel of data contains a full ED-XRF spectrum. Spectra were deconvolved with the software. For 14 thin sections (166 x 110 mm, ~20.3 million pixels), analysis time was 61 hours.

Modal mineralogy quantification from phase mapping

Phase maps were calculated using the Bruker M4 Tornado software using principal component analysis with auto binning (non-fixed bin sizes). The software uses chemical information from each pixel (in this case, Ca, Al, Fe, K, Ti, Si, Na and Mg were selected) and computes a histogram based on intensity of each of these elements in n -dimensional (8 dimensions for these 8 elements) space, where points that plot close together are designated as a phase. The spacing between these is binned automatically, not as constant distance segments. Phase maps are thus images of each of these components by pixel.

Parameters for this analysis specific to the Bruker software were set as follows: sensitivity was set to 95 out of 100 (with higher sensitivity representing how similar each phase is chemically); area was set to 0.05% (the minimum areal percent of pixels in the entire map for a phase to be identified); and edges set to 90 out of 100 (where higher values mean that small phases are merged into single phases). Each phase gives the average chemical composition of that phase across the whole area that it

covers in the section. These compositions were used to manually name phases as the appropriate mineral, corroborated by petrographic examination. Areas with significant alteration and small grains ($<30\text{ }\mu\text{m}$) may be misrepresented by this method, which is an issue for Fe-Ti oxide and chromite, but samples are generally unaltered ($<5\text{-}10\%$) and major phase abundances match petrographic observations. Results are reported in Table S1.

Electron probe microanalysis (EPMA)

San Carlos Olivine was analyzed throughout each run to monitor accuracy. A mean atomic number (MAN) background correction and ZAF or $\phi(\rho Z)$ calculations for matrix correction, with absorption coefficients from $\text{LINEMU} < 10\text{ KeV} / \text{CITZMU} > 10\text{ KeV}$ (Armstrong, 1988) were used. A mean atomic number (MAN) background intensity was calibrated and continuum absorption correction was applied to all elements (Donovan and Tingle, 1996; Donovan et al., 2016). Oxygen was calculated by cation stoichiometry and included in the matrix correction and data was reported as oxides (SiO_2 , TiO_2 , Al_2O_3 , FeO^* —total Fe calculated as FeO , MgO , CaO , Na_2O , K_2O , Cr_2O_3 , MnO , and NiO ; plus CoO in high-current olivine analyses) except for halogens measured in plagioclase, biotite and amphibole (Cl, F). Unknown and standard intensities were corrected for deadtime, and standards were reanalyzed throughout the session to correct for drift over time. Lower limits of detection (Table S11a–d) are based on standard counts and unknown background counts following Scott and Love (1983).

Olivine, pyroxene, plagioclase, spinel, amphibole, and biotite analyses

Operating conditions were 40 degrees takeoff angle, beam energy of 15 kV, 25 nA beam current and 10 μm beam diameter for all phases. V_2O_5 was not analyzed, so no interference corrections were performed for spinel analyses. A summary of detailed conditions, primary standards, detection limits and observed 1σ relative errors for each element setup is in Tables S11a–c. Additional Caltech standards

analyzed during instrument setup during all runs for MAN background correction were synthetic Fayalite (P-669), synthetic MgO (P-85), and synthetic Al₂O₃ (P-472).

High-current olivine analyses with trace elements

Olivine grains in selected dunite samples (EG-19- 59, -67, -75A and -76) were measured with high beam current and long count times to precisely measure trace elements. Operating conditions were 40 degrees takeoff angle, beam energy of 20 kV, beam current of 300 nA and a 10 μ m beam diameter. The off-peak correction method was linear for all elements. A summary of detectors, count times, primary standards, detection limits and observed 1σ relative errors for each element is in Table S11d. Additional Caltech standards analyzed for MAN background correction were synthetic NiO (P-634), Shankland forsterite (P-658) and synthetic fayalite (P-1086).

Amphibole chemistry

Amphibole is present only in trace amounts and only in a few samples from the main mafic series, mostly as patchy igneous peritectic replacements of clinopyroxene. Amphibole abundance is variable in diorite, from trace to \sim 20 modal %, and amphibole is abundant in granodiorite (\sim 2 to $>$ 35 modal %; Wracher, 1991). Amphibole compositions in the main sequence and in the Cisco Butte rocks are magnesio-hornblende to pargasite-edenite replacing clinopyroxene in ultramafic samples (Mg# = 77 to 82). Anhedral to subhedral magnesio-hornblende pseudomorphically replaces or rims pyroxene in intermediate diorite to granodiorite (Mg# = 53 to 59; Table S10). In general, Al₂O₃, CaO, and Na₂O concentrations decrease and K₂O and MnO increase with decreasing Mg#, spanning ultramafic to intermediate rock types.

One sample of melagabbronorite has minor interstitial magnesio-hornblende that is compositionally similar to the trace patchy replacement in ultramafic rock types but with lower concentrations of Al₂O₃ and Na₂O. At one outcrop along the southern contact of gabbronorite with diorite and wallrocks near Mears Meadow,

coarse-grained pargasitic oikocrystic Mg# ~70 amphibole patches and veinlets that are low in CaO (11.8 wt.% compared to >12.3 wt% in patchy amphibole in clinopyroxene in other main suite mafic to ultramafic rocks) and high in TiO₂ (2.1 compared to <1.1 wt% in patchy amphibole) intrude olivine gabbronorite. Notably, that gabbronorite also has high-anorthite (An₈₅) plagioclase. Other than these instances and the trace patchy replacement in some grains of pyroxene, amphibole is notably near-absent from the main sequence rock units.

Crystallization Conditions (*T, P*)

Crystallization temperatures

Thermometry based on average mineral major element compositions by sample (Table 1 and Tables S3–S10) represent subliquidus and potentially subsolidus temperatures recorded during crystallization and potentially re-equilibration during cooling, and thus represent minimum temperatures for the parental magma at the time of crystallization of the relevant minerals. The Ca-in-olivine geothermometer of Shejwalkar and Coogan (2013, eq. 13) corrected for pressure to ~0.3 GPa (see discussion of pressure estimates below) results in temperatures as follows: dunite with minor clinopyroxene and orthopyroxene, >1115 °C; wehrlite and clinopyroxenite, 1050–1130 °C; and olivine gabbronorite, 1080–1100 °C. The olivine-spinel thermometer of Li *et al.* (1995) using chromite in ultramafic rocks yields slightly lower temperature estimates, possibly resulting from diffusive re-equilibration of Fe/Mg in spinel and olivine.

Temperatures calculated for Fe-Mg exchange in clinopyroxene and orthopyroxene using the thermometer of Putirka (2008, eq. 36) are only feasible in plagioclase-bearing samples, as orthopyroxene joined the crystallizing assemblage with plagioclase. Maximum calculated temperatures from core compositions of clinopyroxene-orthopyroxene pairs in olivine gabbronorite and gabbronorite are 1010 and 1000 °C, respectively, down to minimum calculated temperatures of 930 and 870 °C, respectively, using sample-average compositions. These temperatures may be compromised by exsolution in clinopyroxene, especially towards the rims of

grains. Using orthopyroxene compositions from a disaggregating cluster of orthopyroxene in the two-pyroxene diorite yields a maximum calculated temperature of 895 °C, with lower temperatures recorded by disseminated rounded orthopyroxene (down to 830 °C). Two-pyroxene temperatures likely reflect some post-crystallization Fe-Mg exchange or exsolution, as they are lower than orthopyroxene's appearance in most basalt, basaltic andesite, and andesite crystallization experiments.

Amphibole is present as crosscutting veins and patches in one sample of olivine gabbronorite from south of the Lake Valley ultramafic body with coexisting plagioclase that fits within the compositional parameters for plagioclase-amphibole thermometry of Molina et al., 2021. Calculated temperatures using average plagioclase and amphibole compositions are 917–926 °C. Granodiorite amphibole and plagioclase compositions are not within the range allowed for that thermometry, so the parameterization of Holland and Blundy (1994) provides a (likely low) estimate of 745–780 °C for those most evolved rocks of the hornblende-biotite granodiorite pluton. The Cisco Butte suite also contains amphibole in some gabbro, which yield slightly lower temperatures using the Molina et al. (2021) thermometer of 822–830 °C. In general, the Cisco Butte suite yields slightly lower temperatures for all thermometers described above in comparable rock types to the main suite (Table 1).

Crystallization pressure

The metamorphic aureole around the Emigrant Gap complex manifests as andalusite-bearing hornblende-hornfels facies phyllitic argillites and sandstones of the Shoo Fly Complex (James, 1971; Wracher, 1991). This limits the emplacement level of Emigrant Gap intrusive rocks to the upper crust, shallower than ~13 km depth (<~0.35 GPa at ~600 °C; Pattison 1992; Brady, 2019). Calculated pressures of emplacement based on mineral major-element compositions are reported in Table 1. Pressures are most consistent the Al-in-hornblende geobarometer of Mutch et al. (2016), which is applicable to granitic rocks with a specified low-variance mineral assemblage close to the haplogranite solidus. Samples of granodiorite and the two-

pyroxene diorite that meet the phase assemblage criteria of the geobarometer yield pressures of 0.21 to 0.28 GPa, or as shallow as approximately 8 to 10 km depth. Similar pressures of 0.3 GPa are calculated for the plagioclase-amphibole geobarometer of Molina et al. (2021) for both the gabbronorite with patchy crosscutting amphibole and the amphibole-bearing gabbro of Cisco Butte (described above for plagioclase-amphibole thermometry; Table 1).

Barometers for mafic rocks of the series, which lack amphibole, are more scattered (*i.e.*, two-pyroxene barometer, eq. 39 of Putirka, 2008 using eq. 36 temperature, described above); regardless, calculated pressures using average clinopyroxene and orthopyroxene compositions yield pressures of 0.30–0.45 GPa; within uncertainties, these are not discernably different from the amphibole-based pressures (Weiser et al., 2023). Comparison of observed crystallization sequences and mineral chemistry at Emigrant Gap (*i.e.*, Al_2O_3 in clinopyroxene, Fig. 11a) and to experimental studies at variable pressures (*e.g.*, Feig et al., 2006) suggest that the pressure of crystallization was ~0.15 to ~0.3 GPa, or 5.5 to 11 km depth. Note that for low- H_2O primitive basaltic magmas, crystallization at pressures less than ~0.15 GPa would result in early crystallization of plagioclase prior to clinopyroxene (*i.e.*, troctolite), which is not observed at Emigrant Gap.

Cisco Butte suite results

Whole rock geochemistry of Cisco Butte suite

The most primitive compositions in the Cisco Butte ultramafic body are wehrlite (Mg# 80–84, SiO_2 44.3–47.3 wt.%), and olivine clinopyroxenite (Mg# 81–83, SiO_2 48.8–50.1 wt.%). Both of these rock types have low Al_2O_3 , elevated CaO , and low K_2O and other incompatible elements (<2.7 wt.% Al_2O_3 , 8.5–18.6 wt.% CaO , and <0.3 wt.% K_2O , aside from one sample with 5.8 wt.% Al_2O_3 and 0.6 wt.% K_2O).

The olivine gabbro (\pm interstitial amphibole) in the Cisco Butte area has high lower SiO_2 , Al_2O_3 , K_2O and other incompatible elements and higher MgO , FeO^* and CaO compared to gabbronorite of the main suite. In bivariate plots of major elements

(Fig. 7, A4), amphibole-bearing gabbro to gabbronorite trend towards lower SiO_2 , from gabbronorite compositions of the main suite toward compositions of either the olivine gabbro or coarse-grained amphibole gabbro that forms the matrix of the brecciated pyroxenite. The amphibole gabbro comprising the breccia has a unique composition in the sample suite (open crosses in Fig. 7), with comparatively low SiO_2 and Mg#, but high ASI, K_2O , P_2O_5 and other incompatible elements.

Some gabbro(norite) with elevated SiO_2 compared to the amphibole-bearing (gabbro)norites contains late/interstitial quartz, and generally plots in linear arrays between the (gabbro)norites and felsic dikes in most major element bivariate plots, pointing towards contamination by felsic dikes.

Mineral chemistry of Cisco Butte suite

In the amphibole-bearing suite near Cisco Butte, mineral chemistry and mineralogy is similar with a few distinctions. As there is no dunite, there is only limited chromium-bearing spinel, found only in wehrlite and Cr-magnetite in composition. These are similar in composition to Cr-magnetite from the main suite. Olivine compositions in wehrlite, olivine clinopyroxenite \pm amphibole, and olivine gabbro to gabbronorite are similar to those from olivine clinopyroxenite in the main suite, ranging from a maximum of Mg# 83 in wehrlite to a minimum Mg# 73 in gabbro, with overlapping trends in Ni contents for that compositional range in the main suite. Clinopyroxene from wehrlite through gabbro in the Cisco Butte suite have a similar range in Mg# to clinopyroxenite through gabbronorite from the main suite (Mg# = 76 to 86). Despite similar trends in ultramafic rocks of increasing Al_2O_3 and TiO_2 followed by a decrease in plagioclase-bearing rocks, Cisco Butte suite clinopyroxene has systematically lower Al_2O_3 (maximum 2.5 wt.%) and TiO_2 (maximum 0.4 wt.%) than the main suite.

Orthopyroxene is only found in amphibole-bearing and olivine gabbro to gabbronorite, and overlaps in Mg# and Al_2O_3 with the main suite, with slightly lower TiO_2 . Fe-Ti oxides are magnetite in gabbro to clinopyroxenite from the Cisco Butte suite. Frequently, clinopyroxene grains have zones rich in magnetite planes aligned

with cleavage in both directions, creating a hachured ring within clinopyroxenes, which rare, if present at all, in the main suite. Additionally, symplectites of magnetite and orthopyroxene rim large olivine grains or clusters in the most evolved olivine gabbro samples, in which olivine and clinopyroxene host low-Ti rounded magnetite inclusions.

Plagioclase in the Cisco Butte suite is typically reverse-zoned, with high-anorthite rims (An_{71-89}) aside from one normally-zoned altered amphibole gabbronorite, and in a sample with heavily altered plagioclase with sponge textured cores that could not be analyzed. In some cases, plagioclase is associated with rounded anhedral olivine that is interlobate with plagioclase. Biotite in this suite is minor and was not analyzed.

Amphibole is present as up to 5 modal percent patchy replacement and interstitial anhedral greenish to brown magnesiohastingsite with some magnesiohornblende in ultramafic rocks and is similar in chemistry with slightly lower SiO_2 and higher K_2O to the main suite trace amphibole ($Mg\# = 78$ to 81). Some gabbro to gabbronorite has anhedral to interstitial green to brown magnesiohastingsite, occasionally aligned with planes associated with veins. The two most distinct occurrences of amphibole in the Emigrant Gap complex are: (1) one outcrop of amphibole gabbro has pargasitic oikocrystic ~cm-sized $Mg\# 68$ amphibole surrounding and replacing pyroxene; and (2) the coarse pegmatoid amphibole gabbro that brecciates pyroxenite in the pyroxenite breccia unit at Cisco Butte, which is $Mg\# 69$ pargasite-edenite.

Proposed origins of the Cisco Butte suite

The suite at Cisco Butte is distinctive from the main suite indicating that the parental magmas and/or processes that formed this northeastern portion of the mafic complex differed from those of the main suite, and clearly involved more hydrous mafic magmas. First, in the Cisco Butte suite, dunite is absent and the dominant rock types include olivine clinopyroxenite with interstitial igneous amphibole (Fig. A1g,h) and olivine gabbro or amphibole gabbro(norite). Thus, the crystallization sequence

at Cisco Butte was olivine + clinopyroxene \pm chromite followed by plagioclase + titanomagnetite \pm orthopyroxene (minor), and co-crystallizing or subsequent amphibole which typically rims clinopyroxene and is likely a peritectic product. In addition, aspects of the mineral chemistry of the main suite and the Cisco Butte suite are distinct. Plagioclase in gabbronorite of the Cisco Butte suite is also much higher in anorthite content than in the main suite, ranging from An₇₉₋₈₈ in its gabbro (compared to An₄₈₋₅₉ in main suite gabbronorite; Fig. A7), consistent with crystallization from more hydrous melts (Sisson and Grove, 1993).

Finally, although some orthopyroxene-bearing gabbro to gabbronorite is present in the Cisco Butte area, the orthopyroxene grains are routinely small and rounded, like in the two-pyroxene diorite. In some orthopyroxene-bearing Cisco Butte rocks, plagioclase has low-An cores (An_{<50}) surrounded by the typical An_{>80} rims of the Cisco Butte suite. Potentially, the hydrous mafic magmas of the Cisco Butte suite assimilated gabbronoritic rock or crystal mush of the main suite. The pyroxenite breccia intrusion (Fig. A1f), found only in this area, has coarse pegmatoid amphibole gabbro that brecciated pyroxenite, indicating that a late hydrous magma intruded into and interacted with already solidified cumulates.

REFERENCES

Armstrong, J.T., 1988, Quantitative analysis of silicates and oxide minerals: comparison of Monte-Carlo, ZAF and $\phi(\rho Z)$ procedures. *Microbeam Analysis*, 239-246.

Barnes, S.J. and Roeder, P.L., 2001, The range of spinel compositions in terrestrial mafic and ultramafic rocks. *Journal of Petrology*, 42(12), 2279–2302.

Conrey, R.M., Bailey, D.G., Singer, J.W., Wagoner, L.J., Parfitt, B., Hay, J., Keh, O., Chang, Z. and Huang, S., 2023, Combined use of multiple external and internal standards in LA-ICP-MS analysis of bulk geological samples using lithium borate fused glass. *Geochemistry: Exploration, Environment, Analysis*, 23(2): geochem2023-001.

Dick, H.J.B. and Bullen, T., 1984, Chromian spinel as a petrogenetic indicator in abyssal and alpine-type peridotites and spatially associated lavas. Contributions to Mineralogy and Petrology, 86, 54–76.

Donovan, J.J. and Tingle, T.N., 1996, An improved mean atomic number correction for quantitative microanalysis. Journal of Microscopy, 2, 1, 1-7.

Donovan, Singer and Armstrong (2016). A New EPMA method for fast trace element analysis in simple matrices. American Mineralogist, 101, 1839-1853.

Ishii, M., Hiraishi, J. and Yamanaka, T., 1982, Structure and lattice vibrations of Mg-Al spinel solid solution. Physics and Chemistry of Minerals, 8, 64–68.

Jochum K.P., Weis U., Schwager B., Stoll B., Wilson S.A., Haug G.H., Andreae M.O. and Enzweiler J., 2016, Reference values following ISO guidelines for frequently requested rock reference materials. Geostandards and Geoanalytical Research, 40, 333-350.

Johnson D.M., Hooper P.R. and Conrey R.M., 1999, XRF analysis of rocks and minerals for major and trace elements on a single low-dilution Li-tetraborate fused bead. Advances in X-ray Analysis, 41, 843-867.

Molina, J. F., Moreno, J. A., Castro, A., Rodríguez, C. and Fershtater, G.B., 2015, Calcic amphibole thermobarometry in metamorphic and igneous rocks: new calibrations based on plagioclase/amphibole Al-Si partitioning and amphibole/liquid Mg partitioning. Lithos, 232, 286–305.
<http://dx.doi.org/10.1016/j.lithos.2015.06.027>

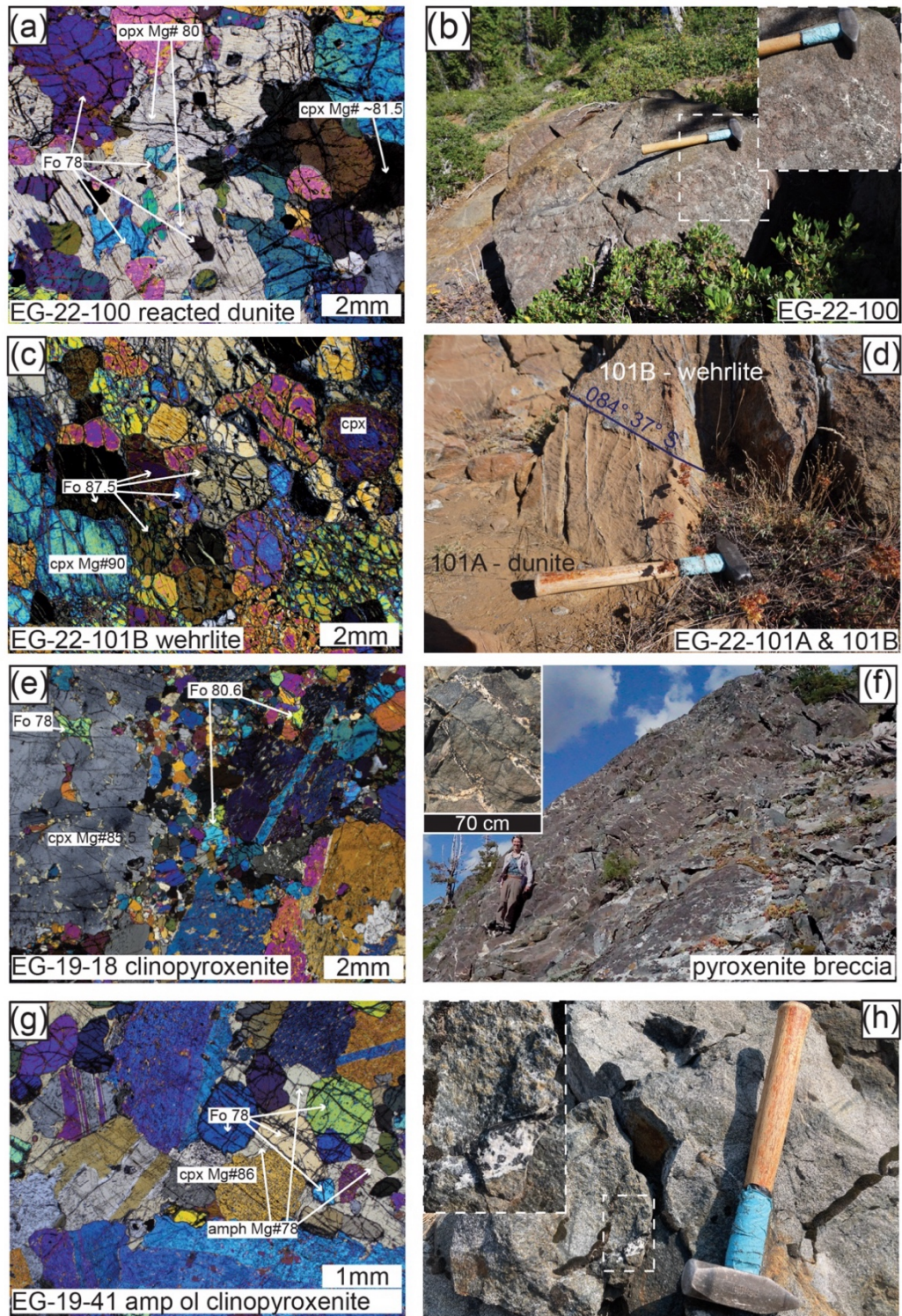
Parkinson, I.J. and Pearce, J.A., 1998, Peridotites from the Izu-Bonin-Mariana forearc (ODP Leg 125): evidence for mantle melting and melt-mantle interaction in a supra-subduction zone setting. Journal of Petrology, 39(9), 1577–1618.

Paton, C., Hellstrom, J., Paul, B., Woodhead, J. and Hergt, J. (2011) Iolite: freeware for the visualization and processing of mass spectrometric data. Journal of Analytical Atomic Spectrometry, 26, 2508–2518.

Pearce, J.A., Barker, P.F., Edwards, S.J., Parkinson, I.J. and Leat, P.T. (2000)
Geochemistry and tectonic significance of peridotites from the South
Sandwich arc-basin system, South Atlantic. Contributions to Mineralogy
and Petrology, 139, 36–53.

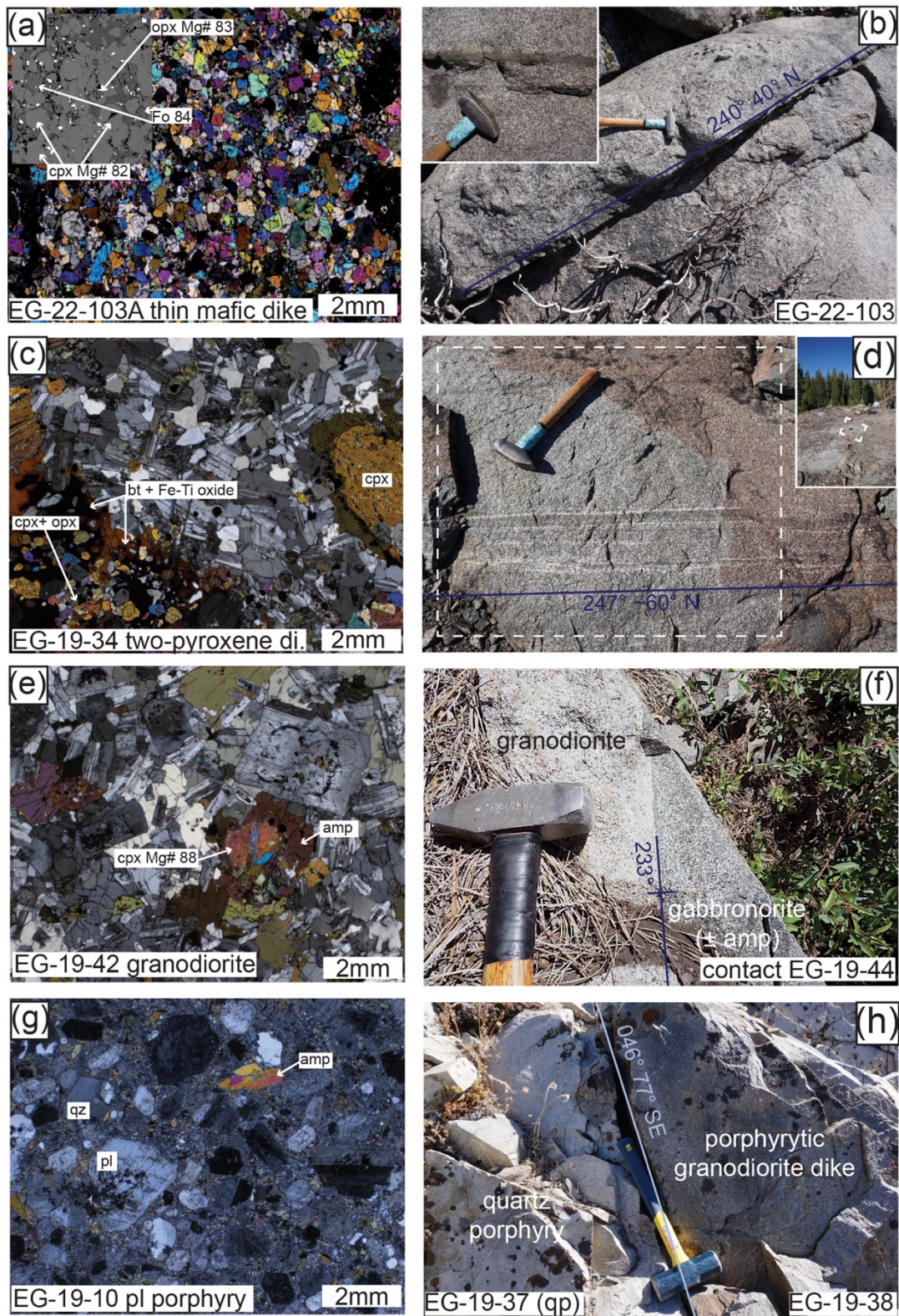
Scott, V.D. and Love, G. (1983) Quantitative electron-probe micronanalysis. Ellis
Horwood LTD., Chichester, England, 345 p.

SUPPLEMENTARY FIGURES



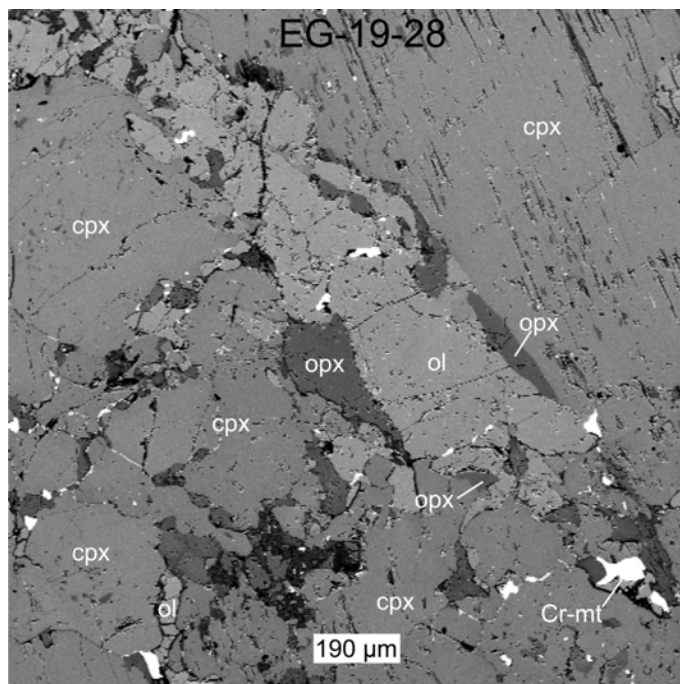
Ch. 2 Figure A 1. Ultramafic rocks of the main and Cisco Butte suites.

(**a, c, e, g**) cross-polarized photomicrographs with measured compositions labeled; (**b, d, f, h**) hammer in all field photos is 37.5 cm long, and handle points roughly north. Mineral names are abbreviated following Warr (2021), Fo is forsterite content expressed as a molar ratio of $100 \times \text{Mg}/(\text{Mg}+\text{FeT})$. (**a**) Oikocryst of orthopyroxene surrounding anhedral olivine inclusions, a few anhedral plagioclase inclusions and rounded olivine grains in the single sample of reacted dunite. Clinopyroxene is abundant (~60 modal percent) outside of the field of view, and oikocrysts of orthopyroxene like the one shown are scattered throughout the outcrop (~3 to 5 modal percent). (**b**) Reacted dunite outcrop, with dashed box (inset is closer view) outlining a region with abundant interstitial plagioclase. (**c**) Wehrlite, with clinopyroxene and olivine intergrown. (**d**) Internal sharp boundary or contact within a dunite lens between dunite and more clinopyroxene-rich wehrlite. (**e**) Amphibole and olivine-bearing clinopyroxenite sampled from a block within the Cisco Butte suite pyroxenite breccia unit. (**f**) Pyroxenite breccia cliffs below Cisco Butte, with thin veinlets of amphibole gabbro between pyroxenite blocks, many dip eastward. Person is 175 cm tall. Inset is a closeup of typical pyroxenite breccia with coarse-grained amphibole gabbro brecciating (olivine-)clinopyroxenite. (**g**) Amphibole-bearing olivine clinopyroxenite (amphibole and olivine abbreviated) from the Cisco Butte suite. Amphibole oikocrysts surround and interstitially fill rounded olivine intergrown with anhedral clinopyroxene. (**h**) Cisco Butte suite amphibole-bearing gabbronorite with crosscutting patches and veinlets of medium to coarse-grained amphibole gabbro, shown in dashed box (inset is closer view).

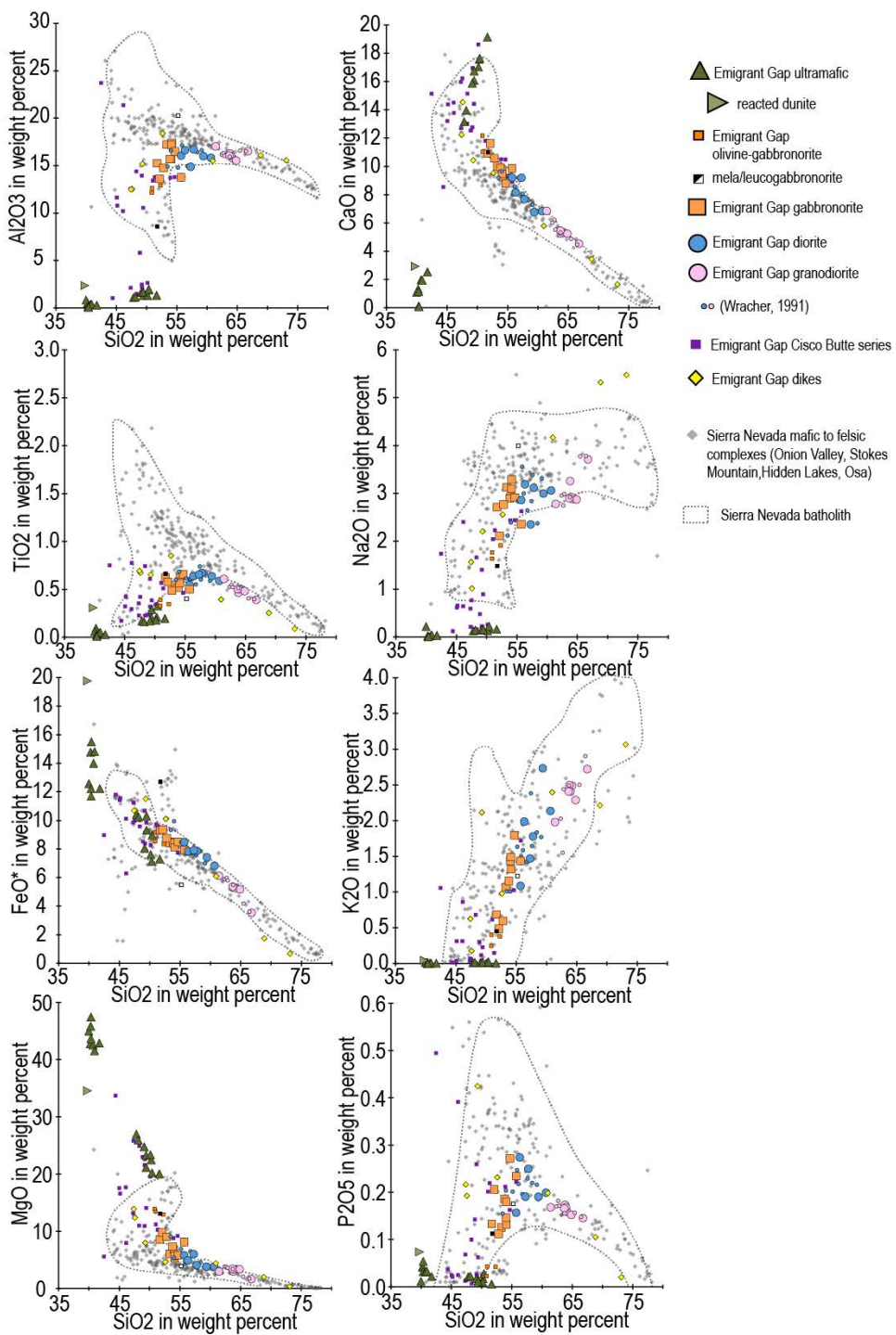


Ch. 2 Figure A 2. Mafic to felsic rocks of the complex.

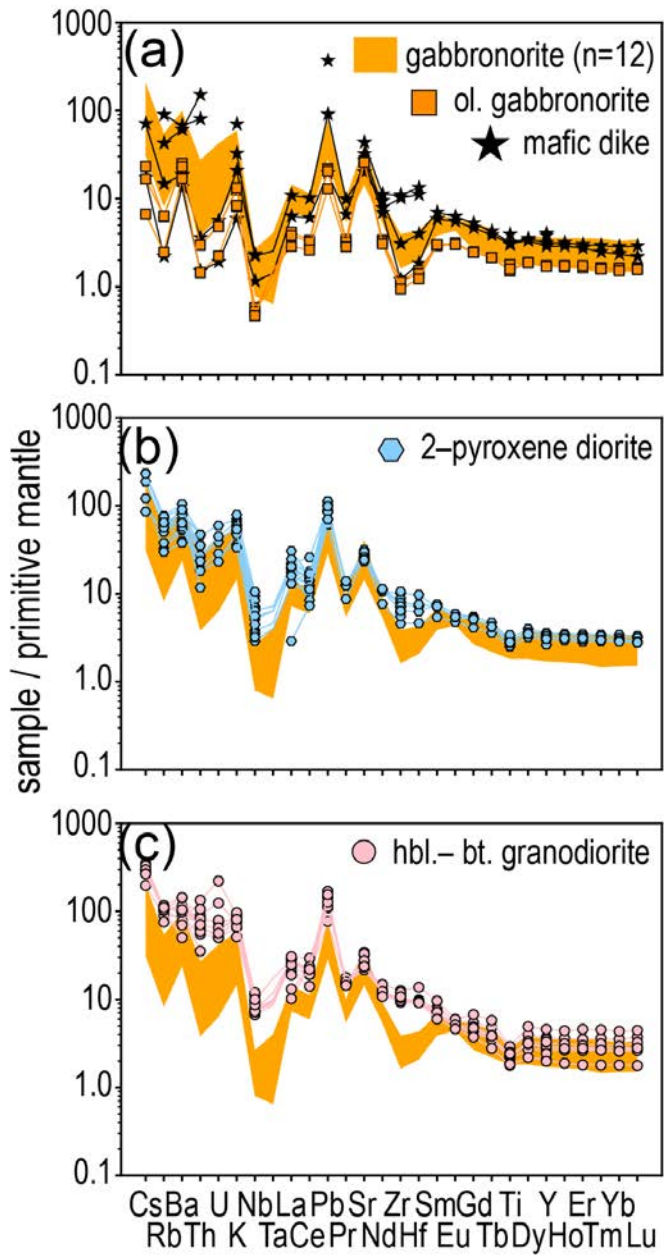
(a, c, e, g) cross-polarized photomicrographs with measured compositions labeled; **(b, d, f, h)** hammer in all field photos is 37.5 cm long and handle points roughly north, vertical in (h). Mineral names are abbreviated following Warr (2021), Fo is forsterite content expressed as a molar ratio of $100 \times \text{Mg}/(\text{Mg}+\text{FeI})$ and An is anorthite content. **(a)** Thin (2 cm) fine-grained mafic dike shown in (b), with mafic mineral Mg#'s in the same range as minerals in olivine clinopyroxenite. Inset backscatter electron image of this sample to show Fe-Ti oxides, distinguish clinopyroxene (light gray) from olivine and orthopyroxene (middle-gray), and interstitial plagioclase. **(b)** Thin fine-grained mafic dikes that crosscut olivine gabbronorite near the summit of Black Mountain. **(c)** Two-pyroxene diorite (abbreviated as di.) showing orthopyroxene (small and rounded) and clinopyroxene with coronas of Fe-Ti oxides and biotite. Plagioclase, potassium feldspar (minor) and quartz are hypidiomorphic granular around mafic phases. **(d)** ~0.5 m of modal layering within gabbronorite-like two-pyroxene diorite near Kelly Lake, continuous for ~100 m across the outcrop. **(e)** Hypidiomorphic granular amphibole-biotite granodiorite with a rounded, resorbed clinopyroxene core surrounded by amphibole and biotite. **(f)** Contact between the amphibole-biotite granodiorite and gabbronorite, near the northernmost exposure of the mafic complex (Cisco Butte suite). There is significant amphibole in a <1 cm zone within gabbronorite at the contact, and amphibole is sparse within gabbronorite farther from the contact. Hammer head is ~3 cm across. **(g)** Plagioclase-porphyritic granodiorite, typically strongly sheared, contains sheared ultramafic xenoliths, and forms dikes within the quartz porphyry unit and some metamorphic rocks along the eastern margin of the complex, shown in (h). **(h)** 1 m wide dike of the plagioclase-porphyritic granodiorite, internally foliated and sheared, within a more isotropic aphanitic quartz porphyry exposed as dikes intruding metamorphic rocks along the eastern margin of the complex.



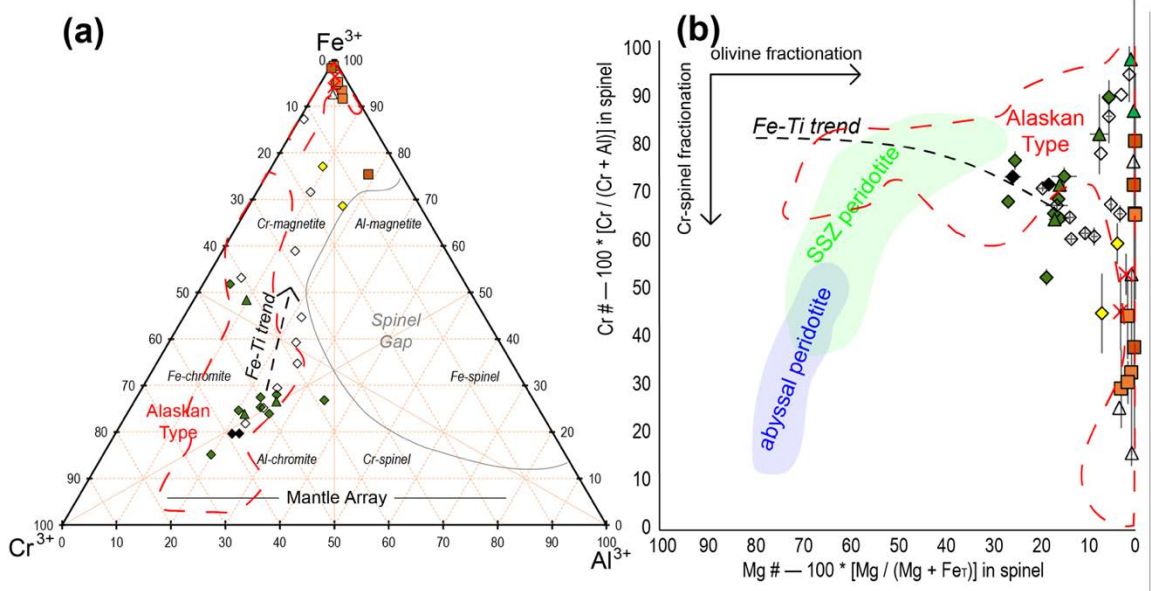
Ch. 2 Figure A 3. BSE image of low-Cr orthopyroxene rimming interstitial olivine patches in olivine clinopyroxenite. Ol = olivine, cpx = clinopyroxene, opx = orthopyroxene, Cr-mt = Cr-magnetite.



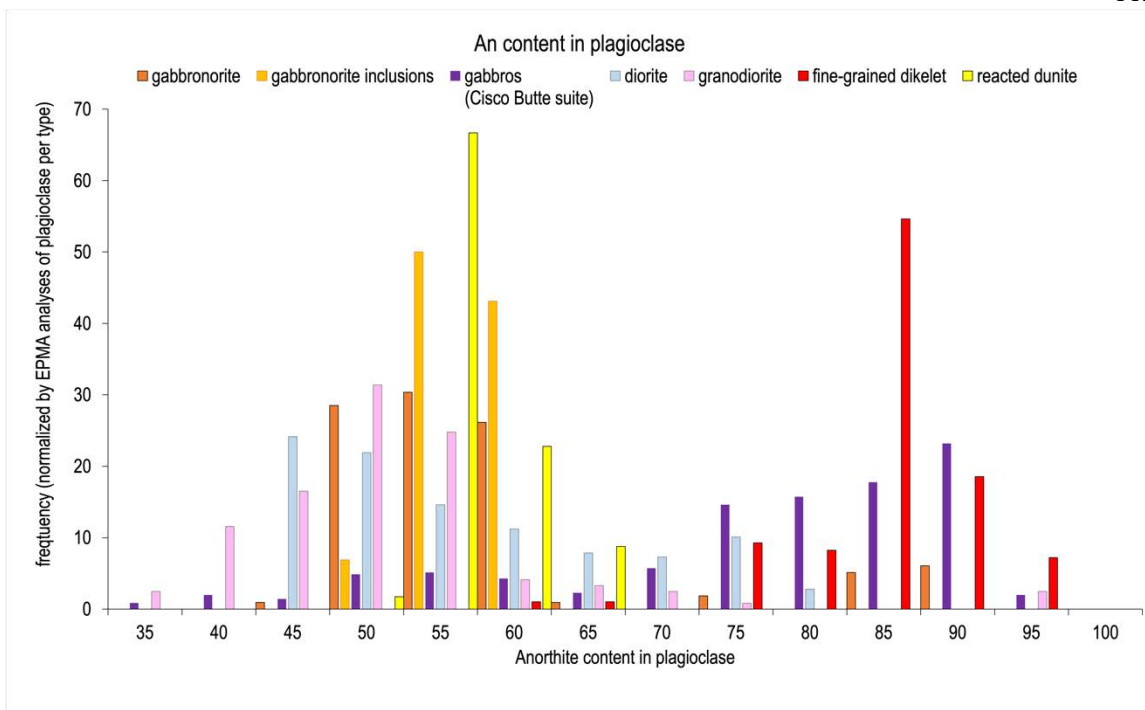
Ch. 2 Figure A 4. Harker diagrams of whole-rock compositions analyzed in this study ($n=81$) and by James (1971; $n=5$) and Wracher (1991; $n=17$) compared to Sierra Nevada batholith compositions including known mafic complexes (Sisson et al., 1996; Clemens-Knott, 1992; Lewis et al., 2021; Clemens-Knott and Gevedon, 2025; Sisson, personal communication).



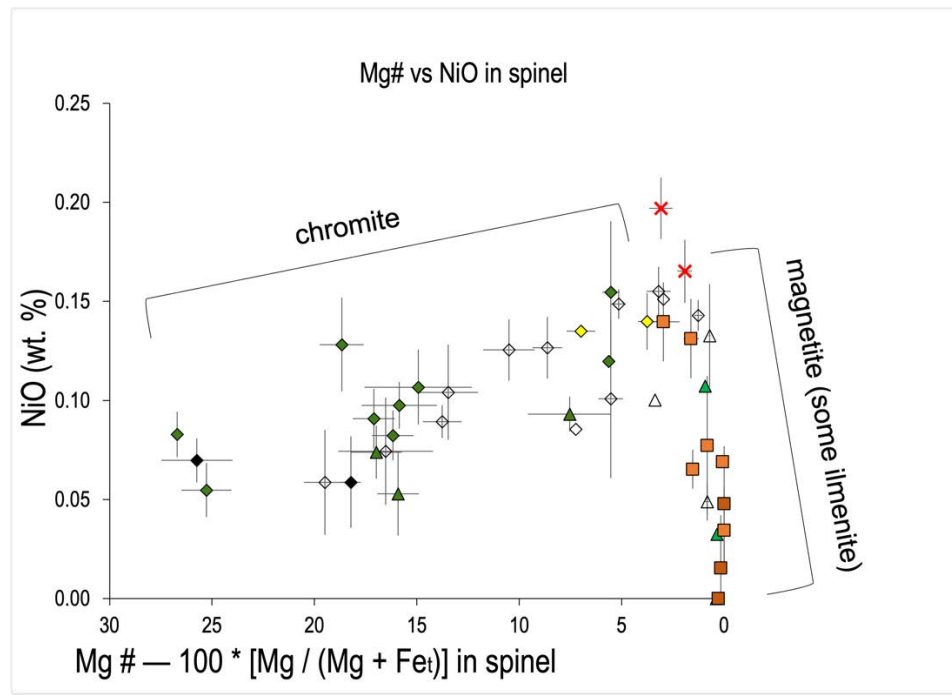
Ch. 2 Figure A.5. Trace-element spider diagrams normalized to primitive mantle (Sun and McDonough, 1989) for feldspar-bearing rocks. Points for Ta are not shown due to likely trace contamination from tungsten-carbide grinding vessels. Orange field outlines the range of 12 gabbronorite and (monzo, mela, leuco)gabbronorite samples, which are compared to **(a)** olivine gabbronorite and mafic dikes; **(b)** two-pyroxene diorite; **(c)** hornblende-biotite granodiorite.



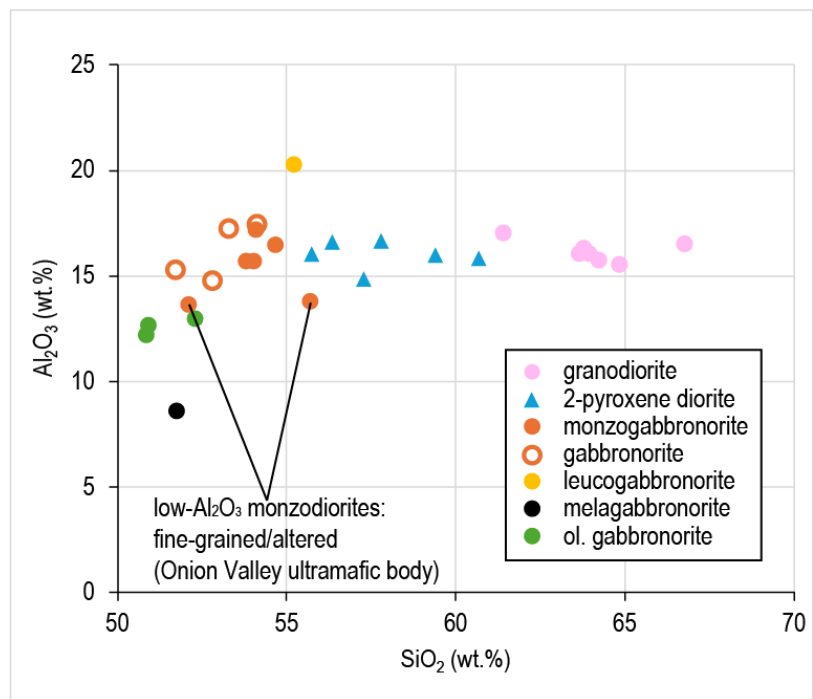
Ch. 2 Figure A 6. Spinel compositions compared to spinel from mantle peridotites, other Alaskan-type complexes (dashed red; Barnes and Roeder, 2001 compilation), and the Fe-Ti trend, which is similar to the Alaskan-type spinel trend but has higher Ti at lower Mg# (Barnes and Roeder, 2001). Symbols the same as in Figure 10 and 11. **(a)** Ternary plot showing spinel compositions; **(b)** Mg# versus Cr# in spinel for chromite through magnetite in dunite through gabbro-norite samples. Blue field of abyssal peridotite spinel compositional range (Dick & Bullen, 1984); green field of supra-subduction zone peridotite spinel compositional range (Ishii et al., 1992; Parkinson and Pearce, 1998; Pearce et al., 2000). The Alaskan-Type trend, which is enriched in Fe and then in Ti at the lowest Mg# compositions, is slightly different from the black dashed line that delineates the Fe-Ti trend that has earlier Ti enrichment due to reaction with melts and/or other silicates (Barnes and Roeder, 2001).



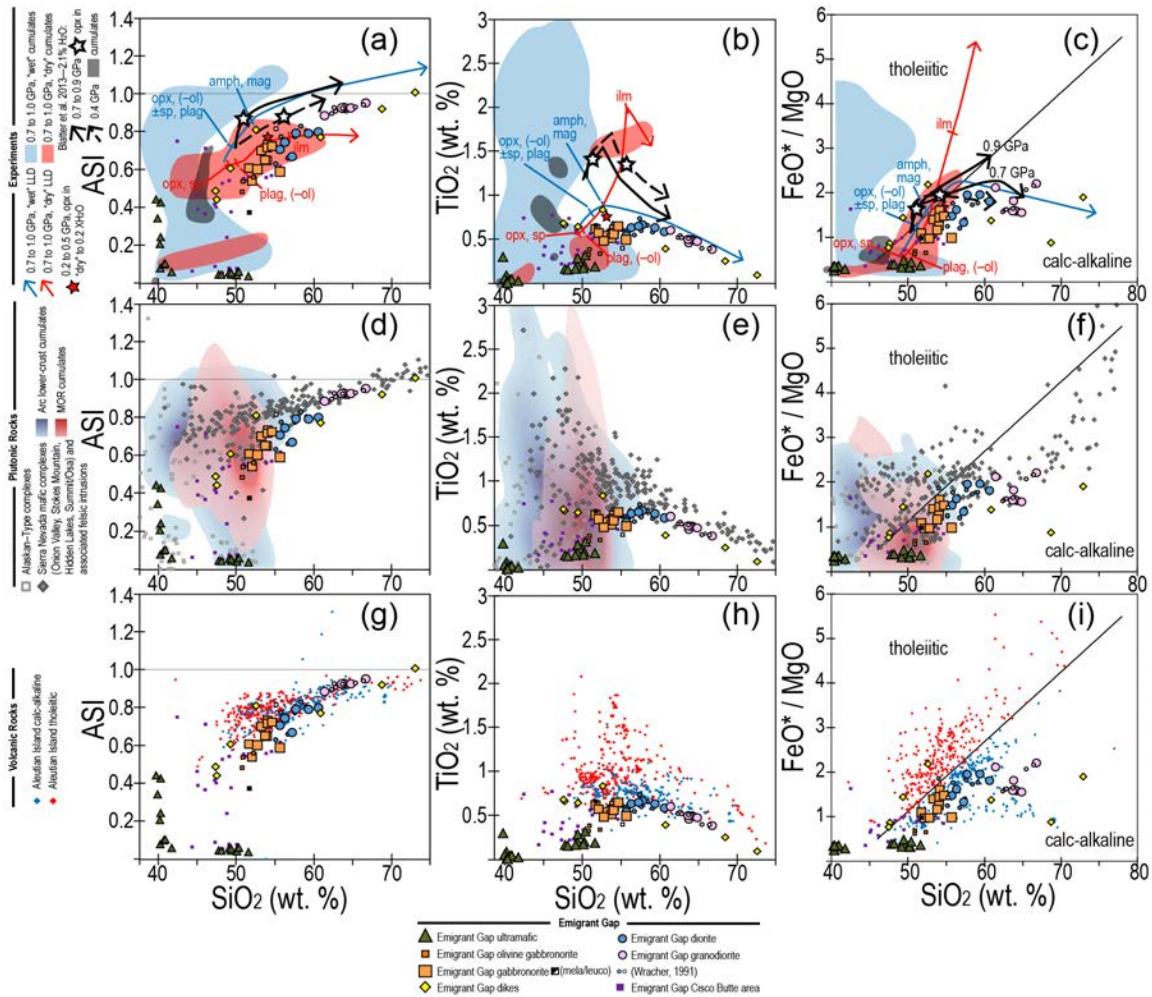
Ch. 2 Figure A 7. Histogram of anorthite (An) content in plagioclase plotting the frequency of EPMA analyses of plagioclase with An content in a given bin (each bin is 5 “An content-units” wide) for each sample type. Cisco Butte suite gabbro has higher An contents than main suite rocks. (Gabbronorite inclusions are plagioclase inclusions in cpx and occasionally opx in (olivine-gabbronorite). Frequency is normalized to the number of EPMA analyses of plagioclase in that sample type.



Ch. 2 Figure A 8. Mg# versus NiO concentration in spinel as sample averages (chromite and Fe-Ti oxides) throughout the main suite. Symbols are the same as in Figures 10 and 11.

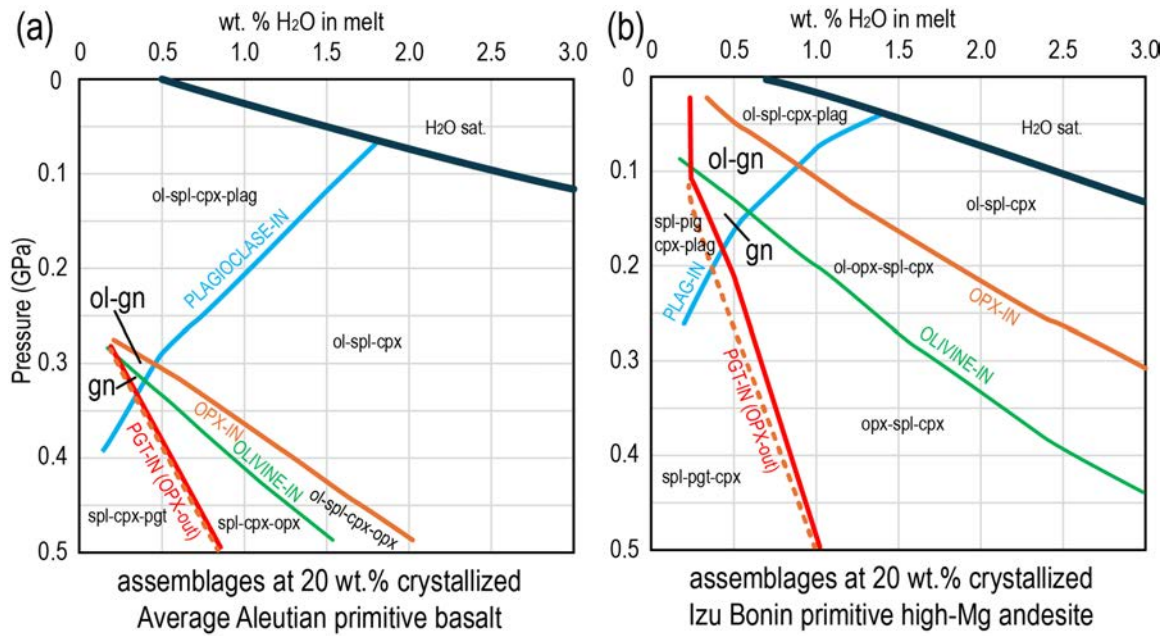


Ch. 2 Figure A 9. Whole rock SiO_2 vs. Al_2O_3 for feldspar-bearing rocks of Emigrant Gap, distinguishing gabbronorite types. Low- Al_2O_3 monzogabbronorite is fine-grained and altered (including silica/quartz), and can be found along the Onion Valley ultramafic body mapped as two-pyroxene diorite. Note the flat trend of two-pyroxene diorite compositions between granodiorite and monzogabbronorite compositions, suggestive of a mechanical mixing origin.



Ch. 2 Figure A 10. Emigrant Gap whole rock compositions showing SiO_2 versus ASI (values $>$ ASI=1 are peraluminous, marked by thin line), TiO_2 and FeO^*/MgO (where FeO^* is total iron as FeO , with tholeiitic and calc-alkaline compositions distinguished by black line; Miyashiro, 1974) compared to: **(a, b, c)** experimental data; **(d, e, f)** natural plutonic samples; **(g, h, i)** volcanic compositions. All compositions normalized anhydrous. Symbology is as follows: **(a, b, c)** schematic liquid lines of descent and fields representing cumulate compositions from experiments with high or low water contents at lower-crustal pressures and mid-crustal pressure. Experimental liquid lines of descent of low- H_2O arc basalt at deep and mid-crustal pressures (Blatter et al., 2013) are shown in black (solid and dashed, respectively), with stars representing orthopyroxene-in and gray fields outlining bulk cumulate compositions from those experiments at all pressures. The red and blue lines and fields approximate lower crustal pressure (0.7 and 1 GPa) fractional crystallization experiments that are anhydrous (Villiger et al., 2004; 2007) and hydrous (Nandedkar et al., 2014; Ulmer et al., 2018). The red star represents the onset of orthopyroxene crystallization in oxidized, upper crustal (0.2 to 0.5 GPa), low- H_2O ($\text{X}_{\text{H}_2\text{O}}$ 0 to 0.2) experiments (Feig et al., 2006). **(d, e, f)** natural plutonic samples as in Fig. 14 including cumulates from mid ocean ridge (MOR) and arc lower-crust (Chin et al., 2018), and

arc-intrusive complexes from Alaskan-Type intrusions (Himmelberg and Loney, 1995) and the Sierra Nevada batholith including other mafic intrusive complexes (Onion Valley, Sisson et al., 1996; Stokes Mountain, Clemens-Knott, 1992; Hidden Lakes, Lewis et al., 2021; Summit/Osa Creek and associated hypabyssal-volcanic series, Clemens-Knott and Gevedon, 2025; Sisson and Moore, 2010); **(g, h, i)** Volcanic rock compositions from Aleutian Islands built on oceanic crust (west of Unimak Island) from tholeiitic and calc-alkaline volcanoes (volcanic rock compositions downloaded on 5 Jan. 2024 from PetDB [<https://search.earthchem.org/>], Table S13).



Ch. 2 Figure A 11. alphaMELTS model results (P versus H_2O) showing (a) high-Mg basalt and (b) high-Mg andesite, at 20 % crystallized, showing phase assemblages over the pressure– H_2O concentration composition space explored. Clinopyroxene and spinel are stable across all pressure– H_2O conditions shown here. The intersection of plagioclase-in and orthopyroxene-in curves are represented as tick marks on the curves in Figure 13. Both compositions are predicted to crystallize near-liquidus olivine + spinel across the lower-pressure and higher- H_2O approximately half of the explored condition space, thus broadly satisfying the requirement of initially producing dunite cumulates. At moderately greater extents of crystallization (≥ 10 wt %), calcic clinopyroxene would have joined the mineral assemblages of both compositions across nearly all of the explored pressure and H_2O conditions, as shown above. For the basalt this widely satisfies the subsequent production of wehrlite or olivine clinopyroxenite cumulates, whereas for the andesite at that degree of solidification, the olivine + clinopyroxene + spinel assemblage is restricted to the low-pressure and high- H_2O ~half of the explored condition space. Orthopyroxene would be present in the andesite across the higher-pressure lower- H_2O ~two-thirds of the explored conditions, and orthopyroxene would have wholly replaced olivine in the lower approximately half of that space, both inconsistent with Emigrant Gap mineral assemblages and appearance sequences.

SIERRA NEVADA UPPER-CRUSTAL MAFIC INTRUSIONS
RECORD ARC MIGRATION INTO THICKENED
CONTINENTAL CRUST

Juliet Ryan-Davis¹, Claire E. Bucholz¹, Jade Star Lackey², Madeline J. Lewis³, Andrew Kylander-Clark⁴, Oliver Wilner¹

¹*Division of Geological and Planetary Sciences, Caltech, Pasadena, California 91104, USA*

²*Pomona College Geology Department, Claremont, California 91711, USA*

³*Department of Geology and Geophysics, University of Wyoming, Laramie, Wyoming 82701, USA*

⁴*Department of Earth Science, University of California, Santa Barbara, California 93106, USA*

ABSTRACT

The formation of silicic arc batholiths and erupted magmas requires primitive basalts to undergo differentiation at subduction zones. Differentiation, however, remains a challenging petrologic problem to understand, due to the many potential ways it can occur (e.g., fractional crystallization, assimilation, partial melting, magma mixing). Although typically small ($\leq 35 \text{ km}^2$ exposure area), mafic intrusions are ubiquitously found throughout the upper crust of arc batholiths and record information about the initial stages of differentiation of mafic (mantle-derived) magmas. In the Sierra Nevada batholith, upper-crustal mafic intrusions provide a record of spatiotemporal variability across heterogeneous, tectonically assembled framework of pre-existing upper plate lithosphere and crust. This framework is best described as four distinct batholith-parallel belts with variable lithospheric and crustal affinity. The mafic magmas parental to all the upper-crustal mafic intrusions along a transect across these belts (~west to east) are not primary, mantle-equilibrated compositions; rather they are low-MgO basalts produced through prior differentiation in the lower crust. The mafic intrusions vary systematically in their geochemistry and field relationships with associated or adjacent felsic intrusions along the transect. The pre-existing upper-plate crustal thickness, composition, and strength—potentially interrelated parameters that vary systematically by belt—thus have a first-order control on the involvement of mafic magmas in production of the silicic batholith.

INTRODUCTION

Although silicic igneous rocks are volumetrically dominant in the upper crust of arcs and as erupted products of subduction zones, mafic magmas are required in their generation as sources of mass and/or heat. There is consensus that differentiation of mafic magmas occurs in the deep crust (Hildreth and Moorbath, 1988; Sisson et al., 2005; Annen et al., 2006; Greene et al., 2006; Jagoutz 2014; Müntener and Ulmer, 2018; Jagoutz and Klein, 2018). However, some mafic

magmas ascend to shallow levels, erupting as basalt to basaltic andesite at arcs and/or crystallizing as upper-crustal mafic intrusions. Because the intrusive record integrates arc-wide activity over hundreds of kilometers and tens (to hundreds) of millions of years, studying mafic intrusions in the upper crust can reveal systematic arc-wide spatial and temporal geochemical changes linked to subduction zone processes.

The Sierra Nevada batholith offers a rich framework for contextualizing and understanding batholith-wide trends, as its evolved intrusions and their host rocks have been well-documented (e.g., Bateman, 1963; Kistler and Peterman, 1973, 1978; Saleeby and Sharp, 1980; DePaolo, 1981; Chen and Moore, 1982; Ague and Brimhall, 1988b; Silver and Chappell, 1988; Chen and Tilton, 1991; Pickett and Saleeby, 1993; Nadin and Saleeby, 2008; Saleeby et al., 2008; Lackey et al., 2008). The composition of the upper-plate lithosphere and crust into which the batholith was emplaced varies laterally in the form of belts that run along the strike of the batholith; these different compositional belts are correlated with compositional and petrologic trends in the evolved intrusions of the batholith (Moore, 1959; Chen and Moore, 1982; Saleeby et al., 2008; Lackey et al., 2008; Chapman et al., 2012, 2017; Ardill et al., 2024).

Several studies have focused on mafic intrusions in the upper crust throughout the Sierra Nevada batholith (Frost and Mahood, 1987; Sisson et al., 1996; Coleman et al., 1992, 1995; Coleman and Glazner, 1997; Clemens-Knott and Saleeby, 1999; Ratajeski et al., 2001; Wenner and Coleman, 2004; Holland et al., 2013; Ratschbacher et al., 2018; Klein et al., 2021; Lewis et al., 2021, 2024). The Emigrant Gap complex of the Northern Sierra and the Stokes Mountain complex in the western Sierra Nevada foothills are distinct among these upper-crustal mafic intrusions in that they provide records of parental magmas at a more primitive stage (James, 1971; Clemens-Knott, 1992; Clemens-Knott and Saleeby, 1999; Ryan-Davis et al., *Chapter 2*). In contrast, most the targeted studies of Sierra Nevada mafic intrusions find that they crystallized not from primitive magmas, but rather, from mafic magmas that have experienced prior differentiation at depth—even deeper than the 0.7–0.9 GPa level of exposures in the southern Sierra Nevada (Sisson et al., 1996; Klein and

Jagoutz, 2021; Lewis et al., 2021, 2023; Rezeau et al., 2021). Despite this, past studies have used their isotopic compositions to infer the mantle source composition. A Mesozoic mantle component with $\varepsilon\text{Nd}_{(\text{Mesozoic})}$ around -4.5 and $^{87}\text{Sr}/^{86}\text{Sr}_{(\text{Mesozoic})}$ around 0.7065 is described as “enriched” relative to depleted MORB mantle (DMM), and has been proposed as the likely source of mafic magmas throughout most of the Sierra Nevada batholith, particularly in the central and eastern portions (Coleman et al., 1992; Sisson et al., 1996; Coleman and Glazner, 1997; Ratajeski et al., 2001). A potentially slightly less “enriched” mantle source composition ($\varepsilon\text{Nd}_{(\text{Mesozoic})}$ around $+1$ and $^{87}\text{Sr}/^{86}\text{Sr}_{(\text{Mesozoic})}$ around 0.7047) was inferred in the western parts of the batholith (Kistler et al., 1986; Clemens-Knott, 1992; Gevedon, 2013; Holland et al., 2013). It is necessary to evaluate the potential role of crustal assimilation in modifying the isotopic composition of the mafic magmas parental to the studied intrusions before they can be used to infer mantle characteristics. Moreover, these studies heavily sample mafic intrusions from the eastern exposures of the Sierra Nevada, with limited focus on the western side of the batholith, and nearly no representation of the central portions.

This study takes a regional, trans-batholithic approach to characterizing upper crustal mafic intrusions along an east-west transect at $37 \pm 0.5^\circ$ N perpendicular to the strike of the belts that comprise the Sierra Nevada (Fig. 1). We evaluate the relationships of mafic intrusions with more evolved rocks of the batholith (generalized as “felsic” in this study), as well as the petrology and geochemistry of the mafic intrusions. By targeting mafic intrusions, which record early stages of arc magma evolution, we document batholith-scale spatiotemporal geochemical trends while avoiding complexities associated with more evolved compositions (*i.e.*, Jacob et al., 2021; Moyen et al., 2021). We target the questions of (1) whether prior differentiation is important for allowing the parental mafic magmas to ascend to shallow levels, and (2) whether there are batholith-wide trends in geochemistry and how these trends may relate to comparable trends identified in the felsic batholith and the pre-existing lithospheric and crustal architecture of the North American upper plate.

Geology of the transect

The Sierra Nevada batholith formed during Mesozoic arc magmatism along the southwestern margin of Laurentia and was constructed on ~NNW trending tectonically assembled lithospheric belts preserved as exposed metamorphic host rocks (Saleeby et al., 2007; Chapman et al., 2012, 2017; Saleeby and Dunne, 2015; Attia et al., 2018; Ardill et al., 2024). Broadly, the western part of the batholith is constructed on accreted oceanic (Panthalassan) lithosphere, whereas the eastern batholith is hosted by continental (Laurentian/North American) lithosphere (DePaolo, 1981; Kistler and Peterman, 1973, 1978; Saleeby, 1981, 1982; Kistler, 1990, 1993; Ducea, 2001; Lackey et al., 2008), with distinctive crustal affinities and sedimentary packages within these NNW-trending belts (Saleeby et al., 1987; Kistler 1990; Stevens and Greene, 2000; Saleeby et al., 2008; Memeti et al., 2010; Saleeby, 2011; Chapman et al., 2012; Saleeby and Dunne, 2015). This framework continues southward into the Peninsular Ranges batholith, where distinctive characteristics in mafic plutons in the western and eastern domains have been identified (Taylor and Silver, 1978; Walawender and Smith, 1980; Silver and Chappell, 1988; Lee et al., 2007; Kimbrough et al., 2015). In addition, the more evolved plutons of the batholith vary by belt, generally increasing in SiO_2 from west to east, with mainly quartz-diorite in the western-most belt, evolving to dominantly granodiorite and granite in the eastern domains (Moore, 1959; Ross, 1989; Saleeby et al., 2011; Chapman et al., 2012).

Following previous studies (*i.e.*, Saleeby, 1981; Kistler et al., 1990, 1993; Lackey et al., 2008; Chapman et al., 2012; Ardill et al., 2024), we define four distinct spatial belts, including the (1) western, (2) central, (3) high Sierra, and (4) eastern belts (Fig. 2A). These subdivisions are based primarily on metamorphic pendant affinities, but also previously documented isotopic variability within the batholith. In detail, documented “breaks” in the batholith delineating the different belts from west to east, are: (1) the Foothills suture (Saleeby, 1982) and the $^{87}\text{Sr}/^{86}\text{Sr}_{(i)} = 0.706$ isopleth of Kistler and Peterman (1973), separating the western and central belts, where $^{87}\text{Sr}/^{86}\text{Sr}_{(i)}$ is the initial strontium isotope ratio of whole rock samples; (2) the

Panthalassan-North American boundary or “interbatholithic break 2” (Saleeby et al., 1986; Kistler, 1993; Lackey et al., 2008; Ardil et al., 2024), separating the central and high Sierra belts; and (3) the Sierra Crest shear zone (Greene and Schweickert, 1995; Tikoff and de Saint Blanquat, 1997), separating the high Sierra and eastern belts. The eastern belt thus extends from the eastern exposures of the Sierra Nevada mountains to the transtensionally-displaced, but lithospherically similar, White-Inyo mountains.

Briefly, the distinctive combinations of lithosphere and crust exposed as metamorphic pendants between intrusions can be summarized by belt as follows. The western belt is built on oceanic lithosphere and hosts the Foothills ophiolite belt (the Kings River ophiolite in the study area) and associated Permian to Triassic metavolcanic to metasedimentary subduction mélange complexes (Kistler and Peterman, 1973; Schweickert et al., 1977; Saleeby, 1982; Snow and Ernst, 2008; Saleeby, 2011). The central belt is transitional between the plainly oceanic western belt and the two plainly continental belts to the east, with multiple potential interpretations for its lithospheric affinity. Broadly, there is consensus that the central belt is constructed on oceanic (Panthalassan) lithosphere, with continent-derived lower-Paleozoic deep marine sedimentary sequences (Kistler and Peterman, 1973; Ague and Brimhall, 1987; 1988b; Kistler, 1990; Saleeby and Busby, 1993; Lackey et al., 2006; Attia et al., 2018, 2021). Mantle xenoliths (garnet websterites and peridotites) in Miocene lavas in the central belt have radiogenic strontium isotope ratios and unradiogenic neodymium isotope ratios compared to depleted mantle (average $^{87}\text{Sr}/^{86}\text{Sr}_{(100 \text{ Ma})}$ around 0.7056 and average $\varepsilon\text{Nd}_{(100 \text{ Ma})}$ around -2), where $^{87}\text{Sr}/^{86}\text{Sr}_{(t)}$ is the strontium isotope ratio of a sample and $\varepsilon\text{Nd}_{(t)}$ is the epsilon-neodymium isotope value of a sample with respect to the chondritic uniform reservoir (CHUR), each calculated at time “ t ”. However, lower-crustal ($>\sim 1$ to 1.5 GPa) granulite and pyroxenite±garnet xenoliths have both mantle and crustal isotopic signatures (Domenick et al., 1983; Dodge et al., 1986; Mukhopadhyay and Manton, 1994; Ducea, 1998; Ducea and Saleeby, 1998; Lee et al., 2006; Chin et al., 2014; Lee et al., 2018).

The suture between oceanic lithosphere and Laurentian/North American continental lithosphere crosses through the Boyden Cave pendant within this study area, which has exposures of mostly metasedimentary rocks to the west and metavolcanic rocks to the east of the suture (Nockleberg, 1983; Saleeby et al., 1990; Kistler, 1990, 1993). Accordingly, the high Sierra belt is also built on continental lithosphere and contains pendants of dominantly Mesozoic metavolcanic and caldera-fill sequences from arc activity just prior to intrusion of the batholith (Kistler, 1993; Saleeby et al., 1990; Fiske and Tobisch, 1994; Klemetti et al., 2014; Raftrey et al., 2016; Barth et al., 2018). The eastern belt is also on continental lithosphere, with metamorphic pendants dominated by Neoproterozoic to mid-Paleozoic shallow marine passive margin metasedimentary sequences, which make up the majority of exposures in the White-Inyo range (Farmer and Ball, 1997; Stevens and Greene, 2000; Stevens et al., 2005; Attia et al., 2018, 2021). Mantle xenoliths from a cinder cone that lies along the eastern range front of the Sierra Nevada have oxygen, strontium and neodymium isotope ratios similar to those found in the central belt (Domenick et al., 1983; Mukhopadhyay and Manton, 1994; Beard and Glazner, 1995; Gao et al., 2017).

Spatiotemporal trends have been documented for the felsic plutons of the batholith that intruded this framework (Fig. 1, 2a). Triassic plutons are restricted to the eastern belt of this study. Jurassic plutons occur mainly along the western and eastern flanks of the range, and were wedged apart and potentially rearranged by magmatism and crustal-scale shear zones active during Cretaceous batholith formation (Fig. 1; Busby-Spera and Saleeby, 1990; Bateman, 1992; Greene and Schweickert, 1995; Tobisch et al., 1995; Nadin and Saleeby, 2008; Saleeby, 2011; Saleeby and Dunne, 2015; Attia et al., 2018). During major episodes of Jurassic intrusive activity, extension is recorded by the ~147 Ma Independence dike swarm that intruded the eastern belt and extends south to the Mojave Desert (*e.g.*, Carl and Glazner, 2002). Most exposed batholith intrusions are Cretaceous, and their ages become younger west to east (Fig. 2B; Evernden and Kistler, 1970; Chen and Moore, 1982; Ague and Brimhall, 1988b; Kistler, 1990; Coleman and Glazner, 1997; Kistler

et al., 2003; Lackey et al., 2008; Cecil et al., 2012; Chapman and Ducea, 2019). This dominant record of magmatism is often identified as a final “flare-up” of magmatic activity of the Sierra Nevada batholith (DeCelles et al., 2009; Paterson and Ducea, 2015; Ducea, 2001; Chapman et al., 2021). The largest felsic intrusions of the Cretaceous batholith are in the high Sierra belt and are also some of the youngest (~83–89 Ma), characterized by enigmatic potassium-feldspar megacrysts (Fig. 1; Moore and Sisson, 2008).

Mafic intrusions were originally considered “forerunners” to the batholith (Mayo, 1941), but have been shown to be contemporaneous and intimately involved in its formation, including as mafic enclaves in more silicic plutons (Dorais et al., 1989; Frost and Mahood, 1987; Bateman, 1992; Coleman et al., 1992, 1995; Sisson et al., 1996; Coleman and Glazner, 1997; Lewis et al., 2021, 2024). Where well-exposed in the high Sierra and eastern belts, the mafic intrusions have tabular (sheet-like, sill or dike) geometries of kilometer to 10-kilometer scale in many cases with tapered ends (Fig. 3). This has been shown at one of the most well-known examples of the region, at Onion Valley (Sisson et al., 1996), and in Yosemite (Ratajeski et al., 2001). Despite their occurrence in all belts, most studies of mafic intrusions focus on the eastern belt, where their age and geochemical relationships to felsic intrusions are inferred to represent the mafic input to the batholith broadly (*i.e.*, Coleman et al., 1992, 1995; Lewis et al., 2024). Thus, this study attempts to broaden this understanding and compare mafic plutons across the arc to identify their relationships to the known batholith-wide framework and trends.

SAMPLING AND ANALYTICAL METHODS

The categorization of the mafic intrusions that we focus on by belt is fundamentally geographical (and thus, geological, as described above; Fig. 2A). We targeted previously mapped mafic intrusions in order to collect 190 samples from the western, central, and high Sierra belts of the Sierra Nevada, and from the eastern belt in the White-Inyo Mountains (Supplementary Data File). Combined with samples collected previously from the eastern belt ($n = \sim 60$, Lewis et al., 2021; $n = 109$ from

Lewis et al., 2024), the sample collection covers 46 mafic plutonic localities along a ~225 km east-west (by ~100 km north-south) transect across the central Sierra Nevada batholith (Fig. 2A). Inaccessibility due to private land, especially in the western belt, prevented comprehensive access to many of the mafic intrusions, so sampling there is limited and biased towards roadside exposures. Thus, this study includes samples from 11 mafic intrusion localities in the western belt, 11 in the central belt, 5 in the high Sierra belt, and 14 in the eastern belt proper plus 2 in the White-Inyo mountains (included as part of the eastern belt).

Although some of the mafic intrusions are composite in nature, comprising both mafic and more silicic lithologies, we focus dominantly on the mafic rocks from each mafic intrusion (Table 1). Our sampling targeted the following lithologies from each intrusion: (1) gabbroic-dioritic rocks representative of the main lithology of the mafic intrusion, (2) the most mafic rocks present (often with cumulate textures), and (3) fine-grained mafic rocks. For ~60% of intrusions, we also sampled intermediate to felsic plutonic rocks from adjacent intrusions and metamorphic country rocks. Rock types are described in detail below, but in general, most mafic rocks range amphibole gabbro or gabbronorite to amphibole+biotite monzodiorite.

Zircon U-Pb ages and trace elements

We analyzed zircon from 69 samples of gabbro to diorite from 44 localities for U(-Th)-Pb geochronology and trace element (TE) concentrations. Zircon was concentrated using traditional magnetic and heavy liquid mineral separation methods at California Institute of Technology, Pomona College, and GeoSep Services (Idaho, USA). A UV light aided in picking zircon for mounts, particularly in samples with low yields, small zircon, and/or abundant apatite. Twenty-one of these samples were previously analyzed for U(-Th)-Pb geochronology and therefore for those samples, we report published ages alongside new trace element analyses of 6 to 13 representative grains analyzed in the same analytical session as the new samples in this study (Lewis et al., 2021; Lewis et al., 2024 and references therein). Zircon was

not recoverable from samples from 3 localities (Hildreth, Humphrey's Station, and Patterson).

Cathodoluminescence images indicated uniform zircon populations for most samples (80%) and guided analytical spot placement. We focused analyses on magmatic rims, but also some cores that appeared inherited. Laser-ablation split-stream inductively-coupled plasma mass spectrometry (LA-SS-ICPMS) was performed at the University of California, Santa Barbara, to measure U(-Th)-Pb dates and TE concentrations of the same zircon zones previously analyzed by secondary ion mass spectrometry for oxygen isotopes and subsequently analyzed by laser-ablation multi-collector ICPMS for hafnium isotopes (Ryan-Davis et al., *Chapter 4*). Additional analyses without corresponding oxygen (or follow-up hafnium) isotope analyses were undertaken to ensure robust age statistics (1179 analyses total; $n = 16$ to 29 measurements per sample, except for samples with few zircon recovered: 8 analyses for 19-JRD-32; 12 analyses for 21-JRD-130A). Detailed methods and analytical parameters, including criteria for exclusion of analyses (*i.e.*, discordant or outlier U-Pb analyses, and analyses affected by mineral or glass inclusion that would not significantly affect U-Pb systematics) are reported in Appendix 2 of this chapter.

Bulk rock geochemistry (XRF and pressed pellet LA-ICPMS)

Whole-rock analyses of 118 representative bulk mafic samples were performed at the California Institute of Technology. Samples were cut on a diamond saw to remove weathered surfaces and alteration, then sanded and sonicated to clean saw blade residue. A minimum of 0.5 kg of each sample was homogenized into powder by crushing in a steel chipmunk crusher, subsampling ~40 g, and powdering in an alumina ball mill. Samples were dried overnight in a 110 °C oven and then ignited at 1050 °C for 1 hour to determine loss on ignition.

Fused glass samples for XRF analysis were prepared using 10:1 Li-borate flux to sample powder in platinum crucibles at 1200 °C. Major, minor and select trace elements (SiO_2 , TiO_2 , Al_2O_3 , Fe_2O_3 , MnO , MgO , CaO , Na_2O , K_2O , P_2O_5 , Cr, Cu, Zn, Rb, Ba, Sr, Nb, Zr, Hf, Y, Zn, Co, V, La, Ce, Nd, Pb, Th) were analyzed using a

Panalytical Zetium wavelength-dispersive XRF spectrometer following the methods of Bucholz and Spencer (2019). Compositions are reported with all iron as FeO* in Table S2, along with whole-rock compositions of samples from other studies from which zircons were separated and analyzed in this study (Sisson (2022). personal communication; Lewis et al., 2021; Lewis et al., 2024). The two samples from Onion Valley (86S52A and 85S57; Sisson, personal communication) were measured by XRF (SiO₂, TiO₂, Al₂O₃, Fe₂O₃^T, MnO, MgO, CaO, K₂O, P₂O₅, Cr, Y, V), flame photometry (Na₂O), ICP (Nb) and INAA (Ba, Co, Ni, Cr, Cs, Hf, Rb, Ta, Th, U, Sc, La, Ce, Nd, Sm, Eu, Gd, Tb, Tm, Yb, Lu), as described by Sisson et al., 1996,

Trace elements (including Li, Be, B, Sc, V, Co, Ni, Ga, As, Rb, Sr, Y, Zr, Nb, Sn, Cs, Ba, La, Ce, Pr, Nd, Sm, Eu, Gd, Tb, Dy, Ho, Er, Tm, Yb, Lu, Hf, Ta, Pb, Th, U) in 55 samples from this study and 16 samples of Lewis et al. (2024) were analyzed as pressed pellets by laser ablation inductively-coupled mass spectrometry (LA-ICPMS) at the California Institute of Technology following the methods described in Wilner et al. (*in prep*). When an element in a given sample was measured by both XRF and pellet LA-ICPMS, the pellet LA-ICPMS value is plotted and reported in the text. The method is briefly described here. Powdered samples were weighed (330 ± 5 mg) and added to 70 ± 5 mg of cellulose binder. The powder and binder were homogenized by passing through 150 and 106 µm sieves and grinding any particles that were larger than 106 µm in a corundum mortar and pestle until all material had passed through. Samples were then pressed into pellets under vacuum at 8.1 tonnes in a 13 mm diameter die set.

Pressed pellets were analyzed using a New Wave Research UP-193 laser ablation system coupled to an Agilent 8800 QQQ ICP-MS operated in no-gas single-quad mode with Ar carrier gas. Groups of analyses included a background blank, three calibration lines on a pressed pellet of NIST SRM 612, seven replicate line analyses on each sample, and a bracketing analysis of NIST SRM 610 between each sample. The concentration of Si, determined by XRF, was used as a normalizing internal standard for all analyses. Reference materials RGM-2 and BHVO-2 were also analyzed as unknowns and are reported with results (Table S2).

Olivine and pyroxene major element chemistry (EPMA)

We analyzed the major and minor element compositions of olivine, clinopyroxene and orthopyroxene from 20 samples from the western, central and high Sierra belts by on a JEOL JXA-iHP200F field emission electron microprobe (EPMA) at Caltech equipped with five wavelength-dispersive X-ray spectrometers. Operating conditions were 25 nA beam current, 15 kV accelerating voltage, and 10 μm beam diameter. Full instrument conditions, including counting times for individual elements, are reported in Table S6.

Elements analyzed include Si, Ti, Al, Fe, Mg, Ca, Na, K, Cr, Mn and Ni, with detection limits of ~ 0.005 wt.% for Si, Al, Mg, Ca, Na and K; and ~ 0.015 wt.% for Ti, Fe, Mn, Cr and Ni. Data reduction used a mean atomic number (MAN) background correction (Donovan and Tingle, 1996; Donovan et al., 2016) and Armstrong/Love Scott ZAF algorithm (Armstrong, 1988). Oxygen was calculated from cation stoichiometry and included in the matrix correction (Moy et al., 2023). Standards for analyzed elements were synthetic anorthite (Si, Al, Ca), forsterite (Mg), fayalite (Fe), Mn-olivine (Mn), Al_2O_3 (for background correction), TiO_2 (Ti), Cr_2O_3 (Cr) and NiO (Ni), and natural Amelia albite (Na), Asbestos microcline (K), and San Carlos olivine (for background correction). Standard intensities were corrected for drift over time on an element-by-element basis. Mineral formulae are reported on a 4 O basis for olivine and a 6 O basis for pyroxenes.

We targeted mineral cores (5 points per grain, 5 grains of each mineral per sample, where possible) that appeared least altered optically in thin section and in backscatter images to collect representative compositions least affected by subsolidus chemical exchange with other minerals. Results for olivine (Table S3), clinopyroxene (Table S4) and orthopyroxene (Table S5) are reported in the Supplementary Data File. Sample averages for each phase are reported in Table 2. These results are presented in combination with reported analyses of these minerals from the eastern belt (Lewis et al., 2024) and from previous detailed studies of Hidden Lakes and Onion Valley (Lewis et al., 2021; Sisson et al., 1996).

FIELD RELATIONSHIPS OF MAFIC INTRUSIONS ACROSS THE TRANSECT

There are several common features shared by most of the mafic intrusions in this study, and also distinct differences that correspond closely to the belt architecture discussed above. A fundamental similarity is the abundance of amphibole in all the mafic intrusions. In addition, small segregations (usually centimeter-scale, rarely approaching a meter in size) of coarse plagioclase and amphibole are commonly found. These pegmatoid segregations have skeletal amphibole with plagioclase cores in many cases (Fig. A-1), and are typically widespread although volumetrically minor constituents throughout each intrusion.

A second similarity among most mafic intrusions is a mingled or heterogeneous zone at their contacts with felsic intrusions (Fig. 4). These fall into two broad categories. First, fine-grained chilled crenulated (Fig. 4H), lens-shaped (Fig. 4A, F), or mingled margins (Fig. 4E, G) of mafic rocks in contact with their felsic hosts indicate that they quenched as magmas intruding into a lower temperature felsic magma. Evidence for co-magmatic intrusion is also less commonly seen as composite dikes (Fig. 4B). Second, previously solidified (at least partly, if not fully) felsic or mafic intrusions have evidence that they were remobilized, depending on which (felsic or mafic) intruded first. This is seen either as wispy, fine-grained felsic plutonic material intermixing at the margin of the mafic intrusion (Fig. 4J), or as angular to rounded blocks of mafic plutonic rock clustered in the marginal zone of an adjacent felsic pluton (Fig. 4C, D, I).

A third similarity among many mafic intrusions is the presence of metamorphic xenoliths (Fig. 5). Typically, these xenoliths are characterized by reaction halos, and the adjacent mafic plutonic rock has distinct modal mineralogy or coarse grain size compared to the typical mafic host rock (Fig., 5C, E, F). Some of the mafic bodies directly intrude metamorphic pendants, yet these xenoliths can be found hundreds of meters from the contact, within the mafic body (Fig. 5B, C, E). Other mafic bodies

do not occur within pendants, yet in many of them, decimeter to several meter-sized blocks of metamorphic rock are still observed (Fig. 5A, D, F).

Differences in mafic intrusion styles by belt

Broadly, the distinctions among the mafic intrusions can be grouped by belt. We ascribe these differences to changes in “styles” of magmatism, discussed further below. The western and central belts host intrusions dominantly characterized by abundant cumulates, including olivine, pyroxene and amphibole-rich cumulates, and plagioclase-rich cumulates. Orthopyroxene occurs in ~30% of the mafic intrusions of the western and central belts as a mafic phenocryst, ranging in modal abundance from ~5 to 20%. These intrusions host exemplary modal and grain size layering and schlieren and comb textures (Fig. 6A, B, E, F). Later felsic intrusions brecciate and disrupt mafic cumulates (Fig. 6C, D, F). In the westernmost exposure of the western belt, mafic complexes occur as “ring dike” complexes that represent feeder systems to arc volcanoes (Clemens Knott et al., 1999; Mack et al., 1979). Additionally, the western mafic intrusions are generally large (up to ~15 km wide) compared to the central and high Sierra belts (<~2.5 km wide). In both the western and central belts, mafic intrusions often occur in metamorphic pendants and belts, including the Ordovician Kings-Kaweah ophiolite in the southwestern part of our study area.

In contrast, in the high Sierra belt along Monarch Divide, mafic intrusions are characterized by small volumes and a paucity of mafic cumulate rocks (texturally and/or chemically defined below). The mafic intrusions are the least mafic of the transect, with far more abundant dioritic rocks than gabbroic rocks (in a general sense). In nearly all cases, the mafic intrusions mingled significantly with their at least partly crystallized felsic host plutons, along margins, as dike-like swarms of enclaves extending into the host, or throughout the entirety of the mafic body (Fig. 3A–B; 4E–H; Fig. 7A–C).

In the eastern belt, the mafic intrusions are exposed along the easternmost face of the Sierra Nevada range front scarp and along the range crest. This belt hosts some of the largest and most heterogeneous mafic intrusions of the transect (*i.e.*, Onion

Valley; Sisson et al., 1996). Like the western belt, several of the eastern intrusions host ultramafic and plagioclase-dominated cumulate rocks in addition to more common amphibole gabbro. These eastern mafic intrusions have been the subject of several studies (Frost, 1987; Frost and Mattinson, 1988; Coleman et al., 1995), including a recent synthesis by Lewis et al., 2023. In many cases, the well-exposed eastern mafic intrusions have sill (or dike) geometries that intrude older felsic plutons, although mingling among co-eval mafic and felsic intrusions also occurs (Frost and Mahood, 1987; Coleman et al., 1995; Lewis et al., 2024). Along the Sierra Crest, at Onion Valley, remobilization of the felsic host pluton between later-injected mafic sills produces flame structures (Fig. 7D; Sisson et al., 1996). The White-Inyo Mountain range to the east, included in this belt, hosts very few mafic intrusions—exposures are dominated by metamorphic rocks, compared to the pluton-dominant Sierra Nevada. The mafic intrusions there are either similar to the eastern Sierra or intrude metamorphic framework rocks and experienced significant chemical exchange with them (*i.e.*, abundant epidote in the mafic rocks and exoskarn formation).

GEOCHRONOLOGY RESULTS

Zircon morphology and textures

Zircons are mostly colorless to pale brown or grayish, and in most samples are either prismatic euhedral to subhedral grains, zircon fragments, or anhedral (resorbed). A few samples, mostly in the western and central belt, have rounded zircon grains. In many samples (~50%) internal igneous zoning is shown by cathodoluminescence (CL) as either widely spaced and broad oscillatory zoning, sector zoning or dark unzoned grains typical of gabbroic zircon (Corfu et al., 2003). About 50% of the samples, including some of the same samples that have zircon with primary igneous zoning, have zircon with patchy to convoluted zoning (Appendix 2). Rounded zircons with overgrowth rims and/or patchy to convoluted zoning resemble metamorphic zircon, but their trace element signatures do not indicate such an origin

(described in more detail in the discussion). Cores with discontinuous or interrupted zoning are present in many samples, but only one sample has rounded xenocrystic or inherited cores with ages drastically different than their rims (20-JRD-94 from Wood Creek, with Jurassic cores and Cretaceous rims).

U-Pb zircon ages

Ages of the mafic intrusions across the transect are Cretaceous to Jurassic, with no Triassic ages in the study area. New U-Pb zircon ages of 58 samples in addition to published ages of 12 samples from the eastern belt (Lewis et al., 2024) are shown in Figure 1 and presented in Table 1, with both analytical uncertainty and propagated external precision reported. CL images of representative zircons from each sample, weighted mean age and concordia plots with analytical uncertainties, and a full discussion of data treatment for each sample are in Appendix 2 of this chapter. Measurements of U-Pb isotopes of each analysis are reported in the Supplementary Data File (Table S1).

Jurassic mafic intrusions are in the western and eastern belts. In the western belt, the Jurassic aged samples (159.4 ± 3.2 from a mafic dike at Fine Gold to 170.4 ± 3.4 Ma from an amphibole gabbro at Mill Creek) are preserved along the “0.706 line,” between the Western Sierra Nevada Metamorphic Belt (Snow and Scherer, 2006) and the central belt dominated by Kings Sequence metasedimentary rocks (Bateman and Clark, 1974; Ague and Brimhall, 1988b; Saleeby and Busby, 1993). In the eastern belt, about half of the exposed mafic intrusions have Jurassic ages (145.1 ± 1.7 from a gabbro-diorite at Mount Tom to 168.2 ± 1.9 Ma from a diorite at Shannon Canyon, plus an early Jurassic age from Pine Creek; Lewis et al., 2024; this study). The oldest age, 194 ± 2.6 Ma, is from Pine Creek (SNB-19-60), reported by Lewis et al., 2024. No Jurassic mafic plutons were observed from the central and high Sierra belts, aside from xenocrystic zircon cores from a fine-grained sample from Wood Creek (central belt) which are Jurassic (168 ± 3.4 Ma), overlapping in age with the Jurassic White Fork pluton that the mafic body intrudes (Mahaffey and Johnston, 2016). However, our sampling of the central belt excluded small

potentially Jurassic mafic intrusions associated with Jurassic plutons that intrude the metavolcanic Goddard pendant (#36, 37 and 38 in Figure 2A), so the lack of any Jurassic ages in that belt may not reflect their absence.

Cretaceous ages of mafic intrusions become younger eastward across the transect. The oldest Cretaceous ages in this study are found in the western belt (117 ± 2.3 Ma to 134.7 ± 2.7 Ma) in foothills ring complexes and mafic intrusions in metamorphic pendants. The youngest western belt mafic intrusion (107.3 ± 2.1 Ma) is farther east and crops out as up to 0.75 km long disseminated diorite bodies (essentially, very large enclaves) in the leucogranite of Big Sandy Bluffs. Ages of mafic intrusions in the central belt range from 96.9 ± 1.9 Ma to 109.6 ± 2.2 Ma. Ages from the mafic intrusions in the high Sierra belt are 87.7 ± 1.8 Ma to 98.9 ± 2.0 Ma. Cretaceous mafic intrusions of the eastern belt are discussed in detail by Lewis et al. (2024), and ages range from 88.8 ± 1.3 to 100.2 ± 1.1 Ma. The two youngest mafic intrusions are in the high Sierra belt (*i.e.*, at Volcanic Lakes, 6 samples span 87.7 ± 1.8 Ma to 90.5 ± 1.8 Ma) and eastern belt (at Keough, 2 samples are 88.8 ± 1.3 Ma and 90.8 ± 1.8 Ma).

WHOLE-ROCK GEOCHEMISTRY

Major-element geochemistry

Whole-rock major- and trace-element compositions, locations, and distance along the A-A' transect (projected for each sample orthogonally to the transect line; Fig. 2A) are reported in Table S2. Samples are classified into three broad lithologic categories—(1) cumulates, (2) gabbroic, or (3) dioritic—using textural observations, modal mineralogy, and bulk-rock chemistry (Fig. 2B, Fig. 8).

Mafic cumulate samples are defined by cumulate textures and chemistry. Textures include interstitial plagioclase that is modally $\sim 35\text{--}40\%$ and in many cases dominantly oikocrystic amphibole ($\sim 50\%$), or plagioclase-dominated cumulate samples, which are more readily identifiable by their chemistry. Cumulate samples for the most part either have low SiO₂ and/or elevated CaO (~ 10 wt.% up to 16.8

wt.%) and MgO (up to 26.3 wt.%) and low Na₂O (0.12 to ~3 wt.%), K₂O (as low as 0.03 wt.% in the western belt, 0.09 wt.% in the central belt, 0.71 wt.% in the high Sierra belt and 0.06 wt.% in the eastern Sierra) and P₂O₅ (typically up to ~0.3 wt.% aside from a few low-SiO₂ apatite-rich samples; Fig. A-2). Chemically, plagioclase-dominated cumulates have Sr/Nd >50 and/or Al/Si >0.25, and pyroxene dominated cumulates have Al/Si <0.13, as was shown for the suite of samples from the Eastern Sierra (Lewis et al., 2024). The cumulate rock category includes a range of rock types (olivine norite/troctolite, leucogabbro, gabbro, gabbronorite, norite, monzogabbro, monzodiorite, quartz monzodiorite and leucodiorite).

We use the term “gabbroic” broadly for gabbro, gabbronorite, norite, monzogabbro, quartz monzogabbro, and monzogabbronorite whose normative plagioclase has anorthite content >50% and that lack cumulate characteristics. Most commonly, samples in this group are varieties of amphibole-gabbro, with variable proportions of amphibole, biotite, clinopyroxene, orthopyroxene and olivine.

Samples whose normative plagioclase has anorthite content <50% are classified as dioritic, and include diorite, monzodiorite to quartz monzodiorite, leucomonzodiorite to quartz leucomonzodiorite, quartz diorite, and a few tonalite and granodiorite samples.

All samples are magnesian (whole-rock FeO^T/[FeO^T+MgO] < [0.0046*SiO₂]+0.486; Frost et al., 2001), aside from two (somewhat altered in outcrop) ferroan amphibole-biotite gabbro and quartz monzodiorite samples from the lower Kings River corridor, which have low whole-rock magnesium numbers of 32 and 36 (Mg#: molar 100*Mg/[Mg+Fe_T]; Fig. 8A). Nearly all samples are metaluminous and follow the typical Sierra Nevada batholith trend of gradually increasing aluminum saturation index (ASI: molar Al/[2*Ca+Na+K]; Fig. 8B) with increasing SiO₂. Exceptions to this include plagioclase-rich cumulates from the western and central belts with an ASI of ~1 and a handful of more felsic samples in the central, high Sierra, and eastern belts. Using the modified alkali-lime index (MALI: Na₂O + K₂O – CaO; Frost et al., 2001), samples from the western and central belts (blue and red symbols) are dominantly calcic, whereas samples from the high-

Sierra belt, which are mostly more evolved diorite, are calc-alkalic (Fig. A-3). Samples from the eastern belt are both calcic and calc-alkalic, particularly with increasing SiO_2 . Some exceptions to these categories are samples that are slightly more Na_2O and K_2O enriched than others from the same or nearby mafic intrusions; these are either close to the margins or represent areas where the mafic intrusions have mingled phases with surrounding evolved plutons.

These characteristic differences from west to east along the transect, with a handful of exceptions, are dominantly controlled by systematic variation in Al_2O_3 , CaO , and K_2O . The maximum K_2O concentrations within each belt are from the most evolved rocks of the belt, with the most K_2O -rich samples in the high Sierra belt (Fig. 9A), but the minimum K_2O across the transect as defined by the cumulates also increases (Fig. 9B). Like K_2O , P_2O_5 enrichment appears to vary slightly across the batholith, with more P_2O_5 -rich dioritic samples in the high Sierra and eastern belts compared to the central belt and the lowest P_2O_5 in the western belt (Fig. A-2).

In the western belt, many samples are cumulates, have low K_2O (<0.5 wt.%), and are biotite-poor, amphibole-rich rocks (Fig. 9; A2). Western belt cumulates also have high Al_2O_3 (14.6 to 25.2 wt.%, and one pyroxenite sample with 6.7 wt.% Al_2O_3) and CaO (9.9 to 16.8 wt.%) due to an abundance of plagioclase (Fig. A-2). Most non-cumulate rocks from the western belt are low-K to medium-K, with gabbroic rocks ranging from 0.05 to 1.6 wt.% K_2O (and a maximum of 2.0 wt.% K_2O in the dioritic rocks) (Fig. 9). In the central belt, mafic cumulates have slightly higher whole-rock K_2O (0.09 to 2.3 wt.% K_2O), and gabbroic to dioritic samples have up to 2.7 wt.% K_2O (Fig. 9A). CaO contents of the central belt cumulates are similar to or lower than those of the western belt (6.0 to 14.3 wt.%), but Al_2O_3 concentrations are distinctly lower (12.5 to 20.1 wt.%) due to less abundant cumulative plagioclase. The high Sierra and eastern belt cumulates have elevated K_2O concentrations similar to the central belt, but gabbroic and dioritic samples typically contain up to ~3 wt.% K_2O (with one sample reaching 3.9 wt.% K_2O) at ~60 wt.% SiO_2 (Fig. 9A).

Trace element chemistry

Compatible trace element concentrations increase with increasing MgO. For example, samples with MgO concentrations >5.5 wt.% are cumulates, and typically have Ni concentrations >55 ppm (up to 203 ppm). Although many of these high-Mg, high-Ni samples are from the western belt, other cumulates from the western belt and elsewhere are amphibole-rich and have low Ni concentrations (<12 ppm). Of the samples with elevated Ni concentrations, only three had identifiable olivine.

Chondrite-normalized ($_{\text{CN}}$; Sun and McDonough, 1989) rare earth element (REE) profiles become generally steeper (that is, more fractionated) from west to east across the batholith, with the highest $(\text{La/Yb})_{\text{CN}}$ in the high Sierra belt (and also in the three samples from the White-Inyo Mountains; Fig. 10). In gabbroic samples along the transect, the average and range of $(\text{La/Yb})_{\text{CN}}$ in each belt are as follows: western belt 2.7 (1.6–4.5, $n = 7$); central belt 4.9 (3.7–6.6, $n = 3$); high Sierra belt 5.7 (5.4–6.0, $n = 2$); eastern belt excluding one White-Inyo sample 5.4 (3.0–9.3, $n = 12$). The excluded epidote-bearing (and likely altered) monzogabbro from Marble Canyon in the White-Inyo Mountains has $(\text{La/Yb})_{\text{CN}}$ 14.2. Even after excluding the altered sample, the eastern domain is the most heterogeneous in REE slope. The slope in light rare earth elements (LREE), expressed by $(\text{La/Sm})_{\text{CN}}$, is constant across most of the traverse (average of 1.5 in gabbroic samples from the western, central and high Sierra belts) before increasing in the eastern belt (average of 2.1). The slope in heavy rare earth elements (HREE), expressed by $(\text{Dy/Yb})_{\text{CN}}$ is roughly constant across all belts (ranging from 1.0–2.0 in all gabbroic samples; Fig. S4).

From west to east, large ion lithophile elements (LILE) and high field strength elements (HFSE) broadly increase in concentration (shown by, for example, Sr/Y and Nb concentrations; Fig. 10; A5). Focusing on Sr/Y, in gabbroic samples along the transect, the average and range in each belt is as follows: western belt 19 (12–33, $n = 7$); central belt 29 (14–47, $n = 3$); high Sierra belt 38 (23–52, $n = 2$); eastern belt 30 (range 12–60, $n = 13$). Again, the eastern domain is the most heterogeneous. Whole-rock Eu anomalies are mostly positive in the plagioclase-rich cumulates and

negative in the gabbroic to dioritic samples, whereas Sr anomalies are nearly all positive. These do not vary systematically along the transect (Fig. A-6).

MINERALOGY AND MINERAL CHEMISTRY

Systematic mineralogical variability occurs along the transect. In the western belt, olivine-bearing and orthopyroxene-rich mafic intrusions with minor clinopyroxene are most abundant. Amphibole is the dominant hydrous mafic silicate, whereas biotite is minor or absent. In the central belt, the mineralogy of mafic bodies is variable. Olivine is rare (only observed with orthopyroxene \pm clinopyroxene and amphibole in one small intrusion with limited exposure at Pineridge), clinopyroxene and orthopyroxene commonly occur together where present, and amphibole is also dominant, with lesser biotite. Titanite is also common in the central belt, particularly in dioritic rocks. In the high Sierra belt, rocks are generally more evolved but clinopyroxene occurs, frequently as cores in amphibole phenocrysts or oikocrysts. In dioritic rocks, which are the dominant lithology in the high Sierra mafic intrusions, biotite is present in subequal or greater proportions to amphibole. Titanite, often occurring as 2 to 3 mm crystals, is abundant. In the eastern belt, olivine is present in about a quarter of mafic intrusions (Casa Diablo, Hidden Lakes, McMurry Meadows and Onion Valley), clinopyroxene is present in nearly all mafic intrusions, and in about a third of the mafic intrusions, orthopyroxene occurs with clinopyroxene (Hidden Lakes, Mount Tom, Bishop Creek, McMurry Meadows, and in one sample from Keough). Although amphibole is the dominant hydrous mafic silicate in the cumulate and gabbroic rocks of the belt, biotite is also common and typically more abundant than amphibole in dioritic rocks.

In all mafic intrusions of the transect, olivine and/or clinopyroxene, followed by orthopyroxene (where present) are the earliest crystallizing mafic minerals, texturally euhedral to subhedral and/or with amphibole as rims or oikocrysts (Fig. 11). They crystallized prior to amphibole and biotite, and were targeted for analysis to assess parental melt Mg#. In our analysis below, we present new analyses from 40 samples in combination with previously reported mineral chemistry from mafic

intrusions from the eastern belt (Lewis et al., 2021; Lewis et al., 2024; Sisson et al., 1996). We attempted to be as comprehensive as possible in analyzing anhydrous mafic silicates across the transect, however for some mafic intrusions, we did not find samples with olivine nor pyroxene. In addition, in the high Sierra only clinopyroxene was analyzed as neither olivine nor orthopyroxene was observed. Mineral chemistry of all analyzed samples is summarized in Table 2.

Olivine, clinopyroxene and orthopyroxene chemistry

Although there are a relatively limited number of samples with olivine ($n = 6$ total), they reveal some systematic trends in olivine chemistry across the batholith. Olivine in samples from the western belt (Mg# 67–72) and central belt (Mg# 65–67) are significantly less magnesian than in the eastern belt (Mg# 75–81.5; Fig. 12). MnO systematically increases with decreasing Mg# in olivine, whereas olivine NiO does not, potentially due to subsolidus exchange with Fe-Ti oxides or to a complex interplay between partition coefficients, primary melt NiO concentration, liquidus olivine composition, and amount of olivine fractionated.

Because clinopyroxene that has experienced metamorphic Mg-Tschermark exchange $[Si_{i+1}Mg_{i+1}Al_{i-2}]$ during cooling can have low-Al₂O₃ and high Mg# compared to unaffected clinopyroxene that crystalized from a melt, we selected the highest Al₂O₃ grains to report sample-average clinopyroxene compositions (Table 2, Table S4; Fig. A-7). Average clinopyroxene Mg# has overlapping ranges in the western belt (69 to 79), central belt (69.8 to 75.9), high Sierra belt (72 to 76), and eastern belt (68.5 to 81; Fig. 12). In general, Al₂O₃ in clinopyroxene decreases with decreasing Mg#, from ~3 to 3.5 wt.% at Mg# 80 to 81, down to 1 to 1.5 wt.% at Mg# ~70, as expected for crystallization in the presence of plagioclase. However, Al₂O₃ in clinopyroxene from most eastern belt samples is higher than clinopyroxene with similar Mg# from the central and western belt by ~1 to 2 wt.% (Fig. A-7A). It is possible that some of the samples with the highest Mg# clinopyroxene (Mg# > 79) have experienced some Mg-Tschermark exchange, and thus that their Mg# is slightly elevated from its original values. Further, all samples from the high Sierra belt are

low in Al_2O_3 , (0.4 to 1.2 wt.% at Mg# 72 to 76), in addition to a few other low- Al_2O_3 clinopyroxene-bearing samples (in the western belt, from Mill Creek; in the eastern belt, from Mount Alice, Tungsten Hills and Marble Canyon of the White-Inyo mountains). These low- Al_2O_3 clinopyroxene compositions are frequently found in cores of amphibole crystals, and/or are in more evolved dioritic samples. Low- Al_2O_3 clinopyroxene also occurs as a second population of interstitial clinopyroxene in samples from McMurry Meadows and Green Lake in the eastern belt, reported by Lewis et al. (2024) but not plotted in this study. They could either be significantly affected by Mg-Tschermark exchange or could potentially be a primary igneous feature—a second low- Al_2O_3 population of pyroxene is reported in fractional crystallization experiments on hydrous basalt at 0.7 GPa (Nandedkar et al., 2014).

Orthopyroxene likely crystallized after olivine and clinopyroxene in all samples, as it has a lower Mg# and in many cases has inclusions of plagioclase and/or Fe-Ti oxides, whereas olivine (and in most cases also clinopyroxene) do not. In some mafic intrusions orthopyroxene is present in dioritic samples. In general, when both olivine and orthopyroxene are present in a sample, orthopyroxene rims olivine, particularly in the western belt, suggesting peritectic formation of orthopyroxene (Fig 11B). The maximum Mg# of orthopyroxene is similar in the western (Mg# 72) and central (Mg# 70.9) belts but is higher on average in the eastern belt (Mg# 67 to 79; Fig. 12). Aside from one sample with very high Al_2O_3 (~3 wt.% Al_2O_3 in Mg# 72 orthopyroxene rims on olivine in a troctolite from Campbell Mountain; Fig. 11B), Al_2O_3 in orthopyroxene follows a decreasing trend with decreasing Mg#, as expected for crystallization in the presence of plagioclase (Fig. A-7B). Al_2O_3 reaches a maximum of 2 wt.% for Mg# 70 orthopyroxene from eastern belt samples, and higher Mg# orthopyroxene have slightly lower Al_2O_3 , indicating possible slight alteration by Mg-Tschermark exchange (reaching up to Mg# 79). Samples from all belts define a trend in Cr_2O_3 decreasing from ~0.6 wt.% at Mg# 75 to ~0.2 wt.% at Mg# ~54. However, about half of the samples (three eastern belt samples in addition to two from the central belt and one from the western belt) have low Cr_2O_3 <0.2 wt.% at Mg# 68–79.

The Mg# of all minerals is lower than would be expected if the whole rock represented a bulk melt (Fig. 12). In other words, the whole-rock Mg# of all samples are elevated compared to a melt in equilibrium with their constituent mafic minerals, which means that the Mg# of the bulk rock is controlled by the mineral compositions. Thus, all samples have accumulated Mg-rich minerals (and none reflects a bulk melt composition). The closest samples to bulk melts are dioritic samples with whole-rock Mg# in the range of 45–55, and Mg# in clinopyroxene in the range of 72 to 76.

Zircon trace element chemistry

As previously mentioned, we targeted zircon rims when analyzing trace elements by LA-SS-ICPMS in conjunction with their U-Pb ages, to avoid inherited autocrystic or xenocrystic cores. We also attempted to avoid inclusions during analysis, but all analyses were screened for accidental analysis of inclusions on the basis of extreme values of certain elements (*e.g.*, P in apatite, Ti in Fe-Ti oxides) and REE patterns (elevated LREE with patterns suggesting monazite, titanite, allanite etc.). We report sample averages of the trace elements for all concordant, non-inherited, and inclusion-free analyses, which the reported sample average values represent the typical chemistry of the latest stages of zircon growth for each sample. All analyses are reported in Table S1.

For all samples, the Hf concentration in zircon ranges from 6100 ppm to 12,150 ppm (average ~9650 ppm Hf). For comparison, the range of Hf concentration in a compilation of 2586 continental arc plutonic zircons is ~5100 to 77,500 ppm (average of ~10,900; Grimes et al., 2015). The average Zr/Hf in zircon of all analyzed samples from the mafic intrusions of this study is ~50. The range in Zr/Hf in zircon in all samples is 39 to 71, with one outlier at 81 (from Mill Creek, 21-JRD-117). Although we focused on representative mafic samples with whole-rock SiO₂ < 60 wt.% from each mafic intrusion, we also analyzed zircon from 8 samples with SiO₂ > 60 wt.%. Excluding those eight samples, the high Zr/Hf sample from Mill Creek, and two low-SiO₂ cumulate samples (20-JRD-73 and 20-JRD-87) from Volcanic Lakes, Zr/Hf in zircon correlates well with SiO₂ in the sample suite (Fig. 13). At the upper limits of

Zr/Hf for the sample suite, low–SiO₂ mafic samples (average whole-rock SiO₂ of ~49 wt.%, with a range in SiO₂ from 45 to 53.8 wt.%) have an average Zr/Hf of 65 (from 61 to 71). At the low end of Zr/Hf, higher SiO₂ mafic samples (average whole-rock SiO₂ of ~55 wt.%, with a range in SiO₂ from 50 to 59 wt.%) have an average Zr/Hf of 42.5 (from 39 to 45).

The Th/U ratio in zircon is often related to differentiation and falling crystallization temperature, decreasing from zircons crystallized from mafic melts towards lower values in those that grew in felsic melts (and metamorphic zircons have Th/U < 0.1; *e.g.*, Hoskin and Schaltegger, 2003). The Th/U in zircon is in general lower in the west than in the east along the transect (Fig. 13). Excluding samples with SiO₂ > 60 wt.%, in the western belt, the range in Th/U in zircon spans 0.27–0.85 (average 0.54); in the central belt, 0.21–1.23 (average 0.72); the high Sierra belt 0.47–1.35 (average 0.91); and in the eastern belt 0.36–1.45 (average 0.87). The Th/U weakly but consistently correlates positively with REE ratios measured in the zircons, including (La/Yb)_{CN} and (Dy/Yb)_{CN} in zircon, and thus displays similar trends across the batholith.

Ce in zircon increases similarly west to east: in the western belt, the average Ce concentration in zircon is 7.5 ppm (1.7–25.3 ppm); in the central belt, the average is 15 ppm (3.6–38.0 ppm); in the high Sierra belt, 42.4 ppm (8.1–115.4 ppm); in the eastern belt, 25.4 ppm (6.5–119.6 ppm). The two eastern-most high Sierra and eastern belts have slightly lower averages if dioritic or White-Inyo Mountains samples are excluded from each—excluding dioritic samples, 20.3 ppm (8.1–32.2 ppm) in the high-Sierra belt, and excluding White-Inyo Mountains samples, 21.0 ppm (6.5–48.1 ppm) in the eastern Belt. This increase from west to east is also true for Ce/Ce* in zircon, though the central belt on average has slightly lower Ce/Ce* in zircon than in the western belt (west: 26.5; central: 23.3; high Sierra: 43.8 or 37.6; eastern: 46.2 or 38.8).

DISCUSSION

Non-primitive mafic magmas ascend after “copious fractionation intervals” at depth

These mafic intrusions must have had low-Mg basalt to basaltic andesite parental magmas ($Mg\# \leq \sim 50$), based on their whole rock and mineral chemistry, and described in other detailed studies of these and similar intrusions (Fig. 8A, 12, 12; Sisson et al., 1996; Ratajeski et al., 2001; Lewis et al., 2021; 2024; Rezeau et al. 2021). As primitive mantle-derived magmas have $Mg\# > 65$ (Kelemen et al., 2014; Schmidt and Jagoutz, 2017), the parental magmas to the mafic intrusions must have experienced crystallization-differentiation deeper in the crust. Lower-crustal (0.7–1.0 GPa) fractional crystallization of hydrous primary (mantle-equilibrated) basalt produces evolved (low-Mg, high-Al) basalt to basaltic andesite compositions (up to ~57 wt.% SiO_2 and as low as $Mg\# \sim 42$ –50) until about ~50% or more of the original melt mass has crystallized (Fig. 14; Nandedkar et al., 2014; Müntener and Ulmer, 2018). This limited increase in SiO_2 at the earliest stages of fractional crystallization is due to limited removal of low- SiO_2 phases, such as amphibole and Fe-Ti oxides. In addition, it occurs in conjunction with a large decrease in melt mass over a small temperature interval (~100 °C) because of multiple saturation of olivine, pyroxenes and spinel—termed a “copious fractionation interval” (CFI) by Jagoutz and Klein (2018; Fig. 14). Higher pressures and/or concentration of H_2O will result in a CFI dominated by clinopyroxene, garnet and amphibole crystallization (Alonso-Perez et al., 2009; Jagoutz et al., 2011). Similar processes can be inferred for erupted basalts, which may erupt in part due to the density minimum of the melts after multiple saturation (Stolper and Walker, 1980).

Considering the “copious fractionation interval,” the H_2O concentration in the melt significantly increases during this limited decrease in SiO_2 that forms low-Mg, high-Al basalt, as H_2O is generally incompatible. For example, starting with a high-Mg basalt (13.3 wt.% MgO) with 3.0 wt.% H_2O (typical for the range of concentration observed in arc basalts, Sisson and Layne, 1993; Plank et al., 2013),

fractional crystallization experiments at 1.0 GPa produce hydrous, low-Mg, high-Al basalt after 56% crystallization (6.8 wt.% H₂O; 6.1 wt.% MgO; ASI=0.88; Ulmer et al., 2018). This results in a decrease in density of 0.3–0.4 g/cm³ and a limited increase in viscosity (<1 log unit), which would facilitate its ascent from the lower crust, and as proposed by Sisson et al. (1996), result in neutral buoyancy in melts of granodioritic composition that would be abundant during batholith formation (Fig. 14C).

We can estimate the Mg# of the least evolved parental melts by calculating the Mg# of melts in equilibrium with the olivine or clinopyroxene, the earliest crystallizing silicates, from the studied intrusions. The maximum sample-average calculated equilibrium melt Mg# represents a minimum possible melt Mg# because we may not have sampled the most primitive material of the intrusion, which clearly experiences further evolution towards lower Mg# once it is emplaced in the upper crust (Reiners et al., 1995; Lewis et al., 2021). These calculated Mg# are 48 to 52 (calculated from Fe²⁺/Mg exchange with olivine, average = 51±1.9) or 33 to 58 (calculated by Fe²⁺/Mg exchange with clinopyroxene, average = 43±7). These calculations assume a melt Fe³⁺/ΣFe of 0.15, assume a calculated Fe³⁺ in clinopyroxene by stoichiometry, and use a mineral-melt partition coefficient (K_D; [Fe²⁺/Mg]_{mineral}/[Fe²⁺/Mg]_{melt}) K_D^{Fe²⁺/Mg} of 0.28 for olivine and 0.23 for clinopyroxene (Sisson and Grove, 1993). All melt compositions calculated from orthopyroxene using a K_D^{Fe²⁺/Mg} of 0.284 (Beattie, 1993); melt Mg# obtained from orthopyroxene is generally lower (< Mg# ~35), although in two samples, orthopyroxene reaction rims on olivine yield an equilibrium melt Mg# estimate as high or slightly higher than their coexisting olivine (CM-1.5 and 19-JRD-32).

Similar mafic intrusions of the Bear Valley Intrusive Suite from deep (~0.7–0.9 GPa) exposures in the southern Sierra Nevada also have non-primitive parental magmas (Mg# ~40–60), meaning that the earliest stages of differentiation must have occurred at even deeper levels (Klein and Jagoutz, 2021; Rezeau et al., 2021). This deeper differentiation to produce low-Mg basalts has been predicted to have left high-pressure cumulates (>1.2 GPa), found as garnet pyroxenite xenoliths in Miocene and

younger lavas in the central Sierra Nevada (Dodge et al., 1986; Ducea and Saleeby, 1998; Lee et al., 2006; Lewis et al., 2024).

The upper-crustal mafic intrusions thus likely represent the crystallization products of residual melts after an earlier “copious fractionation interval” crystallization of more primitive magmas (Fig. 14). The residual mafic magmas (with ~5 to 7 wt.% H₂O) would have viscosities and densities about equal to granodioritic melts, further enhancing their ability to ascend and to mix with more silicic magmas (Sparks and Marshall, 1986; Frost and Mahood, 1987; Laumonier et al., 2014, 2015). Indeed, mixing between a low-Mg, high-Al basaltic composition and felsic melts has been proposed as a solution to the geochemical paradox that lower-crustal fractional crystallization experiments cannot reproduce the compositional trends of arc magmas (Blatter et al., 2013; 2017). The regional perspective on the composition of the mafic mixing endmember that emerges from studying these upper-crustal mafic intrusions provides key constraints on this mixing hypothesis. The felsic mixing endmember could be produced by continued fractionation of a basaltic melt (Sisson et al., 2005; Jagoutz and Klein, 2018) or could have a significant contribution of partially melted or assimilated crust (Huppert and Sparks, 1988; Annen et al., 2006; Taniuchi et al., 2020). Magmatic suites in the Sierra Nevada that span a range in composition from mafic to felsic have been documented as either having the same isotopic signatures across the range, or increased inheritance and crustal assimilation with evolution, suggesting that both possibilities could occur in different cases (Coleman et al., 1992; Coleman and Glazner, 1997).

Importantly, we do not suggest that fractional crystallization is the only process at work in the lower crust—isotopic study of these intrusions indicates that they have experienced early assimilation as well (typically ~10–20% by mass, Ryan-Davis et al., *Chapter 4*). The similar lower-crustal gabbros of the Bear Valley Intrusive Suite also have isotopic and petrologic evidence for significant crustal assimilation (Pickett and Saleeby, 1994; Lackey et al., 2005; Klein et al., 2020; Rezeau et al., 2021). Their geochemistry thus reflects not only crystallization, but also assimilation and interaction with the upper plate.

Gabbroic zircons record crystallization of mafic parental magmas

Before discussing the broader structure and chemical trends of mafic magmatism across the central Sierra Nevada batholith, we discuss the presence of zircon in mafic rocks and its fidelity as an archive of mafic magma chemistry. Although zircon is often presented as uncommon in mafic rocks due to its enhanced solubility in mafic melts, zircon can and does crystallize from mafic magmas, even those with comparatively low Zr concentrations (Bea et al., 2022; Bucholz et al., 2017). It may have crystallized from late, interstitial melt that would be somewhat more evolved than the mafic starting composition (Ratschbacher et al., 2018). In any case, the hydrous, evolved basaltic magmas parental to the mafic intrusions of this study are more favorable for zircon saturation than primitive, dry mafic magmas (Borisov and Aranovich, 2019; Borisov et al., 2025). Alternatively, zircon in the mafic rocks could be xenocrystic, sourced from the local host rocks (or deeper in the crustal column during ascent). However, several lines of evidence suggest that the zircon analyzed in most samples are autocrytic. The zircon populations in most samples (56 of 70) have homogeneous CL characteristics (Appendix 2), and all but 14 samples have age populations broadly consistent with a single crystallization interval (that is, $\text{MSWD} \leq 2$; Table S1, Appendix 3). These attributes are unlikely for populations including abundant xenocrystic zircon, sourced from metasedimentary host rocks with detrital populations or from interaction with a variety of sources during ascent through the crustal column. Zircon crystals separated from more evolved, dioritic to tonalitic samples of this suite have more narrow oscillatory zoning growth bands and euhedral crystal habits, whereas the zircon crystals recovered from gabbroic samples have broad growth bands or sector zoning, and are often broken, typical of mafic rocks (Corfu et al., 2003). The correlation with host rock type and typical mafic characteristics indicate that the zircon crystals from these mafic rocks are unlikely to be sourced from local felsic host plutons. Two caveats to this are that anhedral zircon grains (present in about half of the samples) could have potentially been resorbed and thus not in equilibrium with host melts, at least during the final stages of solidification. Further, grains with patchy or convoluted zoning,

found in about half of the samples, could represent recrystallization of primary igneous zoning. Yet, such resorption and recrystallization could be due to disequilibrium and open-system processes like magma replenishment in the host mafic intrusion, without indicating that they are xenocrystic.

The trace element geochemistry of zircon analyzed here supports an origin by crystallization from mafic melts. For example, Zr/Hf ratios in zircon range from 39 to 81 due to generally low Hf concentrations (<10,000 ppm Hf in 66% of analyzed zircon), whereas the median Zr/Hf in zircon from a compilation of 65 granitic plutons is 38.9, and decreases in more evolved rocks of a given suite (Fig. 13A; Wang et al., 2010; Samperton et al., 2015). The Th/U in zircon analyzed here (median 0.8) is also higher than median granitic zircons, 0.52, in the compilation of Wang et al. (2011); the same study found a median of 0.81 in zircon from mafic to intermediate rocks (Fig. 13A; Wang et al., 2011). In addition, Ce concentrations in the zircon analyzed here range from ~2 to 50 ppm, except for 7 evolved (dioritic) samples which reach ~120 ppm, whereas typical zircon in granodiorite has higher Ce, typically ~120 ppm Ce, for example, in the Bergell intrusion, Central Alps (Samperton et al., 2015).

Thus, we proceed under the assumption that the zircon ages and chemistry in this study record information about the crystallization of the mafic rocks in which they are hosted and can inform our understanding of mafic magmatism in the Sierra Nevada batholith.

Influences of water concentration, oxygen fugacity and pressure on mineral assemblages and chemistry

Potential H₂O variability in mafic parental magmas across the batholith

We begin by summarizing the qualitative evidence for a range in H₂O concentration and oxygen fugacity ($f\text{O}_2$) of the parental mafic magmas of these intrusions, based on their petrography and mineral chemistry. Amphibole occurs in all mafic intrusions, and thus their parental melts were moderately to significantly hydrous, as expected in the Sierra Nevada batholith and arc magmas more broadly (Arculus and Wills, 1980; Sisson and Grove, 1993; Sisson et al., 1996; Plank et al.,

2013). The basalt to basaltic andesite magmas parental to the Onion Valley and Hidden Lakes mafic complexes (in the eastern belt of this study) were estimated by detailed studies to contain ~6 wt.% H₂O and ~2.9–3.5 wt.% H₂O, respectively (Sisson et al., 1996; Lewis et al., 2021). Hornblendite and olivine hornblendite (amphibole cumulates with little to no plagioclase) are common at Onion Valley and no orthopyroxene-bearing rocks occur, whereas the most primitive rocks are orthopyroxene and plagioclase-dominant cumulates at Hidden Lakes followed by clinopyroxene-bearing amphibole gabbros (Sisson et al., 1996; Lewis et al., 2021). In the western belt, the Stokes Mountain complex hosts troctolites and orthopyroxene-rich lithologies in addition to amphibole-rich cumulates with high-anorthite plagioclase, so parental magmas were hydrous (Clemens-Knott, 1992), though potentially varied in composition based on the heterogeneous mineralogy.

Experimental studies on mafic compositions at upper-crustal pressures (0.2–0.4 GPa) show that an increase in melt H₂O concentration suppresses plagioclase (and orthopyroxene) crystallization, and expands stability field of amphibole to higher temperature, resulting in its earlier appearance during crystallization (Berndt et al., 2005; Hamada and Fuji, 2008; Feig et al., 2010; Krawczynski et al., 2012; Melekhova et al., 2015). Conversely, the earlier appearance of plagioclase and orthopyroxene is stabilized at lower H₂O concentration—and/or potentially at higher fO_2 and SiO₂ concentration (Berndt et al., 2005; Pichavant and MacDonald, 2007; Hamada and Fuji, 2008; Feig et al., 2010; Ryan-Davis et al., *Chapter 2*). Early saturation of magnetite is favored by both high H₂O concentration and high fO_2 (Sisson and Grove, 1993; Hamada and Fuji, 2008; Krawczynski et al., 2012; Blatter et al., 2013; Melekhova et al., 2015). Commonly these experimental studies show that delayed crystallization of amphibole and preferential early appearance of plagioclase and/or orthopyroxene occurs at <~3 wt.% H₂O in evolved mafic parental melts, whereas the early appearance of amphibole occurs at >~4 wt.% H₂O. However, pressure also influences the order of crystallization in these and other studies, such as earlier plagioclase crystallization at lower pressures (e.g., Feig et al.,

2006). Furthermore, bulk composition can also significantly affect the phase assemblage (*e.g.*, Sisson et al., 2005).

Further study can elucidate the interplay between H_2O concentration, $f\text{O}_2$ and pressure on the petrography of these mafic intrusions (*i.e.*, plagioclase and amphibole compositions of these samples). Yet, there are first-order petrographic indications of relatively low H_2O concentrations (estimated at $<\sim 3$ wt.% H_2O) in the melts parental to some of these mafic intrusions, particularly in the western and central belts. Plagioclase-olivine-orthopyroxene-rich cumulates with late-crystallizing amphibole are common in the western and (to a lesser extent) central belt (troctolites and orthopyroxene-bearing rocks; *e.g.*, Mack et al., 1979; Ross 1989; Clemens-Knott and Saleeby, 1999; this study). The occurrence of troctolite, with olivine and plagioclase \pm orthopyroxene rims on olivine, and minimal amphibole, indicates early crystallizing plagioclase (prior to clinopyroxene) and the delayed appearance of amphibole. Gabbronorite, with euhedral to subhedral orthopyroxene and plagioclase surrounded by interstitial or poikilitic amphibole, indicates crystallization of orthopyroxene and plagioclase before amphibole (Fig. 11A, C). These rock types, and olivine and orthopyroxene in general, were not observed in the mafic intrusions of the high Sierra belt. Although most compositions there are more evolved than other belts, euhedral amphibole with anhedral plagioclase in even the least evolved gabbroic or cumulate rocks indicates early crystallization of amphibole, and thus higher H_2O concentrations in the parental melts ($>\sim 4$ wt.%; Fig. 11E, G).

These qualitative estimates indicate that parental magmas to these upper-crustal mafic intrusions likely had a range of H_2O concentrations, despite having similarly evolved (low MgO) mafic parental magmas, discussed further below. This difference is presumably inherited from variable H_2O concentrations in the primary magma sources. Such variation has also been described in the deepest exposures of the batholith in the southern Sierra Nevada in the Bear Valley intrusive suite by Rezeau et al. (2021), which has compositions and petrography akin to the upper-crustal mafic intrusions studied here despite its deeper level of emplacement. They suggest that the modest ASI of evolved compositions of the batholith is due to mixing between more

and less hydrous parental magmas, which cannot otherwise be reproduced by lower-crustal fractional crystallization experiments (e.g., Blatter et al., 2013). The presence of such a range in upper-crustal mafic intrusions offers further insight into this issue.

Qualitative relationships between fO_2 and mineral chemistry

An increase in fO_2 for a given magma composition causes a higher $Fe^{3+}/\sum Fe$ in the melt. This would result in a higher Mg# of mafic minerals given a constant $K_D^{Fe^{2+}/Mg}$ between the mineral and melt (and has been demonstrated experimentally in olivine and clinopyroxene; Roeder and Emslie, 1970; Berndt et al., 2005; Feig et al., 2010; Blundy et al., 2020). This effect was documented in biotite in studies that identify zones of variable fO_2 in felsic intrusions across the Sierra Nevada batholith and in particular, a “strongly-contaminated and reduced” belt that corresponds to the central belt of this study (Ague and Brimhall, 1987; 1988a).

In this study, the Mg# in olivine from the western belt (65–73) is significantly lower than in the eastern belt (79–82; Fig. 12), including maximum values reported from Onion Valley and Hidden Lakes (Sisson et al., 1996; Lewis et al., 2021). Clinopyroxene and orthopyroxene have a much less pronounced, though slight, increases in Mg# across the batholith (Fig. 12). Lower fO_2 in the western belt than the eastern belt could thus be a possible explanation for this difference in olivine Mg# across the batholith.

There are several caveats: (1) other factors such as temperature and melt composition (including H_2O concentration) could affect the $K_D^{Fe^{2+}/Mg}$ between melts and minerals; further, fractionation conditions could affect the melt Mg# at which the mineral of interest crystallizes and therefore the mineral Mg# even at constant $K_D^{Fe^{2+}/Mg}$; (2) olivine was only observed and analyzed in eight samples (and found only in the western and eastern belts) so sampling bias could be a factor in these results; (3) low-Mg# olivine could be due to re-equilibration with lower-Mg# phases (for example, orthopyroxene, demonstrated by similar Mg# in olivine and co-existing orthopyroxene rims, and/or potentially amphibole; Fig. A-8). There is independent evidence for the inferred fO_2 gradient across the batholith, based on the zircon

oxybarometer of Loucks et al. (2020), which uses Ce, Ti and U in zircon to calculate fO_2 at zircon crystallization relative to the fayalite-magnetite-quartz buffer. Indeed, zircon analyses indicate an increase in fO_2 from west to east across the batholith is observed (Fig. A-9). We propose that these tentative indicators of a redox gradient merit further study.

Depth of intrusion

We briefly consider variable depth of crystallization and its influence on the style of intrusion from west to east. Limited ($n = 17$) aluminum-in-hornblende pressure estimates from felsic intrusions in the western belt of this transect indicate slightly deeper depths of crystallization ($\sim 0.4\text{--}0.5$ GPa) than in the central (0.3–0.4 GPa) and eastern belt (< 0.2 GPa; Hammarstrom and Zen, 1986; Ague and Brimhall, 1988b; Nadin and Saleeby, 2008; Chapman et al., 2012). Thus, higher-pressure (deeper) exposures in the west could potentially be a reason for more cumulates and ultramafic rocks there compared to the lower-pressure exposures at high elevations to the east (*i.e.*, where limited to no mafic cumulates are found within the high Sierra). However, mafic to ultramafic cumulates are also found in the eastern belt, which yields the lowest pressure estimates. Further, western belt mafic complexes near the study area at Stokes Mountain are shallow (≤ 0.2 GPa), sub-volcanic ring-dike complexes, as inferred from the presence of cordierite in the contact metamorphic aureole (Clemens-Knott and Saleeby, 1999). Rocks from in our transect that resemble the Stokes Mountain suite also appear to have been shallowly emplaced, with early-crystallizing plagioclase (although H_2O could play a role as well, discussed above; Fig. 6A, B, 11A, B). Thus, more information is required to fully assess the effect of pressure on the styles of mafic magmatism across our transect. Nonetheless, initial data suggests that pressure differences played a limited role in mafic intrusion style. Instead, we turn to the heterogeneous, pre-existing upper plate framework as a fundamental control on the expression of mafic magmatism.

Styles and locations of mafic magmatism through time across the Sierra Nevada batholith

Jurassic remnants

Jurassic ages are restricted to two mafic intrusions (of nine dated) in the western belt and eight mafic intrusions (of sixteen dated) in the eastern belt. As Lewis et al. (2024) showed, most of the Jurassic mafic intrusions coincide in age with the regionally extensive Independence dike swarm, a continental-scale extensional magmatic event (Carl and Glazner, 2002), which could have facilitated ascent of mafic magmas into the upper crust. Felsic Jurassic intrusions are more common in the (south)eastern Sierra, the White-Inyo mountains, and the (north)western foothills, but are also exposed as small plutons scattered throughout the batholith that are in many cases associated with metamorphic pendants (Fig. 2A). The Jurassic arc was extensionally wedged apart by later, voluminous Cretaceous magmatism occurring along the central axis of the Sierra Nevada (Fig. 1A; Bateman 1992; Hildreth et al., 2023). Transpressional shear zones that were active during that Cretaceous magmatism (Tobisch et al., 1995; Tikoff and de Saint Blanquat, 1997; Cao et al., 2015) likely offset remaining Jurassic fragments of the arc along strike.

Cretaceous arc migration

The migration of arc magmatism from west to east during the Cretaceous, manifested by decreasing crystallization ages of felsic plutons from west to east (*i.e.*, away from the Mesozoic trench), has long been recognized as a fundamental feature of the construction of the Sierra Nevada batholith (Evernden and Kistler, 1970; Chen and Moore, 1982; Ague and Brimhall, 1988b; Kistler, 1990; Coleman and Glazner, 1997; Kistler et al., 2003; Chapman and Ducea, 2019). This pattern continues in the northern Sierra Nevada (Cecil et al., 2012) and to the south in the related Peninsular Ranges batholith (Silver et al., 1979; Busby, 2004; Lee et al., 2007; Karlstrom et al., 2014). Gabbro samples from the Peninsular Ranges batholith also follow the age trend of the felsic rocks there (Kimbrough et al., 2015). Arc migration away from the

trench and into continental crust has been documented in other arcs globally, and is attributed to various processes like slab shallowing, forearc subduction erosion, or thickening of the arc (Kay et al., 2005; Karlstrom et al., 2014; Ducea and Chapman, 2018; Jicha and Kay, 2018; Chapman et al., 2021).

In detail, the west-to-east migration of arc magmatism may stall and "focus" to form the enigmatic large silicic inward-younging intrusions such as the Tuolumne intrusive complex that comprise the latest intrusions of the batholith (Ardill et al., 2018). The high Sierra belt delineated here is aligned with such large plutons (Fig. 1); specifically, the Mount Givens granodiorite (~98–91 Ma; Frazer et al., 2014; Sendek, 2016) lies within our studied transect. The Whitney intrusive suite, which overlaps in age with the Mount Givens granodiorite, lies to the southeast along strike with the high Sierra belt.

Such west-to-east arc migration, ending with magmatic focusing in the high Sierra belt, is also recorded by the ages of the mafic intrusions of this study (Fig. 2B). Including all Cretaceous mafic intrusion ages and locations from the western to eastern belts, we obtain a slope in the distance versus age plot along the transect that yields a calculated migration rate of up to ~4.0 km/Myr (Fig. 2B). However, the mafic age record indicates that the final stage of Cretaceous magmatism marked a shift from eastward migration of a narrow locus of magmatism to a period of simultaneous activity across a wider swath of the eastern and high Sierra belts (which is also seen in felsic magmas; *i.e.*, Ardill et al., 2018, 2024). Mafic intrusions in this ~50 km wide swath have roughly contemporaneous ages, ranging from ~100 to 88 Ma, potentially even younging inwards towards the high Sierra belt (except for the young ~89–91 Ma Keough mafic intrusion, located along the easternmost exposure of the Sierra Nevada range). Excluding this stalled swath, and therefore considering only early Cretaceous ages from the western belt to the high Sierra belt, we calculate an arc migration rate of 2.6 km/Myr (Fig. 2B). These rates are consistent with a range of west to east migration rates reported by others in felsic plutons slightly to the south (36°N to 37°N; 2.7 km/Myr; Chen and Moore, 1982), slightly to the north crossing through Tuolumne (~37.5°N to 38°N; ~2.7 km/Myr; Ardill et al., 2018) and in the

Northern Sierra (38.5°N to 39.5°N; 2.0–4.8 km/Myr; Cecil et al., 2012). Drill cores from the Great Valley, from ~0 to 50 km west of our western-most sample, contain gabbro, diorite and tonalite with U-Pb zircon ages ~140 to 130 Ma (Fig. 2B; Saleeby, 2007), consistent with the above calculated arc migration rates and extending the record of arc migration back into the latest Jurassic. Following arc migration, active intrusion of mafic magmas into the upper crust occurred in the broad region of the high Sierra and eastern belts (simultaneously?) during the final ~12 million years of activity of the Sierra Nevada batholith.

Crustal structures and strength: a control on mafic intrusive style?

We infer that the variable style of mafic intrusion by belt reflects the interaction between eastward progressing arc magmatism and changes in upper-plate lithosphere-scale structure, density and composition. A similar inference has been offered to explain regional patterns in the felsic intrusions of the batholith (Saleeby and Sharp, 1980; Ague and Brimhall, 1988b; Kistler 1990; Chapman et al., 2017). The felsic plutons are in general more mafic (dioritic to tonalitic) in the western portions of the Sierra Nevada batholith compared to those in the high Sierra and eastern belts (granodioritic to granitic)—this spatial trend has also been documented to the south in the Peninsular Ranges batholith (Moore, 1959; Lee et al., 2007; Saleeby 2011; Chapman et al., 2012).

The western and central belts are constructed on dense and thin oceanic lithosphere, compared to the high Sierra and eastern belts, which are hosted by lower-density continental crust (including pre-Cretaceous batholithic rocks) and lithosphere. Crustal thickness also varies by belt, as the Mesozoic crust of the western and central belts was also comparatively thin (discussed further below). Both the crustal density and the crustal thickness are major factors controlling the ascent of mafic magmas to upper-crustal levels. Lower density is presumably required for mafic magmas to ascend in the high Sierra and eastern belts, which is promoted by higher magmatic H₂O concentrations (Saleeby and Sharp, 1980; Sisson et al., 1996; Saleeby, 2011; Lewis et al., 2021; Clemens-Knott and Saleeby, 1999). Density is not

the only consideration in magma ascent, though; extensional stresses in the eastern belt (similar to the Jurassic instance recorded by the Independence dike swarm) could have further facilitated the ascent of mafic magmas through the thick, low-density crust of the eastern portions of the batholith (Lewis et al., 2024).

In detail, in the western belt, large ($\sim 3\text{--}30\text{ km}^2$) mafic intrusions and associated non-primitive ultramafic cumulates (Fig. 6A–C) intrude dense ophiolitic crust through thin oceanic lithosphere. In the northwestern portion of the western belt in the study area, smaller ($\sim 0.5\text{--}5\text{ km}^2$) mafic intrusions are hosted by Western Metamorphic Belt juvenile arc metavolcanic and metasedimentary crust above oceanic lithosphere. Late-crystallizing amphibole suggests low-H₂O (yet still hydrous and arc-related) parental magmas (Fig. 11A, B).

In the central belt, cumulates are still abundant, but are less commonly ultramafic (and typically feldspar-bearing) compared to the western belt, also with more oikocrystic amphibole and less common orthopyroxene, indicating somewhat more hydrous parental magmas compared to the western belt (Fig. 6D–F; Fig 11C, D). These smaller ($<0.1\text{--}2.5\text{ km}^2$; Fig. 4A) and more sparse central belt intrusions are hosted by continent-derived metasedimentary crust, exposed as Kings Sequence metamorphic rocks, that likely sit atop oceanic or transitional lithosphere (Kistler, 1990). They are frequently crosscut or disaggregated by later felsic plutons, rather than intrusive into them (Fig. 4C, D; 6D–F). Mafic plutons of the central belt—also exposed in the deepest exposures of the southern Sierra Nevada—are intrusive into the host metamorphic sequences, displaying abundant evidence for interaction with the Kings Sequence at both shallow and deep levels (Fig. 5B, C) (Pickett and Saleeby, 1994; Lackey et al., 2005). Felsic plutons of the central belt display field, petrologic, and geochemical evidence for contamination by Kings Sequence rocks, including being relatively reduced and occasionally peraluminous (Ague and Brimhall, 1988b; Lackey et al., 2006).

In contrast, in the high Sierra belt, where the final stages of arc magmatism produced the largest intrusions of the batholith, the mafic rocks are typically dioritic to tonalitic, and almost no mafic cumulates are present. There the mafic intrusions

are commingled with their host felsic plutons and are generally lens to sheet-like intrusions, with enclaves emanating from dike-like regions with obvious syn-intrusion strain (Fig. 3A–B; 4E– G; 7A–C). The exposed pre-existing crustal rocks are nearly all metavolcanic rocks, only slightly older than the batholith (Mesozoic; Fig. 5D), reflecting long-term arc magmatism located there.

Finally, the eastern belt mafic intrusions are more similar in size to the western and central mafic intrusions ($\sim 2\text{--}15\text{ km}^2$) and often intrude as sheets into pre-existing metamorphic rocks or felsic plutons, or syn-magmatically with felsic intrusions (Fig. 3C, D; Frost and Mahood, 1987; Sisson et al., 1996; Coleman et al., 1995). Ages of intrusions in the eastern belt are both Jurassic and Cretaceous, coinciding with the Jurassic Independence dike swarm and with the ages of felsic intrusive suites nearby (Lewis et al., 2024). Amphibole is abundant (and in many cases euhedral, crystallizing early; Fig. 11G, H) in mafic intrusions of both the high Sierra and eastern belts, so parental magmas were likely hydrous—estimates of initial H_2O contents of 3 to 6 wt.% at Onion Valley (Sisson et al., 1996) and Hidden Lakes (Lewis et al., 2021).

The question arises, why are there different styles of mafic intrusion between the high Sierra (smaller and more evolved intrusions) and eastern belts (larger complexes with mafic cumulates) despite many first-order similarities in the upper plate and in their parental magmas?

The metamorphic framework pendants of the high Sierra belt are mainly Mesozoic metavolcanic and caldera fill rocks from slightly earlier stages of arc magmatism (Fiske and Tobisch, 1994; Klemetti et al., 2014; Raftrey et al., 2016; Barth et al., 2018), whereas the eastern belt pendants are Neoproterozoic to mid-Paleozoic shallow marine passive margin metasedimentary sequences (Stevens and Greene, 2000; Stevens et al., 2005). The high Sierra belt could thus have been magmatically and thermally “primed” and weakened by this prior arc activity (DeSilva et al., 2006; Karakas et al., 2017; Ardill et al., 2018). In comparison, the eastern belt would have intruded into more brittle and potentially denser (lacking partial melt) crust. The eastern belt is also separated from the high Sierra belt by the

Sierra Crest Shear Zone, a syn-plutonic region of transpression and crustal weakness recorded as a chain of shear zones active during Cretaceous intrusive activity (Busby-Spera and Saleeby, 1990; Greene and Schweickert, 1995; Tobisch et al., 1995; Tikoff and de Saint Blanquat, 1997). Tectonic stresses have been proposed to affect magma ascent (Watanabe et al., 1999), so the stress fields on either side of the shear zone could have played a role in the magmatic “priming” of the high Sierra belt, and/or in the style of mafic magmatism (*i.e.*, tabular, sill or dike-like bodies in the eastern Sierra, particularly during the Jurassic in association with the Independence dike swarm).

The eastern belt as defined here sits mainly along the steep eastern exposures of the Sierra Nevada (and additionally, separated by Owens Valley, within the White-Inyo Mountains). This region is both the western edge of Basin and Range extension and the axis of the Eastern California Shear Zone (Henry, 2009). It also coincides with the mid-Jurassic (~147 Ma) Independence dike swarm (Carl and Glazner, 2002). Present-day seismicity of the Eastern California Shear zone and volcanism at Long Valley Caldera may be at least partly controlled by these and other nearby plate-scale pre-existing structures (Nevitt et al., 2023; Hildreth et al., 2023). It is possible that the sheet-like style of relatively large mafic intrusions with preserved mafic to ultramafic cumulates is related to fault and fracture-controlled crustal weaknesses that allow mafic magmas to ascend to the upper crust (*i.e.*, Ague and Brimhall, 1988b).

The utility of mafic intrusions for probing crustal thickness across the batholith

From west to east, the $(\text{La}/\text{Yb})_{\text{CN}}$ in non-cumulate samples increases (with a peak in the high Sierra belt) towards the continental interior (Fig. 10). The Sr/Y in these samples increases towards the east as well. These ratios correlate with crustal thickness, or depth to the Moho, due to the stability of plagioclase (in which Sr is compatible) at low pressures, versus amphibole±garnet (in which Y is compatible) at high pressures during differentiation near the base of the crust (Chiaradia, 2015;

Chapman et al., 2015; Profeta et al., 2015). Crustal thickness is calculated using the equations of Profeta et al. (2015) and plotted in Figure 10 (larger symbols are filtered for Rb/Sr between 0.05 to 0.2, to avoid samples that are primitive or have sedimentary melt signatures; Chapman et al., 2015). Mafic compositions (<55 wt.% SiO₂) are not included in the calibration dataset of Profeta et al. (2015) for the crustal thickness calculation, and so the exercise here is illustrative, rather than quantitative. However, at relatively evolved mafic compositions (MgO \leq ~6 wt.%, the composition of parental melts to these mafic intrusions as discussed above), trends in Sr/Y due to fractionation of plagioclase versus amphibole \pm garnet related to crustal thickness are observed (Chiaradia, 2015). As discussed in detail by Lewis et al. (2024), by selecting non-cumulate samples (plainly accumulation of plagioclase or amphibole can cause major changes in Sr/Y) and using evolved mafic compositions that have experienced earlier stages of differentiation (which is the case for all samples of this study), we obtain tentative estimates of the crustal thickness for these mafic samples. Here, this is primarily in recognition of the upper-plate heterogeneity and its controls on geochemistry by belt along the transect. Note that because even the gabbroic and some dioritic samples in our suite contain some amount of cumulate plagioclase, some elevated Sr/Y values may be anomalous and yield artificially high calculated crustal thickness values.

Low (La/Yb)_{CN} cannot be produced if garnet is present in the mantle wedge, and would not be affected by slab melts, which have low concentrations of these elements (Kessel et al., 2005; Hermann and Rubatto, 2009; Turner and Langmuir, 2015). This further corroborates a thinner crust in the west and thicker in the east. Likewise, a similar (Gd/Yb)_{CN} trend was seen in the Peninsular Ranges batholith, suggesting a lack of garnet and thinner crust in the west there as well (Gromet and Silver, 1987; Lee et al., 2007). The Sr/Y of these samples can be influenced by crystallization of plagioclase (in which Sr is compatible) and amphibole (in which Y is compatible). Because the rocks in these mafic intrusions typically have abundant plagioclase and amphibole, and because the gabbroic and some dioritic samples are

likely cumulate in nature, higher Sr/Y values (and corresponding calculated crustal thickness) could reflect plagioclase accumulation (Fig. A-10).

Calculated crustal thickness increases in the eastern ~half of the batholith (high Sierra and eastern belts) compared to the western and central belts. For all non-cumulate samples (not filtered by Rb/Sr), in the western and central belts together, the crustal thickness based on $(La/Yb)_{CN}$ is ~16 to 41 km (average 27 km), and in the high Sierra and eastern belts together, it is ~34 to 60 km (average 45 km). Excluding samples offset to high Sr/Y, which potentially have accumulated plagioclase (20-JRD-50A, SNB-18-53 and SNB-19-52), the values calculated from Sr/Y in the west and central belts are 21 to 41 km (average 31 km) and in the high Sierra and eastern belts 27 to 56 km (average 41 km). To summarize, the calculated Mesozoic crustal thickness in the western half of the Sierra Nevada batholith is on average ~25 to 40% (or up to ~20 km) thinner than the eastern half, which has the relatively thick crust expected in a continental arc.

Lewis et al. (2024) report that in the eastern belt, calculated crustal thickness based on Sr/Y increased by up to ~20 km from the Jurassic (32 to 38 km) to the Cretaceous (40 to 51 km). Crustal thickening from the Jurassic to the Cretaceous has been reported by others based on studies of more felsic compositions of the Sierra Nevada batholith (Chapman et al., 2015; Ardill et al., 2024). Crustal thickening over time from the Jurassic to the Cretaceous is not as obvious in the chemistry of the selected sample suite reported here (particularly based on $(La/Yb)_{CN}$), but such a pattern might emerge in a larger collection of dated samples. It may also be the case that substantial crustal thickening over time only affects the two eastern belts of the arc, where long-term arc magmatism is represented by Jurassic volcanic units and intrusive products of earlier stages of arc magmatism, in comparison to a transient period of arc migration through the western two belts, as discussed above and by Ardill et al. (2018, 2024). Alternatively, a thicker crust in the eastern two belts of the arc could be solely due to pre-existing batholith structure (accreted thin oceanic lithosphere in the west, compared to thicker continental lithosphere eastward; Saleeby et al., 1990; Kistler, 1990, 1993). Rather than actively thickening during

batholith formation, the shifting of the locus of magmatism across this pre-existing framework could have driven the changes in geochemistry.

The $(\text{Dy}/\text{Yb})_{\text{CN}}$ in the melt-like samples studied here does not systematically vary landward (Fig. A-4), although this ratio has been proposed to increase with crustal thickness as well due to the presence of garnet in the deep lithosphere of thicker arcs (Turner and Langmuir, 2015). However, in a compilation of Sierra Nevada batholith whole rock chemistry by Ardill et al. (2018), the opposite trend, a landward decrease in $(\text{Dy}/\text{Yb})_{\text{CN}}$, was observed. Amphibole crystallization affects this ratio, as Dy partitions more strongly into amphibole compared to Yb. Hence, amphibole-rich cumulates would have high $(\text{Dy}/\text{Yb})_{\text{CN}}$, whereas fractional crystallization of amphibole would produce residual melts with low $(\text{Dy}/\text{Yb})_{\text{CN}}$. In the more evolved rocks of that compilation by Ardill et al. (2018), the decreasing trend landward could indicate that amphibole crystallization contributes to the trends during later stages of differentiation than represented by the mafic intrusions of this study, and/or amphibole-rich cumulates of the eastern belts. Thus, we suggest $(\text{Dy}/\text{Yb})_{\text{CN}}$ is not a useful proxy for crustal thickness in these rocks.

An increase in K_2O in these mafic samples from west to east across the batholith follows a pattern similar to these trace element ratios (Fig. 9B). The west to east increasing K_2O trend is also observed in felsic plutonic rocks in the Sierra Nevada batholith (Bateman, 1992; Ardill et al., 2018; Chapman and Ducea, 2019; Chen & Tilton, 1991). In detail, K_2O is lower in the eastern belt than in the high Sierra belt. Also, two exceptions in the western belt (the Big Sandy and Jurassic Fine Gold intrusions) have more evolved compositions and are very small (a $<0.1 \text{ km}^2$ lens and a wide dike, respectively), and thus may have experienced exchange with host felsic plutons. In general, the increase in bulk K_2O for these mafic intrusions corresponds with a general increase in modal biotite abundance within similarly differentiated samples (*i.e.*, biotite-bearing cumulates in the eastern belt). In addition, the trend stays consistent within a given belt with time, from the Jurassic and Cretaceous. Such an increase in K_2O landward occurs in arcs globally, and has been

tied to an increase in the depth to the slab (Dickinson, 1975; Tatsumi and Eggins, 1995).

These increasing geochemical trends by belt landward, with peaks in K_2O and $(La/Yb)_{CN}$ in the high Sierra belt, could reveal either (1) a difference in the upper-plate lithosphere and crust of these belts, imparted into the mafic parental magmas, or (2) temporal changes during the final stages of arc magmatism as magmatism was focused toward the high Sierra belt, as discussed above (Ardill et al., 2018, 2024). The first possibility may be supported by either the MASH hypothesis, wherein thickened crust implies more interaction of the ascending magmas with it (DePaolo, 1981; Hildreth and Moorbath, 1988), or by thicker crust of the upper plate resulting in lower degrees of melting in the mantle, which would increase incompatible elements in any magmas generated (Plank and Langmuir, 1988; Putirka and Busby, 2007; Turner and Langmuir, 2022). However, the second relationship, a temporal evolution in geochemistry and magmatism, has been described in many studies of the Sierra Nevada batholith, where large volumes of magmatism occurred in the latest stages of arc activity, often described as a high-flux magmatic event or “flare-up,” (Ducea 2001; Chapman et al., 2021). Either way, the increase landward in K_2O —as well as $(La/Yb)_{CN}$ and Sr/Y —in these mafic intrusions and the concentration of the most extreme signatures observed in sparse and evolved mafic intrusions emplaced during the latest stages of batholith formation implies a unique dynamic in the high Sierra belt and at the scale of the subduction zone.

In summary, we find that the record of across-arc variation recorded by the mafic intrusions studied here demonstrates that pre-existing upper-plate crustal thickness (and composition) prior to formation of the batholith must have played a significant role in determining the geochemistry of the arc, even at early (basaltic to basaltic andesitic) stages of differentiation.

CONCLUSIONS

Mafic intrusions are often used to estimate mantle-derived endmember compositions, yet we show here that in the upper crust of the central Sierra Nevada

batholith (1) the mafic intrusions are not primitive in composition (parental melt Mg# ~33 to 57.5); (2) they likely were influenced by assimilation; and (3) the bulk rocks are in many cases cumulates whose compositions are controlled by mineralogy and mineral chemistry rather than by melt composition. Nonetheless the variations in mineralogy and chemistry among the mafic intrusions of the Sierra Nevada indicate trends in H₂O concentration and possibly δO_2 likely inherited from primary heterogeneity in their sources. Moreover, the whole rock and mineral chemistry of the mafic intrusions record essential information about the architecture and emplacement history of the batholith, as demonstrated by systematic geochemical changes across four geologic belts. We observe different styles of intrusion and interaction with associated or adjacent felsic intrusions in each belt. We attribute the main cause of this variability to interaction with the different tectonically-assembled lithospheric and crustal belts of the batholith. The influence of the upper plate likely reflects controls via variable crustal thickness and density, rheology of the crust related to prior arc magmatism, and the occurrence of extensional stress regimes. The migration of the locus of arc magmatism led to a final stage that focused activity into the area of the high Sierra belt that had the longest history of magmatic activity. In that region, mafic intrusions are sparse, more evolved than in other belts, and mingled with co-magmatic host intrusions. The mafic magmas that ascended through the thick and potentially ductile, hot crust primed by magmatic activity were likely all more hydrous than the mafic magmas that intruded into the dense oceanic lithosphere and ophiolitic or juvenile arc crust of the western belt.

ACKNOWLEDGEMENTS

Grace Hruska was a major support in the field, in addition to Jennifer Bass, Anahi Carrera, Amanda Bednarick, Xenia Boyes, Ery Hughes, Sarah Zeichner, Barbara Ratschbacher, Stephen Coffer, the Cisco Grove Pack Station, and for sampling permission and access, Daniella Schaeffer (National Park Service), Alan Gallegos and Annette Lambert (Sierra National Forest), Jennifer Lewis (Bureau of Reclamation), Andrew Collum and archeologist Tod Hildebrandt (California State

Parks). Many thanks to Dr. Paul O'Sullivan and Graham Brady for mineral separation support, and Lily Coffin and Emma Bertran for help in the laboratory. We gratefully acknowledge support from U.S. National Science Foundation (NSF) award EAR 2105371.

REFERENCES

Ague, J.J., and Brimhall, G.H., 1987, Granites of the batholiths of California: products of local assimilation and regional-scale crustal contamination. *Geology*, 15, 63–66, doi:10.1130/0091-7613(1987)15<63:GOTBOC>2.0.CO;2.

Ague, J.J., and Brimhall, G.H. (1988a). Regional variations in bulk chemistry, mineralogy, and the compositions of mafic and accessory minerals in the batholiths of California. *Bulletin of the Geological Society of America*, 100, 891–911, doi:10.1130/0016-7606(1988)100<0891:RVIBCM>2.3.CO;2.

Ague, J.J., and Brimhall, G.H. (1988b). Magmatic arc asymmetry and distribution of anomalous plutonic belts in the batholiths of California: Effects of assimilation, crustal thickness, and depth of crystallization. *Bulletin of the Geological Society of America*, 100, 912–927, doi:10.1130/0016-7606(1988)100<0912:MAAADO>2.3.CO;2.

Alonso-Perez, R., Müntener, O., and Ulmer, P., 2009, Igneous garnet and amphibole fractionation in the roots of island arcs: experimental constraints on andesitic liquids. *Contributions to Mineralogy and Petrology*, 157, 541–558, doi:10.1007/s00410-008-0351-8.

Annen, C., Blundy, J.D., and Sparks, R.S.J., 2006, The genesis of intermediate and silicic magmas in deep crustal hot zones. *Journal of Petrology*, 47, 505–539, doi:10.1093/petrology/egi084.

Arculus, R.J., and Wills, K.J.A., 1980, The petrology of plutonic blocks and inclusions from the lesser antilles Island arc. *Journal of Petrology*, 21, 743–799, doi:10.1093/petrology/21.4.743.

Ardill, K., Attia, S., Memeti, V., and Paterson, S.R., 2024, Fingerprinting the geochemical signals of episodic arc activity in the Sierra Nevada batholith in space and time. *Geological Society of America Bulletin*, 1–21, doi:10.1130/B37266.1/6351187/b37266.pdf.

Ardill, K., Paterson, S., and Memeti, V., 2018, Spatiotemporal magmatic focusing in upper-mid crustal plutons of the Sierra Nevada arc. *Earth and Planetary Science Letters*, 498, 88–100, doi:10.1016/j.epsl.2018.06.023.

Armstrong, J. T., 1988, Quantitative analysis of silicate and oxide minerals: comparison of Monte Carlo, ZAF and $\phi(\rho Z)$ procedures. *Microbeam Analysis*, 239–246.

Attia, S., Paterson, S.R., Cao, W., Chapman, A.D., Saleeby, J., Dunne, G.C., Stevens, C.H., and Memeti, V., 2018, Late Paleozoic tectonic assembly of the Sierra Nevada prebatholithic framework and western Laurentian provenance links based on synthesized detrital zircon geochronology. *Special Paper of the Geological Society of America*, 540, 267–295, doi:10.1130/2018.2540(12).

Attia, S., Paterson, S.R., Saleeby, J., and Cao, W., 2021, Detrital zircon provenance and depositional links of Mesozoic Sierra Nevada intra-arc strata. *Geosphere*, 17, 1422–1453, doi:10.1130/GES02296.1.

Barth, A.P., Wooden, J.L., Riggs, N.R., Walker, J.D., Tani, K., Penniston-Dorland, S.C., Jacobson, C.E., Laughlin, J.A., and Hiramatsu, R., 2018, Marine Volcaniclastic Record of Early Arc Evolution in the Eastern Ritter Range Pendant, Central Sierra Nevada, California. *Geochemistry, Geophysics, Geosystems*, 19, 2543–2559, doi:<https://doi.org/10.1029/2018GC007456>.

Bateman, P.C., 1992, Plutonism in the central part of the Sierra Nevada batholith, California. *US Geological Survey Professional Paper*, 1483.

Bateman, P.C., and Clark, L.D., 1974, *Stratigraphic and structural setting of the Sierra Nevada batholith, California*. *Pacific Geology*, 8, 79–89.

Bateman, P.C., Clark, L.D., Huber, N.K., Moore, J.G., and Rinehart, C.D., 1963, The Sierra Nevada batholith—a synthesis of recent work across the central part. U.S. Geological Survey Professional Paper, 414-D, 1–46.

Bea, F., Bortnikov, N., Cambeses, A., Chakraborty, S., Molina, J.F., Montero, P., Morales, I., Silantiev, S., and Zinger, T., 2022, Zircon crystallization in low-Zr mafic magmas: Possible or impossible? *Chemical Geology*, 602, 120898, doi:10.1016/j.chemgeo.2022.120898.

Beard, B.L., and Glazner, A.F., 1995, Trace element and Sr and Nd isotopic compositions of mantle xenoliths from the Big Pine volcanic field, California. *Journal of Geophysical Research*, 100, 4169–4179.

Beattie, P., 1993, Olivine-melt and orthopyroxene-melt equilibria. *Contributions to Mineralogy and Petrology*, 115, 103–111, doi:10.1007/BF00712982.

Berndt, J., Koepke, J., and Holtz, F., 2005, An experimental investigation of the influence of water and oxygen fugacity on differentiation of MORB at 200 MPa. *Journal of Petrology*, 46, 135–167, doi:10.1093/petrology/egh066.

Blatter, D.L., Sisson, T.W., and Hankins, W. Ben, 2017, Voluminous arc dacites as amphibole reaction-boundary liquids. *Contributions to Mineralogy and Petrology*, 172:27, doi:10.1007/s00410-017-1340-6.

Blatter, D.L., Sisson, T.W., and Hankins, W. Ben, 2013, Crystallization of oxidized, moderately hydrous arc basalt at mid- to lower-crustal pressures: Implications for andesite genesis. *Contributions to Mineralogy and Petrology*, 166, 861–886, doi:10.1007/s00410-013-0920-3.

Blundy, J., Melekhova, E., Ziberna, L., Humphreys, M.C.S., Cerantola, V., Brooker, R.A., McCammon, C.A., Pichavant, M., and Ulmer, P., 2020, Effect of redox on Fe–Mg–Mn exchange between olivine and melt and an oxybarometer for basalts. *Contributions to Mineralogy and Petrology*, 175, 1–32 p., doi:10.1007/s00410-020-01736-7.

Borisov, A., and Aranovich, L., 2019, Zircon solubility in silicate melts: New experiments and probability of zircon crystallization in deeply evolved

basic melts. *Chemical Geology*, 510, 103–112, doi:10.1016/j.chemgeo.2019.02.019.

Borisov, A., Aranovich, L. and Antoshechkina, P., 2025, Zircon solubility in silicate melts: New empirical models and thermodynamics. *Chemical Geology*, p.122682.

Bucholz, C.E., Jagoutz, O., VanTongeren, J.A., Setera, J., and Wang, Z., 2017, Oxygen isotope trajectories of crystallizing melts: Insights from modeling and the plutonic record. *Geochimica et Cosmochimica Acta*, 207, 154–184, doi:10.1016/j.gca.2017.03.027.

Bucholz, C.E., and Spencer, C.J., 2019, Strongly Peraluminous Granites across the Archean-Proterozoic Transition. *Journal of Petrology*, 60, 1299–1348, doi:10.1093/petrology/egz033.

Busby-Spera, C.J., and Saleeby, J.B., 1990, Intra-arc strike-slip fault exposed at batholithic levels in the southern Sierra Nevada, California. *Geology*, 18, 255–259, doi:10.1130/0091-7613(1990)018<0255:IASSFE>2.3.CO;2.

Busby, C., 2004, Continental growth at convergent margins facing large ocean basins: A case study from Mesozoic convergent-margin basins of Baja California, Mexico. *Tectonophysics*, 392, 241–277, doi:10.1016/j.tecto.2004.04.017.

Cao, W., Paterson, S., Memeti, V., Mundil, R., Anderson, J.L., and Schmidt, K., 2015, Tracking paleodeformation fields in the Mesozoic central Sierra Nevada arc: Implications for intra-arc cyclic deformation and arc tempos. *Lithosphere*, 7, 296–320, doi:10.1130/L389.1.

Carl, B.S., and Glazner, A.F., 2002, Extent and significance of the Independence dike swarm, eastern California, *in* Glazner, A.F., Walker, J.D., and Bartley, J.M. eds., *Geologic Evolution of the Mojave Desert and Southwestern Basin and Range*, Boulder, Colorado, Geological Society of America Memoir 195, 117–130, doi:10.1130/0-8137-1195-9.117.

Cecil, M.R., Rotberg, G.L., Ducea, M.N., Saleeby, J.B., and Gehrels, G.E., 2012, Magmatic growth and batholithic root development in the northern Sierra Nevada, California. *Geosphere*, 8, 592–606, doi:10.1130/GES00729.1.

Chapman, A.D., Saleeby, J.B., Wood, D.J., Piasecki, A., Kidder, S., Ducea, M.N., and Farley, K.A., 2012, Late cretaceous gravitational collapse of the southern Sierra Nevada batholith, California. *Geosphere*, 8, 314–341, doi:10.1130/GES00740.1.

Chapman, J.B., Ducea, M.N., Kapp, P., Gehrels, G.E., and DeCelles, P.G., 2017, Spatial and temporal radiogenic isotopic trends of magmatism in Cordilleran orogens. *Gondwana Research*, 48, 189–204, doi:10.1016/j.gr.2017.04.019.

Chapman, J.B., and Ducea, M.N., 2019, The role of arc migration in Cordilleran orogenic cyclicity. *Geology*, 47, 627–631, doi:10.1130/G46117.1.

Chapman, J.B., Ducea, M.N., DeCelles, P.G., and Profeta, L., 2015, Tracking changes in crustal thickness during orogenic evolution with Sr/Y: An example from the North American Cordillera. *Geology*, 43, 919–922, doi:10.1130/G36996.1.

Chapman, J.B., Shields, J.E., Ducea, M.N., Paterson, S.R., Attia, S., and Ardill, K.E., 2021, The causes of continental arc flare ups and drivers of episodic magmatic activity in Cordilleran orogenic systems. *Lithos*, 398–399, 106307, doi:10.1016/j.lithos.2021.106307.

Chen, J.H., and Tilton, G.R., 1991, Applications of lead and strontium isotopic relationships to the petrogenesis of granitoid rocks, central Sierra Nevada batholith, California. *Geological Society of America Bulletin*, 103, 439–447, doi:10.1130/0016-7606(1991)103<0439:AOLASI>2.3.CO;2.

Chen, J.H., and Moore, J.G., 1982, Uranium-lead isotopic ages from the Sierra Nevada batholith, California. *Journal of Geophysical Research*, 87, 4761–4784.

Chiaradia, M., 2015, Crustal thickness control on Sr/Y signatures of recent arc magmas: An Earth scale perspective. *Scientific Reports*, 5, 8115, doi:10.1038/srep08115.

Chin, E.J., Lee, C.T.A., and Barnes, J.D., 2014, Thickening, refertilization, and the deep lithosphere filter in continental arcs: Constraints from major and trace elements and oxygen isotopes. *Earth and Planetary Science Letters*, 397, 184–200, doi:10.1016/j.epsl.2014.04.022.

Clemens-Knott, D., 1992, Geologic and isotopic investigations of the early Cretaceous Sierra Nevada batholith, Tulare Co., CA and the Ivrea Zone, NW Italian Alps: examples of interaction between mantle-derived magma and continental crust. California Institute of Technology, 368 p.

Clemens-Knott, D., and Saleeby, J.B., 1999, Impinging ring dike complexes in the Sierra Nevada batholith, California: Roots of the Early Cretaceous volcanic arc. *Bulletin of the Geological Society of America*, 111, 484–496, doi:10.1130/0016-7606(1999)111<0484:IRDCIT>2.3.CO;2.

Coleman, D.S., Glazner, A.F., Miller, J.S., Bradford, K.J., Frost, T.P., Joye, J.L., and Bachl, C.A., 1995, Exposure of a late cretaceous layered mafic-felsic magma system in the central Sierra Nevada batholith, California. *Contributions to Mineralogy and Petrology*, 120, 129–136, doi:10.1007/BF00287110.

Coleman, D.S., Frost, T.P., and Glazner, A.F., 1992, Evidence from the Lamarck granodiorite for rapid late Cretaceous crust formation in California. *Science*, 258, 1924–1926, doi:10.1126/science.258.5090.1924.

Coleman, D.S., and Glazner, A.F., 1997, The Sierra crest magmatic event: Rapid formation of juvenile crust during the late Cretaceous in California. *International Geology Review*, 39, 768–787, doi:10.1080/00206819709465302.

Corfu, F., Hanchar, J.M., Hoskin, P.W.O., and Kinny, P., 2003, Atlas of zircon textures. *Reviews in Mineralogy and Geochemistry*, 53, 469–500.

DeCelles, P.G., Ducea, M.N., Kapp, P., and Zandt, G., 2009, Cyclicity in Cordilleran orogenic systems. *Nature Geoscience*, 2, 251–257, doi:10.1038/ngeo469.

DePaolo, D.J., 1981, A neodymium and strontium isotopic study of the Mesozoic calc-alkaline granitic batholiths of the Sierra Nevada and Peninsular ranges, California. *Journal of Geophysical Research*, 86, 10470–10488.

deSilva, S.L., Zandt, G., Trumbull, R., Viramonte, J.G., Salas, G., and Jimenez, M., 2006, Large-scale silicic volcanism in the Central Andes—a tectonomagmatic perspective, *in* Mechanisms of Activity and Unrest at Large Calderas, Geological Society of London, 47–63.

Dickinson, W.R., 1975, Potash-Depth (K-h) relations in continental margin and intra-oceanic magmatic arcs. *Geology*, 3, 53–56, doi:10.1130/0091-7613(1975)3<53:PKRICM>2.0.CO;2.

Dodge, F.C.W., Calk, L.C., and Kistler, R.W., 1986, Lower crustal xenoliths, Chinese Peak lava flow, central Sierra Nevada. *Journal of Petrology*, 27, 1277–1304.

Domenick, M.A., Kistler, R.W., Dodge, F.C.W., and Tatsumoto, M., 1983, Nd and Sr isotopic study of crustal and mantle inclusions from the Sierra Nevada and implications for batholith petrogenesis. *Bulletin of the Geological Society of America*, 94, 713–719, doi:10.1130/0016-7606(1983)94<713:NASISO>2.0.CO;2.

Donovan, J. J., and Tingle, T. N., 1996, An improved mean atomic number background correction for quantitative microanalysis. *Microscopy and Microanalysis*, 2, 1–7.

Donovan, J. J., Singer, J. W., and Armstrong, J. T., 2016, A new EPMA method for fast trace element analysis in simple matrices. *American Mineralogist*, 101, 1839–1853.

Donovan, J. J., Moy, A., von der Handt, A., Gainsforth, Z., Maner, J. L., Nachlas, W., and Fournelle, J., 2023, A new method for dead time calibration and a

new expression for correction of WDS intensities for microanalysis. *Microscopy and Microanalysis*, 29, 1096–1110.

Dorais, M.J., Whitney, J.A., Roden, M.F., 1990, Origin of mafic enclaves in the Dinkey Creek pluton, central Sierra Nevada batholith, California. *Journal of Petrology*, 31, 853–881, doi:10.1016/j.cossms.2010.07.001.

Ducea, M.N., 1998, A petrologic investigation of deep-crustal and upper-mantle xenoliths from the Sierra Nevada, California; constraints on lithospheric composition beneath continental arcs and the origin of Cordilleran batholiths. California Institute of Technology, 341 p.

Ducea, M.N., and Chapman, A.D., 2018, Sub-magmatic arc underplating by trench and forearc materials in shallow subduction systems; A geologic perspective and implications. *Earth-Science Reviews*, 185, 763–779, doi:<https://doi.org/10.1016/j.earscirev.2018.08.001>.

Ducea, M.N., 2001, The California arc: thick granitic batholiths, eclogitic residues, lithospheric-scale thrusting, and magmatic flare-ups. *GSA Today*, 4–10.

Ducea, M.N., and Saleeby, J.B., 1998, The age and origin of a thick mafic-ultramafic keel from beneath the Sierra Nevada batholith. *Contributions to Mineralogy and Petrology*, 133, 169–185, doi:10.1007/s004100050445.

Evernden J.F., and Kistler, R.W., 1970, Chronology of Emplacement of Mesozoic Batholithic Complexes in California and Western Nevada. US Geological Survey Professional Paper, 623, 1–42.

Farmer, G.L., and Ball, T.T., 1997, Sources of Middle Proterozoic to Early Cambrian siliciclastic sedimentary rocks in the Great Basin: A Nd isotope study. *Geological Society of America Bulletin*, 109, 1193–1205, doi:10.1130/0016-7606(1997)109<1193:SOMPTE>2.3.CO;2.

Feig, S.T., Koepke, J., and Snow, J.E., 2010, Effect of oxygen fugacity and water on phase equilibria of a hydrous tholeiitic basalt. *Contributions to Mineralogy and Petrology*, 160, 551–568, doi:10.1007/s00410-010-0493-3.

Feig, S.T., Koepke, J., and Snow, J.E., 2006, Effect of water on tholeiitic basalt phase equilibria: An experimental study under oxidizing conditions. *Contributions to Mineralogy and Petrology*, 152, 611–638, doi:10.1007/s00410-006-0123-2.

Ferré, E.C., Michelsen, K.J., Ernst, W.G., Boyd, J.D., and Cañón-Tapia, E., 2012, Vertical zonation of the Barcroft granodiorite, White Mountains, California: implications for magmatic processes. *American Mineralogist*, 97, 1049–1059.

Fiske, R.S., and Tobisch, O.T., 1994, Middle Cretaceous ash-flow tuff and caldera-collapse deposit in the Minarets caldera, east-central Sierra Nevada, California. *Geological Society of America Bulletin*, 106, 582–593, doi:10.1130/0016-7606(1994)106<0582:MCAFTA>2.3.CO;2.

Frazer, R.E., Coleman, D.S., and Mills, R.D., 2014, Zircon U-Pb geochronology of the Mount Givens granodiorite: implications for the genesis of large volumes of eruptible magma. *Journal of Geophysical Research: Solid Earth*, 119, 2907–2924, doi:10.1002/2013JB010716.

Frost, T.P., 1987, Sample localities, radiometric ages, descriptions, and major- and trace-element abundances of Late Jurassic mafic plutonic rocks, eastern Sierra Nevada, California. *USGS Open-File Report*, 87-484, 1–32.

Frost, T.P., and Mattinson, J.M., 1988, Late Cretaceous U-Pb age of a mafic intrusion from the eastern Sierra Nevada, California. *Bulletin of Isotopic Geochronology*, 51, 15–18.

Frost, T.P., and Mahood, G.A., 1987, Field, chemical, and physical constraints on mafic-felsic magma interaction in the Lamarck Granodiorite, Sierra Nevada, California. *Geological Society of America Bulletin*, 99, 272–291.

Gao, R., Lassiter, J.C., and Ramirez, G., 2017, Origin of temporal compositional trends in monogenetic vent eruptions: Insights from the crystal cargo in the Papoose Canyon sequence, Big Pine Volcanic Field, CA. *Earth and Planetary Science Letters*, 457, 227–237, doi:10.1016/j.epsl.2016.10.013.

Gevedon, M., 2013, Paired oxygen and hafnium isotopic analysis of zircon from gabbros: Identifying potential Mesozoic mantle heterogeneity in the Sierra Nevada arc. California State University, Fullerton, 77 p.

Greene, A.R., DeBari, S.M., Kelemen, P.B., Blusztajn, J., and Clift, P.D., 2006, A detailed geochemical study of island Arc crust: The Talkeetna Arc section, south-central Alaska. *Journal of Petrology*, 47, 1051–1093, doi:10.1093/petrology/egl002.

Greene, D.C., and Schweickert, R.A., 1995, The Gem Lake shear zone: Cretaceous dextral transpression in the Northern Ritter Range pendant, eastern Sierra Nevada, California. *Tectonics*, 14, 945–961, doi:10.1029/95TC01509.

Grimes, C.B., Wooden, J.L., Cheadle, M.J., and John, B.E., 2015, “Fingerprinting” tectono-magmatic provenance using trace elements in igneous zircon. *Contributions to Mineralogy and Petrology*, 170:46, doi:10.1007/s00410-015-1199-3.

Gromet, P., and Silver, L.T., 1987, REE Variations Across the Peninsular Ranges Batholith: Implications for Batholithic Petrogenesis and Crustal Growth in Magmatic Arcs. *Journal of Petrology*, 28, 75–125, doi:10.1093/petrology/28.1.75.

Hamada, M., and Fujii, T., 2008, Experimental constraints on the effects of pressure and H₂O on the fractional crystallization of high-Mg island arc basalt. *Contributions to Mineralogy and Petrology*, 155, 767–790, doi:10.1007/s00410-007-0269-6.

Hammarstrom, J.M., and Zen, E., 1986, Aluminum in hornblende: An empirical igneous geobarometer. *American Mineralogist*, 71, 1297–1313.

Henry, C.D., 2009, Uplift of the Sierra Nevada, California. *Geology*, 37, 575–576, doi:10.1130/focus062009.1.

Hermann, J., and Rubatto, D., 2009, Accessory phase control on the trace element signature of sediment melts in subduction zones. *Chemical Geology*, 265, 512–526, doi:10.1016/j.chemgeo.2009.05.018.

Hildreth, W., Fierstein, J., and Vazquez, J., 2023, Ages of the granitic basement of Long Valley Caldera, California, USA, and siting of the Quaternary granite-rhyolite pluton. *Geological Society of America Bulletin*, 135, 2753–2766, doi:10.1130/B36589.1.

Hildreth, W., and Moorbath, S., 1988, Crustal contributions to arc magmatism in the Andes of Central Chile. *Contributions to Mineralogy and Petrology*, 98, 455–489, doi:10.1007/BF00372365.

Holland, J.E., Surpless, B., Smith, D.R., Loewy, S.L., and Lackey, J.S., 2013, Intrusive history and petrogenesis of the Ash Mountain Complex, Sierra Nevada batholith, California (USA). *Geosphere*, 9, 691–717, doi:10.1130/GES00890.1.

Hoskin, P.W.O., and Schaltegger, U., 2003, The composition of zircon and igneous and metamorphic petrogenesis. *Reviews in Mineralogy and Geochemistry*, 53, 27–62, doi:10.1515/9781501509322-005.

Huppert, H.E., and Sparks, R.S.J., 1988, The generation of granitic magmas by intrusion of basalt into continental crust. *Journal of Petrology*, 29, 599–624, doi:10.1093/petrology/29.3.599.

Jacob, J.B., Moyen, J.F., Fiannacca, P., Laurent, O., Bachmann, O., Janoušek, V., Farina, F., and Villaros, A., 2021, Crustal melting vs. fractionation of basaltic magmas: Part 2, Attempting to quantify mantle and crustal contributions in granitoids. *Lithos*, 402–403, doi:10.1016/j.lithos.2021.106292.

Jagoutz, O., 2014, Arc crustal differentiation mechanisms. *Earth and Planetary Science Letters*, 396, 267–277, doi:10.1016/j.epsl.2014.03.060.

Jagoutz, O., and Klein, B., 2018, On the importance of crystallization-differentiation for the generation of SiO₂-rich melts and the compositional build-up of arc (and continental) crust. *American Journal of Science*, 318, 29–63, doi:10.2475/01.2018.03.

Jagoutz, O., Müntener, O., Schmidt, M.W., and Burg, J.P., 2011, The roles of flux- and decompression melting and their respective fractionation lines for

continental crust formation: Evidence from the Kohistan arc. *Earth and Planetary Science Letters*, 303, 25–36, doi:10.1016/j.epsl.2010.12.017.

James, O.B., 1971, Origin and emplacement of the ultramafic rocks of the emigrant gap area, California. *Journal of Petrology*, 12, 523–560, doi:10.1093/petrology/12.3.523.

Jicha, B.R., and Kay, S.M., 2018, Quantifying arc migration and the role of forearc subduction erosion in the central Aleutians. *Journal of Volcanology and Geothermal Research*, 360, 84–99, doi:10.1016/j.jvolgeores.2018.06.016.

Karlstrom, L., Lee, C.-T.A., and Manga, M., 2014, The role of magmatically driven lithospheric thickening on arc front migration. *Geochemistry, Geophysics, Geosystems*, 15, 2655–2675, doi:10.1002/2014GC005355. Received.

Kay, S.M., Godoy, E., and Kurtz, A., 2005, Episodic arc migration, crustal thickening, subduction erosion, and magmatism in the south-central Andes. *Geological Society of America Bulletin*, 117, 67–88, doi:10.1130/B25431.1.

Kelemen, P.B., Hanghøj, K., and Greene, A.R., 2014, 4.21 - One View of the Geochemistry of Subduction-Related Magmatic Arcs, with an Emphasis on Primitive Andesite and Lower Crust, *in* Holland, H.D. and Turekian, K.K.B.T.-T. on G. (Second E. eds., Oxford, Elsevier, 749–806, doi:<https://doi.org/10.1016/B978-0-08-095975-7.00323-5>.

Kessel, R., Ulmer, P., Pettke, T., Schmidt, M.W., and Thompson, A.B., 2005, The water-basalt system at 4 to 6 GPa: Phase relations and second critical endpoint in a K-free eclogite at 700 to 1400 °C. *Earth and Planetary Science Letters*, 237, 873–892, doi:10.1016/j.epsl.2005.06.018.

Kimbrough, D.L., Grove, M., and Morton, D.M., 2015, Timing and significance of gabbro emplacement within two distinct plutonic domains of the Peninsular Ranges batholith, southern and Baja California. *Geological Society of America Bulletin*, 127, 19–37, doi:10.1130/B30914.1.

Kistler, B.R.W., Wooden, J.L., and Morton, D.M., 2003, Isotopes and ages in the northern Peninsular Ranges batholith, southern California. US Geological Survey Open-File Report, 1–45.

Kistler, R.W., Chappell, B.W., Peck, D.L., and Bateman, P.C., 1986, Isotopic variation in the Tuolumne intrusive suite, central Sierra Nevada, California. Contributions to Mineralogy and Petrology, 94, 205–220.

Kistler, R.W., and Peterman, Z.E., 1978, Reconstruction of crustal blocks of California on the basis of initial strontium isotopic compositions of Mesozoic granitic rocks. US Geological Survey Professional Paper 1071, 1–17.

Kistler, R.W., 1990, Two different lithosphere types in the Sierra Nevada, California, *in* Anderson, J.L. ed., The nature and origin of Cordilleran Magmatism, Boulder, Colorado, Geological Society of America Memoir, 174, 271–281.

Kistler, R.W., 1993, Mesozoic intrabatholithic faulting, Sierra Nevada, California, *in* Dunne, G. and McDougall, K. eds., Mesozoic Paleogeography of the Western United States-II, Pacific Section SEPM, Book 71, 247–261.

Kistler, R.W., and Peterman, Z.E., 1973, Variations in Sr, Rb, K, Na, and initial $\text{Sr}^{87}/\text{Sr}^{86}$ in Mesozoic granitic rocks and intruded wall rocks in Central California. Bulletin of the Geological Society of America, 84, 3489–3512, doi:10.1130/0016-7606(1973)84<3489:VISRKN>2.0.CO;2.

Klein, B.Z., and Jagoutz, O., 2021, Construction of a trans-crustal magma system: Building the Bear Valley Intrusive Suite, southern Sierra Nevada, California. Earth and Planetary Science Letters, 553, 116624, doi:10.1016/j.epsl.2020.116624.

Klein, B.Z., Jagoutz, O., and Ramezani, J., 2020, High-precision geochronology requires that ultrafast mantle-derived magmatic fluxes built the transcrustal Bear Valley Intrusive Suite, Sierra Nevada, California, USA. Geology, 49, 106–110, doi:10.1130/G47952.1.

Klemetti, E.W., Lackey, J.S., and Starnes, J., 2014, Magmatic lulls in the Sierra Nevada captured in zircon from rhyolite of the mineral king pendant, California. *Geosphere*, 10, 66–79, doi:10.1130/GES00920.1.

Krawczynski, M.J., Grove, T.L., and Behrens, H., 2012, Amphibole stability in primitive arc magmas: Effects of temperature, H₂O content, and oxygen fugacity. *Contributions to Mineralogy and Petrology*, 164, 317–339, doi:10.1007/s00410-012-0740-x.

Lackey, J.S., Robinson Cecil, M., Windham, C.J., Frazer, R.E., Bindeman, I.N., and Gehrels, G.E., 2012, The fine gold intrusive suite: The roles of basement terranes and magma source development in the early Cretaceous Sierra Nevada batholith. *Geosphere*, 8, 292–313, doi:10.1130/GES00745.1.

Lackey, J.S., Valley, J.W., Chen, J.H., and Stockli, D.F., 2008, Dynamic magma systems, crustal recycling, and alteration in the Central Sierra Nevada batholith: The oxygen isotope record. *Journal of Petrology*, 49, 1397–1426, doi:10.1093/petrology/egn030.

Lackey, J.S., Valley, J.W., and Hinke, H.J., 2006, Deciphering the source and contamination history of peraluminous magmas using $\delta^{18}\text{O}$ of accessory minerals: Examples from garnet-bearing plutons of the Sierra Nevada batholith. *Contributions to Mineralogy and Petrology*, 151, 20–44, doi:10.1007/s00410-005-0043-6.

Lackey, J.S., Valley, J.W., and Saleeby, J.B., 2005, Supracrustal input to magmas in the deep crust of Sierra Nevada batholith: Evidence from high- $\delta^{18}\text{O}$ zircon. *Earth and Planetary Science Letters*, 235, 315–330, doi:10.1016/j.epsl.2005.04.003.

Laumonier, M., Scaillet, B., Arbaret, L., Andújar, J., and Champallier, R., 2015, Experimental mixing of hydrous magmas. *Chemical Geology*, 418, 158–170, doi:10.1016/j.chemgeo.2015.10.031.

Laumonier, M., Scaillet, B., Pichavant, M., Champallier, R., Andujar, J., and Arbaret, L., 2014, On the conditions of magma mixing and its bearing on

andesite production in the crust. *Nature Communications*, 5, doi:10.1038/ncomms6607.

Lee, C.T.A., Erdman, M., Yang, W., Ingram, L., Chin, E.J., and DePaolo, D.J., 2018, Sulfur isotopic compositions of deep arc cumulates. *Earth and Planetary Science Letters*, 500, 76–85, doi:10.1016/j.epsl.2018.08.017.

Lee, C.T.A., Cheng, X., and Horodyskyj, U., 2006, The development and refinement of continental arcs by primary basaltic magmatism, garnet pyroxenite accumulation, basaltic recharge and delamination: Insights from the Sierra Nevada, California. *Contributions to Mineralogy and Petrology*, 151, 222–242, doi:10.1007/s00410-005-0056-1.

Lee, C.T.A., Morton, D.M., Kistler, R.W., and Baird, A.K., 2007, Petrology and tectonics of Phanerozoic continent formation: From island arcs to accretion and continental arc magmatism. *Earth and Planetary Science Letters*, 263, 370–387, doi:10.1016/j.epsl.2007.09.025.

Lewis, M.J., Bucholz, C.E., and Jagoutz, O.E., 2021, Evidence for polybaric fractional crystallization in a continental arc: Hidden Lakes mafic complex, Sierra Nevada batholith, California. *Contributions to Mineralogy and Petrology*, 176, 1–27, doi:10.1007/s00410-021-01844-y.

Lewis, M.J., Ryan-Davis, J.R., and Bucholz, C.E., 2024, Mafic intrusions record mantle inputs and crustal thickness in the eastern Sierra Nevada batholith, California, USA. *Geological Society of America Bulletin*, 136, 1808–1826, doi:10.1130/b36646.1.

Loucks, R.R., Fiorentini, M.L., and Henriquez, G.J., 2020, New magmatic oxybarometer using trace elements in zircon. *Journal of Petrology*, 61, egaa034, doi:10.1093/petrology/egaa034.

Mack, S., Saleeby, J.B., and Ferrell, J.E., 1979, Origin and emplacement of the Academy Pluton, Fresno County, California. *Geological Society of America Bulletin*, 90, 633–694, doi:10.1130/0016-7606(1979)90<321:OAEOTA>2.0.CO;2.

Mahaffey, I.R., and Johnston, S.M., 2016, Structure and geochronology of the White Fork pluton, southern Sierra Nevada. Geological Society of America *Abstracts with Programs*, 48. doi:10.1130/abs/2016CD-274566

Mayo, E.B., 1941, Deformation in the interval Mt. Lyell–Mt. Whitney, California. Geological Society of America Bulletin, 52, 1001–1084.

Melekhova, E., Blundy, J., Robertson, R., and Humphreys, M.C.S., 2015, Experimental evidence for polybaric differentiation of primitive arc basalt beneath St. Vincent, Lesser Antilles. *Journal of Petrology*, 56, 161–192, doi:10.1093/petrology/egu074.

Memeti, V., Gehrels, G.E., Paterson, S.R., Thompson, J.M., Mueller, R.M., and Pignotta, G.S., 2010, Evaluating the Mojave-Snow Lake fault hypothesis and origins of central Sierran metasedimentary pendant strata using detrital zircon provenance analyses. *Lithosphere*, 2, 341–360, doi:10.1130/L58.1.

Moore, J.G., 1959, The quartz diorite boundary line in the western United States. *The Journal of Geology*, 67, 198–210.

Moore, J.G., and Sisson, T.W., 2008, Igneous phenocrystic origin of K-feldspar megacrysts in granitic rocks from the Sierra Nevada batholith. *Geosphere*, 4, 387–400, doi:10.1130/GES00146.1.

Moy, A., Fournelle, J., Nachlas, W., Dungan, M., Locock, A., Bullock, E., Donovan, J., & Cathey, H., Allaz, J., and von der Handt, A., 2023, On the importance of including all elements in the EPMA matrix correction. *Microscopy and Microanalysis*, 29, 855–856.

Moyen, J.F., Janoušek, V., Laurent, O., Bachmann, O., Jacob, J.B., Farina, F., Fiannacca, P., and Villaros, A., 2021, Crustal melting vs. fractionation of basaltic magmas: Part 1, granites and paradigms. *Lithos*, 402–403, 106291, doi:10.1016/j.lithos.2021.106291.

Mukhopadhyay, B., and Manton, W.I., 1994, Upper-mantle fragments from beneath the Sierra Nevada Batholith: Partial fusion, fractional crystallization, and metasomatism in a subduction related ancient

lithosphere. *Journal of Petrology*, 35, 1417–1450, doi:10.1093/petrology/35.5.1417.

Müntener, O., and Ulmer, P., 2018, Arc crust formation and differentiation constrained by experimental petrology. *American Journal of Science*, 318, 64–89, doi:10.2475/01.2018.04.

Nadin, E.S., and Saleeby, J.B., 2008, Disruption of regional primary structure of the Sierra Nevada batholith by the Kern Canyon fault system, California, in Wright, J.E. and Shervais, J.W. eds., *Ophiolites, Arcs, and Batholiths*. Geological Society of America Special Paper 438, 429–454, doi:10.1130/2008.2438(15).

Nandedkar, R.H., Ulmer, P., and Müntener, O., 2014, Fractional crystallization of primitive, hydrous arc magmas: An experimental study at 0.7 GPa. *Contributions to Mineralogy and Petrology*, 167, 1, doi:10.1007/s00410-014-1015-5.

Nevitt, J.M., Brooks, B.A., Hardebeck, J.L., and Aagaard, B.T., 2023, 2019 M7.1 Ridgecrest earthquake slip distribution controlled by fault geometry inherited from Independence dike swarm. *Nature Communications*, 14, 1546, doi:10.1038/s41467-023-36840-2.

Nokleberg, W.J., 1983, Wallrocks of the central Sierra Nevada batholith, California: A collage of accreted tectono-stratigraphic terranes: US Geological Survey Professional Paper 1255, doi:10.3133/pp1255.

Paterson, S.R., and Ducea, M.N., 2015, Arc magmatic tempos: gathering the evidence. *Elements*, 11, 91–98, doi:10.2113/gselements.11.2.91.

Pichavant, M., and Macdonald, R., 2007, Crystallization of primitive basaltic magmas at crustal pressures and genesis of the calc-alkaline igneous suite: experimental evidence from St Vincent, Lesser Antilles arc. *Contributions to Mineralogy and Petrology*, 154, 535–558, doi:10.1007/s00410-007-0208-6.

Pickett, D.A., and Saleeby, J.B., 1993, Thermobarometric constraints on the depth of exposure and conditions of plutonism and metamorphism at deep levels

of the Sierra Nevada batholith, Tehachapi Mountains, California. *Journal of Geophysical Research*, 98, 609–629.

Pickett, D.A., and Saleeby, J.B., 1994, Nd, Sr and Pb isotopic characteristics of Cretaceous intrusive rocks from deep levels of the Sierra Nevada batholith, Tehachapi Mountains, California. *Contributions to Mineralogy and Petrology*, 118, 198–215.

Plank, T., and Langmuir, C.H., 1988, An evaluation of the global variations in the major element chemistry of arc basalts. *Earth and Planetary Science Letters*, 90, 349–370.

Plank, T., Kelley, K.A., Zimmer, M.M., Hauri, E.H., and Wallace, P.J., 2013, Why do mafic arc magmas contain ~4wt% water on average? *Earth and Planetary Science Letters*, 364, 168–179, doi:<https://doi.org/10.1016/j.epsl.2012.11.044>.

Profeta, L., Ducea, M.N., Chapman, J.B., Paterson, S.R., Gonzales, S.M.H., Kirsch, M., Petrescu, L., and DeCelles, P.G., 2015, Quantifying crustal thickness over time in magmatic arcs. *Scientific Reports*, 5, 17786, doi:10.1038/srep17786.

Putirka, K., and Busby, C.J., 2007, The tectonic significance of high-K₂O volcanism in the Sierra Nevada, California. *Geology*, 35, 923–926, doi:10.1130/G23914A.1.

Raftrey, M.E., Lackey, J.S., Fulton, A.A., Gaines, R.R., and Davies, G.R., 2016, Tuffs of the Goddard pendant: snapshots of volcanic source during low-flux magmatism in the Sierra Nevada arc. *Geological Society of America Abstracts with Programs*, 48. <https://doi.org/10.1130/abs/2016CD-274617>

Ratajeski, K., Glazner, A.F., and Miller, B. V., 2001, Geology and geochemistry of mafic to felsic plutonic rocks in the Cretaceous intrusive suite of Yosemite Valley, California. *Bulletin of the Geological Society of America*, 113, 1486–1502, doi:10.1130/0016-7606(2001)113<1486:GAGOMT>2.0.CO;2.

Ratschbacher, B.C., Brenhin Keller, C., Schoene, B., Paterson, S.R., Lawford Anderson, J., Okaya, D., Putirka, K., and Lippoldt, R., 2018, A new workflow to assess emplacement duration and melt residence time of compositionally diverse magmas emplaced in a sub-volcanic reservoir. *Journal of Petrology*, 59, 1787–1810, doi:10.1093/petrology/egy079.

Reiners, P.W., Nelson, B.K., and Ghiorso, M.S., 1995, Assimilation of felsic crust by basaltic magma: Thermal limits and extents of crustal contamination of mantle-derived magmas. *Geology*, 23, 563–566.

Rezeau, H., Klein, B.Z., and Jagoutz, O., 2021, Mixing dry and wet magmas in the lower crust of a continental arc: new petrological insights from the Bear Valley Intrusive Suite, southern Sierra Nevada, California. *Contributions to Mineralogy and Petrology*, 176:73, doi:10.1007/s00410-021-01832-2.

Roeder, P.L., and Emslie, R.F., 1970, Olivine-liquid equilibrium. *Contributions to Mineralogy and Petrology*, 29, 275–289.
<https://doi.org/10.1007/BF00371276>

Ross, D.C., 1989, The metamorphic and plutonic rocks of the southernmost Sierra Nevada, California, and their tectonic framework. *US Geological Survey Professional Paper*, 1381, 1–159.

Ryan-Davis, J., Bucholz, C.E. and Sisson, T.W., *Chapter 2*, Shallow differentiation of primitive arc magmas at the Jurassic Emigrant Gap complex, Sierra Nevada, California. *In review: Journal of Petrology*.

Ryan-Davis, J., Bucholz, C.E. Lackey, J.S., Kylander-Clark, A., Lewis, M.J., Kitajima, K. and Valley, J.W., *Chapter 4*, Upper-crustal mafic intrusions fingerprint early, geologically-controlled contamination in a continental arc. *In preparation for: Earth and Planetary Science Letters*.

Saleeby, J.B., 2007, The western extent of the Sierra Nevada batholith in the Great Valley basement and its significance in underlying mantle dynamics. *American Geophysical Meeting Fall Meeting Abstract*, T31E-02.

Saleeby, J., 2011, Geochemical mapping of the Kings-Kaweah ophiolite belt, California— Evidence for progressive mélange formation in a large offset transform-subduction initiation environment, *in* Wakabayashi, J. and Dilek, Y. eds., *Mélanges: Processes of Formation and Societal Significance*. Geological Society of America Special Paper, Geological Society of America, 480, 31–73, doi:10.1130/2011.2480(02).

Saleeby, J.B., 1982, Polygenetic ophiolite belt of the California Sierra Nevada: geochronological and tectonostratigraphic development.. *Journal of Geophysical Research*, 87, 1803–1824, doi:10.1029/JB087iB03p01803.

Saleeby, J.B., Ducea, M.N., Busby, C.J., Nadin, E.S., and Wetmore, P.H., 2008, Chronology of pluton emplacement and regional deformation in the southern Sierra Nevada batholith, California. *Special Paper of the Geological Society of America*, 438, 397–427, doi:10.1130/2008.2438(14).

Saleeby, J., Farley, K.A., Kistler, R.W., and Fleck, R.J., 2007, Thermal evolution and exhumation of deep-level batholithic exposures, southernmost Sierra Nevada, California, *in* Cloos, M., Carlson, W.D., Gilbert, M.C., Liou, J.G., and Sorensen, S.S. eds., *Convergent Margin Terranes and Associated Regions: A Tribute to W.G. Ernst*. Geological Society of America Special Paper 419, 419, 39–66, doi:10.1130/2007.2419(02).

Saleeby, J., and Sharp, W., 1980, Chronology of the structural and petrologic development of the southwest Sierra Nevada foothills, California: Summary. *Geological Society of America Bulletin*, 91, 317–320, doi:10.1130/0016-7606(1980)91<317:COTSAP>2.0.CO;2.

Saleeby, J.B., 1981, Ocean floor accretion and volcanoplutonic arc evolution of the Mesozoic Sierra Nevada, *in* Ernst, W.G. ed., *The Geotectonic Development of California*, Englewood Cliffs, New Jersey, Prentice-Hall, 132–181.

Saleeby, J.B., and Busby, C., 1993, Paleogeographic and tectonic setting of axial and western metamorphic framework rocks of the southern Sierra Nevada,

California, *in* Dunn, G. and McDougall, K. eds., Mesozoic Paleogeography of the Western United States-II, Pacific Section SEPM, 71, 197–226.

Saleeby, J.B., Kistler, R.W., Longiaru, S., Moore, J.G., and Nokleberg, W.J., 1990, Chapter 14: Middle Cretaceous silicic metavolcanic rocks in the Kings Canyon area, central Sierra Nevada, California, *in* Anderson, J.L. ed., The nature and origin of Cordilleran Magmatism, Boulder, Colorado, Geological Society of America Memoir, 74, 251–270, doi:10.1130/MEM174-p251.

Saleeby, J., and Dunne, G., 2015, Temporal and tectonic relations of early Mesozoic arc magmatism, southern Sierra Nevada, California, *in* Anderson, T.H., Didenko, A.N., Johnson, C.L., Khanchuk, A.I., and MacDonald, J.H., J. eds., Late Jurassic Margin of Laurasia—A record of faulting accommodating plate rotation. Geological Society of America Special Paper 513, 223–268, doi:10.1130/2015.2513(05).

Samperton, K.M., Schoene, B., Cottle, J.M., Brenhin Keller, C., Crowley, J.L., and Schmitz, M.D., 2015, Magma emplacement, differentiation and cooling in the middle crust: Integrated zircon geochronological-geochemical constraints from the Bergell Intrusion, Central Alps. Chemical Geology, 417, 322–340, doi:10.1016/j.chemgeo.2015.10.024.

Schmidt, M.W., and Jagoutz, O., 2017, The global systematics of primitive arc melts. Geochemistry, Geophysics, Geosystems, 18, 2817–2854, doi:10.1002/2016GC006699

Schweickert, R.A., Saleeby, J.B., Tobisch, O.T., and Wright, W.H., 1977, Paleotectonic and paleogeographic significance of the Calaveras Complex, western Sierra Nevada, California. Society of Economic Paleontologists and Mineralogists, Pacific Section, Symposium on Pacific Coast Paleogeography, 381–394.

Sendek, C., 2016, Zircon Geochemical and Isotopic Constraints on the Evolution of the Mount Givens Pluton, Central Sierra Nevada Batholith. California State University, San Jose, 153 p.

Silver, L.T., and Chappell, B.W., 1988, The Peninsular Ranges Batholith: An insight into the evolution of the Cordilleran batholiths of southwestern North America: Earth and Environmental Science Transactions of the Royal Society of Edinburgh, 79, 105–121, doi:10.1017/S0263593300014152.

Silver, L.T., Taylor, H.P., Chappel, B., Abbott, P.L., and Todd, V.R., 1979, Some petrological, geochemical and geochronological observations of the Peninsular Ranges batholith near the international border of the USA and Mexico: *in* Mesozoic Crystalline Rocks. Geological Society of America, Annual Meeting, Guidebook, 83–110.

Sisson, T.W., and Layne, G.D., 1993, H₂O in basalt and basaltic andesite glass inclusions from four subduction-related volcanoes. *Earth and Planetary Science Letters*, 117, 619–635, doi:[https://doi.org/10.1016/0012-821X\(93\)90107-K](https://doi.org/10.1016/0012-821X(93)90107-K).

Sisson, T.W., and Grove, T.L., 1993, Temperatures and H₂O contents of low-MgO high-alumina basalts. *Contributions to Mineralogy and Petrology*, 113, 167–184, doi:10.1007/BF00283226.

Sisson, T.W., Grove, T.L., and Coleman, D.S., 1996, Hornblende gabbro sill complex at Onion Valley, California, and a mixing origin for the Sierra Nevada batholith. *Contributions to Mineralogy and Petrology*, 126, 81–108.

Sisson, T.W., Ratajeski, K., Hankins, W.B., and Glazner, A.F., 2005, Voluminous granitic magmas from common basaltic sources. *Contributions to Mineralogy and Petrology*, 148, 635–661, doi: 10.1007/s00410-004-0632-9

Snow, C.A., and Scherer, H., 2006, Terranes of the Western Sierra Nevada Foothills Metamorphic Belt, California: A Critical Review. *International Geology Review*, 48, 46–62, doi:10.2747/0020-6814.48.1.46.

Snow, C.A., and Ernst, W.G., 2008, Detrital zircon constraints on sediment distribution and provenance of the Mariposa Formation, central Sierra Nevada foothills, California, *in* Wright, J.E. and Shervais, J.W. eds., *Ophiolites, Arcs, and Batholiths: A Tribute to Cliff Hopson*. Geological Society of America, doi:10.1130/2008.2438(11).

Sparks, R.S.J., and Marshall, L.A., 1986, Thermal and mechanical constraints on mixing between mafic and silicic magmas. *Journal of Volcanology and Geothermal Research*, 29, 99–124, doi:10.1016/0377-0273(86)90041-7.

Stevens, C.H., and Greene, D.C., 2000, Geology of Paleozoic rocks in eastern Sierra Nevada roof pendants, California, *in* Lageson, D.R., Peters, S.G., and Lahren, M.M. eds., *Great Basin and Sierra Nevada*, Boulder, Colorado, Geological Society of America Field Guide, 237–254, doi:10.1130/0-8137-0002-7.237.

Stevens, C.H., Stone, P., and Miller, J.S., 2005, A new reconstruction of the Paleozoic continental margin of southwestern North America: Implications for the nature and timing of continental truncation and the possible role of the Mojave-Sonora megashear. *Special Paper of the Geological Society of America*, 393, 597–618, doi:10.1130/0-8137-2393-0.597.

Stolper, E., and Walker, D., 1980, Melt density and the average composition of basalt. *Contributions to Mineralogy and Petrology*, 74, 7–12, doi:10.1007/BF00375484.

Sun, S.S., and McDonough, W.F., 1989, Chemical and isotopic systematics of oceanic basalts: Implications for mantle composition and processes. *Geological Society Special Publication*, 42, 313–345, doi:10.1144/GSL.SP.1989.042.01.19.

Taniuchi, H., Kuritani, T., and Nakagawa, M., 2020, Generation of calc-alkaline andesite magma through crustal melting induced by emplacement of mantle-derived water-rich primary magma: Evidence from Rishiri Volcano, southern Kuril Arc. *Lithos*, 354–355, 105362, doi:<https://doi.org/10.1016/j.lithos.2019.105362>.

Tatsumi, Y., and Eggins, S., 1995, *Subduction Zone Magmatism*. Blackwell, Cambridge, MA.

Taylor, H.P., and Silver, L.T., 1978, Oxygen isotope relationships in plutonic igneous rocks of the Peninsular Ranges batholith, southern and Baja California, *in* Zartman, R.E, ed., *Short Papers of the Fourth International Conference, Geochronology, Cosmochronology, Isotope Geology*, 423–426.

Tikoff, B., and de Saint Blanquat, M., 1997, Transpressional shearing and strike slip partitioning in the Late Cretaceous Sierra Nevada magmatic arc, California. *Tectonics*, 16, 442–459.

Tobisch, O.T., Saleeby, J.B., Renne, P.R., McNulty, B., and Weixing Tong, 1995, Variations in deformation fields during development of a large- volume magmatic arc, central Sierra Nevada, California. *Geological Society of America Bulletin*, 107, 148–166, doi:10.1130/0016-7606(1995)107<0148:VIDFDD>2.3.CO;2.

Turner, S.J., and Langmuir, C.H., 2015, The global chemical systematics of arc front stratovolcanoes: Evaluating the role of crustal processes. *Earth and Planetary Science Letters*, 422, 182–193, doi:10.1016/j.epsl.2015.03.056.

Turner, S.J., and Langmuir, C.H., 2022, An Evaluation of Five Models of Arc Volcanism. *Journal of Petrology*, 63, 1–25, doi:10.1093/petrology/egac010.

Walawender, M.J., Smith, T.E., 1980, Geochemical and petrologic evolution of the basic plutons of the Peninsular Ranges batholith, southern California. *Journal of Geology*, 88, 233–242.

Wang, X., Griffin, W.L., and Chen, J., 2010, Hf contents and Zr/Hf ratios in granitic zircons. *Geochemical Journal*, 44, 65–72, doi:10.2343/geochemj.1.0043.

Wang, X., Griffin, W.L., Chen, J., Huang, P., and Li, X., 2011, U and Th contents and Th/U ratios of zircon in felsic and mafic magmatic rocks: Improved zircon-melt distribution coefficients. *Acta Geologica Sinica (English Edition)*, 85, 164–174, doi:10.1111/j.1755-6724.2011.00387.x.

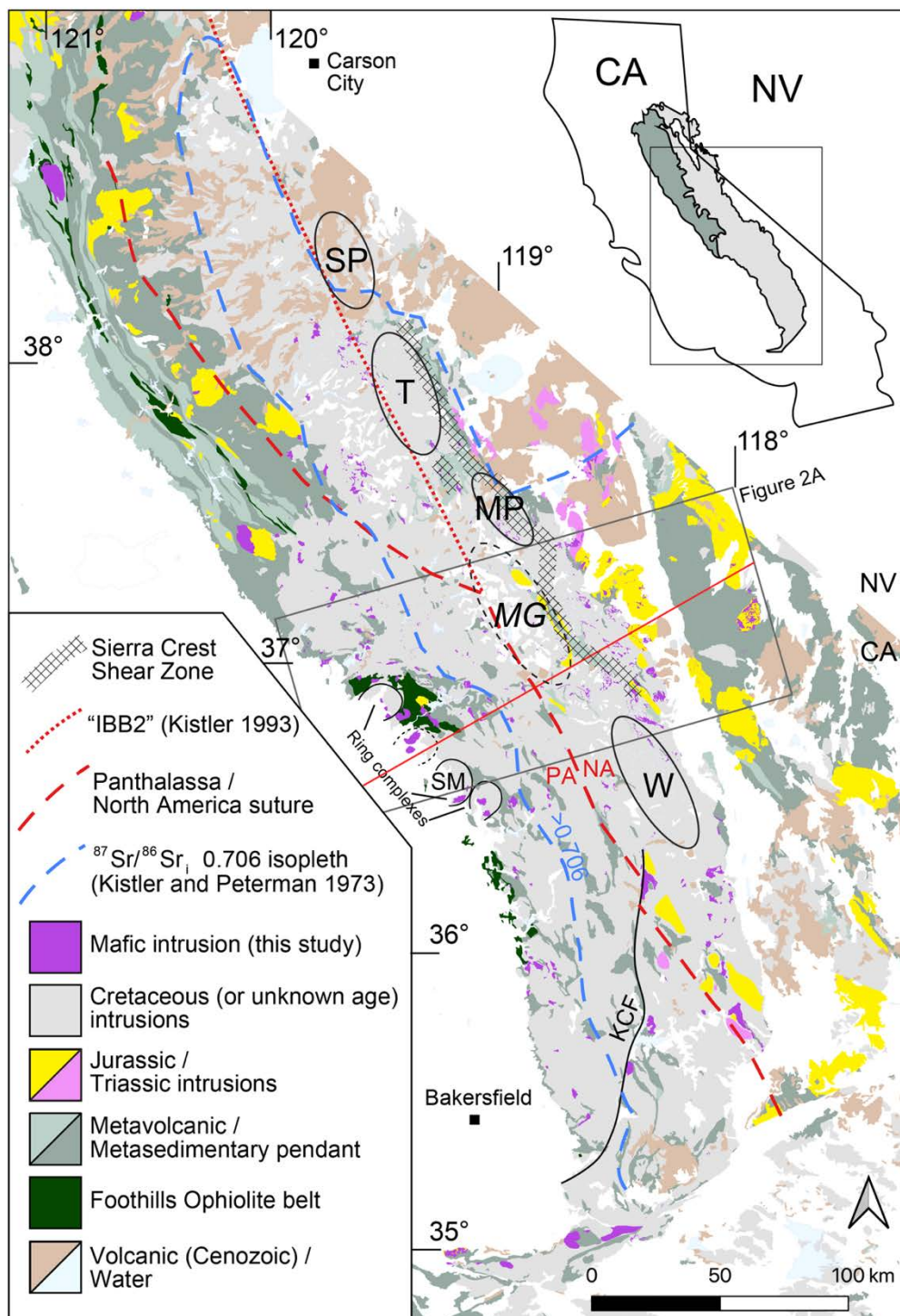
Warr, L.N., 2021, IMA-CNMNC approved mineral symbols. *Mineralogical Magazine*, 85, 291–320, doi:10.1180/mgm.2021.43

Watanabe, T., Koyaguchi, T., and Seno, T., 1999, Tectonic stress controls on ascent and emplacement of magmas. *Journal of Volcanology and Geothermal Research*, 91, 65–78, doi:10.1016/S0377-0273(99)00054-2.

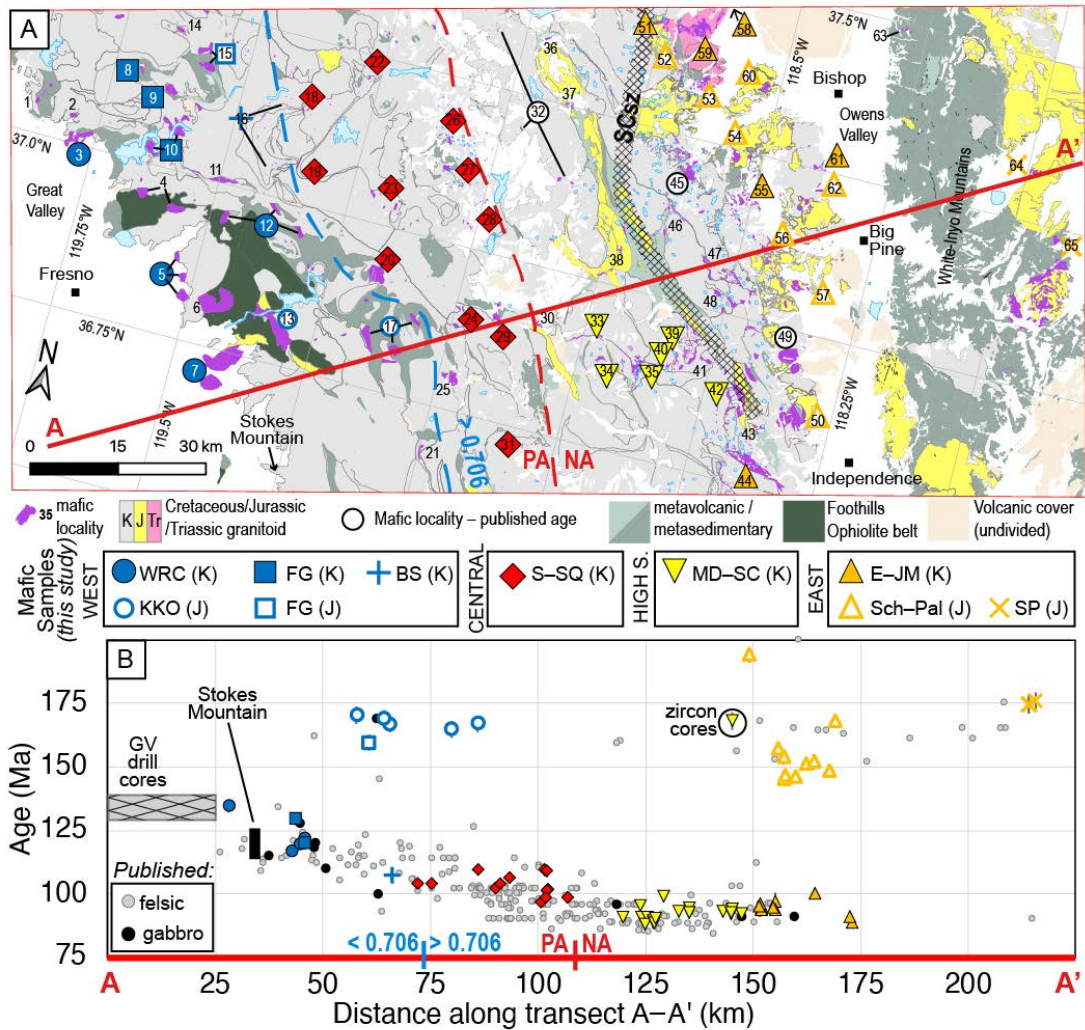
Wenner, J.M., and Coleman, D.S., 2004, Magma mixing and cretaceous crustal growth: Geology and geochemistry of granites in the central Sierra Nevada batholith, California. *International Geology Review*, 46, 880–903, doi:10.2747/0020-6814.46.10.880.

Wilner, O.D., Dalleska, N.F., Asimow, P.D., and Bucholz, C.E., *in prep*, Laser ablation of silicate rock pressed powders as an efficient trace-element analysis method.

FIGURES

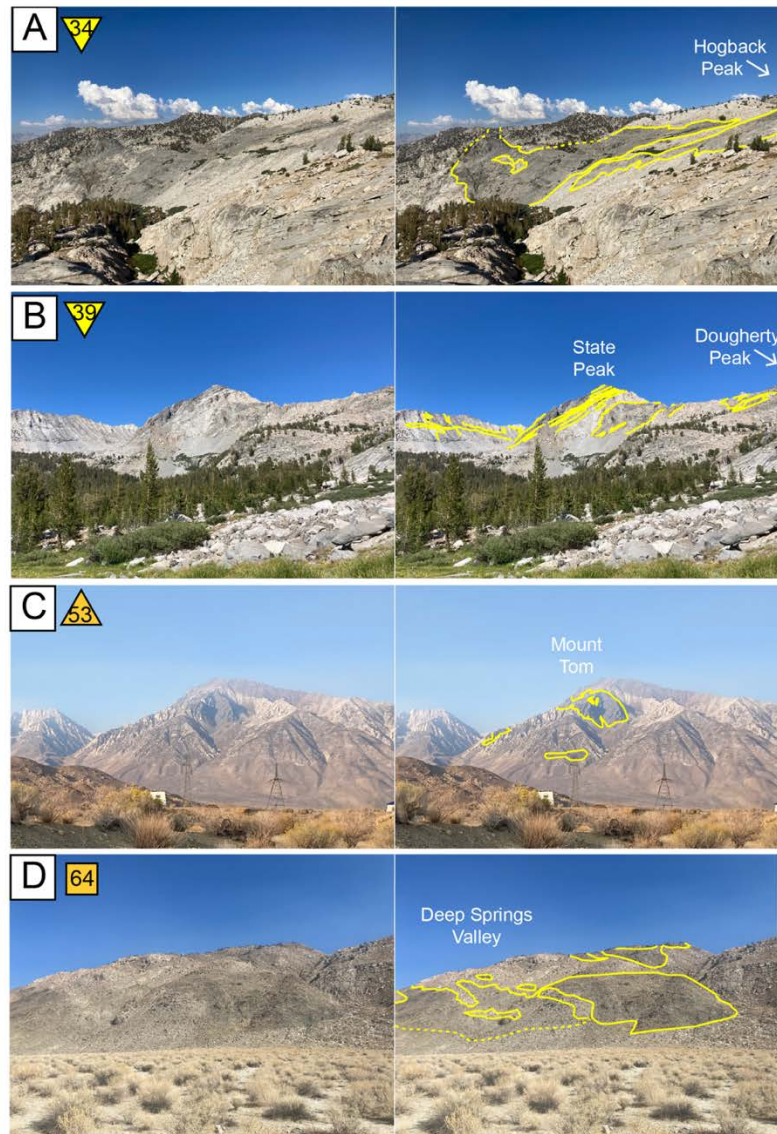


Ch. 3 Figure 1. Overview bedrock map of the Sierra Nevada batholith (modified from Jennings et al., 2010). Small ($<35 \text{ km}^2$) mostly upper-crustal mafic intrusions ubiquitously exposed throughout the batholith are in purple; SM—Stokes Mountain is the most primitive one in the map area. Cretaceous felsic intrusions of the batholith are light gray, and Jurassic and Triassic felsic intrusions are yellow and pink, respectively (based on ages in Irwin and Wooden, 2004; Ferré et al., 2012; Chapman et al., 2012; Saleeby and Dunne, 2015; Hildreth et al., 2024). The metamorphic framework rocks exposed as pendants and septa between intrusions are light green (metavolcanic), olive green (metasedimentary), and dark green (Foothills Ophiolite belt). Younger volcanic sequences are light brown. Dashed lines indicate boundaries interpreted from isotopic analyses of felsic intrusions and metamorphic framework affinity ($^{87}\text{Sr}/^{86}\text{Sr}_{\text{SMOW}}=0.706$) isopleth in blue; the suture between Panthalassan (PA) accreted oceanic and North American (NA) continental lithosphere in red; and the dotted red line the “inter batholith break” IBB2 (Kistler and Peterman, 1973; Saleeby et al., 1987; Kistler, 1993; Lackey et al., 2006; Chapman et al., 2012). The young (83–89 Ma), large intrusive suites along the highest elevations of the range are: SP—Sonora Pass; T—Tuolumne; MP—Mono Pass; W—Whitney, and MG is the Mount Givens granodiorite (98–91 Ma). The Sierra Crest shear zone is a chain of Cretaceous dextral transpressional shear zones to their east (Greene and Schweickert, 1995; Tikoff and de Saint Blanquat, 1997). KCF is the Kern Canyon Fault.



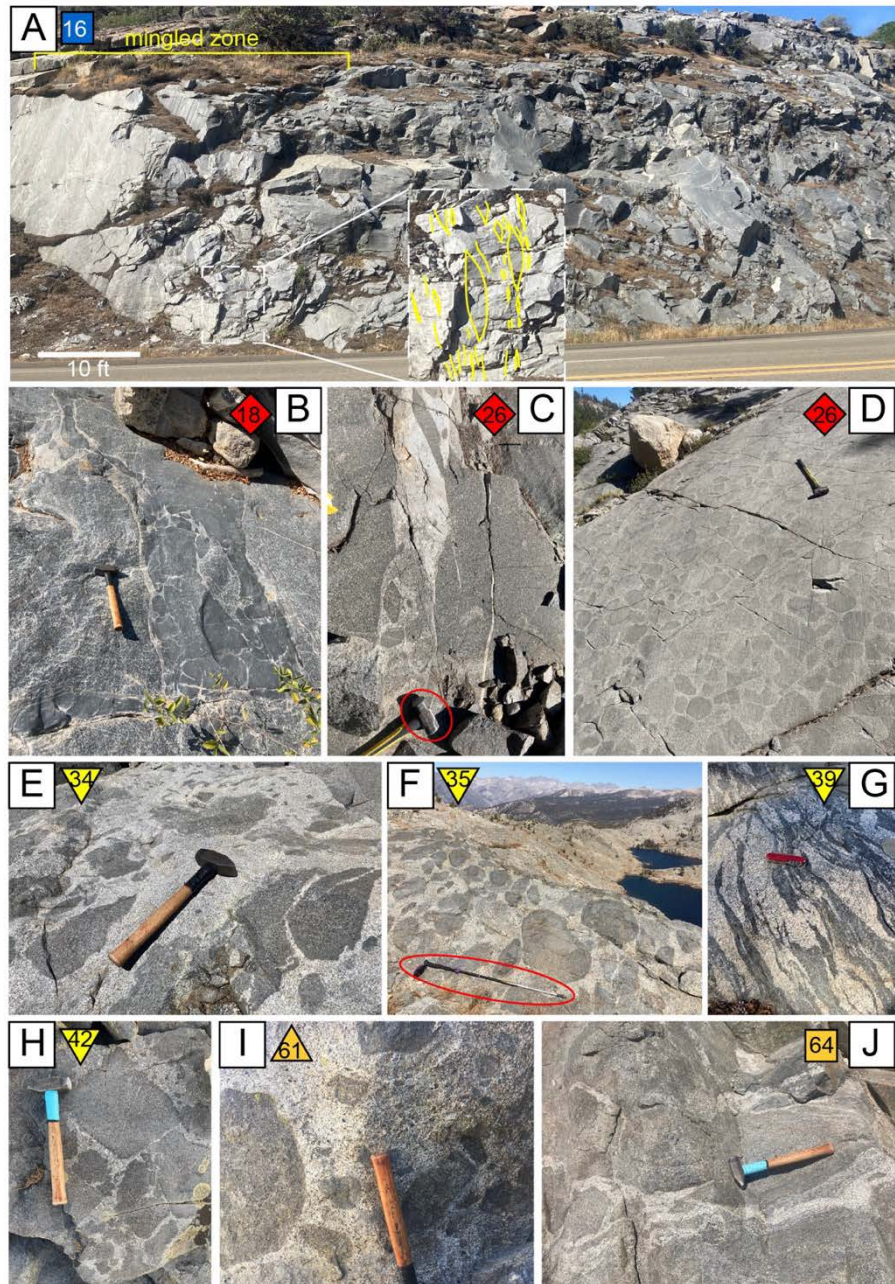
Ch. 3 Figure 2. Study area map with sample locations and ages.

A) Transect map with mafic intrusions numbered as in Table 1. Intrusions with samples included in this study have colored symbols as described by the legend in the figure, where filled symbols are Cretaceous (K) and open symbols are Jurassic (J). Categories are named by intrusive suite and metamorphic pendant affinity. WRC—western ring complexes; FG—Fine Gold; BS—Big Sandy; KK—Kings-Kaweah; S-SQ—Shaver-Sequoia; MD-SC—Monarch Divide/Sierra Crest; E-JM—Eastern/John Muir; Sch-Pal—Scheelite/Palisades; SP—Soldier Pass. White circle symbols for mafic intrusions have published U-Pb zircon ages. **B)** U-Pb zircon ages of mafic samples versus distance along the A–A' transect. Also plotted are previously published ages of mafic intrusions from within and just north and south of the map area (Coleman et al., 1995; Clemens-Knott and Saleeby, 1999; Lackey et al., 2012; Gevedon, 2013; Frazer et al., 2014; Sendek, 2016; Lackey, personal communication), from drill cores in the Great Valley (GV) west of and intersecting with the transect (Saleeby, 2007), and felsic plutons from within and just north and south of the map area (from Lackey et al., 2005, 2006, 2008, 2012).



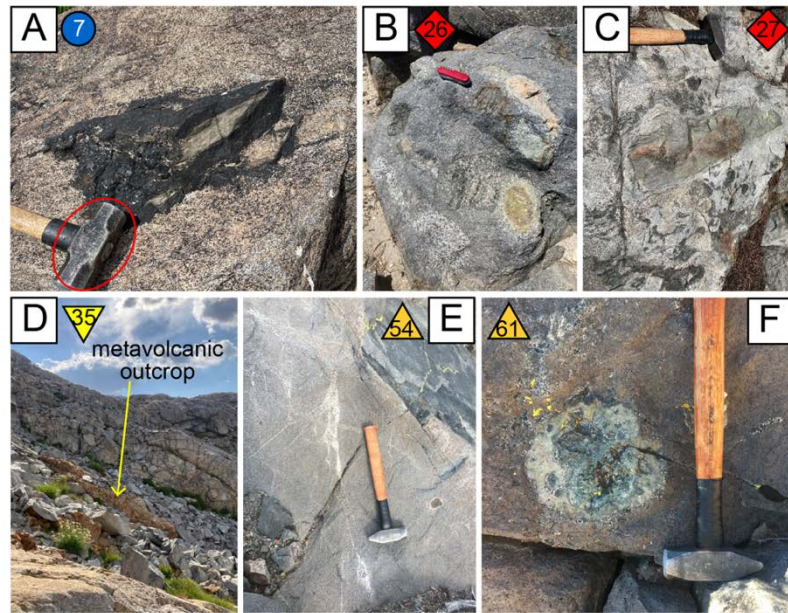
Ch. 3 Figure 3. Overview field photos of mafic intrusions.

Numbers and symbols correspond to mafic intrusions in Fig. 2A and Table 1. Right panels are annotated with yellow outlines around mafic intrusions. **A)** The Hogback mafic intrusion in the high Sierra belt, with tapered, mingled ends. **B)** The Dougherty Peak mafic intrusion in the high Sierra belt with dike-like sheets and mingled margins. **C)** The Mount Tom mafic intrusion in the eastern belt crops out in several patches within the host felsic intrusion (summit is a Cambrian metasedimentary unit). **D)** The Deep Springs mafic intrusion in the White-Inyo mountains (eastern belt) crops out in several patches, with mingled contact zones.



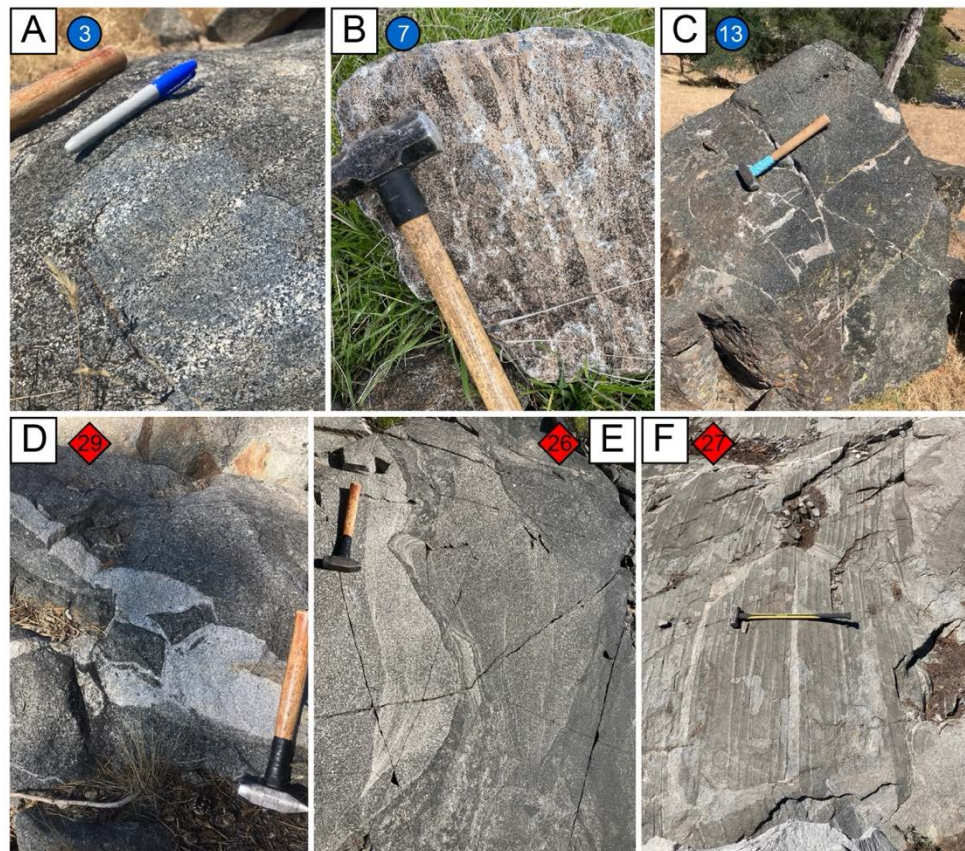
Ch. 3 Figure 4. Field photos of contact relationships of mafic intrusions from each belt. Numbers and symbols correspond to mafic intrusions in Fig. 2A and Table 1. **A)** The Big Sandy intrusion is an ~0.75 km long lens—essentially a very large enclave—and its mingled contact zone with the host leucogranite of Big Sandy Bluffs (inset) is comprised of a swarm of steeply dipping enclaves. **B)** A composite (granitic

and quenched mafic) dike intrudes the mafic intrusion at Jose Creek. **C**) A felsic dike disaggregates and brecciates the gabbroic intrusion. **D**) The margin of the Rainbow Mine mafic intrusion disaggregates into a cluster of round (oval to nearly circular) blocks within the granite of Dinkey Dome. **E**) The tapered margins of the Hogback intrusion (Fig. 3A) are mingled with the host granodiorite of North Dome. **F**) The margins of the Volcanic Lakes mafic intrusion are characterized by swarms of steeply dipping quenched enclaves in the host Pyramid pluton. **G**) Ductile fabrics are developed in the intermingled Dougherty Peak mafic intrusion and the granite of Dougherty Peak (Fig. 3B). **H**) Dark, crenulated margins on blocks of the Wood Creek mafic intrusion that are hosted by the Cotter pluton. **I**) A mingled zone at the margin of the Keough mafic intrusion reactivates the host leucogranite of Rawson Creek, sampled nearby (~7 to 9 million years older; Lewis et al., 2023). **J**) Mingling along the margins of the Deep Springs mafic intrusion with the Beer Creek granite (Fig. 3D).

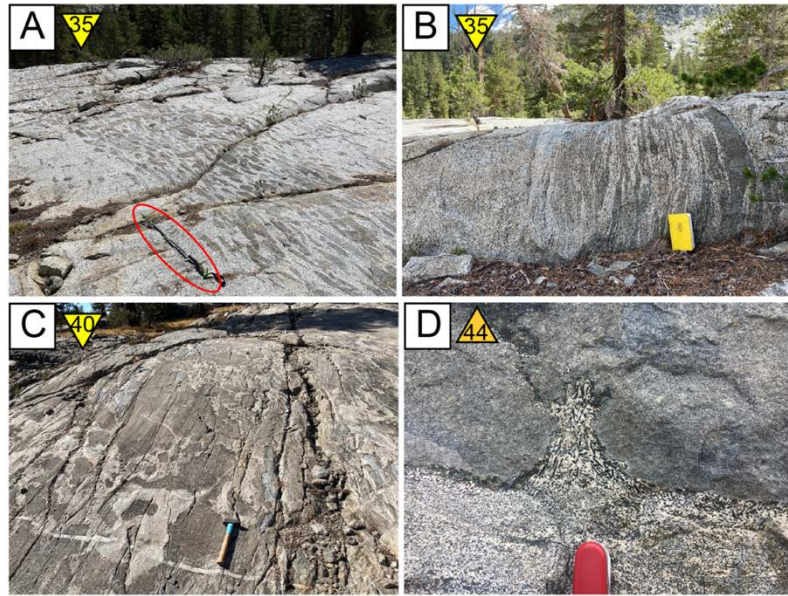


Ch. 3 Figure 5. Field photos of metamorphic xenoliths.

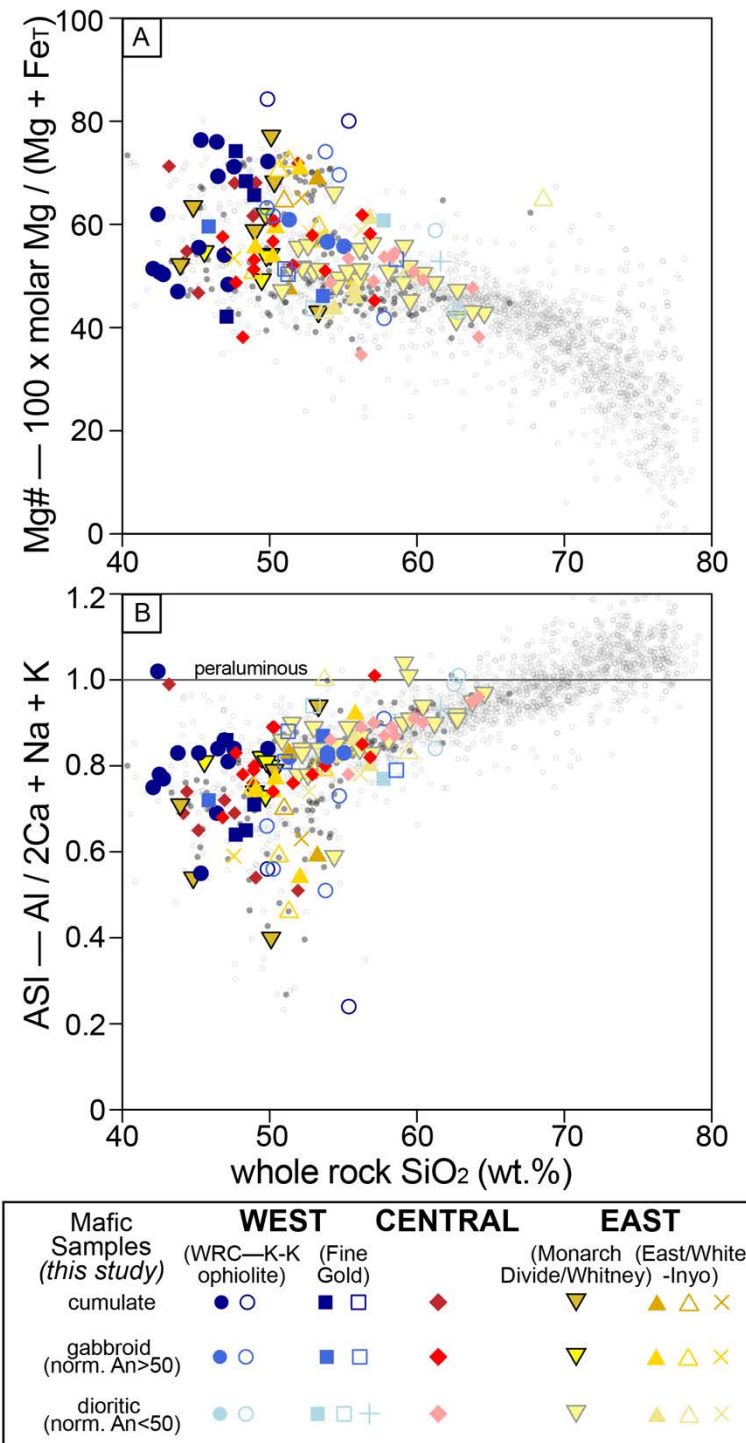
Numbers and symbols correspond to mafic intrusions in Fig. 2A and Table 1. **A)** Ultramafic (ophiolitic) xenolith surrounded by 1-2 cm coarse amphibole crystals (overall ~45 cm including this reaction halo) hosted in amphibole gabbro of the Campbell Mountain mafic intrusion. **B)** A cluster of xenoliths in a block of the Rainbow Mine mafic intrusion (which intrudes the Dinkey Creek metamorphic pendant) with reaction halos that bleach the mafic rock. **C)** A hornfels calc-silicate xenolith in a light gray diorite outcrop of the Mud Lakes mafic body (also intrudes the Dinkey Creek metamorphic pendant). **D)** An isolated meta-rhyolite outcrop (overall ~100–200 m²) with mafic enclaves of the Volcanic Lakes mafic intrusion intruding it, with no mapped metamorphic pendant within or directly in contact with the mafic intrusion. **E)** A 3.5 cm calc-silicate xenolith (to the right of the hammer) with a white colored reaction halo, and nearby wispy light-colored lacy seams and patches of more felsic mineralogy within the Bishop Creek mafic intrusion. **F)** A bright green altered xenolith in the Keough mafic intrusion (weathered surfaces on photo), with micro-pegmatite-like stringers of coarser amphibole+plagioclase emanating from it within the host mafic rock, that must have been brought up from depth as no mapped metamorphic pendant is near the mafic intrusion.



Ch. 3 Figure 6. Field photos of cumulate textures in western and central belt mafic intrusions. Numbers and symbols correspond to mafic intrusions in Fig. 2A and Table 1. **A)** Modal and grain size layering of plagioclase and amphibole in the Four Corners mafic intrusion. **B)** Modal and grain size anorthositic and gabbroic layering in a loose block of the Campbell Mountain mafic intrusion. **C)** Amphibole cumulate brecciated by later felsic intrusions at the Mill Creek mafic intrusion. **D)** Brecciated gabbroic blocks were peeled away into a later felsic dike that intruded the Garlic Meadow mafic body. **E)** Schlieren, ladder structures and comb layering in a modally heterogeneous polished outcrop of the Rainbow Mine mafic intrusion. **F)** Resistant ridges formed along distinct (modal?) layers in the Mud Lakes mafic intrusion, which break into blocks that look very similar to sedimentary rip-up clasts into another phase of the intrusion at the right side of the photo (sledgehammer handle points “up,” though layering dips near vertically).

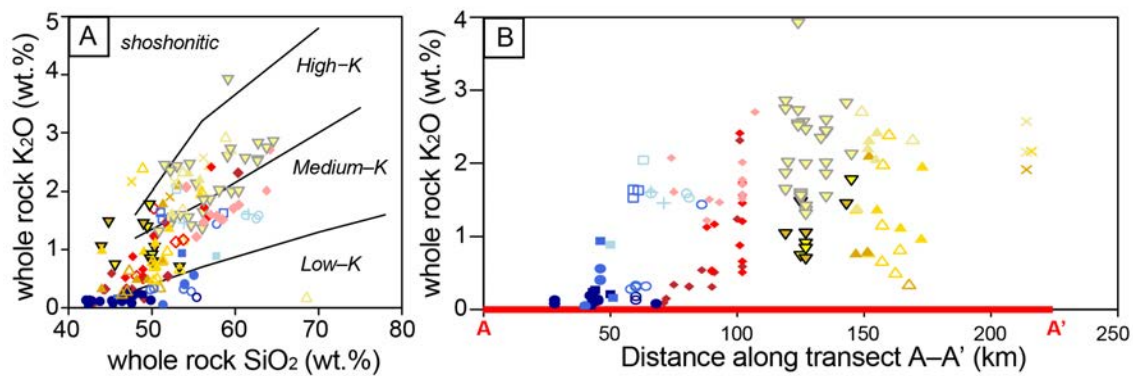


Ch. 3 Figure 7. Field photos of interactions with felsic intrusions in the high Sierra and eastern belts. Numbers and symbols correspond to mafic intrusions in Fig. 2A and Table 1. **A)** A swarm of steeply-dipping mafic enclaves in a dike configuration emanating from the Volcanic Lakes mafic intrusion into the Pyramid pluton. **B)** A side view of another dike-like mafic enclave “swarm” located near the swarm shown in (A) showing mingling between the two phases. **C)** The entirety of the Glacier Lakes mafic intrusion is mingled with the granodiorite of White Divide, well-represented by this polished outcrop. **D)** An inter-sill septum of more evolved, coarser material with a “flame” structure into a fine-grained mafic sill at Onion Valley (see Sisson et al., 1996).



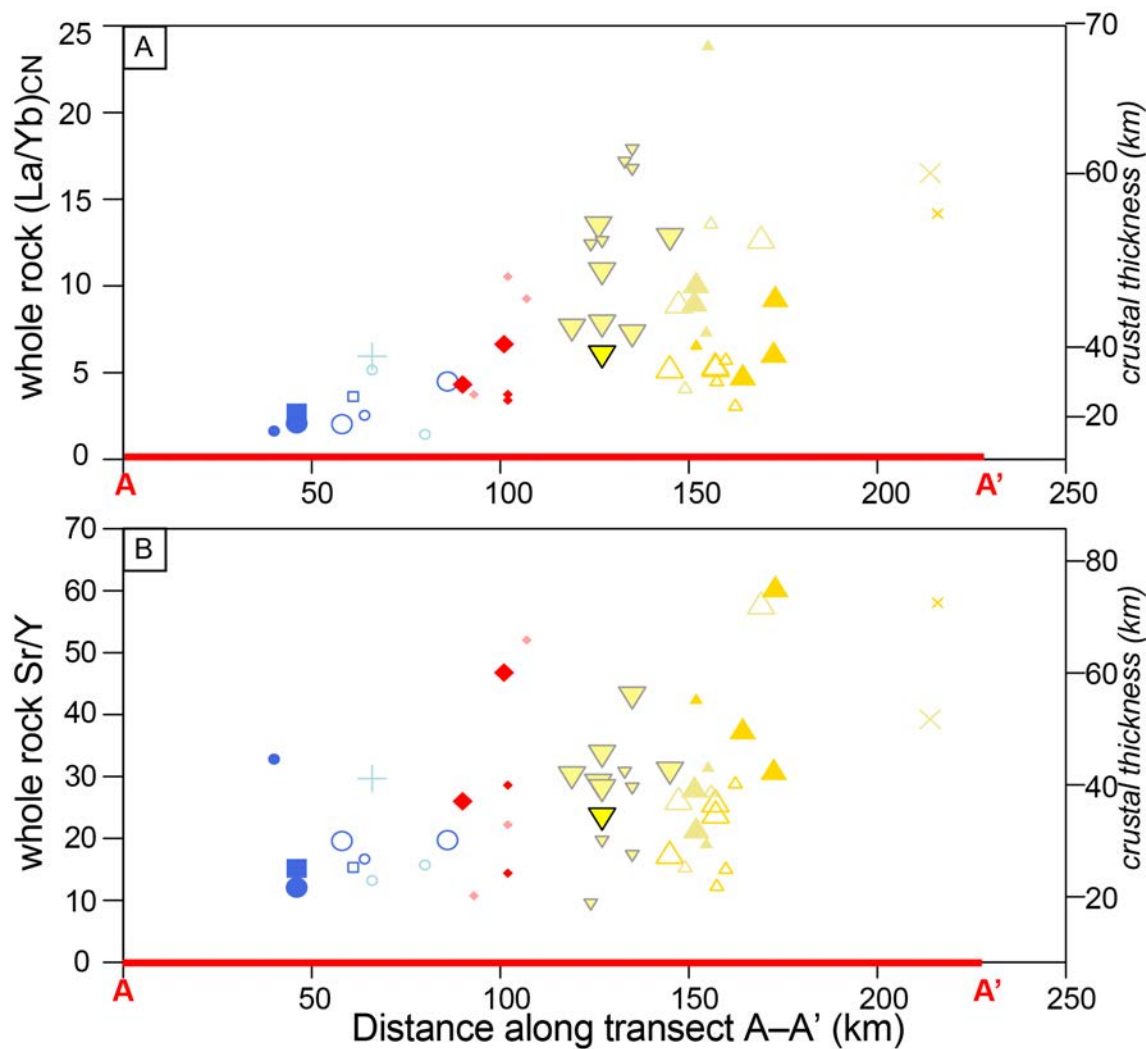
Ch. 3 Figure 8. Whole-rock geochemistry and legend of symbols.

A) Mg# versus SiO₂, with samples from the eastern belt analyzed by Lewis et al. (2024) plotted as small dark gray circles, and a compilation of analyses of the Sierra Nevada batholith plotted in light gray open circles. **B)** ASI versus SiO₂, with symbols the same as in (A). See text for discussion of rock categories.

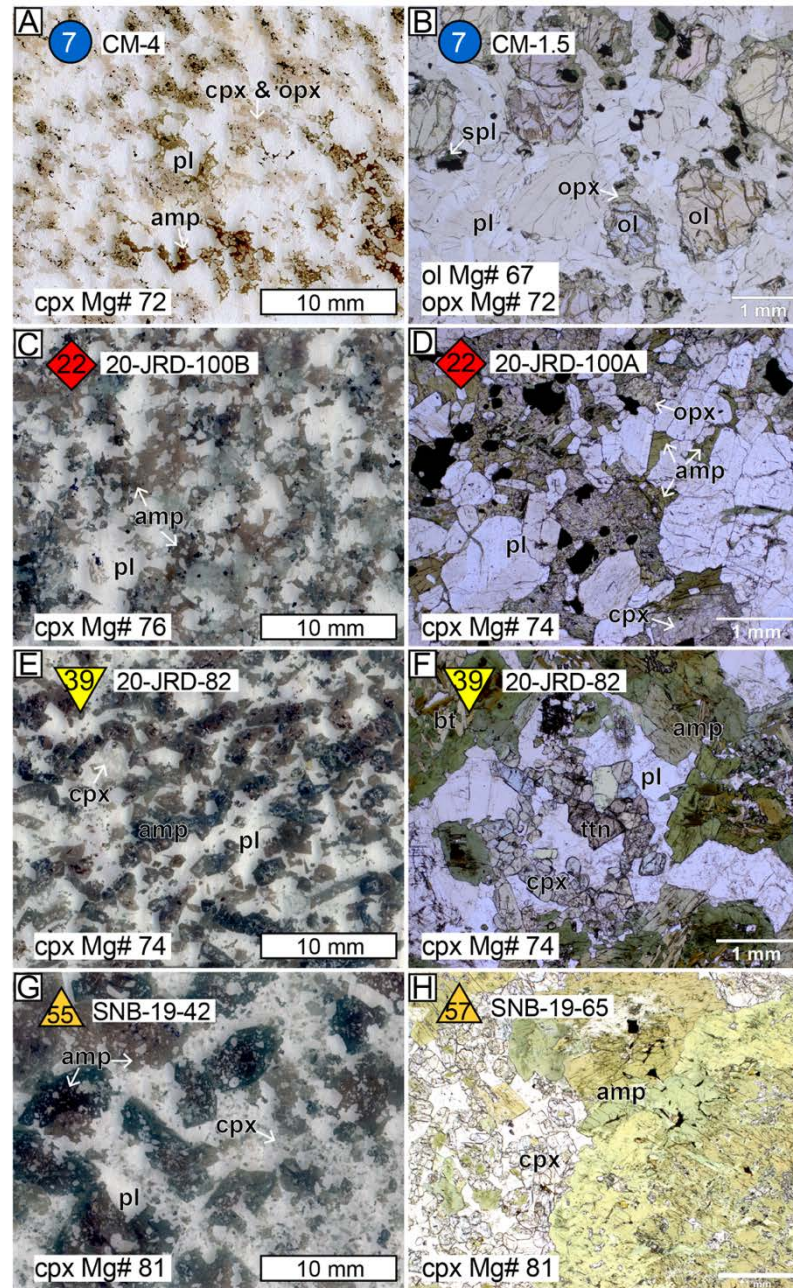


Ch. 3 Figure 9. K₂O in all whole-rock samples across the transect.

A) Whole rock K₂O (wt.%) versus SiO₂ (wt.%). **B)** Whole rock K₂O (wt.%) versus distance along the transect. Symbols as in Figure 8.

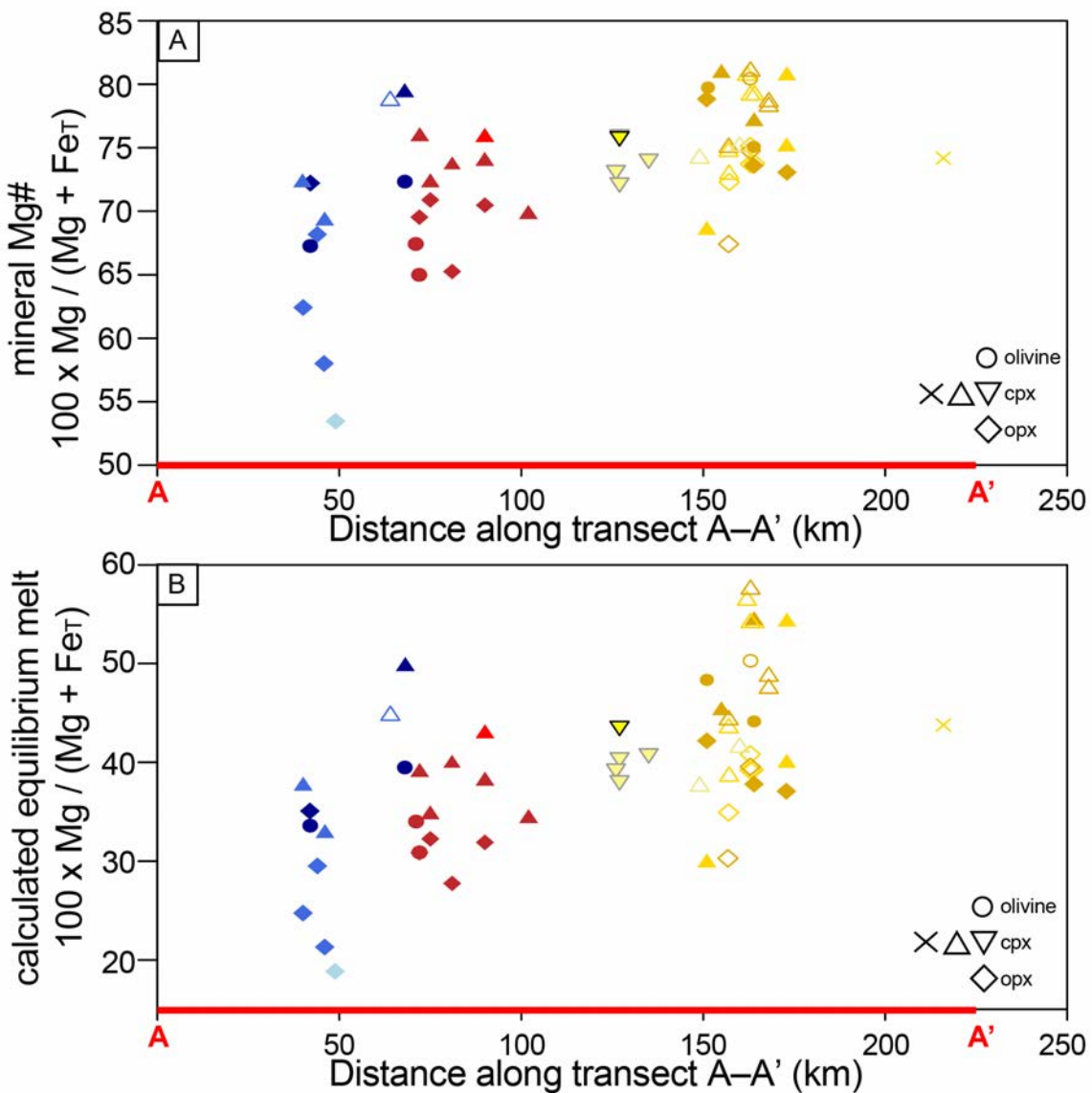


Ch. 3 Figure 10. Whole rock A) $(\text{La}/\text{Sm})_{\text{CN}}$ and B) Sr/Y vs. distance along transect, with calculated crustal thickness according to the equations of Profeta et al., 2015, Symbols as in Figure 8. Only non-cumulate samples are plotted, and large symbols are filtered for Rb/Sr between 0.05 and 0.2.

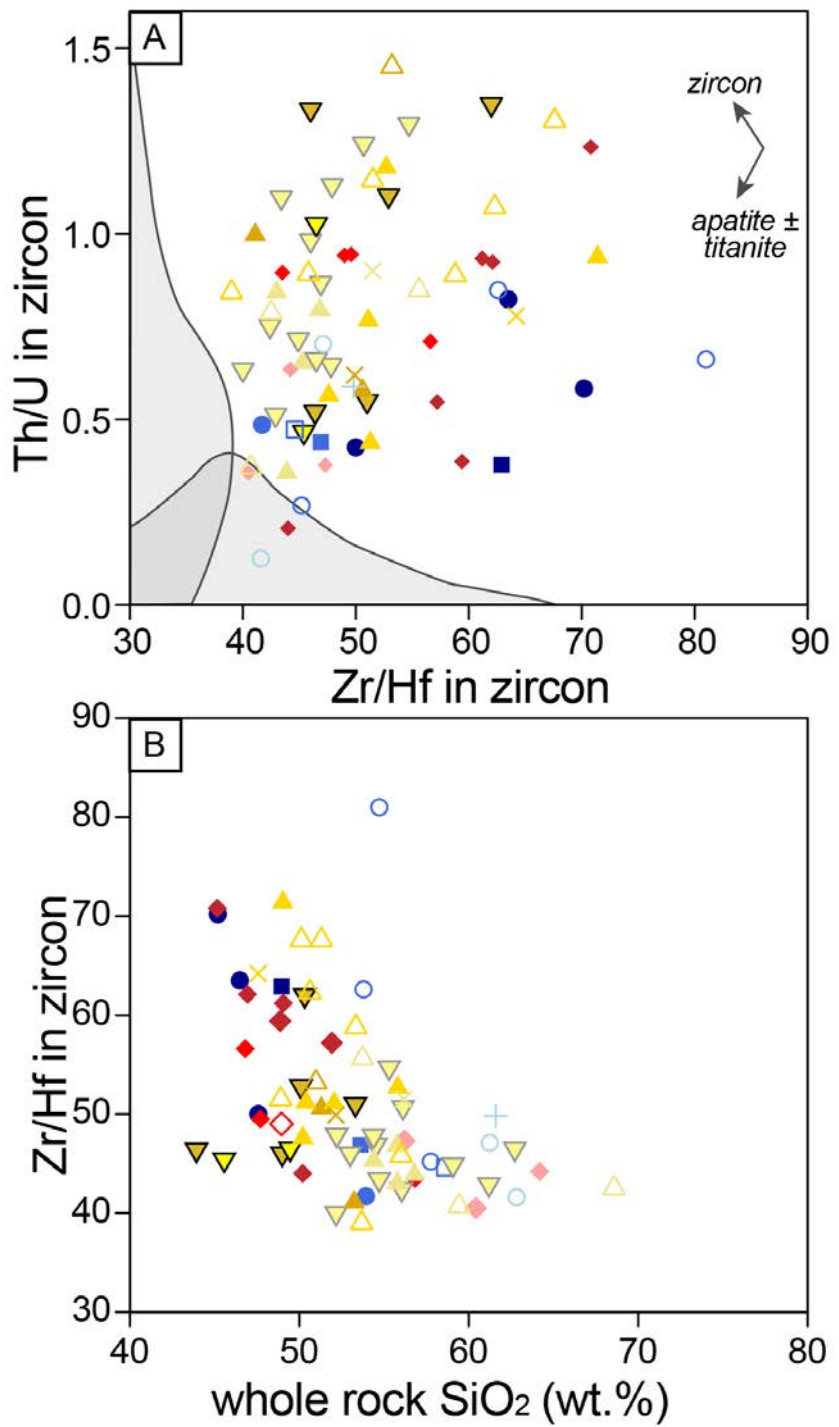


Ch. 3 Figure 11. Representative petrography.

A, C, E, G) scans of thin sections; **B, D, F, H**) photomicrographs (plane polarized light). Mineral abbreviations as in Warr (2021). Sample numbers and Mg# of anhydrous mafic silicates are included as labels.

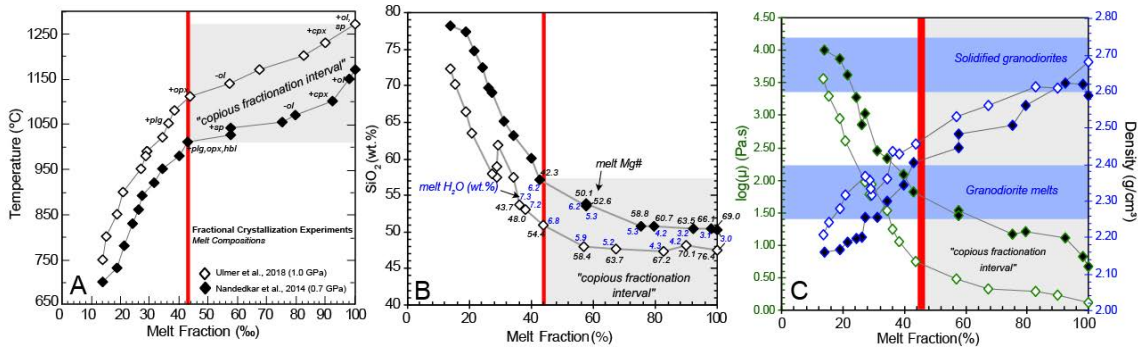


Ch. 3 Figure 12. A) Mineral Mg#, and **B)** Calculated equilibrium melt Mg#. (described in main text) versus distance along the transect. Symbol colors as in Figure 8.



Ch. 3 Figure 13. A) Th/U versus Zr/Hf in zircon.

Gray estimated probability curves are from compilations of Zr/Hf in granitic zircons (Wang et al., 2010) and Th/U in granitic zircons (Wang et al., 2011), scaled so that their peaks roughly intersect. B) Zr/Hf in zircon versus whole rock SiO₂ showing that lower SiO₂ samples have higher Zr/Hf in zircon. Symbols as in Figure 8.



Ch. 3 Figure 14. Plots of “copious fractionation intervals”.

A) Melt fraction (F) versus temperature for two fractional crystallization experimental studies on hydrous high-Mg basalts in the lower crust (white diamonds: 0.7 GPa, Nandedkar et al., 2014; black diamonds: 1.0 GPa, Ulmer et al., 2018). **B)** F versus SiO_2 (wt.%) for the same studies, with each melt fraction step labeled with the $\text{Mg}^{\#}$ of the melt in black and the melt H_2O concentration in blue. **C)** White and black symbols from the same studies showing melt fraction versus viscosity, outlined in green, and density, outlined in blue. Also shown are the density ranges of solid granodiorite and granodiorite melts. After the “copious fractionation interval”, mafic melts reach densities similar to granodiorite melt, and are thus neutrally buoyant.

TABLES

Ch. 3 Table 1. U-Pb zircon ages for mafic intrusions across the transect of the central Sierra Nevada batholith, California ($37 \pm 0.5^\circ\text{N}$). Ages analyzed in this study are MSWD ages, with reported analytical uncertainties (" \pm (Ma)") and propagated uncertainties that reflect $\sim 2\%$ laboratory external reproducibility (" \pm (Ma) ext."). Ages from other studies of samples collected from mafic intrusions within the study area are also included here. (*Continued on following pages*).

*Methods are: 1) Laser-ablation multicollector inductively-coupled mass spectrometry (LA-MC-ICPMS); 2) LA-ICPMS (not multicollector); 3) Isotope dilution thermal ionization mass spectrometry (ID-TIMS); 4) Bulk zircon ID-TIMS; 5) Bulk zircon solution ICP-MS

**References: 1—Saleeby and Sharp (1980); 2—Frost and Mattinson (1993); 3—Coleman et al. (1995); 4—Clemens-Knott and Saleeby (1999); 5—Saleeby (2007); 6—Gevedon (2013); 7—Lackey et al. (2012); 8—Saleeby and Dunne (2015); 9—Sendek (2016); 10—Gevedon et al. (2021); 11—Lewis et al. (2021); 12—Lewis et al. (2024)

Mafic body number	Locality	Category	Sample number	distance along transect (km)	U-Pb zircon age (Ma)	\pm (Ma) ext.	MSWD n	Latitude (°N)	Longitude (°W)	Rock description	Method*	Ref.**
—	Great Valley drill cores	—	(multiple samples)	-25 to 25	130 to 140					amphibole-rich cumulates	2	5
—	Stokes Mountain	WRC	(multiple samples)	~45	114 to 126					gabbros	2	6
—		WBK134		~45	117					biotite-amphibole diorite	4	4
3	Four Corners	WRC	21-JRD-134A	28	134.7	0.8	2.8	2	14	36.4561 -119.0764	1	this study
5	Academy	WRC	21-JRD-130A	43	117.0	0.8	2.5	0.4	10	36.8805 -119.5457	1	this study
			21-JRD-131A	46	122.0	0.7	2.5	0.4	21	36.8955 -119.5227	1	this study
			8S02	48	118		1.6			gabbro	2	7
			KB4	~48	120					quartz norite	5	1
6	Coyote Ridge	WRC	KB20	~44	128		4.0			gabbro	5	1
7	Campbell Mountain	WRC	21-JRD-140B	45	119.8	0.7	2.5	4	17	36.7014 -119.3959	1	this study
8	O'Neals	FG	20-JRD-33	46	120.0	0.6	2.5	1	22	37.1291 -119.6924	1	this study
9	Hildreth	FG	—	~50	—					—		
10	Millerton Lake	FG	20-JRD-58B	43	129.8	0.7	2.7	1	17	37.0289 -119.6451	1	this study
12	Humphrey's Station	KKO	—	~68	—					—		
13	Mill Creek	KKO	21-JRD-115	66	166.9	0.9	3.5	7	18	36.7541 -119.2057	1	this study
		21-JRD-116	64	169	1	3.5	2	12	36.7513 -119.2183	1	this study	
		21-JRD-117	58	170.4	0.9	3.5	1	18	36.8021 -119.3240	1	this study	
		W2	169.5			1.5				quartz monzodiorite	1	this study
15	Fine Gold	FG	20-JRD-35A	61	163.8	0.8	3.4	0.9	15	36.7511 -119.2174	4	8
16	Big Sandy	BS	21-JRD-137	66	107.3	0.5	2.2	1	18	37.0390 -119.4075	1	this study
17	Verplank	KKO	21-JRD-126	86	167	1	3.5	2	13	36.8673 -119.0552	1	this study
18	Jose Creek	S-SQ	20-JRD-47	75	103.8	0.4	2.1	0.9	20	37.1384 -119.3780	1	this study
19	Pineridge	S-SQ	19-JRD-32	72	103.9	0.7	2.2	3	8	37.0628 -119.3598	1	this study
20	Patterson	S-SQ	—	~74	—					—		
22	Mushroom Rock	S-SQ	20-JRD-100B	90	102.2	0.5	2.1	0.8	21	37.2142 -119.2727	1	this study
23	Dinkey Mountain	S-SQ	19-JRD-26	86	109.6	0.6	2.3	0.7	18	37.0289 -119.1806	1	this study
24	Kings River	S-SQ	19-JRD-07	93	106.4	0.6	2.2	6	18	36.8642 -118.9832	1	this study
		19-JRD-09	91	104.1	0.5	2.1	1	17	36.8581 -119.0005	1	this study	
25	Grant Grove	S-SQ	—	89	—					quartz monzogabbro	1	this study
26	Rainbow Mine	S-SQ	20-JRD-39	102	101.8	0.6	2.1	0.9	13	37.1511 -119.0931	1	this study
27	Mud Lakes	S-SQ	20-JRD-50B	101	96.9	0.4	2.0	3	20	37.1092 -119.0797	1	this study

Table 1. Continued:

Table 1. Continued:

Mafic body number	Locality	Category	Sample number	distance along transect (km)	U-Pb zircon age (Ma)	\pm (Ma) ext.	MSWD n	Latitude (°N)	Longitude (°W)	Rock description	Method*	Ref.**		
51	Hidden Lakes	E-JM	SNB-14-30	152	94.2	0.5	0.8	17	37.4176	-118.7447	norite	1	this study	
			SNB-14-34	152	94.5	0.4	0.6	19	37.4176	-118.7447	monzodiorite	1	this study	
			SNB-14-34	152	96.5	0.8	0.8	19	37.4176	-118.7447	monzodiorite	2	11	
			SNB-16-02	152	93.8	0.4	1.9	0.8	19	37.4166	-118.7437	gabbro	1	this study
			SNB-16-06	151	95.9	0.5	2.0	0.4	15	37.4107	-118.7446	monzodiorite	1	this study
			SNB-16-06	151	95.1	1.0	1.0	37.4107	-118.7446	monzodiorite	2	11		
			SNB-16-21	151	95.3	0.4	1.9	1	19	37.4126	-118.7484	leucogabbro	1	this study
		(multiple samples)		90.5 to 96.5	0.7 to 1						mafic complex	2	11	
		52	Pine Creek	Sch-Pal	SNB-19-60	149	194.0	2.6	37.3535	-118.7295	quartz monzodiorite	2	12	
		53	Mount Tom	Sch-Pal	SNB-19-16	157	145.1	1.7	37.3470	-118.6369	quartz diorite	5	2	
54	Bishop Creek	Sch-Pal	SNB-18-23	157	146.5	1.4	37.2417	-118.5561	monzogabbro	2	12			
55	Green Lake	E-JM	SNB-18-43	157	154.0	0.8	3.2	5	13	37.2322	-118.5524	monzogabbro	1	this study
56	Mount Alice	Sch-Pal	SNB-19-44A	155	97.1	3.3	3.3	37.1711	-118.5292	quartz monzodiorite	2	12		
57	McMurry Meadows	Sch-Pal	SNB-18-CB4	160	93.5	0.5	1.9	2	16	37.1719	-118.5307	monzogabbro	1	this study
58	Casa Diablo	E-JM	SNB-19-8	164	100.2	1.1	37.1252	-118.4449	monzogabbro*	2	12			
59	Tamarack Lakes	E-JM	SNB-18-13	155	94.6	1.1	37.0648	-118.3735	gabbro	2	12			
60	Tungsten Hills	Sch-Pal	SNB-19-34	168	148.3	1.8	37.0648	-118.3576	0	1	this study			
61	Keough	E-JM	SNB-18-53	173	88.8	1.3	37.5501	-118.7070	monzogabbro	2	12			
62	Shannon Canyon	Sch-Pal	SNB-18-55A	173	90.8	0.5	1.9	1	17	37.2563	-118.4015	gabbro	1	this study
64	Deep Springs	SP	20-JRD-108	214	174.7	0.9	3.6	2	21	37.2034	-118.3996	leucomonzodiorite	2	12
65	Marble Canyon	SP	20-JRD-109	214	174.7	0.9	3.6	0.9	20	37.3245	-117.9971	monzodiorite	1	this study
			20-JRD-106	216	176	1	3.7	1	17	37.2402	-117.9177	monzogabbro	1	this study

Ch. 3 Table 2. Representative anhydrous mafic mineral compositions (olivine, clinopyroxene and orthopyroxene), with calculated equilibrium melt compositions (see text for details). Thick black boxes are around the maximum sample-average calculated equilibrium melt Mg# for each mafic intrusion. (*Continued on following pages*).

Olivine: $K_D Fe/Mg$ olivine-melt = 0.28; melt : $Fe^{3+}/\Sigma FeT$ = 0.15								
Mafic Body	Campbell Mountain	Humphrey's Station	Pineridge	Pineridge	Onion Valley	Hidden Lakes	McMurry Meadows	Casa Diablo
Sample number	CM-1.5	21-JRD-119	19-JRD-32	20-JRD-44	max. Fo	SNB-14-62	SNB-19-66	SNB-19-06
Transect distance (km)	42	68	72	71	145	151	163	164
Equilibrium melt (calculated)	33.6	39.5	30.9	34.0	~51.5	48.3	50.2	51.7
whole-rock SiO ₂ (wt.%)	42.4	45.3	49.1	43.2		51.3	—	39.1
whole-rock Mg#	62.0	76.4	68.1	71.3		71.7	—	73.4
n (grains)	5	5	2	6			2	9
n (analyses)	25	25	10	30		14	4	33
Max Mg# average group	all grains	all grains	2 highest Mg# grains	all grains	Sisson et al., 1996	Lewis et al., 2021	Lewis et al., 2024	Lewis et al., 2024; MnO<0.4 wt.%
SiO ₂ (wt.%)	36.89	37.69	37.10	36.75		38.81	39.05	37.98
TiO ₂ (wt.%)	0.00	0.00	0.01	0.01		0.02	0.02	0.01
Al ₂ O ₃ (wt.%)	0.00	0.00	0.00	0.00		0.00	0.01	0.02
FeO (wt.%)	29.20	25.30	30.62	29.09		18.60	18.45	22.94
MgO (wt.%)	33.66	37.10	32.21	33.78		40.89	42.28	38.66
CaO (wt.%)	0.01	0.02	0.02	0.01		0.01	0.02	0.09
Na ₂ O (wt.%)	0.00	0.00	0.01	0.00		0.00	0.01	0.00
K ₂ O (wt.%)	0.00	0.00	0.00	0.00		0.00	0.00	0.00
Cr ₂ O ₃ (wt.%)	0.00	0.00	0.00	0.00		0.01	0.01	0.01
MnO (wt.%)	0.42	0.36	0.44	0.38		0.33	0.50	0.37
NiO (wt.%)	0.02	0.04	0.07	0.00			0.05	0.01
Oxides Total (wt.%)	100.20	100.52	100.47	100.04		98.92	100.39	100.09
note			wide spread in data				with magnetite; high MnO...?	
Mg#(Fe _T)	67.3	72.3	65.2	67.4	81.5	79.7	80.3	75.0
Te	0.48	0.39	0.51	0.43		0.36	0.54	0.52
Fo	66.93	72.03	64.87	67.12		79.38	79.88	80.19
Fa	32.58	27.55	34.60	32.43		20.25	19.56	19.24
Mg#(Fe ²⁺ only)	68.0	73.3	65.2	68.4	~81.5	79.7	80.9	81.8
Ca-Olivine	0.01	0.02	0.02	0.02		0.01	0.02	0.04
Si APFU	0.989	0.987	1.001	0.986		1.007	0.992	0.986
Ti APFU	0.000	0.000	0.000	0.000		0.000	0.000	0.000
Al APFU	0.000	0.000	0.000	0.000		0.000	0.000	0.000
Fe ²⁺ APFU	0.022	0.026	0.001	0.028		0.000	0.014	0.028
Fe ²⁺ APFU	0.633	0.529	0.690	0.625		0.404	0.378	0.359
Mg APFU	1.345	1.449	1.295	1.351		1.582	1.602	1.614
Ca APFU	0.000	0.000	0.000	0.000		0.000	0.000	0.001
Na APFU	0.000	0.000	0.001	0.000		0.000	0.000	0.000
K APFU	0.000	0.000	0.000	0.000		0.000	0.000	0.000
Cr APFU	0.000	0.000	0.000	0.000		0.000	0.000	0.000
Mn APFU	0.010	0.008	0.010	0.009		0.007	0.011	0.011
Ni APFU	0.001	0.001	0.002	0.000		0.000	0.001	0.000

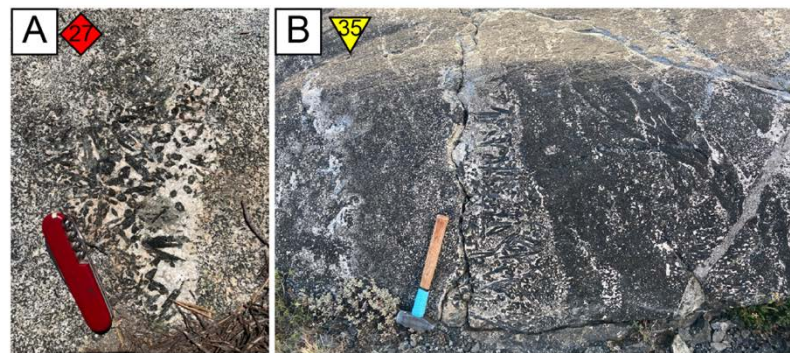
Clinopyroxene: $K_D Fe/Mg$ clinopyroxene-melt = 0.23; melt ; $Fe^{3+}/\Sigma FeT = 0.15$						
Mafic Body	Dougherty Peak	Marble Canyon	Hidden Lakes	Pine Creek	Mount Tom	Mount Tom
Sample number	20-JRD-82	20-JRD-107	SNB-16-01	SNB-19-57	SNB-19-17	SNB-19-18
Transect distance (km)	135	216	151	149	157	157
Equilibrium melt (calculated)	40.9	43.8	29.8	37.6	43.5	44.3
whole-rock SiO_2 (wt.%)	54.4		50.6	58.8	51.8	47.3
whole-rock Mg#	66.1		44.8	46.0	55.9	52.6
n (grains)	5	5		1	1	3
n (analyses)	25	15	3	2	2	7
Max Mg# average group	all grains	$Al_2O_3 > 1$;	Lewis et al., 2021	Lewis et al., 2024	Lewis et al., 2024	Lewis et al., 2024
SiO_2 (wt.%)	53.14	52.36	51.38	52.04	50.74	50.86
TiO_2 (wt.%)	0.07	0.24	0.57	0.35	0.57	0.53
Al_2O_3 (wt.%)	0.66	1.15	2.42	1.99	2.87	2.67
FeO (wt.%)	8.33	8.32	10.01	8.82	8.92	9.01
MgO (wt.%)	13.38	13.41	12.21	14.20	14.76	15.17
CaO (wt.%)	24.08	23.07	22.06	20.86	20.83	20.34
Na_2O (wt.%)	0.39	0.61	0.26	0.39	0.27	0.26
K_2O (wt.%)	0.00	0.01	0.01	0.01	0.00	0.00
Cr_2O_3 (wt.%)	0.04	0.00	0.01	0.02	0.12	0.14
MnO (wt.%)	0.35	0.51	0.31	0.40	0.23	0.29
NiO (wt.%)	0.00	0.00		0.01	0.00	0.01
Oxides Total (wt.%)	100.45	99.68	99.38	99.10	99.31	99.28
note	relatively clustered, low Al_2O_3 data	relatively clustered, low Al_2O_3 data				
$Mg\#(Fe_I)$	74.1	74.2	68.5	74.2	74.7	75.0
Wo	48.95	47.84	47.08	43.92	43.10	41.95
En	37.84	38.70	36.25	41.59	42.50	43.55
Fs	13.21	13.47	16.67	14.49	14.40	14.50
$Mg\#(Fe^{2+} \text{ only})$	78.0	79.9	68.5	75.5	79.7	80.3
Si APFU	1.972	1.954	1.945	1.951	1.894	1.897
Ti APFU	0.002	0.007	0.016	0.010	0.016	0.015
Al APFU	0.029	0.050	0.108	0.088	0.126	0.117
Fe^{3+} APFU	0.049	0.072	0.000	0.019	0.070	0.074
Fe^{2+} APFU	0.209	0.187	0.317	0.258	0.209	0.208
Mg APFU	0.740	0.746	0.689	0.794	0.822	0.844
Ca APFU	0.958	0.922	0.895	0.838	0.833	0.813
Na APFU	0.028	0.044	0.019	0.029	0.020	0.019
K APFU	0.000	0.000	0.001	0.001	0.000	0.000
Cr APFU	0.001	0.000	0.000	0.001	0.003	0.004
Mn APFU	0.011	0.016	0.010	0.013	0.007	0.009
Ni APFU	0.000	0.000	0.000	0.000	0.000	0.000

Clinopyroxene: $K_D Fe/Mg$ clinopyroxene-melt = 0.23; melt ; $Fe^{3+}/\Sigma Fe^+$ = 0.15						
Mafic Body	Bishop Creek	Green Lake	Mount Alice	McMurry Meadows	McMurry Meadows	McMurry Meadows
Sample number	SNB-18-43	SNB-19-42	SNB-19-30	SNB-19-65	SNB-19-66	SNB-19-68
Transect distance (km)	157	155	160	162	163	166
Equilibrium melt (calculated)	38.6	45.2	41.5	56.4	57.5	54.1
whole-rock SiO_2 (wt.%)	52.8	49.5	53.7	50.2		50.1
whole-rock Mg#	54.1	73.1	57.3	73.6		70.1
n (grains)	4	3	1	2	2	2
n (analyses)	8	3	1	5	2	6
Max Mg# average group	Lewis et al., 2024	Lewis et al., 2024: $Al_2O_3 > 2.5$ wt.%				
SiO_2 (wt.%)	51.39	53.08	52.62	51.53	51.11	50.94
TiO_2 (wt.%)	0.57	0.63	0.15	0.42	0.48	0.60
Al_2O_3 (wt.%)	2.82	3.62	1.22	2.77	3.16	2.99
FeO (wt.%)	9.78	6.03	7.98	6.23	6.40	7.13
MgO (wt.%)	14.76	14.29	13.52	14.60	15.33	15.17
CaO (wt.%)	20.39	24.24	23.83	23.65	22.49	21.76
Na_2O (wt.%)	0.23	0.11	0.28	0.32	0.26	0.39
K_2O (wt.%)	0.00	0.00	0.02	0.03	0.01	0.01
Cr_2O_3 (wt.%)	0.06	0.31	0.13	0.13	0.15	0.11
MnO (wt.%)	0.25	0.15	0.45	0.17	0.22	0.24
NiO (wt.%)	0.01	0.01	0.00	0.01	0.02	0.00
Oxides Total (wt.%)	100.27	99.72	100.20	99.85	99.65	99.33
note						
$Mg\#(Fe_1)$	72.9	80.9	75.1	80.7	81.0	79.1
Wo	41.97	49.65	48.76	48.43	46.07	44.93
En	42.30	40.72	38.48	41.61	43.69	43.58
Fs	15.72	9.64	12.75	9.96	10.24	11.49
$Mg\#(Fe^{2+}$ only)	76.3	80.9	78.4	86.9	87.4	85.8
Si APFU	1.905	1.917	1.957	1.903	1.887	1.889
Ti APFU	0.016	0.017	0.004	0.012	0.013	0.017
Al APFU	0.123	0.154	0.053	0.120	0.138	0.131
Fe^{3+} APFU	0.049	0.000	0.042	0.071	0.076	0.082
Fe^{2+} APFU	0.254	0.182	0.206	0.122	0.122	0.139
Mg APFU	0.816	0.770	0.749	0.804	0.844	0.839
Ca APFU	0.810	0.938	0.949	0.936	0.890	0.864
Na APFU	0.016	0.008	0.020	0.023	0.018	0.028
K APFU	0.000	0.000	0.001	0.001	0.000	0.000
Cr APFU	0.002	0.009	0.004	0.004	0.004	0.003
Mn APFU	0.008	0.004	0.014	0.005	0.007	0.008
Ni APFU	0.000	0.000	0.000	0.000	0.001	0.000

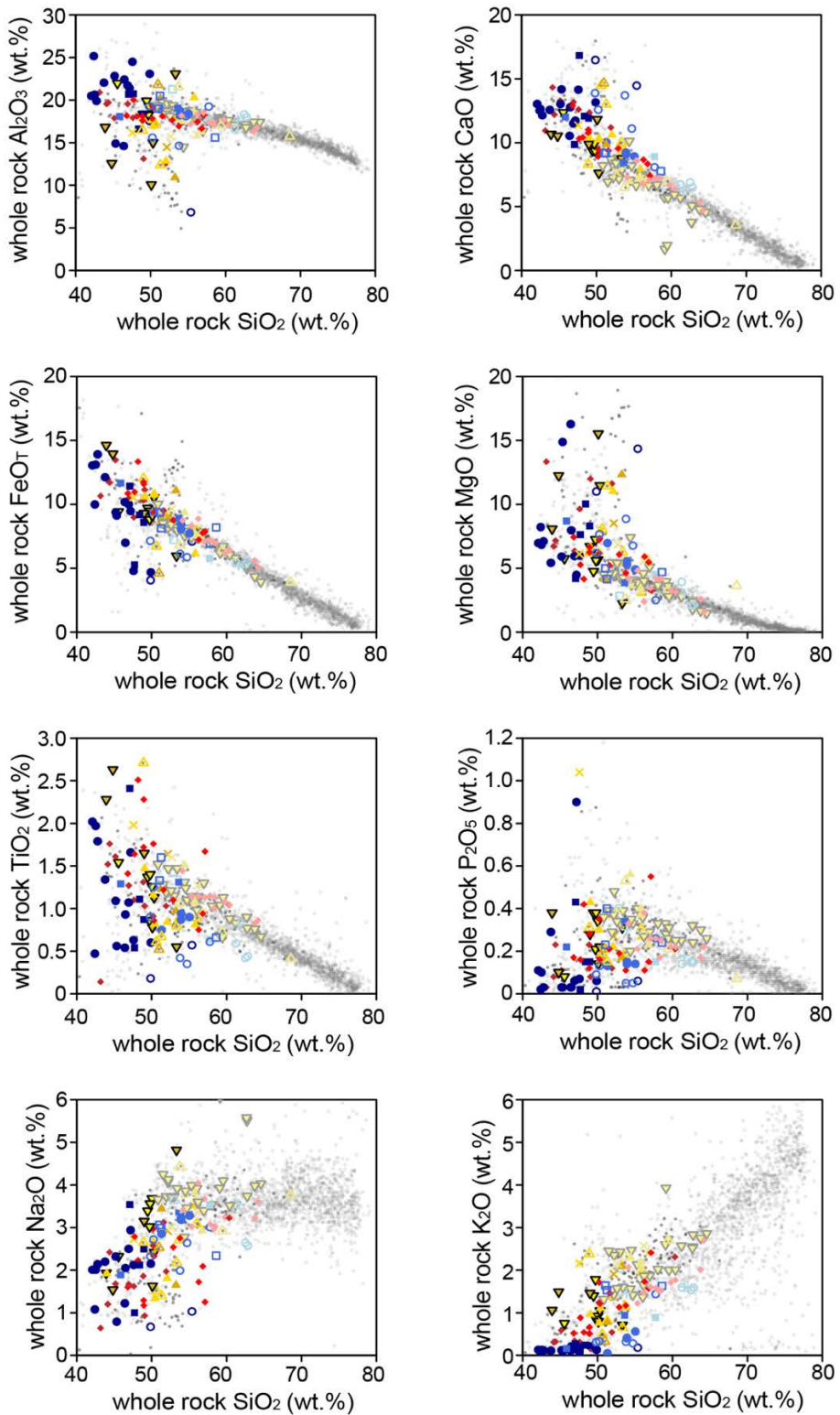
Clinopyroxene: K_D Fe/Mg clinopyroxene-melt = 0.23; melt ; $Fe^{3+}/\Sigma FeT = 0.15$					
Mafic Body	Casa Diablo	Tungsten Hills	Tungsten Hills	Keough	Keough
Sample number	SNB-19-06	SNB-17-26	SNB-17-27	SNB-17-8	SNB-18-53
Transect distance (km)	164	168	168	173	172.927
Equilibrium melt (calculated)	54.4	47.5	48.7	54.2	39.9
whole-rock SiO ₂ (wt.%)	39.1	47.0	46.4	44.0	54.8
whole-rock Mg#	73.4	72.6	71.9	66.9	46.7
n (grains)	1	3	2	1	1
n (analyses)	8	3	2	3	5
Max Mg# average group	Lewis et al., 2024	Lewis et al., 2024: Al ₂ O ₃ >3 wt.%			
SiO ₂ (wt.%)	49.49	52.37	52.29	51.58	51.16
TiO ₂ (wt.%)	0.77	0.17	0.09	0.55	0.75
Al ₂ O ₃ (wt.%)	4.32	1.59	1.52	3.56	3.30
FeO (wt.%)	7.71	7.15	6.80	6.18	8.38
MgO (wt.%)	14.54	14.43	14.02	14.48	14.16
CaO (wt.%)	22.17	23.26	24.32	22.90	20.83
Na ₂ O (wt.%)	0.24	0.30	0.23	0.52	0.45
K ₂ O (wt.%)	0.00	0.01	0.00	0.05	0.03
Cr ₂ O ₃ (wt.%)	0.08	0.03	0.02	0.21	0.01
MnO (wt.%)	0.16	0.25	0.25	0.17	0.33
NiO (wt.%)	0.00	0.02	0.00	0.01	0.00
Oxides Total (wt.%)	99.49	99.59	99.55	100.22	99.40
note					
Mg#(Fe _T)	77.1	78.2	78.6	80.7	75.1
Wo	45.79	47.54	49.50	47.83	44.25
En	41.78	41.04	39.70	42.09	41.85
Fs	12.43	11.41	10.81	10.08	13.89
Mg#(Fe ²⁺ only)	85.9	82.2	82.9	85.8	77.3
Si APFU	1.838	1.946	1.946	1.895	1.908
Ti APFU	0.021	0.005	0.003	0.015	0.021
Al APFU	0.189	0.070	0.067	0.154	0.145
Fe ³⁺ APFU	0.107	0.049	0.052	0.059	0.030
Fe ²⁺ APFU	0.132	0.173	0.160	0.131	0.232
Mg APFU	0.805	0.800	0.778	0.793	0.787
Ca APFU	0.882	0.926	0.970	0.901	0.832
Na APFU	0.018	0.021	0.016	0.037	0.032
K APFU	0.000	0.001	0.000	0.002	0.001
Cr APFU	0.002	0.001	0.001	0.006	0.000
Mn APFU	0.005	0.008	0.008	0.005	0.010
Ni APFU	0.000	0.001	0.000	0.000	0.000

APPENDIX 1

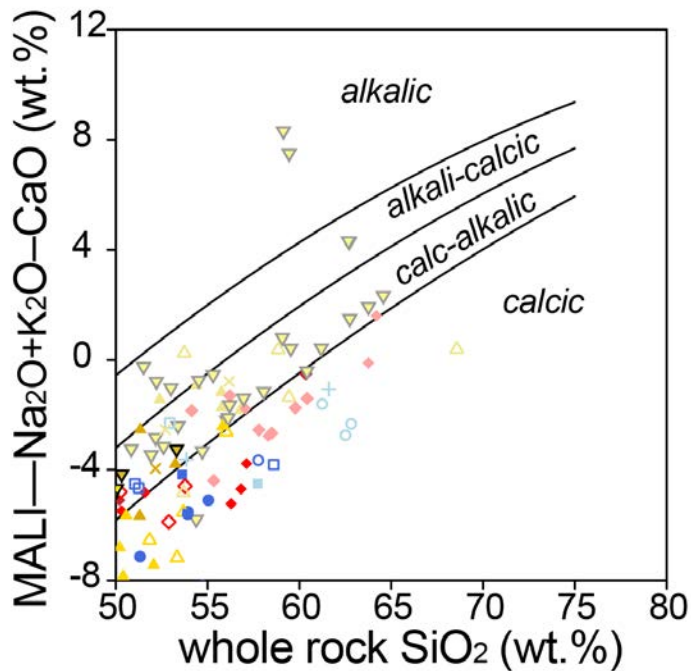
SUPPLEMENTARY FIGURES



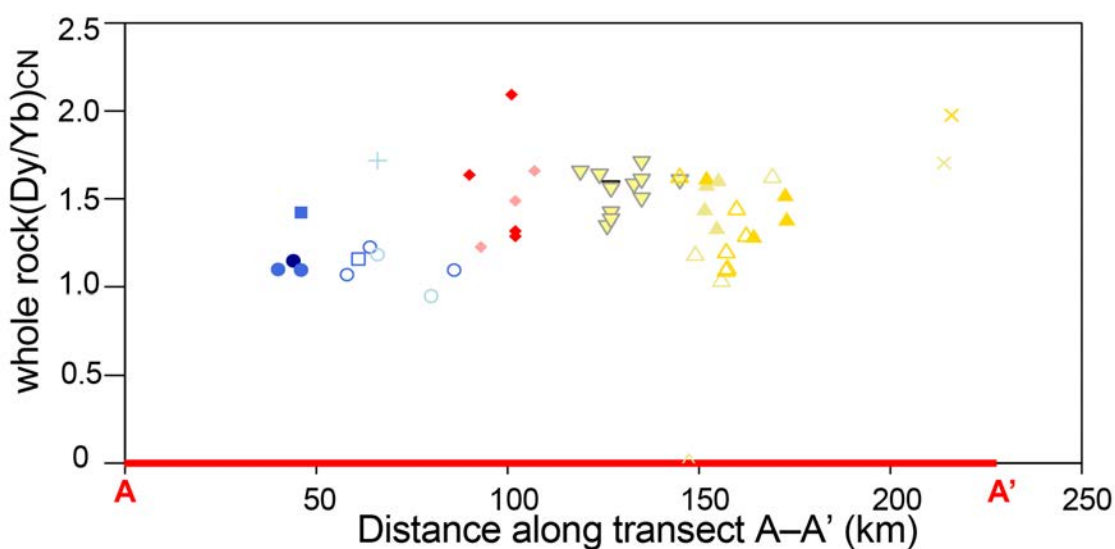
Ch. 3 Figure A-1. Field photos of amphibole pegmatoid segregations from **A)** Mud Lakes and **B)** Volcanic Lakes—these two are some of the coarsest and largest segregations among all mafic intrusions of the transect. Numbers and symbols correspond to mafic intrusions in Fig. 2A and Table 1.



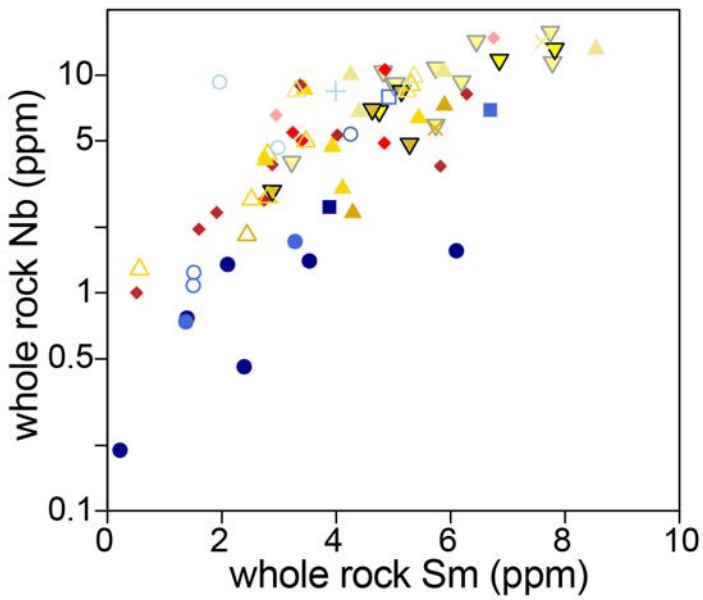
Ch. 3 Figure A-2. Harker diagrams of major and minor oxides versus SiO_2 . Symbols as in Figure 8.



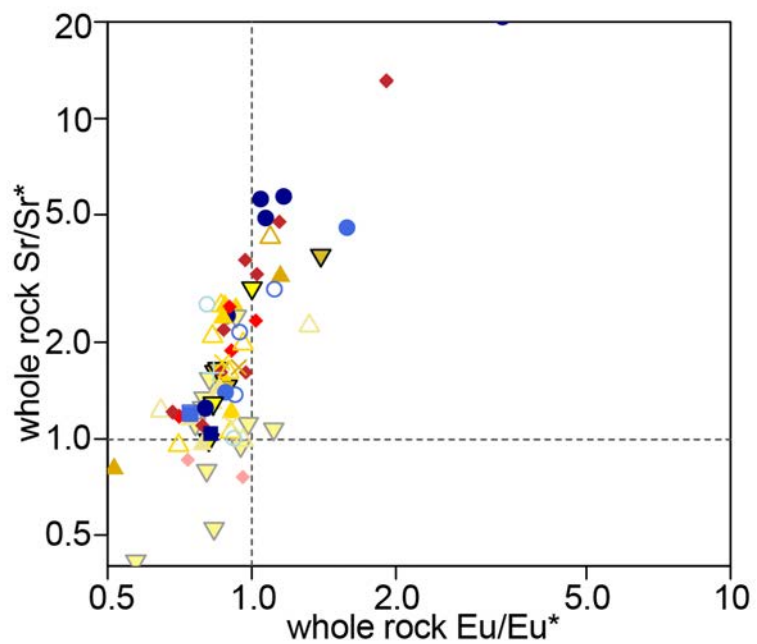
Ch. 3 Figure A-3. Plot of Modified Alkali Lime Index (MALI): whole-rock $\text{Na}_2\text{O} + \text{K}_2\text{O} - \text{CaO}$ versus SiO_2 of Frost et al., 2001, Symbols as in Figure 8.



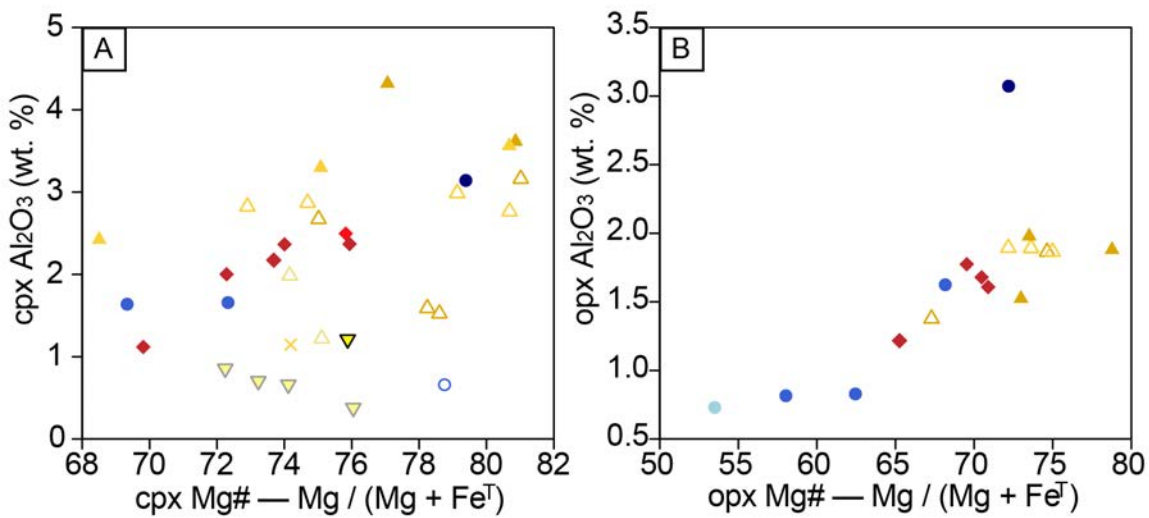
Ch. 3 Figure A-4. Whole rock $(\text{Dy}/\text{Yb})_{\text{CN}}$ versus distance (km) along the transect. Only non-cumulate samples are plotted, and large symbols are filtered for Rb/Sr between 0.05 and 0.2. Symbols as in Figure 8.



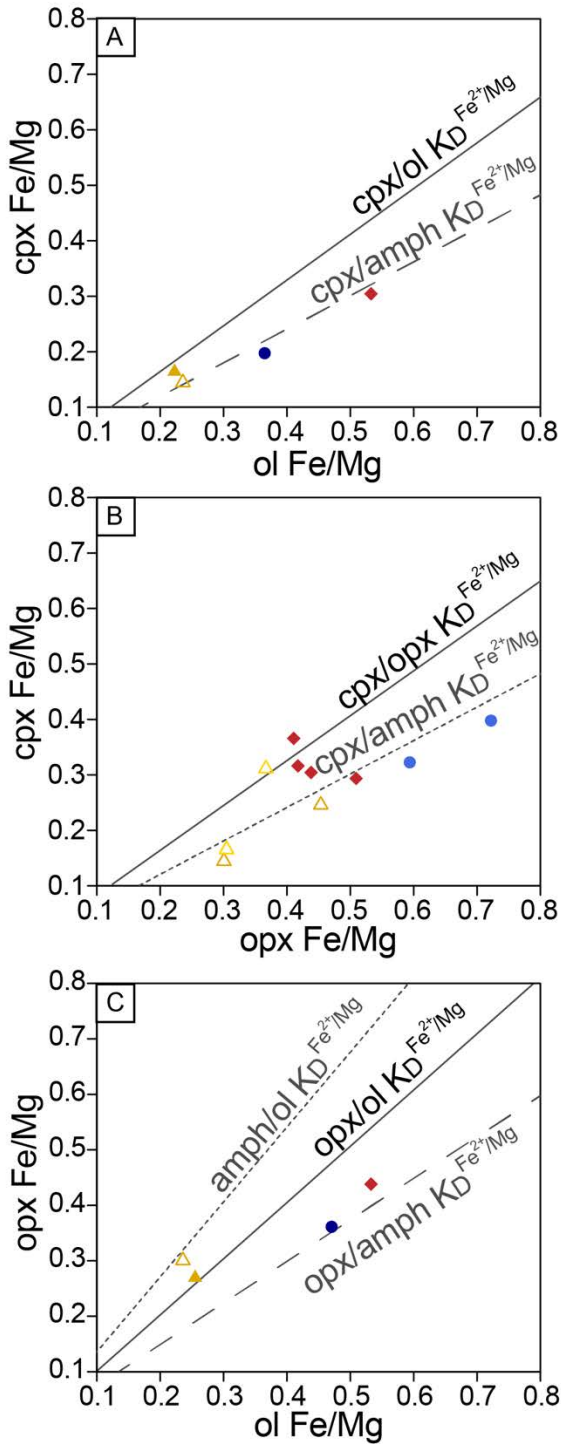
Ch. 3 Figure A-5. Whole-rock Nb versus Sm. Symbols as in Fig. 8.



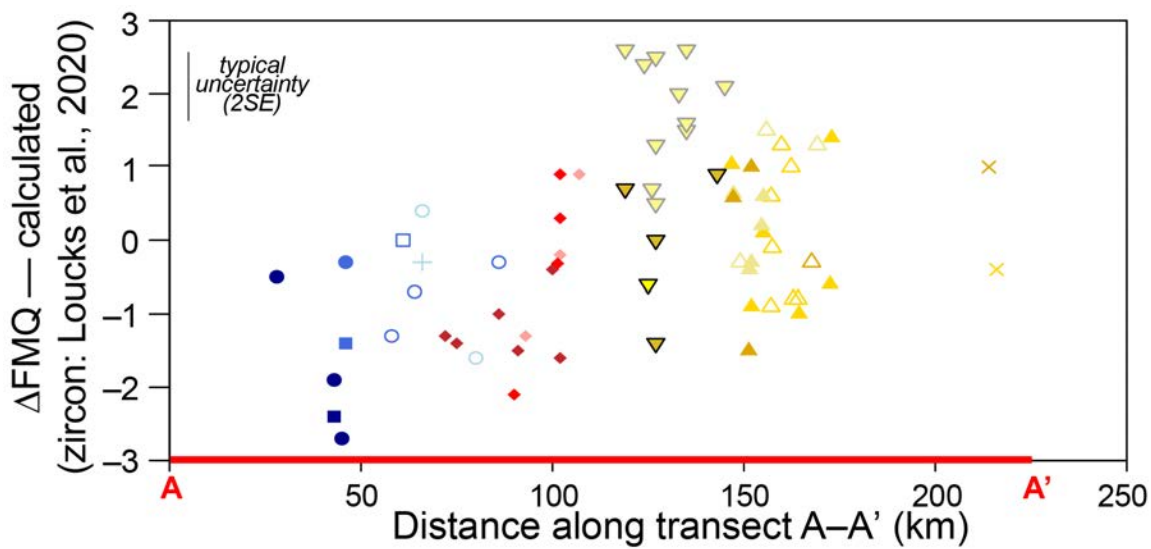
Ch. 3 Figure A-6. Whole rock Sr/Sr* vs Eu/Eu*. Symbols as in Fig. 8.



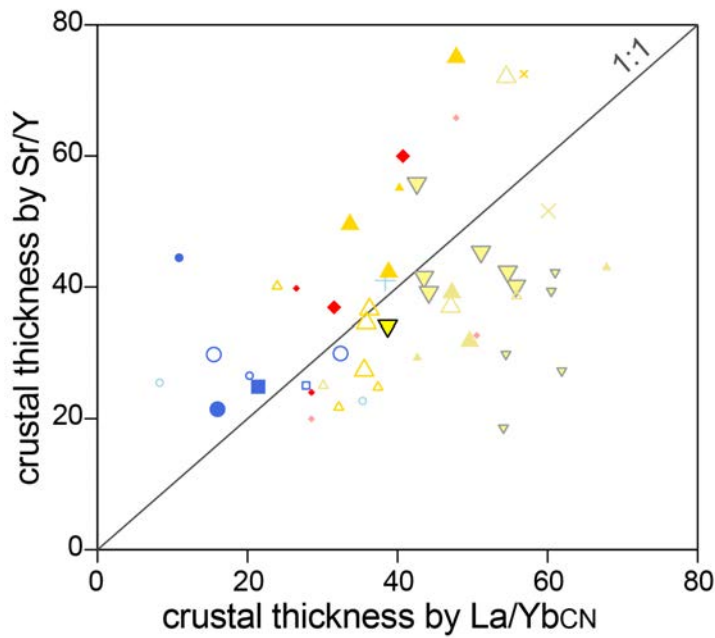
Ch. 3 Figure A-7. Al_2O_3 (wt. %) versus Mg# in **A**) clinopyroxene; **B**) orthopyroxene.
Symbols as in Figure 8.



Ch. 3 Figure A-8. Relations between Fe/Mg in coexisting minerals implied by constant value of the exchange coefficient $K_D^{Fe2+/Mg}$. Solid line shows clinopyroxene or orthopyroxene versus olivine. Dotted and dashed lines indicate predicted amphibole Fe/Mg coexisting with olivine, clinopyroxene, or orthopyroxene as indicated. Symbols as in Figure 8.



Ch. 3 Figure A-9. Calculated oxygen fugacity (by zircon trace elements) relative to the fayalite-magnetite-quartz buffer (ΔFMQ) based on the equation of Loucks et al. (2020), versus distance along the transect. Symbols as in Figure 8.



Ch. 3 Figure A-10. A comparison of crustal thickness calculations by Sr/Y and $(\text{La}/\text{Yb})_{\text{CN}}$ (using equations of Profeta et al., 2015). Samples with high calculated thicknesses by Sr/Y could reflect some amount of plagioclase accumulation in those samples. Only non-cumulate samples are plotted, and large symbols are filtered for Rb/Sr between 0.05 and 0.2. Symbols as in Figure 8.

APPENDIX 2

Laser Ablation Split-Stream Inductively Coupled Mass Spectrometry (LA-SS-ICPMS) Zircon U-Pb Age and Trace Element Analysis

Zircon U-Pb ages and trace element concentrations were analyzed over four days at the University of California, Santa Barbara (UCSB), following the methods outlined in Kylander-Clark et al., 2013. The laser-ablation split-stream system combines a Photon Machines nm ArF Excimer laser with a Hel-Ex ablation cell, Nu Instruments HR Plasma high-resolution and Nu Instruments P3D Plasma MC-ICP-MS systems for collecting U-Pb isotope data, and an Agilent 7700 quadrupole ICP-MS for determining trace-element concentrations. (A building electrical shutdown resulted in a switch from HR to P3C for MC-ICP-MS runs 3 through 6). Cathodoluminescence (CL) images collected prior to SIMS analyses on the JEOL JXA-iHP200F Field Emission Electron Probe Microanalyzer (FE EPMA) at Caltech. Those CL images, in addition to locations of SIMS spots visible in reflected light during analysis, were used to guide spot placement.

Laser ablation analyses consisted of 25 μm spots placed on top of or adjacent to previously analyzed $\delta^{18}\text{O}$ SIMS analysis pits on cores and rims, and on fresh sites on additional grains targeting mostly grain rims with uncomplicated, igneous-looking CL image patterns in addition to any potentially xenocrystic cores, and avoiding inclusions, cracks, and straddling significant growth domains (*i.e.*, core and rim) where possible, with an aim of \sim 20 analyses per sample (more in samples with heterogeneous zircons). Specific settings used are listed in Appendix 2 Table A2-1. Primary and secondary natural reference standards were analyzed throughout the runs bracketing approximately every ten sample analyses.

The laser parameters for analysis for the 25 μm spots were ablation at \sim 1 J/cm^2 and 5 Hz for 12 seconds, following a 20 second baseline and two-shot pre-ablation. Unknowns were bracketed by zircon reference material (RM) 91500 (Wiedenbeck et al., 1995), with RMs GJ-1 (Jackson et al., 2004), Plešovice (Sláma et al., 2008), R33 (Black et al., 2004), and AusZ5 (Kennedy et al., 2014) were included periodically for

quality control; they yielded average ages within 0.06–1.0% of their accepted values. For element concentrations, ^{29}Si was used for internal normalization, assuming 15.2%, and 91500 was used as the reference material for all elements except V and LREE, in which case NIST-612 was used. Raw U-Pb isotope and trace-element data were reduced using Iolite v3 (Paton et al., 2011) to correct for instrument drift, laser-ablation-induced down-hole elemental fractionation, plasma-induced elemental fractionation, and instrumental mass bias.

MSWD plots, concordia ages and analytical errors (2se) were calculated using IsoplotR using a ^{238}U decay constant of $0.000155125 \pm 8.38 \times 10^{-8}$ Myr $^{-1}$, a ^{235}U decay constant of $0.00098485 \pm 6.7 \times 10^{-7}$ Myr $^{-1}$ and a $^{238}\text{U}/^{235}\text{U}$ ratio of 137.818 ± 0.0225 , propagating these external uncertainties with the calculations (Ludwig, 1998; Ludwig, 2003; Paton et al., 2010, 2011). Grains with <95% concordance were excluded. Outliers were identified using the generalized Chauvenet Criterion of IsoplotR when computing a weighted mean, and also excluded from concordia plots and ages. Final reported sample ages in the dataset report the concordia age and analytical error, and also quadratically add propagated error of 2% of the age to reflect reproducibility over time at the UCSB LA-SS-ICPMS center.

About half of the analyzed samples have tightly clustered U-Pb age populations (MSWD ≤ 1), but 10 samples have some spread in individual U-Pb ages (out of 30 samples with an MSWD > 1 , maximum 8). Of these samples, potential reasons for the spread in ages vary: eight are patchy and dark in CL and anhedral, appearing to have been resorbed, and potentially isotopically reset with individual analyses spread to both older and younger ages than the MSWD age (20-JRD-79, 20-JRD-82, 20-JRD-83, 20-JRD-85C, 21-JRD-108; 87S52A); four samples spread to older ages (with disrupted zoning indicative of resorption of cores or xenocrystic zircon; 20-KC-38, 19-JRD-18, 21-JRD-126, 21-JRD-127); four samples appear rounded and have rims that crosscut internal zoning, both features common for metamorphic zircon (19-JRD-14; 20-JRD-50B; 20-JRD-91B; 21-JRD-134); two samples yielded heterogeneous looking zircon (20-JRD-98; 21-JRD-140B); one sample yielded few (and heterogeneous, small) zircon (n=8, 19-JRD-32).

Analyses that produced outlier ages older than the weighted mean age are interpreted to be inherited from older rocks of the batholith or pre-existing crust that mafic magmas transited on their ascent through the crust to their emplacement level. Xenocrystic zircon grains are found in 24 samples, with a maximum of three concordant outlier ages older than the MSWD in any sample; plus the xenocrystic cores as described in 20-JRD-94. In 20-JRD-35A (Fine Gold), four analyses on thin rims visible in CL give a concordia age ~20 million years younger than most zircon analyzed in the sample. The CL textures for these rims could be interpreted as metamorphic overgrowth rims, and the sample is crosscut by a felsic dike and is altered (likely by SiO₂-rich fluids). The surrounding Fine Gold intrusive suite is Cretaceous in age (Lackey et al., 2012), and potentially zircon in this small Jurassic outcrop could have recrystallized.

In addition, 6 samples contain 1 or more outlier ages that are younger than the MSWD age—they may represent protracted crystallization during cooling, as they are either close in age to the rest of the analyses or there is also significant spread in the ages of the rest of the analyses, but in one case (20-JRD-69 from Tehepite), they are offset in age from the main population by ~8 million years. That sample is from the margin of the intrusion adjacent to the younger Volcanic Lakes mafic intrusion, so potentially was affected by this nearby later magmatism.

REFERENCES

Black, L.P., Kamo, S.L., Allen, C.M., Davis, D.W., Aleinikoff, J.D., Valley, J.W., Mundil, R., Campbell, I.H., Korsch, R.J., Williams, I.S., and Foudoulis, C., 2004, Improved $^{206}\text{Pb}/^{238}\text{U}$ microprobe geochronology by the monitoring of a trace-element-related matrix effect: SHRIMP, ID-TIMS, ELA-ICP-MS and oxygen isotope documentation for a series of zircon standards. *Chemical Geology*, 205, 115–140.

Jackson, S. E., Pearson, N. J., Griffin, W. L., and Belousova, E. A., 1995, The application of laser ablation-inductively coupled plasma-mass

spectrometry to in situ U–Pb zircon geochronology. *Chemical Geology*, 211, 47–69, 10.1016/j.chemgeo.2004.06.017.

Kylander-Clark, A. R. C., Hacker, B. R., and Cottle, J. M., 2013, Laser-ablation split-stream ICP petrochronology. *Chemical Geology*, 345, 99-112, 10.1016/j.chemgeo.2013.02.019.

Ludwig, K.R., 1998, On the treatment of concordant uranium-lead ages. *Geochimica et Cosmochimica Acta*, 62, no. 4, p.665-676.

Ludwig, K. R., 2003, User's manual for Isoplot 3.00: A geochronological toolkit for Microsoft Excel. Berkeley Geochronology Center Special Publication.

Paton, C., Woodhead, J.D., Hellstrom, J.C., Hergt, J.M., Greig, A., and Maas, R., 2010, Improved laser ablation U-Pb zircon geochronology through robust downhole fractionation correction. *Geochemistry, Geophysics, Geosystems*, 11, doi:<https://doi.org/10.1029/2009GC002618>.

Paton, C., Hellstrom, J., Paul, B., Woodhead, J., and Hergt, J., 2011, Iolite: Freeware for the visualisation and processing of mass spectrometric data. *Journal of Analytical Atomic Spectrometry*, 26, 2508-2518, 10.1039/c1ja10172b.

Sláma, J., Košler, J., Condon, D. J., Crowley, J. L., Gerdes, A., Hanchar, J. M., Horstwood, M. S. A., Morris, G. A., Nasdala, L., Norberg, N., Schaltegger, U., Schoene, B., Tubrett, M. N., and Whitehouse, M. J., 2008, Plešovice zircon — A new natural reference material for U-Pb and Hf isotopic microanalysis. *Chemical Geology*, 249, 1–35, <https://doi.org/10.1016/j.chemgeo.2007.11.005>.

Weis, D., Kieffer, B., Maerschalk, C., Barling, J., de Jong, J., Williams, G. A., Hanano, D., Pretorius, W., Mattielli, N., Scoates, J. S., Goolaerts, A., Friedman, R. M., and Mahoney, J. B., 2006, High-precision isotopic characterization of USGS reference materials by TIMS and MC-ICP-MS. *Geochemistry, Geophysics, Geosystems*, 7, no. 8, Q08006, doi:[10.1029/2006GC001283](https://doi.org/10.1029/2006GC001283).

Wiedenbeck, M., Allé, P., Corfu, f., Griffin, W. L., Meier, M., Oberli, F., Quadt, A.

V., Roddick, J. C., and Spiegel, W., 1995, Three natural zircon standards

for U-Th-Pb, Lu-Hf, trace element and REE analyses. *Geostandards*

Newsletter, 19, 1–23, <https://doi.org/10.1111/j.1751-908X.1995.tb00147.x>.

TABLES

Ch. 3 Table A2- 1. U-Pb and trace element analysis conditions of the laboratory, laser, mass spectrometer and data processing, and reference materials for laser ablation split-stream ICP-MS on the quadrupole (Q-ICP-MS) and Nu Plasma multicollector (MC-ICPMS) inductively coupled plasma mass spectrometers for trace element and U-Pb analyses, respectively. (*Continued on following pages*).

Laboratory & Sample Preparation	
Laboratory name	Laser Ablation ICP-MS Petrochronology facility at the University of California – Santa Barbara
Sample type/mineral	Zircon
Sample preparation	Conventional mineral separation, 1 inch resin mount, 1 μm polish to finish
CL Imaging	JEOL JXA-iHP200F FE EPMA at Caltech, variable <20 nA, 10.0 or 15.0 kV, ~11 mm WD
Laser ablation system	
Make, Model & type	Photon Machines Analyte 193, ATLEX-SI 193 nm ArF excimer
Ablation cell & volume	Helex ablation cell
Laser wavelength (nm)	193 nm
Pulse width (ns)	~4 ns
Fluence (J.cm⁻²)	~1 J/cm²
Repetition rate (Hz)	5 Hz
Ablation duration (secs)	12 seconds – 2 shot preablation, 20.0 second washout, 60 shot analysis, 3.0 second end delay
Ablation pit depth / ablation rate	~0.08 μm /pulse
Spot diameter (μm) nominal/actual	25 μm (nominal)
Sampling mode / pattern	Static spot ablation
Carrier gas	He
Cell carrier gas flow (l/min)	0.15 L/min in cell, 0.04 L/min in cup
ICP-MS Instrument	
Make, Model & type	<u>U-Pb isotopes:</u> Nu Instruments Plasma HR-ES multicollector ICPMS (run 1 & 2) Nu Instruments Plasma P3D multicollector ICPMS (run 3, 4, 5 & 6) <u>Trace-element concentrations:</u> Agilent 7700 quadrupole ICPMS
RF power (W)	1300W
Make-up gas flow (l/min)	~2.3 L/min; ~1 L/min to MC-ICPMS and ~1.3 L/min to Q-ICPMS
Detection system & masses measured	Nu-HR-ES: two Faraday cups (232, 238) and four ion counters (204, 206, 207, 208) Nu-P3D: three Faraday cups (232, 235, 238) and five Daly detectors (202, 204, 206, 207, 208)

Integration time per peak/dwell times (ms)	500 ms for MC-ICPMS
IC Dead time (ns)	8
Data Processing	
Calibration strategy	Round robin prior to analyses; primary reference for U-Pb analyses is 91500
Reference Material info	Mali, 91500, GJ-1, Plešovice, 9435, R-33, AusZ V and LREE: NIST-612 glass Other trace elements: zircon RM 91500
Data processing package used / Correction for LIEF	Data processed with Iolite software of Patton et al. (2010, 2011), and in-house spreadsheet for age calculation and error propagation. Spreadsheet interfaces with Isoplot/EX Microsoft Excell add-in of Ludwig (2003)
Common-Pb correction	none
Uncertainty level & propagation	Ages are $2s$ absolute, propagation is by quadratic addition. For unknowns, we report analytical error plus quadratic addition of 2% error to reflect long-term reproducibility of the lab consistent with that of standard analyses during the session.
Quality control / Validation	Alternately analyzed 91500 and GJ-1 between every 10 analyses, along with one of the other zircon standards or NIST-612 glass.
Other information	A building electrical shutdown resulted in a switch from HR to P3C for MC-ICP-MS runs 3–6

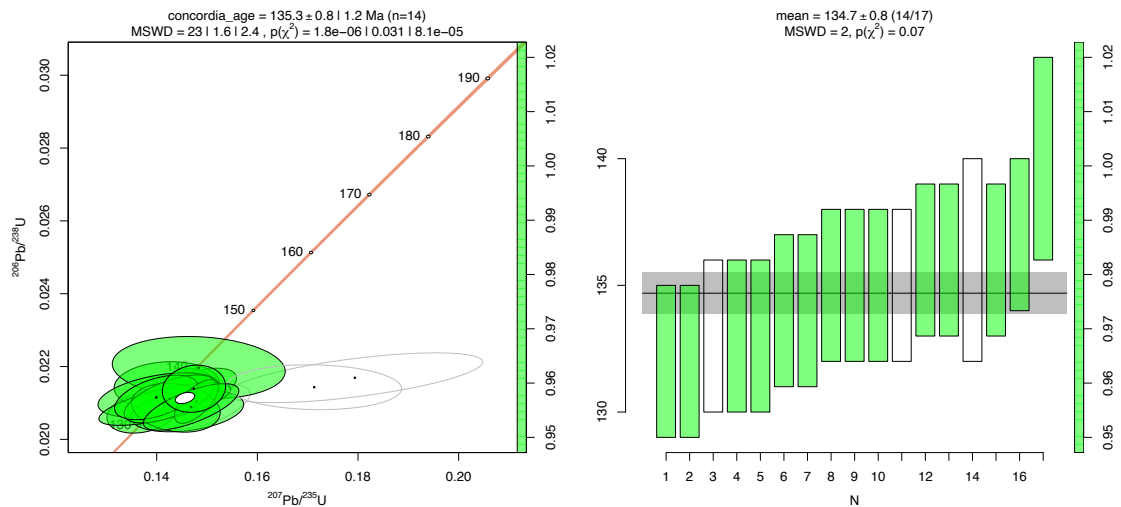
Ch. 3 Table A2- 2. Session averages of Hf isotope measurements on reference materials measured at the start of the session and periodically throughout (every 20 unknowns).

Zircon RM	n (# of analyses)	U-Pb age $\pm 2s$ (Ma)	MSWD	Accepted U-Pb age	Absolute % difference
91500	78	1063.0 \pm 2.3	0.17	1062.4	0.06%
GJ-1	74	603.2 \pm 1.4	0.39	\sim 600 Ma	\sim 0.5%
Plešovice	18	336.8 \pm 1.5	1.5	337.13	0.1%
R33	18	416.2 \pm 2.1	0.98	419.26 \pm 0.39	0.7%
AusZ	16	38.52 \pm 0.21	0.55	38.90	1.0%

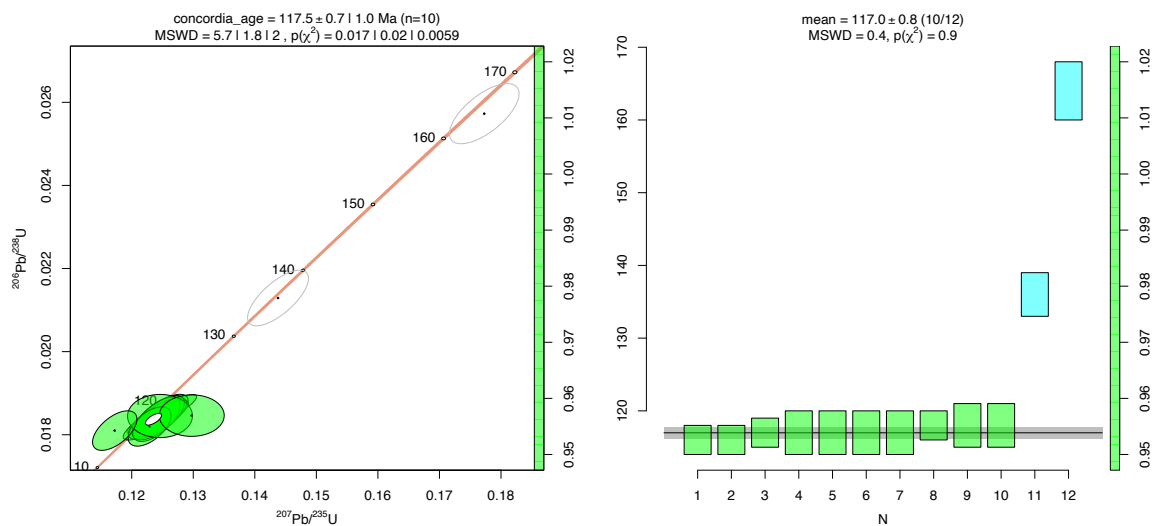
CONCORDIA AND AGE DISPERSION PLOTS

Concordia and age dispersion plots for each sample include concordant analyses (green), discordant analyses (clear) and outliers for a given zircon population (blue). Gray bars represent the mean and 2 s. d. of the population.

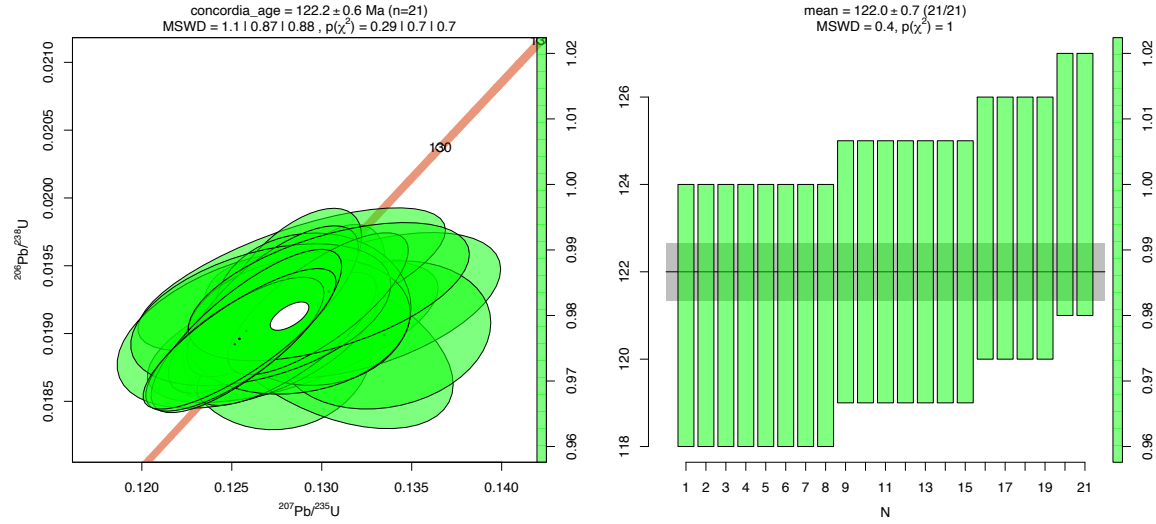
21-JRD-134A:



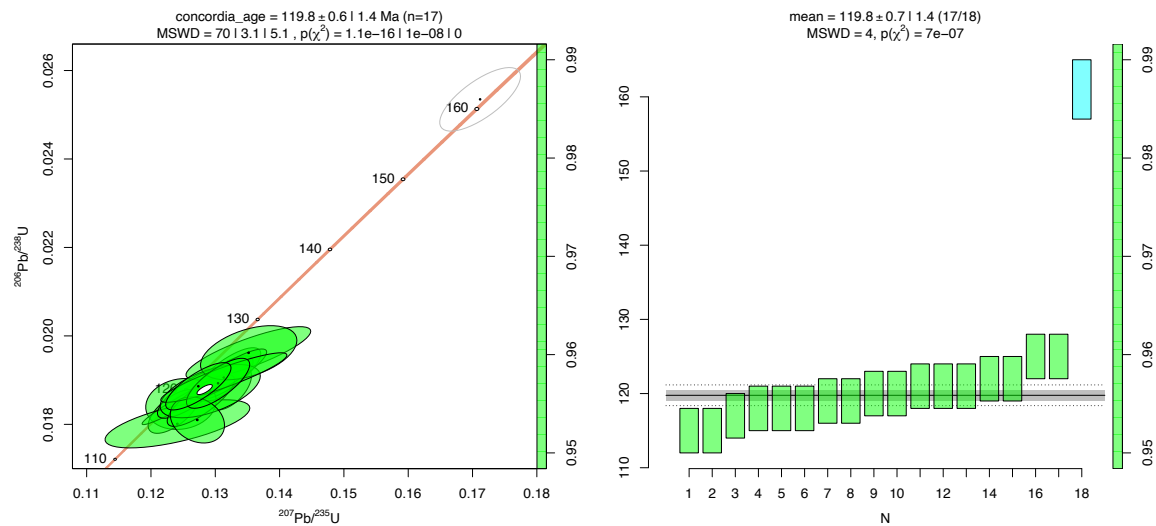
21-JRD-130A:



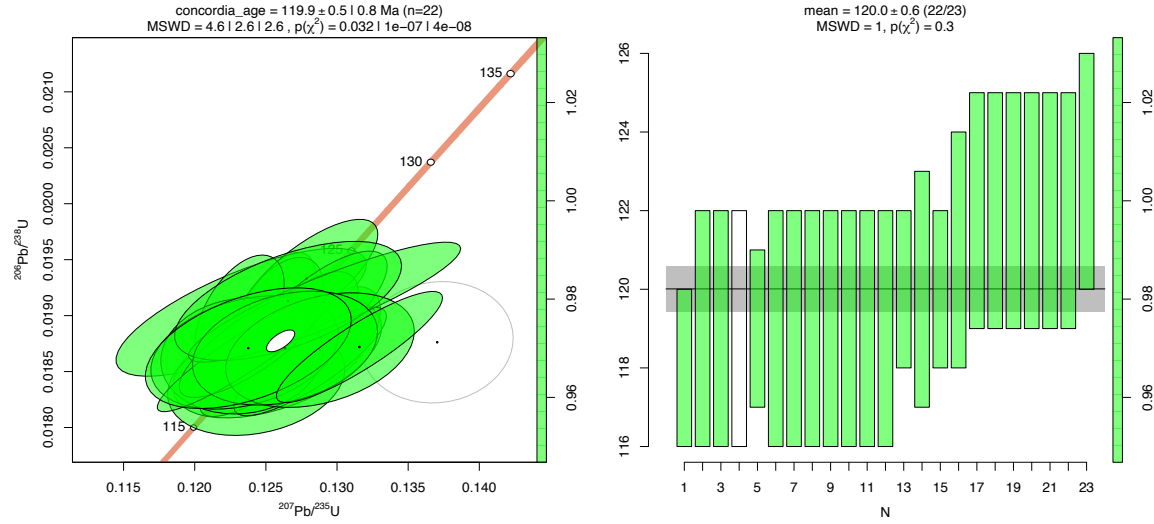
21-JRD-131A:



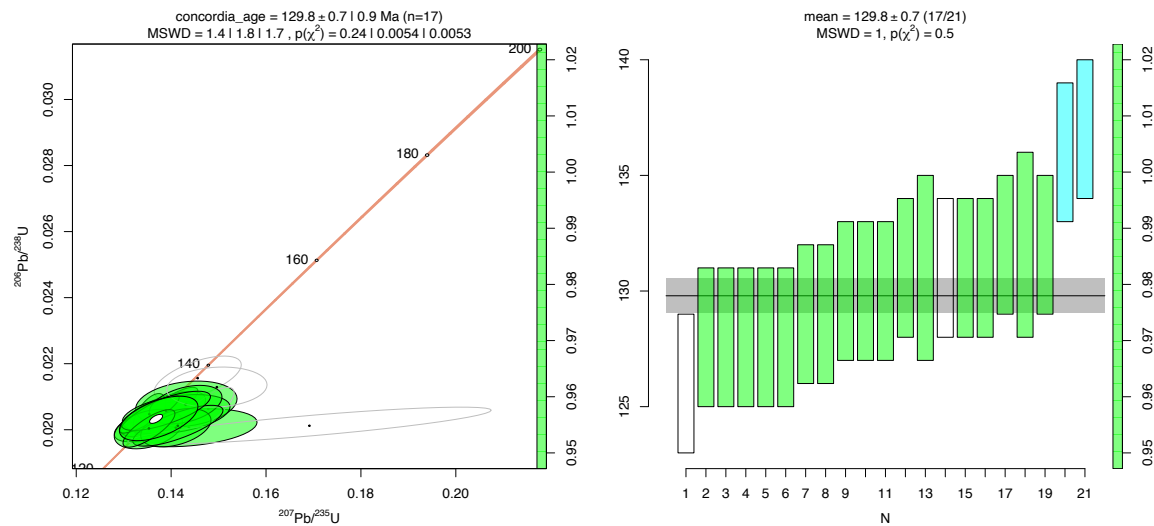
21-JRD-140B:



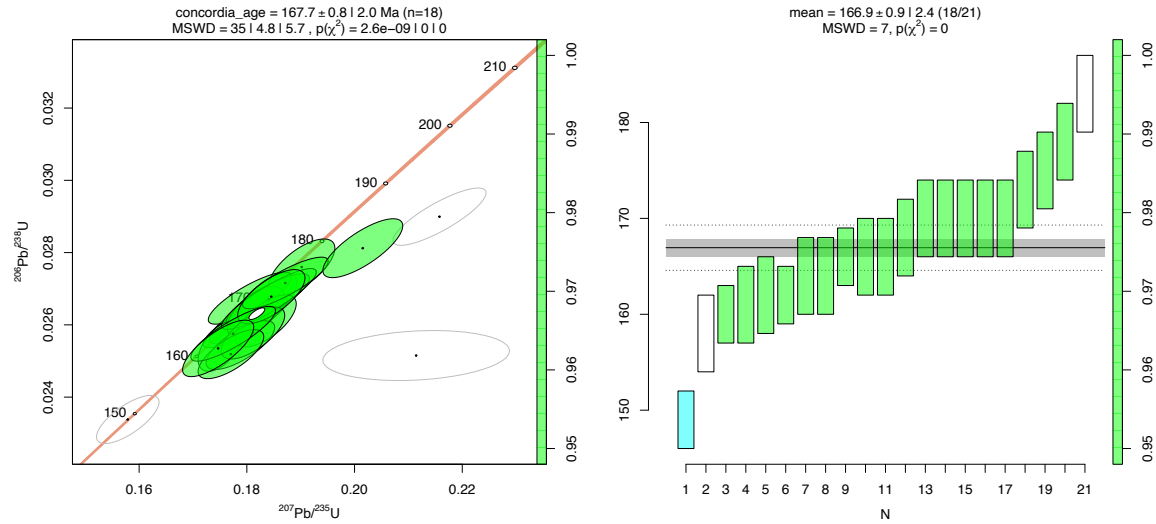
20-JRD-33:



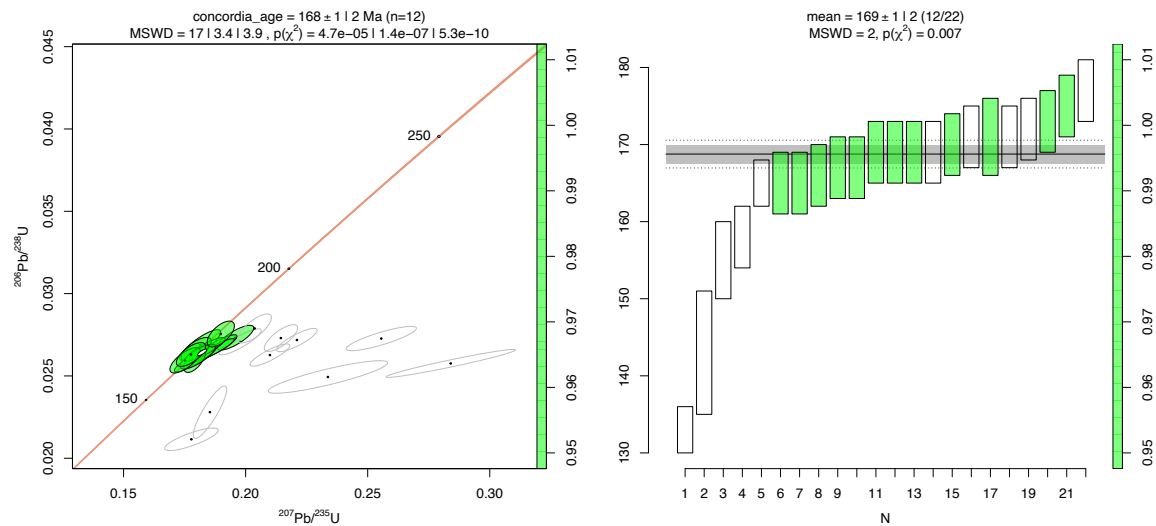
20-JRD-58B:



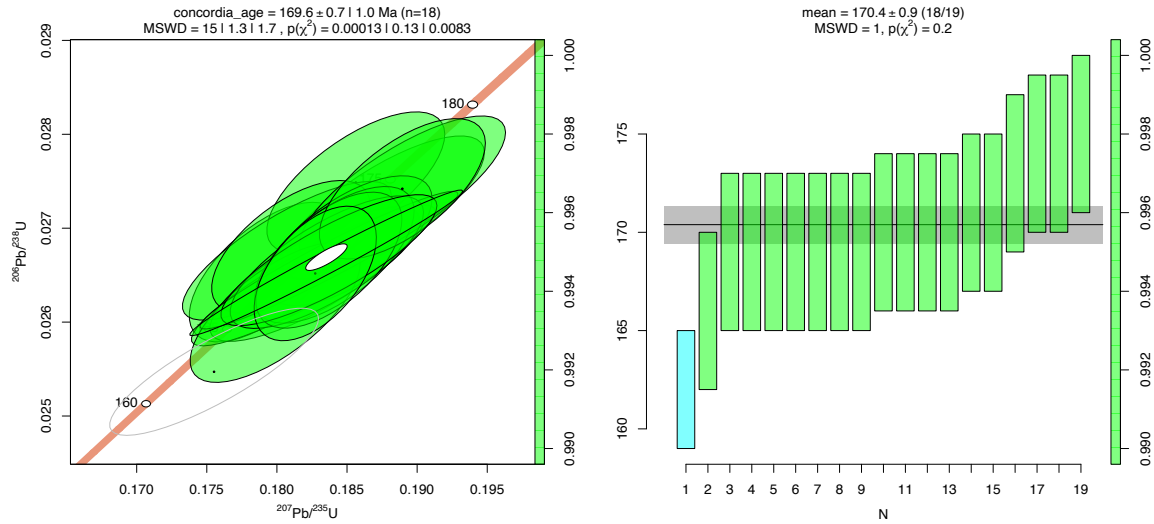
21-JRD-115:



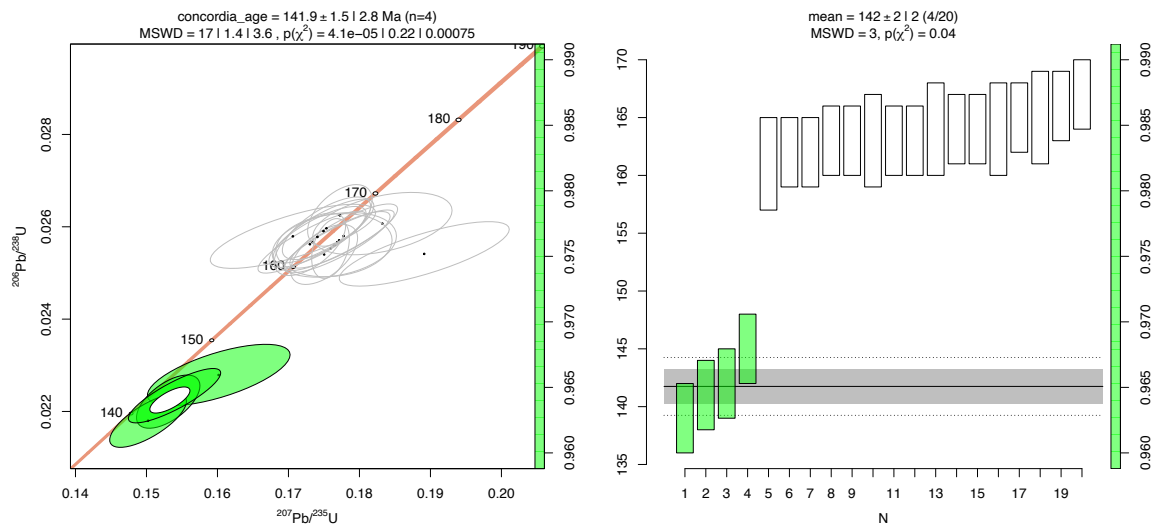
21-JRD-116:



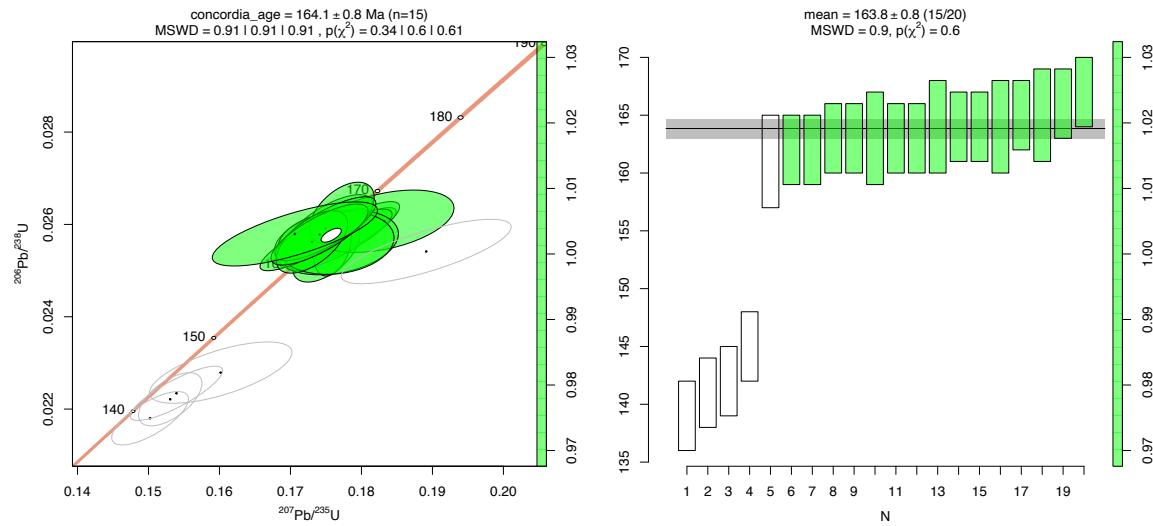
21-JRD-117:



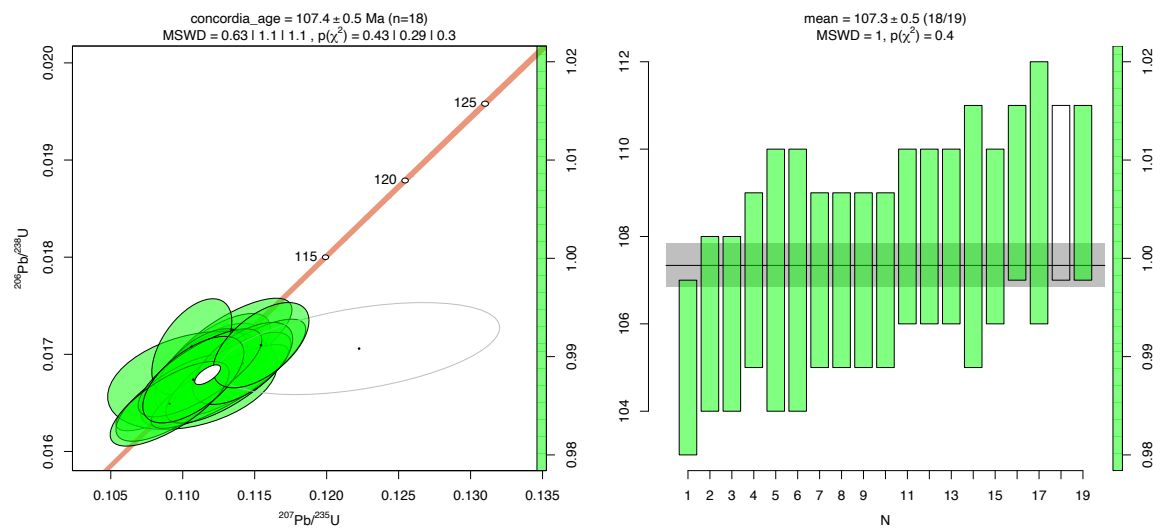
20-JRD-35A-young:



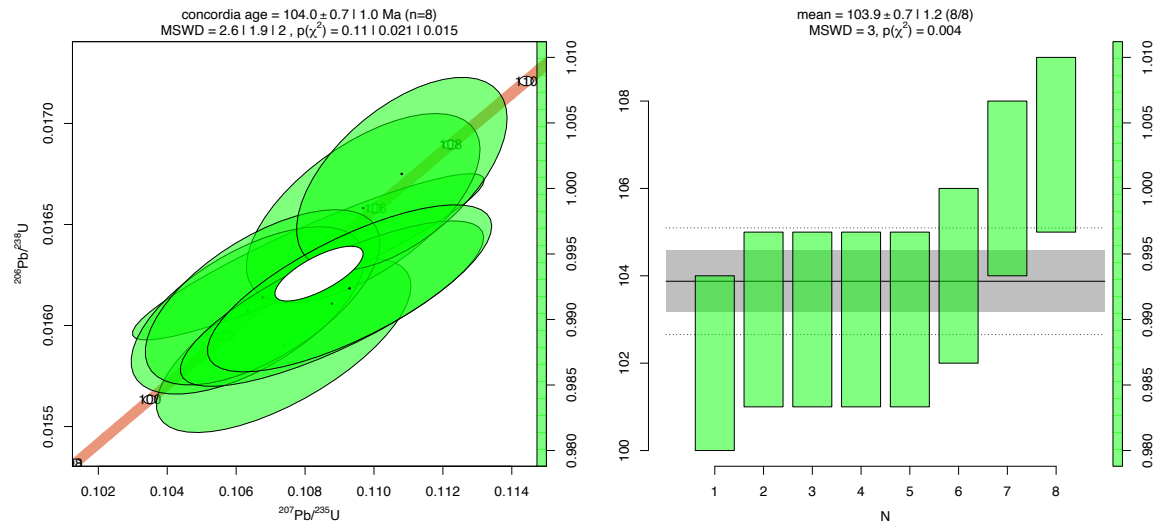
20-JRD-35A-old:



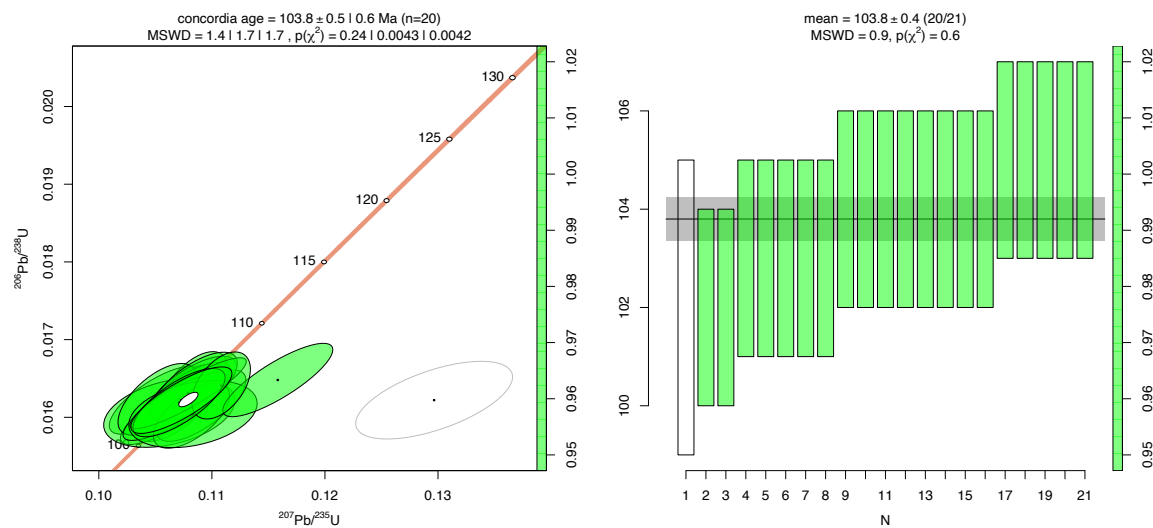
21-JRD-137:



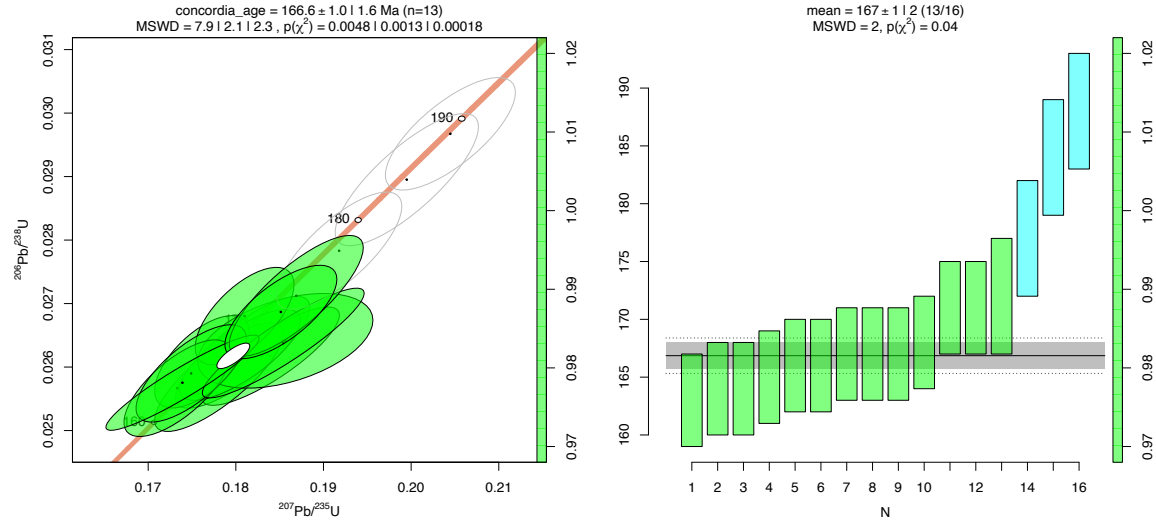
19-JRD-32:



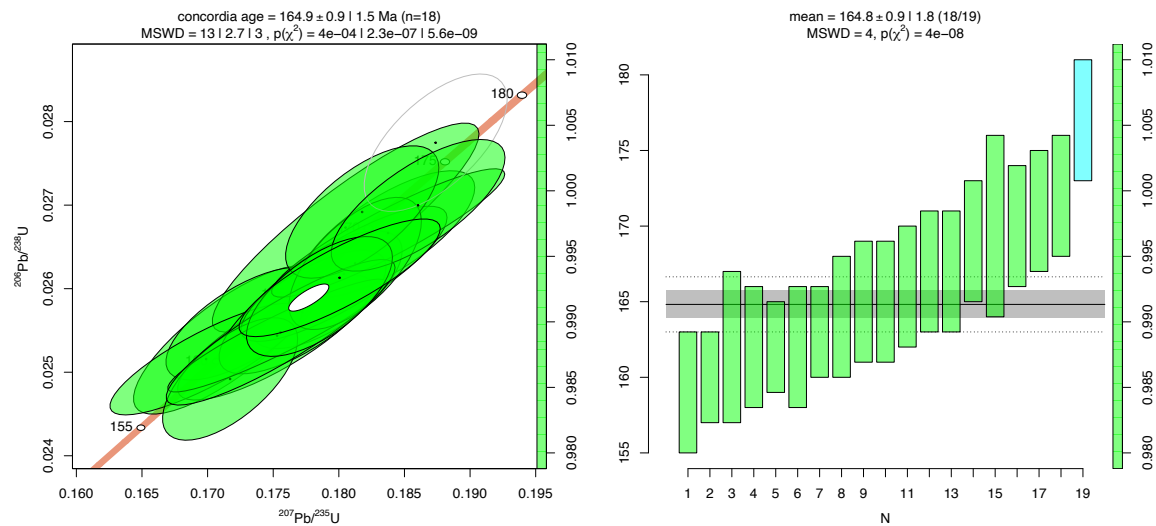
20-JRD-47:



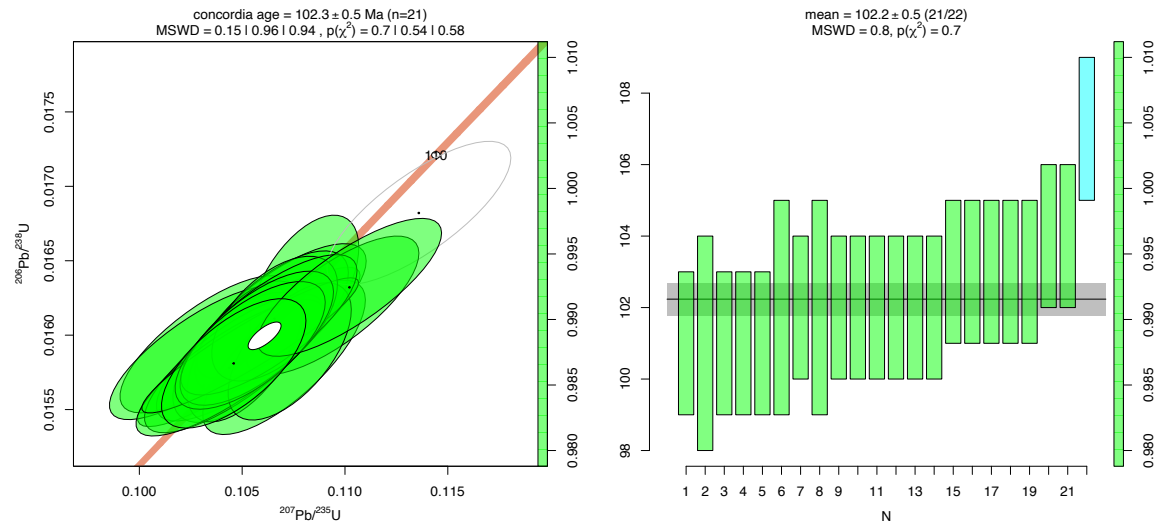
21-JRD-126:



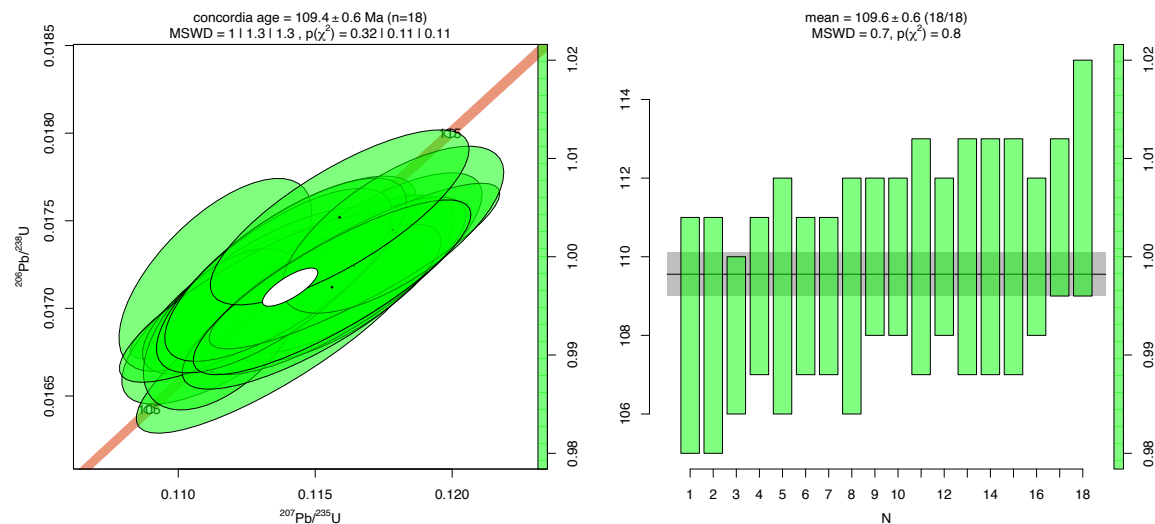
20-JRD-127:



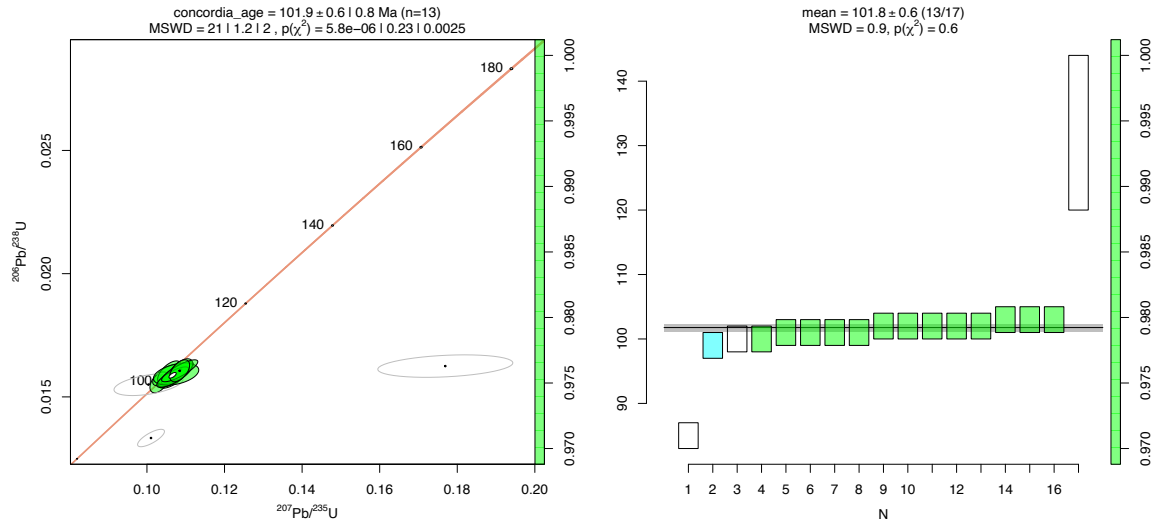
20-JRD-100B:



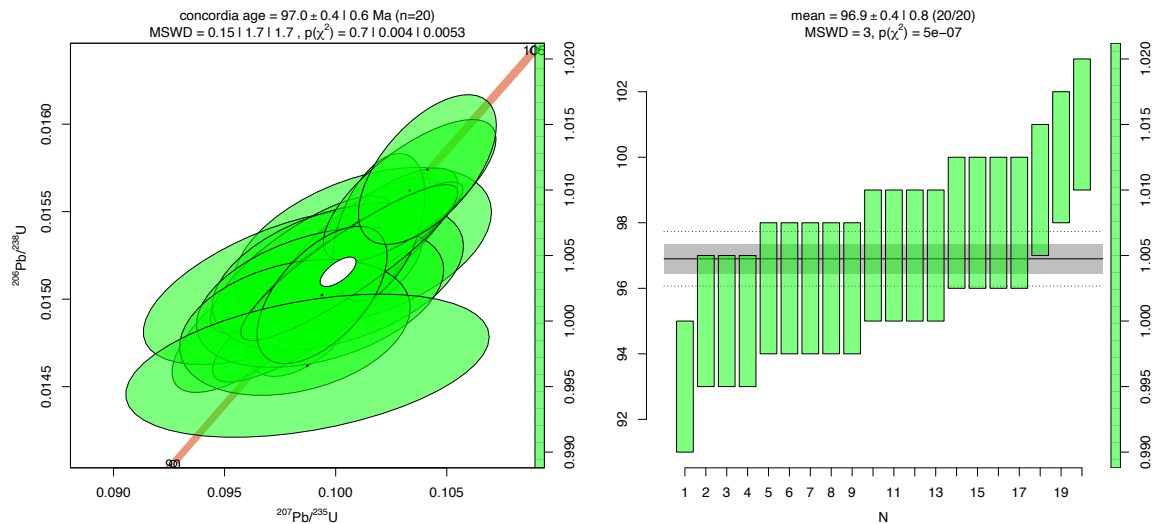
19-JRD-26:



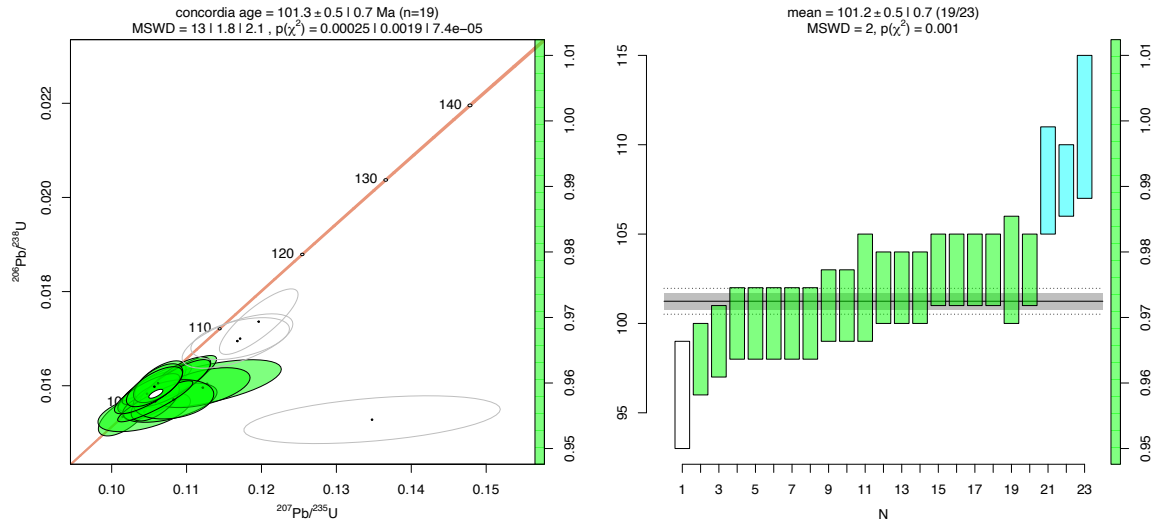
20-JRD-39: (one very discordant old grain not shown on concordia plot)



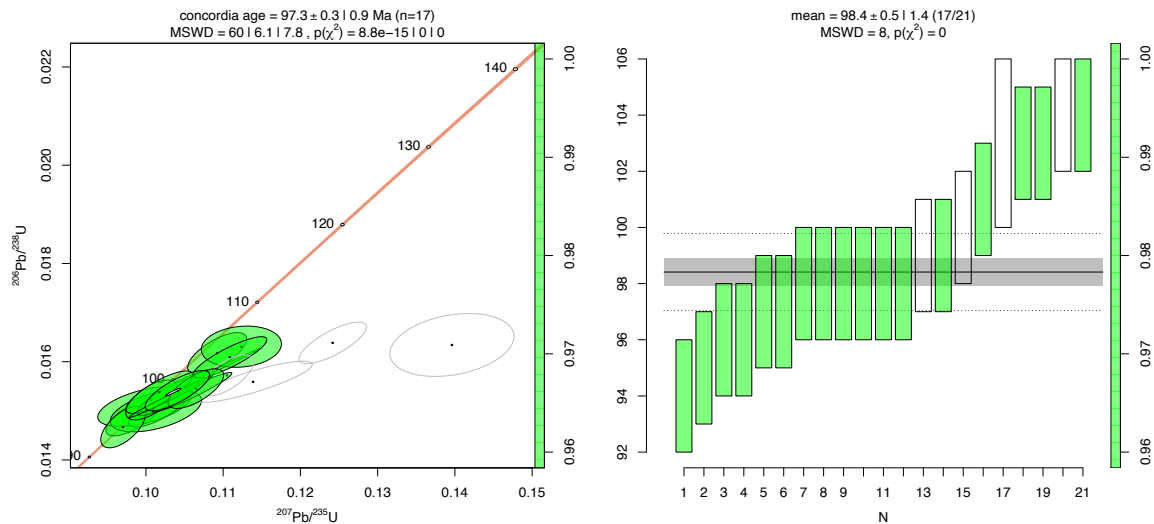
20-JRD-50B:



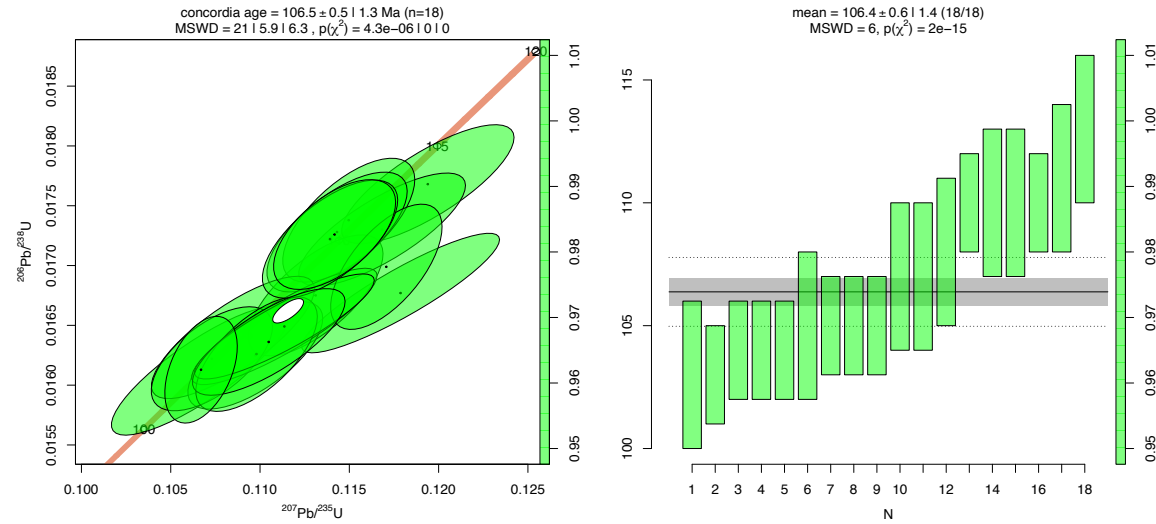
19-JRD-14:



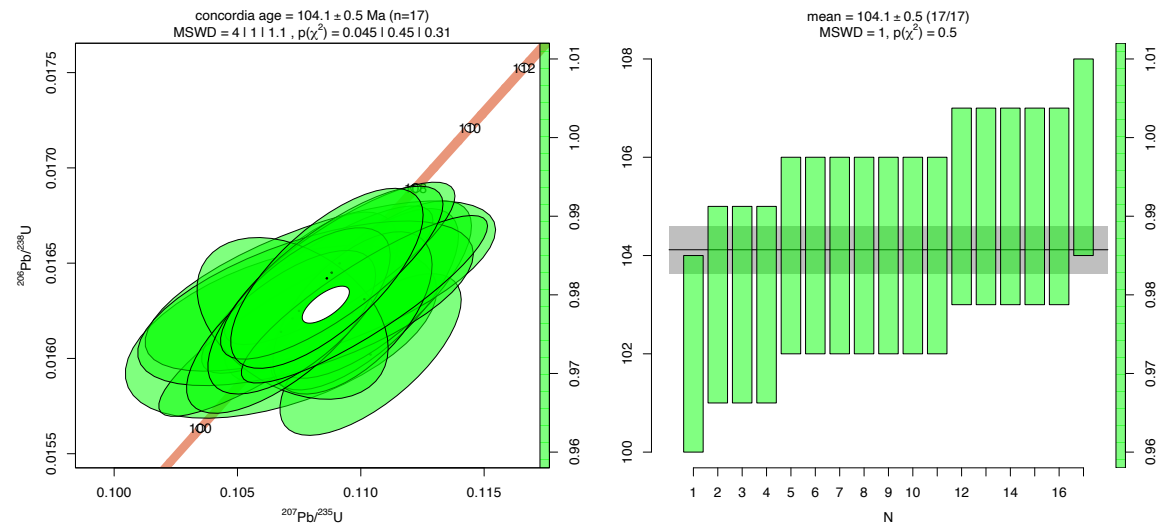
20-JRD-98:



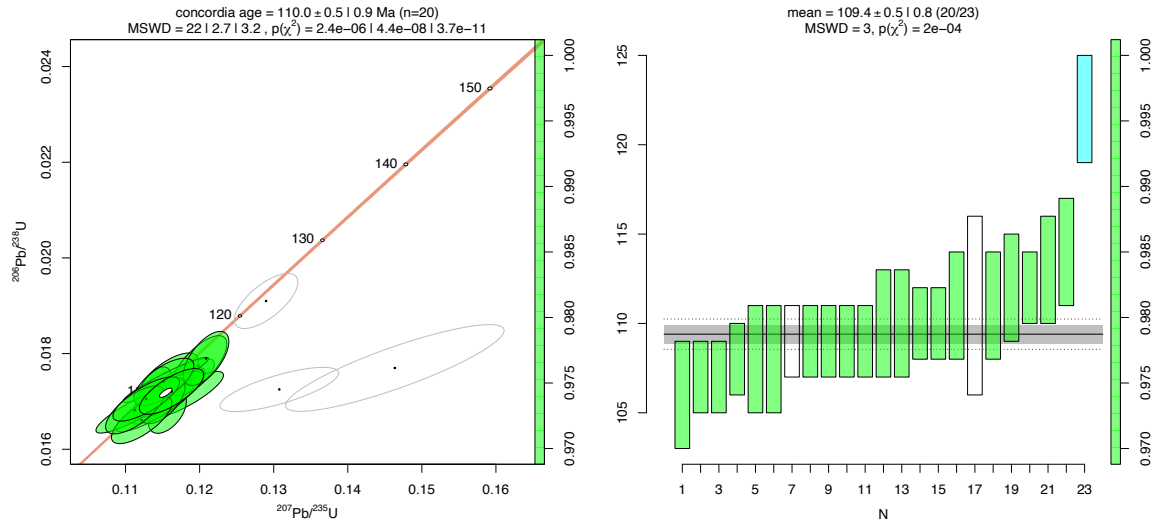
19-JRD-07:



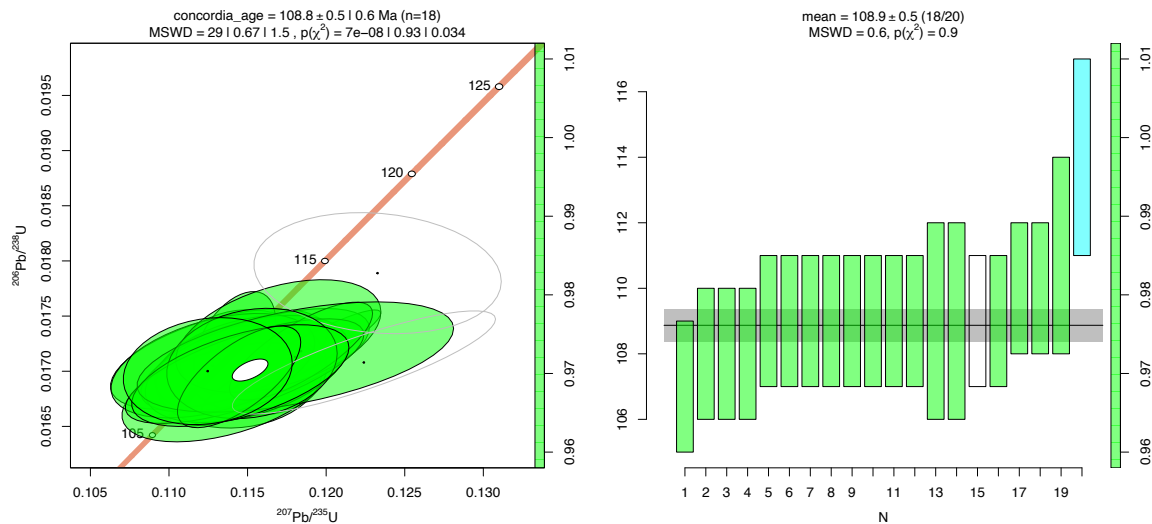
19-JRD-09:



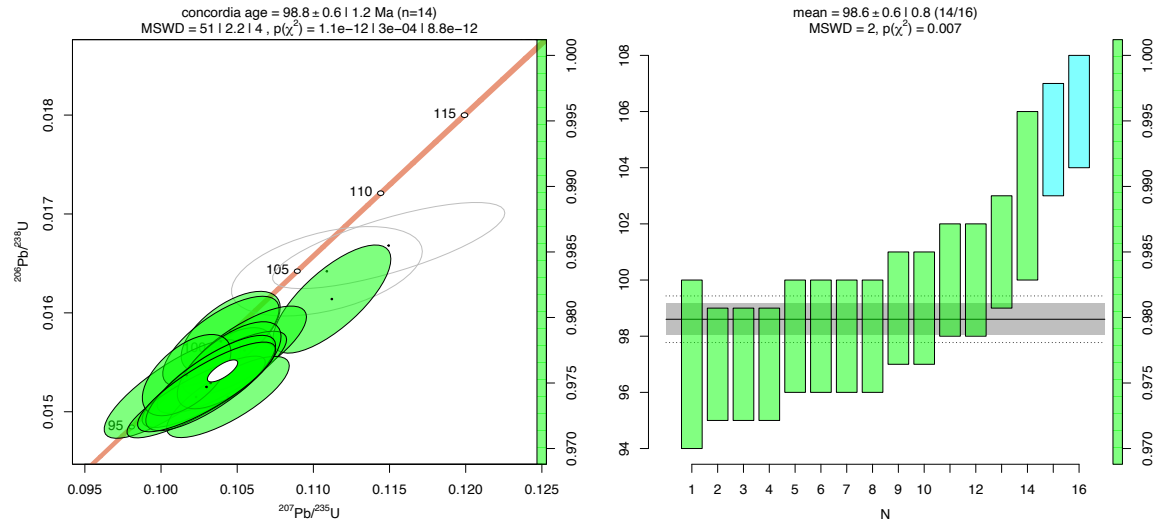
19-JRD-18:



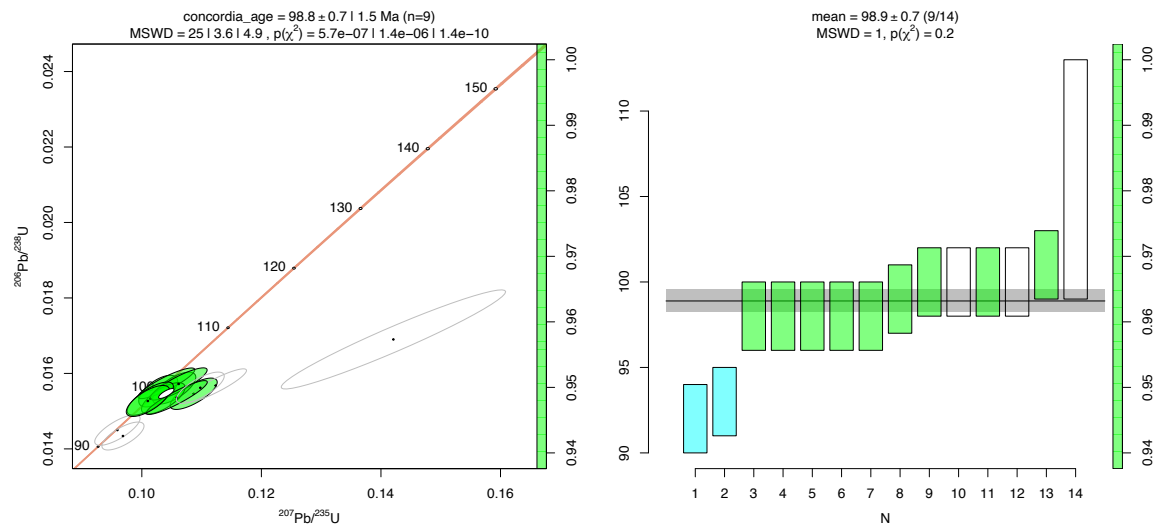
19-JRD-21:



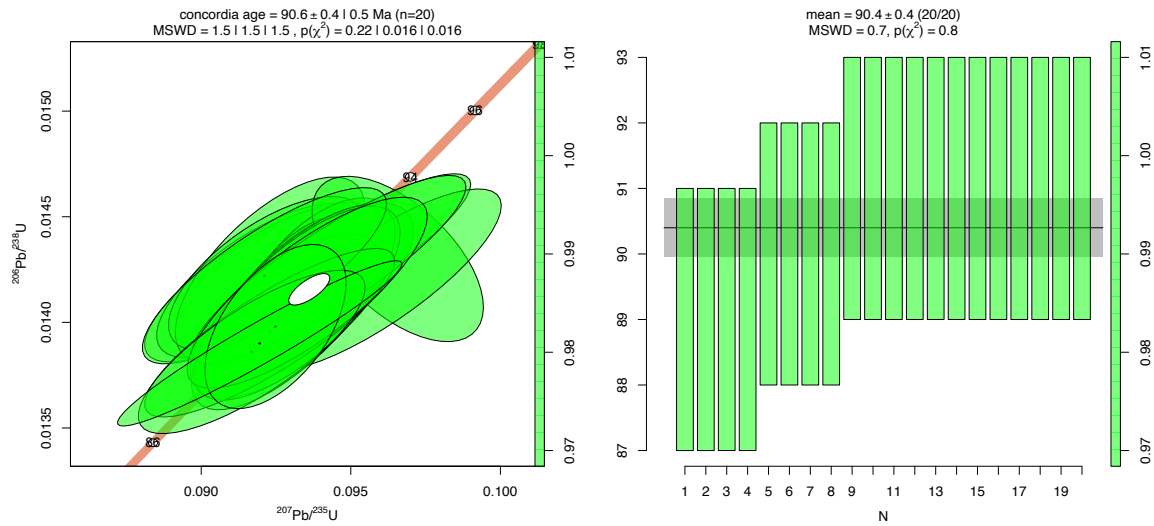
20-KC-38:



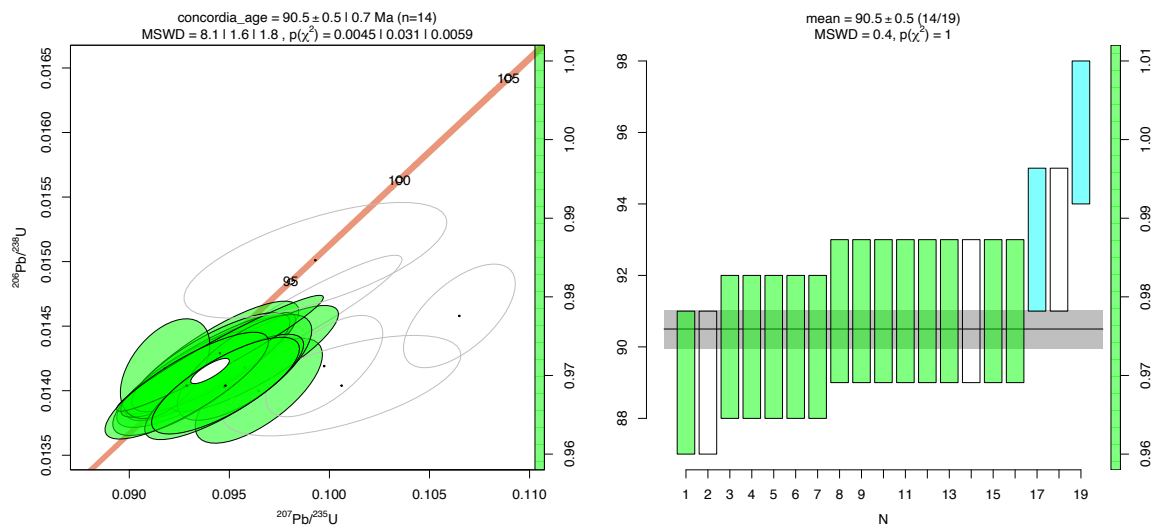
20-JRD-69: (3 discordant grains not plotted, two ~1000 Ma and one 0 Ma/no data):



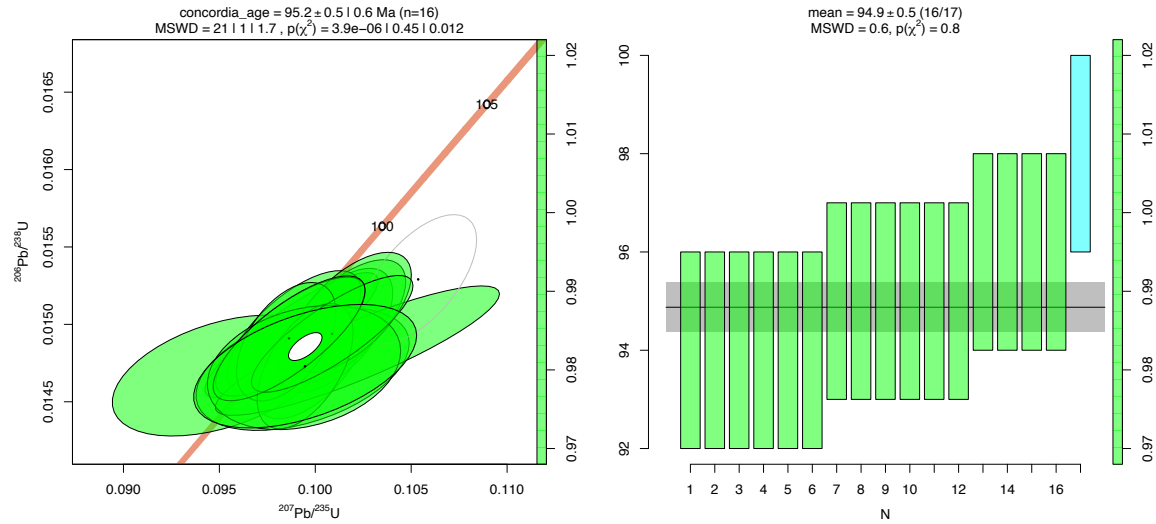
20-JRD-65:



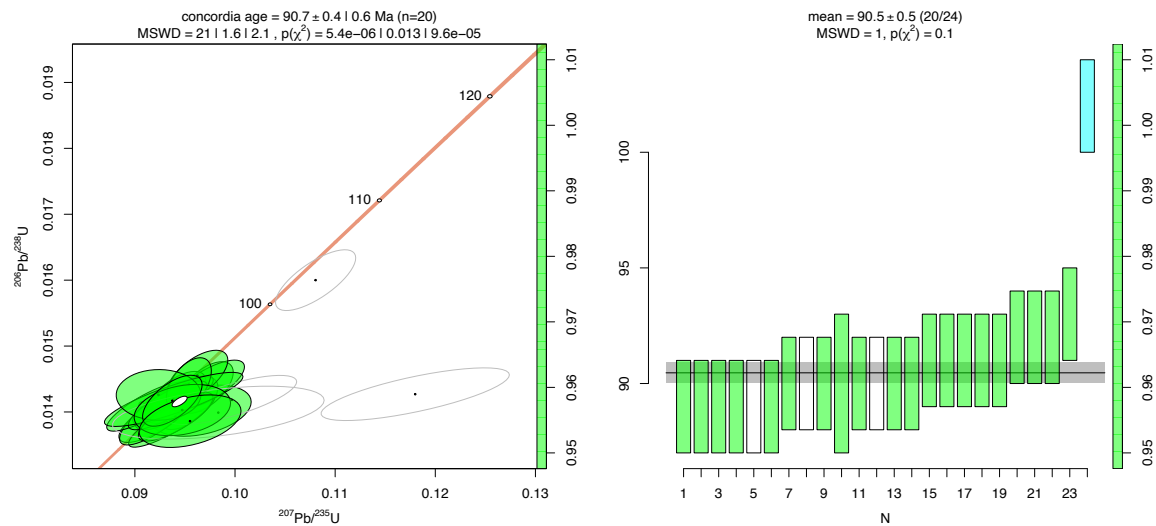
20-JRD-67:



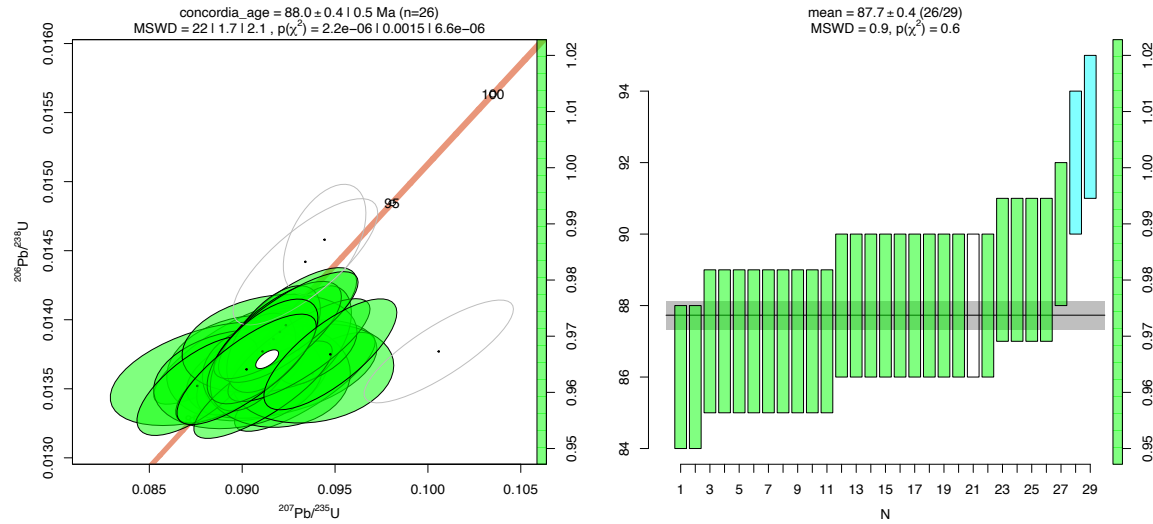
19-JRD-01:



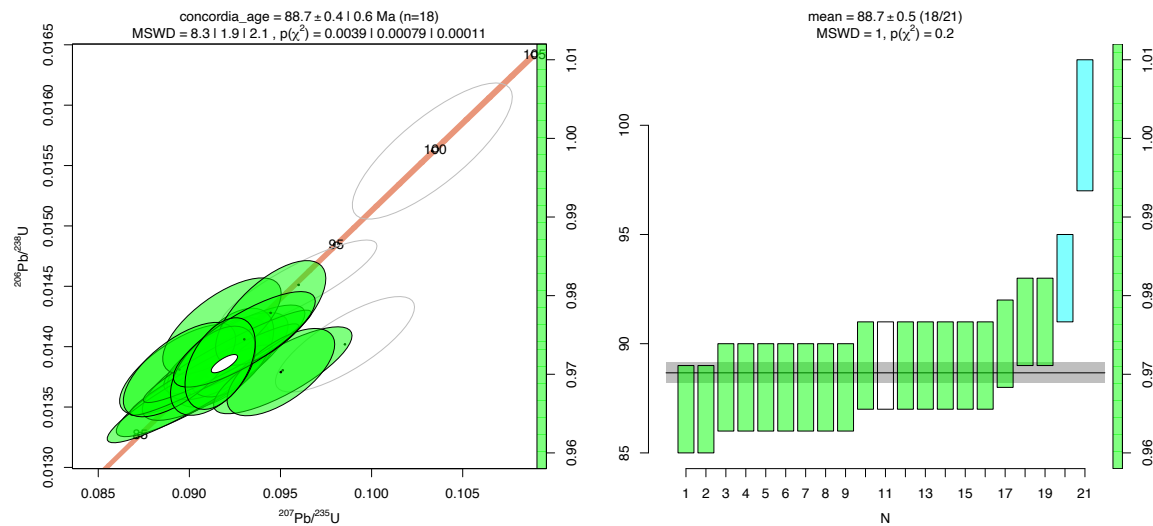
19-JRD-03:



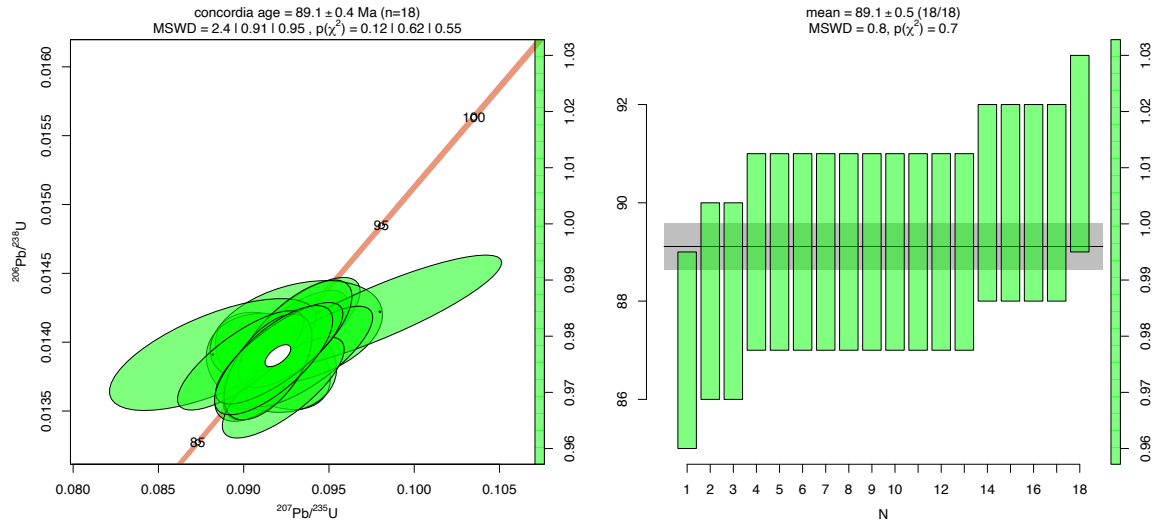
20-JRD-73:



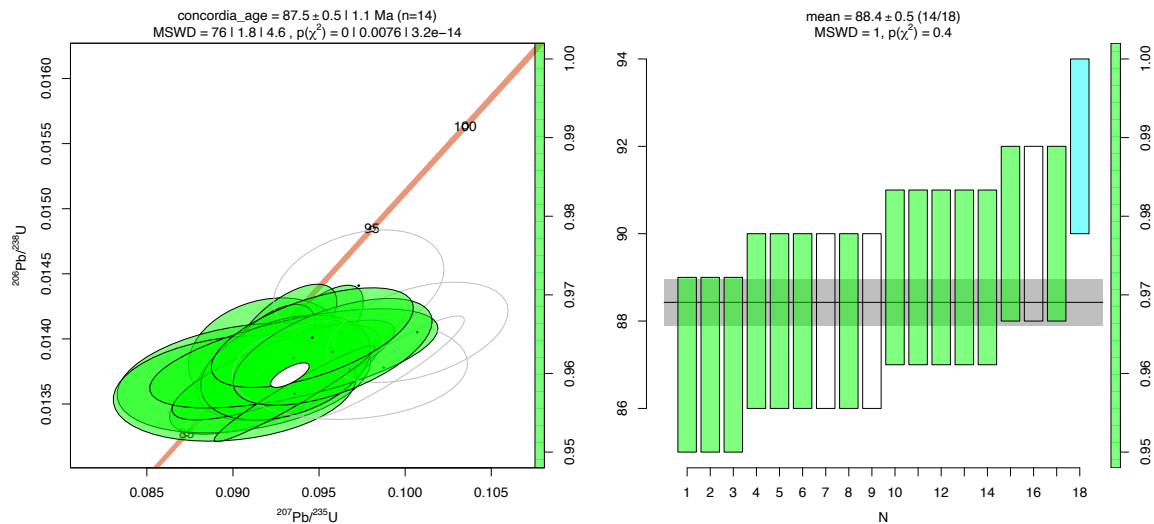
20-JRD-75A:



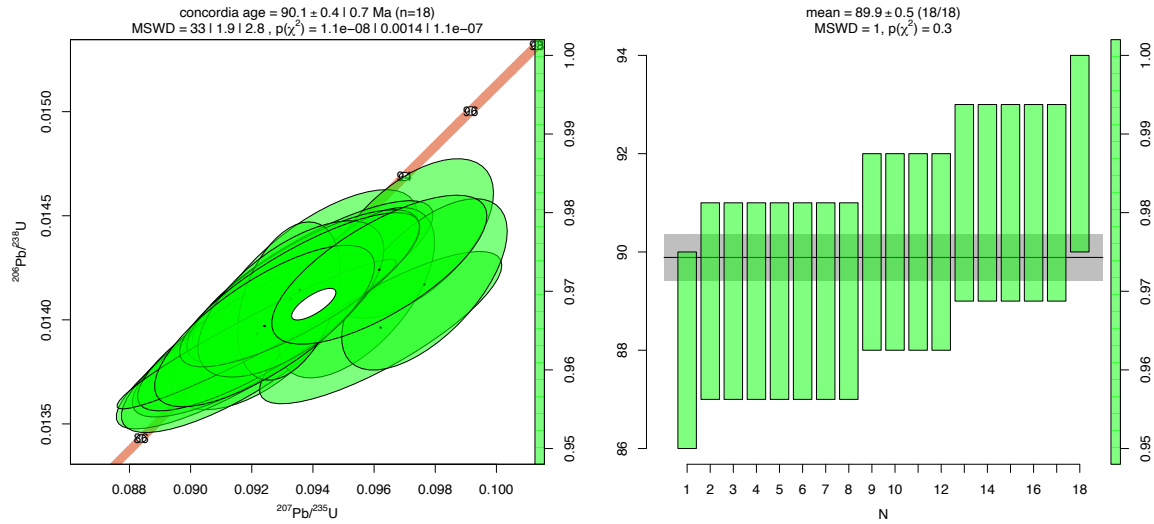
20-JRD-75B:



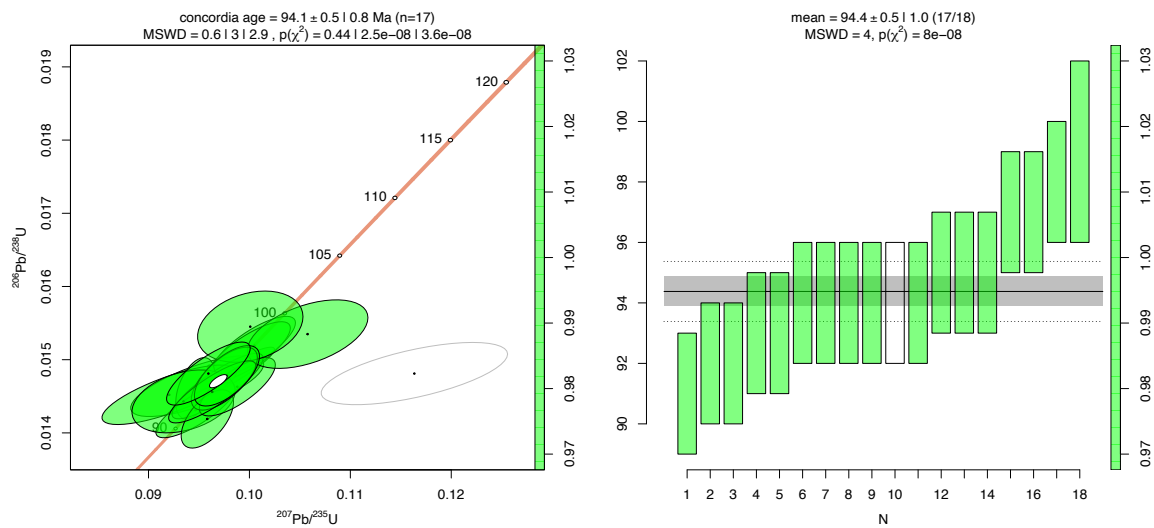
20-JRD-76:



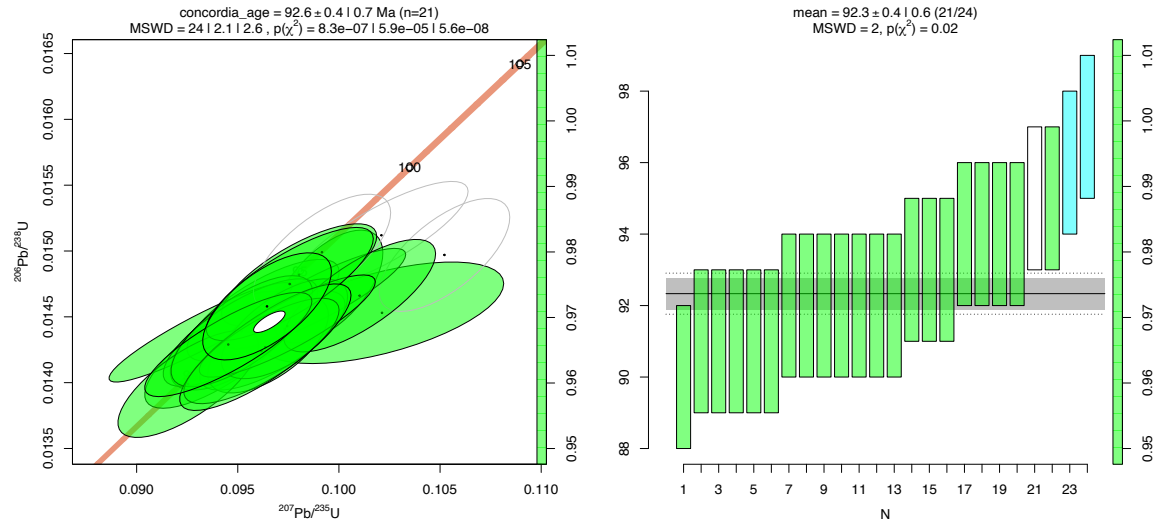
20-JRD-87:



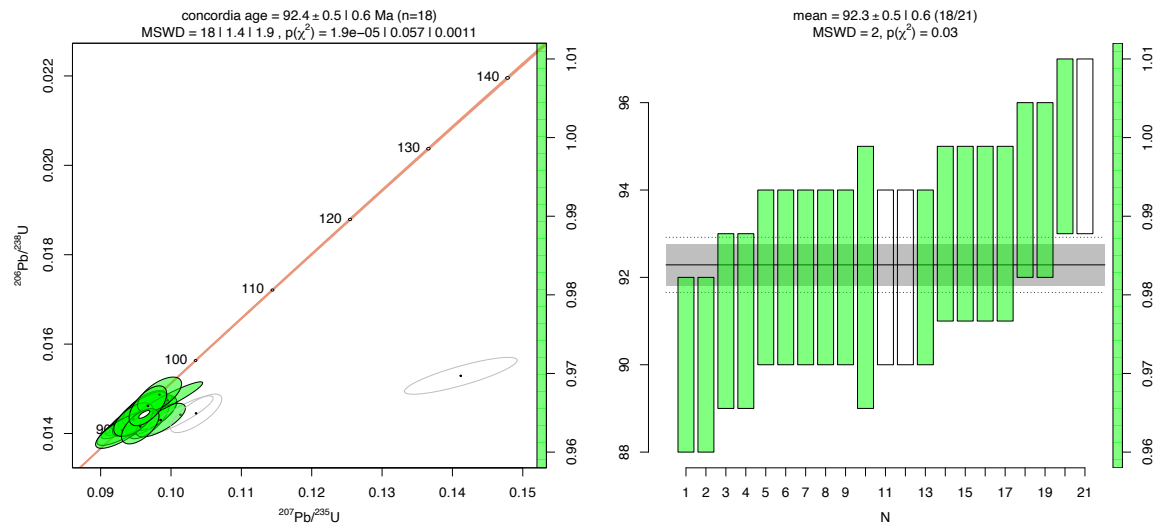
20-JRD-82:



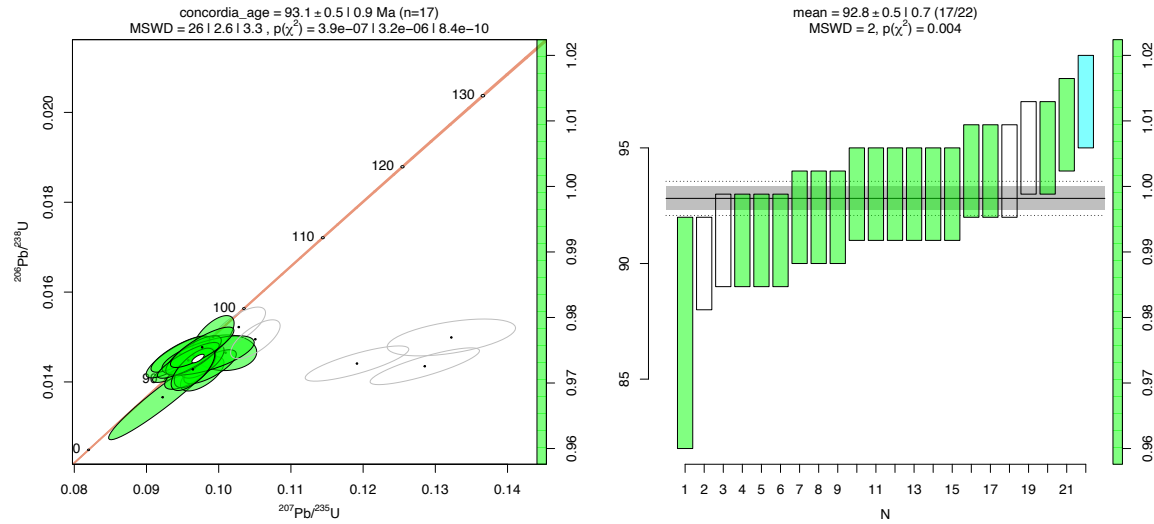
20-JRD-83:



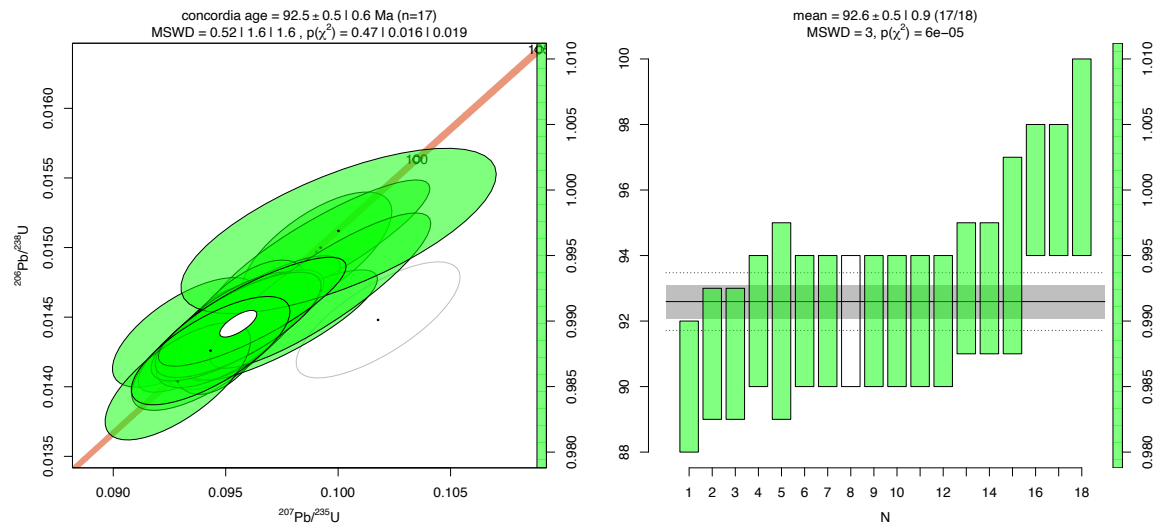
20-JRD-85C:



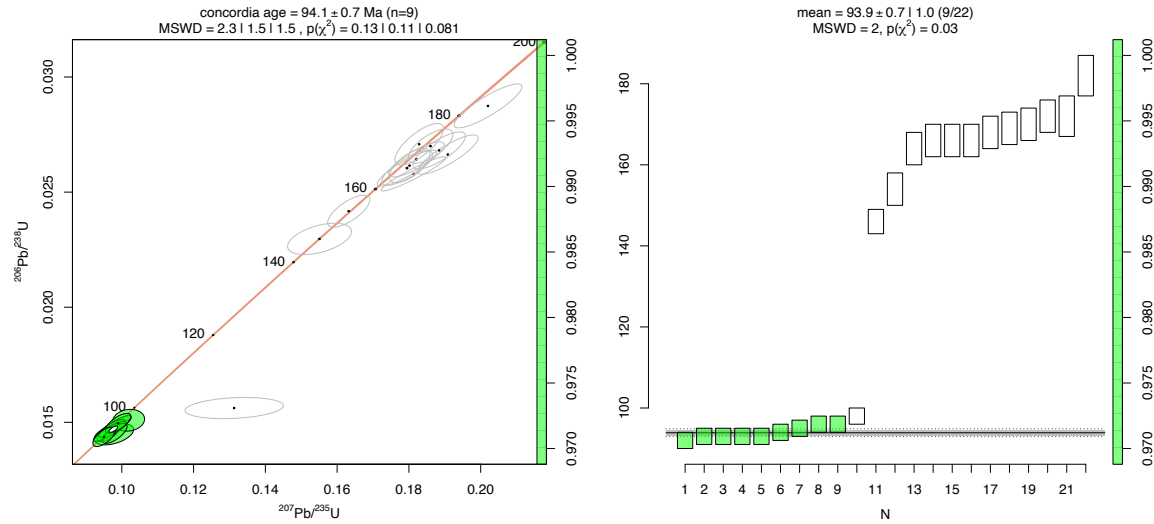
20-JRD-79:



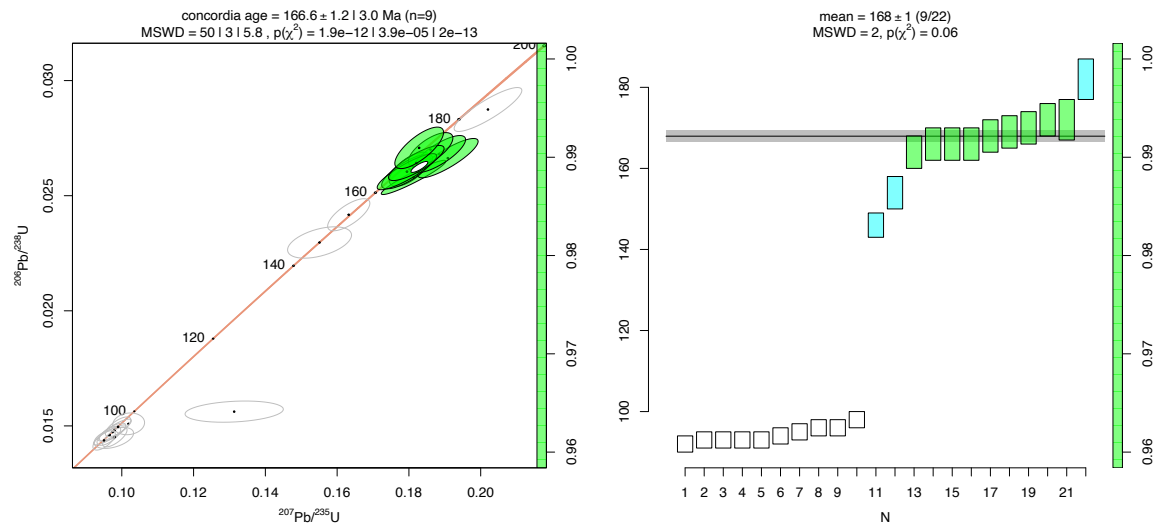
20-JRD-91B:



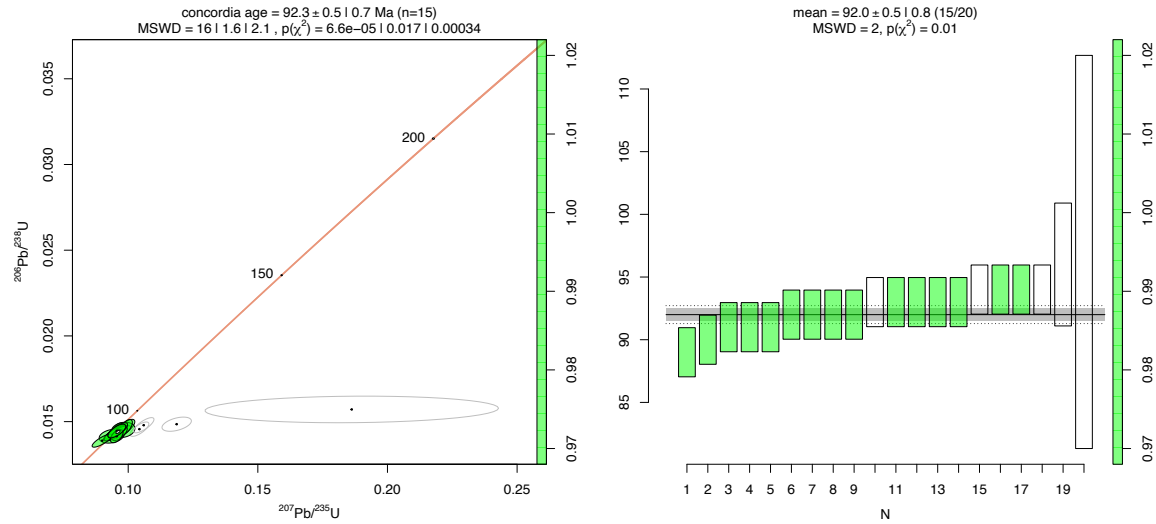
20-JRD-94-young:



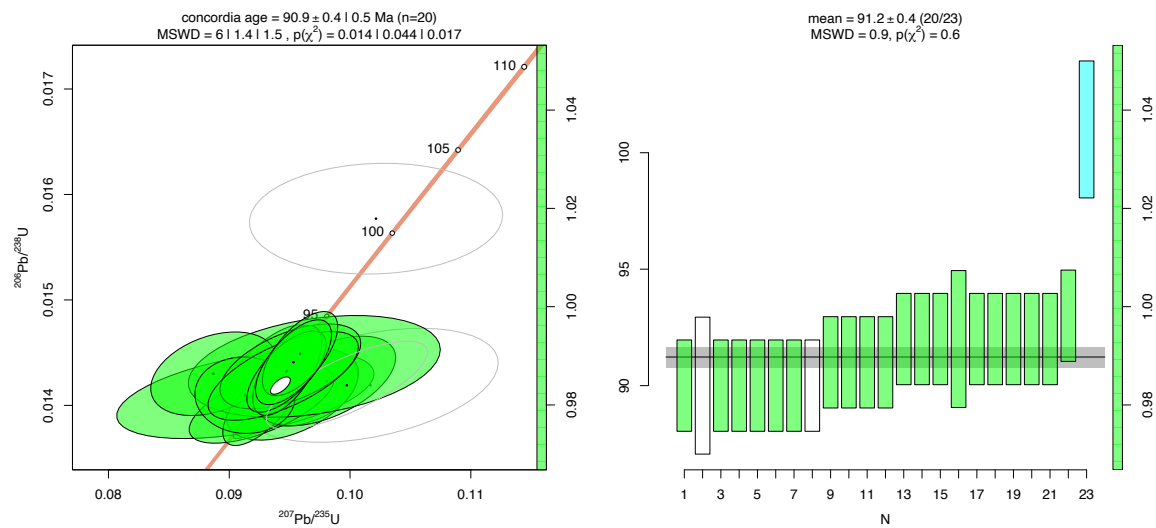
20-JRD-94-old:



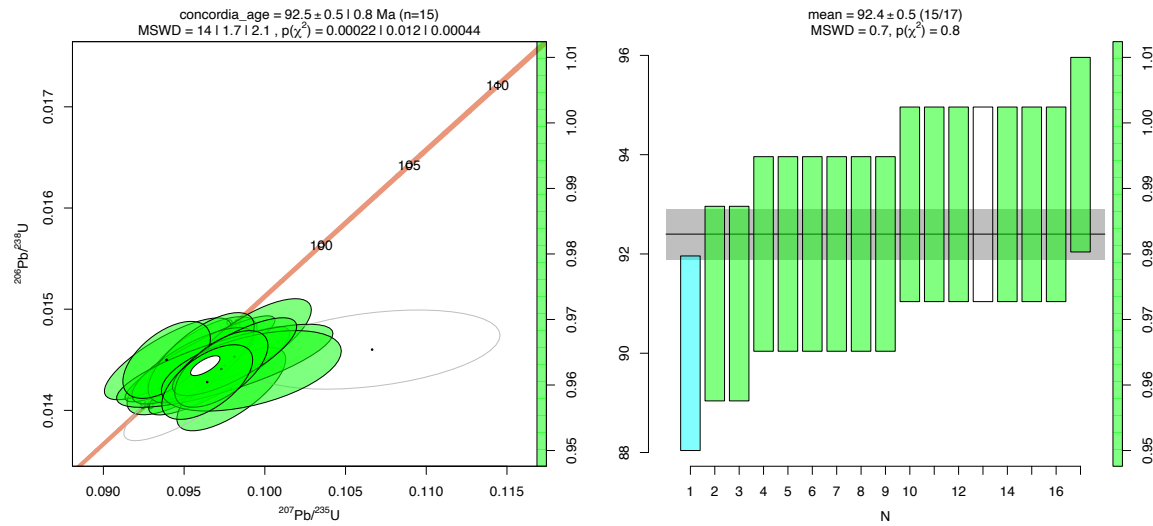
86S52A: (not plotted on Concordia: one very discordant grain)



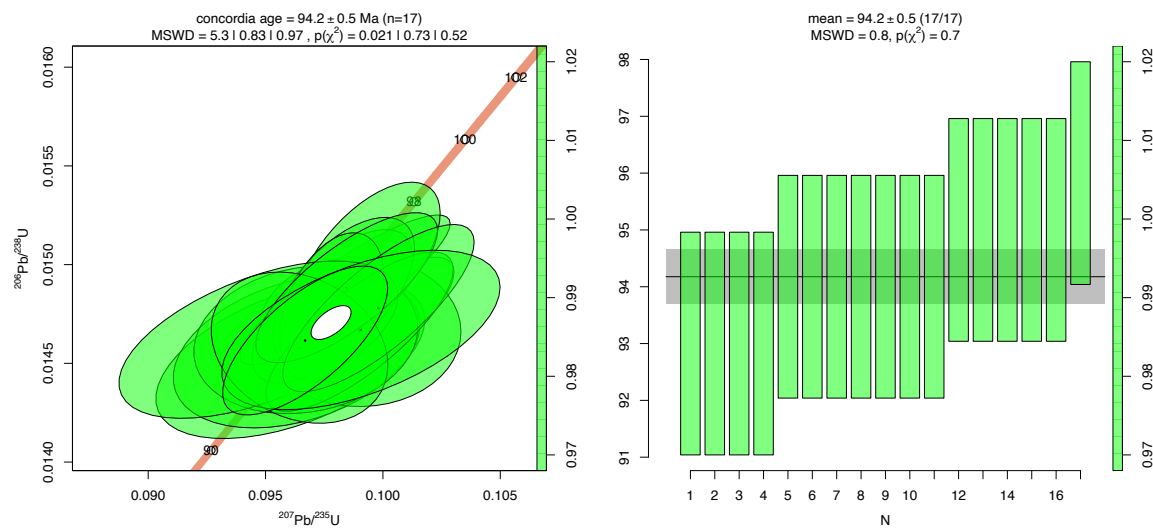
86S57:



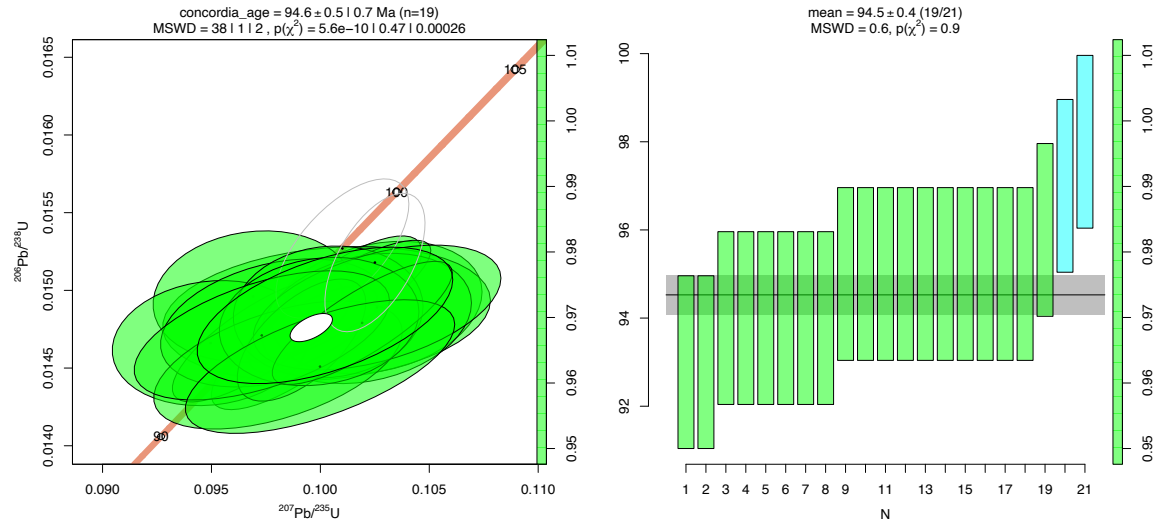
SNB-18-18:



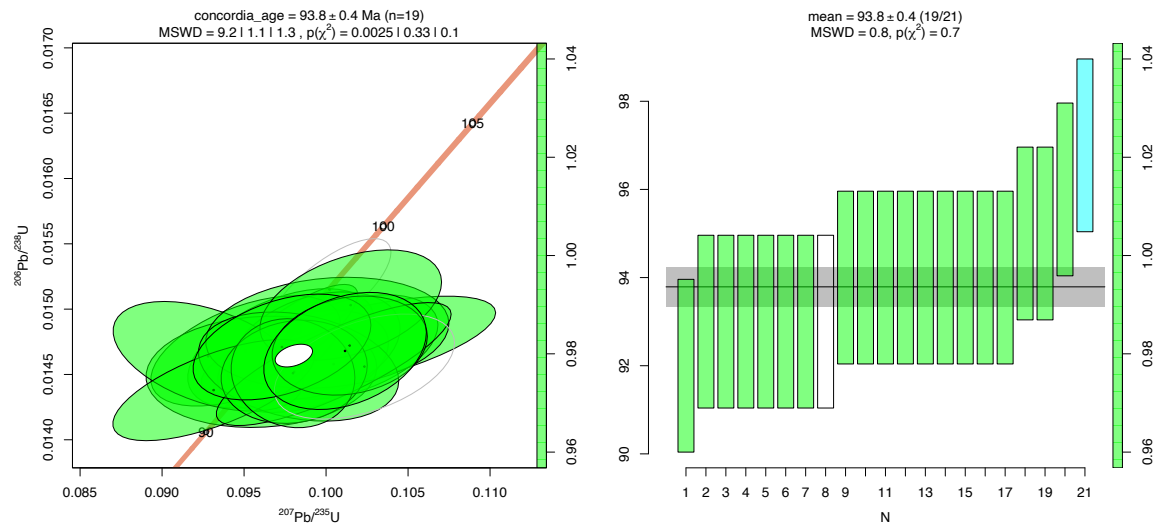
SNB-14-30:



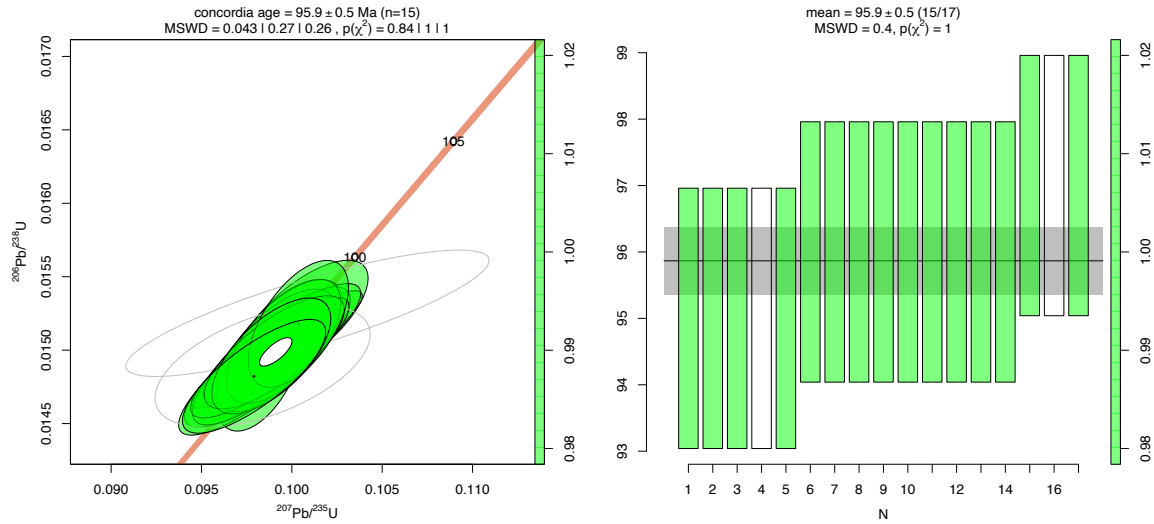
SNB-14-34:



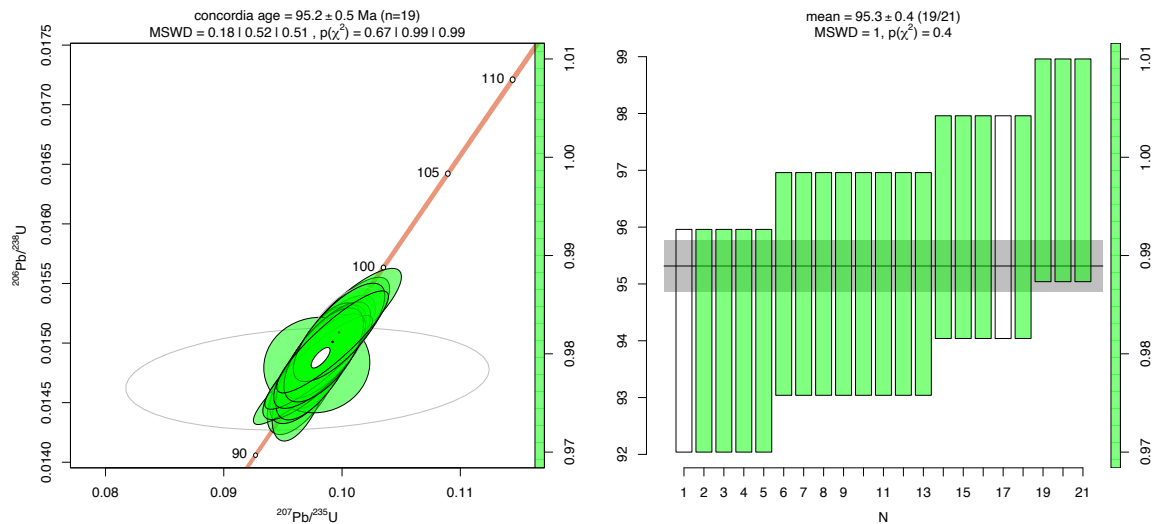
SNB-16-02:



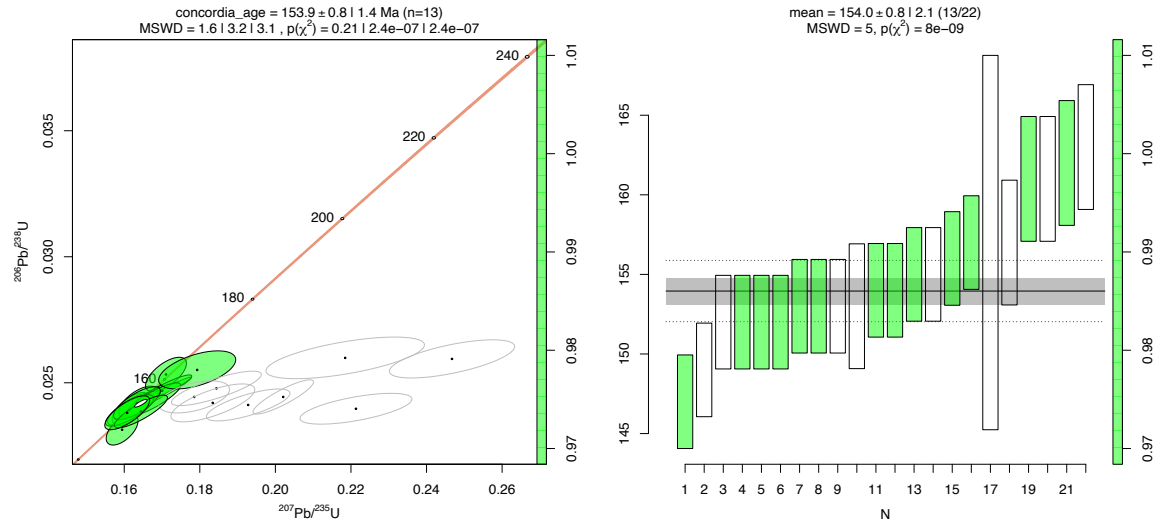
SNB-16-06:



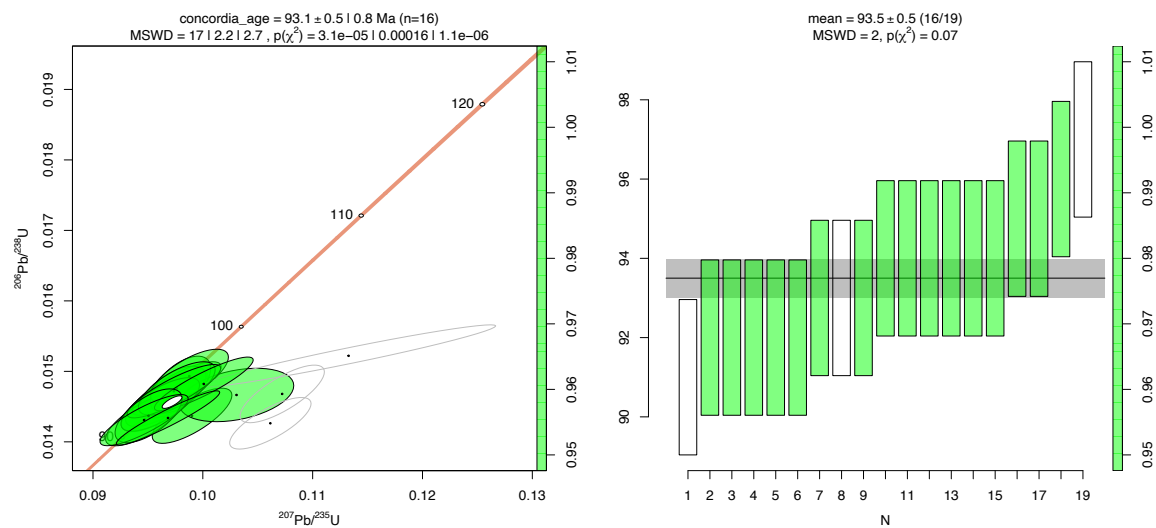
SNB-16-21:



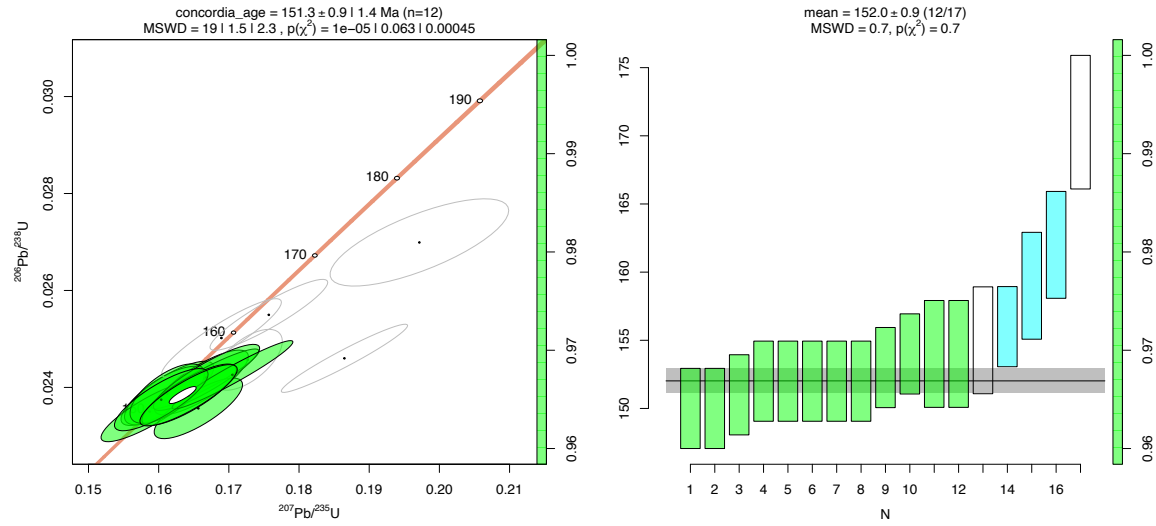
SNB-18-43: (one very discordant grain not plotted on concordia):



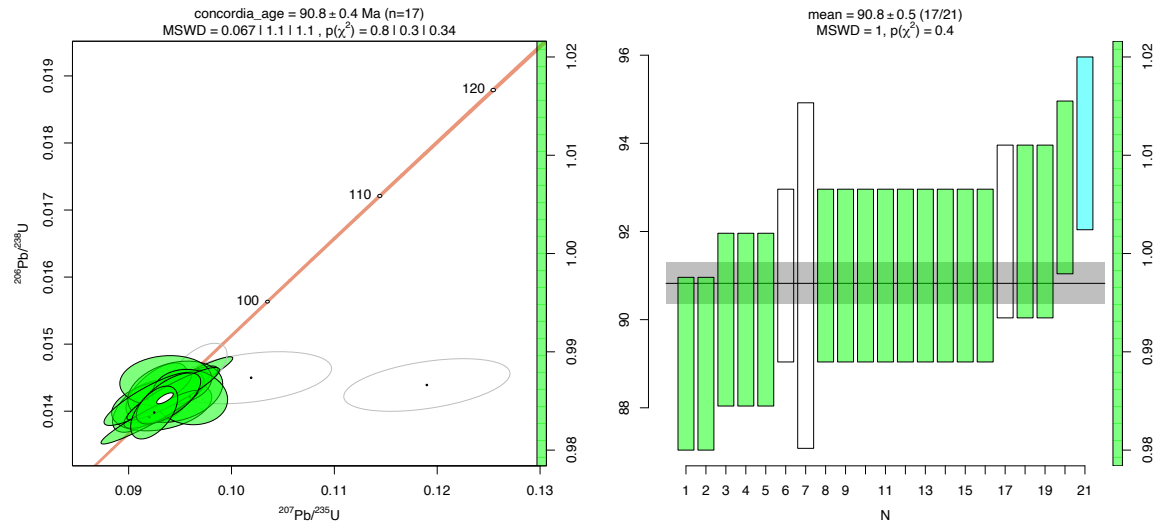
SNB-19-44A:



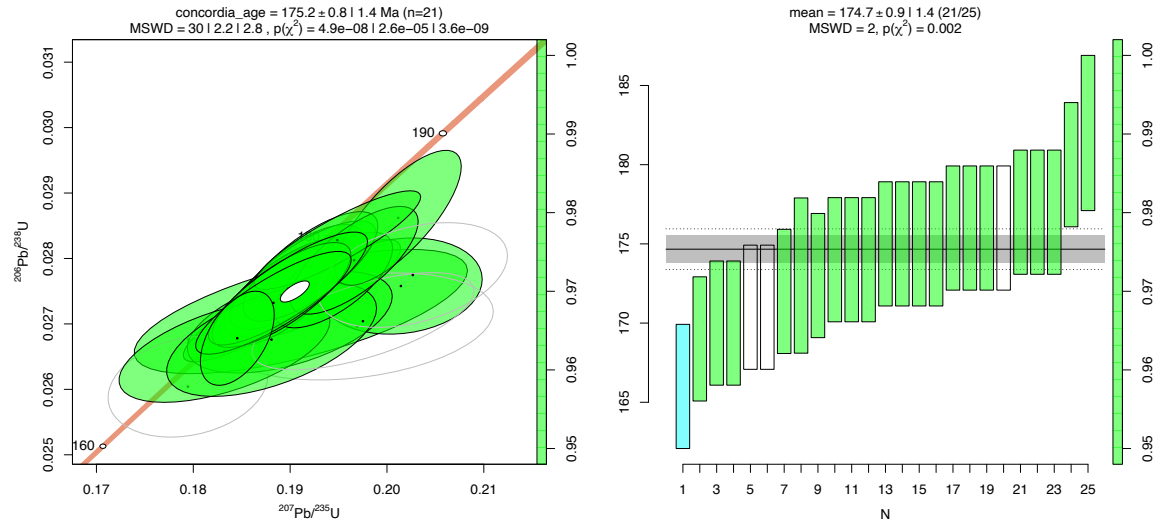
SNB-19-68:



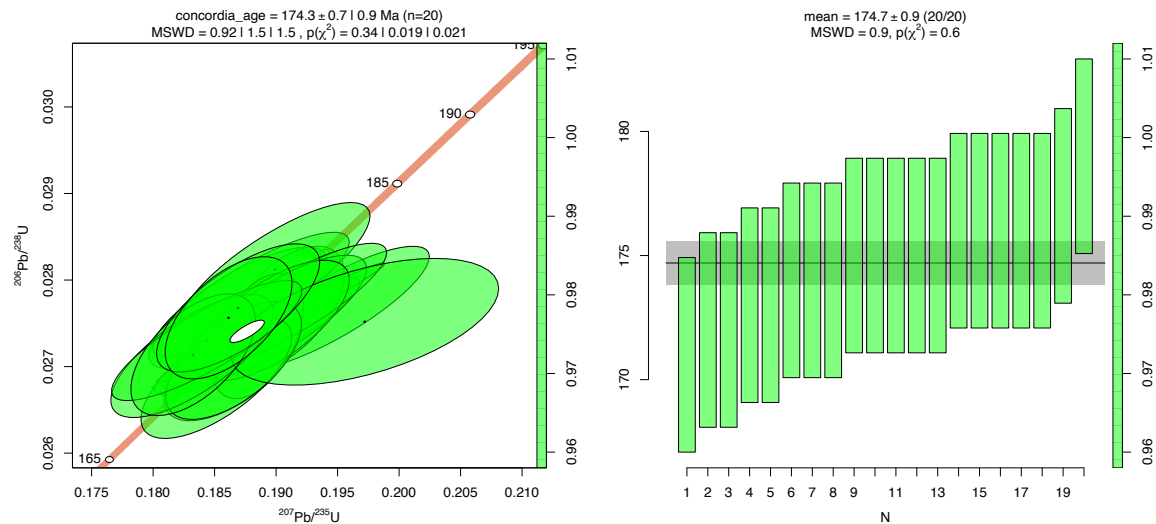
SNB-18-55A: (one very discordant grain not plotted on concordia):



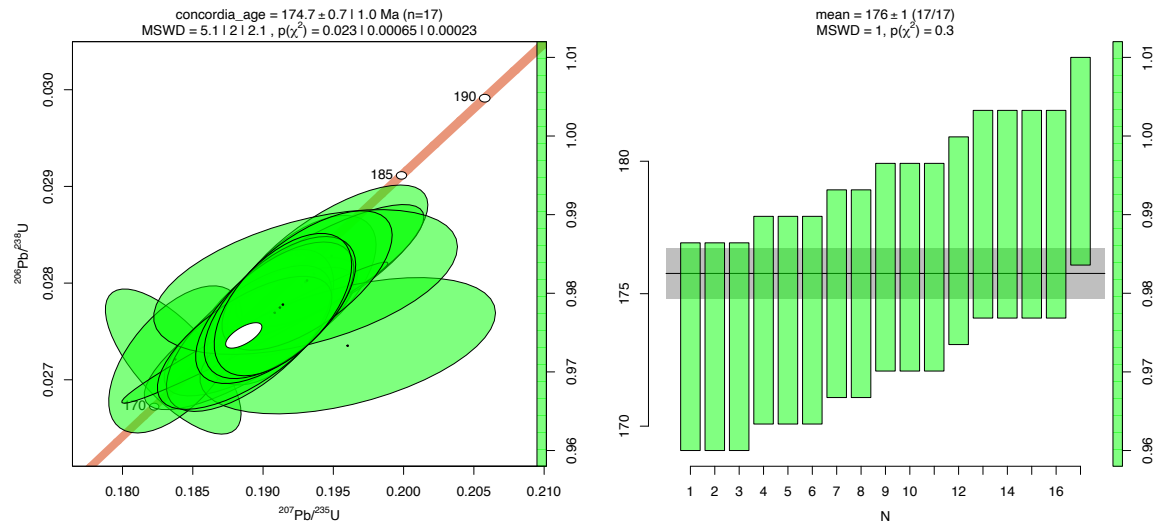
20-JRD-108:



20-JRD-109:

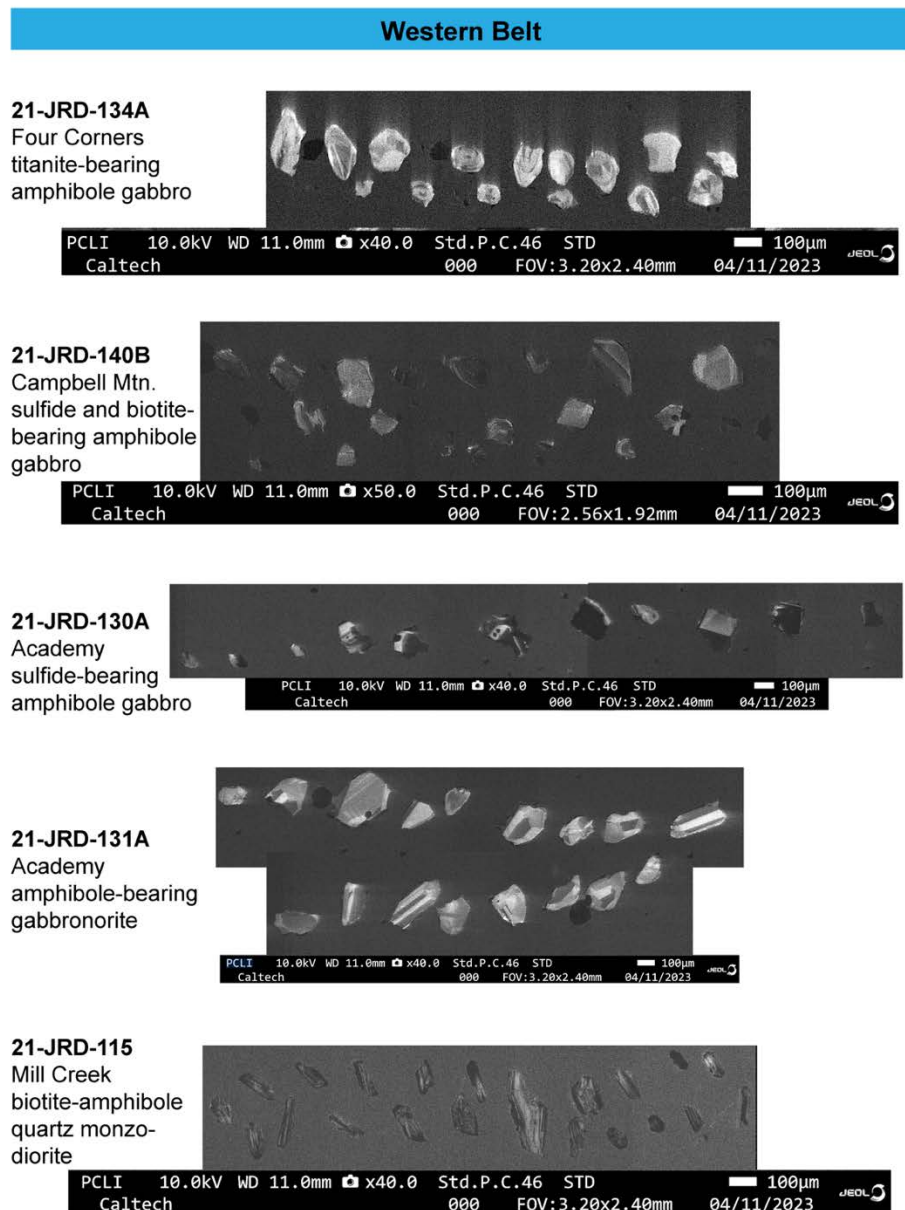


20-JRD-106:



APPENDIX 3

Cathodoluminescence images of representative zircons



Western Belt**21-JRD-116**

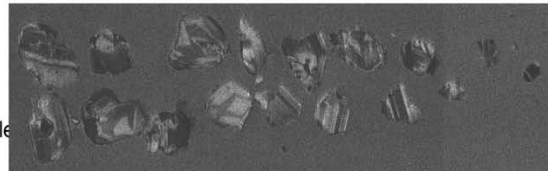
Mill Creek
clinopyroxene-
bearing amphibole
gabbro



PCL1 10.0kV WD 11.0mm x40.0 Std.P.C.46 STD 100µm
Caltech 000 FOV:3.20x2.40mm 04/11/2023 JEOL

21-JRD-117

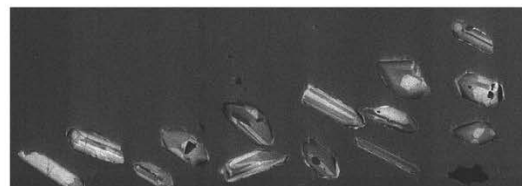
Mill Creek
clinopyroxene-
bearing amphibole
gabbro



PCL1 10.0kV WD 11.0mm x40.0 Std.P.C.46 STD 100µm
Caltech 000 FOV:3.20x2.40mm 04/11/2023 JEOL

21-JRD-126

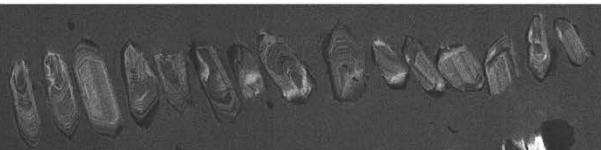
Verplank
amphibole
quartz monzo-
gabbro



PCL1 10.0kV WD 11.0mm x50.0 Std.P.C.46 STD 100µm
Caltech 000 FOV:2.56x1.92mm 04/11/2023 JEOL

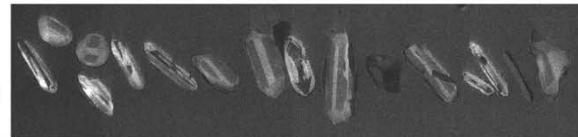
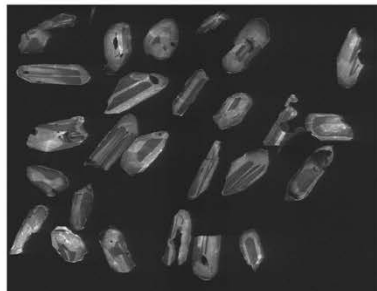
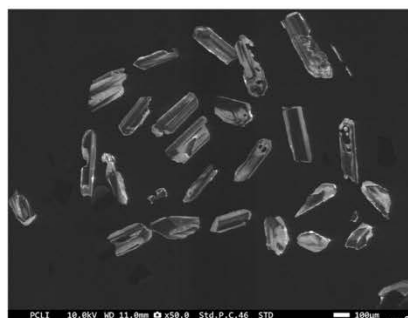
21-JRD-127A

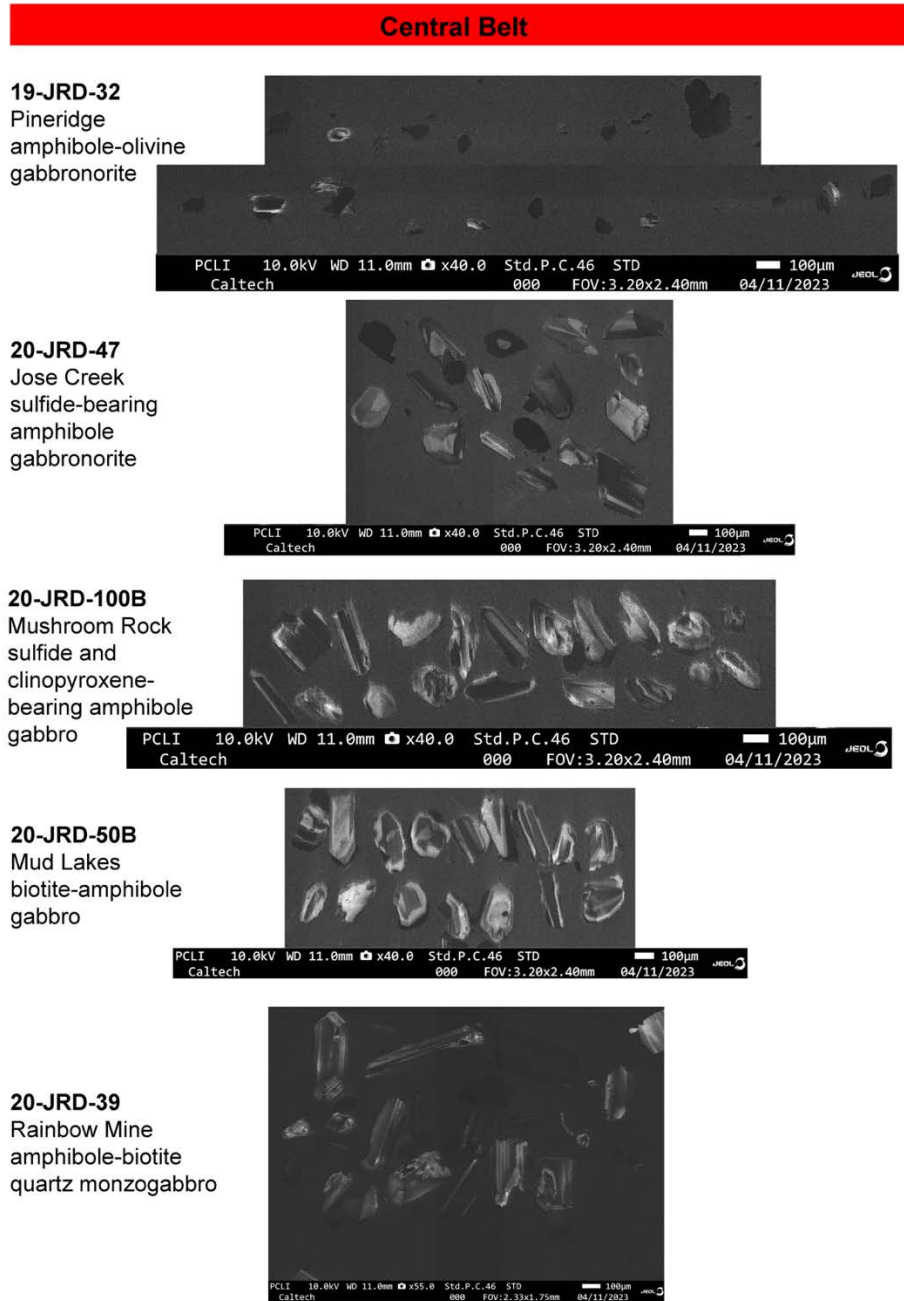
Verplank
porphyritic
biotite
granodiorite



PCL1 10.0kV WD 11.0mm x40.0 Std.P.C.46 STD 100µm
Caltech 000 FOV:3.20x2.40mm 04/11/2023 JEOL

Western Belt

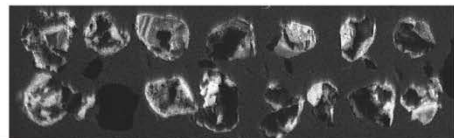
20-JRD-33O'Neals
amphibole-biotite
gabbroPCL1 10.0kV WD 11.0mm x40.0 Std.P.C.46 STD
Caltech 000 FOV:3.20x2.40mm 04/11/2023 JEOL**20-JRD-35A**Fine Gold
amphibole-biotite
quartz monzogabbroPCL1 10.0kV WD 11.0mm x50.0 Std.P.C.46 STD
Caltech 000 FOV:2.13x1.68mm 04/11/2023 JEOL**20-JRD-58B**Millerton Lake
amphibole gabbroPCL1 10.0kV WD 11.0mm x50.0 Std.P.C.46 STD
Caltech 000 FOV:2.13x1.68mm 04/11/2023 JEOL**21-JRD-137**Big Sandy
porphyritic biotite-
amphibole quartz
monzodioritePCL1 10.0kV WD 11.0mm x40.0 Std.P.C.46 STD
Caltech 000 FOV:3.20x2.40mm 04/11/2023 JEOL



Central Belt

19-JRD-14
Hall Mountain
sulfide and
clinopyroxene-
bearing amphibole
gabbro

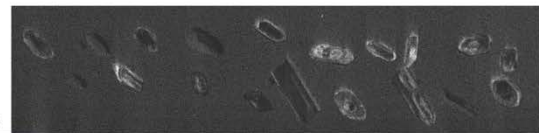
PCLI 10.0kV WD 11.0mm x40.0 Std.P.C.46 STD
Caltech 000 FOV:3.20x2.40mm 04/11/2023



100µm JEOL

20-JRD-98
Short Hair Mdw.
quartz
leucomonzodiorite

PCLI 10.0kV WD 11.0mm x40.0 Std.P.C.46 STD
Caltech 000 FOV:3.20x2.40mm 04/11/2023



100µm JEOL

19-JRD-26
Dinkey Mtn.
amphibole
gabbro

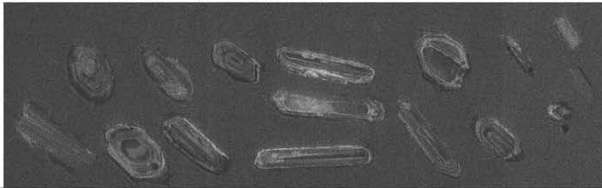
PCLI 10.0kV WD 11.0mm x40.0 Std.P.C.46 STD
Caltech 000 FOV:3.20x2.40mm 04/11/2023



100µm JEOL

19-JRD-07
Lower Kings R.
quartz
monzodiorite

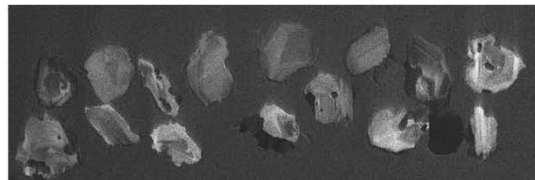
PCLI 10.0kV WD 11.0mm x40.0 Std.P.C.46 STD
Caltech 000 FOV:3.20x2.40mm 04/11/2023



100µm JEOL

Central Belt

19-JRD-09
Lower Kings R.
titanite-bearing
biotite-amphibole
gabbro



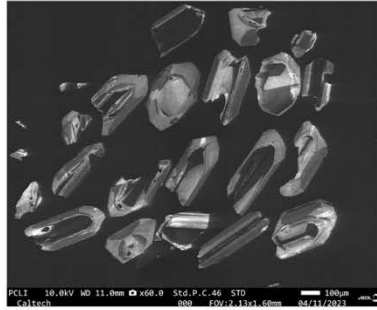
PCLT 10.0kV WD 11.0mm x40.0 Std.P.C.46 STD
Caltech 000 FOV:3.20x2.40mm 04/11/2023 100µm JEOL

19-JRD-18
Garlic Meadow
amphibole-biotite
quartz monzodiorite



PCLT 10.0kV WD 11.0mm x55.0 Std.P.C.46 STD
Caltech 000 FOV:2.33x1.75mm 04/11/2023 100µm JEOL

19-JRD-21
Garlic Meadow
biotite-amphibole
gabbro /
amphibolite *



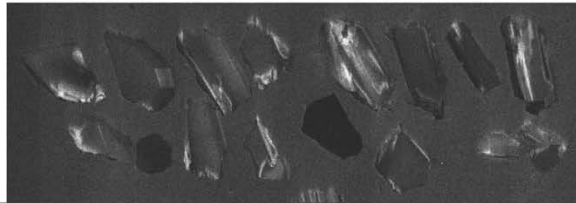
PCLT 10.0kV WD 11.0mm x60.0 Std.P.C.46 STD
Caltech 000 FOV:2.13x1.60mm 04/11/2023 100µm JEOL

20-KC-38
Heart Meadow
sulfide-bearing
amphibole
monzogabbro



PCLT 10.0kV WD 11.0mm x40.0 Std.P.C.46 STD
Caltech 000 FOV:3.20x2.40mm 04/11/2023 100µm JEOL

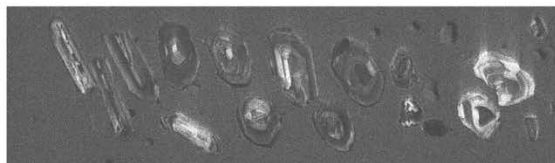
High Sierra Belt

20-JRD-65Hogback
titanite-bearing
amphibole-
biotite
monzogabbro

PCL1 10.0kV WD 11.0mm x40.0 Std.P.C.46 STD 100µm
Caltech 000 FOV:3.20x2.40mm 04/11/2023 JEOL

20-JRD-67Hogback
titanite-bearing
amphibole
quartz
monzodiorite

PCL1 10.0kV WD 11.0mm x40.0 Std.P.C.46 STD 100µm
Caltech 000 FOV:3.20x2.40mm 04/11/2023 JEOL

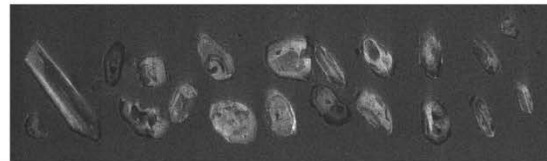
19-JRD-01Kennedy
amphibole-
biotite
quartz
monzodiorite

PCL1 10.0kV WD 11.0mm x40.0 Std.P.C.46 STD 100µm
Caltech 000 FOV:3.20x2.40mm 04/11/2023 JEOL

High Sierra Belt

19-JRD-03

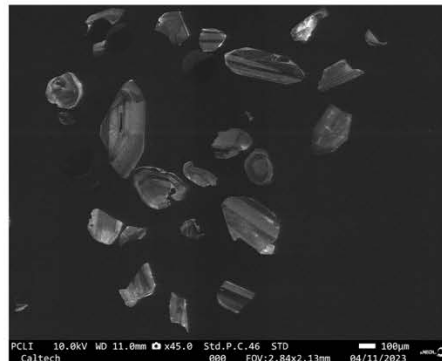
Volcanic Lakes
clinopyroxene
bearing
amphibole
quartz monzodiorite



PCLM 10.0kV WD 11.0mm x40.0 Std.P.C.46 STD 100µm
Caltech 000 FOV:3.20x2.40mm 04/11/2023 JEOL

20-JRD-73

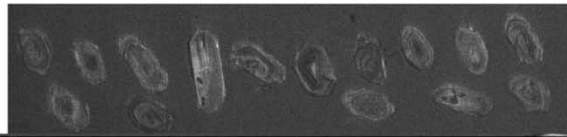
Volcanic Lakes
amphibole
gabbro



PCLM 10.0kV WD 11.0mm x45.0 Std.P.C.46 STD 100µm
Caltech 000 FOV:2.84x2.13mm 04/11/2023 JEOL

20-JRD-75A

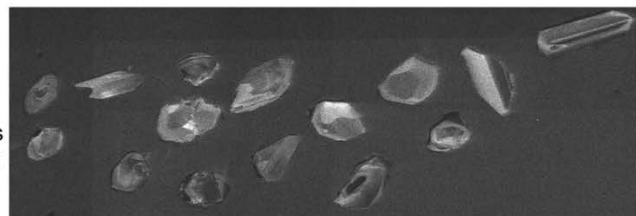
Volcanic Lakes
biotite-amphibole
monzodiorite



PCLM 10.0kV WD 11.0mm x40.0 Std.P.C.46 STD 100µm
Caltech 000 FOV:3.20x2.40mm 04/11/2023 JEOL

20-JRD-75B

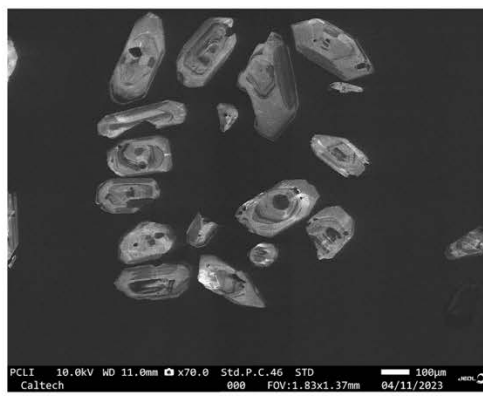
Volcanic Lakes
sulfide-bearing
leucodiorite



PCLM 10.0kV WD 11.0mm x40.0 Std.P.C.46 STD 100µm
Caltech 000 FOV:3.20x2.40mm 04/11/2023 JEOL

High Sierra Belt

20-JRD-76
 Volcanic Lakes
 clinopyroxene-
 bearing biotite-
 amphibole
 quartz monzodiorite



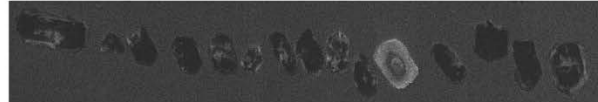
PCLI 10.0kV WD 11.0mm \times 70.0 Std.P.C.46 STD 100 μ m
 Caltech 000 FOV:1.83x1.37mm 04/11/2023

20-JRD-87
 Volcanic Lakes
 titanite-bearing
 amphibole
 monzogabbro



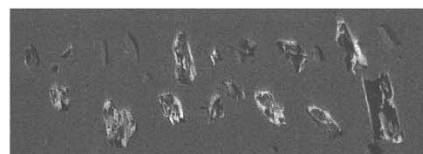
PCLI 10.0kV WD 11.0mm \times 40.0 Std.P.C.46 STD 100 μ m
 Caltech 000 FOV:3.20x2.40mm 04/11/2023 JEOL

20-JRD-69
 Tehepite
 sulfide and
 clinopyroxene-
 bearing
 monzodiorite



PCLI 10.0kV WD 11.0mm \times 40.0 Std.P.C.46 STD 100 μ m
 Caltech 000 FOV:3.20x2.40mm 04/11/2023 JEOL

20-JRD-79
 Glacier Lakes
 amphibole and
 plagioclase
 porphyritic
 monzodiorite



PCLI 10.0kV WD 11.0mm \times 40.0 Std.P.C.46 STD 100 μ m
 Caltech 000 FOV:3.20x2.40mm 04/11/2023 JEOL

High Sierra Belt**20-JRD-82**

Dougherty Peak
titanite and
clinopyroxene-
bearing
amphibole
monzodiorite



PCL1 10.0kV WD 11.0mm $\times 40.0$ Std.P.C.46 STD 100µm JEOL
Caltech 000 FOV:3.20x2.40mm 04/11/2023

20-JRD-83

Dougherty Peak
biotite and
titanite-bearing
amphibole
quartz
monzodiorite



PCL1 10.0kV WD 11.0mm $\times 40.0$ Std.P.C.46 STD 100µm JEOL
Caltech 000 FOV:3.20x2.40mm 04/11/2023

20-JRD-85C

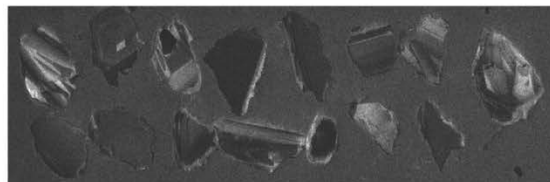
Dougherty Peak
biotite and
titanite-bearing
amphibole-
biotite monzodiorite



PCL1 10.0kV WD 11.0mm $\times 40.0$ Std.P.C.46 STD 100µm JEOL
Caltech 000 FOV:3.20x2.40mm 04/11/2023

20-JRD-91B

Woods Creek
amphibole
monzogabbro



PCL1 10.0kV WD 11.0mm $\times 40.0$ Std.P.C.46 STD 100µm JEOL
Caltech 000 FOV:3.20x2.40mm 04/11/2023

High Sierra Belt**20-JRD-94**

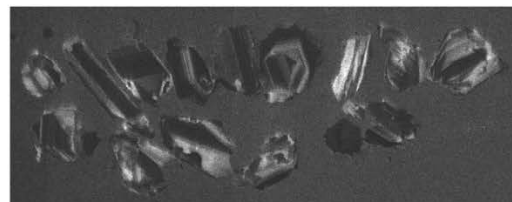
Woods Creek
biotite amphibole
monzodiorite



PCL1 10.0kV WD 11.0mm x40.0 Std.P.C.46 STD 100µm JEOL
Caltech 000 FOV:3.20x2.40mm 04/11/2023

SNB-18-18

Onion Valley
amphibole
monzogabbro



PCL1 10.0kV WD 11.0mm x40.0 Std.P.C.46 STD 100µm JEOL
Caltech 000 FOV:3.20x2.40mm 04/11/2023

86S52A

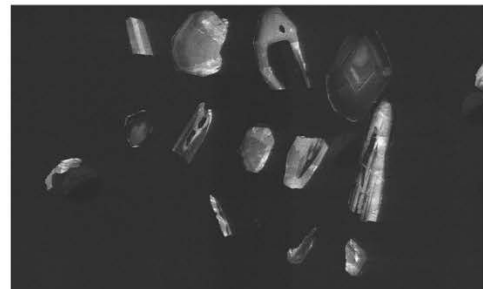
Onion Valley
hornblende-
pyroxene
diorite



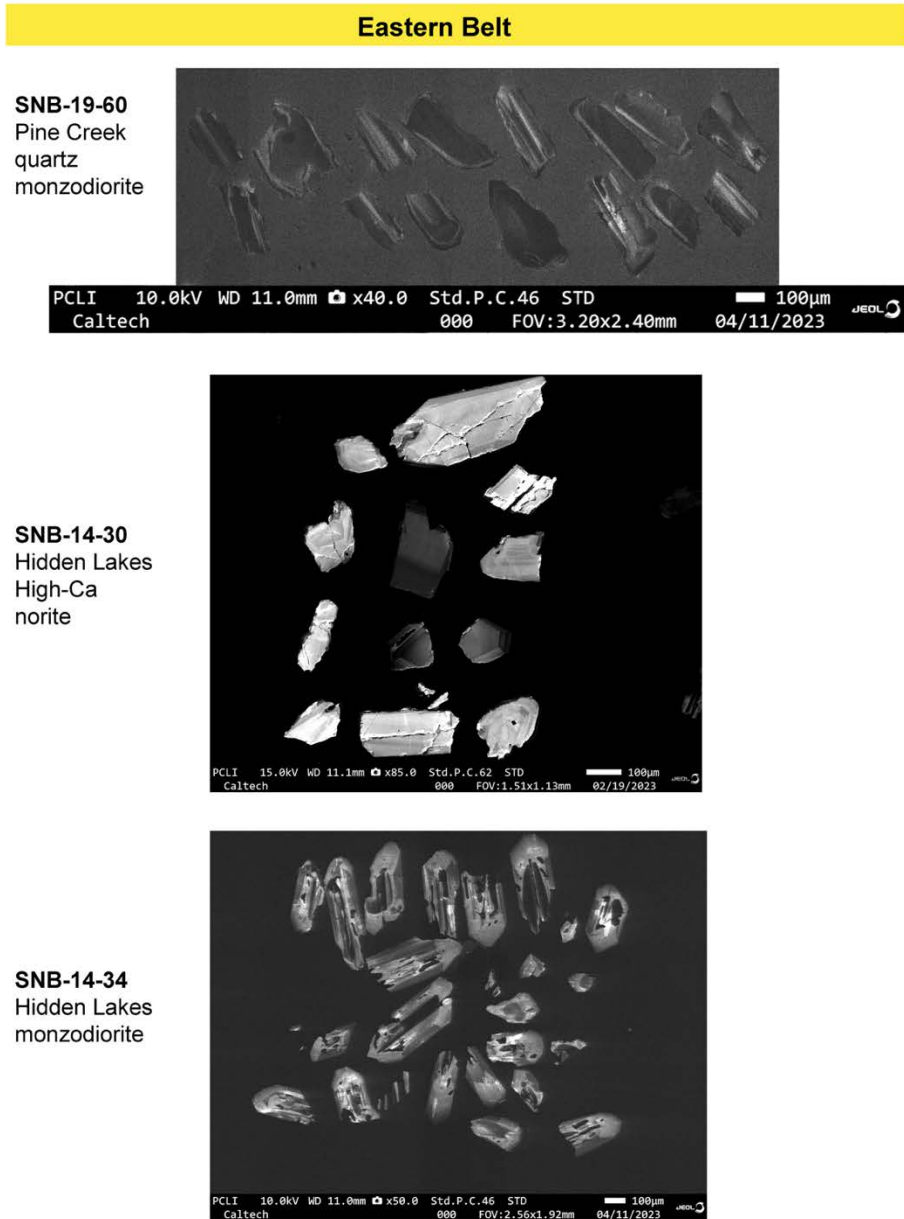
PCL1 10.0kV WD 11.0mm x40.0 Std.P.C.46 STD 100µm JEOL
Caltech 000 FOV:3.20x2.40mm 04/11/2023

86S57

Onion Valley
hornblendeite

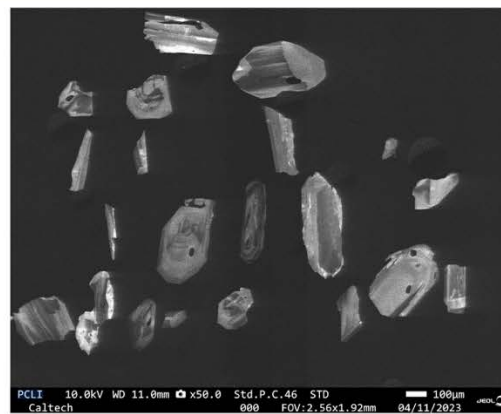


PCL1 10.0kV WD 11.0mm x60.0 Std.P.C.46 STD 100µm JEOL
Caltech 000 FOV:2.13x1.60mm 04/11/2023



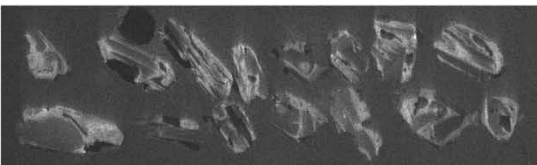
Eastern Belt

SNB-16-02
Hidden Lakes
gabbro



PCLI 10.0kV WD 11.0mm \times 50.0 Std.P.C.46 STD 100 μ m JEOL
Caltech 000 FOV: 2.56x1.92mm 04/11/2023

SNB-16-06
Hidden Lakes
monzodiorite

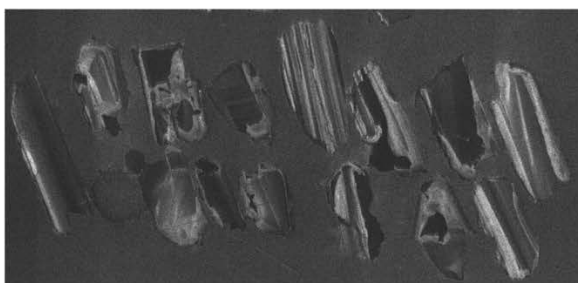


PCLI 10.0kV WD 11.0mm \times 40.0 Std.P.C.46 STD 100 μ m JEOL
Caltech 000 FOV:3.20x2.40mm 04/11/2023

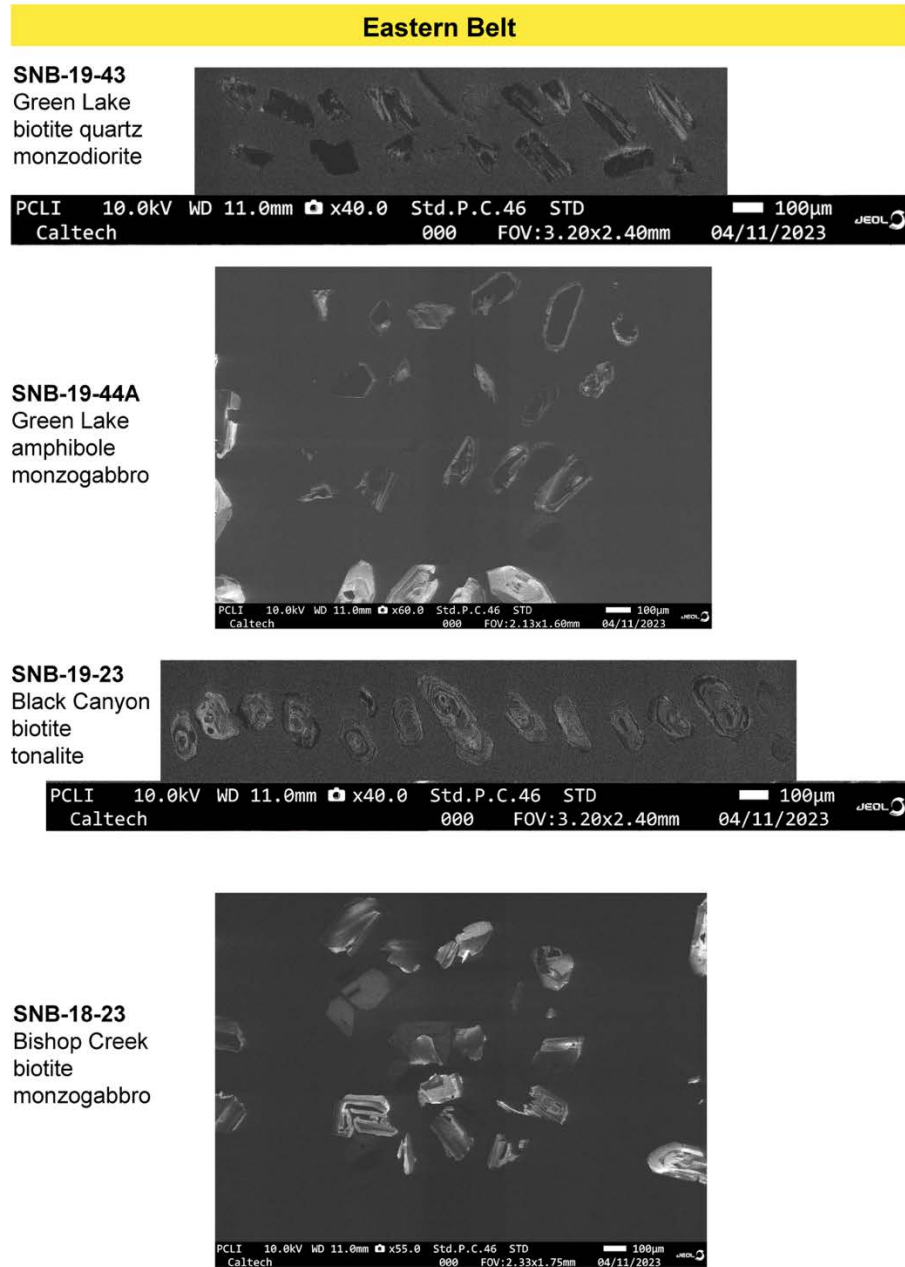
SNB-16-21
Hidden Lakes
High-SiO₂
leucogabbro



SNB-18-13
Tamarack Lakes
amphibole-
biotite
monzodiorite

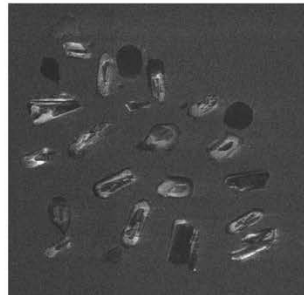


PCLI 10.0kV WD 11.0mm \times 40.0 Std.P.C.46 STD 100 μ m JEOL
Caltech 000 FOV:3.20x2.40mm 04/11/2023



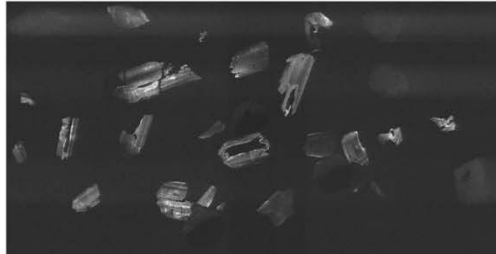
Eastern Belt

SNB-18-43
Bishop Creek
porphyritic
monzogabbronorite



PCLT 10.0kV WD 11.0mm x40.0 Std.P.C.46 STD 100µm
Caltech 000 FOV:3.20x2.40mm 04/11/2023 JEOL

SNB-19-16
Mount Tom
gabbro



PCLT 10.0kV WD 11.0mm x55.0 Std.P.C.46 STD 100µm
Caltech 000 FOV:2.33x1.75mm 04/11/2023 JEOL

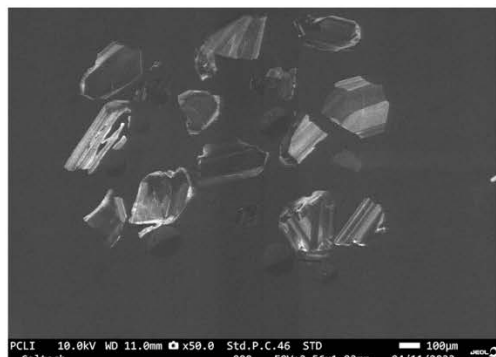
SNB-18-CB4
Mount Alice
amphibole
monzogabbro



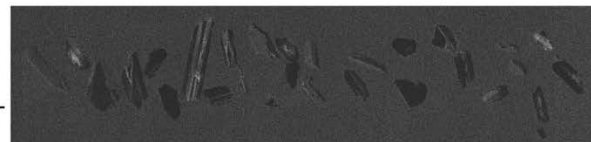
PCLT 10.0kV WD 11.0mm x50.0 Std.P.C.46 STD 100µm
Caltech 000 FOV:2.56x1.92mm 04/11/2023 JEOL

Eastern Belt

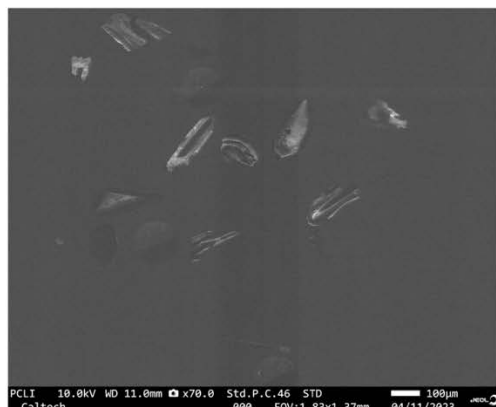
SNB-19-64
McMurry Meadows
amphibole
gabbro



SNB-19-68
McMurry
Meadows
amphibole
monzogabbro-
norite



SNB-19-8
Casa Diablo
amphibole
monzogabbro



Eastern Belt

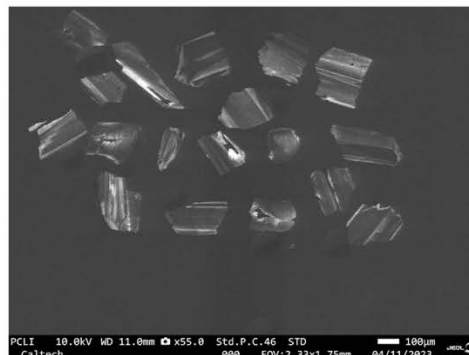
SNB-19-34
Tungsten Hills
leucogabbro



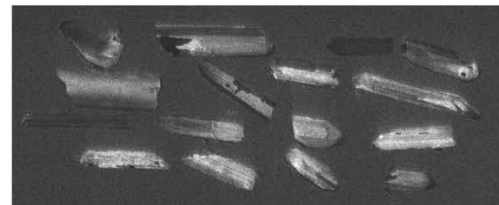
SNB-19-52
Shannon
Canyon
biotite leuco-
monzodiorite



SNB-18-53
Keough
biotite
monzogabbro



SNB-18-55A
Keough
biotite-amphibole
gabbro

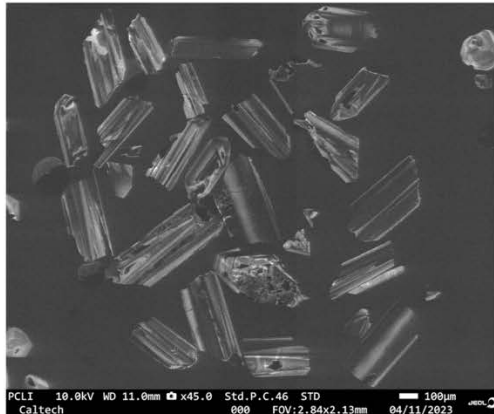


Eastern Belt — White-Inyo Mountains

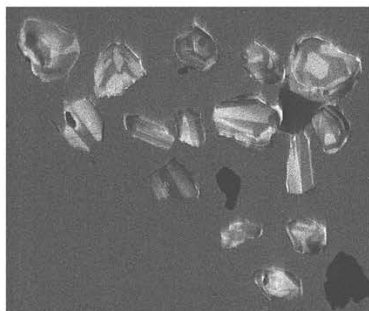
21-JRD-108
Deep Springs
epidote-bearing
biotite-amphibole
monzodiorite



21-JRD-109
Deep Springs
titanite and
epidote-bearing
biotite-amphibole
monzodiorite



21-JRD-106
Marble Canyon
epidote-bearing
amphibole-biotite
monzogabbro



UPPER-CRUSTAL MAFIC INTRUSIONS FINGERPRINT
EARLY, GEOLOGICALLY-CONTROLLED
CONTAMINATION IN A CONTINENTAL ARC

Juliet Ryan-Davis¹, Claire E. Bucholz¹, Jade Star Lackey², Andrew Kylander-Clark³,
Madeline J. Lewis⁴, Kouki Kitajima⁵, and John W. Valley⁵

¹*Division of Geological and Planetary Sciences, Caltech, Pasadena, California 91125, USA*

²*Pomona College Geology Department, Claremont, California 91711, USA*

³*Department of Earth Science, University of California, Santa Barbara, California 93106, USA*

⁴*Department of Geology and Geophysics, University of Wyoming, Laramie, Wyoming 82701, USA*

⁵*Department of Geoscience, University of Wisconsin, Madison, Wisconsin 53706, USA*

ABSTRACT

Upper-plate contamination of subduction-zone magmas is a widely documented process that influences their geochemistry. It is essential to understand such compositional modification in order to interpret global geochemical observations. However, quantifying where and how much material the overriding plate contributes to subduction-zone magmas remains challenging. In particular, the use of correlated age, oxygen and hafnium isotope records from global zircon datasets rely on understanding the mechanisms and efficiency of upper-plate influence on the compositions of continental arc magmas and zircon that they crystallize. In the Sierra Nevada batholith, well-documented lithospheric and crustal heterogeneity of the upper plate takes the form of tectonically-assembled arc-parallel belts with variable affinities into which the batholith intruded. Gabbro to diorite intrusions that intrude this framework represent the products of common mafic magmas parental to the formation of the batholith. Their age progression from west to east across the batholith reflects the migration of Cretaceous magmatism across the pre-existing tectonic belts. The interaction of mafic magmas with different crustal compositions in each belt caused distinctive and highly variable isotopic signatures among the mafic intrusions. The evolving isotopic signatures of zircon in the mafic intrusions can be traced directly to isotopic contributions from the local lithospheric column, rather than arc-wide secular changes. A transect of gabbroic and dioritic intrusions across the Sierra Nevada batholith thus provides a ~110 million-year long time-integrated record of contamination of continental arc magmas during early, mafic stages of their differentiation. This case study informs the interpretation of global datasets—particularly studies wherein zircon are understood separately from their original igneous sources—by showing that the pre-existing geology of continental arc crust and lithosphere exerts a primary control on the composition of arc magmas.

1. INTRODUCTION

The majority of post-Archean continental crust is thought to have formed through subduction zone magmatism (e.g., Rudnick, 1995; Jagoutz and Schmidt, 2012). Thus, quantifying the relative importance in subduction zones of addition of mantle-derived melts to the crust and of reworking of older crustal material is a fundamental, unresolved problem in understanding long term growth of the continental crust. Part of this uncertainty stems from the fact that assigning what fraction of a granitoid—the major constituent of the preserved plutonic record of subduction zone magmatism—was derived from mantle versus crustal materials is complex, often ambiguous, and has been passionately debated since early polarized views about granite petrogenesis (Bowen, 1928; Read, 1948; Pitcher, 1987; summarized by Jacob et al., 2021, and Moyen et al., 2021).

There is widespread agreement that plutonic and volcanic rocks formed in continental subduction zones have at least some contributions from both newly generated mantle-derived magmas and from pre-existing crustal material. Deciding on the best approach to identifying and quantifying these proportions remains challenging at a global scale. Models of crustal growth often use coupled radiogenic and stable (*i.e.*, oxygen) isotopes to interrogate these questions, as they can potentially fingerprint mantle and crustal sources. In particular, oxygen and hafnium isotopes coupled with U-Pb ages are often measured in detrital zircon populations both to understand continental growth over time (*i.e.*, Hawkesworth and Kemp, 2006; Belousova et al., 2010; Dhuime et al., 2017), and at more local scales to trace mantle versus crustal input into arc plutonic and volcanic rocks (Andrews et al., 2022; Cornet et al., 2022).

However, challenges remain in using isotopic systems in zircon to construct a globally unified view of processes through Earth's history. First, the isotopic systematics that fingerprint the sources of arc magmas depend on the type of lithosphere and pre-existing crustal materials that they formed in and interacted with—weathered sedimentary materials impart elevated $^{18}\text{O}/^{16}\text{O}$ ratios, whereas

mantle-derived igneous protoliths will not, and assimilation of ancient, cratonic material will impart distinct radiogenic isotopic signatures compared to juvenile, accreted terranes (Peck et al., 2000; Eiler, 2001). Further, processes such as melting, assimilation, storage and homogenization (MASH) and assimilation and fractional crystallization (AFC) impart geochemical fingerprints of local crustal compositions in arc magmas (DePaolo, 1981; Hildreth and Moorbath, 1988; Annen et al., 2006). Due to the variable nature of preexisting lithosphere at subduction zones, identifying appropriate isotopic compositions of crustal end members can be challenging (*i.e.*, Kistler and Peterman, 1973; Jacob et al., 2021; Sundell and Macdonald, 2022).

Second, mafic arc magmas (basalts to basaltic andesites or intrusive equivalents) are often used to define a mantle endmember. However, even the least contaminated primitive modern mafic volcanic rocks display significant isotopic variability (Mullen, et al., 2017; Schmidt and Jagoutz, 2017; Turner and Langmuir, 2015, 2024). This demonstrates that mantle source regions can vary isotopically and leads to challenges in discerning how, when, and where contamination occurs in arc magma—“source” contamination within the mantle wedge, “path” contamination during ascent through the upper plate of the subduction zone, or both (Cornet et al., 2022). Furthermore, mafic rocks in the lower crust of accreted arcs display isotopic characteristics indicating both contamination of the mantle source, and variable input of different crustal lithologies (Lackey et al., 2005; Walker et al., 2015; Cornet et al., 2022). Heterogeneity in erupted mafic lavas in continental arc volcanoes has been shown to reflect upper-plate, “path” contamination (*i.e.*, MacPherson et al., 1988; Davidson and Harmon, 1989). However, when (at what stage of differentiation), where (upper versus lower crust), and how much “path” contamination occurs is a topic of active debate as it requires detailed knowledge of the upper plate—knowledge which is generally absent in database-scale studies of zircon populations. Disentangling this upper-plate control on isotope ratios in mafic arc magmas can be achieved using a time-transgressive, plutonic record in a location with well-documented across-arc isotopic architecture.

Here, we use the Sierra Nevada batholith as a natural laboratory where extensive prior contextual study allows us to understand the interaction of mafic arc magmas with overlying crust. The Sierra Nevada batholith comprises Triassic to Cretaceous, dominantly tonalitic to granodioritic intrusions that formed in a continental arc. The continental margin upon which the batholith was constructed has been documented in detail as a tectonically assembled framework of belts with variable lithospheric and crustal affinities (Kistler and Peterman, 1973; Farmer and DePaolo, 1983; Saleeby et al., 1992; Lackey et al., 2008). Cretaceous ages across the batholith, and thus migration of the locus of magmatism, become younger from west to east (Evernden and Kistler, 1970; Stern et al., 1981; Chen and Moore, 1982; Chapman et al., 2012; Ryan-Davis et al., *Chapter 3*). The time-integrated history of arc magmatism afforded by the plutonic record reveals arc-wide trends in geochemistry, intrusion geometries, and locations of magmatism (Ardill et al., 2024; Chapman et al., 2017; Ryan-Davis et al., *Chapter 3*).

Mafic (gabbro to diorite) plutons are small in volume, but widespread and nearly ubiquitous across the Sierra Nevada batholith (Frost, 1987; Sisson et al., 1996; Coleman and Glazner, 1997; Wenner and Coleman, 2004; Lewis et al., 2024; Ryan-Davis et al., *Chapter 3*). A handful of these plutons have been studied in conjunction with their associated intermediate to felsic intrusions (Coleman and Glazner, 1997; Wenner and Coleman, 2004; Ratajeski et al., 2001). Such studies have shown that, in many cases, new additions from the mantle result in voluminous crustal growth over relatively short (<10 Ma) timescales by fractionation of already isotopically enriched mafic components to produce intermediate to felsic compositions (e.g., Sisson et al., 1996; Coleman et al., 1992; Coleman and Glazner, 1997). However, these studies are biased towards plutons in the eastern Sierra Nevada, which limits understanding of batholith-wide variability and systematic trends in composition.

Here, we document isotopic heterogeneity of mafic plutons across the Sierra Nevada batholith along a ~225 km-long transect, in the context of well-characterized upper-plate lithospheric heterogeneities. Because the Sierra Nevada has been so well-documented, including the nature of pre-existing crust preserved as pendants or septa

of wallrock between plutons, this provides the opportunity to test for “path” contamination. We analyze O, Hf, Sr, and Nd isotopes in the mafic plutons and present mixing models that constrain the amount of contamination. We show (1) that the upper-plate controls the isotopic heterogeneity of mafic to felsic magmas over \sim 100 Ma of arc activity, and (2) that contamination occurs early in the evolution of arc melts, in mafic (basalt to basaltic andesite) magmas.

2. SAMPLE SUITE AND GEOLOGIC CONTEXT

2.1. Sample suite

We collected samples from 43 mafic plutons along a \sim 225 km long, \sim 100 km wide transect across the central Sierra Nevada batholith at \sim 37 \pm 0.5 °N (Fig. 1A; samples from Sisson et al., 1996; Lewis et al., 2021; Lewis et al., 2024; Ryan-Davis et al., *Chapter 3*). Samples include gabbro, amphibole gabbro, gabbronorite and diorite, with variable amounts of biotite and olivine (described in detail; Ryan-Davis et al., *Chapter 3*). Most of these gabbroic samples are identified texturally and chemically as cumulates, having lost interstitial melt. Nonetheless, the minerals that comprise these rocks, including zircon (which we focus on in this study), crystallized from their mafic parental melts or derivative melt formed during crystallization (Ryan-Davis et al., *Chapter 3*). The parental melts were basalt to basaltic andesite in composition, based on mineral chemistry. Thus, the zircon populations studied from these mafic intrusions did not crystallize from the volumetrically-dominant intermediate to felsic melts of the batholith, but rather from more primitive mafic compositions that occasionally find their way into the upper crust (Lewis et al., 2021; 2024; Ryan-Davis et al., *Chapter 3*). This study expands on previous work (including previously dated samples of Lewis et al., 2024 and Ryan-Davis et al., *Chapter 3*), by associating each of the sampled plutons with its position in the across-arc tectonically-assembled pre-batholithic framework, which is necessary for documenting and quantifying upper-plate contamination.

2.2. The framework for batholith construction

The framework of the Sierra Nevada comprises tectonically-assembled belts built on different types of lithosphere with distinct mantle and crustal domains and thus different isotopic signatures (*i.e.*, Kistler, 1990; Chapman et al., 2017). These complex, tectonically assembled lithospheric belts can be grouped into three distinctive regions (Fig. 1a): (1) a western foothills belt (blue symbols) built on oceanic lithosphere with mafic and juvenile proto-arc crustal assemblages; (2) a central belt (red symbols) built on oceanic lithosphere with Paleozoic to Mesozoic metasedimentary (dominantly siliciclastic) crustal assemblages, with a significant proportion of material derived from Proterozoic sources in the continent; and (3) an eastern belt (yellow symbols) built on Proterozoic continental lithosphere with Paleozoic marine sedimentary sequences and Mesozoic syn-arc volcanic rocks that were intruded at relatively shallow levels by plutons of the batholith. The eastern belt can be divided in detail as two separate belts (high Sierra and eastern belts; Ryan-Davis et al., *Chapter 3*), but they are combined here for parsimony because they are isotopically similar. Mantle xenoliths were brought to the surface by later volcanism in both the central and eastern belts, and both sets have a range in isotopic compositions, but are for the most part isotopically enriched (Fig. A1; Mukhopadhyay and Manton, 1994; Beard and Glazner, 1995; Ducea and Saleeby, 1998).

2.2.1. Lithosphere and crustal wallrocks of the tectonically-assembled belts

In detail, the three regional belts each host a range of specific rock types, exposed at the present-day erosional surface in the transect study area as pendants and septa of wallrock, and also in structurally continuous or geologically comparable regions from deeper (up to \sim 1 GPa) exposures in the Southern Sierra Nevada and other tectonically translated mountain ranges of California (Saleeby et al., 2008; Chapman et al., 2014). First, in the western belt, exposed wallrocks of the batholith are from a proto-forearc environment of the earliest stages of cordilleran subduction in the region (*i.e.*, Saleeby, 2011). Ophiolitic (the Kings River ophiolite in this study

area) and metavolcanic and metasedimentary rocks from late Paleozoic early subduction and Triassic-Jurassic developing arcs were accreted to the active continental margin and intruded by calc-alkaline magmas of the maturing arc (Saleeby, 2011; Lackey et al., 2012; Attia et al., 2018).

Second, eastward in the central belt, crustal rocks comprise Paleozoic (to Mesozoic) deep marine to slope-rise metasedimentary rocks with both cratonic and more juvenile (including volcanic) sources of the Kings sequence (associated with the Northern Sierra terrane northward and Kernville terrane southward; Bateman and Clark, 1974; Saleeby et al., 1978; Ague and Brimhall, 1988; Chapman et al., 2012; Attia et al., 2018). The basement for that region was accreted oceanic lithosphere (Panthalassa) on the western margin of Laurentia (Saleeby et al., 1990; Kistler, 1990; Lackey et al., 2008). The eastern boundary of the central belt is defined by a tectonic “break” with transpressional deformation documented along the length of the entire batholith axis, correlated with a shift in radiogenic isotope systematics in felsic plutons (Kistler and Peterman, 1973, 1978).

Third, in the eastern belt, in the high Sierra Nevada, metamorphic host rocks are mainly Mesozoic arc-related volcanic or volcaniclastic rocks with lesser Paleozoic marine sedimentary rocks (Saleeby et al., 1990). Along the eastern slopes, they are mostly Paleozoic to Neoproterozoic marine (inner- to outer-shelf) sediments (*i.e.*, Morrison block and Inyo facies found in the Inyo and White Mountains); tectonically rearranged correlated exposures occur in Death Valley and the Mojave Desert regions several hundred kilometers southward (Lahren and Schweickert, 1989; Attia et al., 2018). Underlying these rocks, the bulk of the continental crust is understood to be older (Proterozoic) (meta)igneous rocks (*e.g.*, Kistler and Peterman, 1978; Ducea, 2001). No Proterozoic basement outcrops are exposed near the Sierra Nevada batholith, but Proterozoic outcrops do occur in southern California exposures of the broader Mesozoic cordilleran batholith (Table S5).

2.2.2. Mafic contributions to batholith construction within the framework of belts

Mafic intrusions into these belts, the focus of this study, play a major role in the formation of the batholith during the Mesozoic. Jurassic arc activity occurred across the arc, in the western and eastern belts (and may have once been continuous, prior to intrusion by voluminous Cretaceous intrusive complexes of the axial batholith; Fig. 1b). In the Cretaceous, ages of plutons generally young west to east (Chen and Moore, 1982; Bateman et al., 1963; Stern et al., 1981; Bateman, 1992). Mafic plutons of this study follow the same smoothly increasing age progression of the locus of magmatism, sweeping from west to east across the batholith (Fig. 1b; Lewis et al., 2024; Ryan-Davis et al., *Chapter 3*).

Jurassic mafic bodies in the western foothills belt (*i.e.*, Jurassic KK and FG samples, Fig. 1) have been hypothesized to represent island-arc intrusions that are partly responsible for suturing the ophiolitic and proto-forearc assemblages to the western continental margin (Saleeby and Sharp, 1980; Saleeby 2011). Cretaceous mafic plutons in the western foothills belt include ring complexes, similar in their rock types and modal layering to the ring complexes of Stokes Mountain just south of the transect area (Fig. 1: Cretaceous WRC, FG and BS samples, this study; Stokes Mountain, Clemens-Knott and Saleeby, 1999 and Gevedon, 2013). The more felsic intrusions in this belt are less evolved than the batholith, which becomes more evolved eastward (Chapman et al., 2012). This less-evolved western flank has been documented along the entirety of the North American Cordillera (“quartz diorite boundary line,” Moore 1959). Characteristics of these western belt mafic intrusions may be related to the density and rheologic properties of this western belt (Ryan-Davis et al., *Chapter 3*).

Central belt intrusions define the beginning of the $^{87}\text{Sr}/^{86}\text{Sr}_{(i)} = 0.706$ isopleth of the western United States (geographic contour in strontium isotope ratio measurements where the subscript (i) indicates initial values at the time of crystallization; Kistler and Peterman, 1973; 1978; Kistler, 1990). Silicic intrusions of this belt were shown to be “strongly contaminated and reduced” due to assimilating significant proportions of reducing metapelitic rocks of the Kings sequence (Ague

and Brimhall, 1987; 1988), which also affects their isotopic ratios. Thus, $^{87}\text{Sr}/^{86}\text{Sr}_{(\text{i})} > 0.706$ in plutons in this belt is due to contamination by continentally-derived sediment, although the belt is built on Panthalassan, oceanic lithosphere (Kistler, 1990). Mafic plutons of the late Cretaceous Shaver and Sequoia intrusive suites (Fig. 1) are associated with these contaminated felsic plutons.

East of these two belts, the lithosphere is broadly similar across the high Sierra, the eastern Sierra, and into the White-Inyo mountains, which have been separated from the main batholith by Cenozoic (and ongoing) tectonic extension. Intrusions in the highest elevations of the Sierra Nevada along the range crest (high Sierra) are associated with a series of late-Cretaceous, large volume intrusions (from south to north: Whitney granodiorite, Hirt, 2007; Mount Givens granodiorite, Frazer et al., 2014; Mono Pass, Tuolumne, and Sonora Pass, Moore and Sisson, 2008). Mafic intrusions in the high Sierra are sparse, relatively evolved, and often co-mingled with their intermediate hosts (Ryan-Davis et al., *Chapter 3*; Fig. 1, MD-W samples). In the eastern Sierra, Jurassic and Cretaceous mafic plutons are larger in volume, with shallowly-emplaced hydrous basaltic parental magmas (Frost and Mahood, 1987; Sisson et al., 1996; Lewis et al., 2024). Their emplacement is associated with time periods of abundant intrusion, including the Independence dike swarm in the Jurassic and a peak in arc magmatism in the Cretaceous (Chen and Moore, 1979; Lewis et al., 2024; Fig. 1, Jurassic Sch-Pal and E-JM samples, respectively). Four Cretaceous gabbro and diorite bodies in the Lamarck intrusive suite have been isotopically linked to rapid crustal growth, due to the similarity in their isotope ratios to their large host granodiorite (Coleman et al., 1992). In the White-Inyo Mountains, mafic plutons are uncommon (Fig. 1, Jurassic SP samples, this study), but similar in character to others of the eastern belt (Ryan-Davis et al., *Chapter 3*).

3. METHODS

3.1. Zircon O-Hf isotopes

We separated zircon from 70 samples of gabbro to diorite from the 43 mafic intrusions using magnetic and heavy liquid mineral separation methods at Caltech, Pomona College, and GeoSep Services, Idaho. Cathodoluminescence (CL) images of the zircon imaged using the JEOL JXA-iHP200F Field Emission Electron Probe Microanalyzer (FE EPMA) at Caltech indicate uniform zircon populations for 80% of samples (see Ryan-Davis et al., *Chapter 3*) and guided analytical spot placement focusing on rims and some cores of representative grains to identify inherited cores. Oxygen isotope ratios in zircon were measured by secondary ion mass-spectrometry (SIMS) at the University of Wisconsin, Madison (479 analyses total: 6 to 10 measurements per sample), reported as $\delta^{18}\text{O}$ relative to Vienna Standard Mean Ocean Water (VSMOW). Sample averages of $\delta^{18}\text{O}$ exclude irregular SIMS pits (with cracks or inclusions). U-Pb ages and trace element compositions of the same zircons, overlapping the spots analyzed for oxygen isotope ratios via SIMS plus additional analyses for age statistics, are presented separately (Ryan-Davis et al., *Chapter 3*; Lewis et al., 2024), and were measured by split stream laser ablation inductively coupled plasma–mass spectrometry (LA-SS-ICPMS) at the University of California, Santa Barbara. Finally, Lu-Hf isotope analyses were collected in the same zircon grains by multi-collector (MC) LA-MC-ICPMS at the University of California, Santa Barbara on areas adjacent to or overlapping previous SIMS and LA-SS-ICPMS analytical pits within the same growth zone (720 analyses total; 8 to 12 measurements per sample). Values of $\epsilon\text{Hf}_{(i)}$ (initial $^{176}\text{Hf}/^{177}\text{Hf}$ relative to the chondritic uniform reservoir, CHUR, at the time of crystallization) are age corrected to the sample average U-Pb age, with details described in Appendix 1. Full SIMS and LA-SS-ICPMS, and LA-MC-ICPMS analytical methods are provided in Appendix 1 and results in the Supplementary Data File (Table S2, Table S3).

3.2. Whole-rock Sr and Nd isotope analyses

Seventeen representative whole-rock powders were also analyzed for Rb-Sr and Sm-Nd isotopes via MC-ICPMS at the Center for Elemental Mass Spectrometry at the University of South Carolina. Detailed methods and sample and analytical data are reported in Appendix 1 and the Supplementary Data File (Table S4). Isotopic values of $^{87}\text{Sr}/^{86}\text{Sr}_{(i)}$ and $\varepsilon\text{Nd}_{(i)}$ (initial $^{143}\text{Nd}/^{144}\text{Nd}$ relative to the chondritic uniform reservoir, CHUR, at the time of crystallization) are calculated using measured whole-rock Rb, Sr, Sm and Nd concentrations and age corrected to the sample average U-Pb age (Ryan-Davis et al., *Chapter 3*), with details in Appendix 1.

4. ISOTOPIC SYSTEMATICS OF MAFIC PARENTAL MAGMAS ACROSS THE BATHOLITH

4.1 O-Hf isotopes in zircon from mafic plutons

We proceed with the assumption that a non-metamict zircon with a concordant U-Pb age records the oxygen ($\delta^{18}\text{O}$) and initial hafnium ($\varepsilon\text{Hf}_{(i)}$) isotope ratios of the melt from which it crystallized. Zircon has been demonstrated to be a reliable recorder of magmatic oxygen isotope ratios if radiation damage and alteration is limited (Valley, 2003; Gao et al., 2014; Wang et al., 2014). Similarly, zircon is a faithful recorder of its parental melt $\varepsilon\text{Hf}_{(i)}$ due to its elevated Hf concentrations and low Lu/Hf and thus low radiogenic ingrowth (*i.e.*, Vervoort et al., 1996). For both oxygen and hafnium isotope analyses, we targeted zones of zircon displaying oscillatory zoning, and avoided radiation-damaged zones, excluding any analyses with U-Pb discordance ($>5\%$) or evidence of mineral inclusions from trace element concentrations in the corresponding LA-SS-ICPMS analysis (Ryan-Davis et al., *Chapter 3*). We avoided altered zircon by monitoring $^{16}\text{OH}/^{16}\text{O}$ during the session. One high $^{16}\text{OH}/^{16}\text{O}$ analysis was excluded from consideration. Further, one analysis with low relative yield was excluded. Pits from analyses with values and uncertainty outside of two sigma uncertainty of others from the same sample were checked

visually by SEM, and where cracks or irregularities were identified, were also excluded from the final dataset (Appendix 1).

At the liquidus and early stages of crystallization of the parental magmas to the mafic rocks studied here, zircon saturation is not achieved due to high temperatures and mafic melt compositions. Antecrustic (or potentially xenocrystic) zircon are thus more readily dissolved (Bea et al., 2022; Crisp and Berry, 2022). Thus, zircon present in the mafic rocks are more likely to have crystallized upon further cooling and in-situ differentiation of the mafic melts, rather than being antecrustic or xenocrystic. (However, in some cases of rapid cooling such as in dikes, zircon antecrusts and xenocrysts may be present in mafic rocks; Clemens-Knott and Gevedon, 2025). Material (including oxygen and hafnium) from rocks and zircons assimilated into the mafic magmas would be dispersed and incorporated into the composition of those mafic melts; this would have negligible effect on oxygen isotope ratios but might be capable of shifting the Hf isotope ratio enough to influence εHf in the melt and in subsequently crystallized zircons.

In the gabbro and diorite samples of this study, we infer that zircon crystallized from more evolved, interstitial melts during cooling of the parental basalt to basaltic andesite magmas. The increase in $\delta^{18}\text{O}$ of the melt expected during this crystallization process is mostly offset by an increase in the fractionation factor between zircon (zrc) and melt ($\Delta^{18}\text{O}_{\text{zrc-melt}} = \delta^{18}\text{O}_{\text{zrc}} - \delta^{18}\text{O}_{\text{melt}}$) due to a decrease in temperature and increase in melt silica content (*i.e.*, Kemp et al., 2007; Lackey et al., 2008; Bucholz et al., 2017). Thus, zircon $\delta^{18}\text{O}$ values are expected to be nearly identical throughout crystallization differentiation within a closed system. By using a $\Delta^{18}\text{O}_{\text{zrc-melt}}$ of 0.2‰ in basalt (~50% SiO_2), estimated from basaltic magmas from the Kohistan arc and hydrous experiments (Bucholz et al., 2017), we calculate the isotopic composition of the parental basaltic magma for each sample.

The sample average $\delta^{18}\text{O}_{\text{zrc}}$ for all gabbro and diorite samples in this study ranges from 5.2–8.5‰, excluding one amphibole-rich cumulate from the central belt ($8.7 \pm 0.4\text{‰}$; Fig. 2a). The range in error at the 2σ level (2 standard deviation of all

analyses from a sample) for these analyses is 0.1–0.9‰, as the spread in oxygen isotope composition within a given sample is typically small; external reproducibility for the session is 0.2‰ (Appendix 1). Over half of the samples from this study (42 out of 69) overlap in composition (including errors) with the $\delta^{18}\text{O}$ range expected for zircon from magmas differentiated directly from un-contaminated mantle-derived magma ($5.3 \pm 0.6\text{\textperthousand}$; Valley et al., 1998; Cavosie et al., 2009; Grimes et al., 2011). A slightly higher range of $5.5 \pm 0.7\text{\textperthousand}$ for zircon from igneous rocks directly differentiated from the mantle is given by Valley et al. (2005), so we consider a conservative range of $\delta^{18}\text{O}_{\text{zrc}}$ 4.7–6.2‰ as having potentially crystallized from uncontaminated mantle-derived magmas (Fig. 2a). Out of five quartz dioritic (to granodioritic) samples (whole-rock $\text{SiO}_2 > 60.0$ wt.%; Ryan-Davis et al., *Chapter 3*) that represent the most mafic sampled rock from a given mapped mafic intrusion, four fall within this range. Importantly, just under half of the samples (28 out of 69), including 5 out of the 22 gabbroid samples (with normative plagioclase having anorthite content >50%, as compared to dioritic samples, defined in Ryan-Davis et al., *Chapter 3*) have elevated $\delta^{18}\text{O}_{\text{zrc}}$ values ($6.5 \text{--} 8.7\text{\textperthousand} \pm 0.1 \text{--} 0.7\text{\textperthousand}$) that are outside of the mantle-derived range (Fig. 2a). The majority of these are from the Fine Gold Intrusive suite in the western belt (Lackey et al., 2012) which has a range in $\delta^{18}\text{O}_{\text{zrc}}$ of 6.8–8.5‰, and in the central belt ($\delta^{18}\text{O}_{\text{zrc}}$ 6.3–8.7‰), which includes the “strongly-contaminated and reduced” belt of Ague and Brimhall (1987).

Sample-average $\varepsilon\text{Hf}_{\text{(i)}}$ in zircon ranges from –9.5 to +13.2 epsilon units, excluding the amphibole-rich cumulate with the most elevated $\delta^{18}\text{O}_{\text{zrc}}$, which has an extremely low hafnium isotope ratio ($\varepsilon\text{Hf}_{\text{(i)}} = -24.2$; Fig. 2b). Most sample populations of zircons define tight clusters (2 s.d. on averages varies from 1.1–3.8 epsilon units), however six samples have larger spreads in their zircon $\varepsilon\text{Hf}_{\text{(i)}}$ values compared to analytical error (2 s.d.= 5.0–10.0). One of these samples, from the 93.9 Ma Wood Creek mafic intrusion in the Sierra Nevada range crest, has distinctive 168 Ma xenocrystic zircon cores that are 2.5 epsilon units lighter than the rims ($\varepsilon\text{Hf}_{\text{(i)}} = -5.0$ cores with –2.4 rims; and, $\delta^{18}\text{O}_{\text{zrc}} = 6.5 \pm 0.6\text{\textperthousand}$ cores with $5.8 \pm 0.3\text{\textperthousand}$ rims). This

is the only sample with a confirmed, visually distinct population of xenocrystic cores (in CL) whose an isotope ratios, trace element compositions, and ages are distinct from the rims. Samples from the western belt have the highest sample-average Hf isotope values ($\epsilon\text{Hf}_{(i)} = +3.0$ to $+13.1$), which are distinctly elevated compared to the central and eastern belts. In fact, the western belt has two distinctive groups of samples, those that intrude ophiolitic and other juvenile arc assemblages ($\epsilon\text{Hf}_{(i)} = +8.6$ to $+13.1$) and those that intrude metasedimentary rocks and are part of the Fine Gold intrusive suite ($\epsilon\text{Hf}_{(i)} = +3.0$ to $+6.9$). The Fine Gold-associated samples are from relatively small mafic intrusions located within large masses of metasedimentary wallrock, and have the highest $\delta^{18}\text{O}_{\text{zrc}}$ values for the belt. The central belt, with some of the highest $\delta^{18}\text{O}_{\text{zrc}}$, has a range of $\epsilon\text{Hf}_{(i)}$ from -9.5 to $+1.6$, excluding the exceptionally low amphibole-rich cumulate ($\epsilon\text{Hf}_{(i)} = -24.2$). The eastern belt, spanning from the Sierra Nevada range crest to the White-Inyo Mountains, has a nearly overlapping range of $\epsilon\text{Hf}_{(i)} = -8.6$ to $+2.8$.

Importantly, these isotope ratios vary by location but not by sample age (Fig. 2). Jurassic and Cretaceous samples, ~ 50 million years apart in age, have identical isotope ratios within error in the same general location for both O and Hf isotopes. This is true locally, comparing between nearby mafic intrusions, and more broadly by belt in both the eastern and western belts, which have Jurassic and Cretaceous mafic intrusions, considering the Fine Gold intrusive suite separately from the rest of the western foothills belt that intrudes ophiolitic and related wallrocks. No isotopic evolution occurs with time within a geologically defined area.

4.2 Sr-Nd isotopic systematics of mafic plutons

Representative samples (Fig. 3b, d) from the western foothills belt, including the Fine Gold intrusive suite, are characterized by low $^{87}\text{Sr}/^{86}\text{Sr}_{(i)} = 0.70311$ – 0.70366 . For three samples from the western belt, that intrude ophiolitic and related wallrocks, the range in Nd isotope compositions is $\epsilon\text{Nd}_{(i)} = +5.95$ to $+7.27$. Central and eastern belt representative samples almost all have distinctly higher $^{87}\text{Sr}/^{86}\text{Sr}_{(i)}$, with the most

radiogenic composition (0.70727) measured in a gabbro from the Rainbow Mine mafic intrusion. There is evidence of local assimilation there, with blocks of the metasedimentary wall rock entrained in the gabbro in some places (Ryan-Davis et al., *Chapter 3*). The Sierra Nevada range crest and eastern Sierra samples have narrow ranges of Sr-Nd isotope ratios ($^{87}\text{Sr}/^{86}\text{Sr}_{(i)} = 0.70574\text{--}0.70691$; $\varepsilon\text{Nd}_{(i)} = -6.69$ to -2.06) aside from two samples with $^{87}\text{Sr}/^{86}\text{Sr}_{(i)} = 0.70418\text{--}0.70479$ and $\varepsilon\text{Nd}_{(i)} = -0.91$ to -0.38 . These are from McMurry Meadows, which has abundant olivine phenocrysts and the highest Mg# equilibrium melt in the whole sample suite, Mg# ~ 55 (calculated by clinopyroxene-melt Fe-Mg exchange; Ryan-Davis et al., *Chapter 3*), and from Deep Springs in the Inyo Mountains (no olivine or pyroxene measured for calculation of melt Mg#; Ryan-Davis et al., *Chapter 3*).

5. ISOTOPIC FINGERPRINTS DEPEND ON LOCATION ACROSS THE UPPER PLATE

Tectonic-scale upper-plate structures have the potential to influence the geochemistry of mafic arc magmas as they transit the lithosphere and assimilate pre-existing material. Although many studies, particularly of volcanic rocks, focus on primitive mafic magmas in hopes of constraining the initial, primary mafic inputs into arcs (*e.g.*, Turner and Langmuir, 2015; Turner and Langmuir, 2022), products of such primitive compositions are rare in the California Mesozoic batholiths (Clemens-Knott, 1992; Bushey et al., 2006; Ryan-Davis et al., *Chapter 2*). The samples of this study are representative of more common gabbros and diorites formed from crystallization of evolved (low-Mg, high-Al) basalts to basaltic andesites that ascended to the shallow crust (Sisson et al., 1996; Lewis et al., 2021, 2023; Ryan-Davis et al., *Chapter 3*). Thus, they have experienced prior differentiation deeper in the crust and represent mafic end-member compositions that can either further differentiate or mix with more evolved magmas to form intermediate compositions that construct the bulk of the batholith (Blatter et al., 2013; Lewis et al., 2024; Ryan-Davis et al., *Chapter 3*).

The O-Hf and Sr-Nd isotope ratios of mafic plutons in this study fall into three categories that correspond to their geographic location and thus the underlying lithosphere and upper-crustal metamorphic rocks into which they intruded (Fig. 3). Mafic plutons that intrude into the western belt, which consists of oceanic lithosphere with ophiolitic and juvenile crustal assemblages, typically have mantle-like radiogenic isotopic signatures and mostly low, though locally variable, $\delta^{18}\text{O}$. In contrast, the central belt is built on juvenile (Paleozoic-Mesozoic) oceanic lithosphere covered by continent-derived pelitic metasedimentary assemblages (Kistler, 1990; Saleeby and Busby, 1993; Attia et al., 2018, 2021). Mafic plutons of this belt have high $\delta^{18}\text{O}_{\text{zrc}}$ (typically $>7\text{\textperthousand}$), high $^{87}\text{Sr}/^{86}\text{Sr}_{(\text{i})}$, and low $\varepsilon\text{Nd}_{(\text{i})}$, as expected from significant assimilation of weathered sedimentary material. This is consistent with observations of significant contamination in the felsic plutons of this belt (Ague and Brimhall, 1987; Lackey et al., 2006).

Finally, the eastern belt (yellow symbols, Fig. 2) is built on continental lithosphere interpreted as having enriched (sub-continental lithospheric) mantle based on enriched isotope signatures of mafic intrusions and mantle xenoliths (Fig. A1; Coleman et al., 1992; Beard and Glazner, 1995). Overlying metasedimentary and metaigneous materials have the elevated $^{87}\text{Sr}/^{86}\text{Sr}_{(\text{i})}$ and low $\varepsilon\text{Nd}_{(\text{i})}$ signatures expected of old crustal materials (Kistler and Peterman, 1973; Farmer and Ball, 1997). Correspondingly, mafic plutons from this belt have $\delta^{18}\text{O}_{\text{zrc}} < 7\text{\textperthousand}$, but crust-like radiogenic isotopes. In detail, different upper-crustal wallrock assemblages in the eastern belt correspond to slight differences in isotopic signatures in the mafic plutons. While samples from east of the range crest (yellow symbols, Fig 2) may be explained by assimilation of Proterozoic materials, plus potentially Paleozoic metasedimentary sequences, the more westerly samples from the Monarch Divide and Whitney intrusive suite (MD-W samples, bright yellow downward-pointing triangles, Fig. 2) intrude into a region that sparsely preserves only metavolcanic host rocks between large intrusive suites, rather than Paleozoic metasedimentary sequences. The country rocks are mostly Mesozoic metavolcanic rocks from slightly earlier episodes of arc magmatism in the same area, which have low- $\delta^{18}\text{O}$ (~ -6 to

+11 ‰; Saleeby et al., 1990; Kistler, 1993; Raftrey et al., 2016; Lackey, personal communication). Local contamination in the upper crust with the volcanic rocks could have contributed to lower $\delta^{18}\text{O}_{\text{Zrc}}$ in the mafic plutons in the MD-W samples (5.5–6.5‰), which were shallowly emplaced.

Whether or not upper-crustal assimilation contributes significantly to the signatures of these mafic magmas is unclear. The crustal assemblages described above as potential assimilants are exposed in the upper crust, but similar (though more highly metamorphosed) metasedimentary rocks are found in high pressure exposures of the batholith in southern California (Saleeby et al., 1987; Pickett and Saleeby, 1994; Chapman et al., 2014). Their presence in the lower crust has been explained as downward displacement of these assemblages, potentially during batholith growth (e.g., Saleeby et al., 2003; Chapman et al., 2014; Cao et al., 2016). Prior to batholith growth, the transpressional tectonic assembly of the framework belts could potentially have brought high- $\delta^{18}\text{O}$ weathered sedimentary materials to deeper levels of the crust. In addition, lower-crustal granulite outcrops and xenoliths from the region have metasedimentary protoliths that record high pressures, even up to ~2.5 GPa in xenoliths (*i.e.*, Ducea and Saleeby, 1998, Domenick et al., 1983; Hanchar et al., 1994). Thus, the upper crustal assemblages described above are thought to be representative of the entire crust during batholith construction.

6. QUANTIFICATION OF THE DEGREE OF ASSIMILATION IN THE PARENTAL MAFIC MAGMAS

To quantify how mafic magmas are affected by the upper plate lithosphere that they transit, we modeled binary mixing between potential primitive arc magma compositions and geologically relevant assimilants in each belt (Fig. 3). There is significant uncertainty regarding the isotope ratios of the parental magmas and potential assimilants, however we attempt to address this by using two candidate end-member primitive arc magma compositions and existing data for potential assimilants from each of the lithospheric belts. We chose simple compositional

models with binary endmembers and not more complex thermodynamically constrained models or mixing between multiple endmembers due to the compositional (and lithological) heterogeneity of crustal assimilants, plus additional factors such as variable fusibility of these lithologies and the potential for disequilibrium and nonmodal partial melting (Zeng et al., 2005).

End-member first quartile, median, and third quartile values used for these mixing models are reported in Table 1, with initial radiogenic isotope values calculated at 100 Ma for comparison with the Mesozoic samples of this study. Compiled data and sources for each of these endmembers is in Table S5. We discuss these endmembers and considerations for their isotopic compositions, with further details and additional sources of data for oxygen isotope data and hafnium concentration for several of the endmembers in Appendix 1 and Table S5. Hf isotopes were not reported for any of the compiled samples aside from oceanic arc lavas and instead were calculated for compiled samples using the terrestrial correlation with Nd isotopes of Vervoort et al., 2011,

6.1. Arc basaltic mixing endmembers

We considered two isotopically distinct arc basaltic endmembers, chosen to represent (1) primitive magmas with a more depleted source, as found in oceanic arcs, and (2) primary magmas of a continental arc that originated from an enriched source. The first, which we call “primitive arc magma”, is isotopically suggestive of a depleted mantle-like source and uses the average Sr-Nd isotopic and elemental composition of modern high-Mg oceanic arc basalts given by Turner and Langmuir (2022), and a range of oxygen isotope values from oceanic arc basalts of 5.2–5.8 ‰ (Eiler et al., 2000; Eiler, 2001). Elemental concentrations are the average of high-Mg basalts from the Cascades arc (Turner and Langmuir, 2022).

The second endmember, called “enriched arc magma” represents a continental arc basalt and is isotopically similar to EM1 mantle composition. In the Sierra Nevada batholith, an enriched sub-continental lithospheric mantle source east of the $^{87}\text{Sr}/^{86}\text{Sr}_{(i)} = 0.706$ isopleth has been described as metasomatized or reacted

subduction-related ancient lithosphere, revealed by the mantle xenoliths brought to the surface by later volcanic activity (Fig. A1; Mukhopadhyay and Manton, 1994; Beard and Glazner, 1995; Ducea and Saleeby, 1998). The enriched endmember isotope ratios (Table 1) are the average of measurements of these xenoliths. Calculating an equilibrium melt based on oxygen isotope ratios in unaltered olivine measured in these xenoliths (5.2–5.7‰; Gao et al., 2017; Chin et al., 2014) and a basaltic melt-olivine oxygen isotope fractionation ($\Delta_{\text{melt-olivine}}$) ranging from 0.2 to 0.6‰ (representing a range of 0.4 ± 0.2 , 2σ ; Eiler et al., 2000) gives a potential range for the enriched melt composition of 5.4–6.3‰. Concentrations of Lu and Hf were measured in several xenoliths (Chin et al., 2014) and are used to calculate Lu/Hf for initial Hf isotopic compositions.

6.2. Assimilant endmembers and amount of assimilation

Endmember compositions of potential assimilants within the transect study area selected for each of the three belts. Each has distinctive sedimentary packages and, more importantly, different types of basement material that form the bulk of the crust (Fig. 4a). For details of compiled samples and values used for each endmember composition, refer to Appendix 1 and the Supplementary Data File (Table S5).

In the western belt, the ophiolitic basement and wallrocks are isotopically similar to mantle-derived arc magmas, but, sediments that were shed from the continent into the trench of the paleo arc-trench system are exposed in the Franciscan complex farther to the west (Ghatak et al., 2013). It has been suggested that such materials underplated the arc system (Wakabayashi, 2015; Snow et al., 2010; Dumitru et al., 2010). Isotopically, these rocks are similar to the Pelona-Orocopia-Rand schist—a similarly-formed subduction complex from earlier (Laramide) subduction that can be found at the base of the crust (*i.e.*, Chapman et al., 2021). Considering these subduction complex rocks from the Franciscan complex as an endmember assimilant (Fig. 3a–b, Table 2a), up to 20% assimilation within a primitive arc magma could produce most of the western belt mafic intrusion isotope data. Up to 40% assimilation of this endmember in a primitive arc magma would

produce the higher oxygen isotope signature in mafic rocks of the Fine Gold intrusive suite, which intruded into metasedimentary crust rather than ophiolitic material as described above.

In the central belt, metapelitic rocks of the Kings sequence are exposed as upper-crustal wallrock. The isotope ratios of central belt mafic plutons that intruded the Kings sequence can be reproduced through 20-50% assimilation of that endmember by a primitive arc magma (Fig. 3a–b). Assimilation of Proterozoic metasedimentary rock (more crustal radiogenic isotopes) would result in less total assimilation required (10-20%) to reproduce the observations from the mafic samples of that belt (Fig. 3; Table 2). Further, some metamorphic pendants of the central belt host Paleozoic metasedimentary shallow-water continental margin sequences (*i.e.*, Saleeby and Busby, 1993; Attia et al., 2018), and thus in our model could be represented by assimilation of Paleozoic metasedimentary rocks in the central belt. The mafic intrusions that require the most assimilation based on their isotope ratios intrude such Paleozoic metasedimentary rocks, so the best-fitting modeled proportions of assimilation for the central belt mafic plutons is ~10 to 35%.

In all regions of the eastern belt, modeled assimilation using these Proterozoic endmembers into a primitive arc magma allows for 5–20% metasedimentary or up to ~25% metaigneous contribution in the mafic intrusions. Instead, mixing with an “enriched” arc basalt could require as little as 0% assimilation, or up to similar (20–25%) proportions of Proterozoic metasedimentary and metaigneous assimilants (Fig. 3; Table 2). Pre-existing Proterozoic metasedimentary and metaigneous basement samples are highly heterogeneous isotopically. The values we use to model these endmember assimilants are derived from xenoliths and basement outcrops (Table 1; Table S5), including lower-crustal granulite xenoliths (mostly metasedimentary) from the Mojave and basement exposures in Southern California (Table S5). No oxygen isotope data exists for these rocks, so the average oxygen isotope ratios of lower-crustal metasedimentary and metaigneous rocks compiled for the central belt were used. A final separate potential assimilant found in the eastern belt includes Paleozoic metasedimentary rocks of the Mount Morrison roof pendant, the Inyo

facies, and similar rocks sampled in the Mojave Desert. Up to 30% assimilation of Paleozoic metasedimentary assimilant by primitive or enriched arc magmas is permissible to explain the isotopic characteristics of the eastern belt mafic plutons (Fig. 3; Table 2).

6.3. Likely 10–20% assimilation in mafic compositions across the batholith

In summary, these models indicate that the mafic rocks from each belt incorporated approximately 10 to 20% of assimilants of their local crustal column, with potentially higher values up to ~35–40% in the central belt and Fine Gold suite. These models represent a first-order estimate of the proportion of assimilation in these mafic rocks—they are not energy-constrained, and the ranges in these estimates in part reflect large uncertainties in the model end-member components (Fig. A2, A3).

To change the isotopic composition of the mafic magmas parental to these intrusions, the leverage that the assimilant has depends on its compositional and isotopic difference compared to the parental magma. In a homogeneous, isotopically mantle-like crustal column, such as in an oceanic arc or accreted terrane with juvenile radiogenic isotope signatures and a restricted range in oxygen isotope values, that leverage will be small. However, in a heterogeneous, tectonically assembled setting, like the Sierra Nevada, there will be a range in the radiogenic and oxygen isotope leverage depending on the particular crustal assemblage that the magma interacts with (Fig. 4).

Broadly, these results are consistent with thermal models for assimilation in basaltic magmas, where up to ~20 % assimilation can occur without significant corresponding melt evolution. The early (*i.e.*, olivine-only) stages of crystallization of primitive mantle-derived basalts can accommodate significant assimilation and corresponding isotopic and trace element compositional changes, in part due to suppression of crystallization (Bowen, 1922; Reiners et al., 1995). Higher water concentration of parental mafic magmas further increases assimilation (Reiners et al., 1995).

Depending on the crustal composition and depth (and thus temperature of the surrounding crust), thermodynamic simulations by Heinonen and others (2021) on arc basaltic magma compositions allow for at least 10–20% assimilation relative to the mass of the parental melt while remaining basaltic (<52 wt.% SiO₂, <5 wt.% Na₂O+K₂O) in composition and <50% crystallinity—necessary for the magmas to be able to further ascend. Compositions of assimilants in those models are relatively mafic average crustal compositions. Those compositional constraints are likely stricter than required for the upper-crustal mafic intrusions of this study, as their parental melts are likely non-primitive basalt to basaltic andesite compositions (Fig. A4; Lewis et al., 2024; Ryan-Davis et al., *Chapter 3*). Potentially 30–40 wt.% assimilation in the models of Heinonen et al. (2021) would produce basaltic andesite (to andesite) compositions, which is allowable by the whole-rock chemistry of these mafic intrusions (Fig. A4; Lewis et al., 2024; Ryan-Davis et al., *Chapter 3*). Perhaps most importantly, these thermal models show that crustal isotopic signatures (for example, up to –7 unit decrease in ε Nd while maintaining a basaltic composition) are readily produced by these relatively low amounts of assimilation (Reiners et al., 1995; Bohrson and Spera, 2001).

It is worth exploring the implications of these results for the use of mafic intrusions to define mantle end-member compositions. Potentially, the Four Corners intrusion of the western belt could have experienced no assimilation and be representative of the most primitive endmember basaltic magmas of the batholith. However, the ophiolitic basement of the western belt has a primitive mantle-like isotopic signature (Saleeby, 2011), and thus was not modeled as an assimilant. Assimilation of the ophiolite and associated rocks would not be identifiable, if it occurred (*i.e.*, Fig. 4b). Likewise, some intrusions of the eastern belt could represent 0% assimilation if an enriched source is assumed. However, this leads us to the question—why would no assimilation and thus an enriched mantle source be the explanation for the eastern belt mafic intrusions? They are in a setting with much thicker crust and lithosphere to interact with compared to the western (and central)

belt, where it is more readily apparent that assimilation affected the mafic intrusions. This remains an open question.

7. IMPLICATIONS FOR THE GENERATION OF FELSIC CRUST

7.1. Relationships between mafic plutons and the evolved batholith

The current understanding of arc magmas is that most differentiation and contamination occurs in the lower crust (*e.g.*, Pimenta-Silva et al., 2024). Interaction between granitoid magmas and metasedimentary or granulite rocks has been documented with field and geochemical evidence globally (Voshage et al., 1990; Otamendi et al., 2008; Lackey et al., 2005; Rezeau et al., 2024). It is possible that mid- to upper-crustal assimilation contributes to the signatures of these mafic magmas (*i.e.*, Kemp et al., 2007), but lower-crustal assimilation is likely (*i.e.*, MASH model, Hildreth and Moorbath, 1988). Assimilation at or deeper than ~ 0.7 GPa has been documented in the Sierra Nevada batholith (Lackey et al., 2005; Rezeau et al., 2024).

Granitoids from the Sierra Nevada batholith have isotopic trends across the batholith similar to those observed in the mafic rocks (Fig. 2). Indeed, similar estimates, ~ 5 – 20% with up to ~ 35 – 40% assimilation to generate felsic rocks, have been proposed on the basis of measurements of the oxygen, neodymium, and strontium isotope ratios observed (Lackey et al., 2005, 2008, 2012; Holland et al., 2013). This means that significantly different processes of assimilation are not required to generate intermediate-felsic compositions, but rather, that assimilation occurs early in the differentiation process, in the mafic endmembers. Further crystallization-differentiation of these contaminated mafic parents could produce many of the more evolved intrusions of the batholith, as could mixing of these mafic magmas with isotopically similar felsic endmembers.

However, though rare in these mafic plutons, zircon inheritance and xenocrystic zircon cores are not uncommon in associated evolved plutons throughout the Sierra. This must be due to assimilation of older crust (*e.g.*, Coleman and Glazner,

1997; Ryan-Davis et al., *Chapter 2*). In some of the largest and most thoroughly studied Sierra Nevada intrusive suites (*i.e.* Tuolumne), ancient (Proterozoic) crust must have been involved in forming the more evolved rocks of the suites compared to mafic rocks of the same suite, as the felsic end-members of the suite have isotope ratios indicating more assimilation of pre-existing crust (Coleman and Glazner, 1997).

7.2. Isotopic variations with time are due to heterogeneous crustal columns, not arc maturation

The results of this study and Ryan-Davis et al. (Chapter 3) show that, as the locus of Cretaceous magmatism in the Sierra Nevada batholith shifted from west to east (Fig. 1B), the geochemistry and field relationships of mafic intrusions also changed, and that these changes depend upon geographic belt.

The spatial migration of the magmatic locus may be linked at least in part to thermal maturation of the arc system or stress-field changes, potentially leading to migration and/or spatial focusing of magmatism (*e.g.*, Cao et al., 2015; Ardill et al., 2018; Chapman et al., 2021). Similarly, an external driver of magmatic activity was likely responsible for the timing of intrusion of mafic plutons in the eastern belt of this study, with ages that correspond to an episode of extensional diking in the Jurassic and abundant Cretaceous mafic intrusions that correspond to locally enhanced magmatism (Lewis et al., 2024).

The controls on where, geographically, magmatism occurs in heterogeneous arc crust (*i.e.*, along a continental margin; Fig. 4c) primarily drives these observed geochemical shifts. This does not exclude heterogeneity that already exists in the primary mantle-derived mafic magmas of an arc (*e.g.*, Turner and Langmuir 2022), but such heterogeneity would not be expected to correlate with the geologic belts of the upper plate. Most importantly, shifts in isotope ratios in these mafic intrusions are indeed linked to the geologic belts, showing that upper-plate geochemical signatures are imparted upon products of early stages of differentiation, while magmas are still mafic. Thus, what appears to be temporal shifts in isotope ratios with time (Fig. 5)

are, we conclude, not the result of secular changes in how much crust is assimilated and recycled over time. Instead, our results demonstrate that the time progression is an induced correlation brought about by the time-transgressive shift of the locus of Sierra Nevada magmatism from west to east through pre-existing crust with heterogeneous isotopic signatures (Fig. 4a). We have shown that ~10–20% assimilation is consistently required for all of the mafic intrusions across the central Sierra Nevada batholith, which all represent a similar, early stage of differentiation (Fig. 3, Table 2). This means that temporal shifts in isotope ratios (and by extension, other compositional aspects such as trace element signatures) do not reflect variable amounts of assimilation related to secular changes in arc dynamics.

Instead, a unified process wherein magmas interact with the crustal column across the arc, potentially to a consistent degree, is modulated by the pre-existing geology. In detail, thermal maturation of a given region can result in isotopic evolution within a single system (Pimenta-Silva et al., 2024). However, at a broader arc-wide and even global scale, secular changes in isotopic signatures are instead a reflection of tectonic processes that control the locus of magmatism of an arc. Similar spatial isotopic trends have been documented globally, including in erupted volcanic rocks (Rogers and Hawkesworth, 1989; Haschke et al., 2006; Mamani et al., 2010; Chapman et al., 2017). Sundell and Macdonald (2022) have shown that the spatial pattern of hafnium isotope ratios in global datasets depends upon the type of crust that is being reworked (*i.e.*, young accreted terranes versus older continental crust). Thus, changes in isotopic signatures do not necessarily reflect a change in reworking or recycling of crust by arc magmas, but rather, a change in the type of crust involved.

When isotopic variations are placed in spatial context, the observation that their changes are controlled by local geology is readily evident, as shown here. In detrital studies one loses such geographic and geologic context. A comparison between the results of this study and detrital zircons from Nevada show that the isotopic shifts with time are the same (Fig. 5b). Such isotopic shifts, when inferred from detrital zircon studies, are often interpreted as arc-wide or potentially globally unified processes such as cyclicity within orogenic subduction systems or changes in crustal

recycling or reworking with time (e.g., DeCelles et al., 2009; Dhuime et al., 2012; Storck et al., 2020). Our results demonstrate that variability of the crust is a primary control on arc-related isotopic signatures that could easily be overlooked with missing geographic context.

8. CONCLUSIONS

The diversity of isotope ratios in evolved mafic arc magmas may be understood by a simplified model wherein mafic magmas inherit isotopic fingerprints of the particular lithospheric and crustal column through which they ascend. Where pre-existing crust has variable isotopic “leverage,” such as in the Sierra Nevada batholith, this process can be identified by linking isotopic heterogeneity to the composition of tectonically assembled belts of upper-plate lithosphere and crust. Potentially, such a process would not be evident in a juvenile/oceanic arc setting where the upper plate is isotopically homogeneous.

The mafic intrusions of the Sierra Nevada vary across the batholith from west to east in a predictable way, and their isotopic signatures mirror those of intermediate to felsic plutons. This implies upper-plate control on the isotopic signature of mafic magmas of the batholith as magmatism shifted locations (sweeping from west to east during Cretaceous arc activity). Mafic magmas may thus assimilate crust in modest proportions, early during differentiation. This process occurs with only limited evolution of the major-element melt composition, but strongly affects isotopic (and trace element) signatures. The gabbros and diorites of the batholith represent products of mantle-derived melts that have been modified by relatively minor assimilation (10–20%, with more extreme cases up to ~40%). Thus, extensive crustal melting to produce more evolved compositions is not required to observe crustally-influenced signatures in arc plutons.

Temporal variations in isotopic compositions of magmas via the direct rock record or the detrital zircon record must be interpreted within the regional context of the lithosphere through which magmas transited and with which they interacted.

ACKNOWLEDGEMENTS

Funding was provided by the National Science Foundation (EAR-2105371). We thank Mike Spicuzza and Drae Rogers at the University of Wisconsin, Madison, for assistance and advice on zircon mount preparation for SIMS analyses, and Michael Bizimis at the University of South Carolina for Sr and Nd isotope analyses.

REFERENCES

Ague, J.J., Brimhall, G.H., 1987, Granites of the batholiths of California: products of local assimilation and regional-scale crustal contamination (USA). *Geology* 15, 63–66. [https://doi.org/10.1130/0091-7613\(1987\)15<63:GOTBOC>2.0.CO;2](https://doi.org/10.1130/0091-7613(1987)15<63:GOTBOC>2.0.CO;2)

Ague, J.J., Brimhall, G.H., 1988, Magmatic arc asymmetry and distribution of anomalous plutonic belts in the batholiths of California: Effects of assimilation, crustal thickness, and depth of crystallization. *Geological Society of America Bulletin*, 100, 912–927. [https://doi.org/10.1130/0016-7606\(1988\)100<0912:MAAADO>2.3.CO;2](https://doi.org/10.1130/0016-7606(1988)100<0912:MAAADO>2.3.CO;2)

Andrews, G.D., Busby, C.J., Brown, S.R., Fisher, C.M., Davila-Harris, P., Strickland, A., Vervoort, J.D., Pettus, H.D., McDowell, F.W. and Murray, B.P., 2022, Petrogenesis of voluminous silicic magmas in the Sierra Madre Occidental large igneous province, Mexican Cordillera: Insights from zircon and Hf-O isotopes. *Geosphere*, 18(3), pp.946-984.

Annen, C., Blundy, J.D., Sparks, R.S.J., 2006, The genesis of intermediate and silicic magmas in deep crustal hot zones. *Journal of Petrology*, 47, 505–539. <https://doi.org/10.1093/petrology/egi084>

Ardill, K., Attia, S., Memeti, V., Paterson, S.R., 2024, Fingerprinting the geochemical signals of episodic arc activity in the Sierra Nevada batholith in space and time, *Geological Society of America Bulletin*, 1–21. <https://doi.org/10.1130/B37266.1/6351187/b37266.pdf>

Attia, S., Paterson, S.R., Cao, W., Chapman, A.D., Saleeby, J., Dunne, G.C., Stevens, C.H., Memeti, V., 2018, Late Paleozoic tectonic assembly of the Sierra Nevada prebatholithic framework and western Laurentian provenance links based on synthesized detrital zircon geochronology. *Special Paper of the Geological Society of America*, 540, 267–295. [https://doi.org/10.1130/2018.2540\(12\)](https://doi.org/10.1130/2018.2540(12))

Attia, S., Paterson, S.R., Saleeby, J., Cao, W., 2021, Detrital zircon provenance and depositional links of Mesozoic Sierra Nevada intra-arc strata. *Geosphere*, 17, 1422–1453. <https://doi.org/10.1130/GES02296.1>

Balgord, E.A., Yonkee, W.A., Wells, M.L., Gentry, A. and Laskowski, A.K., 2021, Arc tempos, tectonic styles, and sedimentation patterns during evolution of the North American Cordillera: constraints from the retroarc detrital zircon archive. *Earth-Science Reviews*, 216, 103557. <https://doi.org/10.1016/j.earscirev.2021.103557>

Bateman, P.C., 1992, Plutonism in the central part of the Sierra Nevada batholith, California. *US Geological Survey Professional Paper* 1483.

Bateman, P.C., Clark, L.D., Huber, N.K., Moore, J.G., Rinehart, C.D., 1963, The Sierra Nevada batholith—a synthesis of recent work across the central part. *US Geological Survey Professional Paper* 414D, 1–46.

Bateman, P.C., Clark, L.D., 1974, Stratigraphic and structural setting of the Sierra Nevada batholith, California. *Pacif. Geol.* 8, 79–89.

Bea, F., Bortnikov, N., Cambeses, A., Chakraborty, S., Molina, J.F., Montero, P., Morales, I., Silantiev, S., Zinger, T., 2022, Zircon crystallization in low-Zr mafic magmas: Possible or impossible? *Chemical Geology*, 602, 120898. <https://doi.org/10.1016/j.chemgeo.2022.120898>

Beard, B.L., Glazner, A.F., 1995, Trace element and Sr and Nd isotopic compositions of mantle xenoliths from the Big Pine volcanic field, California. *Journal of Geophysical Research*, 100, 4169–4179.

Belousova, E.A., Kostitsyn, Y.A., Griffin, W.L., Begg, G.C., O'Reilly, S.Y., Pearson, N.J., 2010, The growth of the continental crust: Constraints from

zircon Hf-isotope data. *Lithos*, 119, 457–466.
<https://doi.org/10.1016/j.lithos.2010.07.024>

Blatter, D.L., Sisson, T.W., Hankins, W. Ben (2013). Crystallization of oxidized, moderately hydrous arc basalt at mid- to lower-crustal pressures: Implications for andesite genesis. *Contributions to Mineralogy and Petrology*, 166, 861–886. <https://doi.org/10.1007/s00410-013-0920-3>

Bohrson, W.A., Spera, F.J., 2001, Energy-constrained open-system magmatic processes II: Application of energy- constrained assimilation - Fractional crystallization (EC-AFC) model to magmatic systems. *Journal of Petrology*, 42, 1019–1041. <https://doi.org/10.1093/petrology/42.5.1019>

Bowen, N.L., 1922, The Reaction Principle in Petrogenesis. *Journal of Geology*, 30, 177–198. <https://doi.org/10.1086/622871>

Bowen, N., 1928, *The Evolution of the Igneous Rocks*. Princeton University Press, Princeton, New Jersey.

Bucholz, C.E., Jagoutz, O., VanTongeren, J.A., Setera, J., Wang, Z., 2017, Oxygen isotope trajectories of crystallizing melts: Insights from modeling and the plutonic record. *Geochimica et Cosmochimica Acta*, 207, 154–184. <https://doi.org/10.1016/j.gca.2017.03.027>

Bushey, J.C., Snock, A.W., Barnes, C.G., Frost, C.D., 2006, Geology of the bear mountain intrusive complex, Klamath Mountains, California. *Special Paper of the Geological Society of America*, 410, 287–315.
[https://doi.org/10.1130/2006.2410\(14\)](https://doi.org/10.1130/2006.2410(14))

Cao, W., Paterson, S., Memeti, V., Mundil, R., Anderson, J.L., Schmidt, K., 2015, Tracking paleodeformation fields in the Mesozoic central Sierra Nevada arc: Implications for intra-arc cyclic deformation and arc tempos. *Lithosphere* 7, 296–320. <https://doi.org/10.1130/L389.1>

Cao, W., Paterson, S., Saleeby, J., Zalunardo, S., 2016, Bulk arc strain, crustal thickening, magma emplacement, and mass balances in the Mesozoic Sierra Nevada arc. *Journal of Structural Geology*, 84, 14–30.
<https://doi.org/10.1016/j.jsg.2015.11.002>

Cavosie, A., Kita, N., Valley, J., 2009, Primitive oxygen-isotope ratio recorded in magmatic zircon from the Mid-Atlantic Ridge. *American Mineralogist*, 94, 926–934. <https://doi.org/10.2138/am.2009.2982>

Chapman, A.D., Ducea, M.N., Kidder, S., Petrescu, L., 2014, Geochemical constraints on the petrogenesis of the Salinian arc, central California: Implications for the origin of intermediate magmas. *Lithos*, 200–201, 126–141. <https://doi.org/10.1016/j.lithos.2014.04.011>

Chapman, A.D., Saleeby, J.B., Wood, D.J., Piasecki, A., Kidder, S., Ducea, M.N., Farley, K.A., 2012, Late cretaceous gravitational collapse of the southern Sierra Nevada batholith, California. *Geosphere*, 8, 314–341. <https://doi.org/10.1130/GES00740.1>

Chapman, J.B., Ducea, M.N., Kapp, P., Gehrels, G.E., DeCelles, P.G., 2017, Spatial and temporal radiogenic isotopic trends of magmatism in Cordilleran orogens. *Gondwana Research*, 48, 189–204. <https://doi.org/10.1016/j.gr.2017.04.019>

Chapman, J.B., Shields, J.E., Ducea, M.N., Paterson, S.R., Attia, S., Ardill, K.E., 2021, The causes of continental arc flare ups and drivers of episodic magmatic activity in Cordilleran orogenic systems. *Lithos*, 398–399, 106307. <https://doi.org/10.1016/j.lithos.2021.106307>

Chen, J.H., Moore, J.G., 1982, Uranium-lead isotopic ages from the Sierra Nevada batholith, California. *Journal of Geophysical Research*, 87, 4761–4784.

Chin, E.J., Lee, C.T.A., Barnes, J.D., 2014, Thickening, refertilization, and the deep lithosphere filter in continental arcs: Constraints from major and trace elements and oxygen isotopes. *Earth and Planetary Science Letters*, 397, 184–200. <https://doi.org/10.1016/j.epsl.2014.04.022>

Clemens-Knott, D., 1992, Geologic and isotopic investigations of the early Cretaceous Sierra Nevada batholith, Tulare Co., CA and the Ivrea Zone, NW Italian Alps: examples of interaction between mantle-derived magma and continental crust. California Institute of Technology.

Clemens-Knott, D., Gevedon, M., 2025, Zircon U-Pb-Hf isotope evidence from gabbros of the Summit Igneous Complex for a latest Jurassic rift through the southern Sierra Nevada arc crust, California, USA, in: Riggs, N., Putirka, K., Wakabayashi, J. (Eds.), *The Virtue of Fieldwork in Volcanology, Sedimentology, Structural Geology, and Tectonics—Celebrating the Career of Cathy Busby*. Geological Society of America Special Paper, 1–34. [https://doi.org/https://doi.org/10.1130/2025.2563\(08\)](https://doi.org/10.1130/2025.2563(08))

Clemens-Knott, D., Saleeby, J.B., 1999, Impinging ring dike complexes in the Sierra Nevada batholith, California: Roots of the Early Cretaceous volcanic arc. *Geological Society of America Bulletin*, 111, 484–496. [https://doi.org/10.1130/0016-7606\(1999\)111<0484:IRDCIT>2.3.CO;2](https://doi.org/10.1130/0016-7606(1999)111<0484:IRDCIT>2.3.CO;2)

Coleman, D.S., Frost, T.P., Glazner, A.F., 1992, Evidence from the Lamarck granodiorite for rapid late Cretaceous crust formation in California. *Science*, 258, 1924–1926. <https://doi.org/10.1126/science.258.5090.1924>

Coleman, D.S., Glazner, A.F., 1997, The sierra crest magmatic event: Rapid formation of juvenile crust during the late cretaceous in California. *International Geology Review*, 39, 768–787. <https://doi.org/10.1080/00206819709465302>

Cornet, J., Laurent, O., Wotzlaw, J.F., Antonelli, M.A., Otamendi, J., Bergantz, G.W., Bachmann, O., 2022, Reworking subducted sediments in arc magmas and the isotopic diversity of the continental crust: The case of the Ordovician Famatinian crustal section, Argentina. *Earth and Planetary Science Letters*, 595, 117706. <https://doi.org/10.1016/j.epsl.2022.117706>

Crisp, L.J., Berry, A.J., 2022, A new model for zircon saturation in silicate melts. *Contributions to Mineralogy and Petrology*, 177. <https://doi.org/10.1007/s00410-022-01925-6>

Davidson, J.P., Harmon, R.S., 1989, Oxygen isotope constraints on the petrogenesis of volcanic arc magmas from Martinique, Lesser Antilles. *Earth and Planetary Science Letters*, 95, 255–270. [https://doi.org/10.1016/0012-821X\(89\)90101-5](https://doi.org/10.1016/0012-821X(89)90101-5)

DePaolo, D.J., 1981. A neodymium and strontium isotopic study of the Mesozoic calc-alkaline granitic batholiths of the Sierra Nevada and Peninsular ranges, California. *Journal of Geophysical Research*, 86, 10470–10488.

Dhuime, B., Hawkesworth, C.J., Cawood, P.A. and Storey, C.D., 2012. A change in the geodynamics of continental growth 3 billion years ago. *Science*, 335, 1334–1336. <https://doi.org/10.1126/science.1216066>

Dhuime, B., Hawkesworth, C.J., Delavault, H., Cawood, P.A., 2017. Continental growth seen through the sedimentary record. *Sedimentary Geology*, 357, 16–32. <https://doi.org/10.1016/j.sedgeo.2017.06.001>

Domenick, M.A., Kistler, R.W., Dodge, F.C.W., Tatsumoto, M., 1983. Nd and Sr isotopic study of crustal and mantle inclusions from the Sierra Nevada and implications for batholith petrogenesis. *Geological Society of America Bulletin*, 94, 713–719. [https://doi.org/10.1130/0016-7606\(1983\)94<713:NASISO>2.0.CO;2](https://doi.org/10.1130/0016-7606(1983)94<713:NASISO>2.0.CO;2)

Ducea, M.N., 1998. A petrologic investigation of deep-crustal and upper-mantle xenoliths from the Sierra Nevada, California; constraints on lithospheric composition beneath continental arcs and the origin of Cordilleran batholiths. California Institute of Technology.

Ducea, M.N., 2001. The California arc: Thick granitic batholiths, eclogitic residues, lithospheric-scale thrusting, and magmatic flare-ups. *GSA Today* 4–10.

Ducea, M.N., Saleeby, J.B., 1998. The age and origin of a thick mafic-ultramafic keel from beneath the Sierra Nevada batholith. *Contributions to Mineralogy and Petrology*, 133, 169–185.
<https://doi.org/10.1007/s004100050445>

Dumitru, T.A., Wakabayashi, J., Wright, J.E., Wooden, J.L., 2010. Early Cretaceous transition from nonaccretionary behavior to strongly accretionary behavior within the Franciscan subduction complex. *Tectonics*, 29, TC5001. <https://doi.org/10.1029/2009TC002542>

Eiler, J. M., Crawford, A., Elliott, T., Farley, K.A., ValleyJ.W., Stolper, E.M., 2000, Oxygen Isotope Geochemistry of Oceanic Arc Lavas. *Journal of Petrology*, 41, 229–256. <https://doi.org/10.1180/minmag.1998.62a.1.221>

Eiler, J.M., 2001, Oxygen isotope variations of basaltic lavas and upper mantle rocks. *Reviews in Mineralogy and Geochemistry*, 43, 319–364. <https://doi.org/10.1515/9781501508745-008>

Evernden J.F., Kistler, R.W., 1970, Chronology of Emplacement of Mesozoic Batholithic Complexes in California and Western Nevada. US Geological Survey Professional Paper 623, 1–42.

Farmer, G.L., DePaolo, D.J., 1983, Origin of Mesozoic and Tertiary granite in the western United States and implications for Pre-Mesozoic crustal structure. 2. Nd and Sr isotopic studies of unmineralized and Cu- and Mo-mineralized granite in the Precambrian craton. *Journal of Geophysical Research*, 88, 3379–3401. <https://doi.org/10.1029/jb089ib12p10141>

Frazer, R.E., Coleman, D.S., Mills, R.D., 2014, Zircon U-Pb geochronology of the Mount Givens granodiorite: implications for the genesis of large volumes of eruptible magma. *Journal of Geophysical Research, Solid Earth* 119, 2907–2924. <https://doi.org/10.1002/2013JB010716>

Frost, T.P., 1987, Sample localities, radiometric ages, descriptions, and major- and trace-element abundances of Late Jurassic mafic plutonic rocks, eastern Sierra Nevada, California. USGS Open-File Rep. 87–484, 1–32.

Frost, T.P., Mahood, G.A., 1987, Field, chemical, and physical constraints on mafic-felsic magma interaction in the Lamarck Granodiorite, Sierra Nevada, California. *Geological Society of America Bulletin*, 99, 272–291.

Gao, R., Lassiter, J.C., Ramirez, G., 2017, Origin of temporal compositional trends in monogenetic vent eruptions: Insights from the crystal cargo in the Papoose Canyon sequence, Big Pine Volcanic Field, CA. *Earth and Planetary Science Letters*, 457, 227–237. <https://doi.org/10.1016/j.epsl.2016.10.013>

Gao, Y.Y., Li, X.H., Griffin, W.L., O'Reilly, S.Y., Wang, Y.F., 2014, Screening criteria for reliable U-Pb geochronology and oxygen isotope analysis in uranium-rich zircons: A case study from the Suzhou A-type granites, SE China. *Lithos*, 192–195, 180–191.
<https://doi.org/10.1016/j.lithos.2014.02.002>

Gevedon, M., 2013, Paired oxygen and hafnium isotopic analysis of zircon from gabbros: identifying potential Mesozoic mantle heterogeneity in the Sierra Nevada arc. California State University, Fullerton.

Ghatak, A., Basu, A.R., Wakabayashi, J., 2013, Implications of Franciscan Complex graywacke geochemistry for sediment transport, provenance determination, burial-exposure duration, and fluid exchange with cosubducted metabasites. *Tectonics*, 32, 1480–1492.
<https://doi.org/10.1002/tect.20078>

Grimes, C.B., Ushikubo, T., John, B.E., Valley, J.W., 2011, Uniformly mantle-like $\delta^{18}\text{O}$ in zircons from oceanic plagiogranites and gabbros. *Contributions to Mineralogy and Petrology*, 161, 13–33. <https://doi.org/10.1007/s00410-010-0519-x>

Hanchar, J.M., Miller, C.F., Wooden, J.L., Bennett, V.C., Staude, J.-M.G., 1994, Evidence from xenoliths for a dynamic lower crust, eastern Mojave desert, California. *Journal of Petrology*, 35, 1377–1415.

Haschke, M., Günther, A., Melnick, D., Echtler, H., Reutter, K.-J., Scheuber, E. and Oncken, O., 2006, Central and Southern Andean tectonic evolution inferred from arc magmatism, in Oncken, O., Chong, G., Franz, G., Giese, P., Götze, H.-J., Ramos, V.A., Strecker, M.R., Wigger, P., eds. *The Andes. Frontiers in Earth Sciences*. Springer, Berlin, Heidelberg.
https://doi.org/10.1007/978-3-540-48684-8_16

Hawkesworth, C.J., Kemp, A.I.S., 2006, Using hafnium and oxygen isotopes in zircons to unravel the record of crustal evolution. *Chemical Geology*, 226, 144–162. <https://doi.org/10.1016/j.chemgeo.2005.09.018>

Heinonen, J.S., Spera, F.J., Bohrson, W.A., 2022, Thermodynamic limits for assimilation of silicate crust in primitive magmas. *Geology* 50, 81–85. <https://doi.org/10.1130/G49139.1>

Hildreth, W., Moorbath, S., 1988, Crustal contributions to arc magmatism in the Andes of Central Chile. *Contributions to Mineralogy and Petrology*, 98, 455–489. <https://doi.org/10.1007/BF00372365>

Hirt, W.H., 2007, Petrology of the Mount Whitney Intrusive Suite, eastern Sierra Nevada, California: Implications for the emplacement and differentiation of composite felsic intrusions. *Geological Society of America Bulletin*, 119, 1185–1200. <https://doi.org/10.1130/B26054.1>

Holland, J.E., Surpless, B., Smith, D.R., Loewy, S.L., Lackey, J.S., 2013, Intrusive history and petrogenesis of the Ash Mountain Complex, Sierra Nevada batholith, California (USA). *Geosphere*, 9, 691–717. <https://doi.org/10.1130/GES00890.1>

Jacob, J.B., Moyen, J.F., Fiannacca, P., Laurent, O., Bachmann, O., Janoušek, V., Farina, F., Villaros, A., 2021, Crustal melting vs. fractionation of basaltic magmas: Part 2, Attempting to quantify mantle and crustal contributions in granitoids. *Lithos*, 402–403. <https://doi.org/10.1016/j.lithos.2021.106292>

Jagoutz, O., Schmidt, M.W., 2012, The formation and bulk composition of modern juvenile continental crust: The Kohistan arc. *Chemical Geology*, 298–299, 79–96. <https://doi.org/10.1016/j.chemgeo.2011.10.022>

Kemp, A.I.S., Hawkesworth, C.J., Foster, G.L., Paterson, B.A., Woodhead, J.D., Hergt, J.M., Gray, C.M., Whitehouse, M.J., 2007, Magmatic and crustal differentiation history of granitic rocks from Hf-O isotopes in zircon. *Science*, 315, 980–983. <https://doi.org/10.1126/science.1136154>

Kistler, R.W., 1990, Two different lithosphere types in the Sierra Nevada, California, in: Anderson, J.L. (Ed.), *The Nature and Origin of Cordilleran Magmatism*. Geological Society of America Memoir, Boulder, Colorado, 271–281.

Kistler, R.W., Peterman, Z.E., 1973. Variations in Sr, Rb, K, Na, and initial $\text{Sr}^{87}/\text{Sr}^{86}$ in Mesozoic granitic rocks and intruded wall rocks in Central California. *Geological Society of America Bulletin*, 84, 3489–3512.
[https://doi.org/10.1130/0016-7606\(1973\)84<3489:VISRKN>2.0.CO;2](https://doi.org/10.1130/0016-7606(1973)84<3489:VISRKN>2.0.CO;2)

Kistler, R.W., Peterman, Z.E., 1978, Reconstruction of crustal blocks of California on the basis of initial strontium isotopic compositions of Mesozoic granitic rocks. *US Geological Survey Professional Paper* 1071, 1–17.

Lackey, J.S., Robinson Cecil, M., Windham, C.J., Frazer, R.E., Bindeman, I.N., Gehrels, G.E., 2012, The fine gold intrusive suite: The roles of basement terranes and magma source development in the early Cretaceous Sierra Nevada batholith. *Geosphere*, 8, 292–313.
<https://doi.org/10.1130/GES00745.1>

Lackey, J.S., Valley, J.W., Chen, J.H., Stockli, D.F., 2008, Dynamic magma systems, crustal recycling, and alteration in the Central Sierra Nevada batholith: The oxygen isotope record. *Journal of Petrology*, 49, 1397–1426. <https://doi.org/10.1093/petrology/egn030>

Lackey, J.S., Valley, J.W., Hinke, H.J., 2006, Deciphering the source and contamination history of peraluminous magmas using $\delta^{18}\text{O}$ of accessory minerals: Examples from garnet-bearing plutons of the Sierra Nevada batholith. *Contributions to Mineralogy and Petrology*, 151, 20–44.
<https://doi.org/10.1007/s00410-005-0043-6>

Lackey, J.S., Valley, J.W., Saleeby, J.B., 2005, Supracrustal input to magmas in the deep crust of Sierra Nevada batholith: Evidence from high- $\delta^{18}\text{O}$ zircon. *Earth and Planetary Science Letters*, 235, 315–330.
<https://doi.org/10.1016/j.epsl.2005.04.003>

Lahren, M.M., Schweickert, R.A., 1989, Proterozoic and Lower Cambrian miogeoclinal rocks of Snow Lake pendant, Yosemite-Emigrant Wilderness, Sierra Nevada, California: evidence for major Early Cretaceous dextral translation. *Geology*, 17, 156–160.
[https://doi.org/10.1130/0091-7613\(1989\)017<0156:PALCMR>2.3.CO;2](https://doi.org/10.1130/0091-7613(1989)017<0156:PALCMR>2.3.CO;2)

Lewis, M.J., Bucholz, C.E., Jagoutz, O.E., 2021, Evidence for polybaric fractional crystallization in a continental arc: Hidden Lakes mafic complex, Sierra Nevada batholith, California. *Contributions to Mineralogy and Petrology*, 176, 1–27. <https://doi.org/10.1007/s00410-021-01844-y>

Lewis, M.J., Ryan-Davis, J.R., Bucholz, C.E., 2024, Mafic intrusions record mantle inputs and crustal thickness in the eastern Sierra Nevada batholith, California, USA. *Geological Society of America Bulletin*, 136, 1808–1826. <https://doi.org/10.1130/b36646.1>

Macpherson, C.G., Gamble, J.A., Matthey, D.P., 1998, Oxygen isotope geochemistry of lavas from an oceanic to continental arc transition, Kermadec-Hikurangi margin, SW Pacific. *Earth and Planetary Science Letters*, 160, 609–621. [https://doi.org/10.1016/S0012-821X\(98\)00115-0](https://doi.org/10.1016/S0012-821X(98)00115-0)

Mamani, M., Wörner, G., Sempere, T., 2010, Geochemical variations in igneous rocks of the Central Andean orocline (13°S to 18°S): Tracing crustal thickening and magma generation through time and space. *Geological Society of America Bulletin*, 122(1–2), 162–182. <https://doi.org/10.1130/B26538.1>

Moore, J.G., 1959, The Quartz Diorite Boundary Line in the Western United States. *Journal of Geology*, 67, 198–210.

Moore, J.G., Sisson, T.W., 2008, Igneous phenocrystic origin of K-feldspar megacrysts in granitic rocks from the Sierra Nevada batholith. *Geosphere*, 4, 387–400. <https://doi.org/10.1130/GES00146.1>

Moore, N.E., Grunder, A.L., Bohrson, W.A., Carlson, R.W., Bindeman, I.N., 2020, Changing Mantle Sources and the Effects of Crustal Passage on the Steens Basalt, SE Oregon: Chemical and Isotopic Constraints. *Geochemistry, Geophysics, Geosystems*, 21, 1–33. <https://doi.org/10.1029/2020GC008910>

Moyen, J.F., Janoušek, V., Laurent, O., Bachmann, O., Jacob, J.B., Farina, F., Fiannacca, P., Villaros, A., 2021, Crustal melting vs. fractionation of

basaltic magmas: Part 1, granites and paradigms. *Lithos*, 402–403, 106291. <https://doi.org/10.1016/j.lithos.2021.106291>

Mukhopadhyay, B., Manton, W.I., 1994, Upper-mantle fragments from beneath the Sierra Nevada Batholith: Partial fusion, fractional crystallization, and metasomatism in a subduction related ancient lithosphere. *Journal of Petrology*, 35, 1417–1450. <https://doi.org/10.1093/petrology/35.5.1417>

Mullen, E.K., Weis, D., Marsh, N.B., and Martindale, M., 2017, Primitive arc magma diversity: New geochemical insights in the Cascade Arc. *Chemical Geology*, 448, 43–70, doi:10.1016/j.chemgeo.2016.11.006.

Otamendi, J.E., Tibaldi, A.M., Vujovich, G.I., Viñao, G.A., 2008, Metamorphic evolution of migmatites from the deep Famatinian arc crust exposed in Sierras Valle Fértil-La Huerta, San Juan, Argentina. *Journal of South American Earth Science*, 25, 313–335.
<https://doi.org/10.1016/j.jsames.2007.09.001>

Peck, W.H., King, E.M., Valley, J.W., 2000, Oxygen isotope perspective on Precambrian crustal growth and maturation. *Geology*, 28, 363–366.
[https://doi.org/10.1130/0091-7613\(2000\)28<363:OIPOPC>2.0.CO;2](https://doi.org/10.1130/0091-7613(2000)28<363:OIPOPC>2.0.CO;2)

Pickett, D.A., Saleeby, J.B., 1994, Nd, Sr and Pb isotopic characteristics of Cretaceous intrusive rocks from deep levels of the Sierra Nevada batholith, Tehachapi Mountains, California. *Contributions to Mineralogy and Petrology*, 118, 198–215.

Pimenta Silva, M., Giuliani, A., Schaltegger, U., Chiaradia, M., Nowak, A., Schoene, B., Ulmer, P., Müntener, O., 2024, Tracing Lower Crustal Contamination in Continental Arc Magmas Using Sr-Nd-Hf Isotopes: A Combined in Situ and Bulk Rock Approach Applied to the Adamello Batholith. *Journal of Petrology*, 65, egae084.
<https://doi.org/10.1093/petrology/egae084>

Pitcher, W.S., 1987, Granites and yet more granites forty years on. *Geologische Rundschau*, 76, 51–79. <https://doi.org/10.1007/BF01820573>

Raftrey, M.E., Lackey, J.S., Fulton, A.A., Gaines, R.R., Davies, G.R., 2016, Tuffs of the Goddard pendant: snapshots of volcanic source during low-flux magmatism in the Sierra Nevada arc. Geological Society of America Abstracts with Programs, 48. <https://doi.org/10.1130/abs/2016CD-274617>

Ratajeski, K., Glazner, A.F., Miller, B. V., 2001, Geology and geochemistry of mafic to felsic plutonic rocks in the Cretaceous intrusive suite of Yosemite Valley, California. *Geological Society of America Bulletin*, 113, 1486–1502. [https://doi.org/10.1130/0016-7606\(2001\)113<1486:GAGOMT>2.0.CO;2](https://doi.org/10.1130/0016-7606(2001)113<1486:GAGOMT>2.0.CO;2)

Read, H.H., 1948. Granites and granites, in: Gilluly, J. (Ed.), *Origin of Granite*, Geological Society of America Memoir, 28, 1–19.

Reiners, P.W., Nelson, B.K., Ghiorso, M.S., 1995, and Extents of Crustal Contamination of Mantle-Derived Magmas. *Geology*, 23, 563–566.

Rezeau, H., Jagoutz, O., Beaudry, P., Klein, B.Z., Izon, G., Ono, S., 2024, Lower crustal assimilation revealed by sulfur isotope systematics of the Bear Valley Intrusive Suite, southern Sierra Nevada Batholith, California, USA. *Contributions to Mineralogy and Petrology*, 179, 34. <https://doi.org/10.1007/s00410-024-02123-2>

Rogers, G. and Hawkesworth, C.J., 1989, A geochemical traverse across the North Chilean Andes: evidence for crust generation from the mantle wedge. *Earth and Planetary Science Letters*, 91(3–4). 271–285.

Rudnick, R.L., 1995, Making continental crust. *Nature* 378, 571–578.

Ryan-Davis, J., Bucholz, C.E. and Sisson, T.W., *Chapter 2*, Shallow differentiation of primitive arc magmas at the Jurassic Emigrant Gap complex, Sierra Nevada, California. *In review: Journal of Petrology*.

Ryan-Davis, J., Bucholz, C.E., Lackey, J.S., Lewis, M.J., Kylander-Clark, A. and Wilner, O.D., *Chapter 3*, Sierra Nevada upper-crustal mafic intrusions record arc migration into thickened continental crust. *In preparation for: GSA Bulletin*.

Saleeby, J.B., 1992, Petrotectonic and paleogeographic settings of U.S. Cordilleran ophiolites, in Burchfiel, B.C., Lipman, P.W., and Zoback, M.L., (Eds.), *The Cordilleran Orogen: Conterminous U.S.*: Boulder, Colorado, Geological Society of America, *Geology of North America*, G-3, 653–682.

Saleeby, J., 2011, Geochemical mapping of the Kings-Kaweah ophiolite belt, California— Evidence for progressive mélange formation in a large offset transform-subduction initiation environment, in: Wakabayashi, J., Dilek, Y. (Eds.), *Mélanges: Processes of Formation and Societal Significance*: Geological Society of America Special Paper. Geological Society of America, 31–73. [https://doi.org/10.1130/2011.2480\(02\)](https://doi.org/10.1130/2011.2480(02))

Saleeby, J.B., Sams, D.B., Kistler, R.W., 1987, U/Pb zircon, strontium, and oxygen isotopic and geochronological study of the southernmost Sierra Nevada batholith, California (USA). *Journal of Geophysical Research*, 92, 10443–20466. <https://doi.org/10.1029/jb092ib10p10443>

Saleeby, J., Sharp, W., 1980, Chronology of the structural and petrologic development of the southwest Sierra Nevada foothills, California: summary. *Geological Society of America Bulletin*, 91, 1416–1535. [https://doi.org/10.1130/0016-7606\(1980\)91<1416:COTSAP>2.0.CO;2](https://doi.org/10.1130/0016-7606(1980)91<1416:COTSAP>2.0.CO;2)

Saleeby, J.B., Busby, C., 1993, Paleogeographic and tectonic setting of axial and western metamorphic framework rocks of the southern Sierra Nevada, California, in: Dunn, G., McDougall, K. (Eds.), *Mesozoic Paleogeography of the Western United States-II*. Pacific Section SEPM, 197–226.

Saleeby, J.B., Kistler, R.W., Longiaru, S., Moore, J.G., Nokleberg, W.J., 1990, Chapter 14: Middle Cretaceous silicic metavolcanic rocks in the Kings Canyon area, central Sierra Nevada, California, in: Anderson, J.L. (Ed.), *The Nature and Origin of Cordilleran Magmatism*. Geological Society of America Memoir, Boulder, Colorado, 251–270. <https://doi.org/10.1130/MEM174-p251>

Saleeby, J., Ducea, M., Clemens-Knott, D., 2003, Production and loss of high-density batholithic root, southern Sierra Nevada, California. *Tectonics*, 22, 1604. <https://doi.org/10.1029/2002TC001374>

Saleeby, J.B., Farley, K.A., Kistler, R.W., Fleck, R., 2007, Thermal evolution and exhumation of deep-level batholithic exposures, southernmost Sierra Nevada, California, in Cloos, M., Carlson, W.D., Gilbert, M.C., Liou, J.G., and Sorensen, S.S., (Eds.), *Convergent Margin Terranes and Associated Regions: A Tribute to W.G. Ernst*: Geological Society of America Special Paper 419. doi: 10.1130/2007.2419(02).

Sendek, C., 2016, *Zircon Geochemical and Isotopic Constraints on the Evolution of the Mount Givens Pluton, Central Sierra Nevada Batholith*. California State University, San Jose.

Sisson, T.W., Grove, T.L., Coleman, D.S., 1996, Hornblende gabbro sill complex at Onion Valley, California, and a mixing origin for the Sierra Nevada batholith. *Contributions to Mineralogy and Petrology*, 126, 81–108.

Snow, C.A., Wakabayashi, J., Ernst, W.G., Wooden, J.L., 2010, Detrital zircon evidence for progressive underthrusting in Franciscan metagraywackes, west-central California. *Geological Society of America Bulletin*, 122, 282–291. <https://doi.org/10.1130/B26399.1>

Stern, T.W., Bateman, P.C., Morgan, B.A., Newell, M.F., Peck, D.L., 1982, Isotopic U-Pb ages of zircon from the granitoids of the central Sierra Nevada, California. U.S. US Geological Survey Professional Paper 1185, 1–17.

Storck, J.C., Wotzlaw, J.F., Karakas, Ö., Brack, P., Gerdes, A., Ulmer, P., 2020, Hafnium isotopic record of mantle-crust interaction in an evolving continental magmatic system. *Earth and Planetary Science Letters*, 535, 116100. <https://doi.org/10.1016/j.epsl.2020.116100>

Sundell, K.E., Macdonald, F.A., 2022, The tectonic context of hafnium isotopes in zircon. *Earth and Planetary Science Letters*, 584, 117426. <https://doi.org/10.1016/j.epsl.2022.117426>

Tatsumi, Y., Kogiso, T., 2003, The subduction factory: its role in the evolution of the Earth's crust and mantle, in: Larter, R.D., Leat, P.T. (Eds.), Intra-Oceanic Subduction Systems: Tectonic and Magmatic Processes. Geological Society, London, Special Publications, 55–80.

Turner, S.J., Langmuir, C.H., 2022, An Evaluation of Five Models of Arc Volcanism. *Journal of Petrology*, 63, 1–25.
<https://doi.org/10.1093/petrology/egac010>

Turner, S.J., Langmuir, C.H., 2024, An alternative to the igneous crust fluid + sediment melt paradigm for arc lava geochemistry. *Science Advances*, 10, 44–46. <https://doi.org/10.1126/sciadv.adg6482>

Turner, S.J., Langmuir, C.H., Dungan, M.A., Escrig, S., 2017, The importance of mantle wedge heterogeneity to subduction zone magmatism and the origin of EM1. *Earth and Planetary Science Letters*, 472, 216–228.
<https://doi.org/10.1016/j.epsl.2017.04.051>

Valley, J.W., 2003, Oxygen isotopes in zircon. *Reviews in Mineralogy and Geochemistry*, 53, 343–385.
<https://doi.org/https://doi.org/10.2113/0530343>

Valley, J.W., Kinny, P.D., Schulze, D.J., Spicuzza, M.J., 1998, Zircon megacrysts from kimberlite: Oxygen isotope variability among mantle melts. *Contributions to Mineralogy and Petrology*, 133, 1–11.
<https://doi.org/10.1007/s004100050432>

Vervoort, J.D., Patchett, P.J., Gehrels, G.E., Nutman, A.P., 1996, Constraints on early Earth differentiation from hafnium and neodymium isotopes. *Nature*, 379, 624–627. <https://doi.org/10.1038/379624a0>

Vervoort, J.D., Blichert-Toft, J., 1999, Evolution of the depleted mantle: Hf isotope evidence from juvenile rocks through time. *Geochimica et Cosmochimica Acta*, 63, 533–556. [https://doi.org/10.1016/S0016-7037\(98\)00274-9](https://doi.org/10.1016/S0016-7037(98)00274-9)

Vervoort, J.D., Plank, T., Prytulak, J., 2011, The Hf-Nd isotopic composition of marine sediments. *Geochimica et Cosmochimica Acta*, 75, 5903–5926. <https://doi.org/10.1016/j.gca.2011.07.046>

Voshage, H., Hofmann, A.W., Mazzucchelli, M., Rivalenti, G., Sinigoi, S., Raczek, I., Demarchi, G., 1990, Isotopic evidence from the Ivrea Zone for a hybrid lower crust formed by magmatic underplating. *Nature*, 347, 731–736. <https://doi.org/10.1038/347731a0>

Wakabayashi, J., 2015, Anatomy of a subduction complex: Architecture of the Franciscan Complex, California, at multiple length and time scales. *International Geology Review*, 57, 669–746. <https://doi.org/10.1080/00206814.2014.998728>

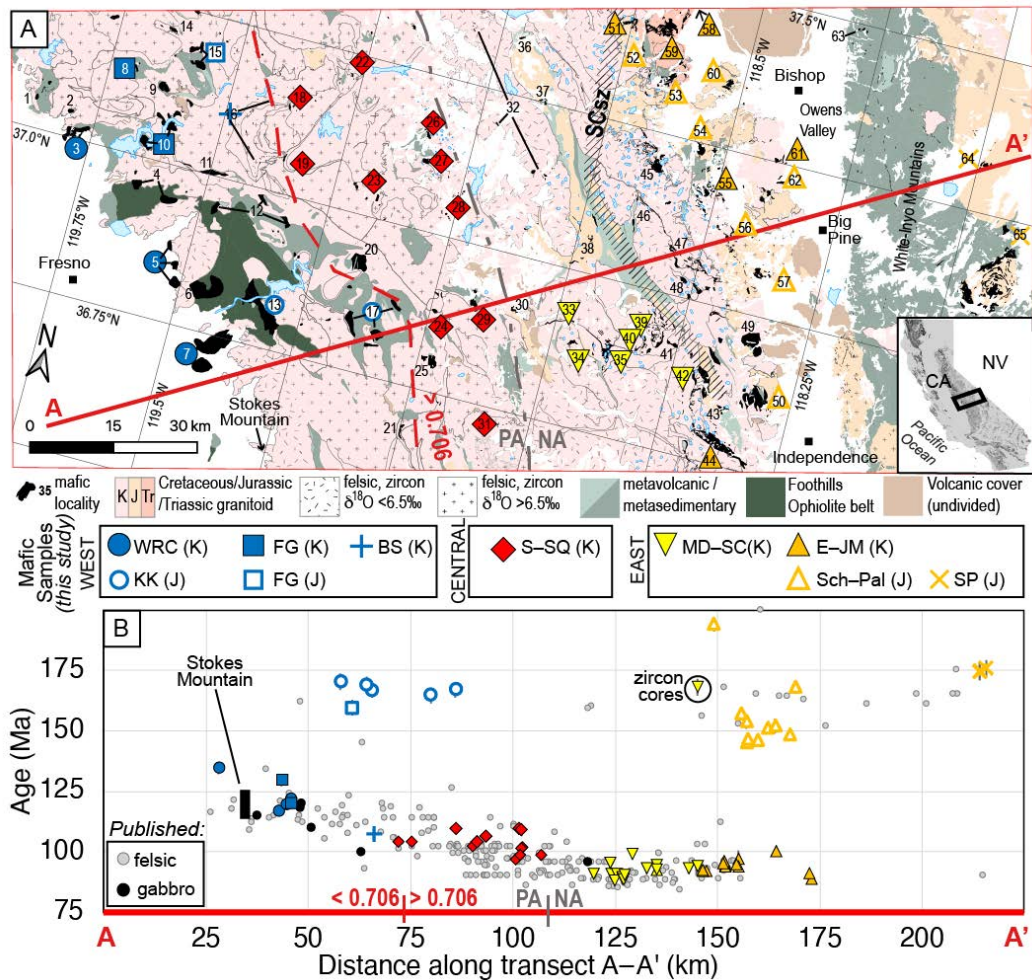
Walker Jr, B.A., Bergantz, G.W., Otamendi, J.E., Ducea, M.N., Cristofolini, E.A., 2015, A MASH Zone Revealed: the Mafic Complex of the Sierra Valle Fértil. *Journal of Petrology*, 56, 1863–1896. <https://doi.org/10.1093/petrology/egv057>

Wang, X.L., Coble, M.A., Valley, J.W., Shu, X.J., Kitajima, K., Spicuzza, M.J., Sun, T., 2014, Influence of radiation damage on Late Jurassic zircon from southern China: Evidence from in situ measurements of oxygen isotopes, laser Raman, U-Pb ages, and trace elements. *Chemical Geology*, 389, 122–136. <https://doi.org/10.1016/j.chemgeo.2014.09.013>

Wenner, J.M., Coleman, D.S., 2004, Magma mixing and cretaceous crustal growth: Geology and geochemistry of granites in the central Sierra Nevada batholith, California. *International Geology Review*, 46, 880–903. <https://doi.org/10.2747/0020-6814.46.10.880>

Zeng, L., Saleeby, J.B., Ducea, M., 2005, Geochemical characteristics of crustal anatexis during the formation of migmatite at the Southern Sierra Nevada, California. *Contributions to Mineralogy and Petrology*, 150, 386–402. <https://doi.org/10.1007/s00410-005-0010-2>

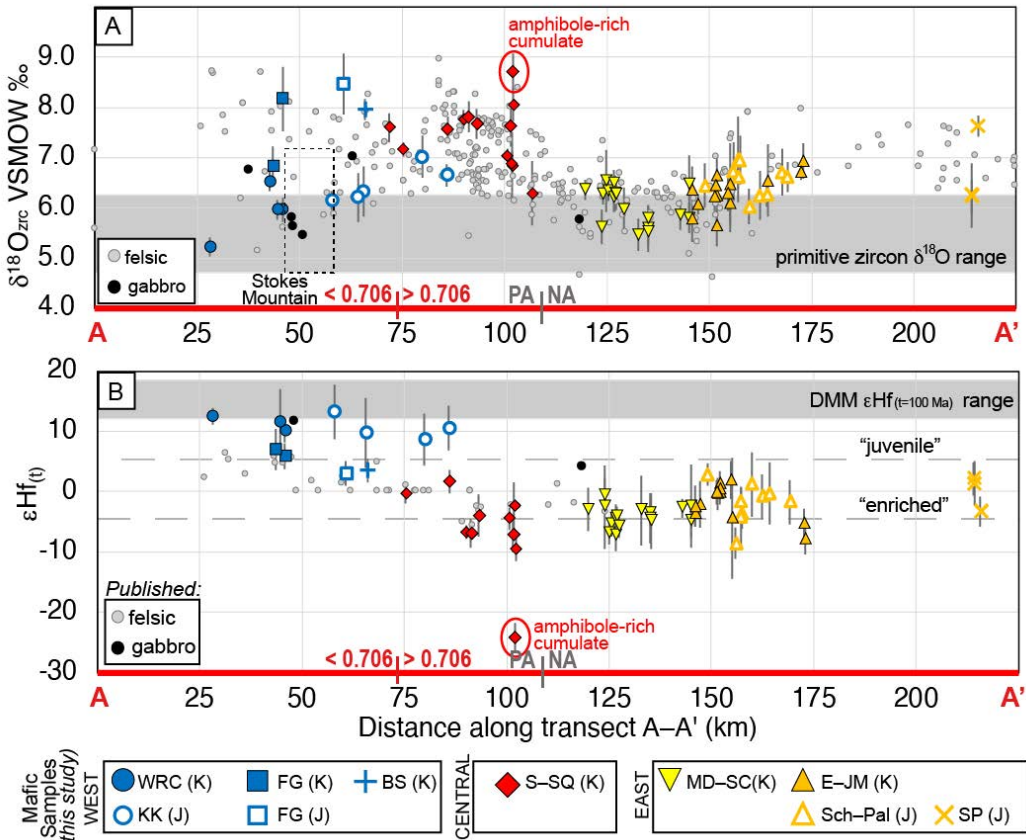
FIGURES



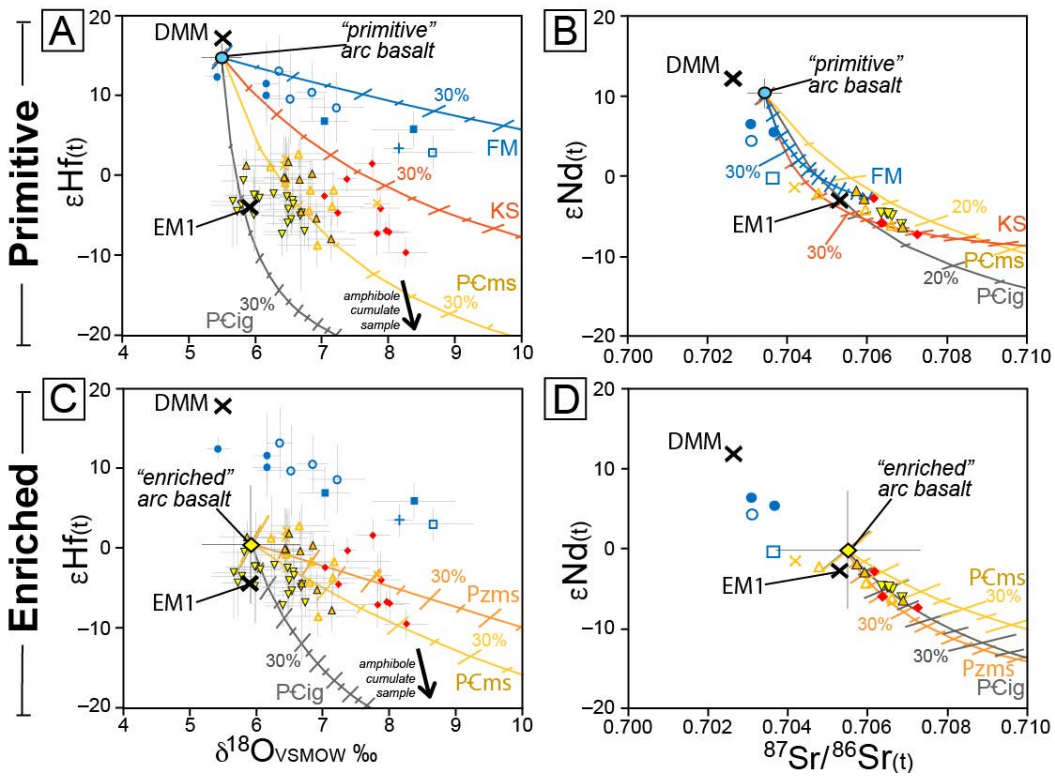
Ch. 4 Figure 1. Overview of the study area and ages.

A)—Geologic map of transect A–A' across the Sierra Nevada batholith with mafic localities (numbered—location details are in Table S1). Transect endpoint locations: 36.5044° , -119.7409° and 37.3595° , -117.9070° (WGS84). Inset shows location within the Sierra Nevada, California. NAD83(HARN) CA State Plane IV (EPSG:2769). Geographic/tectonic boundaries: dashed red line—adjusted $^{87}\text{Sr}/^{86}\text{Sr}_{\text{J}}=0.706$ isopleth (Kistler and Peterman, 1973; Kistler, 1990); dash-dot gray line—Panthalassan (PA)–North American (NA) lithospheric break (Saleeby et al., 1986; Kistler, 1990, 1993; Saleeby and Busby, 1993); diagonal patterned line—Sierra Crest shear zone (SCsz). Sample categories (K—Cretaceous; J—Jurassic): WRC—Western ring complexes; FG—Fine Gold; BS—Big Sandy; KK—Kings-Kaweah ophiolite belt; S-SQ—Shaver and Sequoia intrusive suites; MD-SC—Monarch Divide—Sierra Crest; E-JM—East-John Muir; Sch-Pal—Scheelite—Palisade Crest; SP—Soldier Pass. **B)**—Distance along transect versus zircon U-Pb age (Ma), 2% error smaller than symbols where hidden, from Ryan-Davis et al. (*Chapter 3*). Gray and black circles are published data from the central Sierra Nevada (35.9° – 38.35° N; Lackey et al., 2006;

2008; 2012; Frazer et al., 2014; Sendek 2016) and the most primitive mafic complex at Stokes Mountain (Clemens-Knott and Saleeby, 1999; Gevedon, 2013).

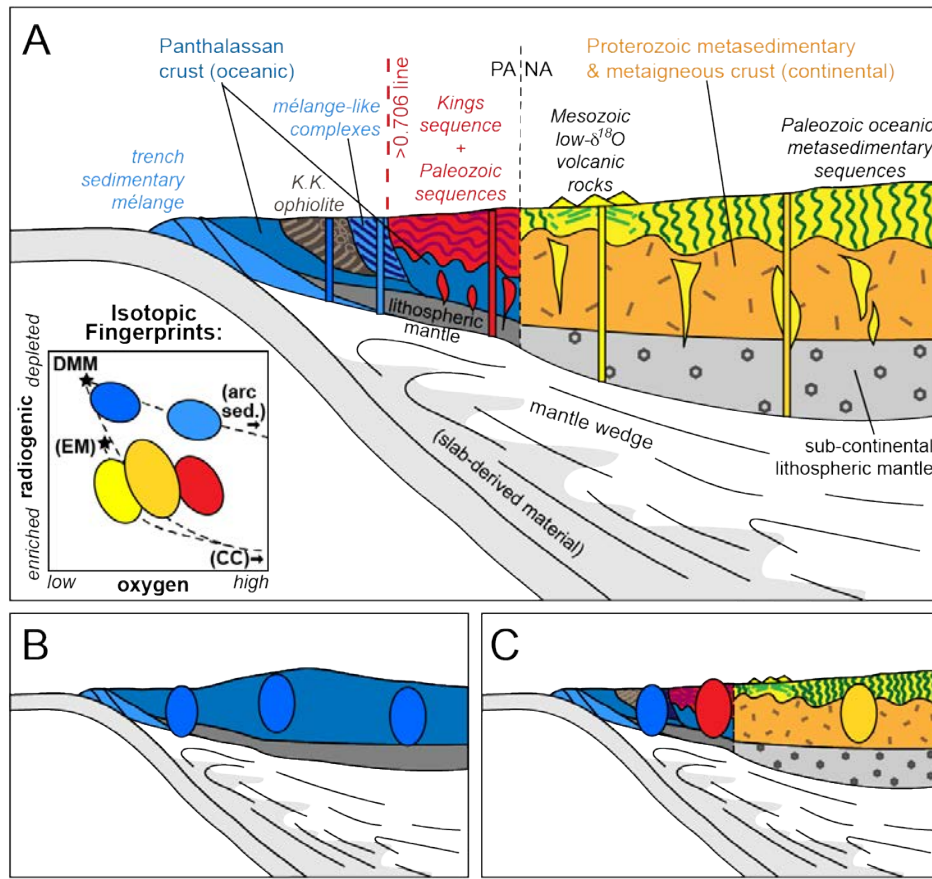


Ch. 4 Figure 2. Distance versus isotope ratios in zircon. Symbols are the same as in Figure 1. **A**—Distance versus sample average zircon $\delta^{18}\text{O}$. Dashed box is Stokes Mountain ring complex gabbro zircon range, which is just south of this transect (Clemens-Knott and Saleeby, 1999; Gevedon, 2013). Primitive zircon $\delta^{18}\text{O}$ range $5.3 \pm 0.6 \text{\textperthousand}$ is in equilibrium with mantle-derived primary melts (see text for details). **B**—Distance versus sample average zircon $\epsilon\text{Hf}_{(t)}$ at the zircon U-Pb age analyzed within the same zone as the hafnium isotope analysis. Depleted MORB mantle (DMM) isotopic range of $+15.3 \pm 1.5$ (calculated at 100 Ma based on Vervoort and Blichert-Toft, 1999, values), with "juvenile" and "enriched" values plotted at 10 and 20 epsilon units beneath DMM, respectively.

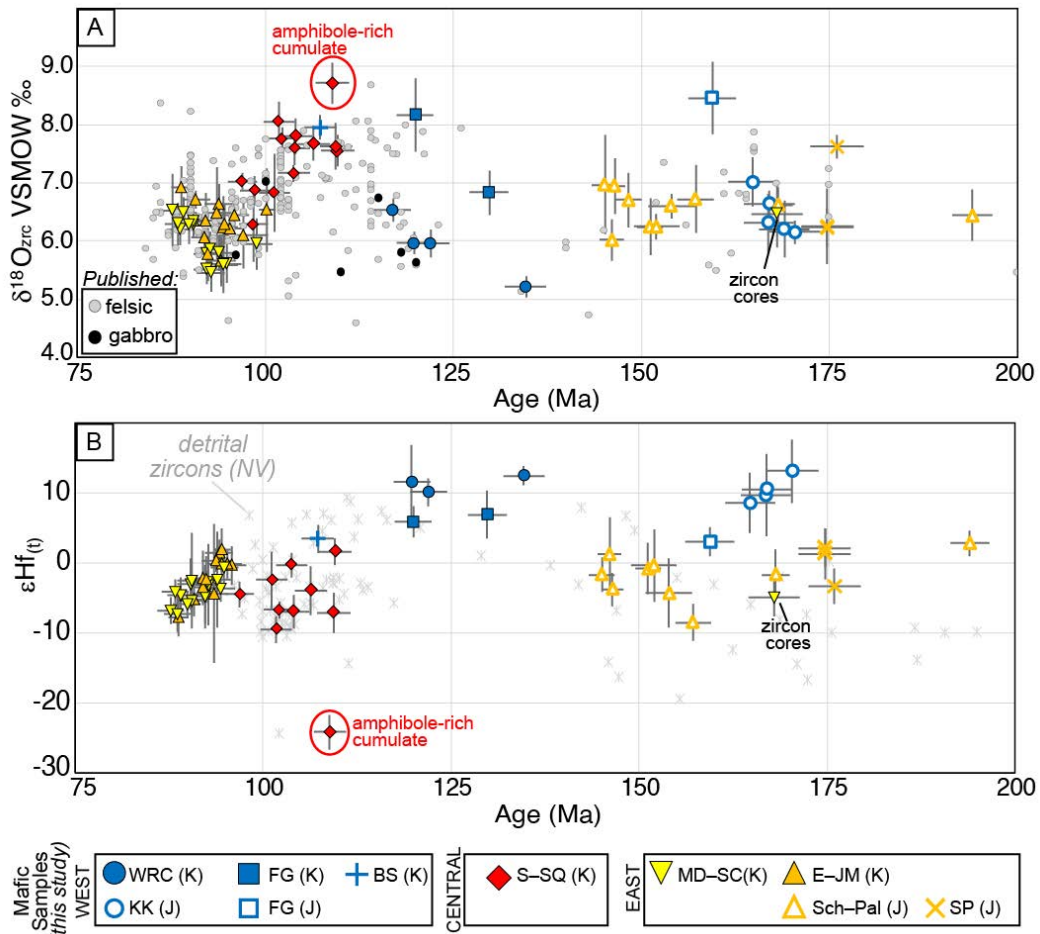


Ch. 4 Figure 3. Binary mixing models of assimilants.

Plots include isotopic data from the mafic plutons of this study, with $\delta^{18}\text{O}$ measured in zircon and plotted as equilibrium melt composition ($\Delta_{\text{zrc-melt}} = 0.2\text{‰}$), $\varepsilon\text{Hf}_{(t)}$ measured in zircon, and $^{87}\text{Sr}/^{86}\text{Sr}_{(t)}$ and $\varepsilon\text{Nd}_{(t)}$ measured in whole rock powders. All initial isotopic values are calculated at the U-Pb zircon age of crystallization for the samples, with sample symbols the same as in Figure 1. Errors on samples are 2σ (smaller than symbols where not seen). DMM is depleted MORB mantle and EM1 is enriched mantle in all plots (see Table 1 and S4 for details). **A** and **B**— $\delta^{18}\text{O}$ versus $\varepsilon\text{Hf}_{(t)}$ and $^{87}\text{Sr}/^{86}\text{Sr}_{(t)}$ versus $\varepsilon\text{Nd}_{(t)}$ with mixing curves between a "primitive" basalt endmember (bright blue circle, error bars 2SD) and (1) Franciscan metasedimentary mélange (FM – blue curve), (2) Kings sequence and comparable lower-crustal metasedimentary rocks (KS – red curve), (3) Proterozoic metasedimentary rocks (pCms – yellow curve), and (4) Proterozoic igneous rocks (pCig – gray curve). **C** and **D**—Same as A and B, with mixing curves between an "enriched" basalt endmember (yellow diamond, error bars 2 s.d.) also including a mixing curve with (5) Paleozoic metasedimentary rocks of the eastern Sierra Nevada (Pzms – orange curve).



Ch. 4 Figure 4. Schematic cartoon of isotopic fingerprints of the upper plate imparted on mafic magmas. **A**—Cartoon cross section of the transect of this study, showing the crust and lithosphere of each tectonically assembled belt that forms the pre-existing framework of the Sierra Nevada batholith, with colored bars representing mafic magmas that ascend through the crust of each belt acquiring its particular isotopic fingerprint. Inset shows a schematic plot of oxygen versus radiogenic isotope signatures and mixing curves between depleted MORB mantle (DMM) or enriched mantle (EM) and juvenile (recently mantle-derived) arc sediment or old continental crust (CC). **B**—Homogeneous and **C**—heterogeneous pre-existing crust in an arc (for example, in a more juvenile arc versus a continental arc, respectively) may both impart their isotopic fingerprints on arc magmas, but without isotopic leverage and/or heterogeneity, the signature of assimilation could be unidentifiable.



Ch. 4 Figure 5. Age versus O and Hf isotope ratios in zircon showing that trends in isotopic composition with age that could be interpreted as secular variation in arc magmatic processes (*i.e.*, more mantle input versus crustal recycling) correspond to interaction of mafic magmas with crust by geographic belt (by symbol). Symbols are the same as in Figure 1. Zircon cores in one sample from the Whitney intrusive suite (bright yellow triangle) are xenocrystic and Jurassic in age, but isotopically nearly the same as the rims. **A**—Sample age versus sample average zircon δ¹⁸O. **B**—Sample age versus average zircon εHf_(t). Also plotted are analyses of detrital zircons from southern Nevada (Balgord et al., 2021).

TABLES

Ch. 4 Table 1. Endmember arc magma and assimilant composition values used for binary mixing models, with all radiogenic isotope ratios calculated at 100 Ma.

	Primary arc magmas		Median (see Supplementary Data File for references):	Crustal assimilants				
	primitive arc magma (oceanic arc; depleted mantle-like)	enriched arc magma (continental arc; EMI-like)		Mesozoic Franciscan mélange metasedimentary rocks	Kings sequence and similar lower-crustal metasedimentary rocks	Proterozoic metasedimentary rocks	Proterozoic metagneous rocks	Paleozoic metasedimentary rocks (Mt. Morrison, White-Inyo & Mojave)
$\delta^{18}\text{O}$ (WR)	5.6	5.7	$\delta^{18}\text{O}$ (WR)	16.2	13.6	16.8	8.4	14.9
first quartile	5.5	5.5	first quartile	12.7	12.3	14.0	7.7	13.1
third quartile	5.7	5.9	third quartile	18.5	16.8	17.9	9.1	16.1
(n)	72	9	(n)	18	38	7*	20*	256*
$^{176}\text{Hf}/^{177}\text{Hf}_{100\text{ Ma}}$	0.283090	0.282624	$^{176}\text{Hf}/^{177}\text{Hf}_{100\text{ Ma}}$	0.282601	0.282297	0.281896	0.282002	0.281988
first quartile	0.283061	0.282558	first quartile	0.282501	0.282248	0.281883	0.281985	0.281906
third quartile	0.283111	0.282723	third quartile	0.282770	0.282332	0.282012	0.282344	0.282087
(n)	48	18	(n)	8**	12**	16**	5**	13***
[Hf] ppm	1.16	3.5	[Hf] ppm	1.6	4.5	7.8	9.3	3.5
first quartile	0.84	3.5	first quartile	1.4	3.5	4.9	5.0	2.7
third quartile	1.44	3.7	third quartile	1.8	6.4	9.8	12.5	4.2125
(n)	48	9	(n)	9	5*	14	5	124*
$^{87}\text{Sr}/^{86}\text{Sr}_{100\text{ Ma}}$	0.703439	0.705409	$^{87}\text{Sr}/^{86}\text{Sr}_{100\text{ Ma}}$	0.706072	0.713517	0.722030	0.727012	0.713583
first quartile	0.703329	0.705134	first quartile	0.704487	0.710417	0.714132	0.719507	0.712179
third quartile	0.703544	0.706141	third quartile	0.706380	0.716761	0.733536	0.763116	0.714474
(n)	48	22	(n)	9	19	16	11	4
[Sr] ppm	227.6	500.5	[Sr] ppm	166.0	143.7	263.5	229.3	257.4
first quartile	157.9	483.0	first quartile	81.0	97.9	136.3	201.8	198.9
third quartile	277.8	507.5	third quartile	221.0	191.8	564.3	379.5	314.9
(n)	48	22	(n)	9	19	16	11	4
$^{143}\text{Nd}/^{144}\text{Nd}_{100\text{ Ma}}$	0.512899	0.512447	$^{143}\text{Nd}/^{144}\text{Nd}_{100\text{ Ma}}$	0.512353	0.512010	0.511595	0.511377	0.511664
first quartile	0.512874	0.512337	first quartile	0.512248	0.511970	0.511481	0.510845	0.511564
third quartile	0.512916	0.512583	third quartile	0.512529	0.512063	0.511732	0.511605	0.511776
(n)	52	18	(n)	8	12	35	21	13
[Nd] ppm	5.98	18.4	[Nd] ppm	15.4	42.7	31.5	48.6	38.9
first quartile	4.25	18.1	first quartile	13.6	26.5	19.2	30.9	33.6
third quartile	7.10	19.3	third quartile	16.1	47.5	46.6	75.5	42.1
(n)	54	19	(n)	9	13	35	21	13

*estimated from other literature data—see Appendix A for details.

**number of Hf isotopic values used in average, calculated from Nd isotopes using the terrestrial correlation of Vervoort et al., 2011, Value in parentheses is number of measured samples used.

***Calculated from average Nd isotope value for this endmember using the present day terrestrial correlation of Vervoort et al., 2011,

¹Reported by Eiler et al., 2000, for primitive arc basalts

Ch. 4 Table 2. Amount of assimilation, by belt, of likely endmembers recorded by mafic intrusions across the Sierra Nevada batholith. Values reported are to the nearest 5% by weight and are only shown for assimilants present within the same tectonically assembled geologic belt for each geographic region that are plausible (mixing curves intersect the data).

a. Assimilation modeled using a primitive (oceanic) arc magma endmember.

Mafic pluton region		Franciscan metasedimentary mélange rocks	Kings sequence & lower-crustal metasedimentary	Proterozoic metasedimentary rocks	Proterozoic metaigneous rocks	Paleozoic metasedimentary rocks
West / (Fine Gold)	$\delta^{18}\text{O}$	0–20% / (20–40%)	~0–20% (20–35%)	—	—	—
	$^{176}\text{Hf}^{177}\text{Hf}$					
	$^{87}\text{Sr}^{86}\text{Sr}$	0–20% / (~40%)	0–5% / (~10%)	—	—	—
Central	$\delta^{18}\text{O}$	—	20–45%	10–20%	—	~15–35%
	$^{176}\text{Hf}^{177}\text{Hf}$					
	$^{87}\text{Sr}^{86}\text{Sr}$	—	~25–50%	~15–20%	—	20–35%
high Sierra (East)	$\delta^{18}\text{O}$	—	—	5–15%	~5–25%	~10–25%
	$^{176}\text{Hf}^{177}\text{Hf}$					
	$^{87}\text{Sr}^{86}\text{Sr}$	—	—	15–20%	~10–15%	~20–30%
East	$\delta^{18}\text{O}$	—	—	5–15%	~5–30%	~10–25
	$^{176}\text{Hf}^{177}\text{Hf}$					
	$^{87}\text{Sr}^{86}\text{Sr}$	—	—	10–20%	~5–15%	~10–30
$^{143}\text{Nd}^{144}\text{Nd}$	$^{143}\text{Nd}^{144}\text{Nd}$	—	—			

b. Assimilation modeled using an enriched mantle (SCLM) derived arc magma endmember.

Mafic pluton region		Franciscan metasedimentary mélange rocks	Kings sequence & lower-crustal metasedimentary	Proterozoic metasedimentary rocks	Proterozoic metaigneous rocks	Paleozoic metasedimentary rocks
West / (Fine Gold)	$\delta^{18}\text{O}$	—	—	—	—	—
	$^{176}\text{Hf}^{177}\text{Hf}$					
	$^{87}\text{Sr}^{86}\text{Sr}$	—	—	—	—	—
Central	$\delta^{18}\text{O}$	—	—	~5–20%	—	10–30%
	$^{176}\text{Hf}^{177}\text{Hf}$					
	$^{87}\text{Sr}^{86}\text{Sr}$	—	—	10–25%	—	~10–35%
high Sierra (East)	$\delta^{18}\text{O}$	—	—	0–10%	0–25%	0–15%
	$^{176}\text{Hf}^{177}\text{Hf}$					
	$^{87}\text{Sr}^{86}\text{Sr}$	—	—	15–20%	10–15%	20–30%
East	$\delta^{18}\text{O}$	—	—	0–15%	~0–30%	0–20%
	$^{176}\text{Hf}^{177}\text{Hf}$					
	$^{87}\text{Sr}^{86}\text{Sr}$	—	—	~0–25%	0–15%	0–30%
$^{143}\text{Nd}^{144}\text{Nd}$	$^{143}\text{Nd}^{144}\text{Nd}$	—	—			

APPENDIX 1

This appendix describes methods of this study, including details of oxygen and hafnium isotope measurements in zircon, and strontium and neodymium isotopes in whole-rock powders. Additionally, details about endmembers used in binary mixing models are described, and supplementary figures are included at the end of the document.

METHODS

Zircon $\delta^{18}\text{O}$ by secondary ion mass spectrometry (SIMS)

Zircon grains were mounted within the inner 1 cm of two separate epoxy resin mounts—one mount with small zircon grains (JRD-SM) and one mount with large zircon grains (JRD-L), to avoid losing small grains during polishing. At least 15 zircons per sample were aligned on Kapton double sided tape in rows or squares, and ~5 fragments of standard zircon UWZ-1 from the University of Wisconsin, Madison were placed in the center of each mount. Both mounts were ground flat and polished on diamond lapping films (sequentially finer: 30, 15, 9, 6, 3, 1, and 0.5 μm) to expose the interior of the grains and obtain a flat surface, with cleaning in DI water in an ultrasonic bath between polishing steps to avoid scratches. A third mount with small grains (JRD-S) from another project included one sample from this study, SNB-14-30.

The SM zircon mount is set in EpoFix epoxy, and was polished with minimal polishing relief ($\sim 2 \mu\text{m}$ relief on grains). The L zircon mount is set in EpoThin epoxy which cured poorly with bubbles and some waviness within the epoxy surrounding grains upon polishing. To avoid electrostatic deflection of secondary ions by minor ($\sim 10 \mu\text{m}$) relief at the edge of grains (*i.e.*, Kita et al., 2009), analytical spots were placed closer to the center of grains on that mount. We observed that zircon splits from the same mafic intrusion mounted on both the L and SM mounts had statistically homogeneous oxygen isotope ratios, so the slight topography on the L mount is considered to have negligible effect on the results.

Cathodoluminescence (CL) images prior to analyses were collected on the JEOL JXA-iHP200F Field Emission Electron Probe Microanalyzer (FE EPMA) at Caltech. Efforts to avoid damaging epoxy for samples that would be subsequently analyzed by SIMS included analyses either at 10 kV or at 15.0 kV beam energy, and with beam current kept below \sim 20 nA.

Samples were cleaned and coated in gold to generate a conductive surface at the University of Wisconsin, Madison. Spot locations were placed on grains using micro QGIS via the WiscSIMS Tool and plugins (https://github.com/wiscsims/wiscsims_tool). This enabled reflected light and CL images to guide spot placement on areas with no cracks, inclusions, and representative zoning.

Zircon grains were analyzed during a three-day session with overnight runs measuring $\delta^{18}\text{O}$ and $^{16}\text{OH}/^{16}\text{O}$ using the large-radius double-focusing CAMECA IMS 1280 Secondary Ion Mass Spectrometer (SIMS) with multicollection Faraday cup (FC) detectors at the University of Wisconsin, Madison WiscSIMS lab. A focused (“Gaussian”) beam of Cs^+ ions with an accelerating voltage of +10 kV was sputtered onto the sample surface, using an 11 μm oval-shaped spot size ($\leq\sim 1 \mu\text{m}$ depth) and a -10 kV secondary voltage at the sample surface, producing a 20 kV primary ion impact energy, using the settings of Kita et al., 2009. Ions of $^{18}\text{O}^-$, $^{16}\text{O}^1\text{H}^-$ and $^{16}\text{O}^-$ were simultaneous collected by three Faraday cup detectors. Recorded primary beam currents of 1.89 to 2.15 nA stayed consistent throughout the session (these were offset from the primary 2.5 nA beam current due to charge compensation by the electron gun). Each analysis lasted for \sim 3.5 minutes, including pre-sputtering, automated centering of secondary ions, and 80 seconds of signal integration.

Zircon running standard (UWZ-1, $\delta^{18}\text{O}_{\text{SMOW}} = 4.98\text{\textperthousand}$) was analyzed to monitor instrument stability and for quantification of instrumental mass bias, OH, and reproducibility. Four analyses of the running standard were made before and after every 18-20 unknown analyses, except for twice when analyzing additional grains on a mount before a sample change (30 and 9 unknowns between brackets). Raw measured ($^{18}\text{O}/^{16}\text{O}$) ratios are converted to delta notation by normalizing to Vienna

Standard Mean Ocean Water ($^{18}\text{O}/^{16}\text{O}$)_{VSMOW}=0.0020520 (Baertschi, 1976; Kita et al., 2009). Using the average measured bracketing analyses of the running standard, values for each spot are corrected for an instrumental bias of -0.70 to $-0.18\text{\textperthousand}$ throughout the session; equations 2.1, 2.2, and 2.5 of Kita et al., 2009, The variability of repeated standard measurements represented by 2 s.d. of the eight bracketing measurements of the running standard is on average $\pm 0.19\text{\textperthousand}$ (± 0.04 to $\pm 0.38\text{\textperthousand}$ on all brackets), so we assume $\pm 0.2\text{\textperthousand}$ analytical error for all analyses. This is consistent with other sources of analytical error.

Stage height was not adjusted for each spot, so large values for DTFA X and Y deflectors that center secondary ions to the Field Aperture (FA) occurred on samples that are far from the center or on a tilted mount (DTFA>40). A test of the effect of the DTFA was conducted by re-measuring the spots with an adjusted stage height to lower the DTFA values (≤ 15). This test produced consistent $\delta^{18}\text{O}$ values within 0.3% even for spots with DTFA values >60 , comparable to the 2s.d. of the bracket.

Zircon grains from two other unrelated projects were analyzed during the session and are thus “missing” rows in Table S2. Otherwise, the table shows groups of analyses bracketed by running standard UWZ-1. Mass bias and instrument stability were monitored through the bracketing analysis of the running standard (UWZ-1). The $^{16}\text{OH}/^{16}\text{O}$ of this nominally anhydrous running standard are used for a background correction on $^{16}\text{OH}/^{16}\text{O}$. This measurement is not quantitative, as it varies between sessions, but rather is an internally consistent relative measure of elevated water content, and correlates with alteration (Liebmann et al., 2021). All background corrected values of $^{16}\text{OH}/^{16}\text{O}$ measured during the session are $<1.0 \times 10^{-3}$ which is reliable except for one analysis which was excluded from further consideration. Further, the relative yield calculated for each analysis was on average ~ 0.99 (0.92–1.03, except for one spot (0.88) which was discarded from further consideration due to being outside of the acceptable range of 0.90 to 1.10.

After analyses, samples were carbon coated and 64 analytical pits ($\leq 1 \text{ }\mu\text{m}$ depth) with values that produced statistically lower or higher values than others within a sample were inspected on the Zeiss 1550 VP Field Emission Scanning

Electron Microscope (FE SEM) using SE and BSE detectors to identify any irregularities in the SIMS pits shapes (fractures, inclusions, or very warped pits) to ensure reproducible consistent sputtering dynamics. Seven analyses were excluded from the final data set due to cracks or irregularities. A summary of all samples is in Table S1.

ϵ Hf in zircon by laser-ablation multicollector inductively-coupled mass spectrometry (LA-MC-ICPMS)

Zircon Lu-Hf isotopic compositions were analyzed in the same zircons as $\delta^{18}\text{O}$, U-Pb ages and trace elements over two days at the University of California, Santa Barbara, following the methods outlined in Kylander Clark et al., 2013, A Photon Machines nm ArF Excimer laser with a Hel-Ex ablation cell and Nu Instruments P3D Plasma MC-ICP-MS system were used for collecting Hf isotope data. Laser ablation analyses consisted of 35, 40 or 50 μm spots depending on inclusion-free zircon availability placed on top of or adjacent to previously analyzed $\delta^{18}\text{O}$ SIMS analysis pits and U-Pb and trace element laser ablation pits within the same zone, on cores and rims and on some fresh sites on additional grains. Like previous analyses, Hf analysis sites targeted mostly grain rims with uncomplicated, igneous-looking CL image patterns in addition to any potentially xenocrystic cores, and avoided inclusions and straddling significant growth domains (*i.e.*, core and rim) where possible, with an aim of 12 analyses per sample. Representative CL images are in Ryan-Davis et al., *Chapter 3*. Samples were not analyzed if grains were too small and/or full of inclusions to fit the laser spot (SNB-19-8, SNB-19-34, SNB-19-43, 20KC38, 19-JRD-32, 20-JRD-69, 20-JRD-98, 21-JRD-116, 21-JRD-130A). Specific settings used are listed in Table A1. Primary and secondary natural reference standards were analyzed throughout the runs bracketing approximately every twenty sample analyses.

The laser parameters for analysis were ablation at $\sim 1 \text{ J/cm}^2$ and 5 Hz for 20 seconds, following a 45 second baseline and two-shot preablation. Unknowns were bracketed by zircon reference material (RM) 91500 (Wiedenbeck et al., 1995), GJ1

(Jackson et al., 2004), Plešovice (Sláma et al., 2008), MUN4 (Fisher et al., 2011, 2014) and Mud Tank (Black and Gulson, 1978; Table A1). They yielded $^{176}\text{Hf}/^{177}\text{Hf}$ averages within $<0.001\text{--}3.7\%$ of their accepted values (Table A2). Raw Hf isotope data was reduced using Iolite v3 (Paton et al., 2011) to correct for instrument drift, laser-ablation-induced down-hole elemental fractionation, plasma-induced elemental fractionation, and instrumental mass bias.

The initial $^{176}\text{Hf}/^{177}\text{Hf}_{(i)}$ and $\epsilon\text{Hf}_{(i)}$ values were calculated for each spot corrected to the U-Pb age of the same zone in the zircon measured prior to the Hf isotope analyses. In some samples (that were dated by Lewis et al., 2024), grains with no U-Pb analysis were analyzed for Hf isotopes, so these were corrected to the sample MSWD age. These calculations used a value of $\lambda^{176}\text{Lu}$ of $1.867 \times 10^{-11} \text{ y}^{-1}$ and values for the chondritic uniform reservoir (CHUR) of $^{176}\text{Lu}/^{177}\text{Hf}_0 = 0.0332 \pm 0.0002$ and $^{176}\text{Hf}/^{177}\text{Hf}_0 = 0.282772 \pm 0.000029$ (Blichert-Toft and Albarède, 1997; Söderland et al., 2004).

Strontium and neodymium isotopes measured in whole-rock powders

Whole rock Sr and Nd isotope data are reported in Table S1 and S3. Measurements were performed on a representative selection of bulk powders from across the transect at the Center for Elemental Mass Spectrometry, University of South Carolina following established methods for the lab (e.g., Frisby et al., 2016; Béguelin et al., 2017). Powdered samples were dissolved in a 3:1 mixture of Teflon-distilled HF:HNO₃ in Teflon vessels for ~3 days, dried down with HNO₃, and split into two fractions for further Sr and Nd measurements. Sr was separated on Eichrom Sr-SPEC resin in HNO₃ media. REE were separated from the bulk sample on Eichrom TRU spec resin with further isolation of Nd on an Ln-resin in HCl media.

Sr and Nd isotope ratios were measured on a Thermo Scientific Neptune Plus MC-ICP-MS with a PFA 100 μL nebulizer coupled to APEX (Elemental Scientific, Inc.) introduction system and a Jet, X-cone interface. Measured $^{87}\text{Sr}/^{86}\text{Sr}$ ratios were corrected for mass fractionation using $^{86}\text{Sr}/^{88}\text{Sr} = 0.1194$, and krypton interference on ^{86}Sr was corrected using $^{83}\text{Kr}/^{86}\text{Kr} = 0.66474$. Full procedural blank

measurements during Sr analyses were <25 pg. The NIST SRM987 standard was determined at $^{87}\text{Sr}/^{86}\text{Sr} = 0.710310 (\pm 0.000008; 2 \text{ standard deviations, } n=8)$ and the Sr isotope data is reported relative to a value of 0.710250 (Ehrlich et al., 2001). Measured $^{143}\text{Nd}/^{144}\text{Nd}$ ratios were corrected for mass fractionation using $^{146}\text{Nd}/^{144}\text{Nd} = 0.7219$. Full procedural blank measurements during Nd analyses were <5 pg. The JNd-i-1 standard was determined at $^{143}\text{Nd}/^{144}\text{Nd} = 0.512080 (\pm 0.000004; 2 \text{ standard deviations, } n=8)$ and the Nd isotope data is reported relative to the value of 0.512115 (Tanaka et al., 2000, The BCR-2 standard was run with samples and is reported in Table S3, and is consistent with literature values (Weis et al., 2006).

Ratios of $^{87}\text{Rb}/^{86}\text{Sr}$ and $^{147}\text{Sm}/^{144}\text{Nd}$ were calculated from the Rb/Sr and Sm/Nd measured by ICP-MS on each whole rock powder, respectively. Initial Sr isotope ($^{87}\text{Sr}/^{86}\text{Sr}_{(i)}$) ratios were calculated using a decay constant for ^{87}Rb of $1.3972 \times 10^{-11} \text{ y}^{-1}$, and initial Nd isotope ratios ($^{143}\text{Nd}/^{144}\text{Nd}_{(i)}$) were calculated using a decay constant for ^{147}Sm of $6.524 \times 10^{-12} \text{ y}^{-1}$ (Villa et al., 2022) and the U-Pb zircon age and elemental concentrations measured in the same sample (Ryan-Davis et al., Chapter 3). Epsilon neodymium ($\varepsilon_{\text{Nd}_{(i)}}$) calculations use values for the chondritic uniform reservoir (CHUR) of $^{147}\text{Sm}/^{144}\text{Nd}_0 = 0.1960 \pm 0.0004$ and $^{143}\text{Nd}/^{144}\text{Nd}_0 = 0.512630 \pm 0.000011$ (Bouvier et al., 2008). A summary of all samples is in Table S1.

Discussion of binary mixing models and endmembers

Binary mixing uses the equations of Albarède (1995). Isotopic and trace element analyses of bulk rock samples for all mixing endmembers are compiled in Table S4. Most samples did not have all isotopes (oxygen, hafnium, strontium and neodymium) and/or trace elements measured (within the same rock). Thus, the median, first and third quartile values for each endmember may represent a different number of samples. Further, in some cases, an endmember has no analyses of trace elements or oxygen isotopes for any samples. In that case, we turn to global compilations of similar materials. Each endmember compilation is described in the following sections.

Arc basalt endmembers

The “primitive” arc basalt endmember composition is the median, first, and third quartile values of a compilation of 56 high-Mg lavas from oceanic arc front stratovolcanoes (Turner and Langmuir, 2022), with oxygen isotopes from measurements of 72 olivine-phyric samples of oceanic arcs from arc and back-arc settings at five arcs and three back-arc regions with a range in magma isotopic composition (Eiler et al., 2000). For oxygen isotopes, we used analyses of olivine from all samples to calculate an equilibrium melt compositional range using a $\Delta_{\text{melt-olivine}}$ of 0.36‰, as reported in the study. For samples where olivine was not analyzed, we used the reported olivine composition calculated based on glass or plagioclase.

The “enriched” arc basalt endmember isotopic composition is from mantle xenoliths erupted in the central Sierra Nevada brought to the surface by Miocene volcanic eruptions (Domenick et al., 1983; Mukhopadhyay and Manton, 1994; Ducea, 1998; Ducea and Saleeby, 1998), and eastern Sierra Nevada, brought to the surface by Quaternary volcanic eruptions (Domenick et al., 1983; Mukhopadhyay and Manton, 1994; Beard and Glazner, 1995; Fig. A1). Enrichment of these xenoliths likely occurred in the Neoproterozoic (~820 Ma) based on a Sm-Nd isochron (Beard and Glazner, 1995). We used oxygen isotopes of olivine measured in these xenoliths (Chin et al., 2014; Gao et al., 2017) to calculate the equilibrium melt compositional range also using a $\Delta_{\text{melt-olivine}}$ of 0.36‰, as above. Concentrations of Sr, Nd and Hf for mixing calculations are from the compilation of high-Mg basalts from continental arc front stratovolcanoes, from the Cascades arc (Turner and Langmuir, 2022).

Assimilant endmembers

Franciscan complex and other subduction complex rocks

Subduction complex-like, juvenile sedimentary rocks are associated with accreted rocks in the western belt that are part of the Western Metamorphic Belt, and Foothills Ophiolite Belt (Snow and Scherer, 2006). These are represented by the metasedimentary rocks associated with the Kings-Kaweah ophiolite belt in addition

to the Mariposa Formation and Calaveras Complex locally in the western part of the study area, but few analyses exist for those sequences (a total of 6 composite samples), and their average compositions are plotted in figure A2 and A3 (Kistler and Peterman, 1973; DePaolo, 1981). Of those, the Mariposa Formation is somewhat similar isotopically to the Franciscan complex, which is exposed in the Coast Ranges of California, which were tectonically separated from the Sierra Nevada batholith by later faulting. To explore this potential contribution to the western belt, we consider the Franciscan Complex as a mixing endmember.

The Franciscan complex metasedimentary rocks represent the paleo (Mesozoic and younger, ~170 Ma to ~35 Ma) arc-trench subduction complex, shed from the continent (Wakabayashi and Dumitru, 2007). They are sheets that have been tectonically scraped and underplated during subduction, younging downwards (Wakabayashi, 1999; Dumitru et al., 2010). They are mainly graywacke, schist, shale, conglomerate and cherts, ranging from prehnite-pumpellyite to blueschist facies. Radiogenic isotopes and whole-rock trace element concentrations were measured in nine samples (Ghatak et al., 2013), and oxygen isotopes were measured in eighteen samples (Margaritz and Taylor, 1976).

The Pelona-Orocopia-Rand schists have had few radiogenic isotopic measurements reported, but twenty-two oxygen isotope measurements on quartzite, schist and graywacke (Ross, 1989; Glazner and O'Neill, 1989). They are similarly a subduction complex that was thrust under the continental arc in the late Mesozoic, and are exposed in the southern regions of the batholith outside of the study area. Due to their limited measurements, they were not considered with the Franciscan complex, but are compositionally similar based on the limited data, and thus are plotted for comparison (with ϵ Hf roughly estimated based on their reported strontium isotope range) in Figure A2.

Kings Sequence

The Mesozoic Kings Sequence is exposed along the axis of the Sierra Nevada, and is associated with “strongly contaminated reduced” felsic intrusions (Saleeby and Busby, 1993; Ague and Brimhall, 1988). Kings sequence metapelitic rocks are also found in high-pressure lower-crustal exposures of the southern Sierra Nevada (Saleeby and Busby, 1993; Zeng et al., 2005), and as xenoliths erupted from depths up to 2.5 GPa from the Central Sierra Nevada (Ducea and Saleeby, 1998). In addition to the upper-crustal Kings sequence rocks, we included similar lower-crustal metasedimentary rock and xenolith compositions in the modeled endmember composition. Eight analyses of radiogenic isotopes of metapelites of the Kings Sequence in the southern Sierra Nevada (Zeng et al., 2005) and thirty-one analyses of oxygen isotopes from ten central-Sierra Nevada pendants (Lackey et al., 2006) represent the Kings Sequence proper. We also include three analyses of lower-crustal metasedimentary xenoliths erupted with the mantle xenoliths, described above (DePaolo, 1981; Masi et al., 1981; Domenick et al., 1983; Ducea and Saleeby, 1998). For these xenoliths, lutetium and hafnium concentrations (for calculating hafnium isotope compositions and mixing curves) are estimated based on Proterozoic granulite and quartzose xenoliths from the Mojave (Hanchar et al., 1994). In addition, we include analyses of lower-crustal metasedimentary rocks, possibly part of the Kings sequence, from high-pressure, exposures of the Mesozoic arc, including two samples from the Salinian arc of the Coast Ranges (two samples; Chapman et al., 2014) and ten samples from the San-Emigdio/Tehachapi region (Saleeby et al., 1987; Ross, 1989; Pickett and Saleeby, 1994; Saleeby et al., 2007).

The single amphibole-rich cumulate sample from our study ($\delta^{18}\text{O}_{\text{zc}}=8.71\pm0.36\text{\textperthousand}$; $\epsilon\text{Hf}_{\text{(i)}}=-24.2$) may represent a more appropriate endmember composition for the central belt, as it lies along the O-Hf trajectory of the rest of the samples of the central belt (Fig. A2). However, the age of the zircon from that sample are the same as the other dated sample from the same mafic intrusion within error, and the reason for its extreme isotopic composition is uncertain, and so it was not used for considering model endmembers for the central belt.

Proterozoic metasedimentary and metaigneous rocks

Proterozoic rocks closest to the Sierra Nevada batholith are found as lower-crustal xenoliths found in the North Piute dike in Mojave desert (Hanchar et al., 1994), and in lower-crustal outcrops around southern and eastern California. We include analyses of radiogenic isotopes in thirteen of these metasedimentary xenoliths, and in twenty-four metasedimentary rocks from outcrops located at Mount Pinos, the White-Inyo Mountains, the Death Valley-Pahrump group, and the Mojave desert (Kistler and Peterman, 1973; DePaolo, 1981; Bennett and DePaolo, 1987; Martin and Walker, 1992; Miller and Wooden, 1994; Farmer and Ball, 1997). Rock types are mainly metapelitic, with a few samples that are quartzite, arkose, and hornfels. No oxygen isotopes were measured in these samples, so averages of lower-crustal rocks (part of the compilation with the Kings sequence) were used.

Metaigneous Proterozoic rocks are from the same localities and studies (in addition to two samples from Miller and Glazner, 1995). One xenolith from the North Piute dike was included, in addition to twenty-three samples from the Proterozoic outcrop localities listed above. Again, oxygen isotopes were not analyzed, so lower-crustal sample averages were used.

Paleozoic metasedimentary rocks

Paleozoic marine metasedimentary rocks near the Sierra Nevada batholith that have been analyzed isotopically are exposed in the eastern Sierra in the Mount Morrison pendant, White-Inyo range and the Mojave. These rocks comprise siltstone, sandstone, shale, schist and hornfels, plus a composite sample that also includes some limestone (Kistler and Peterman, 1973; Smith and Suemnicht, 1991; Miller and Glazner, 1995; Farmer and Ball, 1997). Due to limited (two) analyses of oxygen isotopes from Paleozoic metasedimentary samples, we calculated oxygen isotope values for the endmember from 250–540 Ma samples from a compilation of siliciclastic sedimentary rocks (Bucholz and Hernandez-Montenegro, 2025). Additionally, lutetium and hafnium concentrations were estimated from a compilation of marine sedimentary rocks (Vervoort et al., 2011).

Additional data from Mesozoic metavolcanic pendants

Additional data from Jurassic to Cretaceous metavolcanic rocks in pendants in the high Sierra and eastern Sierra is included in Table S4 (Kistler and Peterman, 1973; DePaolo, 1981; Saleeby et al., 1990; Kistler, 1993; Lackey et al., 2008; Barth et al., 2011; Raftrey et al., 2016; Lackey, unpublished). A number of these samples have low oxygen isotope ratios (16 of 51 analyses below 4.5‰, as low as -5.8‰). As the high Sierra belt has intrusions with low oxygen isotope ratios, we include these metavolcanic compositions to show that either, a) they could have been assimilated very soon after they were formed—which would suggest upper-crustal assimilation, or, b) our preferred interpretation is that the nearby intrusions underwent similar processes to lower their oxygen isotope compositions, likely by infiltration of meteoric fluids at shallow levels (Ryan-Davis et al., 2019; Ramos et al., 2018).

REFERENCES

Ague, J.J., Brimhall, G.H., 1988, Magmatic arc asymmetry and distribution of anomalous plutonic belts in the batholiths of California: Effects of assimilation, crustal thickness, and depth of crystallization. Geological Society of America Bulletin, 100, 912–927. [https://doi.org/10.1130/0016-7606\(1988\)100<0912:MAAADO>2.3.CO;2](https://doi.org/10.1130/0016-7606(1988)100<0912:MAAADO>2.3.CO;2)

Albarède, F., 1995, Introduction to Geochemical Modeling. Cambridge: Cambridge University Press.

Baertschi, P., 1976, Absolute ^{18}O content of standard mean ocean water. Earth and Planetary Science Letters, 31, 341–344.
[https://doi.org/https://doi.org/10.1016/0012-821X\(76\)90115-1](https://doi.org/https://doi.org/10.1016/0012-821X(76)90115-1)

Barth, A.P., Walker, J.D., Wooden, J.L., Riggs, N.R., Schweickert, R.A., 2011, Birth of the Sierra Nevada magmatic arc: Early Mesozoic plutonism and volcanism in the east-central Sierra Nevada of California. Geosphere, 7, 877–897. <https://doi.org/10.1130/GES00661.1>

Beard, B.L., Glazner, A.F., 1995, Trace element and Sr and Nd isotopic compositions of mantle xenoliths from the Big Pine volcanic field, California. *Journal of Geophysical Research*, 100, 4169–4179.

Béguelin, P., Bizimis, M., Beier, C., Turner, S., 2017, Rift–plume interaction reveals multiple generations of recycled oceanic crust in Azores lavas. *Geochimica et Cosmochimica Acta*, 218, 132–152.
<https://doi.org/https://doi.org/10.1016/j.gca.2017.09.015>

Bennett, V.C., DePaolo, D.J., 1987, Proterozoic crustal history of the western United States as determined by neodymium isotopic mapping. *Geological Society of America Bulletin*, 99, 674–685.

Black, L.P., Gulson, B.L., (1978). The age of the mud tank carbonatite, strangways range, northern territory. *BMR Journal of Australian Geology and Geophysics*, 3, 227-232.

Blichert-Toft, J., Albarède, F., 1997, The Lu-Hf isotope geochemistry of chondrites and the evolution of the mantle-crust system. *Earth and Planetary Science Letters*, 148, 243–258.
[https://doi.org/https://doi.org/10.1016/S0012-821X\(97\)00040-X](https://doi.org/https://doi.org/10.1016/S0012-821X(97)00040-X)

Bucholz, C.E. and Hernández-Montenegro, J.D., 2025, Temporal variation in oxygen isotopes of peraluminous granites derived from sedimentary sources. *Lithos*, 492–493, 107864.

Chapman, A.D., Ducea, M.N., Kidder, S., Petrescu, L., 2014, Geochemical constraints on the petrogenesis of the Salinian arc, central California: Implications for the origin of intermediate magmas. *Lithos*, 200–201, 126–141. <https://doi.org/10.1016/j.lithos.2014.04.011>

Chin, E.J., Lee, C.T.A., Barnes, J.D., 2014, Thickening, refertilization, and the deep lithosphere filter in continental arcs: Constraints from major and trace elements and oxygen isotopes. *Earth and Planetary Science Letters*, 397, 184–200. <https://doi.org/10.1016/j.epsl.2014.04.022>

DePaolo, D.J., 1981. A neodymium and strontium isotopic study of the Mesozoic calc-alkaline granitic batholiths of the Sierra Nevada and Peninsular ranges, California. *Journal of Geophysical Research*, 86, 10470–10488.

Domenick, M.A., Kistler, R.W., Dodge, F.C.W., Tatsumoto, M., 1983. Nd and Sr isotopic study of crustal and mantle inclusions from the Sierra Nevada and implications for batholith petrogenesis. *Geological Society of America Bulletin*, 94, 713–719. [https://doi.org/10.1130/0016-7606\(1983\)94<713:NASISO>2.0.CO;2](https://doi.org/10.1130/0016-7606(1983)94<713:NASISO>2.0.CO;2)

Ducea, M.N., 1998. A petrologic investigation of deep-crustal and upper-mantle xenoliths from the Sierra Nevada, California; constraints on lithospheric composition beneath continental arcs and the origin of Cordilleran batholiths. California Institute of Technology.

Ducea, M.N., Saleeby, J.B., 1998. The age and origin of a thick mafic-ultramafic keel from beneath the Sierra Nevada batholith. *Contributions to Mineralogy and Petrology*, 133, 169–185.
<https://doi.org/10.1007/s004100050445>

Dumitru, T.A., Wakabayashi, J., Wright, J.E., Wooden, J.L., 2010. Early Cretaceous transition from nonaccretionary behavior to strongly accretionary behavior within the Franciscan subduction complex. *Tectonics*, 29, TC5001. <https://doi.org/10.1029/2009TC002542>

Ehrlich, S., Gavrieli, I., Dor, L.-B., Halicz, L., 2001. Direct high-precision measurements of the $^{87}\text{Sr}/^{86}\text{Sr}$ isotope ratio in natural water, carbonates and related materials by multiple collector inductively coupled plasma mass spectrometry (MC-ICP-MS). *Journal of Analytical Atomic Spectrometry*, 16, 1389–1392. <https://doi.org/10.1039/B107996B>

Eiler, J. M., Crawford, A., Elliott, T., Farley, K.A., Valley, J.W., Stolper, E.M., 2000. Oxygen Isotope Geochemistry of Oceanic Arc Lavas. *Journal of Petrology*, 41, 229–256. <https://doi.org/10.1180/minmag.1998.62a.1.221>

Farmer, G.L., Ball, T.T., 1997. Sources of Middle Proterozoic to Early Cambrian siliciclastic sedimentary rocks in the Great Basin: A Nd isotope study.

Geological Society of America Bulletin, 109, 1193–1205.
[https://doi.org/10.1130/0016-7606\(1997\)109<1193:SOMPTE>2.3.CO;2](https://doi.org/10.1130/0016-7606(1997)109<1193:SOMPTE>2.3.CO;2)

Fisher, C.M., Hanchar, J.M., Samson, S.D., Dhuime, B., Blichert-Toft, J., Vervoort, J.D., Lam, R., 2011, Synthetic zircon doped with hafnium and rare earth elements: A reference material for in situ hafnium isotope analysis. *Chemical Geology*, 286, 32–47.
<https://doi.org/https://doi.org/10.1016/j.chemgeo.2011.04.013>

Fisher, C.M., Vervoort, J.D., DuFrane, S.A., 2014, Accurate Hf isotope determinations of complex zircons using the “laser ablation split stream” method. *Geochemistry, Geophysics, Geosystems*, 15, 121–139.
<https://doi.org/https://doi.org/10.1002/2013GC004962>

Frisby, C., Bizimis, M., Mallick, S., 2016, Hf–Nd isotope decoupling in bulk abyssal peridotites due to serpentinization. *Chemical Geology*, 440, 60–72.
<https://doi.org/https://doi.org/10.1016/j.chemgeo.2016.07.006>

Gao, R., Lassiter, J.C., Ramirez, G., 2017, Origin of temporal compositional trends in monogenetic vent eruptions: Insights from the crystal cargo in the Papoose Canyon sequence, Big Pine Volcanic Field, CA. *Earth and Planetary Science Letters*, 457, 227–237.
<https://doi.org/10.1016/j.epsl.2016.10.013>

Ghatak, A., Basu, A.R., Wakabayashi, J., 2013, Implications of Franciscan Complex graywacke geochemistry for sediment transport, provenance determination, burial-exposure duration, and fluid exchange with cosubducted metabasites. *Tectonics*, 32, 1480–1492.
<https://doi.org/10.1002/tect.20078>

Glazner, A.F., O’Neil, J.R., 1989, Crustal structure of the Mojave Desert , California: inferences from Sr and O isotope studies of Miocene volcanic rocks. *Journal of Geophysical Research*, 94, 7861–7870.

Hanchar, J.M., Miller, C.F., Wooden, J.L., Bennett, V.C., Staude, J.-M.G., 1994, Evidence from xenoliths for a dynamic lower crust, eastern Mojave desert, California. *Journal of Petrology*, 35, 1377–1415.

Jackson, S.E., Pearson, N.J., Griffin, W.L., Belousova, E.A., 2004, The application of laser ablation-inductively coupled plasma-mass spectrometry to in situ U–Pb zircon geochronology. *Chemical Geology*, 211, 47–69. [https://doi.org/https://doi.org/10.1016/j.chemgeo.2004.06.017](https://doi.org/10.1016/j.chemgeo.2004.06.017)

Kistler, R.W., 1993, Mesozoic intrabatholithic faulting, Sierra Nevada, California, in: Dunne, G., McDougall, K. (Eds.), *Mesozoic Paleogeography of the Western United States-II*. Pacific Section SEPM, Book 71, 247–261.

Kistler, R.W., Peterman, Z.E., 1973. Variations in Sr, Rb, K, Na, and initial $\text{Sr}^{87}/\text{Sr}^{86}$ in Mesozoic granitic rocks and intruded wall rocks in Central California. *Geological Society of America Bulletin*, 84, 3489–3512. [https://doi.org/10.1130/0016-7606\(1973\)84<3489:VISRKN>2.0.CO;2](https://doi.org/10.1130/0016-7606(1973)84<3489:VISRKN>2.0.CO;2)

Kita, N.T., Ushikubo, T., Fu, B., Valley, J.W., 2009, High precision SIMS oxygen isotope analysis and the effect of sample topography. *Chemical Geology*, 264, 43–57. <https://doi.org/https://doi.org/10.1016/j.chemgeo.2009.02.012>

Kylander-Clark, A.R.C., Hacker, B.R., Cottle, J.M., 2013, Laser-ablation split-stream ICP petrochronology. *Chemical Geology*, 345, 99–112. <https://doi.org/https://doi.org/10.1016/j.chemgeo.2013.02.019>

Lackey, J.S., Valley, J.W., Chen, J.H., Stockli, D.F., 2008, Dynamic magma systems, crustal recycling, and alteration in the Central Sierra Nevada batholith: The oxygen isotope record. *Journal of Petrology*, 49, 1397–1426. <https://doi.org/10.1093/petrology/egn030>

Lackey, J.S., Valley, J.W., Hinke, H.J., 2006, Deciphering the source and contamination history of peraluminous magmas using $\delta^{18}\text{O}$ of accessory minerals: Examples from garnet-bearing plutons of the Sierra Nevada batholith. *Contributions to Mineralogy and Petrology*, 151, 20–44. <https://doi.org/10.1007/s00410-005-0043-6>

Lewis, M.J., Ryan-Davis, J.R., Bucholz, C.E., 2024, Mafic intrusions record mantle inputs and crustal thickness in the eastern Sierra Nevada batholith, California, USA. *Geological Society of America Bulletin*, 136, 1808–1826. <https://doi.org/10.1130/b36646.1>

Liebmann, J., Spencer, C.J., Kirkland, C.L., Xia, X.-P., Bourdet, J., 2021, Effect of water on $\delta^{18}\text{O}$ in zircon. *Chemical Geology*, 574, 120243.
<https://doi.org/https://doi.org/10.1016/j.chemgeo.2021.120243>

Magaritz, M., Taylor, H.P., 1976, Oxygen, hydrogen and carbon isotope studies of the franciscan formation, Coast Ranges, California. *Geochimica et Cosmochimica Acta*, 40, 215–234.
[https://doi.org/https://doi.org/10.1016/0016-7037\(76\)90179-4](https://doi.org/https://doi.org/10.1016/0016-7037(76)90179-4)

Martin, M.W., Walker, J.D., 1992, Extending the western North American Proterozoic and Paleozoic continental crust through the Mojave Desert. *Geology*, 20, 753–756. [https://doi.org/10.1130/0091-7613\(1992\)020<0753:ETWNAP>2.3.CO;2](https://doi.org/10.1130/0091-7613(1992)020<0753:ETWNAP>2.3.CO;2)

Masi, U., O’Neil, J.R., Kistler, R.W., 1981. Stable isotope systematics in mesozoic granites of Central and Northern California and Southwestern Oregon. *Contributions to Mineralogy and Petrology*, 76, 116–126.
<https://doi.org/10.1007/BF00373691>

Miller, J.S., Glazner, A.F., 1995, Jurassic plutonism and crustal evolution in the central Mojave Desert, California. *Contributions to Mineralogy and Petrology*, 118, 379–395. <https://doi.org/10.1007/s004100050021>

Miller, C.F., Wooden, J.L., 1994, Anatexis, hybridization and the modification of ancient crust: Mesozoic plutonism in the Old Woman Mountains area, California. *Lithos*, 32, 111–133.
[https://doi.org/https://doi.org/10.1016/0024-4937\(94\)90025-6](https://doi.org/https://doi.org/10.1016/0024-4937(94)90025-6)

Mukhopadhyay, B., Manton, W.I., 1994, Upper-mantle fragments from beneath the Sierra Nevada Batholith: Partial fusion, fractional crystallization, and metasomatism in a subduction related ancient lithosphere. *Journal of Petrology*, 35, 1417–1450. <https://doi.org/10.1093/petrology/35.5.1417>

Paton, C., Hellstrom, J., Paul, B., Woodhead, J., Hergt, J., 2011, Iolite: Freeware for the visualisation and processing of mass spectrometric data. *Journal of Analytical Atomic Spectrometry*, 26, 2508–2518.
<https://doi.org/10.1039/C1JA10172B>

Pickett, D.A., Saleeby, J.B., 1994, Nd, Sr and Pb isotopic characteristics of Cretaceous intrusive rocks from deep levels of the Sierra Nevada batholith, Tehachapi Mountains, California. Contributions to Mineralogy and Petrology, 118, 198–215.

Raftrey, M.E., Lackey, J.S., Fulton, A.A., Gaines, R.R., Davies, G.R., 2016, Tuffs of the Goddard pendant: snapshots of volcanic source during low-flux magmatism in the Sierra Nevada arc. Geological Society of America Abstracts with Programs, 48. <https://doi.org/10.1130/abs/2016CD-274617>

Ramos, E.J., Hesse, M.A., Barnes, J.D., Jordan, J.S., Lackey, J.S., 2018, Reevaluating Fluid Sources During Skarn Formation: An Assessment of the Empire Mountain Skarn, Sierra Nevada, USA. *Geochemistry, Geophysics, Geosystems*, 19, 3657–3672. <https://doi.org/https://doi.org/10.1029/2018GC007611>

Ryan-Davis, J., Lackey, J.S., Gevedon, M., Barnes, J.D., Lee, C.T.A., Kitajima, K., Valley, J.W., 2019, Andradite skarn garnet records of exceptionally low $\delta^{18}\text{O}$ values within an Early Cretaceous hydrothermal system, Sierra Nevada, CA. Contributions to Mineralogy and Petrology, 174, 1–19. <https://doi.org/10.1007/s00410-019-1602-6>

Ross, D.C., 1989, The metamorphic and plutonic rocks of the southernmost Sierra Nevada, California, and their tectonic framework. US Geological Survey Professional Paper 1381, 1–159.

Saleeby, J.B., Sams, D.B., Kistler, R.W., 1987, U/Pb zircon, strontium, and oxygen isotopic and geochronological study of the southernmost Sierra Nevada batholith, California (USA). *Journal of Geophysical Research*, 92, 10443–20466. <https://doi.org/10.1029/jb092ib10p10443>

Saleeby, J.B., Kistler, R.W., Longiaru, S., Moore, J.G., Nokleberg, W.J., 1990, Chapter 14: Middle Cretaceous silicic metavolcanic rocks in the Kings Canyon area, central Sierra Nevada, California, in: Anderson, J.L. (Ed.), The Nature and Origin of Cordilleran Magmatism. Geological Society of

America Memoir, Boulder, Colorado, 251–270.
<https://doi.org/10.1130/MEM174-p251>

Saleeby, J.B., Busby, C., 1993, Paleogeographic and tectonic setting of axial and western metamorphic framework rocks of the southern Sierra Nevada, California, in: Dunn, G., McDougall, K. (Eds.), Mesozoic Paleogeography of the Western United States-II. Pacific Section SEPM, 197–226.

Saleeby, J., Farley, K.A., Kistler, R.W., Fleck, R.J., 2007, Thermal evolution and exhumation of deep-level batholithic exposures, southernmost Sierra Nevada, California, in: Cloos, M., Carlson, W.D., Gilbert, M.C., Liou, J.G., Sorensen, S.S. (Eds.), Convergent Margin Terranes and Associated Regions: A Tribute to W.G. Ernst. Geological Society of America Special Paper 419. 39–66. [https://doi.org/10.1130/2007.2419\(02\)](https://doi.org/10.1130/2007.2419(02))

Sláma, J., Košler, J., Condon, D.J., Crowley, J.L., Gerdes, A., Hanchar, J.M., Horstwood, M.S.A., Morris, G.A., Nasdala, L., Norberg, N., Schaltegger, U., Schoene, B., Tubrett, M.N., Whitehouse, M.J., 2008, Plešovice zircon — A new natural reference material for U–Pb and Hf isotopic microanalysis. *Chemical Geology*, 249, 1–35.
<https://doi.org/https://doi.org/10.1016/j.chemgeo.2007.11.005>

Smith, B.M., Suemnicht, G.A., 1991, Oxygen isotope evidence for past and present hydrothermal regimes of Long Valley caldera, California. *Journal of Volcanology and Geothermal Research*, 48, 319–339.
[https://doi.org/10.1016/0377-0273\(91\)90049-6](https://doi.org/10.1016/0377-0273(91)90049-6)

Snow, C.A., and Scherer, H., 2006, Terranes of the Western Sierra Nevada Foothills Metamorphic Belt, California: A Critical Review. *International Geology Review*, 48, 46–62. <https://doi.org/10.2747/0020-6814.48.1.46>

Söderlund, U., Patchett, P.J., Vervoort, J.D., Isachsen, C.E., 2004, The ^{176}Lu decay constant determined by Lu–Hf and U–Pb isotope systematics of Precambrian mafic intrusions. *Earth and Planetary Science Letters*, 219, 311–324. [https://doi.org/https://doi.org/10.1016/S0012-821X\(04\)00012-3](https://doi.org/https://doi.org/10.1016/S0012-821X(04)00012-3)

Tanaka, T., Togashi, S., Kamioka, H., Amakawa, H., Kagami, H., Hamamoto, T., Yuhara, M., Orihashi, Y., Yoneda, S., Shimizu, H., Kunimaru, T., Takahashi, K., Yanagi, T., Nakano, T., Fujimaki, H., Shinjo, R., Asahara, Y., Tanimizu, M., Dragusanu, C., 2000, JNdI-1: A neodymium isotopic reference in consistency with LaJolla neodymium. *Chemical Geology*, 168, 279–281. [https://doi.org/https://doi.org/10.1016/S0009-2541\(00\)00198-4](https://doi.org/https://doi.org/10.1016/S0009-2541(00)00198-4)

Turner, S.J., Langmuir, C.H., 2022, An evaluation of five models of arc volcanism. *Journal of Petrology*, 63, 1–25. <https://doi.org/10.1093/petrology/egac010>

Vervoort, J.D., Plank, T., Prytulak, J., 2011, The Hf-Nd isotopic composition of marine sediments. *Geochimica et Cosmochimica Acta*, 75, 5903–5926. <https://doi.org/10.1016/j.gca.2011.07.046>

Wakabayashi, J., 1999, Subduction and the rock record: Concepts developed in the Franciscan Complex, California, in: Moores, E.M., Sloan, D., Stout, D.L. (Eds.), *Classic Cordilleran Concepts: A View from California*. Geological Society of America. <https://doi.org/10.1130/0-8137-2338-8.123>

Wakabayashi, J., and Dumitru, T.A., 2007, *40Ar/39Ar Ages from Coherent, High-Pressure Metamorphic Rocks of the Franciscan Complex, California: Revisiting the Timing of Metamorphism of the World's Type Subduction Complex*. *International Geology Review*, 49, 873–906. <https://doi.org/10.2747/0020-6814.49.10.873>

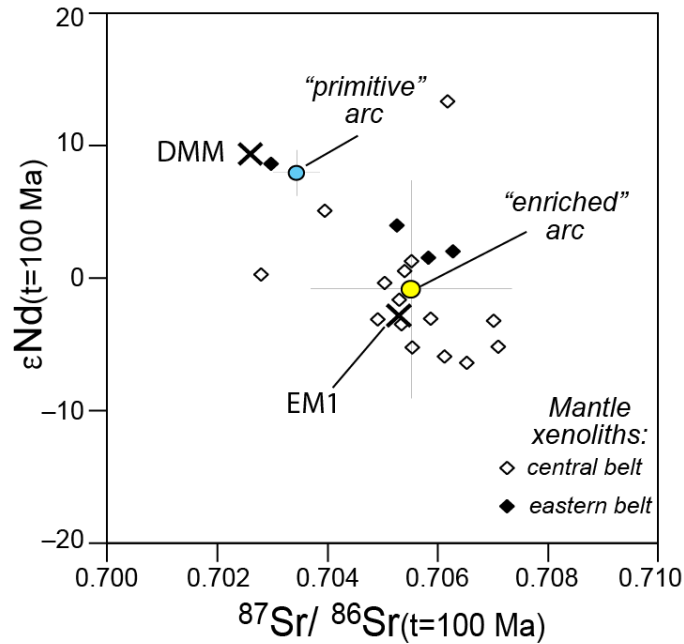
Weis, D., Kieffer, B., Maerschalk, C., Barling, J., de Jong, J., Williams, G.A., Hanano, D., Pretorius, W., Mattielli, N., Scoates, J.S., Goolaerts, A., Friedman, R.M., Mahoney, J.B., 2006, High-precision isotopic characterization of USGS reference materials by TIMS and MC-ICP-MS. *Geochemistry, Geophysics, Geosystems*, 7. <https://doi.org/https://doi.org/10.1029/2006GC001283>

Zeng, L., Saleeby, J.B., Ducea, M., 2005, Geochemical characteristics of crustal anatexis during the formation of migmatite at the Southern Sierra Nevada,

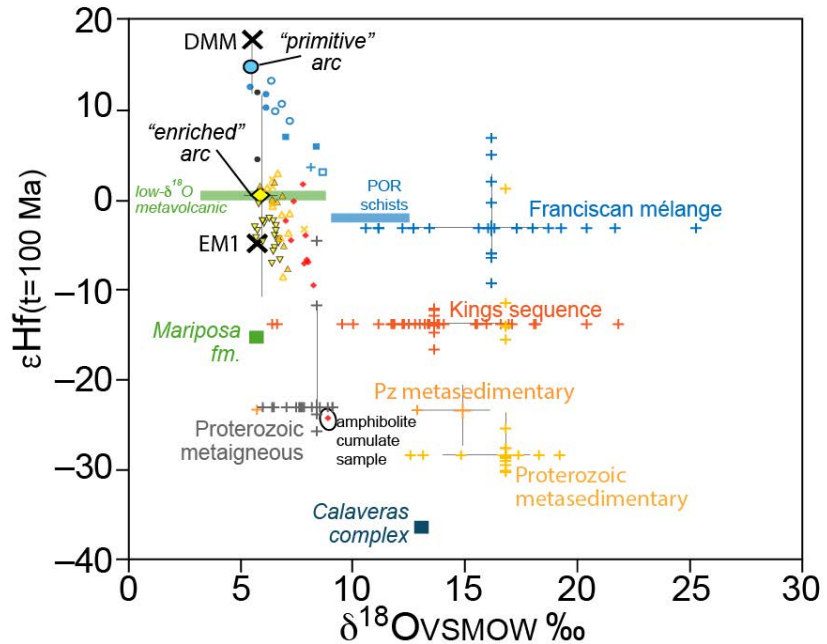
California. Contributions to Mineralogy and Petrology, 150, 386–402.

<https://doi.org/10.1007/s00410-005-0010-2>

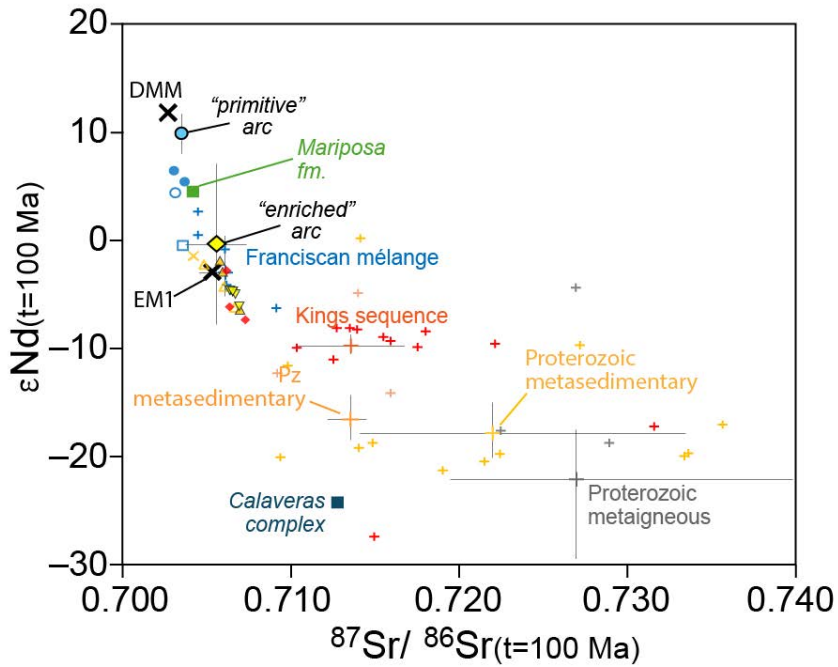
SUPPLEMENTARY FIGURES



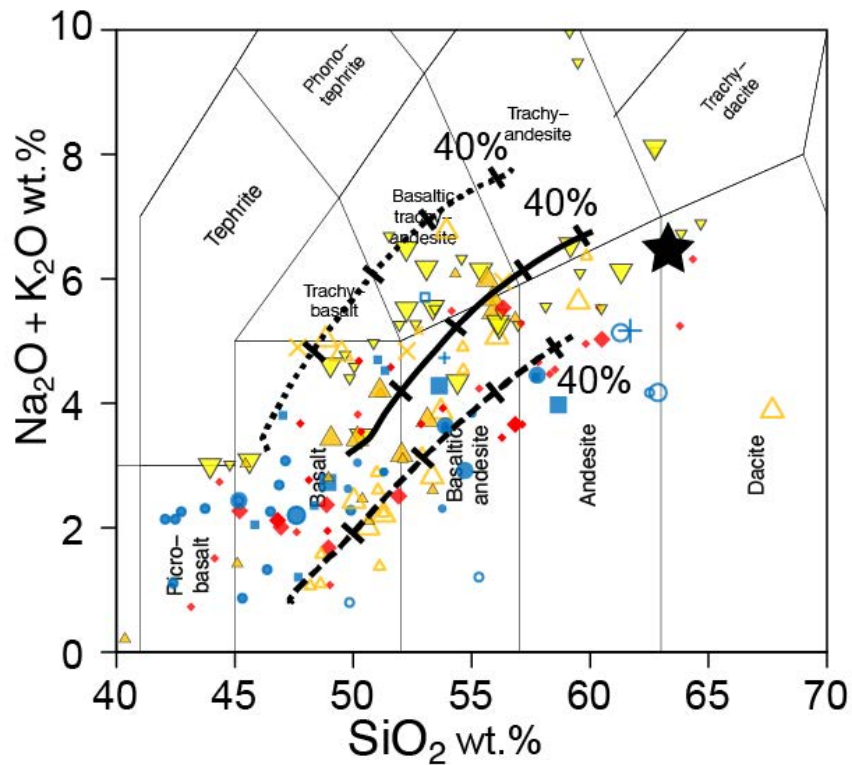
Ch. 4 Figure A 1. Mantle xenolith Sr and Nd isotope compositions from the central and eastern belts. Also plotted are the composition of depleted MORB mantle (DMM) and enriched mantle (EM1), and the “primitive” and “enriched” arc basalt endmembers used in mixing models, described above and in Table 1 and Table S4



Ch. 4 Figure A 2. Plot of the range in $\delta^{18}\text{O}$ versus $\epsilon\text{Hf}_{(t)}$ of compiled data of model endmember compositions, with samples as symbolized in all other figures. Hafnium isotopes are calculated based on measurements of neodymium isotopes and the terrestrial correlation of Vervoort et al. (2011), as described in this appendix and Table S4. Measurements of oxygen isotopes were almost always performed on different samples than radiogenic isotope measurements, so here, we plot the compositions separately, at the average value of the other isotope system (resulting in plus-shaped arrays of samples). Also plotted are the average (larger plus symbols) and first and third quartile values (thin gray error bars) for each endmember. POR schists—Pelona-Orocopia-Rand schist subduction complex metasedimentary rocks. References for all model endmember compositions are in Table S4.



Ch. 4 Figure A 3. Plot of $^{87}\text{Sr}/^{86}\text{Sr}_{(t)}$ versus $\epsilon\text{Nd}_{(t)}$ where t is the isotope ratio calculated at 100 Ma, like Figure A2, plotting only compositions from the endmember compilations for which both Sr and Nd isotopes were measured in the same sample. The average and first and third quartile error bars of these and additional samples (Table S4) are plotted as larger plus symbols. References for all model endmember compositions are in Table S4.



Ch. 4 Figure A 4. Plot of whole-rock TAS diagram (total alkalis versus silica, SiO_2 vs. $\text{Na}_2\text{O} + \text{K}_2\text{O}$; Le Bas et al., 1986) with all mafic intrusion samples of Ryan-Davis et al. (Chapter 3) plotted—larger symbols have isotopic measurements included in this study. Overlaid are thermodynamically modeled assimilation-fractional crystallization of crustal partial melts using Magma Chamber Simulator (MCS-AFC; Bohrson et al., 2014, 2020) for three arc basaltic compositions at 0.4 GPa up to 50% crystallinity (Heinonen et al., 2021). The assimilant is shown as a black star, and is the composition of average mid-crust of Rudnick and Gao (2003). Starting compositions are from the Kurile-Kamchatka arc (dotted line), Aleutian arc (solid line) and Central American arc (dashed line).

SUPPLEMENTARY TABLES

Ch. 4 Table A 1. Analytical conditions for hafnium isotope analyses. (*Continued on following pages*).

Laboratory & Sample Preparation	
Laboratory name	Laser Ablation ICP-MS Petrochronology facility at the University of California – Santa Barbara
Sample type/mineral	Zircon
Sample preparation	Conventional mineral separation, 1 inch resin mount, 1 μm polish to finish
CL Imaging	JEOL JXA-iHP200F FE EPMA at Caltech, variable nA, 10.0 or 15.0 kV, ~11 mm WD
Laser ablation system	
Make, Model & type	Photon Machines Analyte 193, ATLEX-SI 193 nm ArF excimer
Ablation cell & volume	Helex ablation cell
Laser wavelength (nm)	193 nm
Pulse width (ns)	~ 4 ns
Fluence (J.cm⁻²)	~1 J/cm²
Repetition rate (Hz)	
Ablation duration (secs)	~60 seconds – 2 shot preablation, 45 second washout, 20 second analysis
Ablation pit depth / ablation rate	~ 0.08 μm /pulse
Spot diameter (μm) nominal/actual	35, 45 and 50 μm (zircon dependent)
Sampling mode / pattern	Static spot ablation
Carrier gas	He
Cell carrier gas flow (l/min)	0.15 L/min in cell, 0.04 L/min in cup
ICP-MS Instrument	
Make, Model & type	Nu Instruments Plasma P3D multicollector ICPMS
Sample introduction	(see above)
RF power (W)	1300W
Make-up gas flow (l/min)	~1 L/min to MC-ICPMS
Detection system & masses measured	Nu-P3D: static measurements on Faraday cups, masses 180 to 171
Integration time per peak/dwell times (ms)	500 ms for MC-ICPMS
IC Dead time (ns)	8
Data Processing	
Calibration strategy	Round robin prior to analyses, with primary reference MUN4

Reference Material info	MUN4, Mud Tank, 91500, GJ-1, Plešovice
Data processing package used / Correction for LIEF	Data processed with Iolite software of Patton et al. (2010, 2011), with peak mass bias corrections and peak stripping using a modified version of the Iolite Hf routine (Fisher et al., 2014)
Quality control / Validation	Analyzed GJ-1 and 91500 or Mud Tank, Plešovice and MUN4 alternately between every 20 unknowns.

Ch. 4 Table A 2. Session averages of Hf isotope

Measurements on reference materials, which were measured at the start of the session and periodically throughout (every ~20 unknowns).

Zircon RM	n (# of analyses)	Session average measured $^{176}\text{Hf}/^{177}\text{Hf} \pm 2\sigma$	MSWD	Accepted $^{176}\text{Hf}/^{177}\text{Hf}$ value	Absolute % difference
MUN4	41	0.2821306 ± 0.0000096	1.07	0.282140	0.003%
GJ-1	21	0.282015 ± 0.000019	0.52	0.282	$\sim <0.01\%$
Mud Tank	21	0.282527 ± 0.000019	1.15	0.272507	3.6%
Plešovice	31	0.282482 ± 0.000012	0.44	0.282484	$<0.001\%$
91500	29	0.282315 ± 0.000019	0.61	0.282306	0.003%

